Laser-cooled mercury to search for physics beyond the standard model

Dissertation
zur
Erlangung des Doktorgrades (Dr. rer. nat.)
der
Mathematisch-Naturwissenschaftlichen Fakultät
der
Rheinischen Friedrich-Wilhelms-Universität Bonn

vorgelegt von
Thorsten Georg Groh
aus
Stuttgart

Bonn, 2025

Angefertigt mit Genehmigung der Mathematisch-Naturwissenschaftlichen Fakultät der Rheinischen Friedrich-Wilhelms-Universität Bonn.

Gutachter/Betreuer:	Prof. Dr. Simon Stellmer
Gutachter:	Jun. Prof. Dr. Daqing Wang
Tag der Promotion:	04.12.2025
Erscheinungsjahr:	2026

Abstract

This thesis explores the development and application of laser-cooled mercury atoms for precision measurements relevant to fundamental physics. A primary motivation is the search for a permanent electric dipole moment in mercury, that could shed light on the baryon asymmetry of the universe. We present the design and construction of a custom experimental apparatus for producing and trapping cold mercury atoms, detailing challenges associated with working with mercury in an ultra-high vacuum environment and considering deep-ultraviolet optics. A magneto-optical trap operating on the $^1S_0 \rightarrow {}^3P_1$ intercombination line at 254 nm is realized for all seven stable isotopes, achieving atom numbers up to 5×10^7 and phase-space densities up to 1×10^{-6} suitable for optical dipole trap loading. Cooling efficiency for all bosonic and fermionic isotopes are characterized over a wide parameter space, and we show sub-Doppler cooling in ^{199}Hg and ^{201}Hg. The successful loading of mercury into a high-power optical dipole trap is demonstrated, forming the basis for future electric dipole moment experiments of laser cooled mercury atoms. Prospects of evaporatively cooling mercury down to quantum degeneracy could allow for a quantum-enhanced metrology tool kit for the planned measurements. Apart from this, we are exploring the use of ultracold fermionic gases made of mercury as a quantum simulator for impurity physics. As a promising versatile and tunable platform for studying impurity-bath interactions, we are assessing the feasibility of observing Friedel oscillations in ultracold quantum gases. Further, we perform precision isotope shift spectroscopy on several dipole-allowed atomic transitions in mercury. Via King plot analysis this allows investigations of the mercury nuclear structure – also relevant for electric dipole moment bounds – and lays the foundation for probing a potential fifth force carrier coupling electrons to neutrons. We also propose upgrades to the machine for improvements in laser cooling, extensions of the spectroscopy search and a proposed experimental setup for probing the atomic electric dipole moment in an optical dipole trap of cold mercury atoms.

Publications

Parts of this thesis have been published in a peer-reviewed journal [1]:

> Quentin Lavigne, Thorsten Groh and Simon Stellmer, *Magneto-optical trapping of mercury at high phase-space density*, Physical Review A **105**, 033106 (2022). DOI: 10.1103/PhysRevA.105.033106

It is considered as the one of the main results of this thesis and therefore included as part of chapter 4. A reprint of the publication is included in appendix A of this thesis.

The results presented in chapter 6 are also available as the preprint [2]:

> Thorsten Groh, Felix Affeld and Simon Stellmer, *Probing Nuclear Interactions Through Isotope Shift Spectroscopy of Mercury*, arXiv:2510.18514 (2025). DOI: 10.48550/arXiv.2510.18514

Contents

1 Introduction

"Like a tiger defying the laws of gravity."
Freddie Mercury, *Don't Stop Me Now.*

New physics beyond the standard model

The standard model (SM) of particle physics is arguably the most successful scientific theory of all time. It describes the wide spectrum of known elementary particles and their interactions through three of the the four fundamental driving forces of nature – the strong, the weak and the electromagnetic interaction. Its predictive power has been confirmed repeatedly across an impressive range of experiments: from high-energy collider results at the Large Hadron Collider (LHC), to precision low-energy laboratory tests, to astrophysical and cosmological observations. The SM therefore serves as the cornerstone of modern physics.

The SM of physics is however incomplete. It fails to include gravity via a quantum description and provides no explanation for the dominant components of the universe's energy density: dark matter and dark energy. Furthermore, it contains a number of internal puzzles and deficiencies that point towards new physics (NP).

A particular issue is its inability to explain the observed baryon asymmetry of the universe. This is linked to the strong charge and parity symmetry (CP) problem of quantum chromodynamics (QCD) via the Sakharov condition: an imbalance of matter and antimatter production in the early universe necessarily requires CP-symmetry violation. While the SM does allow for CP violation through the complex phase in the Cabibbo-Kobayashi-Maskawa (CKM) matrix and the $\bar{\theta}_{\mathrm{QCD}}$ vacuum term in the QCD Lagrangian, its magnitude is by more than ten orders of magnitude too small to explain the observed matter-antimatter imbalance [3]. This mismatch underscores the need for new mechanisms of CP-violation beyond the SM.

Additionally, the SM fails to give an explanation to the flavor puzzle – the small but non-zero masses of neutrinos and the hierarchical pattern in the masses of quarks and leptons. Within the SM, fermion masses arise from their Yukawa-couplings to the Higgs field. Because these couplings are much smaller than their experimental bounds, they are not stringent enough to significantly rule out larger couplings. This allows the possibility that the Higgs boson may not account alone for the complete masses of the light fermions [4].

Several experimental results also hint at possible shortcomings of the SM, such as the muon $g-2$ anomaly, flavor anomalies in rare B-meson decays, and tensions in the Hubble constant. All these shortcomings motivate the existence of new sources of CP violation of fundamental particles, beyond those present in the SM and point to the potential existence of new particles and fifth force interactions. The broad search for physics beyond standard model (BSM) is a central goal of modern physics.

Experimental frontiers of new physics searches

Traditionally, high-energy colliders such as the LHC have served as the primary tool to probe the SM, directly searching for new particles at the TeV scale. While no new fundamental particles beyond the Higgs boson have been discovered so far, the LHC continues to provide stringent bounds on a wide range of BSM physics scenarios. The future of collider physics lies in extending these capabilities with upgraded detectors, improved analysis techniques, and exploration of more subtle or rare signatures. Nonetheless, the absence of direct signs of NP at the LHC in the last decade has led to an increased focus on complementary approaches.

The main motivation for the existance of dark matter and dark energy, which the SM fails to account for, comes from astrophysical observations. Observations of large-scale structure formation, galaxy rotation curves, and gravitational lensing all point toward the need for dark matter [5]. Direct detection experiments – such as XENONnT [6], PandaX [7], and LUX-ZEPLIN [8] – are probing weakly-interacting ultralight dark matter (WIMP) candidates, axion-like particles (ALPs), and ultralight scalar dark matter. Upcoming gravitational-wave observatories are being considered as probes of exotic dark-sector physics, such as primordial black holes and phase transitions in the early universe.

Non-accelerator experiments also provide important insights. The Karlsruhe Tritium Neutrino Experiment (KATRIN) aims to directly measure the absolute neutrino mass scale with sub-eV sensitivity [9], providing essential input for constraining neutrino sector models and their implications on BSM physics. Searches for neutrinoless double beta decay test whether neutrinos are Majorana particles, directly probing lepton number violation [10]. Proton decay searches in large underground detectors like Super-Kamiokande [11] can test predictions of BSM theories.

A complementary approach to probe BSM physics via collider physics arises from the precision frontier via low-energy, high-precision table-top experiments. Advances in atomic physics and quantum metrology now enable measurements at extreme levels of precision, where even tiny deviations from SM predictions become experimentally accessible. State-of-the-art optical lattice clocks achieve fractional frequency uncertainties below the 1×10^{-18} level [12–14], and hydrogen spectroscopy has tested quantum electrodynamics (QED) with relative uncertainties below 1×10^{-15} [15, 16]. In addition, the electron g-factor is measured to part-per-trillion precision [17, 18]. These capabilities open new ways for BSM searches, including constraints on couplings to ultralight scalar dark matter, signatures of new force-mediating bosons, violations of Lorentz and charge, parity and time reversal symmetry (CPT), and potential variations of fundamental constants [19–21].

Multiple experimental platforms – such as optical clocks, highly charged ions, and nuclear transitions – are now being used to search for oscillatory or transient variations in these constants. Such effects could be induced by interactions with topological dark matter structures like domain walls or by passing dark sector fields [22, 23]. To enhance sensitivity, proposals include distributed networks of atomic clocks capable of detecting coherent, large-scale signals from such phenomena. Worldwide, many additional precision-based, low-energy approaches are underway. They provide constraints on a broad array of BSM models (see reviews [19, 20, 24]). As experimental precision improves precision table-top measurements are becoming increasingly comparable to and complementary of high-energy collider searches in the quest for NP.

Electric dipole moment searches

One of the most sensitive precision probes of new sources of CP violation is the search for a permanent electric dipole moment (EDM) of elementary particles, atoms, and molecules (see, e.g., reference [25] for a review). Permanent EDMs violate both parity (P) and time-reversal (T) symmetries and, through the CPT theorem, also signal CP violation. New sources of CP violation are predicted by many BSM theories, such as supersymmetry (SUSY), left-right symmetric models, and models with extended Higgs sectors, which often naturally predict EDMs within or just beyond current experimental reach. These theories aim to address the shortcomings of the SM, including the baryon asymmetry, and thus provide strong motivation for increasingly precise EDM measurements. It however remains unknown which system or fundamental particle, if any, might exhibit an EDM within measurable range, motivating searches across a wide variety of systems.

Since different systems are sensitive to different underlying CP-violating operators (e.g., electron EDM, nucleon EDM, CP-odd electron-nucleon interactions, etc.), only a comprehensive program combining multiple EDM measurements in atoms, molecules, and particles [26] can disentangle the origin of CP violation and discriminate between SM and BSM contributions. Global analyses that incorporate theoretical input, such as hadronic and nuclear matrix elements, are essential in this effort (see e.g., reference [3]), allowing constraints on the CP-violating parameter space and offering clues to the nature of NP. Continued progress in experimental precision, system diversity, and theoretical interpretation makes EDM searches one of the most promising attempts for uncovering BSM CP violation.

While no EDM has yet been observed, current experiments have set stringent limits on new sources of CP-violating interactions. EDM searches in composite systems, particularly those with enhanced internal sensitivity such as heavy atoms and polar molecules, provide some of the most stringent constraints. These systems amplify the effects of fundamental CP violation, making them powerful probes for BSM physics.

For the electron electric dipole moment (eEDM), the tightest constraints currently come from polar molecules. These molecules possess extremely large internal effective electric fields – often tens of GV/cm – which couple directly to a potential intrinsic eEDM. They also offer favorable features such as nearly complete polarization in modest external fields, long coherence times, and, in polyatomic species, internal states providing built-in co-magnetometry to suppress systematics. Using trapped HfF^+, the Cornell group has set a limit $|d_e| < 4.1 \times 10^{-30}\,\mathrm{e} \cdot \mathrm{cm}$ at 90 % confidence level (CL) [27]. Ongoing and planned experiments with ThO (ACME II/III) [28] and advanced interrogation schemes promise significant further sensitivity gains.

Atomic electric dipole moments (aEDMs) predominantly arise from nuclear contributions, primarily the CP-violating Schiff moment, which encodes the effects of intrinsic nucleon EDMs and CP-odd nucleon-nucleon interactions. Direct sensitivity to the intrinsic electron EDM is strongly suppressed in closed-shell (diamagnetic) atoms due to electronic screening and the near-cancellation enforced by Schiff's theorem. As a result, atom EDMs provide a clean probe of hadronic and nuclear sources of CP violation and are complementary to direct neutron and proton EDM searches. Experiments with heavy, octupole-deformed nuclei such as $^{225}\mathrm{Ra}$ benefit from a strong enhancement of the nuclear Schiff moment due to their pear-shaped asymmetric nuclear structure, resulting in an amplification by two to three orders of magnitude compared to spherical nuclei [29, 30].

The most precise probe of an atomic electric dipole moment (aEDM) to date comes from diamagnetic, neutral mercury ^{199}Hg atoms. Here, measurements in a vapor-cell setup set $d_{\mathrm{Hg}} = (2.20 \pm 2.75_{\mathrm{stat}} \pm 1.48_{\mathrm{sys}}) \times 10^{-30}\,\mathrm{e} \cdot \mathrm{cm}$, which provides an upper bound of $|d_{\mathrm{Hg}}| < 7.4 \times 10^{-30}\,\mathrm{e} \cdot \mathrm{cm}$ at 95 % CL [31]. This bound translates into one of the strongest indirect constraints on hadronic CP violation currently available. Mercury also plays an important role in the direct measurement of the neutron electric dipole moment (nEDM), where it acts as one of the most precise atomic co-magnetometers [32, 33]. Here the latest limit was recently pushed to $|d_n| < 1.8 \times 10^{-26}\,\mathrm{e} \cdot \mathrm{cm}$ at 90 % CL [32] and future measurements within the PanEDM collaboration [34] are on the way.

The current ^{199}Hg EDM measurement has reached fundamental technical limitations in its room-temperature vapor cell implementation. These challenges motivate the development of a next-generation approach based on cold, trapped ^{199}Hg atoms. Compared to thermal vapor cells, such systems allow substantially higher atom densities, smaller trap geometries supporting stronger applied electric fields, and reduced systematic errors. In addition, quantum-enhanced measurement strategies (e.g., Heisenberg scaling) promise further sensitivity gains. These developments are central to the "quMercury" project, which is presented here and which is explicitly included in the current European strategy for EDM searches [26]. Future nEDM measurements will also benefit from better knowledge of (nuclear) properties of mercury, isotope shifts (ISs) for AC light shift mitigation [33], as well as improved laser systems and experimental control in the deep-ultraviolet (UV).

Isotope shift spectroscopy

Another powerful technique at the precision frontier is atomic isotope shift spectroscopy (ISS). IS arises from nuclear mass and charge distribution differences between isotopes of the same element. Differential measurements, which compare transition frequencies across isotopes and transitions, can suppress common-mode systematics and enhance sensitivity to both SM and BSM effects that have not yet been studied. ISS is particularly sensitive to new parity-conserving electron-neutron interactions, potentially mediated by hypothetical bosons beyond the SM [4, 35] and therefore connects to fundamental questions in particle physics. This sensitivity allows atomic ISS experiments to probe new forces at subatomic scales with remarkable precision. This is particularly relevant in regard to the fermion mass hierarchy, where the LHC constraints of the electron Yukawa coupling allow for $y_e \lesssim 1.3 \times 10^{-3}$, much larger than the $y_e \approx 2 \times 10^{-6}$ SM prediction [4], as noted above. This leaves room for extended Higgs sectors or alternative mass-generation mechanisms.

The search for low-energy BSM physics is also motivated by the observation of anomalies in the 17 MeV electron-positron pairs excess in ^{8}Be nuclear decays observed by the ATOMKI collaboration [36], interpreted as evidence for a potential new vector boson [37]. ISS is a sensitive probe of a potentially scalar-mediated fifth force coupling electrons to neutrons, which are inaccessible to collider experiments. Here, King plots (KPs) provide a sensitive method for detecting nonlinearities in ISs that may signal NP. Although no definitive signals have yet emerged from ISS or KP analysis, these experiments already constrain new scalar and vector bosons in previously unexplored parameter space or support astronomical observations. Continuos improvements in experimental precision and theoretical modeling promise to further tighten these bounds and may eventually uncover NP signatures in atomic spectra.

Interpreting such deviations requires careful modeling of SM effects, particularly higher-order nuclear deformation. The sensitivity of IS experiments depends strongly on atomic number Z: in low-Z systems like calcium ($Z = 20$) BSM signals are weak, while in high-Z atoms like ytterbium ($Z = 70$) BSM effects are enhanced but SM-induced nonlinearities especially from nuclear deformation complicate the analysis. Mercury ($Z = 80$) offers an ideal compromise: it has a relatively simple electronic structure, high-Z enhancement, and near-spherical nuclei close to the proton shell closure at $Z = 82$, reducing deformation effects. It also provides narrow optical transitions and several stable even-even isotopes, making it well-suited for high-precision IS and KP studies.

ISS also enables precise mapping of nuclear charge radii across isotopic chains, revealing features such as the charge radii kink at the $N = 126$ shell closure and shape staggering in neutron-deficient isotopes of mercury. These observables provide stringent benchmarks for nuclear structure models, looking at shell effects and shape coexistence in heavy nuclei. Potentially also probing EDM enhancing nuclear structure effects like Schiff moments, ISS in Hg may also help to improve BSM bounds for new CP-violating interactions from EDM measurements.

Thesis overview

In this thesis, we lay the foundation for a measurement of the permanent EDM of laser-cooled mercury atoms and the use of ISS as a precision probe of potential new BSM physics. The structure of this thesis is as follows:

Chapter 2 provides a brief overview of the nuclear and electronic structure of mercury relevant for precision measurements of laser-cooled mercury atoms, particularly in the context of searches for a permanent EDM and ISS.

Chapter 3 discusses the technical challenges associated with handling mercury in an ultra-high vacuum environment and details the design and construction of a custom experimental vacuum chamber for producing and trapping cold mercury atoms.

Chapter 4 contains one of the main results of this thesis and describes the realization of a magneto-optical trap (MOT) operating on the ${}^1\mathrm{S}_0 \rightarrow {}^3\mathrm{P}_1$ intercombination line at 254 nm, capable of trapping all stable isotopes of mercury with atom numbers up to 5×10^7 and phase-space densities in the order of 1×10^{-6}. We present the construction of the optical and electronic setup including laser frequency stabilization, magnetic field control and imaging. We characterize the MOT cooling performance for all bosonic and fermionic isotopes, demonstrating sub-Doppler cooling in the latter.

Chapter 5 demonstrates the successful loading of cold mercury into a high-power optical dipole trap, which serves as the platform for future EDM measurements. We also outline the prospects for evaporative cooling toward quantum degeneracy, which has not yet been achieved in mercury, enabling quantum-enhanced metrology. Additionally, we are investigating ultracold fermionic mercury gases as a highly controllable quantum platform to simulate solid-state impurity physics, benefiting from the wide range of isotopes and thus tunable impurity-to-bath scattering properties. Our focus is on evaluating the feasibility of observing Friedel oscillations arising from impurity-bath interactions under realistic experimental conditions.

Chapter 6 reports precision ISS on several dipole-allowed electronic transitions in mercury. The data, analyzed through KP analysis, provide a starting point for probing subtle nuclear structure effects that are relevant to setting stringent constraints on the EDM. Furthermore, these measurements lay the groundwork for sensitive searches of hypothetical BSM interactions, enhancing our understanding of fundamental physics beyond the SM.

Throughout the chapters we also propose future upgrades to the experimental system, including improvements in laser cooling, extensions of the spectroscopy measurements, and the construction of a science chamber to measure the aEDM in an optical dipole trap.

2 Mercury

Mercury is the chemical element with atomic number $Z = 80$ and an atomic mass of about 200 u. Its chemical symbol, Hg, derives from the ancient Greek word “ὑδράργυρος” (“hydr argyros”) meaning “water silver,” reflecting its unique property of being a liquid metal at room temperature. Though extremely rare in the Earth’s crust, mercury’s remarkable physical and chemical properties have made it central to a long history of scientific discoveries and technological application. Its silvery appearance and strong wetting characteristics enabled its use in early optical mirrors, even by ancient Mayan civilizations. With a freezing point of $-38.8\,°\mathrm{C}$ and a boiling point of $356.7\,°\mathrm{C}$, mercury extended the operational range of sealed liquid-in-glass thermometers beyond that of alcohol-based designs. Its high density and thermal expansion coefficient made it ideal for barometers and manometers, and it remains the reference for the torr pressure scale. Michelson and Morley floated their apparatus on mercury, whose density and fluidity enabled frictionless rotation of the optical elements to detect shifts relative to the hypothesized aether. Due to its high vapor pressure and monatomic vapor phase, mercury became a preferred source for early molecular beam experiments. Superconductivity was discovered in mercury by Heike Kamerlingh Onnes in 1911 at 4.19 K, and its excellent electrical conductivity saw widespread use in switches and relays throughout the 19th and 20th centuries. Mercury fluorescence vapor lamps were also used in many applications here, some of which are still in use today.

Its atomic structure made mercury central to the early development of quantum and atomic physics. The Franck-Hertz experiment (Nobel Prize 1925), the demonstration of the Hanle effect (Nobel Prize 1924), the first optical pumping by Alfred Kastler (Nobel Prize 1966), and the first Einstein-Podolsky-Rosen (EPR) experiment using lasers by Fry and Thompson in 1976 were all performed using mercury. Thomas Walther therefore refers to mercury as the “Rosetta Stone of physics”, pointing out that, prior to the advent of laser cooling, it was the preferred element for quantum physics [38]. Mercury was also used in early optical pumping experiments, pioneered magnetic resonance studies by Isidor Isaac Rabi and $^{199}\mathrm{Hg}$ and $^{201}\mathrm{Hg}$ are considered the most studied nuclear magnetic resonance active nuclei. Together, these properties and applications have made mercury not only a practical tool but also a foundational element in the advancement of modern physics.

Today, the field of precision metrology and quantum optics is especially interested in mercury as a promising candidate for an optical lattice clock [39–43]. Its deep-ultraviolet (UV) clock transition and low sensitivity to black body radiation shifts increases its sensitivity to variations in fundamental constants [44, 45] and coupling to dark matter [21]. Comparisons of optical clocks to UV mercury transition achieve fractional uncertainties beyond the current realization of the second [46], also including clocks based on single mercury ions [47]. A two-photon E1-M1 excitation scheme in a hot mercury vapor is suggested to provide a compact, transportable optical clock with a stability down to $1 \times 10^{-15}\,\sqrt{\mathrm{Hz}}^{-1}$ [48]. With a long-time fractional stability of 3×10^{-15} a compact clock based on mercury ions was already launched into space as part of NASA's Deep Space Atomic Clock (DSAC) program, designed to improve the precision of deep space and real-time autonomous spacecraft navigation [49].

The green line of ^{198}Hg at 546 nm was favored as a calibration standard for the meter in the form of a monoisotopic, electrodeless lamp, which provides a sharp, stable spectral line with minimized Doppler broadening and a very simple hyperfine structure [50]. The wavelengths of four visible ^{198}Hg lines are still recommended by the International Committee for Weights and Measures for practical realization of the meter at the 5×10^{-8} level [51, 52]. And the $^1\mathrm{S}_0 \rightarrow {}^3\mathrm{P}_1$ intercombination line is considered as a precise thermometer that could serve as a practical realization of the kelvin temperature scale [53].

Mercury's high nuclear charge makes it a strong candidate for fundamental tests of parity violation and searches for physics beyond the standard model. Nuclear-spin comagnetometers based on atomic mercury are used to compensate magnetic field drifts in the direct search for a permanent electric dipole moment (EDM) of the neutron [34] and can also be used to search for a new physics gravity spin coupling at earth's range [54]. In the context of nuclear physics the heavy mercury nucleus also shows a staggering of the nuclear charge radius at higher masses, a feature that is still being investigated and might improve our understanding of nuclear structure theory.

Generation of ultra-cold diatomic Hg-molecules by photo-association promises new platforms for quantum simulation, precision magnetometers and beyond standard model searches of baryon interactions or the EDM of the electron [55]. They are considered potential source of entangled atoms and could be used in a loophole-free experimental test of Bell's inequalities [56]. The weak van der Waals interactions of Hg-dimers render them an interesting molecule to test computational models [57] and to probe hypothetical fifth forces or short-range modifications to gravity [58].

This chapter will give a description of the nuclear and electronic structure of mercury laying a foundation for laser cooling, precision spectroscopy and EDM searches. It will motivate the use of isotope shift spectroscopy (ISS) to benchmark nuclear structure theory, that currently limit beyond standard model bounds of latest EDM measurements in mercury.

2.1 Nuclear structure

The potential source of a permanent atomic EDM of mercury lies mainly in its nucleus. The rich nuclear structure of mercury makes both the naturally abundant and stable, but also artificially created and radioactive isotopes very intriguing for ISS.

2.1.1 Isotopes

Mercury is a very heavy element, that can be found in form of seven naturally occurring isotopes with mass numbers between $A = 196$ and 204 as shown in table 2.1. Five of these isotopes are bosonic with nuclear spin $I = 0$ with natural abundances between 0.15 % for ^{196}Hg and 29.74 % for the most abundant ^{202}Hg. About one third of natural occurring mercury exists as fermionic mercury ^{199}Hg with nuclear spin $I = 1/2$ and ^{201}Hg with nuclear spin $I = 3/2$. Next to the stable isotopes, the radioactive isotope ^{194}Hg is quite long-lived with a half lifetime of about 444 yr and decays via electron capture via ^{194}Au into ^{194}Pt, while all other radioisotopes have life times of a few days or less.

Mass number A	Natural abundance p_{nat} (%)	Nuclear spin I	Atomic mass m (u)	Binding energy E_b/A (keV)
196	0.15(1)	0	195.965 833(3)	7914.370(15)
198	9.97(20)	0	197.966 769 2(5)	7911.553(2)
199	16.87(22)	1/2	198.968 281 0(6)	7905.279(3)
200	23.10(19)	0	199.968 326 9(6)	7905.896(3)
201	13.18(9)	3/2	200.970 303 1(8)	7897.561(4)
202	29.86(26)	0	201.970 643 6(8)	7896.850(4)
204	6.87(15)	0	203.973 494 0(5)	7885.546(3)

Table 2.1: All naturally occurring isotopes of mercury, their natural abundance and nuclear properties. Data for the abundances p_{nat} are taken from reference [59]. The atomic masses m and binding energies per nucleon E_b/A are taken from the most recent atomic mass evaluation AME2020 [60].

Nuclear mass The isotope masses, given in table 2.1, are the respective atomic masses, which we denote as m. Important for isotope shift (IS) contributions discussed in section 6.1, the nuclear mass – denoted as m_A in dependence on the mass number A – is obtained by correcting m for the total mass $Z\,m_e$ and binding energy $E_b(Z)$ of all electrons

$$m_A = m - Z\,m_e + E_b(A, Z)\,. \tag{2.1}$$

For mercury ($Z = 80$) this correction is dominated by the large electron binding energy, which can be approximated by the semi-empirical Bethe-Weizsäcker mass formula. The binding energy per nucleon E_b/A is maximal for ^{62}Ni and gradual decreases for larger A, as the strong binding force is weakened by electromagnetic repulsion. For the stable mercury isotopes $\langle E_b(A, Z)/A\rangle = 7.804(14)\,\text{MeV}/c^2$, which results in binding energy corrections of about $< E_b(A, Z) >= 1.676(17)\,\text{u}$, while the electron mass contribution is much smaller $Z\,m_e = 0.043\,886\,392\,725\,2(13)\,\text{u}$. Experimentally determined binding energies are given in table 2.1. Adapted to the mass and binding energy data given in [60], we use the recommended values of the fundamental physical constants (CODATA) from 2018 [61].[1]

2.1.2 Nuclear shape

With $Z = 80$ protons mercury lies just below the closed proton shell of lead located at $Z = 82$ and close to the neutron shell closure of $N = 126$ – the magic quantum numbers of the nuclear shell model, where nuclei are more stable and exhibit a usually spherical shape due to the strong binding forces. While the mercury nucleus at first glance therefore follows the simple liquid drop model of a spherical, incompressible nucleus with radius $r = r_0\,A^{1/3}$ (with $r_0 = 1.2\,\text{fm}$) the large nucleon number renders the nucleus to be soft (= easily deformable). Just adding or removing a single neutron from the nucleus can alter the shape drastically. This gives rise to multiple nuclear states with different shapes (spherical, oblate, prolate) coexisting at energies close to the nuclear ground state. This shape

---

[1] A precise conversion to mass units is possible by the electron volt to atomic mass unit relationship $1\,\text{eV}/c^2 = 1.073\,544\,102\,33(32) \times 10^{-9}\,\text{u}$ and the electron mass $m_e = 5.485\,799\,090\,65(16) \times 10^{-4}\,\text{u}$, given in units of the unified atomic mass unit $1\,\text{u} = 1.660\,539\,066\,60(50) \times 10^{-27}\,\text{kg}$ [61].

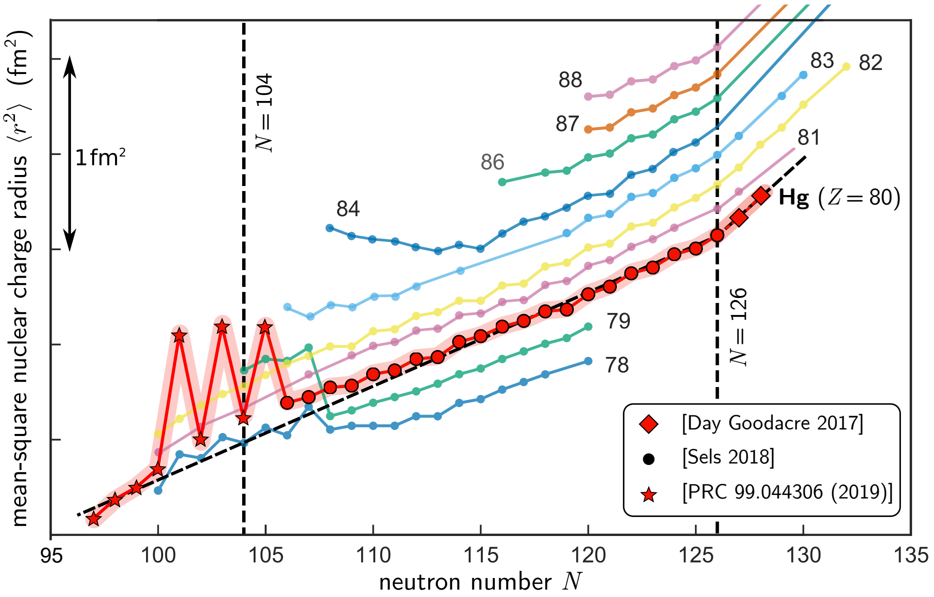

Figure 2.1: Mean-square nuclear charge-radii $\langle r^2 \rangle$ of the nuclear ground state of elements in the lead region. Highlighted (red) are the charge-radii of mercury showing the strong shape staggering close to the $N = 104$ midshell and the charge-radii kink at the nuclear shell closure at $N = 126$. Figure taken from reference [64] and data (circles) from the references within: [71–76]. The figure is modified to also show the mean-square nuclear charge-radii of mercury beyond the nuclear shell closure and its staggering. The additional data for the neutron-rich isotopes (black-bordered red diamonds) is taken from reference [65, 77], the data for the neutron-deficient isotopes from [68]. Black-dashed lines indicate the slope of $\langle r^2 \rangle$ before and after the nuclear shell closure.

coexistence is well-behaved for stable mercury nuclei but slightly affects neutron-rich isotopes and strongly affects neutron-deficient isotopes. For the latter, the spherical shape abruptly transforms into a prolate spheroid resembling a rugby ball. However, this only occurs for odd A nuclei, an effect called shape staggering.

Shape staggering of neutron-deficient isotopes

The neutron-deficient mercury nucleus is one of the most extensively studied examples of shape coexistence. This for instance leads to changes of the nuclear charge radius between even and odd isotopes that strongly disagree with a simplified droplet nuclear shell model. This shape staggering was indeed first discovered in neutron-deficient ^{183}Hg to ^{187}Hg via optical pumping and β-decay at the on-line mass separator ISOLDE at CERN [62] and later described as “one of the most remarkable discoveries in nuclear structure physics in the last 50 years” [63, 64]. For mercury, it is dominant near the $N = 104$ neutron midshell – in-between the $N = 82$ and $N = 126$ shell closures – and very pronounced in comparison to other nuclei in the neutron-deficient lead region [65] as shown in figure 2.1. While studied extensively especially in mercury ([62, 64–68], [69, and the references within]) there are still many open questions to the main interactions that drive nuclear deformation, and it is still an active field of research [70]. Recently it was identified that the staggering stops at around ^{180}Hg, where the nuclear charge radii return to follow the slope trend of lead [68].

Charge-radii kink at $N = 126$

On the other side of the isotopic chain of heavy elements a strong change in the generally rather smooth gradient of nuclear charge radii can be observed when crossing a specific number of neutrons [65, 71]. This kink appears at the $N = 28$, 50, 82 and 126 shell closures and was recently investigated for mercury at around $N = 126$ [77, 78]. Here, "the gradient of the trend of isotope shifts is not consistent immediately prior to and following the $N = 126$ shell closure" [65]. This means that while the ^{206}Hg is the most interesting mercury isotope to study, nuclear deformation effects are also present around the shell closure and therefore will also affect for instance ^{204}Hg.

Onsets of the nuclear deformations of the nuclear charge radius are also being probed close to the neutron midshell, where charge radii behave much smoother due to increased degrees of freedom for deformation far away from the stabilizing influence of the surrounding shell closures. Here the form of the neutron skin – the thin outer layer of neutrons in neutron-rich nuclei – and its influence on shape coexisting states and therefore nuclear deformation is studied and being probed by optical ISS, as for example in even proton-magic $Z = 82$ lead isotopes near the $N = 104$ neutron midshell [79]. Studying the mercury nucleus therefore acts as a benchmark for nuclear structure models, that still requires improvements in this region of the nuclear table [65, 80, 81].

These nuclear deformation effects require more sophisticated nuclear structure models, especially for predicting the interplay between the nucleus and electronic structure in optical ISs, as well as the exposure and enhancement of nucleon EDMs via nuclear Schiff moments.

Description of nuclear deformations

Extension of the liquid drop model to arbitrary nuclear shapes is allowed in the more precise droplet nuclear structure model [82]. It enables spatial separation of the proton and neutron density, introduces surface diffuseness instead of a sharp boundary and allows for a finite compressibility of the nucleus [64]. This for instance allows the description of an outer-lying neutron-skin for neutron rich isotopes like mercury.

While both of these macroscopic models roughly predict nuclear charge radii and deformation parameters, they cannot explain fine structure effects arising from individual nucleon interaction. To address these, the mercury nucleus needs to be described within the context of nuclear shell models, where the nucleus is treated as a system of individual protons and neutrons occupying quantized orbits within a mean nuclear potential. The underlying shape of the nucleus is therefore not imposed, but rather emerges from collective nucleon-nucleon interactions. To solve the resulting many-body Schrödinger equation the configuration space is restricted to often only one or two major shells in the framework of traditional nuclear shell model theory. More recent developments of Monte Carlo shell model calculations however try to fix the problem of diagonalizing large Hilbert spaces by sampling the most dominant many-body configurations stochastically, which is needed to describe shape coexistence and deformation in heavy nuclei such as mercury.

The extension to a deformed shell model or Nilsson model [83] allows the description of deformed nuclear potentials via parametrization of the nuclear surface r as a sum of (real-valued) spherical harmonics and corresponding multipole deformation parameters [64]. In spherical coordinates and

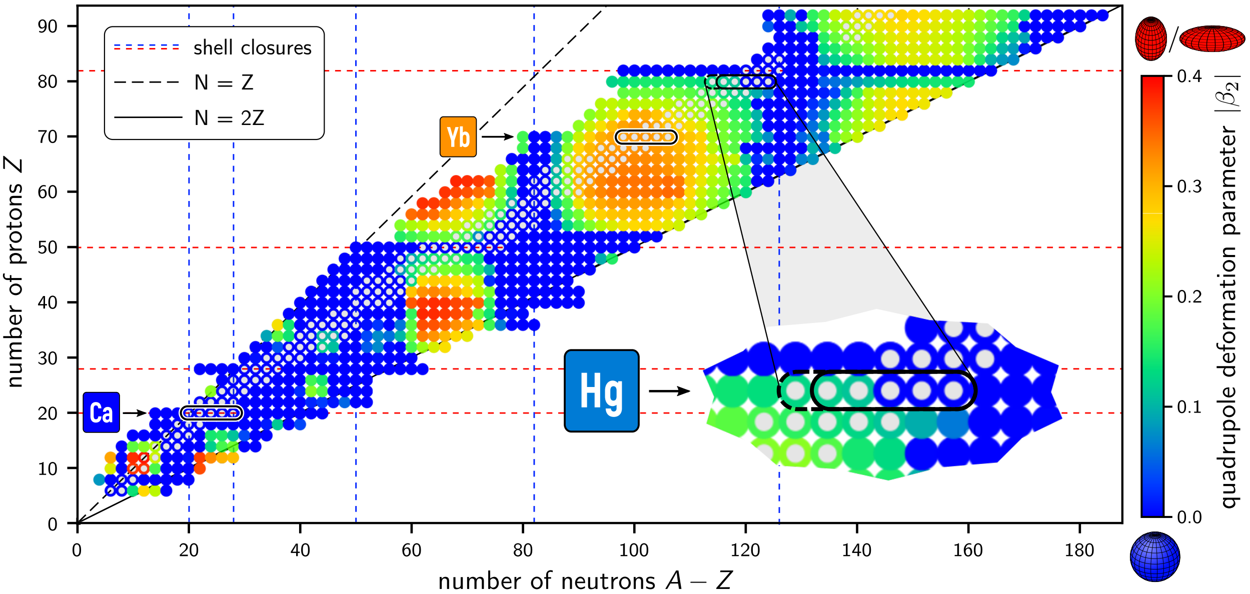

Figure 2.2: The absolute value of the nuclear quadrupole deformation parameter, β_2, of the nuclear ground state of even even isotopes across the nuclear table. Open circles represent stable or close to stable nuclei. Nuclei close to a nuclear shell closure (as indicated by the red and blue dashed lines) feature a rather spherical nucleus given by a quadrupole deformation parameter close to $\beta_2 = 0$. Nuclei with a non-zero quadrupole deformation parameter have a prolate or oblate nuclear structure instead. The five naturally occurring mercury isotopes sit close to the nuclear shell closures of doubly-magic lead ^{208}Pb and therefore only show a weak quadrupole deformation for the lighter isotopes. Note that ^{194}Hg (enclosed by a dashed line) is only semi-stable with a half lifetime of $T_{1/2} = 444\,\mathrm{yr}$. We also indicate the location of the natural abundant calcium and ytterbium isotopes as a comparison for isotope shift spectroscopy, discussed in chapter 6. The figure is taken and adapted from reference [85].

under assumption of axial symmetry[1] the nuclear surface radius is then given by

$$r(\theta,\phi) = r_0\, c_V \left(1 + \sum_{l=2}^{\infty} \beta_l\, Y_{l,m=0}(\theta,\phi)\right), \qquad \text{where} \qquad c_V = 1 - \frac{1}{\sqrt{4}\,\pi} \sum_{l=2}^{\infty} \beta_l^2 \tag{2.2}$$

normalizes the nuclear radius to scale as $\propto A^{1/3}$ identical to the liquid drop model [84]. The β_l are the 2^l-pole deformation parameters, where $\beta > 0$ are considered prolate and $\beta < 0$ oblate deformation. The dominating correction term to the spherical nucleus is the electric quadrupole deformation described by the deformation parameter β_2, which can be measured via low-energy Coulomb excitation or hyperfine spectroscopy and a table of nuclear quadrupole deformation across the elements is illustrated in figure 2.2. Being close to both the proton shell closure at $Z = 82$ and the neutron shell closure at $N = 126$ the even isotopes of mercury are rather spherical and only slightly oblate and therefore less deformed compared to other elements like for instance ytterbium, a comparison we will revisit in the question of nuclear contributions to optical ISs.

In more advanced theories, such as the interacting boson model, pairs of nucleons are treated as effective bosons with angular momentum 0 or 2 in a collective description. In these theories, shapes emerge as phases, and transitions between spherical and deformed shapes correspond to

---

[1] This removes all $m \neq 0$ components.

quantum phase transitions in the bosonic Hamiltonian. The kink in the mean-square nuclear charge radius can be explained by the nuclear relativistic mean-field approximation [86] as resulting from shifts in the neutron levels due to the spin-orbit interaction. This affects the proton density and consequently the charge radius [65]. Alternative explanation of the kink based on spherical relativistic Hartree-Bogoliubov and spherical nonrelativistic Hartree-Fock-Bogoliubov approaches – indicating an occupation of close lying nuclear orbitals above the $N = 126$ shell gap – are still being studied and potentially promise to unify both the explanation of the shape staggering and charge radius kink [77]. Shape staggering can then be described to arise from a quantum phase transition – particle-hole excitations across a shell gap – between monopole and quadrupole nucleon-nucleon interactions and occupation of specific proton and neutron orbitals [64, 68, 70].

2.2 Electronic level structure

With two valence electrons mercury possesses an alkaline-earth-like electronic level structure featuring a [Xe] $4f^{14}\,5d^{10}\,6s^2\;{}^1S_0$ electronic ground state, as shown in figure 2.3. As the orbital angular momentum of the atomic ground state is $J = 0$ and the spin $S = 0$, only the nuclear spin $\vec{I}$ contributes to the total atomic spin $\vec{F}$. While we will utilize and probe other states in the electronic level structure, both the measurement of EDMs and ISs are linked to this nuclear structure dependency.

Clock lines

Mercury in its ground state can just be excited using deep-UV light. Therefore, its energy shifts negligibly when exposed to blackbody radiation. The excited clock states, ${}^3P_0$ and ${}^3P_2$, can only be addressed using visible to deep-UV light. This combination results in a very small blackbody radiation shift of the optical clock transitions compared to other elements used for optical clock operation. The ${}^1S_0 \rightarrow {}^3P_0$ clock transition at 266 nm is affected only as little as $\Delta\nu_{BBR}/\nu_0 = -1.6 \times 10^{-16}$, which is a an order of magnitude lower shift compared to strontium or ytterbium [92]. This makes mercury an ideal candidate for an optical lattice clock [39–43] without the need for cryogenic shielding to suppress blackbody radiation. Here both the 266 nm and 227 nm transitions connecting the ${}^1S_0$ ground state to the metastable ${}^3P_0$ and ${}^3P_2$ excited state feature sub-Hz narrow linewidths, ideal for clock operation [93, 94].

Laser cooling and high-resolution imaging

For laser cooling, discussed in more detail in chapter 4, we ideally require a broad and closed cycling transition that starts in the atomic ground state. Alkaline-earth metals, like magnesium, calcium and strontium are typically slowed and magneto-optically trapped on the very broad (≥30 MHz) dipole allowed ${}^1S_0 \rightarrow {}^1P_1$ singlet transition and further cooled on the narrow (≤100 kHz) dipole allowed ${}^1S_0 \rightarrow {}^3P_1$ triplet transition.

While the singlet transition in mercury with $\Gamma = 2\pi \times 120\,\text{MHz}$ is similarly broad allowing large photon scattering rates, it lies at a wavelength of $\lambda = 184.9\,\text{nm}$, deep in the UV, where so far no continuous-wave laser exists and prospects in building one did not yet promise enough power for efficient laser cooling. However, the 184.9-nanometer line is an excellent candidate for high-resolution imaging of cold atomic clouds. Its broad linewidth promises high photon scattering rates, and its

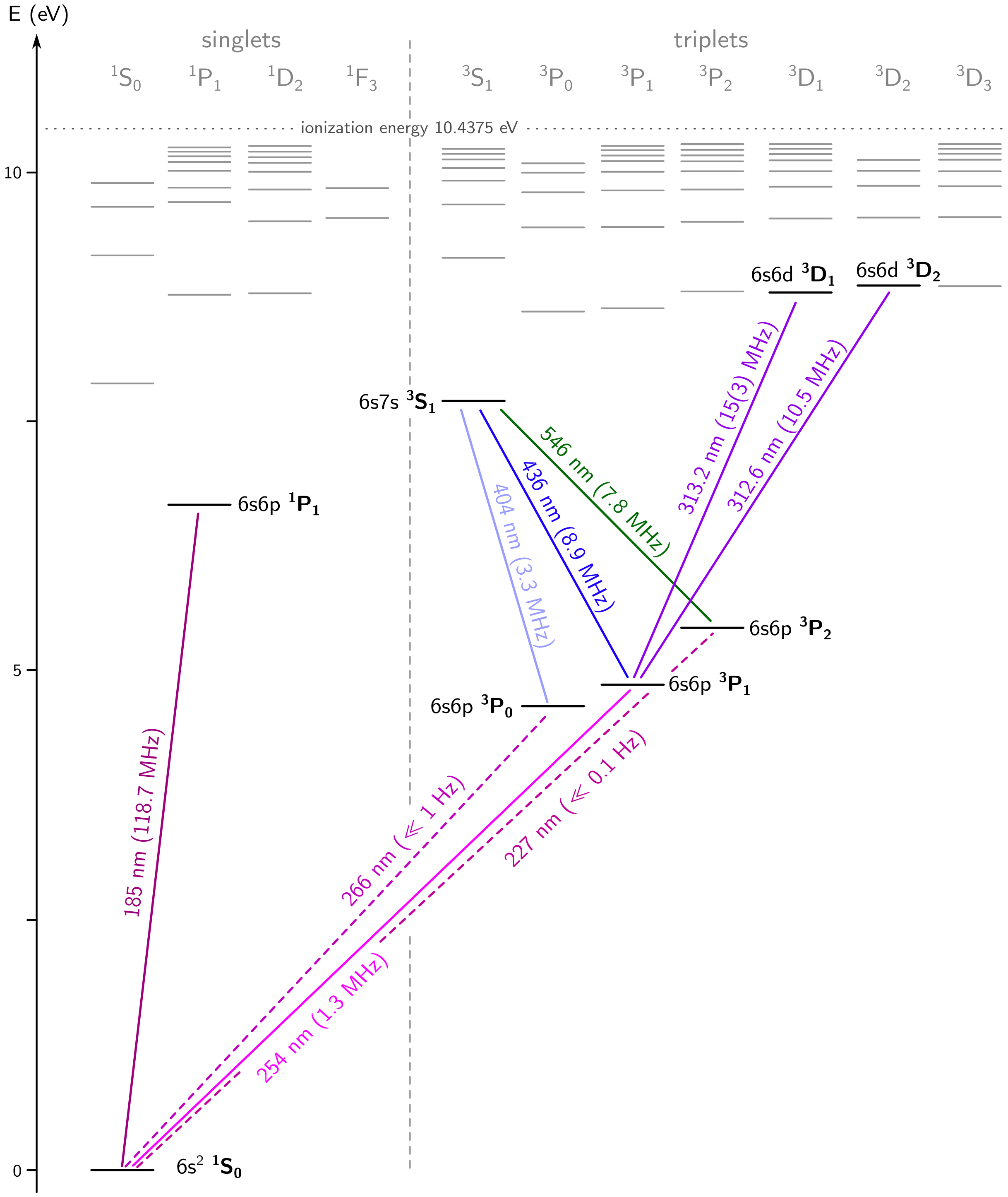

Figure 2.3: Grotrian diagram of neutral mercury showing only the electronic levels and transitions relevant for the work discussed here. The transition energies are given as vacuum wavelengths, the number in brackets denotes the natural linewidth. Data is taken from reference [87], except for linewidth of the clock line transitions and $^3P_1 \rightarrow {}^3D_1$ transition, the latter being determined from excited state lifetime measurements [88–90] as explained in [91].

small wavelength allows for resolution down to around 100 nm when diffraction-limited. This enables e.g., the study of solid-state physics in ultracold Fermi gases, as discussed in 5.3.2. In section 4.8.2, we will discuss laser development at 184.9 nm aimed at this goal.

Due to enhanced mixing of the 6s 6p $^3\mathrm{P}_J$ ($J = 0, 1, 2$) fine structure manifold with the singlet 6s 6p $^1\mathrm{P}_1$ level [95–97] the triplet transition is with $\Gamma = 2\pi \times 1.3\,\mathrm{MHz}$ slightly broader.[1] While still two orders of magnitude smaller than the singlet transition linewidth, this line represents a compromise for efficient slowing and low temperatures.

Hyperfine structure and magnetic field interaction

The hyperfine structure of an atom arises from interactions between the nuclear spin and the surrounding electron cloud, most notably through magnetic dipole and electric quadrupole couplings. These interactions are sensitive to both the nuclear spin and the electronic state of the atom and play a critical role in laser cooling, dipole trapping, and especially in high-precision spectroscopy such as optical clock operation and EDM measurements. For isotope $^{199}\mathrm{Hg}$ with nuclear spin $I > 0$ magnetic dipole coupling dominates, as the nucleus interacts with the magnetic field generated by the electrons. The $^{201}\mathrm{Hg}$ isotope with spin $I \geq 1$ exhibits coupling of the nuclear quadrupole moment to the gradient of the electronic electric field. This interaction reflects the non-spherical charge distribution of the nucleus and can cause additional hyperfine structure shifts. Historically, mercury was instrumental in identifying the existence of a nuclear quadrupole moment, as early studies of its hyperfine structure revealed deviations inconsistent with purely magnetic dipole interactions [99].

In neutral mercury, the ground state $^1\mathrm{S}_0$ and metastable triplet state $^3\mathrm{P}_0$ have total electronic angular momentum $J = 0$ and thus exhibit no hyperfine splitting. For bosonic isotopes with $I = 0$, the absence of nuclear spin further eliminates all hyperfine interactions. As a result, for bosonic isotopes these states are magnetically insensitive, which is advantageous for precision metrology and quantum state control. The magnetic sensitivity of excited states with $J \neq 0$ plays an important role in the operation of the magneto-optical trap (MOT) and must be accounted for when analyzing systematic shifts in high-precision ISS.

The fermionic isotopes, $^{199}\mathrm{Hg}$ ($I = 1/2$) and $^{201}\mathrm{Hg}$ ($I = 3/2$), do exhibit hyperfine splitting in states with non-zero total electronic angular momentum $J \neq 0$. For the work here this is especially relevant for the $^3\mathrm{P}_1$ excited state, where hyperfine splitting shifts the $^1\mathrm{S}_0 \rightarrow {}^3\mathrm{P}_1$ intercombination line by multiple gigahertz, exceeding the isotope shift. The specific properties of individual hyperfine levels influence their suitability for laser cooling and EDM measurements, as discussed in Chapters 4 and 7. In the $^1\mathrm{S}_0$ and $^3\mathrm{P}_0$ states, the total electronic angular momentum remains zero, and thus no hyperfine splitting occurs even for fermionic nuclei. This absence of hyperfine coupling in the clock states is essential for achieving narrow linewidths and long coherence times in optical clocks. Nevertheless, weak magnetic interactions still occur due to nonzero nuclear magnetic moments, resulting in small Zeeman shifts under external magnetic fields.

Aligned with the total spin $\vec{F} = \vec{I} + \vec{J}$, the mercury atom possesses an associated magnetic moment $\vec{\mu} = \mu_B\, g_F\, \vec{F}$, where μ_B is the Bohr magneton and g_F the Landé hyperfine g-factor. Its interaction with an externally applied magnetic field $\vec{B}$ leads to a Zeeman shift of the atomic hyperfine structure

---

[1] Note that the exact linewidth of the $^1\mathrm{S}_0 \rightarrow {}^3\mathrm{P}_1$ transition in mercury is actively debated [98].

levels $|F, m_F\rangle$:

$$\Delta E_Z = -\vec{\mu} \cdot \vec{B} = m_F \, g_F \, \mu_B \, B \,. \tag{2.3}$$

For bosonic isotopes ($I = 0$), the atomic ground state $|^1\mathrm{S}_0; F = 0, m_F = 0\rangle$ is therefore magnetically insensitive. For the fermionic isotopes ^{199}Hg and ^{201}Hg, the gyromagnetic ratios are [61, 100]

$$g_L = 1 - \frac{m_e}{m} \approx 1 \,, \quad g_S \approx 2.0023193 \,, \quad g_I = \begin{cases} +1.008(1) \,, & ^{199}\mathrm{Hg} \\ -0.3720(5) \,, & ^{199}\mathrm{Hg} \end{cases} . \tag{2.4}$$

The Zeeman shift in the weak field limit follows equation (2.3), with the Landé g-factor given by

$$g_F = g_J \, \frac{F\,(F+1) - I\,(I+1) + J\,(J+1)}{2\,F\,(F+1)} + g_I \, \frac{\mu_N}{\mu_B} \, \frac{F\,(F+1) + I\,(I+1) - J\,(J+1)}{2\,F\,(F+1)} \,, \tag{2.5}$$

which for the ground state reduces to $g_F = g_I \, \mu_N/\mu_B = 5.49(1) \times 10^{-4}$ and $g_F = -2.026(3) \times 10^{-4}$ for ^{199}Hg and ^{201}Hg, respectively, as the ratio of nuclear and Bohr magneton is small, $\mu_N/\mu_B \approx 1/1836$. This renders magnetic trapping of mercury in the $^1\mathrm{S}_0$ ground or metastable $^3\mathrm{P}_0$ excited state impossible for bosons and extremly challenging for fermions, restricting quantum degeneracy approaches to evaporative cooling in an optical dipole trap (ODT). Note that mercury atoms in the metastable $^3\mathrm{P}_2$ state can, in principle, be magnetically trapped using standard techniques such as magnetic quadrupole or Ioffe-Pritchard traps.

3 Integrating mercury into ultra-high vacuum systems

Unlike most other elements used in quantum gas experiments, mercury presents a unique set of challenges due to its physical and chemical properties. First, it is liquid at room temperature, with a vapor pressure of 1.7×10^{-3} mbar, requiring not heating but cooling to achieve vapor pressures compatible with the ultra-high vacuum (UHV) conditions necessary for laser cooling. Second, mercury readily forms amalgams with many metals, which complicates its use in UHV systems typically built from stainless steel, titanium, or copper. Third, laser cooling of mercury relies on transitions in the ultraviolet (UV) wavelength range, which imposes additional constraints on the optical components and vacuum windows used. The combination of these factors makes the design and operation of vacuum systems for mercury particularly demanding. In this chapter, we discuss the individual challenges in detail and present new developments aimed at overcoming them.

Mercury has a long history being used in vacuum environment and was used almost from day one as an early barometer that even defined the torr pressure scale, as the pressure generated by a 1 mm high column of mercury. A high speed jet of liquid mercury was used in mercury diffusion pumps to reach high vacuum regimes, where the jet accelerates gas molecules out of the pumping volume, similar to the working principle of a turbo molecular pump. Pressure levels in the UHV (1×10^{-7} mbar to 1×10^{-12} mbar) and towards the extreme high vacuum (XHV) ($\leq 1 \times 10^{-12}$ mbar) relevant for laser cooling of mercury towards quantum degeneracy are however still challenging to achieve, as experimental setups and knowledge about mercury pumping speeds of relevant pumping technologies is rare[1]. Integrating mercury into UHV systems is therefore still an ongoing quest and optimal source chamber designs and vacuum pumping strategies are still unknown.

The following chapter presents the vacuum apparatus constructed during this thesis and will try to answer some of these questions. Two mercury sources were constructed in this work based on two different design principles. A review of existing source chambers is followed by a discussion of relevant design criteria for material selection and cooler design, and the construction and performance of the two solutions are presented. A short section about vacuum viewports will discuss reliability of anti-reflection (AR) coatings in the deep ultraviolet. An outlook for a collimated atomic beam source for Zeeman slowing of mercury and a versatile quantum gas chamber for future electric dipole moment (EDM) measurements will be given.

---

[1] Personal communication to Agilent Vacuum Technology and SAES Getters.

3.1 Source chamber

3.1.1 Design considerations

The vapor pressure of mercury can be approximated with a logarithmic regression model [101],

$$\ln\left(p_{\mathrm{sat}}/p_c\right) = (T/T_c)\left(a_1\,\tau + a_2\,\tau^{1.89} + a_3\,\tau^2 + a_4\,\tau^8 + a_5\,\tau^{8.5} + a_6\,\tau^9\right)\,, \tag{3.1}$$

where $\tau = 1 - T/T_c$ with $T_c = 1764\,\mathrm{K}$ and $p_c = 1.67\times10^6\,\mathrm{mbar}$. The coefficients a_1 to a_6 are adapted to a collection of experimental data and can be found in reference [101]. The vapor pressure in dependence of temperature is shown in figure 3.1. Even at its melting point at −38.8 °C the resulting equilibrium vapor pressure is as high as 3×10^{-6} mbar. Considering the most simple vacuum chamber design where mercury is laser cooled directly from the background gas, a vacuum pressure in the magneto-optical trap (MOT) region below 1×10^{-8} mbar is desired to achieve good atomic lifetimes, which are fundamentally limited by collisions with background atoms. Experiments towards quantum degeneracy typically aim for 1×10^{-10} mbar to 1×10^{-11} mbar, at which Bose-Einstein condensate (BEC) and Fermi gas lifetimes – limited by collisions between trapped atoms and residual background gas in the system – of tens of seconds can be achieved.

By spatially separating the magneto optical trap chamber from the source chamber a reduction of the mercury background pressure via differential pumping of one to two orders of magnitude is easily achieved. This indicates that a cooling to about −50 °C is desired to reach mercury vapor pressures of below 1×10^{-6} mbar. For the two vacuum chamber layouts discussed here we set our goal to source temperatures < −50 °C for loading from the background gas and < −30 °C for operation of a Zeeman slower (ZS). Assuming typical vacuum pumping speeds of the ion getter pumps (IGPs) mass transport rates in the order of $\ll 1$ g/yr from the source should be achieved, see also the discussion of ZS construction in section 4.8. This results in a required mercury quantity of a few grams to be loaded into the source chamber. With a density of about 13.5 g/cm^3 this corresponds to a few hundred mm^3 in volume.

Review of existing designs

Cooling a small container of mercury to temperatures around or below its melting point has already been accomplished in a few ways. The machine described in reference [102] is using a copper vacuum feedthrough with an air-sided attached $Q_{\mathrm{max}} = 18\,\mathrm{W}$, $\Delta T_{\mathrm{max}} = 100\,\mathrm{K}$ two-stage thermoelectric cooler (TEC) pre-cooled by a 240 W vapor-compressor refrigerator cooler reaching temperatures down to −74.7 °C. In the later reconstruction John et al. are using a $Q_{\mathrm{max}} = 22\,\mathrm{W}$, $\Delta T_{\mathrm{max}} = 111\,\mathrm{K}$ TEC achieving temperatures down to −55 °C [103]. The compressor cooler however requires vibration isolation from the MOT chamber (via a 250 mm long ConFlat (CF) DN16 bellows) and has a rather high energy consumption.

Alternative approaches [58, 104, 105] utilize a TEC element in vacuum. This has the benefit of suppressing the thermal conductivity via convection between the cold and hot side of the TEC, the main performance limitation of Peltier based cooling in air. Furthermore, this design requires no additional insulation to prevent condensation on the cold TEC surface. The only challenge is to remove the thermal heat of the TEC from within the vacuum chamber. In reference [104] a small

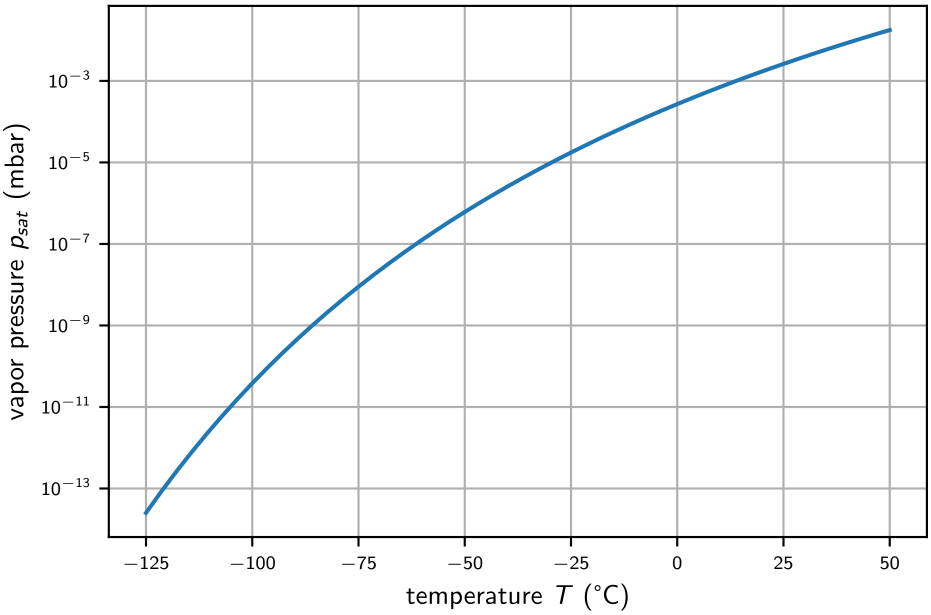

Figure 3.1: Saturation vapor pressure p_{sat} of mercury in dependence of temperature T.

copper cup is cooled by a $\Delta T_{\mathrm{max}} = 80\,\mathrm{K}$ TEC backed by a 12 °C water cooled copper heatsink. The thermal contact between cup, TEC and heatsink are realized via EPO-TEK H72 heat-conductive epoxy. Inspired by the design Paul et al. [105] is using a $Q_{\mathrm{max}} = 10.4\,\mathrm{W}$, $\Delta T_{\mathrm{max}} = 93\,\mathrm{K}$ multi-stage TEC contacted via EPO-TEK H72 to a custom-made copper feedthrough. Similarly, [58] stacked two $Q_{\mathrm{max}} = 55\,\mathrm{W}$, $\Delta T_{\mathrm{max}} = 93\,\mathrm{K}$ TEC elements using cryogenic heat conductive paste[1] reaching a temperature difference of about 40 K with about 100 W of electrical power [106]. In both designs a small copper cup containing a drop of mercury is cooled, and the TEC is contacted to a copper heatsink cooled by a water loop. [107] is also using a multistage TEC in vacuum backed by a 10 °C water cooled copper vacuum feedthrough reaching temperatures of down to −70 °C. There are no available claims or data on long-term reliability.

For the proven performance a purely Peltier based cooling solution backed by a water cooling loop is chosen. Within the scope of this thesis two designs were tested with respect to their performance and reliability. The first system inspired by [58, 104, 105] is using an in-vacuum housed TEC and the second generation source chamber is based on a TEC element in air.

Material selection

Selecting a material for holding a small amount of mercury within the vacuum chamber is not straight forward. Most materials with high heat conductivity that are vacuum-compatible and convenient to machine are metals, like oxygen-free copper (390 W/(m K)) or aluminum (237 W/(m K)) and are therefore wetted by and form amalgams with mercury leading to corrosion. This can dissolve the metal leading to structural weaknesses creating vacuum leaks or malfunction of the cooling apparatus.

Strongly depending on the chemical conditions, especially temperature and mass ratio of the mixing elements, exceptions can be found in the lighter elements of the first transition metals chromium, iron and cobalt, as well as in heavier transition elements molybdenum, tantalum, platinum and tungsten

---

[1] Apiezon N, 0.194 W/(m K) thermal conductivity at room temperature.

[108–111]. Iron needs to be excluded due to its impure form and risk of corrosion making it not compatible with UHV, platinum due to its high cost. Tantalum (54 W/(m K)), tungsten (175 W/(m K)) and alloys of molybdenum (142 W/(m K)) have high thermal conductivities and corrosion resistance, but are however quite challenging to machine.[1]

Higher grade stainless steel alloys like 1.4404 / AISI 316L contain 2 % to 2.5 % of molybdenum are preferred and – being used in industrial machines and applications for handling mercury – known to be mercury corrosion resistant. Note that lower grade stainless steel AISI 304 should be avoided as it can be embrittled by mercury contact at room temperature [112]. With a rather low heat conductivity of about 15 W/(m K) AISI 316L is not the ideal choice for cooling, but easily to source and machine, as well as proven vacuum compatible and therefore adding no additional unknown variables a new material might do. Depending on the surface finish it also features a quite low thermal emissivity, which is important for reducing the thermal heat load of the source cup.

Alternatively, applying a corrosion resistant coating on for instance oxygen free copper was discussed. Later with the observation of corrosion of copper vacuum gaskets, see section 3.2, chromium (15 W/(m K)) plating copper via evaporation was investigated as a potential corrosion inhibitor. This could have been a viable alternative to the choice made here.

3.1.2 In-vacuum cooled source chamber

The first generation source chamber, as shown in figure 3.2, consists of a small 9 mm inner diameter stainless steel 316LN cup with a volume of 585 mm^3 that can hold up to 8 g of mercury. It is contacted to a four-stage TEC that is supported by water cooling consisting of a custom copper vacuum feedthrough transferring the heat to a spiral-shaped aluminum water cooler. The cup features a 20 mm diameter brim, which together with a ring-shaped stainless steel disc forms a differential pumping stage, that reduces the amount of mercury entering the lower part of the source chamber. This protects the copper heatsink as well as the metallic components of the TEC and other electronics housed here and prevents condensation of mercury on the TEC itself.

Vacuum pumping

The source chamber is pumped by a small IGP[2] connected via a CF16 vacuum flange on the side of the chamber. The pump has a specified pumping speed of 2 L/s for nitrogen, the pumping speed for mercury was not quantifiable, but it is expected to be noticeably lower than this. It is known that mercury is pumped only inefficiently by IGPs, poisoning the pump, leading to overheating and complete failures especially when exposed to high vapor pressures in the 1×10^{-4} mbar to 1×10^{-5} mbar range [113, 114]. The authors of [113] state, that “mercury atoms do not combine with titanium and are only loosely trapped on the anode by the sputtered titanium film; repeated temperature changes caused by operating the pump in this pressure region are sufficient to cause the titanium film to break away”. During the operation of the source chamber this behavior could be reproduced. Due to a power outage, the TEC cooling of the mercury sample failed and the vapor pressure in the source chamber rose to about 1×10^{-3} mbar which overheated the pump. It could be brought back to life for a short

---

[1] Limited by our mechanical workshop capabilities. Tantalum for its hardness and gumminess and tungsten both for its hardness requiring high strength tungsten carbide tools and for its dust to cause irritations of the lung and mucous membranes.

[2] Agilent VacIon 2 L/s ion pump 9190520.

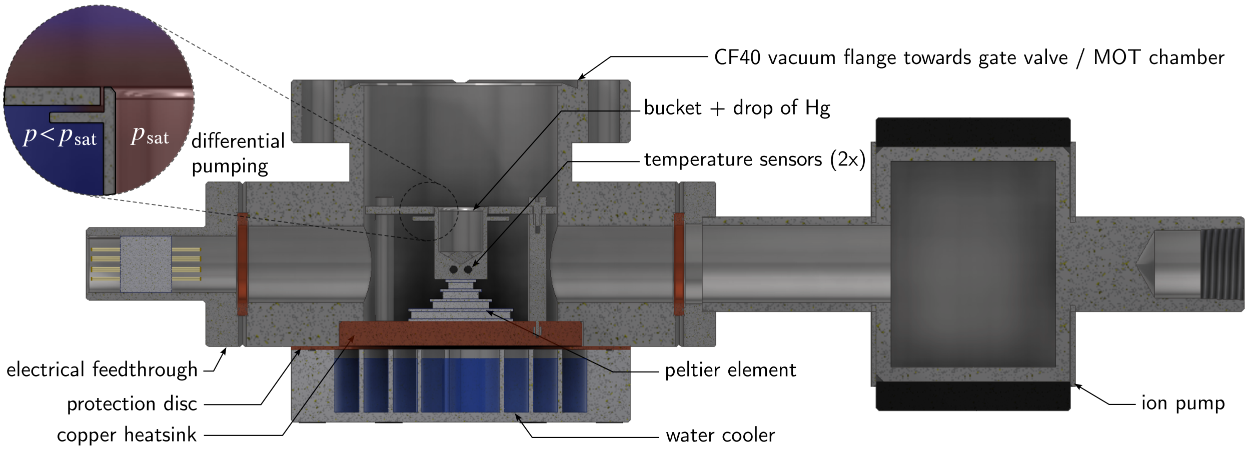

Figure 3.2: CAD render of the first generation source chamber design. A drop of mercury is contained in a small 9 mm inner diameter stainless steel cup cooled by a four stage TEC, which is contacted to a copper heatsink supported by an aluminum water cooler. Components are contacted via UHV compatible epoxy to each other and to the 316LN stainless steel vacuum chamber. A ring shaped copper disc protects the glue from the erosion through the water. Two cylindrical PT100 sensors monitor the temperature close to the base of the bucket. Two lateral CF16 flanges host an electrical feedthrough and a small 2 L/s IGP. The electronics are protected from the corrosive mercury vapor by a differential pumping stage consisting of a brim at the cup and a ring shaped stainless steel disc.

time by heating the pump to above 80 °C for a few hours during which the cooling of the TEC was ramped up again. Additionally, the pump required to be high potted by applying 7 kV of voltage – two times the normal operation voltage – to its electrodes for a few seconds, which was repeated multiple times in a row and is expected to remove the high spots in the anode material caused by the loosely trapped mercury via spark discharge. Over the following year the pump performance degraded again multiple times, which required repeated rounds of high potting. Alternatively gentle hits on the pump body (with removed magnet) with a hammer showed similar improvements, probably removing the flaky anode surface mechanically.

To protect the IGP, the authors of [113] suggest the use of a refrigerated vapor trap baffle, which operated at −70 °C successfully protected the IGP at higher chamber vapor pressures. Liquid nitrogen cooled cryoshields are also used in molecular beam epitaxy (MBE) applications where much higher amounts of mercury are used in high vacuum (HV) to UHV environment [115, 116]. Adding a TEC powered cold point pump to the main vacuum chamber was indeed already discussed in the planning phase of the experiment, but discarded for added complexity and increased outgassing. After replacing the IGP in the source chamber and with reliable cooling of the source cup, no additional pump failures could be observed, since the source itself acts as the cold point trap. Adding a redundant power supply together with an uninterruptible power supply could add more safety here. Future source chamber designs, see outlook, potentially operating at higher vapor pressures however might need to revisit this problem.

Temperature monitoring & interlock

The cup is additionally equipped with two 1.3 mm diameter, 10 mm length platinum resistance PT100 temperature sensors[1] glued into the bottom of the cup using EPO-TEK H74. To reduce the thermal load via the electrical contacts to the bucket, the temperature sensors are crimped to 0.1 mm thin Kapton isolated copper wire[2] and its open leads isolated using vacuum compatible Kapton tubes[3]. Accounting for the added electrical resistance of the wires this setup allows monitoring the temperature of the source precisely. All in-vacuum contacts are crimped to a 12-pin UHV electrical feedthrough[4] housed in a stainless steel CF16 flange.

One of the temperature sensor is hooked up to a programmable temperature monitor and limiter[5] that allows to set a critical upper temperature for interlock triggering a pneumatic operated all metal gate valve[6] separating the source from the main vacuum chamber in case of cooling failures. The interlock also triggers more directly in case of a cooling water failure, which is monitored via an adjustable flow meter watchdog. The other source temperature sensor is connected to a lab surveillance system and can send a warning to the user in case of temperature changes.

Thermoelectric cooling and heat load estimation

TECs are based on the Peltier effect, where a current flowing through a pn-doped semiconductor interface induces a temperature difference by either absorbing or releasing heat when jumping the gap between the two conduction bands. They are mostly manufactured in form of many few millimeter thick semiconductor stacks that are sandwiched between two thermally conductive sheets of aluminum or beryllium oxide. Their size limits the achievable temperature difference and the heat load that can be removed. The efficiency of thermoelectric materials is quite low; the main limiting effect is the resistive heat generated by the TEC itself. TEC elements are specified by the maximum heat load $Q_{\max}$ they are able to cool at a temperature difference of $\Delta T \to 0\,\mathrm{K}$ and by the maximum temperature difference $\Delta T_{\max}$ they can reach in the limit of negligible heat load $Q = 0\,\mathrm{W}$. Stacking TEC elements (in manufacturing) can increase the required temperature difference, while reducing the cooling power, since the resistive heat load of the upper – mostly smaller – stages need to be dissipated as well. A TEC achieving large temperature differences of up to 100 K is at the limit of Peltier based cooling even if the heat load is reduced to a few hundred mW. For this in vacuum operation is crucial, since the added thermal load from convection in air between the cold and hot side of the TEC is dominating the otherwise really low intrinsic conductivity of the thermoelectric semiconductor materials.

The heat load of the mercury source cup is the sum of the thermal conductivity through the TEC element and the electrical connections of the temperature sensors as well as the radiative heat load from the warm chamber walls, that dominantly sit at room temperature. The thermal conductivity of the electrical connections is reduced by the choice of the wire diameter (0.1 mm) and is in the order of 0.1 mW for a temperature difference of 100 K and a 100 mm long connection to the room temperature outside and can therefore be neglected. The radiative heat load can be estimated from the Stefan Boltzmann radiation law. Assuming two gray surfaces that form an enclosure, the transferred heat

---

[1] Allectra 343-PT100-1.3-B. [2] Allectra 311-KAP-010-5M [3] Allectra 312-KAP-TUBE-03-300. [4] Vacom CF16-VB-2B-12. [5] JUMO safetyM TB/TW08. [6] VAT 79043C.

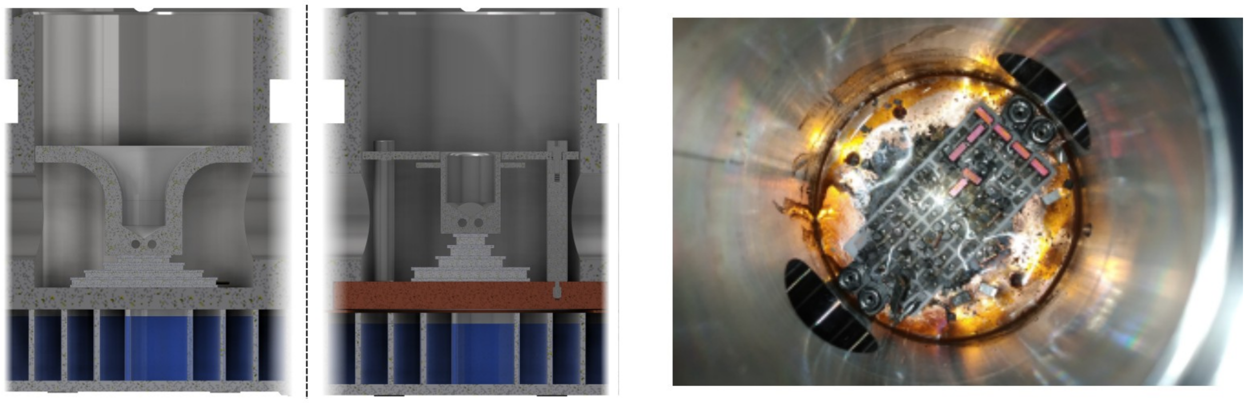

Figure 3.3: First generation source chamber construction and challenges. Comparison of the two source chamber cups: The first design (left), where the differential pumping is realized by the cup rim and the surrounding 38 mm inner diameter CF40 flange port itself and the improved design (center), reducing the thermal heat load of the cup by reducing the overall surface area. The differential pumping stage is formed by the added brim and a surrounding stainless steel disc, as displayed also in figure 3.2. Gallium corrosion of the thermoelectric cooler made of aluminum oxide (right). The liquid metal used as a thermal interface material between copper heat sink and TEC attacked and broke the bottom and top surface of the TEC leaving a clear liquid in the vacuum chamber behind. After removal of the TEC a silvery stain remained on the copper surface that required mechanical removal.

rate $\dot{Q}_{12}$ from surface A_1 at temperature T_1 and surfaces A_2 at temperature T_2 is given

$$\dot{Q}_{12} = \frac{\sigma \left({T_1}^4 - {T_2}^4\right)}{\frac{(1-\epsilon_1)}{A_1\,\epsilon_1} + \frac{(1-\epsilon_2)}{A_2\,\epsilon_2} + \frac{1}{A_1\,F_{12}}} \tag{3.2}$$

where σ is the Stefan Boltzmann constant and ϵ_i the emission coefficient of the gray surface i ($\epsilon = 1$ for a blackbody) [117]. F_{12} is the radiation view factor of the two surfaces, describing the fraction of light emitted from surface 1 reaching surface 2 due to geometric constraints with $A_1\,F_{12} = A_2\,F_{21}$. These view factors are tabulated for typical geometric shapes and arrangements [117, 118] or can be calculated numerically via ray tracing. With a simplified geometry of the cup and its surrounding, assuming an emissivity of $\epsilon = 0.3$ for the stainless steel walls, the heat load of the source chamber at a temperature of −80 °C is estimated to be about 250 mW. This improved the here shown source cup design by reducing the overall surface area over a previous attempt, where the differential pumping stage was formed by a much larger cup rim and the surrounding wall of the CF40 vacuum port, as shown in figure 3.3.

Heatsink design

With a high thermal conductivity and heat capacity water cooling is the preferred choice for removing the thermal heat load of the TEC element. A spiral shaped cooling loop of rectangular cross section (5 mm wide, 13 mm height) was milled into an aluminum water cooler attachment, that mounts to the underside of the vacuum chamber sealing with an FKM o-ring. Two threaded water fitting bores allow connection of the heatsink to the installed house cooling water loop – providing 17 °C cold cooling water at a pressure difference of about 2 bar. We later replaced the house cooling water loop with an external water-to-air chiller[1] after identifying galvanic corrosion due to metal mixes in the loop.

With the TEC elements described below dissipating about 50 W to 80 W at their hot side we require the thermal resistance of the heatsink to be ≤50 mK/W at a target temperature difference of in versus outflowing water of $\Delta T \leq 3\,\mathrm{K}$. With a cooling channel length of ~0.3 m and an effective hydraulic diameter of ~9 mm we estimate a required water flow of about 1.7 L/s. Following the Darcy-Weissbach equation for the worst case assumption of turbulent flow a pressure difference of $\Delta p = 1.4\,\mathrm{bar}$ is therefore required[2], which is sufficiently provided by the house cooling water and the chiller.

In the first iteration the 5 mm thick interface between the TEC and the water cooling loop was integrated into the chamber design itself and therefore made out of stainless steel to avoid any amalgamation. The thickness was chosen to avoid bulging of ~50 mm diameter disc shaped chamber bottom due to the 1 bar atmosphere pressure as simulated by a finite element method (FEM). Under testing this however showed insufficient cooling performance and quickly overheated the TEC. We later estimated the thermal resistance to ≥ 160 mK/W – further increased by the thermal contact material discussed in the next paragraph – not compatible with the design requirement and replaced the stainless steel bottom with one made out of copper. This improves thermal conductivity and thermal resistance by a factor of 24. An epoxy seal (EPO-TEK H74) of the recessed copper plate allowed a vacuum-tight connection. As we however observed erosion of the epoxy from the water flow, a 0.5 mm thin rectangular copper plate with a circular hole covering just the circular epoxy interface was machined and contacted via heat conductive paste[3] to the chamber. In hindsight mechanically connecting the copper baseplate to a stainless steel CF knife edge would have possibly been the better solution.

In-vacuum thermal contacts

Options for thermal heat contacting the TEC with cup and copper heat sink are much more limited in an UHV environment than at atmospheric pressure. Options exist in form of low viscosity thermal pastes, heat curable two-component epoxies, soft metals like indium or gallium, or vacuum-compatible solder. Except for the liquid metal options and vacuum-compatible soldering, most of the potential contact materials have a thermal heat conductivity one to two orders of magnitude lower than typical non-vacuum compatible heat conductive pastes and epoxies. Additionally to the heat conductivity, the thermal expansion coefficient is equally important and needs to be matched to the materials contacted to avoid stress induced damage during temperature changes. In this work, four options were investigated: vacuum compatible solder, heat curable epoxy, as well as gallium/indium based liquid metal and thermal contact pads.

Soldered connection Soldering using gold-plated TEC was investigated, but discarded due to its complexity and no external company or research center could be sourced for manufacturing. It is a proven solution used for instance in electron-multiplying charge-coupled device (EMCCD) cameras,

---

[1] SolidState Cooling Systems TCube Edge, 240 W cooling capacity, 2 L/min flow rate. [2] Darcy-Weissbach is an empirical generalization of the Hagen-Poiseuille equation for all flow regimes. For the heatsink described here we estimate a Reynolds number of $\mathrm{Re} \approx 4344$ and assuming smooth pipes (Karman-Prandtl equation) a Darcy friction factor of $\Lambda \approx 11.2$ for the approximatively turbulent flow regime ($\mathrm{Re} > 4000$). The estimated pressure difference requirement in laminar flow regime is orders of magnitude smaller than the given value.

[3] Arctic Silver 5 (8.9 W/(m K)).

like the ANDOR iXon 3 camera used for imaging (see section 4.4), whose sensor chips allows Peltier based cooling in vacuum down to −100 °C to reduce dark counts. Connecting large surface areas for UHV applications however ideally requires a vacuum soldering oven to avoid trapping air or flux in between the two surfaces and all soldered parts needs to be properly cleaned from any remaining flux. Regarding the temperature of the solder used in the construction of the TEC itself caution need to be taken by precise temperature control and selection of low temperature solders, like 117 °C indium/tin or 183 °C tin/lead based solder. It might be a viable option if the soldering process is investigated further.

Liquid metal interface High thermal conductivity can also be realized using an alloy of gallium and indium. The one tested here[1] features a melting point below room temperature (8 °C), but UHV compatible vapor pressures even at high temperatures ($<1 \times 10^{-8}$ mbar at 500 °C). With a specified thermal conductivity of 32 W/(m K) it seemed to be an ideal choice for the application here and showed promising performance in first tests. To our surprise it however strongly corroded the TEC used for testing as shown in figure 3.3. Leaving it over the weekend in vacuum, the liquid metal attacked, weakened and broke the TEC surfaces and left a clear liquid behind. While gallium corrosion of aluminum is known, a reaction with the chemically stable aluminum oxide Al_2O_3 substrates or electronic components (e.g., metal interconnects) of the TEC was not expected.[2] This also ruled out the further use of indium gallium alloy based thermal pads[3], that after melted above 60 °C promises a thermal conductivity of 125 W/(m K) and in first testing showed promising cooling performance.

Heat-conductive epoxies for use in UHV The remaining option that could be realized at location was therefore the use of UHV compatible thermal conductive epoxies. Most heat curable epoxies however have rather low thermal conductivity of 1 W/(m K) or below. The best option found is EPO-TEK H74, a heat curable epoxy with a specified thermal conductivity of 1.3 W/(m K) and a linear thermal expansion coefficient of 21×10^{-6} m/(m K) roughly matching the thermal expansion coefficients of oxygen free copper ($\sim 17 \times 10^{-6}$ m/(m K)) and stainless steel 316 ($\sim 17.5 \times 10^{-6}$ m/(m K)), and just slightly above the expansion coefficient of aluminum oxide (4.5×10^{-6} m/(m K) to 10.9×10^{-6} m/(m K)). The product was also recommended by the manufacturer over the available EPO-TEK H72 used in references [104, 105]. The epoxy was mixed, carefully degassed under vacuum for at least 20 min and applied to the previously cleaned parts, which were held in place with small clamps, applying a slight pressure to the surfaces during curing. This should allow minimum glue thickness, just filling in the voids of the joining surfaces, that were machined as flat as possible. The epoxy then was cured in air in a self-built oven, where the temperature was ramped slowly (about ±1 K/min) to avoid any additional stress formed at the contact interface. Curing temperature were selected to not melt the internal solder of the TEC, but at least over 130 °C to stay as close to the recommended cure of 150 °C for 1 h.

---

[1] Allectra 317-TCL-1. [2] Gallium can hypothetically diffuse through micro-cracks or grain boundaries and react with unbound pure aluminum. Here the vacuum environment could have enhanced gallium wetting and surface diffusion. [3] Allectra 317-TCP.

Thermoelectric cooler selection

In this work, multiple TECs, heat sink configurations, and thermal contact materials were tested. The first TEC selected for the application was a four-stage, $\Delta Q_{\mathrm{max}} = 5.0\,\mathrm{W}$, $\Delta T_{\mathrm{max}} = 124\,\mathrm{K}$ cooler[1] featuring a 27 mm × 27 mm square baseplate and 10 mm × 10 mm cold top plate. The TEC was specifically selected for our application by the manufacturer for a heat load of 0.25 W up to 0.75 W and a target temperature of −90 °C given a 17 °C cold heatsink supporting an expected power usage of about 35 W to 43 W. Reaching just −23 °C at a TEC power of 17 W indicated that the EPO-TEK H74 contact and stainless steel heat sink, as shown in figure 3.3, was not sufficient.

A stack of two TECs[2] contacted using gallium indium based thermal pads reached temperatures of only −18 °C at a combined input power of 19 W. Exchanging the thermal pad by gallium indium based liquid metal reached a temperature of down to −61 °C at an input power of 27 W, but failed due to gallium bases corrosion as described above.

Finally, with the redesign of the source cup to reduce the thermal heat load and the updated copper heatsink, a Marlow SP2394 ($\Delta Q_{\mathrm{max}} = 4.5\,\mathrm{W}$, $\Delta T_{\mathrm{max}} = 130\,\mathrm{K}$) TEC was contacted using EPO-TEK H74 heat conductive epoxy. Due to the melting point of 138 °C of the internal solder used in the TEC, a curing temperature of 130 K was selected and to avoid any thermal stress a heating ramp of about 1 K/min was chosen. Without the source cup just contacting a PT100 temperature sensor to the top, this combination reached a promising temperature of −100.6 °C at a TEC input power of 30 W (4.0 A, 7.5 V). With the source cup attached afterward (curing at 130 °C for 1.5 h) and measuring the temperature within the cup the minimum temperature reached was −57.4 °C at an input power of 13 W (2.3 A, 5.7 V). After fixing a vacuum leak caused by erosion of the epoxy seal through the water cooling, the cooling performance was reduced again due to the thermal cycling when curing the additional epoxy.

Conclusion

Obtained vacuum & mercury vapor pressure The final performance of the source chamber with about 0.5 mL (≈6.8 g) mercury is shown in figure 3.4. It reaches a minimum temperature of −55 °C at an input power of 18 W. With a resulting background pressure in the low 1×10^{-8} mbar range, as read by the small IGP in the source chamber, this cooling performance was considered to meet the requirements for magneto optical trap operation from the background gas. As the IGP reading does not necessarily give the mercury vapor pressure (as the pumping speed is unknown), figure 3.4 also shows a measurement of the partial mercury pressure analyzed by a quadrupole mass spectrometer. It is installed on the main vacuum chamber close to the primary ion getter vacuum pump, shown in section 3.2, and connects to the source chamber with a molecular flow regime vacuum conductance of about 9.7 L/s. The measurement scaling with temperature agrees relatively well with the IGP reading as shown by scaled nonlinear fits of the vacuum pressure temperature dependency, as given in figure 3.1.

Long-term reliability The here presented source design allowed for efficient cooling down to −57 °C and enabled magneto-optical trapping from the background gas (chapter 4) and was used both

---

[1] TEC Microsystems 4TC31-0116-155.D. [2] Quick-Cool QC-63-1.0-3.0 ($\Delta Q_{\mathrm{max}} = 14.8\,\mathrm{W}$, $\Delta T_{\mathrm{max}} = 100\,\mathrm{K}$) as the bottom and Quick-Cool QC-35-1.4-3.7 ($\Delta Q_{\mathrm{max}} = 9.6\,\mathrm{W}$, $\Delta T_{\mathrm{max}} = 71\,\mathrm{K}$) as the top TEC.

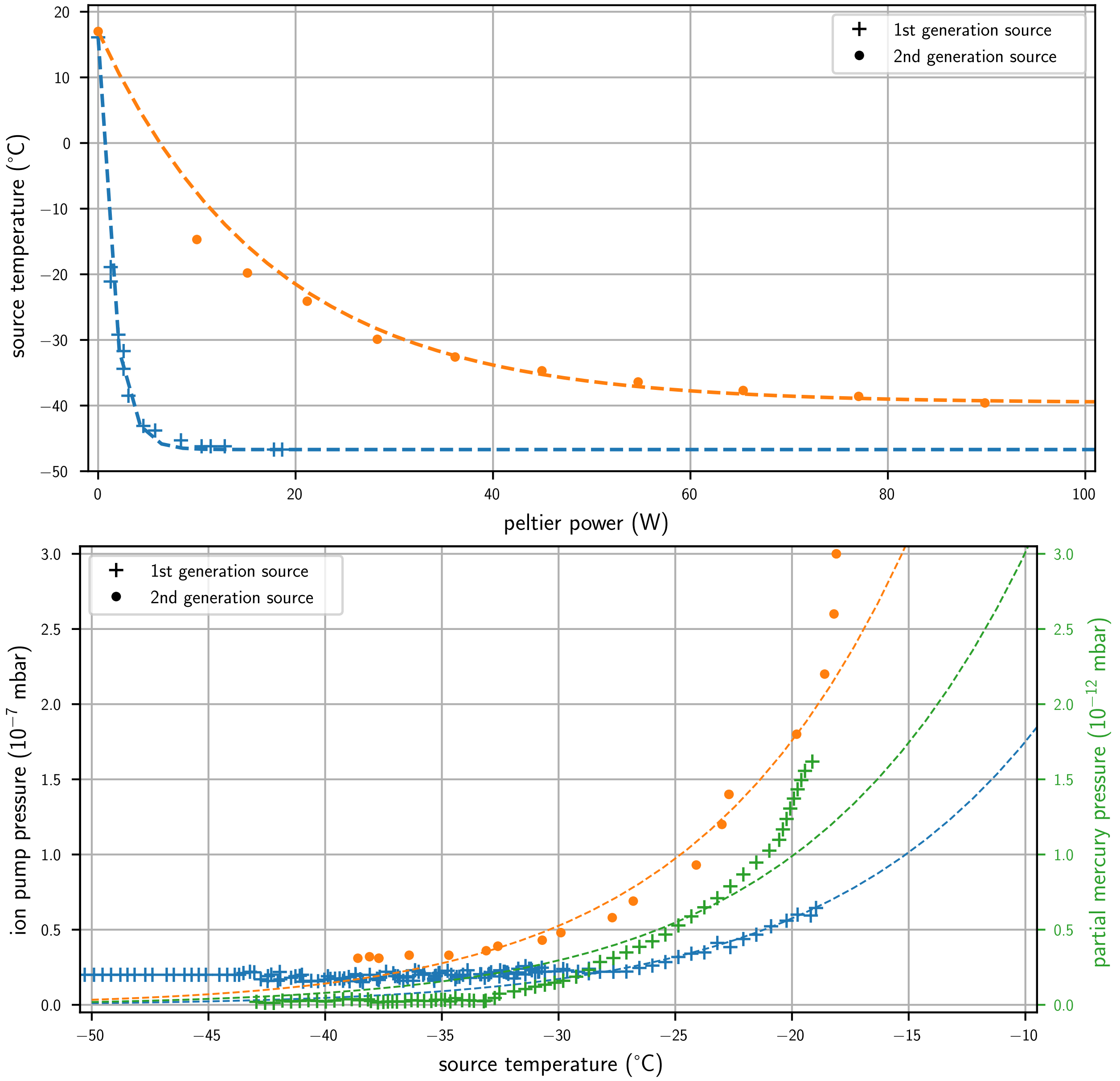

Figure 3.4: Cooling performance of the first (cross, blue) and second generation (dot, orange) source chamber. Source chamber temperature in dependence of peltier power (top) and chamber pressure in dependence on temperature (bottom) as recorded by the small IGP. For the first generation source, we also show a quadrupole mass spectrometer measurement of the partial mercury pressure in the main chamber (cross, green).

for realization of the first optical dipole trap (ODT) (chapter 5) and the first isotope shift spectroscopy (ISS) of laser cooled mercury (chapter 6). Its long-term reliability was however a bit troublesome and the source chamber failed completely after two and a half years of continuous operation. The main limiting factor appeared to be the thermal interfaces between the bucket, TEC element and heat sink, that due to the greater differences in the thermal expansion coefficient was not sufficiently stable against thermal shocks. These shocks were especially introduced by two power failures in the lab, that first reduced the cooling performance by a few °C, and the second completely led to detachment of the source bucket from the TEC element.

3.1.3 A collimated atomic beam source for mercury

In need of a replacement for the broken source, we reviewed the failure points listed above and created a new design for the source chamber. In the long term, we also aim to upgrade the vacuum chamber and install a ZS for more efficient MOT loading, as described in section 7.3.1. To this end, an extension of the source to a beam source of cold mercury is required. This results in a slight reduction of the source chamber requirements in terms of cooling performance, as the new source can be separated from the main UHV/XHV chamber via a strong differential pumping stage. For reliable long-term operation of this source, we decided to not rebuild the old source, but implement an updated source chamber design with optional integration of a micro-nozzle array for creation of a collimated atomic beam.

Source chamber design

With the main limitation of the previous source design being the thermal contact in vacuum, the new source chamber design places the TEC outside the vacuum to improve thermal performance. The second generation source is shown in figure 3.5. It is based on a two-stage TEC[1], that cools a small vacuum container made out of stainless steel 316L holding the mercury. With an outer size of $(30 \times 30 \times 18)\,\mathrm{mm}^3$ and a wall thickness of 3 mm the container is designed to both withstand deformations induced by the atmospheric pressure and to generously hold up to 45 g of mercury. A ~38 mm long, $7\,\mathrm{mm} \times 0.5\,\mathrm{mm}$ (OD × wall thickness) sized tube connects the source chamber to a CF16 vacuum flange and a CF16 to CF40 flange adapter. This acts both as a differential pumping section with a molecular vacuum conductance of ~0.7 L/s and as a thermal insulator with a thermal resistance of ~248 K/W bridging between the TEC cooled and room temperature side. The container is constructed from two pieces, with the top plate being tungsten inert gas welded to the connecting tube from the vacuum side and featuring a large chamfer to allow deep weld penetration to avoid any virtual leaks.

Thermal contact between TEC and stainless steel container is established via a sub-zero temperature compatible thermal paste, where we tested a few options including liquid metal and observed up to 4 °C performance difference. We finally chose an aluminum, zinc-oxide based thermal paste[2]. The $(40 \times 40)\,\mathrm{mm}^3$ large TEC hotside is contacted to a water-cooled copper heatsink with a similar spiral loop channel design as before, see figure 3.5, designed to dissipate the $\leq$100 W heat load. The heatsink is again backed by the water chiller described before. While not used permanently, operating the chiller with a 2:1 water to 1, 2-propandiol mixture and insulated tubing this even allowed reducing the heatsink temperature by up to 15 K, resulting in about 5 K lower source temperatures.

The surrounding of the TEC element and source container is enclosed in an aluminum tube, that is tightly sealed[3] to the main CF40 vacuum flange and the copper heat sink. Electrical connections for the TEC element and a PT100 temperature sensor are guided through a small bore in the heatsink, that is also sealed once the cables are in place. This shell is then actively purged by dry nitrogen to prevent excessive formation of ice around the cooler.

---

[1] Adaptive (European Thermodynamics Ltd) AP2-162-1420-1118, $P_{\mathrm{max}} = 29.3\,\mathrm{W}$, $\Delta T_{\mathrm{max}} = 95\,°\mathrm{C}$. [2] Thermal Grizzly Kryonaut, −250 °C to 350 °C. [3] Using Würth Bond and Seal Power structural and elasticated adhesive.

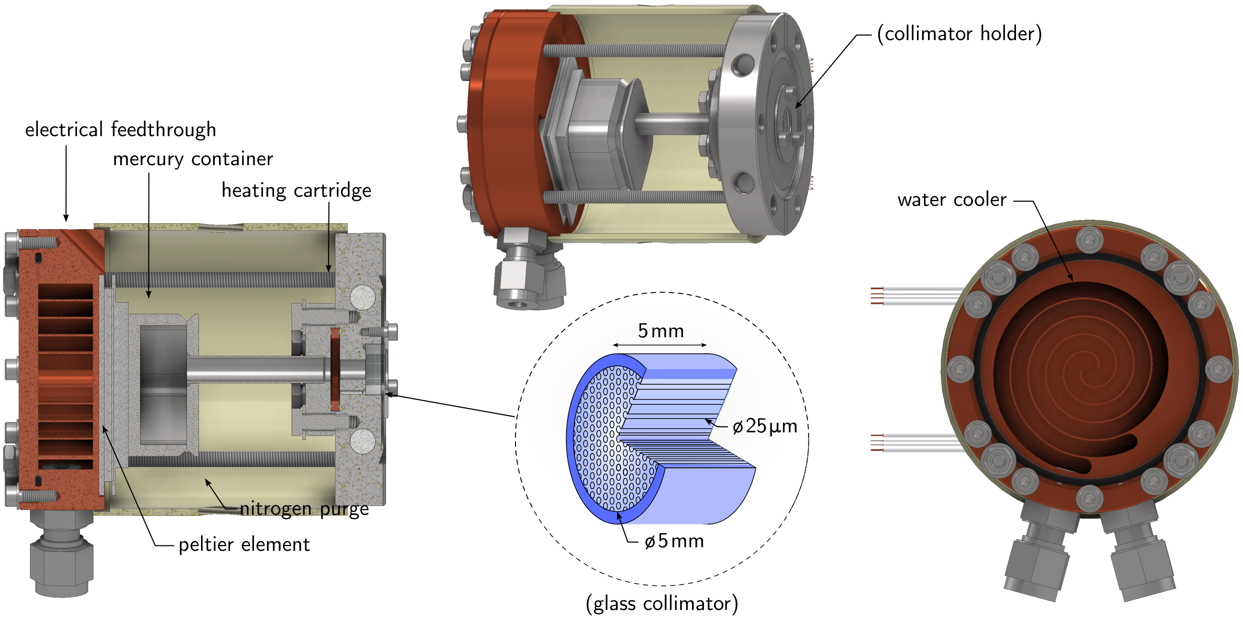

Figure 3.5: CAD render of the second generation source chamber. Detailed description see text.

Cooling performance

We successfully installed the upgraded source chamber onto the MOT chamber, as shown below and operated the source for more than two years for MOT operation from the background gas and first steps towards quantum degeneracy of mercury trapped in a high power optical dipole trap. The cooling performance is also shown in figure 3.4, showing the temperature as measured by a PT100 temperature sensor attached to the front of the mercury container and the pressure being monitored by the small IGP that pumps the source section. The plot shows the raw temperature measurement of the two-wire connected platinum resistance temperature detector, where the cable adds about 1 K of temperature offset. We further estimate that due to a temperature gradient in the stainless steel container, the temperature sensor measures about 4 K to 5 K higher temperatures than the coldest point in the source chamber. With this information the source chamber performs only about 5 K to 10 K worse than the lowest temperatures reached in the previous in-vacuum cooled design, while keeping the overall system more long-term reliable and serviceable. This is more than sufficient for ZS operation, as discussed below and allowed very similar background pressures in the MOT vacuum chamber for loading from the background gas, as also indicated by the IGP reading. We did not observe any big changes in MOT lifetimes between the two source chamber implementations.

Outlook – Atomic beam generation

Collimated atomic beams for ZS operation are commonly generated using either mechanical apertures or microchannel arrays, which spatially filter thermal atomic vapor to produce a directed flux. While also used for ZS operation, aperture designs are especially found in the semiconductor industry for molecular beam epitaxy and other applications, where uniform vapor deposition on semiconductor targets is required. In comparison, microchannel arrays [119–121] offer enhanced collimation by allowing only atoms with nearly parallel trajectories to exit. This reduces the transverse velocity spread, thereby increasing beam brightness. Increasing the channel count [122] further enhances this effect. Compared to simple pinhole apertures, microchannel arrays provide better angular selectivity and higher atomic flux within the capture angle of the slower [123, 124]. Lithographically etched microchannel structures [125, 126], while currently limited to two-dimensional, planar silicon wafer structures, offer tailoring of the spatial velocity distributions and therefore allow for more controlled beam shaping.

Microchannel arrays are often constructed from stacking of needle tubes with microscopic inner diameters (see for example [124]). The here presented design features a microscopic nozzle array made out of glass instead. These are microscopic glass structures precision-engineered using techniques like laser micromachining, wet etching, or anodic bonding. This enables reproducible nozzle geometries, large channel packing densities and minimal beam divergence. Due to the chemical inertness, thermal stability, and smooth internal surfaces of glass, these nozzles are also well-suited for high-vacuum and high-temperature environments. We do not expect any chemical reaction or wetting of the glass surfaces by mercury.

Micro-nozzle glass collimator We purchased two cylindrical 13 mm diameter, 5 mm long Borosilicate glass capillary plates[1] with 50 µm and 25 µm diameter holes respectively. With a specified nominal opening area of 50 % to 60 % they feature about 5500(500) and 22,000(2000) cylindrical microchannels respectively within a 5 mm diameter active aperture, that we expose to the atom source, as shown in figure 3.5. The capillary plate is mounted in a cylindrical pocket in the CF40 vacuum flange, held by a thin stainless steal disk and three vacuum-vented socket-head screws. The rim of the plate, which does not feature microchannel holes, is additionally vented by a groove and small bore towards the source.

As we require a temperature gradient between source and collimator to avoid clogging [124], two cylindrical 4.5 mm diameter, 40 mm long heating cartridges[2] are installed into the CF40 vacuum flange and allow for a source independent temperature control. At elevated temperatures they can also be used both for initial vacuum baking of the flange and due to the high vapor pressure of mercury also for freeing the nozzle if channels would get clogged.

Flow regime For analysis of the flow dynamics we need to estimate the flow regime and mean free path length ℓ at the given nozzle temperature and source vapor pressure. Empirical data for mercury found $\ell\, p = 3.1 \times 10^{-5}\,\mathrm{m\,hPa}$ at a temperature of 0 °C [127]. With a scaling of $\ell \propto T/p$, this gives a mean free path length $\ell \approx 9\,\mathrm{mm}$ at a nozzle temperature of 30 °C. This agrees with the value of $\ell \approx 7\,\mathrm{mm}$ interpolated from the graph in reference [128]. Another approach is to determine the mean free path from a hard sphere approximation of the colliding Hg atoms. Assuming a diameter d_0, the mean free path is then given as [128]

$$\ell = \frac{k_B T}{\sqrt{2}\, p\, \sigma} \tag{3.3}$$

with $\sigma = \pi\, d_0^2$ the collisional cross-section. With a Van der Waals radius estimate of $d_0/2 \approx 1.55\,\text{Å}$ [129] we obtain $\ell \approx 25\,\mathrm{mm}$, which is much larger than the values above. We can also estimate the cross-

---

[1] Collimated Holes Inc. capillary plates.

[2] HORST S/HS-4,5/40/80/24-B high power heat cartridge, 80 W, 24 V, TL/AP-300 (2-pole), $T_{\mathrm{max}} = 250\,°\mathrm{C}$.

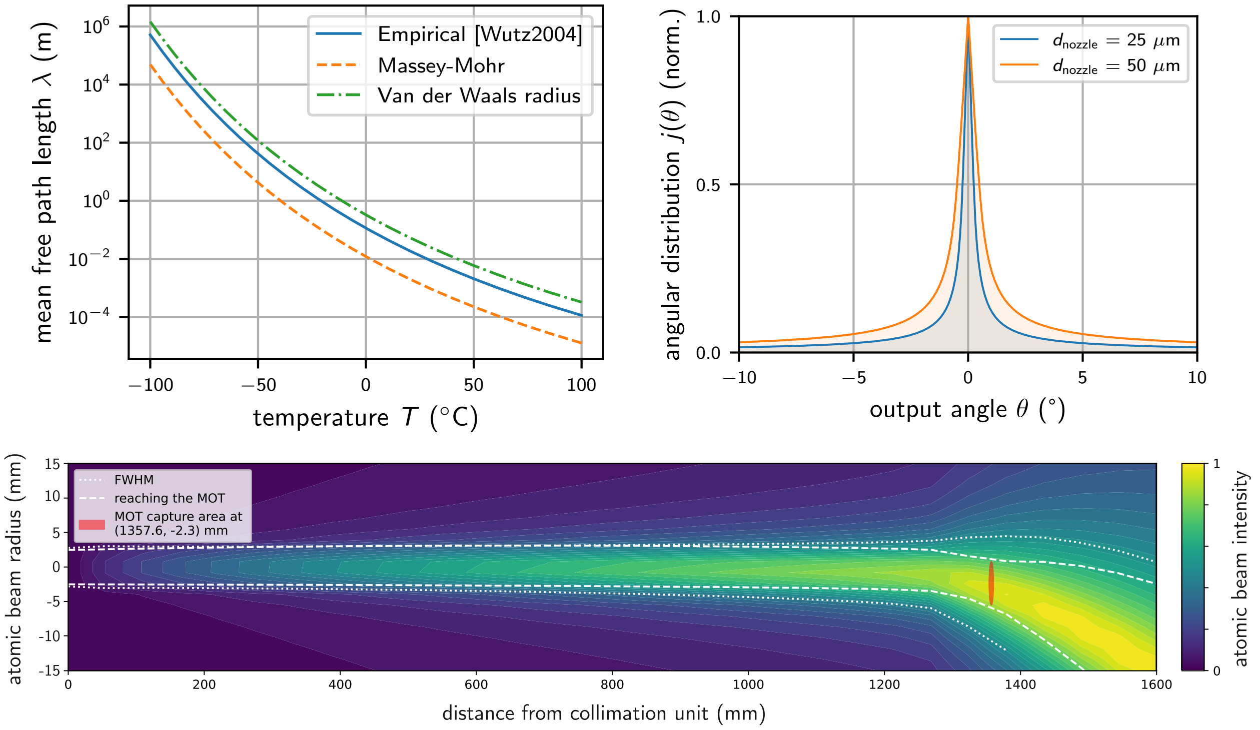

Figure 3.6: Mean free path of atomic mercury as computed from various methods (top left) and angular distribution of the collimated atomic beam flux of a single microchannel of length $L_{\text{coll}} = 5\,\text{mm}$ and temperature $T_{\text{coll}} = 30\,°\text{C}$ (top right). Simulation of the atomic beam propagation from source chamber microchannel nozzle through the ZS to the MOT (bottom). We assume 22,000 microchannels of $d_{\text{coll}} = 25\,\mu\text{m}$ inner diameter distributed over the source chamber aperture of 5 mm emitting under experimentally realistic parameters including gravitational sag, that displaces atoms by −1.9 mm to −5.1 mm along the vertical for the range of velocities ($v = 57\,\text{m/s}$ to $190\,\text{m/s}$) that can be captured by the combination of ZS and MOT.

section via the Massey-Mohr-formula[1] [131] $\sigma_S \approx 7\,(C_6/\langle v\rangle_{\text{th}})^{2/5}$, which gives $\ell \approx 0.9\,\text{mm}$ – a much smaller result. The mean free path is shown in dependence on the temperature in figure 3.6. From this we estimate the associated Knudsen number $\text{Kn} = \ell/D$ for the inner diameter $D \equiv d_{\text{coll}} = 25\,\mu\text{m}$ or $50\,\mu\text{m}$ as $\text{Kn} = 18$ to 1000 and for the length $D \equiv L_{\text{coll}} = 5\,\text{mm}$ as $\text{Kn} = 0.2$ to 5 and conclude that the nozzle channels operate in the molecular ($\text{Kn} > 10$) to transition $0.1 < \text{Kn} \leq 10$ gas flow regime. Following the description in reference [124] the resulting atomic flux per microchannel can then be estimated by obtaining the transmission probability from the Clausing factor and approximating the nozzle length as $L_{\text{eff}} \approx \sqrt{L_{\text{coll}}\,\ell(T)}$ for computation of the angular dependency. The latter is shown in figure 3.6, which is expected to slightly deviate from a purely molecular cosine emitter of collimation $\beta \approx d_{\text{coll}}/L_{\text{coll}} = 5.0\,\text{mrad}$.

We can then simulate the full atomic beam dynamics and estimate capturable atomic flux emitted by the source for Zeeman slowing. An example for atomic beam propagation is simulated for the

---

[1] The semi-empirical Massey-Mohr formula relates scattering cross-section σ_S and molecular ground state potential. From the C_6 Van der Waals coefficient – $C_6 = 392(4)$ au determined for the mercury dimer [130] – and the mean thermal velocity of mercury atoms $\langle v\rangle_{\text{th}}$ at the nozzle temperature, the resulting scattering length is $a = \sqrt{\sigma_S/(4\pi)} \approx 15.1\,a_0 \approx 8\,\text{Å}$. Note the use of atomic units: $\text{au} = E_h\,a_0^6$ with E_h the Hartree energy and a_0 the Bohr radius.

$d_{\text{coll}} = 25\,\mu\text{m}$ diameter microchannel plate with an active aperture of 5 mm and nozzle temperature of 30 °C and is also shown in figure 3.6. Next to the beam broadening resulting from the angular distribution, here we additionally take into account gravitational sag and transversal broadening mechanism through photon scattering of the ZS beam, that results in a three-dimensional random walk in velocity space. The explicit usage of the collimated beam source for Zeeman slowing will be discussed in more details in section 4.8.3, where we motivate the choice of the collimator design by comparing various nozzle diameter via a simulation of the capturable atomic flux from the calculations above, as shown in figure 4.24.

3.2 Magneto-optical trap vacuum chamber

The vacuum chamber used for the measurements presented in this thesis is shown in figure 3.7. As integrating mercury into UHV systems is still being studied and optimal vacuum pumping strategies unknown, in our first design we opted for a relatively compact and simple setup for learning about the system and its performance.

The central section for MOT operation and dipole trapping is an off-the-shelf stainless steel 316L cube with 70 mm edge length featuring six CF40 flanges for optical access. Four of these ports are directly equipped with UV fused silica optical viewports, as discussed in more detail below. The main chamber is surrounded by the magnetic gradient field coils, that fit tightly around the four corners, and all the optics used for atom trapping and investigation (not shown), their location restricting the rest of the vacuum chamber layout. Two custom-made 296 mm long CF40 distribution tubes each featuring three additional CF40 junctions connect to the rest of the vacuum components. An inverted magnetron Pirani vacuum gauge[1] and a Faraday quadrupole mass spectrometer / residual gas analyzer[2] are connected close to the main chamber for vacuum diagnostics. Pumping from atmospheric pressure to UHV is established by a combination of a ~50 L/s turbo molecular pump (TMP)[3] backed by a dry scroll roughing pump[4] (not shown), a titanium sublimation pump (TSP)[5] (TSP) and held by a ~55 L/s IGP[6]. To optimize pumping speed, the vacuum pumps are also mounted as close to the chamber center as the simple design allows. The estimated molecular regime vacuum conductance is about ~100 L/s for both the IGP and for the TSP.

The vacuum chamber is supported in a height of 250 mm over the optical table by water-jet-cut flange support clamps (not shown) made from stainless steel to match the thermal expansion coefficient of the chamber itself (as recommended in reference [122]). A four-point support of the vacuum flanges reduces stress on the flange welds and vacuum viewports. The clamps support as many flanges as possible and are mounted to the optical table with 1 in-diameter stainless steel pedestal posts. A low-profile support for the main chamber cube was added when upgrading the gradient field coils, as we identified the chamber center sagging under the additional weight.

---

[1] Agilent FRG-700 full range gauge (5×10^{-9} mbar to 1013 mbar). [2] Pfeiffer PrismaPro QMG, 1 to 300 u mass range. [3] Agilent TwisTorr 74 FS. [4] Agilent IDP-7 [5] Agilent 916-0050 TSP Filament Catridge, 2.7 g filament (85 % Ti, 15 % Mo), 0.09 g/h to 0.1 g/h sublimation rate. [6] Agilent VacIon Plus 55.

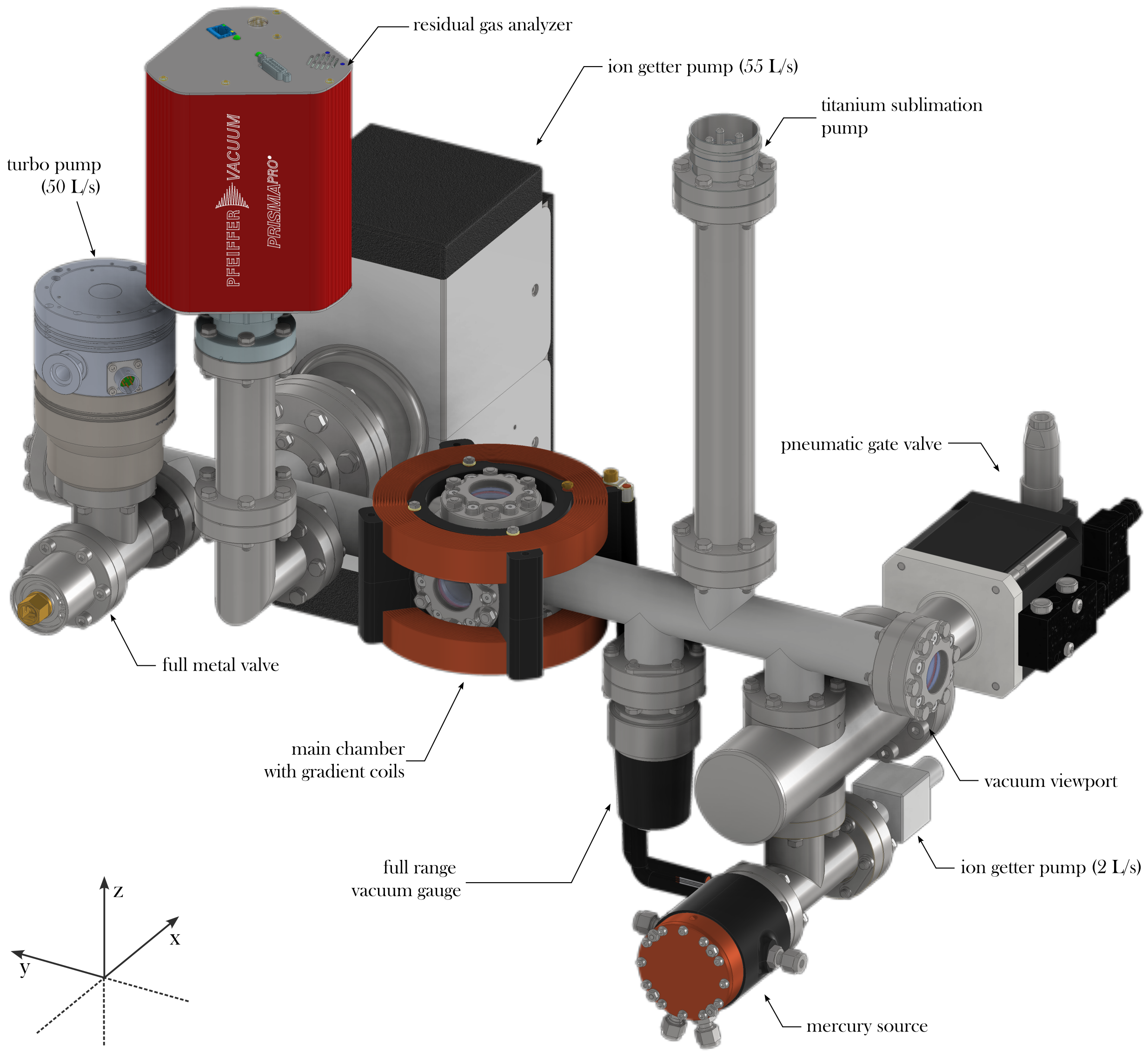

Figure 3.7: CAD render of vacuum chamber. For a detailed description see the text.

3.2.1 Ultra-high vacuum operation

Pumping from atmospheric pressure to UHV is initially established by the TMP backed by a dry scroll roughing pump. The chamber is then baked under vacuum at around 200 °C to 350 °C for a two to four weeks to remove water and reduce hydrogen outgassing from the steel walls of the chamber. For the initial bake, viewports are replaced by blind flanges to allow for higher temperatures, as the glass to metal seals are sensitive to thermal stress. While we replace the viewports under a clean, dry nitrogen atmosphere in self-built glove boxes, a subsequent additional bake-out at slightly lower temperatures for one to two weeks removes residual water, as confirmed by the residual gas analyzer. We ramp temperature by $\leq 1\,^{\circ}\mathrm{C/min}$ and wrap everything in layers of glass wool and aluminum foil to avoid thermal stresses in all connections. After baking the multiple rounds of activating the TSP allows reducing the chamber pressure by up to an order of magnitude while the chamber is still hot. After activation of the IGP and a slow cool-down vacuum pressures down to 1×10^{-10} mbar are achieved. The latest vacuum bake-out and residual gas analyzer (RGA) analysis can be found in reference [132].

Figure 3.8: Overview of CF DN40 vacuum gaskets used in the experimental setup. The first three – cube towards source, main chamber IGP and gate valve – are gaskets used in the vacuum chamber for about 4.5 years being exposed to mercury vapor. They show green to dark gray colored corrosion along the vacuum sided edge of the gasket, that also leave a corrosive residue on the underlying aluminum foil. The corrosion on the outer air-sided edge stems from baking. The last gasket shows a chromium plated copper gasket tested in the rebuild of the vacuum chamber to prevent mercury corrosion.

As already discussed above, pumping mercury with IGPs is challenging due to its high mass, as its acceleration is insufficient to penetrate deep into the anode material of the pump. Bigger reservoirs, loosely trapped under the anode surface, can break loose and create leakage currents and destroy the pump. However, so far no degradation of the large IGP could be observed.

Gaskets Since other groups did not communicate corrosion problems of standard oxygen-free copper CF gaskets so far, we initially did not consider any alternative. Analysis of copper gaskets after four and half years of use in 1×10^{-9} mbar mercury environment, see figure 3.8, however showed significant signs of corrosion and could be a source of vacuum leaks preventing deeper vacuum operation. Excluding Viton gaskets, so far no commercially available mercury-compatible gasket alternative could be found. Readily available nickel-, gold-, and silver-plated CF gaskets are all prone to amalgamation. To prevent amalgamation and potential UHV contaminations we chrome plated copper gaskets via evaporation deposition in vacuum, but the resulting gaskets were too brittle to conform to the stainless steel knife edges resulting in leak rates only compatible with HV. Future analysis of corrosion protection is advised.

Filling the source chamber Filling the mercury source with about 1 mL of mercury (about 13 g) is also performed under nitrogen atmosphere and after pre-baking the source beforehand. We pre-cool the Peltier slightly and fill the source via a clean needle syringe in a glovebox. As re-heating the mercury source container itself is not impossible, this opening can in theory introduce impurities like water vapor into the source chamber that are then cooled by the Peltier cooler. While RGA analysis showed no significant contaminations, considering the limited end pressure in the main vacuum chamber that we achieve this could – next to the amalgamation issues – be a potential virtual leak.

Conclusion Long-term operation of the chamber increased the vacuum pressure as read by the IGP up to 2×10^{-9} mbar, where stable operation was found. So far we could not identify whether the problem indeed originates from a (virtual) leak or a false reading in the IGP current. Later installation of an additional non-evaporable getter pump[1] with a quoted hydrogen pumping speed of 400 L/s to

---

[1] SAES Getter CapaciTorr Z 400.

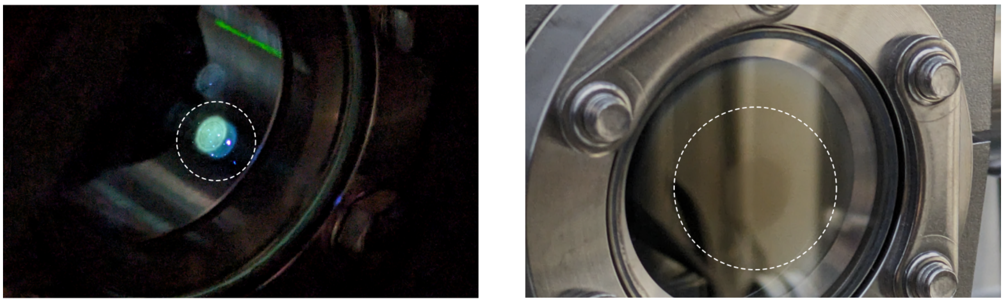

Figure 3.9: UV degradation on the AR coating of the vacuum viewports after four years of use, visible as a dark, blurry spot at the location of the MOT beams (right) and fluorescing under UV light (left).

the previous location of the RGA hoped to remove potential water vapor and hydrogen sources, but did improve vacuum quality only slightly. Better characterization of the atomic lifetimes in the optical dipole trap should hopefully answer this question.

3.2.2 Viewports

Low reflectivity vacuum viewports are critical for the realization of high power (hundreds of watt) optical dipole traps. However, AR-coated vacuum windows also strongly benefit MOT operation, polarization-sensitive spectroscopy, and EDM measurements.

For establishing magneto optical trapping we initially purchased vacuum soldered CF40 viewports, which were custom AR coated optimized for the UV wavelengths required[1]. As also present in all other optics – mirrors, lenses, waveplates, AOMs and more – we however observed strong UV degradation of the AR coating over time, as shown in figure 3.9. High-energy UV photons can break chemical bonds in the coating materials that lead to the formation of color centers and can create permanent photochemical damage. Oxygen vacancies or impurities in fused silica glass are also subject to solarization and both coating and glass substrates are more prone to damage in vacuum environment, where no ambient oxygen can repair these damages. After four years of use and a few hundred hours of UV exposure at 254 nm transmission decreased to about 68.6 %, the increased UV damage at the vacuum side is easily visible on the viewport coatings.

Random AR nano-textures Given the need to integrate a high-power optical dipole trap laser and the severe degradation, the viewports were replaced with 1.5 in diameter nano-textured random anti-reflection (RAR) windows[2]. Instead of thin-film AR coating layers, RAR surfaces use sub-wavelength nanostructures that gradually match the refractive index between air and substrate, enabling broadband, wide-angle AR performance. While specifications for the UV-C wavelength range were not available, the RAR texture showed excellent transmission of 99.5(1) % at 254 nm and reflectivity of 0.38(13) % at 1070 nm, both at 10° incidence [132].

To suppress UV degradation inside the glass, we selected high purity, non-crystalline, UV-grade Corning 7980 fused silica substrates with minimal impurity inclusions (inclusion class 0: $\leq 0.03\,\mathrm{mm}^2$ total inclusion cross-section per $100\,\mathrm{cm}^3$ of glass) and high homogeneity (grade A: ≤ 1 ppm maximum

---

[1] Laseroptik UV VAR, ≤0.25 % reflectivity at 250 nm to 330 nm.

[2] TelAztec RAR-M, fused silica C7980 grade 0A.

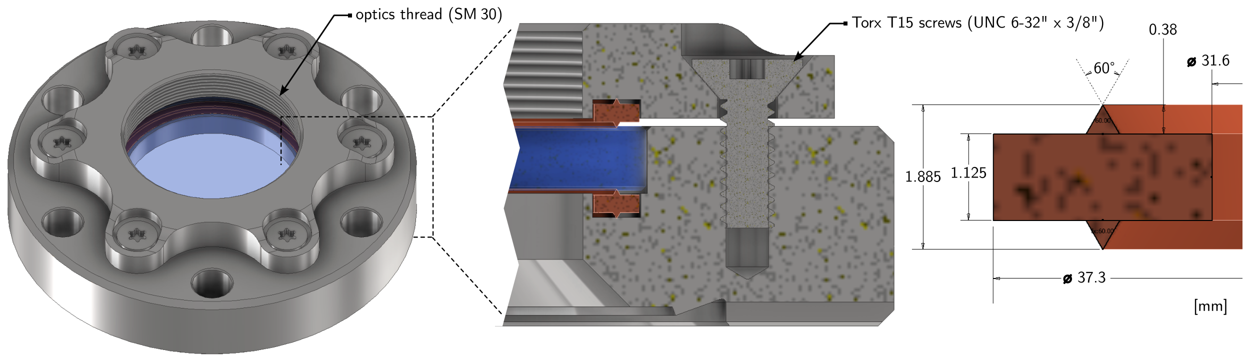

Figure 3.10: Upgraded vacuum viewports with the copper to glass UHV seal. The flanges are commercially available (Thorlabs VC234) stainless steel CF40 flanges originally made for sealing via Viton gaskets, that are replaced with a custom-made double-sided copper knife edge. The custom stainless steel retaining clamp compresses the copper ring to ≥90 µm per knife edge, establishing a UHV tight and nanostructure viewport compatible seal.

index variation). These substrates promise high transmission in the deep-UV (≥ 99.9 %/cm) and demonstrate good damage resistance in comparable applications.

Sealing the nano-textured windows for UHV use was challenging, as vacuum-soldered glass-to-metal bonded viewports were unavailable. After recommendations from other groups, Viton o-rings in commercial vacuum flanges were used[1]. However, the RAR surfaces are fragile, prone to contamination, and difficult to clean. A mild ≤80 °C bake-out caused fluorocarbon outgassing from the o-rings, contaminating the nano-texture and increasing absorption to 8(1) % and 2.3(2) % in the UV and infrared (IR), respectively [132]. Multiple cleaning attempts, including oxygen plasma and UV exposure, failed – plasma increased UV absorption, while UV exposure raised vacuum pressure by over an order of magnitude. New windows were installed using a custom-designed upgraded viewport with a glass-to-copper seal, developed in this thesis and inspired by concepts in references [133, 134]. As shown in figure 3.10, the design modifies commercially available CF40 flanges (Thorlabs VC234) by replacing the original Viton sealing mechanism with a custom double-sided copper knife edge and retaining clamp, achieving a UHV-tight and nanostructure-compatible seal that proved reliable and leak-tight to below 5×10^{-11} mbar L/s. Details on installation, characterization, contamination, and cleaning can be found in reference [132].

3.2.3 Outlook

A future vacuum chamber design supporing high-resolution EDM measurements and the production of quantum degenerate gases is presented in section 7.3.1. This design incorporates a Zeeman slower, as discussed in section 4.8.3, for improved MOT loading and employs differential pumping stages to achieve a strong pressure gradient, enabling operation in the UHV to XHV range. In addition to improving vacuum quality, the new setup enables separation of the source and science chambers. This reduces background gas collisions and allows installation of magnetic shielding for future EDM measurements. The proposed system lays a solid foundation for future experimental advances.

---

[1] Thorlabs VC234, rated to 1×10^{-8} mbar, with reported operation down to 1×10^{-10} mbar. Viton outgassing should be reduced by vacuum bake (100 °C to 150 °C, four hours). A UHV seal requires an untextured rim of 3 mm on the vacuum side.

4 Magneto-optical trapping of mercury at high phase-space density

The investigation of radiation pressure of light dates way back to the beginning of the 17th century when Johannes Kepler tried to explain why comet tails point away from our sun [135]. While supported by theory and experiment suggestions by Leonard Euler (1746), James Clerk Maxwell (1873), Adolfo Bartoli (1876) and Albert Einstein (1917) it took nearly 200 years for the first experimental verification in a light mill radiometer [136, 137] – as suggested by Wiliam Crookes (1873) – and the first observation of recoil forces in an atomic beam by Otto Robert Frisch in 1933 [138].

Only with the development of the (tunable) laser at around 1960, a tool for efficient atom-light interaction was born and the concept of laser cooling atoms utilizing the dipole force – as initially proposed by Arthur Ashkin in 1978 [139], as well as Ted Hänsch and Arthur L. Schawlow in 1975 [140] among others – began to gain momentum. The first three-dimensional optical molasses was then realized by Steven Chu and colleagues in 1985 [141]. They slowed a beam of neutral sodium atoms down from tens of m/s to tens of cm/s and cooled them from hundreds of Kelvin to the Doppler temperature limit of 240 µK.

Suggestions and experiments using chirped laser light for addressing and cooling multiple velocity classes in a hot gas of atoms were made, a technique that still finds application today. In parallel, ideas to utilize magnetic fields and the Zeeman shift in optical transitions for a position and velocity-dependent cooling force [142] then led to the development of the magneto-optical trap (MOT). Proposed by Jean Dalibard in the late 1980s [143] and first realized in the group of Steven Chu and David Pritchard in 1987 [144], the MOT adds a position-dependent restoring force to the velocity compression of the molasses. This not only allowed much higher atomic densities and atom numbers, but surprisingly allowed to reach sub-Doppler temperatures down to a few times the recoil limit. The latter was explained by discovery of the Sisyphus cooling mechanism in alkali vapors, a mechanism relying on ground-state Zeeman sublevels and polarization gradients [145, 146]. Most importantly, magneto-optical trapping allowed direct trapping from a thermal background vapor without the need for atomic beam slowing techniques based on chirped lasers or Zeeman shift compensation. In 1997, the Nobel Prize in physics honored the advancements in this field while highlighting potential applications and the award went to Steven Chu, Claude Cohen-Tannoudji and William D. Phillips “for their development of methods to cool and trap atoms with laser light” [147].

Today, magneto optical trapping is the workhorse tool for a wide range of (ultra-)cold physics creating millimeter-sized clouds of cold atoms or molecules with densities on the order of $1 \times 10^{11}\,\mathrm{cm}^{-3}$ and temperatures down to the recoil limit. This enables Bose-Einstein condensation [148, 149], Fermi degeneracy [150], as well as quantum information experiments and precision metrology probing the physics beyond the standard model, and much more. Recent advances have extended MOT techniques to certain diatomic molecules, such as monofluorides and, more recently, hydroxides of Sr, Ca, Ba and Al [151], overcoming challenges related to their complex internal structure through carefully engineered laser cooling schemes. Laser cooling has also recently been successfully applied to antimatter systems, most notably in the cooling and trapping of antihydrogen [152], which opens up new frontiers in precision tests of fundamental symmetries, such as charge, parity and time reversal symmetry (CPT) invariance and gravitational interactions involving antimatter.

Magneto optical trapping in mercury was started in the group of Hidetoshi Katori at RIKEN (University of Tokyo) [153] and at SYRTE in Paris [154, 155] motivated by its low sensitivity to blackbody radiation in the context of an optical lattice clock. At the same time, the group of Thomas Walther in Darmstadt set up a mercury MOT for photo-association of cold mercury dimers and to study lasing without inversion in the deep-ultraviolet (UV) region [56, 57, 102, 103, 156]. Interest in laser-cooling mercury also A dual-species mercury-rubidium MOT was also developed in Toruń [58], primarily aimed at investigating cold collision dynamics between Hg and Rb, as well as enabling future studies of ultracold molecule formation. More recently, mercury cooling and trapping efforts there have also supported the development of a molecular Hg_2 clock to probe potential variations of fundamental constants [157]. Magneto-optical trapping for optical lattice clock operation was also established in Shanghai [107] and Arizona [105, 158]. While mercury was established as the heaviest non-radioactive element trapped in a MOT, its high vapor pressure and deep-UV wavelengths make handling and cooling mercury quite challenging. These works demonstrated that a MOT of Hg is feasible; however, to the best of our knowledge, none of these experiments were designed with evaporative cooling or quantum gas production in mind. Consequently, atom number and phase-space density remain parameters with potential for further optimization.

Relevant for the optical dipole force in magneto-optical trapping, but also for describing dipole trapping, Zeeman slowing and the interaction between the probe beam and the atomic cloud during spectroscopy in chapter 6, it is helpful to revise atom-field interaction on the fundamental level. The following section will therefore lay a theoretical basis of atom-field interactions for laser cooling. Sections 4.2 to 4.6 will give a detailed construction of the optical and electronic setup required for trapping and analysis of cold mercury atoms. With the technical foundation laid out, the chapter will conclude in demonstration of high-phase space densities and a thorough characterization of the Hg-MOT and will give an outlook to planned upgrades and future improvements. The MOT characterization section 4.7 will include results published in reference [1].

4.1 Atom-field interaction

The derivation presented follows the description in reference [159] and [145].

The interaction between a two-level atom with states $|g\rangle$, $|e\rangle$ and a monochromatic electric field $\vec{E}(\vec{r},t)$ is described by the sum $H = H_A + H_{AF}$ of the atomic free-evolution Hamiltonian $H_A = \vec{p}^2/(2m) + \hbar\omega_0|e\rangle\langle e|$ and the atom-field interaction $H_{AF} = -\vec{d}\cdot\vec{E}$, where $\vec{d}$ is the induced atomic dipole moment and $\vec{p} = -i\hbar\nabla$ the atomic momentum operator. Rewriting $\vec{d} = \langle g|\vec{d}|e\rangle\,(\sigma + \sigma^\dagger)$, where $\sigma = |g\rangle\langle e|$ is the atomic lowering operator[1] and also decomposing the electric field $\vec{E}(\vec{r},t) = \hat{\epsilon}\, E^{(+)}(\vec{r})\, e^{-i\,\omega\, t}$ + c.c. into positive and negative rotating terms, we can write the Hamiltonian in the form

$$H = \frac{\vec{p}^2}{2\,m} + \hbar\,\omega_0\,\sigma^\dagger\sigma + \frac{\hbar}{2}\,(\sigma + \sigma^\dagger)\,\left(\Omega(\vec{r})\,e^{-i\,\omega\,t} + \Omega^*(\vec{r})\,e^{+i\,\omega\,t}\right) \tag{4.1}$$

where the Rabi frequency is defined as $\Omega(\vec{r}) = -2\,\langle g|\vec{d}\cdot\hat{\epsilon}|e\rangle\,E^{(+)}(\vec{r})/\hbar$. In the rotating-wave approximation $|\omega-\omega_0| \ll \omega+\omega_0$ we can neglect the fast oscillating terms $e^{\pm i\,(\omega+\omega_0)}$ in the product $\vec{d}\cdot\vec{E}$ and the total atom-field interaction Hamiltonian can be written as $H_{AF} = \hbar/2\,\left(\Omega(\vec{r})\,\sigma^\dagger\,e^{-i\,\omega\,t} + \Omega^*(\vec{r})\,\sigma\,e^{+i\,\omega\,t}\right)$. Here we can absorb the explicit time dependence by transforming to a rotating frame governed by the unitary transformation $U = \exp\left(i\,\omega\,t\,|e\rangle\langle e|\right)$. The resulting Hamiltonian then reads

$$\tilde{H} = \frac{\vec{p}^2}{2\,m} - \hbar\,\Delta\,\sigma^\dagger\sigma + \frac{\hbar}{2}\,\left(\Omega(\vec{r})\,\sigma^\dagger + \Omega^*(\vec{r})\,\sigma\right) \tag{4.2}$$

where $\Delta = \omega - \omega_0$ is the detuning of the angular frequency of the light field with respect to the resonance frequency of the atomic resonance.

4.1.1 Absorption cross-section and lineshape

To also include dissipation by spontaneous emission to the description of the two-level atom governed by $\tilde{H}$, we change to the density matrix description $\tilde{\rho}$ and solve the associated Liouville-von Neumann master equation. Under the Born-Markov approximation of separable system and reservoir and the assumption that the dissipation is dominated by homogeneous (natural) line broadening this leads to the optical Bloch equations,

$$\frac{\partial\tilde{\rho}}{\partial t} = \mathscr{L}\rho = -\frac{i}{\hbar}\,\left[\tilde{H},\tilde{\rho}(t)\right] + \Gamma\,\mathscr{D}[\sigma]\,\tilde{\rho}(t)\,,\ \text{with}\ \mathscr{D}[\sigma]\,\tilde{\rho} = \sigma\tilde{\rho}\,\sigma^\dagger - \frac{1}{2}(\sigma^\dagger\tilde{\rho}\,\sigma + \tilde{\rho}\,\sigma^\dagger\sigma)\,, \tag{4.3}$$

where $\mathscr{D}[\sigma]$ is the Lindblad superoperator of the raising operator σ. The transition rate is given in terms of the dipole matrix transition element as

$$\Gamma = \frac{\omega_0^3}{3\pi\,\epsilon_0\,\hbar\,c^3}|\langle g|\hat{\epsilon}\cdot\vec{d}|e\rangle|^2 \tag{4.4}$$

and in detail depends on the exact electronic level structure involved. It is most often referenced to the lifetime $\tau = 1/\Gamma$ of the relevant transition between total angular momentum eigenstates $|J_e\rangle \longrightarrow |J_g\rangle$. The dipole matrix element is then written using the Wigner-Eckart theorem in terms of the reduced matrix element $\langle J_g||\vec{d}||J_e\rangle$, which encapsulates the transition strength independent of the magnetic sublevels. In the given form it allows to determine the polarization-dependence of the optical dipole force in section 5.1.1.

In steady state $t \longrightarrow \infty$ the master equation can be solved, and we obtain the diagonal $\rho_{ee}(t \longrightarrow \infty)$ (= excitation) and off-diagonal $\rho_{eg}(t \longrightarrow \infty)$ (= coherence) elements of the two-level system's density

---

[1] We can choose the phase of $\langle g|\vec{d}|e\rangle$ to be real. The diagonal matrix elements of the atomic dipole moment operator vanish due to parity arguments, see for instance [159, section 5.1.1]. Similarly, we can write $H_A = \vec{p}^2/(2\,m) + \hbar\,\omega_0\,\sigma^\dagger\sigma$, showing that σ evolves under the unperturbed atomic Hamiltonian as $e^{-i\,\omega_0\,t}$. The dipole matrix element can therefore be written as a positive and negative rotating term $\vec{d} = \langle g|\vec{d}|e\rangle\,(\sigma + \sigma^\dagger) = \vec{d}^{(+)} + \vec{d}^{(-)}$.

matrix. The diagonal term relevant for absorption and emission reads

$$\rho_{ee}(t \to \infty) = \frac{1}{2}\,\frac{s}{1+s}\,, \quad \text{with} \quad s(\Delta, \vec{r}) = \frac{|\Omega(\vec{r})|^2/2}{\Delta^2 + (\Gamma/2)^2} = \frac{s_0}{1 + (2\,\Delta/\Gamma)^2}\,, \tag{4.5}$$

where $s_0 = s(\Delta = 0, \vec{r}) = I(\vec{r})/I_{\mathrm{sat}}$ is the (position-dependent) on-resonant saturation parameter and $I_{\mathrm{sat}} = \hbar\,\omega_0^3\,\Gamma/(12\pi\,c^2)$ the associated saturation intensity. As it describes the excited state decay rate, it is also a measure of the (coherent) photon scattering rate $R_{\mathrm{sc}} = \Gamma\,\rho_{ee}(t \to \infty)$ and following the optical Wiener-Khinchin theorem [159] gives us the associated scattering cross-section,

$$\sigma_{\mathrm{sc}} = \frac{\sigma_0}{1 + s_0 + (2\Delta/\Gamma)^2}\,, \quad \text{with} \quad \sigma_0 = \frac{3\,\lambda^2}{2\pi}\,, \tag{4.6}$$

relevant especially for (absorption) imaging as described in section 4.4. The dependency on detuning Δ and saturation parameter s_0 resembles a Lorentzian lineshape of power-broadened effective width $\Gamma' = \Gamma\sqrt{1 + s_0}$ that can be probed with near resonant laser light.

As we will see in chapter 6 on isotope shift spectroscopy, multiple photon scattering events can alter this dependency by introducing a Doppler shift $\Delta \to \Delta + \hbar\,\vec{k} \cdot \vec{v}$ due to directed photon recoil of the probe beam. An accumulative velocity change by multiples of $v_{\mathrm{rec}} = \hbar\,k/m$ can then lead to an asymmetric line shape, easily resolvable at small wavelengths λ in the ultraviolet even for only a few scattered photons per atom. We will derive a semi-empirical model in section 6.2.2, that describes the data well, but a more thorough analysis would need to solve equation 4.3 for a Hamiltonian $\tilde{H}$ with time varying Doppler shifted lightfield frequency / detuning.

4.1.2 Laser cooling – dipole and radiation pressure force

Given the Hamiltonian in the rotating frame from equation (4.2), the force acting on the atom can be derived in the Heisenberg-picture from

$$\vec{F} = \frac{\partial \vec{p}}{\partial t} = \frac{i}{\hbar}\,\left[\tilde{H}, \vec{p}\right] = -\nabla\,\tilde{H}_{AF} = -\frac{\hbar}{2}\,\left(\nabla\Omega(\vec{r})\,\sigma^{\dagger} + \nabla\Omega^{*}(\vec{r})\,\sigma\right)\,. \tag{4.7}$$

Separating the Rabi frequency into amplitude and phase $\Omega(\vec{r}) = |\Omega|\,e^{i\,\phi(\vec{r})}$ and expressing the Rabi frequency amplitude in terms of the saturation parameter $s(\Delta, \vec{r}, \Delta)$ from equation (4.5), the mean force can be written[1] as

$$\begin{aligned} \langle\vec{F}\rangle &= -\frac{\hbar\,\Omega^{*}(\vec{r})}{2}\,\left[\nabla \log|\Omega(\vec{r})| - i\nabla\phi(\vec{r})\right]\,\langle\sigma\rangle \\ &= -\frac{\hbar\,\Delta}{2}\,\nabla\,\log\left[1 + s(\Delta, \vec{r})\right] + \frac{\Gamma}{2}\,\frac{s(\Delta, \vec{r})}{s(\Delta, \vec{r}) + 1}\,\nabla\phi(\vec{r}) \\ &= \langle\vec{F}_{\mathrm{dip}}(\vec{r}, \Delta)\rangle + \langle\vec{F}_{\mathrm{rad}}(\vec{r}, \Delta)\rangle\,. \end{aligned} \tag{4.8}$$

Dipole force The first term in the last expression is the mean dipole force $\langle\vec{F}_{\mathrm{dip}}\rangle$, which depends on the detuning Δ and the Rabi frequency $\Omega(\vec{r})$ and therefore on the field amplitude / intensity. It originates in the coherent scattering and interference of photons that change their wavevector ori-

---

[1] For this step the author of [159] uses the fact that the gradient can then be rewritten as $\nabla\Omega(\vec{r}) = \Omega(\vec{r})\,\left(\nabla \log\left(|\Omega(\vec{r})|\right) - i\nabla\phi(\vec{r})\right)$ and $\nabla s(\vec{r}) = 2\,s(\vec{r})\,\nabla \log|\Omega(\vec{r})|$.

entation during the absorption and re-emission process. While this vanishes for a plane wave for which the Rabi frequency has no spatial dependency, it is the main driving force in optical dipole traps (ODTs), where a strongly focussed laser beam can create a conservative trapping potential $\langle \vec{F}_{\text{dip}}(\vec{r}, \Delta)\rangle = -\nabla U_{\text{dip}}(\vec{r}, \Delta)$.

The second term in equation (4.8) is the mean radiation pressure force $\langle \vec{F}_{\text{rad}}\rangle$, which compared to the steady state solutions of the optical Bloch equations from equation (4.5), is just the scattering rate $\Gamma\,\rho_{ee}(\vec{r}, t \to \infty)$ multiplied with the photon recoil momentum.[1] This is the main driving force in optical molasses, magneto-optical trapping, and for slowing atoms in a Zeeman slower (ZS).

Optical molasses

The simplest model of a one-dimensional optical molasses involves two counter-propagating laser beams that are red-detuned ($\Delta < 0$). These beams create a velocity-dependent friction force that opposes and dampens the motion of the atoms. For this, we need to consider that the moving atom of velocity v experiences the frequency of the two beams Doppler shifted $\Delta \to \Delta \pm k\,v$ with opposite signs. The resulting force of the co-propagating ($\Delta \to \Delta - k\,v$) and counter-propagating ($\Delta \to \Delta + k\,v$) light field can therefore be written as the sum

$$\begin{aligned}\langle F_{\text{rad}}\rangle^{\text{(molasses)}} &= \hbar k\,\frac{\Gamma}{2}\,s_0\left[\frac{1}{1+s_0+(2(\Delta-k\,v)/\Gamma)^2}-\frac{1}{1+s_0+(2(\Delta+k\,v)/\Gamma)^2}\right]\\ &= \frac{8\hbar\,k^2\,s_0\,|\Delta|/\Gamma}{\left(1+s_0+(2\Delta/\Gamma)^2\right)^2}\,v+\mathcal{O}(v^2)\equiv -\alpha\,v+\mathcal{O}(v^2)\end{aligned} \tag{4.9}$$

and is shown in figure 4.1. Note that this treatment only really holds for a two-level system in the low intensity regime of negligible saturation $s_0 \ll 1$, such that we can treat the two beams and their radiation pressure forces as independent. For $\sigma_\pm$ orthogonally polarized beams it is however still a good approximation that holds even at moderate intensities [145].

The damping coefficient α is positive for red-detuned laser light and therefore results in cooling by decelerating the atoms and compressing them in velocity space. When we consider the spatial intensity profile of finite sized laser beams and extend the above picture to three dimensions this cooling also leads to an accumulation and therefore resembles (unstable) trapping of atoms at the interception point of the beams. Damping is maximal for $\Delta \approx -\Gamma/2$ and $s_0 \approx 2$, and we can see that only a small range of velocities can be trapped. The maximal trapping velocity is approximately given by the location of the two extrema ($v = \pm\Delta/k$), which at maximum damping gives us $v_c^{\text{(molasses)}} \approx \Gamma/(2\,k) = \lambda\,\gamma/2$. While generally being quite small for most cooling transitions, the narrow linewidth ($\gamma = \Gamma/(2\pi) = 1.3\,\text{MHz}$) and deep ultraviolet cooling transition ($\lambda = 253.7\,\text{nm}$) available in mercury makes the maximum trapping velocity more than an order of magnitude smaller ($\approx 0.16\,\text{m/s}$) compared to typical cold atom experiments.

Temperature limit of laser cooling

Doppler cooling limit Equation 4.9 describes a deceleration to $v = 0$, i.e. $T = 0$, which is nonphysical. For an estimate of the cooling limit, we therefore have to consider not only the mean radiation pressure force $\langle F_{\text{rad}}\rangle$ but all its fluctuations over time. Every photon that is absorbed or emitted

---

[1] For a plane wave $\hbar\,\nabla\phi(\vec{r}) = \hbar\,\vec{k}$.

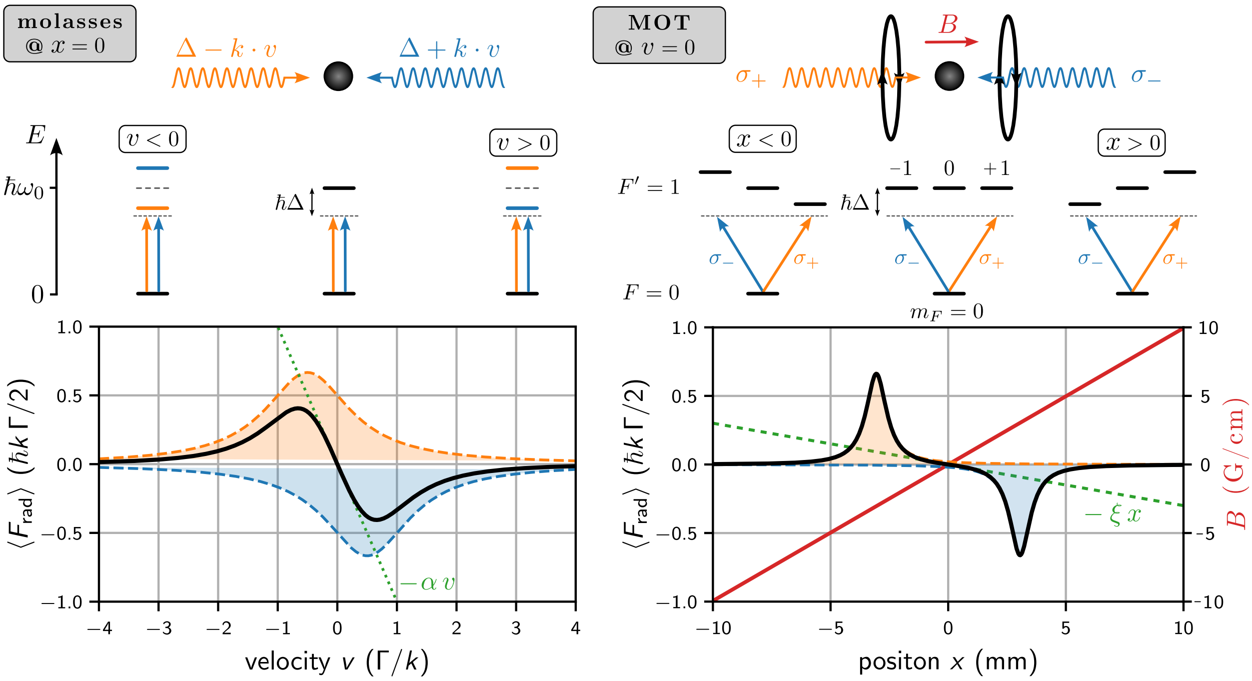

Figure 4.1: The radiation pressure force (black curve) for a one-dimensional model of optical molasses cooling (left) and magneto-optical trapping (right) of mercury. The optical molasses is shown for a detuning of $\Delta = -\Gamma/2$ and a saturation parameter of $s_0 = 2$ for which maximal damping (α) is predicted. In the MOT example $\Delta = -5\,\Gamma$ and $s_0 = 2$ to visualize the large capture radius achievable when increasing the light field detuning $|\Delta|$. The orange and blue shaded curves (dashed) show the force contributions from the two opposing, red-detuned ($\Delta < 0$) light fields, that the atom perceive as being shifted further and closer into resonance depending on their velocity v and position x. In the optical molasses this shift originates in the Doppler effect $\Delta \to \Delta - \vec{k}\cdot\vec{v}$. In the MOT for $v = 0$ the magnetic gradient field ($\partial B/\partial x = 10\,\mathrm{G/cm}$) shifts the $m_{F'} = \pm 1$ hyperfine states, such that $\Delta \to \Delta + \Delta\mu\, B(x)/\hbar$ with $\Delta\mu > 0$, as probed by the circular polarized laser fields. The depiction of the energy shifts is valid for small v, x for which the linear approximation of the radiation pressure force (dotted, green) holds.

changes the atom's momentum by one recoil $\hbar k$. A comparison of the cooling and heating rate [145] gives the resulting temperature limit of radiation pressure cooling:

$$T \geq T_D = \frac{\hbar\,\Gamma^2}{8\,k_B\,|\Delta|}\left(1 + s_0 + (2\,\Delta/\Gamma)^2\right) \geq \frac{\hbar\,\Gamma}{2\,k_B} = T_D^{(min)} \tag{4.10}$$

where the second inequality indicates the minimum achievable temperature for a detuning of $\Delta = -\Gamma/2$ and $s_0 \to 0$. For the extension to three dimensions, the saturation parameter needs to be computed for the sum of all laser intensities $s_0 = I_{\rm tot}/I_{\rm sat} = 6\,I_{\rm beam}/I_{\rm sat}$ for three orthogonal pairs of counter-propagating laser beams.[1] The minimal temperature is typically referred to as the Doppler temperature, for mercury it lies at $T_D^{(min)} = 30.5\,\mu\mathrm{K}$.

Polarization gradient sub-Doppler cooling As first observed in Lett et al. [145], orthogonally linear (lin ⊥ lin) or circular polarized ($\sigma_+\,\sigma_-$) lightfields in combination with a Zeeman substructure

---

[1] Note that in the publication attached to this work and described in section 4.7 we use the notation $s \equiv s_0/6$.

of the atomic ground state allows reducing the temperature even further. In the MOT compatible $\sigma_+\,\sigma_-$ scheme employed within this thesis, two counter-propagating laser beams with opposite circular polarizations[1] $\hat{\epsilon}_\pm = (1, \pm i)^\intercal/\sqrt{2}$ interfere in a standing wave. If we assume the two waves to have identical amplitude the resulting polarization is always linear $\hat{\epsilon} = (\sin(k\,x), \cos(k\,x))^\intercal$, but rotates in a corkscrew-like helix with pitch λ.[2] For a multilevel atom with degenerate ground-state Zeeman sublevels, this leads to a velocity-dependent redistribution of population among magnetic sublevels through optical pumping. The associated friction force originates from non-adiabatic transitions between the various hyperfine levels for which the Clebsch-Gordon coefficients need to create a population asymmetry. Therefore, polarization gradients lead to cooling beyond the Doppler limit. This simpler explanation of the $\sigma_+\,\sigma_-$ scheme is only valid for ^{201}Hg. Due to the lack of sufficiently asymmetric optical pumping between ground state Zeeman sublevels in any atom with $F_g < 1$, polarization gradient cooling based on unbalanced radiation pressures in the $\sigma_+\,\sigma_-$ corkscrew scheme is however prohibited in ^{199}Hg ($F_g = 1/2$) [146]. The complex polarization topography of three-dimensional light fields that occurs in the interference of the six MOT light fields considered within this thesis however again allows sub-Doppler cooling schemes based e.g., on opposing linear polarization induced gradients [160]. Here, the lin ⊥ lin cooling scheme is based on a spatial polarization gradient induced modulation of light shifts and population redistribution via optical pumping between ground-state sublevels with different potentials and is therefore referred to as Sisyphus cooling [146].

The absolute limit of polarization gradient cooling via radiation pressure is then given by the residual random walk due to the recoil that atoms experience when absorbing and re-emitting single photons of momentum $\hbar k$. The associated temperature limit – the recoil temperature – is then given by

$$T \geq T_\text{recoil} = \frac{(\hbar k)^2}{m\,k_B} = \frac{h^2}{m\,\lambda^2\,k_B}\,. \tag{4.11}$$

The derivation here is simplified and experiments typically can only reach temperatures of a few to a few tens of T_recoil. Especially residual magnetic fields and the resulting Zeeman shift can cause atom loss and heating. For mercury this limit is approachable only for the fermionic, odd mass number isotopes ^{199}Hg and ^{201}Hg with ground state hyperfine structure and is given by $T_\text{recoil} = 1.5\,\mu\text{K}$ limited by the large recoil of the UV photons.

Magneto-optical trapping

So far, the optical molasses has no position-dependent restoring force and therefore cannot provide stable trapping. Magneto optical trapping adds a spatially dependent magnetic quadrupole field and requires circular polarization from the opposing laser beams. In the simplest case, applicable for the bosonic mercury isotopes, the atom features a $F = 0$ ground state and $F' = 1$ excited state (hyper)fine structure. In the one dimensional case of two opposing laser beams with orthogonal $\sigma_\pm$ polarization, a coaxial magnetic gradient field $B(x) = (\partial B/\partial x)\,x$ shifts the $m_{F'} = \pm 1$ sublevel due to the Zeeman effect, as illustrated in figure 4.1. Due to the selection rules the $\sigma_\pm$-polarized laser beams therefore

---

[1] Note that the polarization handedness here is defined with respect to a fixed basis. In their respective co-propagating reference frames the two laser beams have the same circular polarization. If the atomic spin is aligned with the wavevector $\sigma_\pm$ refers to left-handed (right-handed) circularly polarized light. [2] For unequal field amplitudes the following explanation is still valid. The resulting polarization is elliptical and rotates with constant ellipticity.

can only address the $m_F = 0 \longrightarrow m_{F'} = \pm 1$ transition with $\Delta m_F = \pm 1$. If we consider that the energy level degeneracy of the hyperfine levels is lifted according to $\Delta E_Z = (m_{F'}\, g_{F'} - m_F\, g_F)\, \mu_B\, B(x)$, an atom at rest located at $x < 0$ ($x > 0$) therefore will be addressed dominantly by the σ_+ (σ_-) polarized lightfield. The opposing lightfield driving the $\Delta m_F = -1$ ($\Delta m_F = +1$) transition is further red detuned and the atom therefore experiences a position-dependent radiation force towards the center of the trap.

We introduce the Zeeman shift into the detuning $\Delta \longrightarrow \Delta \pm k\, v \pm \Delta\mu\, B(x)/\hbar$, where we assume $|\Delta E_Z| = \Delta\mu\, B(x)$ for the outermost hyperfine transitions. From equation 4.9, in the limit of small x, v we then obtain a damped oscillator like force:

$$\begin{aligned}\langle F_{\text{rad}} \rangle^{(\text{mot})} &= \hbar k\, \frac{\Gamma}{2}\, s_0 \left[\frac{1}{1 + s_0 + (2(\Delta - k\, v - \beta\, x)/\Gamma)^2} - \frac{1}{1 + s_0 + (2(\Delta + k\, v + \beta\, x)/\Gamma)^2} \right] \\ &= -\alpha\, v - \kappa\, x + \mathcal{O}(x^2, v^2)\,, \qquad \text{where} \quad \kappa = \frac{\alpha\, \beta}{k}\,, \quad \beta = \frac{\Delta\mu}{\hbar}\, \frac{\partial B}{\partial x}\,. \end{aligned} \tag{4.12}$$

The spring constant κ depends on the applied gradient field strength $\partial B/\partial x$ – typically in the 5 G/cm to 50 G/cm range – and the velocity damping constant α of the optical molasses. Extending this scheme to three dimensions is straight forward. A three-dimensional magnetic gradient field can be realized by e.g., a pair of coils in anti-Helmholtz configuration, the laser beam polarization of the six MOT beams then needs to be adapted to the magnetic field orientation on the three spatial axes.

Cooling of fermionic mercury isotopes with $F \neq 0$ works nearly identical to the here described simple $F = 0 \longrightarrow F' = 1$ model, since the atom quickly aligns its spin to the outermost $m_F = \pm F$, $m_{F'} = \pm F'$ Zeeman states due to optical pumping by the $\sigma_\pm$-polarized lightfields [161].

Capture velocity & radius Under the assumption of equation 4.12 the capture velocity of a (1D) MOT can be approximated [161] as

$$v_c^{(\text{mot})} = \sqrt[3]{\frac{2\pi\, \hbar^2\, k^3\, \Gamma^2\, |\Delta|}{m^2\, \beta^2}\, \frac{s_0^2}{(1 + s_0)^{3/2}}\, \frac{1}{1 + s_0 + (2\, \Delta/\Gamma)^2}} \tag{4.13}$$

With $v_c^{(\text{mot})}$ typically in the tens of m/s range, this makes magneto-optical trapping from a thermal background gas much more efficient than pure optical molasses cooling. The latter is often just applied as a second cooling stage once the atoms mean velocity is already reduced by the MOT. At strongly reduced laser intensity and detuning, this additional cooling scheme can allow further reduction of the achievable cloud temperatures. For reasonable experimental parameters of $\Delta = -15\,\Gamma$, $s_0 = 2$ ($s_0 = 20$) and a gradient field strength of $\partial B/\partial z = 10\,\text{G/cm}$, for mercury we obtain a capture velocity of just $v_c^{(\text{mot})} \lesssim 5.2\,\text{m/s}$ ($9.0\,\text{m/s}$). The radius in which a MOT can roughly capture atoms is relevant when loading from an atomic beam source. It can be roughly estimated from the resonance condition $\Delta\mu\, B(r_c^{(\text{mot})}) \overset{!}{=} \hbar\, |\Delta|$ giving us $r_c^{(\text{mot})} = |\Delta|/\beta$, which for the parameters given above is $r_c^{(\text{mot})} \approx 1.5\,\text{mm}$. The capture velocity and radius computations were compared to a 1D Monte-Carlo simulation of atom trajectories simulated using a python implementation of the heuristic force equation 4.12 based on the python package PyLCP [162]. The simulation roughly agrees with the above numbers.

Atom numbers and shape While the typically Gaussian beam profile of the MOT cooling light roughly determines the capture and roughly also the trapping volume, the exact shape of the MOT can be really complex and is determined by many parameters. Under the assumption of a perfectly symmetric cloud, the cloud temperature given can be related to its average via the equipartition theorem. Assuming the atom is dominated by the position-dependent force in equation 4.12 and cooled to the Doppler temperature given in equation 4.10, in 1D we get $1/2\, k_B\, T^2 = 1/2\, \kappa\, r^2$ and the resulting MOT radius is given by

$$r^{(mot)} = \sqrt{\frac{\hbar\, \Gamma^3}{64\, \Delta^2\, s_0\, \beta} \left[1 + s_0 + \left(\frac{2\, \Delta}{\Gamma}\right)^2\right]^3}\,, \tag{4.14}$$

where we again define $\beta = \Delta\mu\, \partial_x B\, /\hbar$.

4.2 Optical setup

We will now present the optical setup for magneto-optical trapping of mercury. Care is taken to both reduce the number of optical components to a minimum and to work with as large beams as possible to reduce the intensity and avoid UV damage to optical components. Furthermore, the optical beam path is chosen as short as possible, since the lack of good (polarization maintaining, low loss, UV damage resistance) optical fibers at the wavelength requires good beam stability up to the atoms. This is furthermore complicated by the beam pointing instability of the laser system as discussed below.

4.2.1 254 nm laser system

The 254 nm light required for cooling and imaging is generated by a commercial Toptica fourth-harmonic generation (FHG) system that was built specifically for this application and, at the time of construction, exceeded the continuous wave laser power available at this deep ultraviolet wavelength. The optical setup is shown in figure 4.2. An external-cavity diode laser (ECDL) at 1015 nm (top right) successively seeds a tapered amplifier (TA) and an external fiber amplifier (FA). Optical isolators (OI) prevent back reflections into the laser. Two bow-tie-cavity enhanced second-harmonic generation (SHG) processes in nonlinear crystals (NC) successively convert the light from the infrared to the ultraviolet. The cavity lengths are stabilized via piezo-driven cavity mirrors ($\mathrm{M^p}$) over the photodiode (PD) monitored cavity reflections in a Pound-Drever-Hall (PDH) locking scheme. Here the first doubling stage (labeled as SHG) is stabilized via sidebands modulated onto the laser diode (LD) current and the second doubling stage (labeled as FHG) via an additional electro-optic modulator (EOM). Incoupling to the tapered amplifier, SHG and FHG, as well as the crystal positions can be optimized successively by pairs of motorized (servo-driven) mirrors ($\mathrm{M^m}$) and (motorized) crystal mounts with the output power being monitored via photodiodes (not shown for the doubling cavities). While the SHG is housed in a low humidity environment, the FHG stage features an additional inert gas atmosphere.

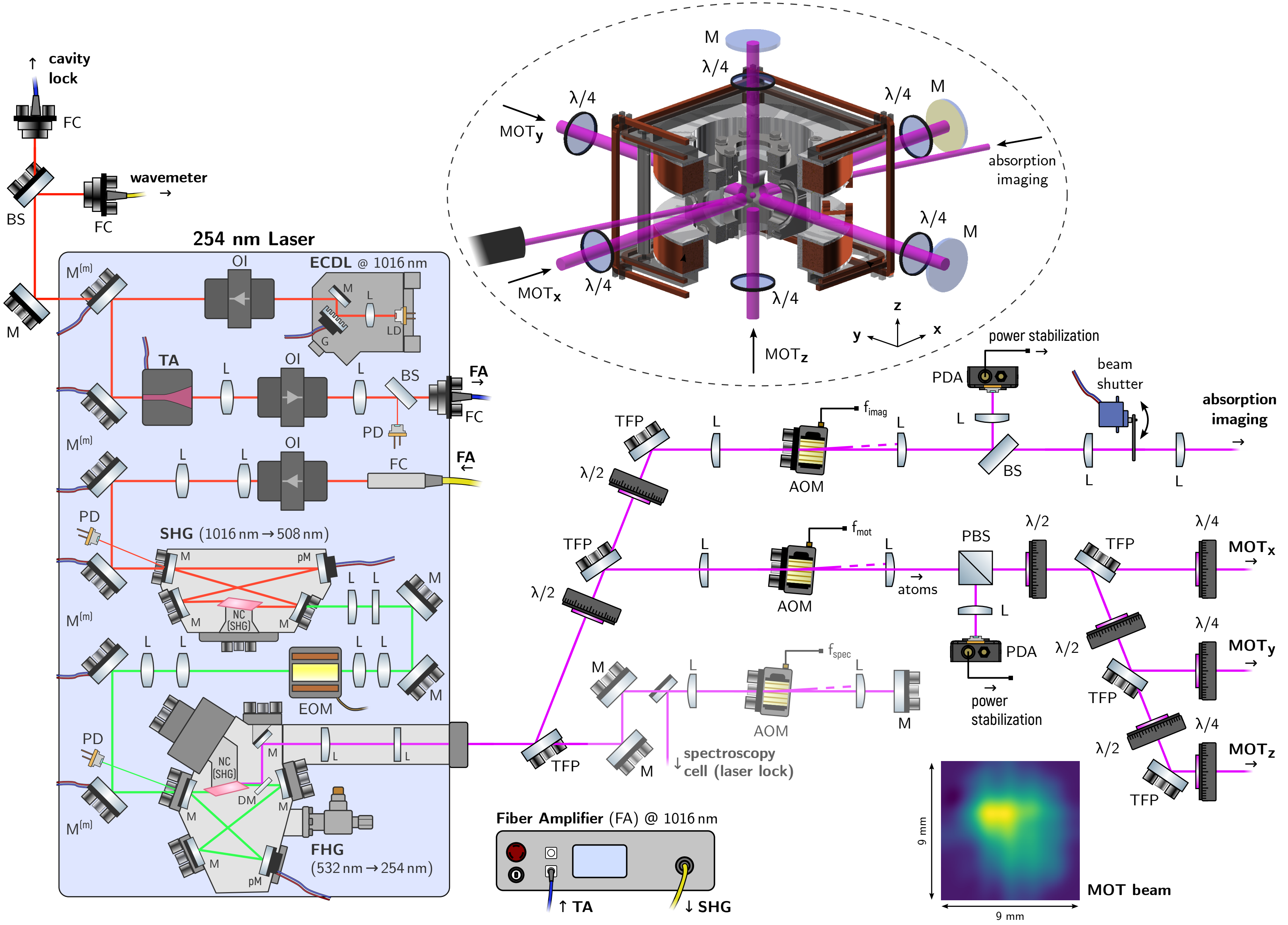

Figure 4.2: Laser system at 254 nm (left) and sketch of the optics providing light for MOT, imaging and spectroscopy (right). The inset (bottom right) shows the MOT beam profile reconstruction from scanning slit analysis data. The inset of the vacuum chamber is taken from reference [1]. Description see main text.

Beam profile & beam pointing

Beam profile The UV laser beam profile does not follow a pure Gaussian TEM_{00}-mode. It contains higher-order cylindrical transverse TEM_{p1} modes with $p \geq 1$, which have additional intensity patterns oriented along the horizontal axis. These modes propagate differently than the main central mode and therefore alter the beam profile along its propagation path. This is confirmed by a measurement of the overall beam quality factor, obtaining $M^2 \approx 1.1$ to 1.2 along the vertical and $M^2 \approx 1.4$ to 1.9 along the horizontal beam axis, which also depends on the crystal position and UV degradation of external laser optics. Beam profiling at 254 nm is not trivial, as standard silico-based charge-coupled device (CCD) cameras are not sensitive in this wavelength region. Initially we performed beam profile analysis via manual knife-edge technique, but also attempted imaging strongly attenuated, acousto-optic modulator (AOM) pulsed light onto the Andor emCCD camera used for atom imaging. The latter was quite sensitive to beam shape distortions of the high-power UV laser beam, which became apparent after passing through several optical elements, especially AOMs and polarization optics. The most consistent beam profile measurements were obtained using a high-power compatible scanning slit beam profiler[1], which records intensity slices along two orthogonal axes. A two-dimensional reconstruction of the beam profile from multiple angular scans was attempted using the inverse Radon transform, a standard algorithm from computed tomography. An beam profile of the MOT beam is shown in figure 4.2.

Over the time of this thesis, slight alterations in the FHG output beam profile were observed. A more drastic change likely occurred during transit when the laser system was sent for repair, affecting both beam waists and focus positions. We shipped the system back to the manufacturer, who opened the protective enclosure of the final beam-shaping optics and adjusted the lens setup.

Beam pointing instability Beam pointing in SHG enhancement cavities can vary due to thermal effects in the nonlinear crystal, cavity misalignments, birefringent walk-off, and at high power also nonlinear optical phenomena like intensity-dependent refractive index changes (Kerr effect). Instabilities can also worsen by environmental factors such as vibration, thermal drift, and power fluctuations, and can be mitigated through thermal stabilization, vibration isolation, and careful alignment. We observed strong beam pointing instability of the UV beam directly after locking the second SHG cavity, but also long-term drifts and fluctuations, as characterized with the UV-sensitive Andor CCD camera and a scanning slit beam profiler. Overall, peak to peak beam pointing changes of 0.1° amplitude could be observed. This is estimated to be the main limitation for the Doppler-free absorption spectroscopy attempts as discussed below and also limits the shot-to-shot stability of MOT atom numbers, cloud size, and temperature.

4.2.2 Cooling and imaging setup

For the MOT a retroreflected three beam configuration was chosen as a compromise of available laser power and power balance of the six effective MOT beams. The top right inset in figure 4.2 shows the selected beam orientation including the quarter-wave plates[2] used for creating the desired handedness of the light field polarization and the 0°-mirrors for retroreflection. While more power

---

[1] Thorlabs BP209-VIS/M. [2] Eksma Optics zero-order $\lambda/4$ waveplate, front and back surface anti-reflection coated for 254 nm ($R \lesssim 1.78\,\%$ for both surfaces) (custom order).

efficient MOT setups exist e.g., in form of single beam setups, sending the beam successively through all 6 optical viewports or using a grating mirror within the vacuum chamber, these configurations were considered to create imperfections in the optical beam polarizations and a too high power imbalance between opposing MOT beams. The MOT appeared to be rather sensitive to the power balance, also just caused by imperfections of the beams' intensity profile. This leads to parts of the MOT cloud having horizontal and vertical velocity components, that during time-of-flight imaging can even lead to the atom cloud not falling straight down along the direction of gravity. When we observed strong ultraviolet degradation of the optical viewports, as described in section 3.2.2, we switched the horizontal axes from a retroreflected configuration to four individual beams. This allowed balancing the intensities of opposing beams, which lead to an even stronger elongation of the MOT cloud. The vertical MOT beam was chosen to be sent against the direction of gravity and retroreflected from above the vacuum chamber, such that the slightly weaker retroreflected beam scattering force is opposing the gravitational force. The gravitational force is usually stronger than the imbalance of forces induced by the two MOT beams. This imbalance depends on the intensity of the cooling beams ($s_0 \lesssim 5$ per beam, typically) and its detuning ($\Delta = -15\,\Gamma$ to $-\Gamma/2$, typically), and on the transmission of the viewports ($T > 99\,\%$ if not UV-degraded). This results in a net downward acceleration of $a_{\downarrow} = \Delta F_{\mathrm{rad}}/m \approx -0.01\,\mathrm{m/s^2}$ to $-2.5\,\mathrm{m/s^2}$ opposing gravity.

The UV laser beam exiting the laser system (see figure 4.2) is split into separate paths for cooling and imaging, each independently adjusted in polarization, beam size, and frequency. Standard polarization beam splitter (PBS) cubes are difficult to construct in the deep-UV due to material absorption and stringent flatness and alignment requirements for optical contacting or air-spacing. Their numerous coated surfaces must also withstand high-intensity UV light. For these reasons, we use polarization-sensitive thin film polarizerss (TFPs) as beam splitters. These reflect s-polarized light under the Brewster's angle ($\sim 56.4°$). Successive $\lambda/2$ waveplates and TFPs allow splitting the light into MOT and imaging beam, in early optical setups a separate spectroscopy beam was present as well.

Frequency control

For frequency control we use Gooch & Housego AOMO 3200-1220 acousto-optic modulators. They are specified for up to 75 % diffraction efficiency at 257 nm at reasonable radio frequency (RF) power requirements ($\leq 1\,\mathrm{W}$), but with an active aperture of only $0.25 \times 2.5\,\mathrm{mm^2}$ they require quite small beam diameter ($\lesssim 100\,\mu\mathrm{m}$). This leads to quite long optical beam paths when using single lenses (to reduce the number of optical elements susceptible to UV damage) for focussing and recollimation, requiring focal lengths of 300 mm to 500 mm to reach high diffraction efficiencies. This degrades the beam quality further and exposes the AOM to high beam intensities. With the diffraction efficiency being optimal at around 225 MHz and a given natural linewidth of ~1.3 MHz for the intercombination line the MOT AOM is set fixed to $f_{\mathrm{mot}} = 225\,\mathrm{MHz}$, where available power is crucial and the center frequency of the imaging AOM is set to $f_{\mathrm{imag}} = f_{\mathrm{mot}} + |\delta_{\mathrm{mot}}|$ for addressing the atomic resonance, as illustrated in figure 4.10. Imaging AOM frequencies within ~200 MHz to ~230 MHz therefore allows performing spectroscopy scans resolving the slightly Doppler-broadened atomic lineshape for any MOT detuning. We reach diffraction efficiencies up to 75 % to 80 % at 254 nm. The AOMs are

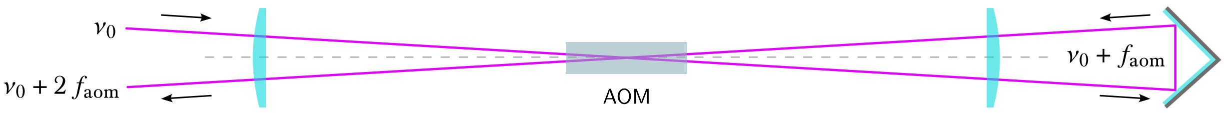

Figure 4.3: Sketch of the double-pass AOM setup, shown from a side view, illustrating the vertical angle used to separate the two beam passes. The AOM diffracted beam is deflected in a direction normal to the page.

powered by voltage controlled oscillator (VCO) frequency generators[1] with integrated phase lock loop (PLL) for frequency reference and stabilization against our Rubidium atomic clock, amplified by matching RF amplifiers[2]. Later the oscillators were replaced by multichannel Urukul direct digital synthesizer (DDS) boards within the Sinara/ARTIQ time control system as discussed in section 4.6 to allow for power stabilization of both MOT and imaging beam via the RF frequency amplitude.

Double-pass AOM A double-pass AOM setup would benefit both the MOT cooling and imaging light. It allows dynamic tuning of the MOT detuning during loading without displacing the MOT cloud and removes intensity variations at the position of the MOT due to beam movement for high resolution spectroscopy. The accessible diffraction efficiency in the UV however limits its application. While a double-pass configuration was set up for both a Doppler-free saturation spectroscopy lock and for absorption imaging, this excluded the application of a double-pass configuration for the MOT light. The anisotropic nature of the AOM crystal material makes the diffraction efficiency in the UV strongly polarization-dependent. For our model it drops to $\leq 20\,\%$ for linear polarization parallel to the acoustic wave propagation direction. This prevents the use of typical double-pass configurations where the first and second pass are separated via their polarization. The light therefore was sent into the AOM under a shallow vertical angle (~1°) and the first and second pass beam were separated geometrically in their vertical position. As illustrated in figure 4.3, the focusing and collimating lenses are arranged in a cat's eye configuration. This allows the single-pass beam to be reflected a few millimeters into the vertical direction and back into the AOM. With the optimal AOM frequency for the cooling light in single-pass configuration being at ~225 MHz, the double-pass imaging / spectroscopy AOM frequency was necessarily adjusted to about 100 MHz to 120 MHz. This furthermore lowered the efficiency to about 8 % in the upper frequency range.

The high intensity impacting the AOMs and other optics lead to strong UV degradation, necessitating us to replace mirrors, waveplates, thin film polarizers and AOMs after about 6 months of operation, as transmission reduced down to about 50 % or below. A future optical setup including a protective oxygen gas atmosphere for solarization mitigation is shown in figure 4.4 and discussed in more detail in the outlook of this chapter.

4.3 Frequency stabilization

Laser frequency stabilization is necessary to allow for stable atom numbers and reproducible and precise resonance addressing during imaging and spectroscopy. With a natural linewidth of $\gamma \approx 1.3\,\mathrm{MHz}$ in the UV, the linewidth of the infrared (IR) master laser is therefore ideally in the range

---

[1] Rhode & Schwarz SML-01 [2] MiniCircuit ZHL-2-S+

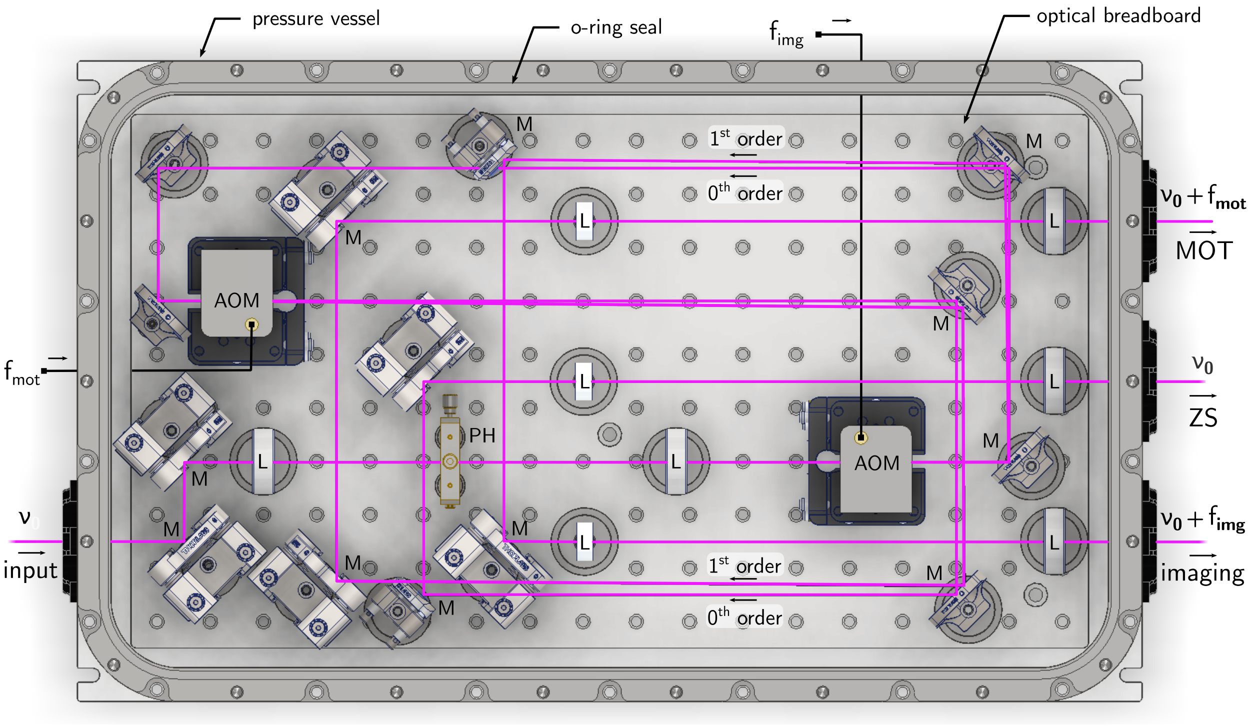

Figure 4.4: Upgrade of the 254 nm laser system to a compact setup with a protective enclosure. The UV beam enters through a sealed window, where a set of plano-convex lenses (L) in combination with a pinhole (PH) clean the mode. Mirrors (M) direct the beam into the two 5-axis stage-mounted AOMs, which feature Brewster-cut fused silica substrates, that diffract and displace the output beams by ±10 mm along the vertical axis. The zeroth and first diffraction orders exit separated in the horizontal plane by the Bragg angle. They are split by D-shaped mirrors and pass through Galilean telescopes for magnification. To protect against solarization, the breadboard can be sealed under an inert gas mixture of oxygen and argon.

$\ll \gamma/16$, since both SHG stages increase the linewidth by a factor of two to four depending on the dominating phase noise sources. The doubling crystal itself is expected to contribute with a factor of about two, but technical noise due to the cavity lock or from additional amplifier stages, like the fiber amplifier, the latter contributing with a white noise like spectrum can increase this to a factor of up to four [103].[1]

4.3.1 Doppler-free saturation spectroscopy

First attempts of laser locking were based on optical spectroscopy in a vapor cell. Multiple Doppler-free nonlinear spectroscopy techniques were tested and initially employed for locking the cooling and spectroscopy laser. While this enabled first stable magneto-optical trapping of mercury at the beginning of this thesis, long-term drifts of the laser frequency up to 10 MHz/h strongly limited MOT operation. After a long debugging process involving many variations of spectroscopy and locking techniques, it is now believed that these drifts are mostly due to residual power dependency in the locking scheme, especially in the beam pointing instability of the UV output of the FHG enhancement cavity. We were only able to characterize the latter observation after long-term MOT operation and

---

[1] In the thesis work of H. John [103] a really similar system is discussed, here the first doubling stage contributes with a factor of 2.18(8) to the linewidth of the fundamental.

purchase of a scanning slit beam profiler. These drifts were partly compensated for by increasing the beam diameter of the spectroscopy lock setup, which however came with a higher power demand for the spectroscopy and limited the available precious UV power for MOT operation. Additionally, all spectroscopy schemes were limited in some way by the poor quality and ease of use of polarization optics in the deep-UV. While our Glan-Taylor laser prisms provide the best polarization purity, they are impractical for splitting polarized beams in both the forward and reverse directions. The more affordable thin-film polarizers lack in polarization extinction ratio even when carefully aligned. PBS cubes with custom coatings were ordered, but strongly lacked in extinction ratio and transmission. Therefore, alternative approaches – locking to a stable wavemeter and finally to an ultrastable high-finesse cavity – were pursued. The section here gives just a very brief overview over the technical advances as well as the spectroscopy and locking schemes used.[1]

Vapor cell design In mercury, the absorption length in a vapor cell at room temperature is quite short due to the high vapor pressure (1.7×10^{-3} mbar, see figure 3.1). Most spectroscopy setups for the 254 nm-line therefore choose rather short spectroscopy cells of only a few mm length [33] to spectroscopically address the more abundant species, while reducing the amount of power needed in pump and probe beam for a proper absorption signal. To also properly resolve isotope ^{196}Hg with a natural abundance of just 0.15 % (see table 2.1), we opted for much longer cells, a 1.9 cm and a 10.6 cm long one. A Peltier-based cooling system is set up to individually control the vapor pressure in the cell for the isotope of choice. Here a two-stage Peltier element[2] was chosen to cool a small ($(30 \times 30)\,\mathrm{mm}^2$ base area) block of copper acting as a thermal mass that houses a glass tip extension of the spectroscopy cell and a small drop of mercury (~1 g) contained within. With a ~3 cm thick styrofoam insulation around the copper block and a water-cooled copper heat sink backing the underside of the Peltier, temperature control from ≥50 °C down to −40 °C was established. This allows to tune the saturation vapor pressure of the mercury droplet within the cell, which dominates the partial mercury cell pressure within the probe volume of the spectroscopy beam. The cell is made of Pyrex and features two 1 in diameter wedged windows for optical access. The experimental spectroscopy cell setup and temperature control is shown in figure 4.5.

The Zeeman substructure of the excited state additionally requires magnetic field control in the interaction region of probe beam and atoms within the spectroscopy cell. To zero the Earth's magnetic field and, optionally, apply a guiding field along the optical beam axis for sub-Doppler dichroic atomic vapor laser locking (DAVLL), three pairs of magnetic coils in a Helmholtz configuration were designed and constructed from enameled copper wire wound onto a nylon frame, as displayed in figure 4.5.

Broadening mechanisms It is noted that the temperature control does not allow to fully set the Doppler, collisional and transit time broadening. These are dominated by the temperature of the spectroscopy cell walls that are not contained within the cooler and therefore sit very close to room temperature. If we assume the thermal velocity of the atoms to follow a Maxwell-Boltzmann distribu-

---

[1] While optical and electronic setup as well as optimization were shared work, I want to thank Quentin Lavigne for the intensive literature research as well as guiding the selection and characterization of spectroscopy locking schemes presented, which is why not all details are specifically given here.

[2] Adaptive (European Thermodynamics Ltd) AP2-162-1420-1118, $P_{\max} = 29.3\,\mathrm{W}$, $\Delta T_{\max} = 95\,°\mathrm{C}$.

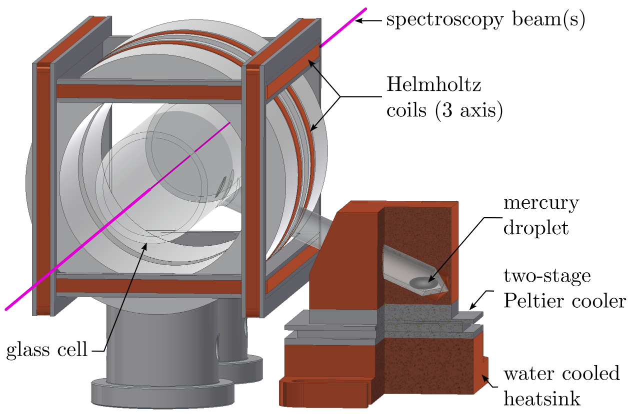

Figure 4.5: Doppler-free saturation spectroscopy cell design including temperature and magnetic field control. Here showing the 1.9 cm long Pyrex cell.

tion,

$$P_{\text{th}}(v)\,\mathrm{d}v = \sqrt{\frac{m}{2\pi\,k_B\,T}}\,\exp\left(-\frac{m\,v^2}{2\,k_B\,T}\right)\mathrm{d}v = \frac{1}{v^\star(T)\,\sqrt{\pi}}\,e^{-(v/v^\star(T))^2}\,\mathrm{d}v\,, \tag{4.15}$$

with $v^\star(T) = \sqrt{2\,k_B\,T/m}$ the most probable speed, the resulting lineshape is described by a Voigt profile. The full width at half maximum (FWHM) linewidth of the temperature-induced Doppler prodile is given by $\Gamma_D(T) = 2\sqrt{\log(2)}\,v^\star(T)\,\omega_0/c = 2\pi$. Within the given achievable temperature range, we obtain a value of $\Gamma_D = 2\pi \times 1.3\,\text{GHz}$ to $1.5\,\text{GHz}$, which is much larger than the natural linewidth. Thus, the Doppler-broadened lineshape is approximately Gaussian. This broadening is compensated for using the Doppler-free saturation spectroscopy technique, which features Doppler-free resonances on top of a Gaussian background.

Transit time broadening originating from the finite travel time of an atom through the interaction region of the probe beam can be estimated from the atomic thermal velocities as well. At a probe beam diameter of $d = 1\,\text{mm}$ the resulting FWHM width is about $\Gamma_T = 2\pi\,v^\star(T)/d = 2\pi\, \times 0.14\,\text{MHz}$ at $T = 20\,°\text{C}$ for the line studied here. It does not impose any further constraints on the spectroscopy lock performance.

Collisional broadening is hard to estimate precisely, since the mean free path length ℓ between Hg – Hg collisions varies strongly with the derivation. Following the discussion for atomic beam generation in microtube nozzles in section 3.1.3, we obtain a mean free path of $\ell \approx 1.5\,\text{mm}$ to $5.5\,\text{mm}$, which corresponds to a conservative estimate for the collisional broadening of $\Gamma_C \approx 2\pi\,\langle v(T)\rangle/\ell(T) \gtrsim 0.5\,\text{kHz}$ to $1.5\,\text{kHz}$ (FWHM). While experimentally measured values are often much larger than these approximations, the resulting broadening should still be negligible in comparison to the natural line width.

Spectroscopy schemes

Multiple spectroscopy schemes were set up, tested and compared regarding maximal error signal amplitude and slope and minimal long-term drifts. For all other spectroscopy schemes the fundamental UV laser output was frequency shifted using the double-pass AOM setup explained in section 4.2.2. For MOT operation at a detuning of δ_{mot} a modulation frequency of $f_{\text{spec}} = (f_{\text{mot}} + |\delta_{\text{mot}}|)/2$ is required when locking the spectroscopy light to the atomic resonance, as can be seen from figure 4.2. This made AOM diffraction rather inefficient and led to MOT detuning-dependent power level of pump and probe beam. Initially a standard Doppler-free saturation spectroscopy was set up with varying diameters ($\sim 0.5\,\mathrm{mm}$ to $4\,\mathrm{mm}$) and saturation parameters for pump and probe beam. The Doppler background in the probe beam signal was later subtracted by adding and simultaneously recording a third reference beam that passes the spectroscopy cell displaced to the pump-probe interaction volume and therefore probes the atoms Doppler-broadened. This was important to suppress residual power dependency of the locking error signal offset.

For a **frequency modulation spectroscopy (FMS)** [163] scheme sidebands for a PDH locking were generated using a free-space EOM in the UV[1], operated at a modulation frequency of $f_{\mathrm{eom}} = 20\,\mathrm{MHz} \gg \Gamma/(2\pi)$ (optimized for minimum RF reflection) and a modulation depth of $\beta \approx 1.082\,\mathrm{rad}$ ($\mathrel{\widehat{\approx}} 19\,\mathrm{dBm}$) for optimal slope of the error signal. Residual amplitude modulation was observed and mitigated by the use of higher quality polarization optics – Glan-Laser α-BBO polarizers – and careful alignment of the polarization axis of the EOM via a five-axis mount[2]. To remove potential drifts due to amplitude modulation we also tested frequency modulation via the AOM, with no improvement observed. Residual amplitude modulation can also be compensated further by employing additional reference beams and lock-in detection techniques by intentionally intensity modulating the probe beam [164, 165] a technique we did not tested at the time.

PDH demodulation and general locking was performed via a Toptica PDD module with integrated photodiode amplification and phase control and a Toptica FALC laser lockbox respectively. The latter feeds back to the ECDL diode laser both via the diode current – the fast locking branch, establishing initial locking and compensating most laser noise sources – and via the external cavity grating angle controlled by a piezo – the slow locking branch, correcting long-term drifts out of the range of the current feedback. Details on reducing noise and optimizing PDH locking performance are given below. High signal-to-noise detection of the probe beam is challenging in the UV as fast Si detectors decrease strongly in spectral responsivity compared to the visible and near infrared range. Various amplified UV-enhanced Si photodetectors were tested for optimal probe and reference beam recording.

While the modulation was applied to the probe beam for the frequency modulation spectroscopy (FMS), a **frequency modulation transfer spectroscopy (FMTS)** [166, 167] setup was tested, where the EOM modulates the pump beam instead. Here four-wave mixing between pump and probe beam transfers the probe beam acquires frequency sidebands at harmonics of the modulation frequency. Since this modulation transfer just occurs for atoms in the $v = 0$ Doppler-free velocity class, the resulting probe beam signal is fully Doppler-free. This removes potential sensitivity of the demodulated error signal [167]. We believe that this modified optical setup was still mostly limited by optical beam pointing of the FHG cavity, which might explain why we did not find any big improvements in locking performance and especially long-term stability.

Doppler-free **polarization spectroscopy (PS)** [169] was established with a stronger circularly polarized pump and a 45° tilted linearly polarized spectroscopy beam, whose polarization components are split and the signals amplitude difference recorded. Here residual magnetic fields (Earth's magnetic field and surrounding electronics) inside the interaction volume were controlled and cancelled

---

[1] QUBIG PM7-UV, $f_{\mathrm{res}} = 20.0(3)\,\mathrm{MHz}$, $3 \times 3\,\mathrm{mm}^2$ aperture, $200\,\mathrm{nm}$ to $400\,\mathrm{nm}$ anti-reflection (AR) coating ($R < 1\,\%$), accepting vertical polarized light.

[2] Thorlabs PY005/M, ±3.5° pitch, ±5° yaw and 3 mm linear translation adjustment.

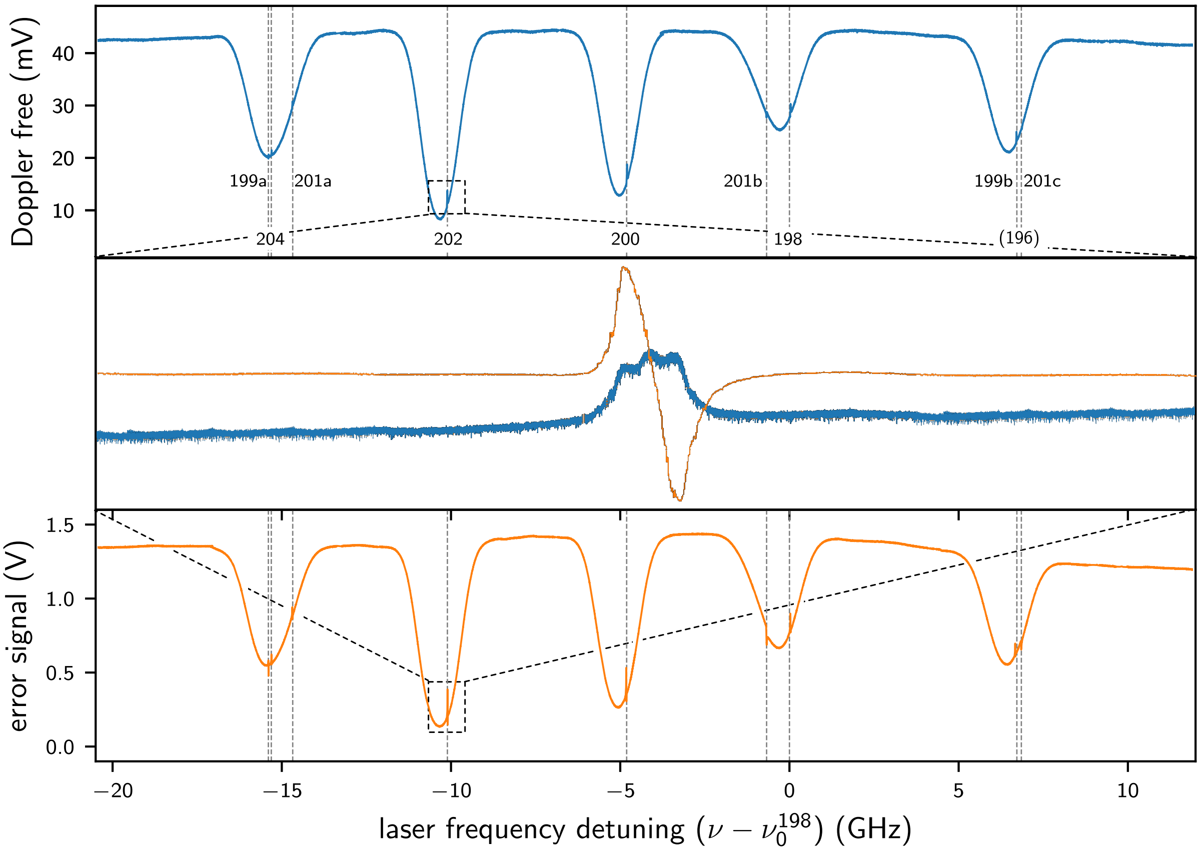

Figure 4.6: Doppler-free saturation spectroscopy signal in the DAVLL scheme (top) and the respective error signal as recorded by the balanced photodetector (bottom). The dashed lines indicate the location of the various isotopes and hyperfine transitions as given in reference [168]. The signal is recorded by a scan of ECDL piezo voltage, the frequency axis is adjusted to the these locations. A zoom into the ^{202}Hg resonance shows the triple structure of the Zeeman split $F = 0 \rightarrow F = 1$ transition and the resulting error signal.

for maximizing the contributions from multiple magnetic m_F-sublevels in the excited and for the fermionic isotopes also in the ground state to the natural dispersion. This is then observed as an error signal. We quickly converted this setup into a sub-Doppler **dichroic atomic vapor laser locking (DAVLL)** scheme [170] by instead applying a controlled magnetic field (typically a few Gauss) along the spectroscopy cell and beam axis.[1] This modifies the polarization spectroscopy (PS) scheme by not trying to zero and instead utilizing the Zeeman shift of the excited state m_F-sublevels, the former which we found was not so easy over the full length of the interaction region. In the DAVLL scheme (for the bosons) the $m_F = \pm 1$ Zeeman levels addressed with a $\sigma_\pm$-polarized probe light (superposition of the linear polarization orthogonal to the magnetic field orientation) are shifted equally but with opposite sign with respect to the atomic resonance. This creates a dispersive error signal when carefully splitting and subtracting the amplitude of the two components. To address this, a combination quarter waveplate and thin film polarizer in the probe beam behind the spectroscopy cell split the linear polarized beam into its circular components. Splitting the probe beam after the spectroscopy cell was achieved using a 50 : 50 non-polarizing plate beam splitter, that showed a slight polarization

---

[1] A Doppler-broadend DAVLL spectroscopy scheme was already established in mercury at ~200 G magnetic fields provided by a pair of Helmholtz coils [171].

sensitivity and increased the power need for the pump beam by a factor of two. Overall it was however the better choice in comparison to introducing a slight angle between probe and pump beam and splitting them using a UV-enhanced silver coated D-shaped mirror for pick-off. The latter version was strongly limited by our need for relatively small beam diameters for the pump beam, which therefore reduced the interaction region of the angled beams within the cell. For the PS and DAVLL locking scheme, the two polarization components of the probe beam were split by thin film polarizers under Brewster's angle and recorded via a free-space balanced amplified photodiode[1]. This was also used for subtracting the reference beam in the standard Doppler-free spectroscopy scheme. Increasing the transimpedance gain via two individual photodiodes and a custom differential op-amp circuit[2] could indeed increase the error signal slope, but resulted in increased non-common-mode noise to be an overall improvement.

A broad scan of all mercury isotopes and exemplary error signal for locking to the ^{202}Hg resonance is shown in figure 4.6. While still being sensitive to beam pointing and residual amplitude variations the DAVLL scheme allowed the best signal-to-noise ratio in the slope of the error signal and allowed first stable trapping of a high number of mercury atoms in the MOT over longer time scales.

4.3.2 Wavemeter stabilization

Alternatively locking the master laser to a high resolution Fizeau-interferometer wavemeter[3] with 10 MHz absolute accuracy and sub 100 kHz resolution was used successfully, but limited stability. We calibrated the wavemeter to an off-site helium-neon laser for obtaining an absolute frequency reference that enabled trapping of all naturally occurring mercury isotopes. Here measurements of some of the isotopic transition against a frequency comb with absolute frequencies given in reference [172], see also figure 4.10, allowed relatively easy localization. With no external absolute optical frequency reference at the point in time the out-of-box stability of the wavemeter could just been characterized via the performance and spectroscopy of our MOT, which showed drifts in the order of ~ 5 MHz/h, not sufficient for reliable long-term operation.

Inspired by the work of Stefan Truppe (at that time: Fritz Haber Institute Berlin) we tried to actively temperature stabilize the wavemeter by enclosing it into a 10 mm thick aluminum box equipped with heating pads. An layer of insulation foam and a PVC box enclosure provides an additional heat shielding. In practice a transfer stability down to 100 kHz referenced to a He-Ne calibration laser can be reached, when the wavelength of the locked laser is in the same range as the reference, while slightly larger wavelength-dependent drifts are expected for larger wavelength differences.[4] While successful in Berlin just in passive mode this resulted in much stronger drifts of about ~ 20 MHz/h (later measured against the ultra-low expansion cavity at 1015 nm as introduced below), which we guess originate in the wavemeter not being able to get rid of heat and/or incompatible temperature settings of the internal stabilization. Active stabilization from our side did not improve things. A future design should therefore increase the box size for better heat circulation and eventually cool – via fan supported convection cooling or a water cooling baseplate – the system as well. Alternatively an active calibration to an optical atomic frequency reference is another option, that then also allows

---

[1] Thorlabs PDB220A2, ∅ 4.1 mm UV-enhanced Si/PIN detector (190 nm to 1100 nm), ~0.1 A/W responsivity, 175×10^3 V/A transimpedance gain, 1 MHz bandwidth. [2] Based on a Texas Instruments THS4551 low noise, 150 MHz bandwidth, fully differential amplifier. [3] Highfinesse WS8-10 [4] Personal communication with Stefan Truppe.

more precise absolute frequency determination.

4.3.3 Ultrastable cavity stabilization

Also motivated by the application as a frequency ruler for high precision isotope shift spectroscopy alternatively locking the IR fundamental of the 254 nm laser system to a high-finesse ultrastable cavity was pursued. Here, the frequency stabilization is transferred to a length stabilization of an ultra-low expansion glass ceramic spacer. With a zero-crossing of the thermal expansion coefficient at a specific temperature (ideally above room temperature) the frequency stabilization can be replaced by a precise temperature stabilization. To achieve this, the cavity spacer is carefully mounted using e.g., thermally insulating mm-diameter FKM fluoroelastomer (Viton) balls to avoid length changes due to bending moments from the temperature-sensitive support structure. It is additionally surrounded by a multi-layer thermal shield that is temperature stabilized by Peltier elements or a heating jacket. The heat shield dampens residual temperature variation of the outside by introducing a thermal mass that introduces a time constant of up to multiple days for the remaining dominating radiative heat exchange towards the spacer. Optical path length changes due to pressure-dependent refractive index changes of the air [173] between the cavity mirrors are strongly suppressed by enclosing the spacer including the thermal shield and temperature control within a vacuum system. Pumped to a pressure of $\leq 1 \times 10^{-7}$ mbar this suppresses daily pressure variations of the atmosphere by many orders of magnitude.

Cavity spacer design Initially, an own design of a $L = 10\,\mathrm{cm}$ long cavity spacer with optically contacted mirror substrates and thermal expansion compensation rings guided by the work in references [174–178] was created.[1] Detailed plans for copper heat shield and vacuum housing were made including a finite element stress analysis simulation for the physical support location of the glass ceramic. A CAD drawing of the reference cavity spacer including heat shield and vacuum enclosure is shown in figure 4.7. We found an optimal solution for laying the glass ceramic on four 3 mm diameter Viton balls that lead to a static stability of $< 10^{-10}\,\mathrm{m}$ and keep the faces at least $10^{-11}\,\mathrm{m}$ even.

With a frequency stability objective of $< 8\,\mathrm{kHz}$ in the IR – providing $\ll 0.05\,\gamma$ fluctuations in the UV when considering the linewidth increase in the FHG system – an active fractional length stability of $\Delta L/L \leq 2.8 \times 10^{-11}$ ($\Delta L \leq 2.8\,\mathrm{pm}$) is required from the spacer, its mechanical support and from the mirror coatings Brownian motion. Given a free spectral range of $\delta_{\mathrm{fsr}} = c/(2\,L) = 1.5\,\mathrm{GHz}$ and a target finesse of $\mathcal{F} > 10\,000$ the 10 cm long cavity design features a $\delta_{\mathrm{fsr}}/\mathcal{F} < 150\,\mathrm{kHz}$ linewidth that should easily allow locking to below the target stability using a standard PDH locking scheme.

The titanium-silicate glass ceramic[2] spacer features a mean linear coefficient of thermal expansion (CTE) of $\alpha_{\mathrm{CTE}} = 0(30)\,\mathrm{ppb/^\circ C}$ around the zero CTE temperature which nominally is located at room temperature [179]. The required temperature stabilization $\Delta T = (\Delta L/L)\,\alpha_{\mathrm{CTE}} \leq 1\,\mathrm{mK}$ is achieved using a three-layer copper heat shield design backed by a Peltier-based temperature control together with a precision proportional-integral-differential (PID) controller[3]. The pressure sensitivity

---

[1] The first choice for an $L = 485\,\mathrm{mm}$ long spacer design (based on the work in references [174, 175]) that allows easy addressing of cavity resonances within a free spectral range of $\delta_{\mathrm{fsr}} \approx 309\,\mathrm{MHz}$ using a standard free-space double-pass AOM setup without resorting to complicated GHz-AOMs was revised and discarded with regard to cost of the spacer material and copper shield and stability against vibration.

[2] Corning ULE 7972.

[3] Thorlabs TED200C benchtop temperature controller (12 W, ≤ 2 mK stability).

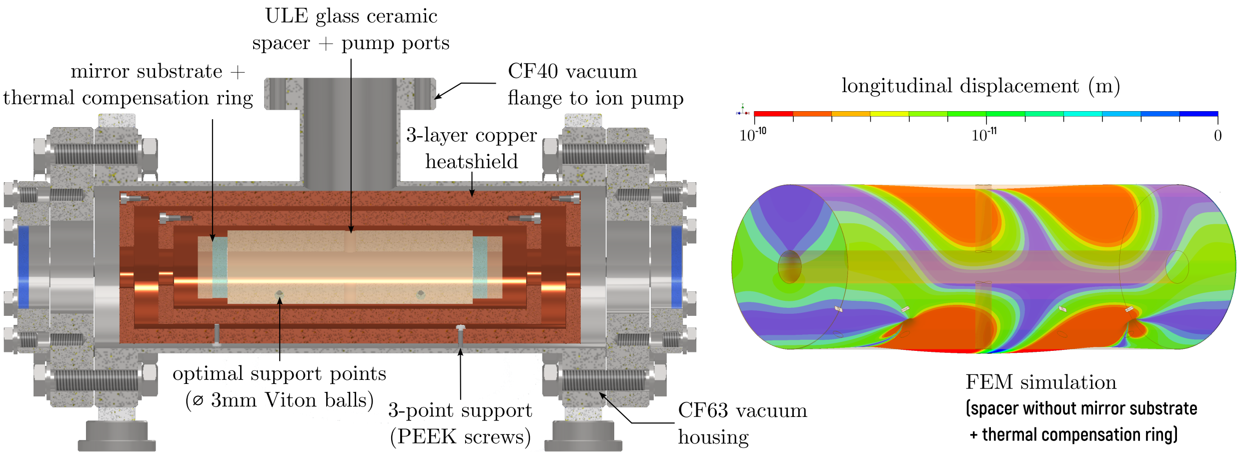

Figure 4.7: Reference cavity design (left) of the 30 mm diameter, $L = 10$ cm length cavity spacer supported by four 3 mm diameter Viton balls on optimal support locations that minimize bending and length change of the spacer in response to vertical accelerations as identified by finite element method (FEM) (right). The three-layer 6 mm thick nested copper heat shields are each supported on three points via PEEK screws for thermal insulation and enclosed in an off-the-shelf 208 mm long CF63 vacuum tube with a CF40 side port for connection to a small ion getter pump (IGP) and gate valve. 3 mm thick, 6 mm inner diameter ultra-low expansion (ULE) glass substrate rings optically contacted to the back of the half-inch diameter mirror fused silica (Corning 7979/7980) substrates compensate for the difference in thermal expansion of the two materials. The latter is omitted in the FEM simulation displaying the longitudinal displacement of the cavity spacer under the influence of gravity for optimized support location.

to the refractive index of air of about 2.7×10^{-7}/mbar (extracted from reference [173]) considering the tidal induced daily atmospheric pressure fluctuations with diurnal and semidiurnal periodicity is compensated for by inserting the cavity spacer into vacuum, where a resulting pressure demand of $\leq 1 \times 10^{-3}$ mbar is reached with a 2 L/s IGP .

High-finesse ultra-low expansion cavity Additional funding for a commercial system then allowed to save development effort, and instead we purchased an optical reference cavity based on a $L = 5$ cm cubic cavity spacer manufactured from ultra-low expansion glass with calibrated thermal expansion zero crossing temperature[1]. Featuring a loaded symmetric support structure – see [174] and a similar design in reference [180] – instead of laying the spacer on horizontal optimized support spots [181] via e.g., four Viton balls, here the cavity spacer is clamped on all corners. This allows the design to be transportable while maintaining low mechanical and low frequency instability.

The cavity stabilization setup is shown in figure 4.8. It is located on a separate optical table and connected via a polarization maintaining fiber to the master ECDL laser. A fiber EOM (fEOM) generates the required PDH sidebands at f_{pdh} and allows offsetting the laser by a frequency offset f_{eom} with respect to the cavity mode used for locking. A typical PDH locking scheme stabilizes the ECDL via the ULE cavity reflection signal monitored with an amplified photodiode (PDA). The fiber coupler (FC) lens mode matches the TEM_{00} cavity mode and a combination of optical attenuator (A) and $\lambda/4$ retardation waveplate act as an optical isolator avoiding back reflections into the fiber

---

[1] Menlo ORC-Cubic.

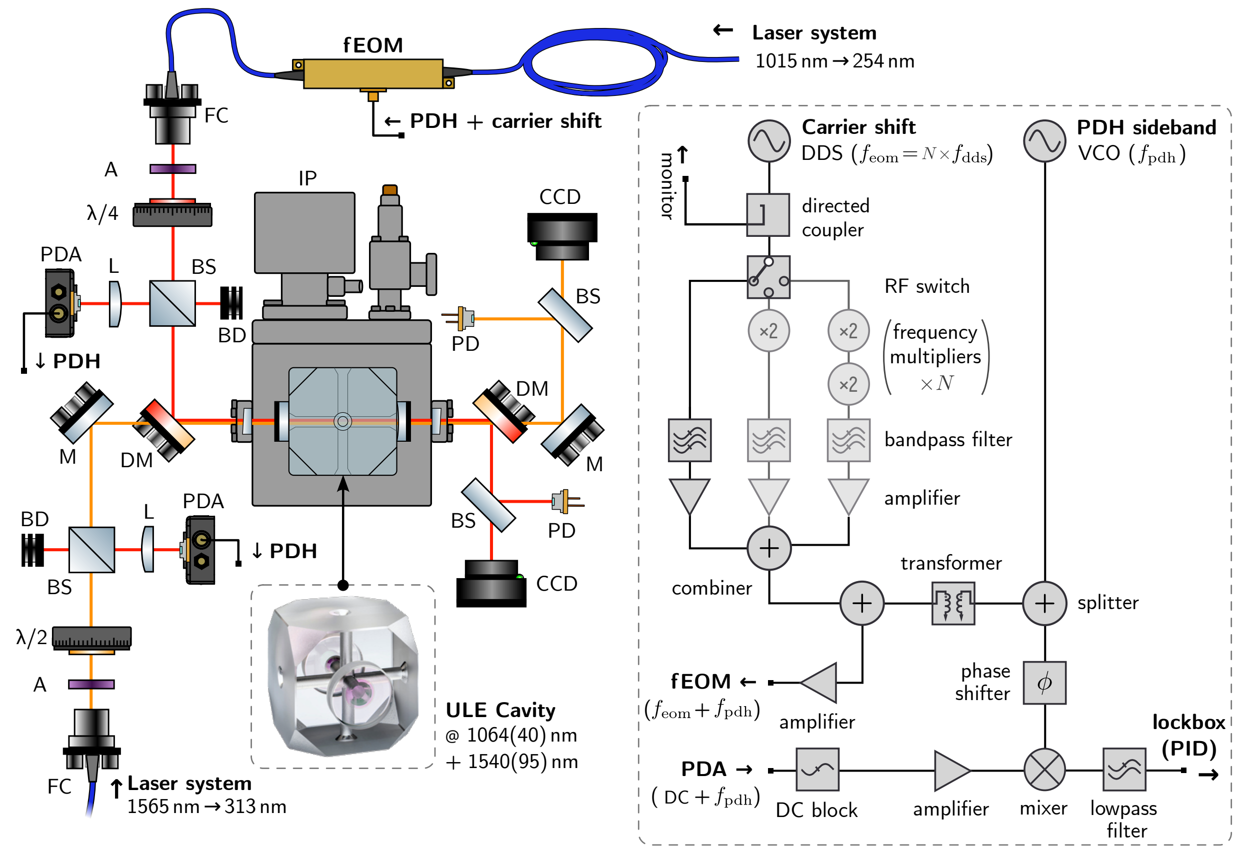

Figure 4.8: Optical (left) and electronic setup (right) of the laser lock to the ultrastable cavity. The setup shows the combined optical path of the 1015 nm (top left, red) and 1565 nm (bottom left, orange) path and the PDH demodulation and locking electronics for the former (right). For a detailed description see the main text. The photo of the ULE cavity spacer (inset) is taken from reference [182].

EOM and laser.[1] A CCD camera and a PD monitor the locking status via the cavity transmission. Dichroic (long-pass) mirrors (DM) allow stabilization of multiple lasers to the cavity that features a high-finesse mirror coating: $\mathcal{F} > 30\,000$ for 1020(75) nm; $\mathcal{F} > 100\,000$ for 1540(95) nm. Also shown is the 1565 nm stabilization of the quintupled 313 nm spectroscopy laser system, introduced in chapter 6. Long term stability of the cavity is provided by pumping the temperature stabilized cube-shaped ULE glass ceramic via an IGP to $\leq 1 \times 10^{-7}$ mbar.

Frequency control & locking The fiber-based electro-optic phase modulators[2] (fEOM) allows sideband modulation of up to $f_{\mathrm{eom}} \geq 7$ GHz, not reachable by standard AOM technology[3]. The only disadvantage compared to AOM frequency shifters is the lack of spatial separation between the modulated and non-modulated light. This increases incident power to the cavity that otherwise does only contribute to the PDH cavity reflection signal as a DC offset and slightly decreases its signal-to-noise.

The fiber EOM is fed by the sum of the two radio frequencies that allows offsetting the laser by a

---

[1] Without the isolator, we could observe laser frequency-dependent sinusoidal modulation of the error signal offset caused by etalon effects in the beam path. [2] JENOPTIK PM1064 phase modulator with a spectral bandwidth of 1064(40) nm that was modified/specified to also work at 1015 nm. [3] For optimum modulation depth, larger frequencies require increasing the RF power, as the half-wave voltage increases from 6 V ($f_{\mathrm{eom}} \leq 1$ GHz) to 18 V at $f_{\mathrm{eom}} = 7$ GHz.

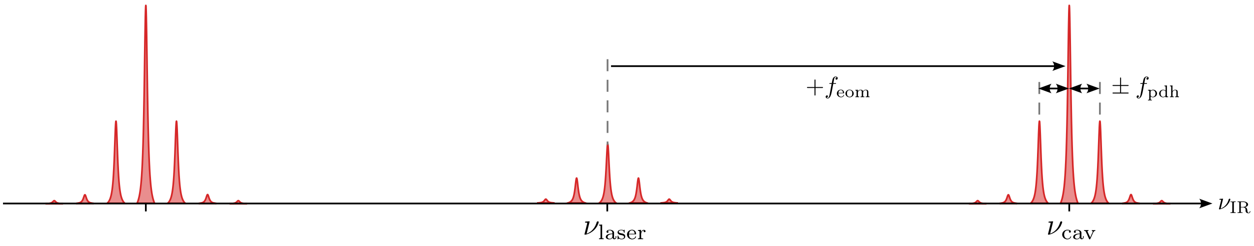

Figure 4.9: Fiber EOM frequency spectrum fed by the sum of two sinusoidal RF signals at f_{eom} (carrier shift) and f_{pdh} (PDH sideband frequency for demodulation), respectively.

frequency offset f_{eom} with respect to the cavity mode and generates the PDH sidebands $\pm\beta_{\text{pdh}}$ used for locking. This creates three PDH triplets in the infrared laser frequency, as illustrated in figure 4.9. At optimized modulation depth β the fundamental is suppressed ($\beta_{\text{eom}} \approx 1.841$) and the $\pm f_{\text{eom}}$ carrier shifted triplet features a sideband-to-carrier power ratio that maximizes the resulting PDH error signal ($\beta_{\text{pdh}} \approx 1.082$).[1]

The carrier shift f_{eom} frequency is generated by a DDS board[2], that is extended from $f_{\text{dds}} \leq 400$ MHz to the GHz-range by (consecutive) RF multipliers. The resulting higher harmonics are carefully filtered with a selection of bandpass filters and the fundamental frequency is monitored via a Rb microwave clock referenced spectrum analyzer. A Toptica PDD module with integrated VCO generates the required PDH sidebands at $f_{\text{pdh}} \approx 10$ MHz for locking and demodulates the amplified and filtered cavity reflection photodiode signal to generate the PDH error signal. The master laser is controlled via a PID laser lockbox[3] with its slow and fast circuit branch acting back on the ECDL diode current and piezo-driven external grating (G) angle, respectively. The use of low-pass filters for the demodulated signal at a cut-off frequency of 10 MHz allows efficient elimination of noise in the error signal while not restricting the bandwidth of the laser lock. We typically reach −3 dB locking bandwidths of a few hundred kHz to just below <1 MHz as identified by investigating the (locked) error signal on a spectrum analyzer. Additionally, DC-blocking and therefore isolating the frequency modulated probe beam photodiode signal is crucial to remove unwanted error signal offset fluctuations caused by ground loop currents in the lab electronics. A typical PDH error signal, corresponding cavity transmission spectrum and a ring-down finesse measurement are shown in figure 4.10. We measure a finesse of $\mathcal{F} = 74\,115(656)$ at 1015 nm and $\mathcal{F} = 166\,458(352)$ at 1565 nm.

Individual isotopes can be addressed via their isotope shift. To achieve this, we select the closest cavity resonance line – gray dashed line in figure 4.10 – and adjust the EOM carrier shift frequency f_{eom} to the respective atom cavity detuning, taking into account the additional frequency shift by the absorption imaging and MOT path AOM. The $^1\text{S}_0 \rightarrow {}^3\text{P}_1$ transition in mercury is spread over 23 GHz for all natural-abundant isotopes, corresponding to about 6 GHz in the IR. Here the cavity features resonances located every integer multiple of its free spectral range $\delta_{\text{fsr}} \approx 3$ GHz, which restricts the maximum EOM carrier shift frequency required to $f_{\text{eom}} \leq \delta_{\text{fsr}}/2 = 1.5$ GHz. The UV imaging beam

---

[1] This condition shifts to smaller β when supplying the EOM with all desired frequencies by electronic mixing, which we found requires overall less RF power, but results in a reduced error signal slope. Furthermore, note that high modulation depths cause unwanted sidebands at higher harmonics, which can lead to residual amplitude modulation.

[2] Sinara Urukul 4-channel frequency synthesizer based on a AD9910 DDS.

[3] Toptica Fast Analog Linewidth Control FALC 110.

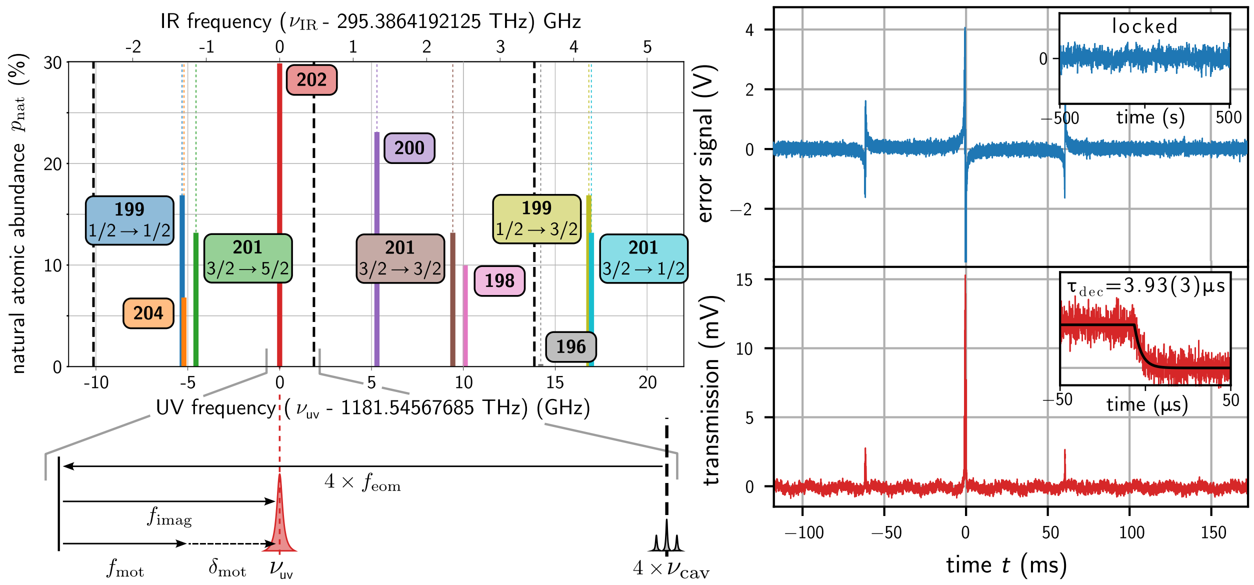

Figure 4.10: Cavity lock of the 254 nm laser system for laser cooling and spectroscopy. The bottom left shows a zoomed in sketch of the EOM frequencies (f_{eom}) and AOM frequencies needed for MOT operation (f_{mot}) and resonant imaging (f_{imag}) on ^{202}Hg. A typical error signal (right top) of the PDH scheme and the corresponding cavity transmission (right bottom) close to cavity resonance is shown on the right. The insets show the error signal during locking and a ring down measurement after enabling/disabling the lock respectively. More details are given in the text.

frequency is given by

$$\begin{aligned} \nu_{\mathrm{img}} &= 4\,(\nu_{\mathrm{cav}} \pm f_{\mathrm{eom}}) + f_{\mathrm{img}} \\ &= 4\,\left(\nu_{\mathrm{cav},\,0} + i_{\mathrm{cav}}\,\delta_{\mathrm{fsr}} \pm f_{\mathrm{eom}}\right) + f_{\mathrm{img}}\,, \end{aligned} \tag{4.16}$$

where we introduced a cavity line index $i_{\mathrm{cav}} \in \mathbb{N}$ that references all isotopic resonances to a fixed cavity line $i_{\mathrm{cav}} = 0$. Here f_{img} is again the imaging beam AOM frequency, as defined above. We define the cavity detuning with respect to this fixed line as

$$\delta_{\mathrm{cav}} \equiv \nu_{\mathrm{img}} - 4\,\nu_{\mathrm{cav},\,0} = 4\,(i_{\mathrm{cav}}\,\delta_{\mathrm{fsr}} \pm f_{\mathrm{eom}}) + f_{\mathrm{img}}\,. \tag{4.17}$$

The atomic resonance is then denoted by $\nu^{\star}$ and $\delta^{\star}_{\mathrm{cav}}$ respectively. We will utilize the stability of the cavity resonance lines and this reference for precision isotope shift spectroscopy in chapter 6, where we also present a precise measurement of the cavity free spectral range.

The achieved laser lock is quite stable against environmental disturbances including daily pressure and temperature variations and especially acoustic noise from power supplies, chillers, lab doors and more. At the beginning of each experimental sequence, and upon request, the laser is slowly ramped to the desired frequency (~ MHz/s) by adjusting the carrier-shift DDS frequency in small steps. The system remains locked during the day, requiring relocking only when switching between isotopes, as the latter mostly requires frequency changes that extend the free spectral range (FSR). Faster frequency changes of tens of megahertz within milliseconds for MOT compression are also possible and discussed in more detail in section 4.8. Linewidth, frequency stability and lock reproducibility is also discussed in chapter 6.

4.4 Imaging

Imaging the atomic cloud for determination of its atom number and size is the main diagnostic tool and provides the main observable for the experiments discussed in this thesis. Collecting the fluorescence of the atoms stimulated by e.g., scattered MOT light gives us a good knowledge of cloud position, shape and a rough estimate of atom number. This allows initial alignment of the MOT gradient field zero with respect to the center of the cooling beams. The latter are aligned to the physical center of the vacuum chamber with the help of irises within the beam path and additional ones mounted to the six vacuum viewports. The number of scattered fluorescence photons is directly proportional to the atom number. But a rough estimate of the atom number is only possible with knowledge of the cooling beam detuning and an estimate of the photon collecting efficiency, which is determined by viewing angle, viewport transmission and camera efficiency. Additionally, temperature determination via fluorescence imaging can lead to trap re-formation during the imaging exposure with MOT light. This then alters the measured temperature in dependence on exposure time [105]. With these limitations for atom number and temperature determination we decided to directly implement an additional absorption imaging setup, that acts as the main detection and analysis routine. The combined setup is described below.

4.4.1 Fluorescence imaging

Imaging in the deep-UV is challenging since the spectral responsivity of standard Si-based detector materials breaks down at around 300 nm. Here a charge-coupled device camera with electron-multiplying gain (emCCD)[1] is selected as the imaging sensor. With a thermoelectric cooled, UV-enhanced Si sensor with a quantum efficiency of $\epsilon_{\mathrm{qe}} \geq 30\,\%$ at $\lambda > 200\,\mathrm{nm}$, the camera technology allows detection down to single photon level while keeping background counts low. To achieve this, the camera exposure is controlled by an external trigger via our time control system, while the sensor chip is in a clean cycle state before and after to remove background counts of stray light.

When illuminating the atoms with MOT light, fluorescence imaging is mainly limited by scattered light at the vacuum viewports. To compensate this, an additional camera exposure is triggered at a later point in time in the sequence, where the gradient field is switched off and therefore no atoms are present. The resulting reference image is subtracted from atom image to correct for background counts. An optionally inserted optical bandpass filter[2] at $(254 \pm 5)\,\mathrm{nm}$ allows to further reduce unwanted counts in the visible to infrared range. This includes UV laser induced fluorescence of the glass and especially the coating substrates, which is visible by eye as diffuse blueish white light. While fluorescence detection via an amplified (avalanche) photodetector was considered and tested, the presence of background induced counts in the current system and the lack of flexibility in spatial filtering options for non-camera-based detection was reason enough to not pursue it any further.

The camera position and imaging system are restricted by the vacuum chamber geometry and selected to maximize the viewing angle for fluorescence while allowing absorption imaging on the same axis. The horizontal imaging axis tilted by $\alpha \approx {\sim}10^\circ$ with respect to the y-axis MOT beams is shown in figure 4.2 and 5.2. With the camera sensor at a distance of $d_{oi} \approx 273\,\mathrm{mm}$ to the center of

---

[1] Andor iXon3 885. 1004×1002 pixel resolution, $8 \times 8\,\mu\mathrm{m}$ pixel size. 31.4 fps maximum frame rate in video mode. [2] Edmund Optics 39-312 hard-coated UV fused silica bandpass filter, 254(2) nm center wavelength, 10(2) nm FWHM transmission band, OD ≥ 4 blocking and $\geq 50\,\%$ transmission.

the vacuum chamber, a very simple imaging system in form of a single lens collects the fluorescence light. A $D_\mathrm{lens} = 1\,\mathrm{in}$ (or $2\,\mathrm{in}$) diameter, $f \approx 68.25\,\mathrm{mm}$ focal length plano-convex lens[1] in $2f : 2f$ configuration allows imaging a $8 \times 8\,\mathrm{mm}$ area at a $|M| = 1:1$ magnification. The lens diameter limits the collection efficiency of atomic fluorescence to a solid angle fraction of

$$\frac{\delta\Omega}{\Omega} \lesssim \frac{\pi\,(D_\mathrm{lens}/2)^2}{4\pi\, d_\mathrm{lens}^2}\,, \tag{4.18}$$

where $d_\mathrm{lens} = 2f$ is the object distance. For the 1 in diameter lens given above this fraction is just about 0.22 %, but sufficient for MOT characterization. We increased the lens diameter to 2 in when optical access (MOT beams, ODT beam reflections from the viewports) allowed for it. The magnification – important for cloud size determination – was calibrated using a reference target of known size illuminated at 254 nm. By simply replacing a lens tube on the camera with a $f' \approx 45.5\,\mathrm{mm}$ lens at a principal plane distance of $d_o \approx 215\,\mathrm{mm}$ the magnification can be quickly reduced to $|M'| \approx 1:3.7$ without moving the camera. This allows imaging a much larger $\sim 30 \times 30\,\mathrm{mm}^2$ area, helpful during initial MOT alignment and for debugging purposes. The camera lens system is mounted on top of a linear translation stage to precisely adjust its position with respect to the atoms.

The fluorescence counts n_fluo collected by the camera can be used to infer the approximate atom number N. The photon flux of $\lambda = 254\,\mathrm{nm}$ photons – induced by either the MOT beams or a separate imaging beam – that is emitted by the cloud is directly proportional to the atom number $\Phi = N\,\sigma\,I$, where σ is the photon scattering cross-section from equation (4.6) and I the beam laser beam intensity. Given the geometrical constraints of the imaging system, equation (4.18), and the quantum efficiency of the camera sensor ϵ_qe itself, the fluorescence counts are then given as

$$n_\mathrm{fluo} = \epsilon_\mathrm{qe}\,\frac{\delta\Omega}{\Omega}\,\frac{1}{E_\nu}\int_0^{t_\mathrm{exp}} \mathrm{d}t\;\Phi(t) = \epsilon_\mathrm{qe}\,\frac{\delta\Omega}{\Omega}\,\frac{\sigma\,I}{E_\nu}\,N\,, \tag{4.19}$$

where $E_\nu = h\,c/\lambda$ is the photon energy and in the last step we assumed atom number and intensity to be constant over the exposure time t_exp.

For typical MOT characterization a camera exposure time of $t_\mathrm{exp} = 20\,\mathrm{ms}$ was chosen when illuminating the atoms via the MOT beams. The camera is fully controlled via a self-written python server that controls the cooling (typically to −60 °C) and the optimized horizontal and vertical readout speed of the CCD sensor, as well as the mechanical shutter. It fully integrates into the ARTIQ control system, see section 4.6, prepares the camera for acquisition of multiple images and transfers them to the data storage and analysis tools.

Vertical imaging system A second imaging system observing the MOT through the top viewport that increases the numerical aperture of the horizontal system was installed later. Here a $f = 68.4\,\mathrm{mm}$ objective lens with its optical axis under 13.4° with respect to the vertical MOT beams at a distance of $d_o = 2f \approx 137\,\mathrm{mm}$ increases the fluorescence capture angle by a factor of ~6.5. By illuminating the atoms not with the MOT cooling light, but using the horizontal absorption imaging beam, whose viewports are out of line-of-sight from the top, this imaging system is much less limited by laser

---

[1] Focal lengths are corrected for the refractive index of UV fused silica at 254 nm.

induced background counts. Therefore, the fluorescence counts can be increased by multiple orders of magnitude by activating the electron-multiplying gain of the camera. While not explicitly used for the calibration and spectroscopy measurements presented in this thesis, the system therefore especially allowed amplification of small atom number signals experienced in ^{196}Hg spectroscopy, where our absorption imaging implementation struggles to resolve the small cloud densities. The imaging system was therefore included into the standard experiments imaging sequence, where the two cameras were then triggered simultaneously during absorption beam illumination. This results in an approximate 2D projection of the MOT cloud in the $x-z$ plane from the absorption and an additional 2D projection in the $x-y$ plane from the fluorescence image. Binning of the vertical cameras CCD pixels ($2x2$ to $4x4$) and increasing the imaging beam pulse and vertical camera exposure time up to 1 ms proved to be beneficial for small signal amplification.

We initially attempted to image the atoms using a large 2 in diameter $f = 54.6\,\mathrm{mm}$ plano-convex lens positioned exactly vertically along the z-axis MOT beams. Here the 1 in diameter $\lambda/4$-waveplate and 0° retroreflection mirror for the MOT beam were glued directly onto the flat side of the lens, such that the atoms are just imaged via the circular non-covered section of the lens. A 2 in threaded kinematic mirror mount positioned on a vertical breadboard above the vacuum chamber aligns and holds the imaging system while allowing adjustment of the MOT beam reflection. While this system in theory allows for even better collection efficiency when mounting the lens close to the vacuum viewport, a later ray tracing analysis using Ansys Zemax OpticStudio revealed that the thick lens introduces spherical aberrations that are too large for the object size imaged here. The current system is also limited by a slight astigmatism introduced by the transmission of the top viewport under the angle of 13.4°, which is why a future upgrade to a carefully designed aspheric lens systems along the z-axis might be beneficial.

4.4.2 Absorption imaging

A collimated UV laser beam around the resonance frequency of the intercombination line is sent under a slight angle (~10°) through the short horizontal axis of the MOT chamber, as shown in figure 4.2. The beam diameter is selected to be much larger than the MOT cloud size to ensure relatively homogeneous saturation of the atoms. Initially set to a waist of $w_0 = 7.5\,\mathrm{mm}$, we later increased the beam drastically to >1 in diameter for improved isotope shift spectroscopy, since the frequency-dependent diffraction angle in the single-pass AOM setup leads to intensity variation at the location of the atoms even when power stabilizing the imaging beam. For this, the beam is expanded in a telescope to a waist of about 15 mm, such the resulting central beam area follows approximately a flat top profile when compared to the MOT size. This leads to clipping of the beam at the periscope optics and beam shaping lenses and introduces slight fringe patterns in the camera images, which however did not alter the performance in atom number and temperature determination.

Atom number and temperature determination Absorption imaging probes the three-dimensional optical density $\mathrm{od}(\vec{r})$ of the atomic cloud via detecting the absorption of the probe beam using a camera. Following the Lambert-Beer absorption law $\mathrm{d}I(\vec{r}) = \mathrm{od}(\vec{r})I(\vec{r})\,\mathrm{d}s$ the absorption imaging beam experiences the attenuation along its propagation axis path $\vec{r}(s) = \vec{k}_{\mathrm{img}}\,s$ and the transmitted

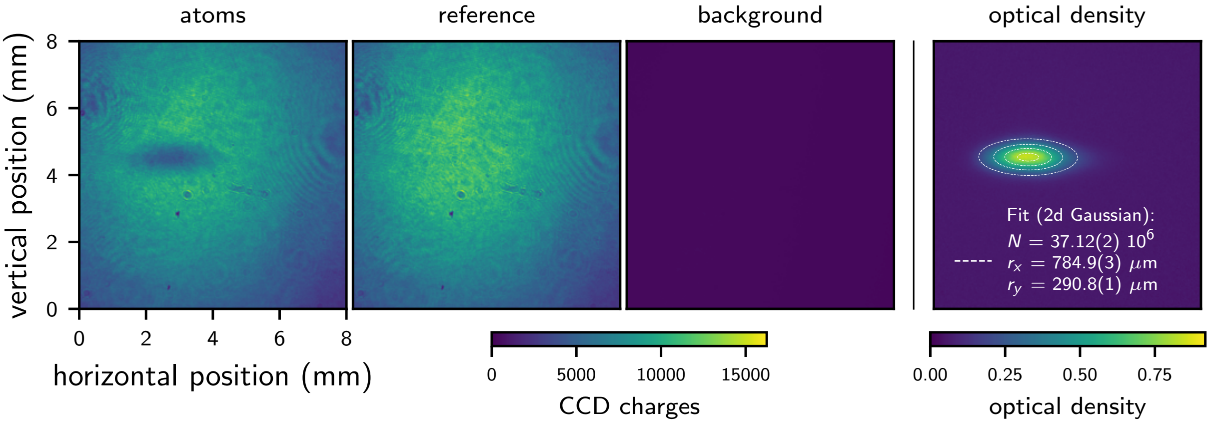

Figure 4.11: Typical set of absorption images and resulting optical density estimate for ^{202}Hg. The CCD camera electron counts are shown unprocessed in false colors, all scaled to the same color scheme limits. We show a 1000×1000 pixel sized section of the sensor area, where the given axis are converted to millimeter from the pixel size and magnification (= 1). The optical density is obtained following equation (4.21), the atom number and cloud radii are determined from a two-dimensional Gaussian fit following equation (4.23).

intensity is the two-dimensional projection given by

$$I(x', z') = I_0(x', z') \int_{\text{sample}} \mathrm{d}s\ \mathrm{od}(\vec{r}(s)) \approx I_0(x, z) \int_{\text{sample}} \mathrm{d}y\ \mathrm{od}(x, y, z)\,, \tag{4.20}$$

where x', z' denote the axes of the camera. For the setup here, the imaging beam axis lies in the (x, y)-plane as shown in figure 4.2 with the axes defined by the MOT beams and gradient field orientation. With the imaging beam wavevector given by $\vec{k}_{\text{img}} = (-k\ \sin\alpha,\ -k\ \cos\alpha,\ 0)^T \approx (0,\ -k,\ 0)^T$ for $\alpha \approx 10°$ we approximately image the atomic cloud profile in the $(x' \approx x, z' = z)$-plane as noted above, an approximation we will use throughout this thesis. The camera records the intensity profile as the photon counts integrated over the individual sensor pixel area $A_{\text{px}} = 8 \times 8\,\mu\text{m}^2$ and imaging beam exposure time t_{img} given by $\mathrm{img}(x', z') = \mathrm{QE} \int_{A_{\text{px}}} \mathrm{d}x'\mathrm{d}y'\ I(x', y')\ t_{\text{img}}$. Recording both an absorption image of the atomic cloud $\mathrm{img}_a(x', z') \propto I(x', z')$ and one of the unperturbed reference beam $\mathrm{img}_r(x', z') \propto I_0(x', z')$ the two-dimensional projection of the optical density of the atomic cloud can be estimated from

$$\mathrm{od}(x', z') = -\log\left(\frac{\mathrm{img}_a(x', z') - \mathrm{img}_b(x', y')}{\mathrm{img}_r(x', z') - \mathrm{img}_b(x', z')}\right)\,, \tag{4.21}$$

where $\mathrm{img}_b(x', y')$ is a background image taken without any imaging beam to correct for dark counts and stray light detected by the camera.

Given the optical resonance cross-section σ_0 defined in equation 4.6, the atom number can then be estimated from the sum of the optical density as

$$N = \frac{1}{\sigma_0} \int \mathrm{d}x'\mathrm{d}z'\ \mathrm{od}(x', z') \approx \frac{A_{\text{px}}}{\sigma_0} \sum_{x',\, z'} \mathrm{od}(x', z')\,. \tag{4.22}$$

Alternatively and more stable against power fluctuations between atom and reference image, a two-dimensional Gaussian profile,

$$\mathrm{od}_{\mathrm{gauss}}(x', y') \supset A \, \exp\left(-\frac{(x' - x_0')^2}{2\, {r_x}^2}\right) \exp\left(-\frac{(z' - z_0')^2}{2\, {r_z}^2}\right), \tag{4.23}$$

can be fitted to the optical density estimate. This is implemented in the time control system as a fixed analysis routine running asynchronously to data acquisition for most efficient timing, giving us live information about atomic cloud density and cloud radii r_x, r_z for optimization purposes. The number of atoms is then given by

$$N \approx \frac{1}{\sigma_0} \int \mathrm{d}x'\mathrm{d}z' \; \mathrm{od}_{\mathrm{gauss}}(x', z') = \frac{2\pi \, A \, r_x \, r_z}{\sigma_0}. \tag{4.24}$$

A typical absorption image including optical density calculation and atom number estimate from a two-dimensional Gaussian fit is shown in figure 4.11.

The atomic cloud temperature can then be estimated from a time-of-flight sequence, where the atoms are imaged after increasing fall times t_{tof}. For this, the measurement sequence of loading and imaging the atoms, figure 4.13, is repeated multiple times. Under the assumption of a thermalized atomic cloud at temperature T its radius r $(= r_x,\ r_z)$ will then expand according to

$$r(t_{\mathrm{tof}}) = \sqrt{r_0^2 + \frac{k_B \, T}{m} \, t_{\mathrm{tof}}^2}\,. \tag{4.25}$$

Ideally the atomic cloud will then follow a free fall trajectory $(x_0(t_{\mathrm{tof}}),\ z_0(t_{\mathrm{tof}})) = (x_0,\ z_0 - \frac{1}{2}\, g \, {t_{\mathrm{tof}}}^2)$. This can be used to calibrate the imaging magnification. Furthermore, analyzing the atom trajectory in free fall for nonzero initial velocities allows studying and compensating residual power imbalance in the MOT beams. The latter can also originate from absorption at the vacuum viewports, when recycling the beam via retroreflection. A typical time-of-flight sequence and temperature estimate for a configuration of nearly perfectly balanced cooling beams is shown in figure 4.12.

Optimization Exposure time and imaging beam intensity are mainly restricted by MOT dynamic timescales and recoil shifts, the latter being discussed in section 6.2. They are optimized for best signal-to-noise by maximizing the camera counts, nearly filling the 30 000 electron well depth per pixel in the active area of the sensor chip. An imaging beam pulse duration of $t_{\mathrm{img}} = 150\,\mu\mathrm{s}$ and a power of $\leq 1\,\mathrm{mW}$ corresponding to a beam intensity of $\leq 0.1\, I_{\mathrm{sat}}$ were found to be optimal. With these settings, each atom scatters approximately 20 photons on resonance. This results in a slight recoil shift and a slightly asymmetric lineshape, as discussed in more detail in section 6.2.2.

Intensity stabilization For intensity stabilization the magnified beam is monitored using a variable-gain amplified photodetector[1] behind a AR-coated wedged window for pickup. The signal is read out via an ARTIQ Sampler digital-analog converter that controls the AOM RF power via a PID feedback loop operating on the main field programmable gate array (FPGA) chip of the time control

---

[1] Thorlabs PDA25K2 GaP, 150 nm to 550 nm spectral bandwidth, ~0.03 A/W responsivity at 254 nm, variable 0.75×10^3 V/A to 4.75×10^6 V/A transimpedance gain at 2.6 kHz to 9500 kHz bandwidth. Sadly this model was discontinued and sourcing GaP sensor material became more challenging due to global trade restrictions.

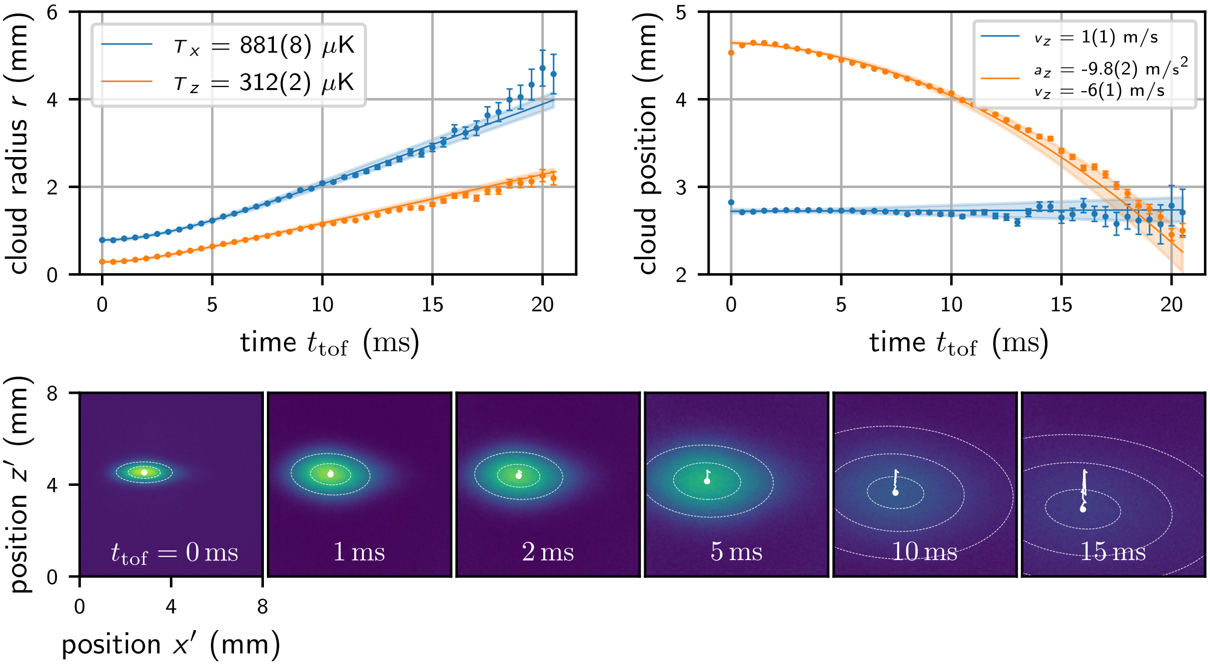

Figure 4.12: Time of flight (TOF) sequence and temperature estimation for ^{202}Hg. After extracting MOT size and position from the optical density via a two-dimensional Gaussian fit for varying fall times t_{tof} (bottom), we fit the cloud radii in horizontal and vertical direction according to equation (4.25) to extract the temperature (top right). Analyzing the cloud position in time (top left) we can determine the residual velocities and accelerations in both directions, confirming the magnification of the imaging system. With larger MOT clouds, we can observe TOFs of up to 20 ms limited by the decreasing density and the absorption imaging contrast.

system. The bandwidth of the ARTIQ SuServo PID lock is limited to $\lesssim$ 100 kHz, which successfully compensates long timescale power drifts of the UV laser system up to acoustic noise induced power fluctuations (including air vibrations from the table air conditioning). It is however too slow to power stabilize the short imaging beam pulses ($t_{\text{img}} \approx 150\,\mu\text{s}$) necessary for absorption imaging without introducing more advanced feed-forward locking schemes. For this, the main imaging beam is then sent through a 1:1 Keplerian telescope. Here, a self-built servo-based mechanical shutter in the focus between the two plano-convex lenses allows fast switching (about 10 ms to 15 ms) of the imaging light due to the reduced beam diameter. Active beam power stabilization is then operated only with the shutter in the closed state and halted shortly before the required imaging beam pulse for which the shutter is opened briefly, as illustrated in figure 4.13. This reduces the power stabilization bandwidth drastically to lower frequencies, but a detailed relative laser intensity noise (RIN) characterization of the UV laser system showed that acoustic noise should not limit any of our measurements.

4.5 Magnetic field control

Various magnetic fields are required for preparation and analysis of the atomic clouds within the main chamber of the vacuum system. Magneto-optical trapping requires a magnetic field with a spatial gradient at the location of the atoms is required. To address individual Zeeman sublevels during

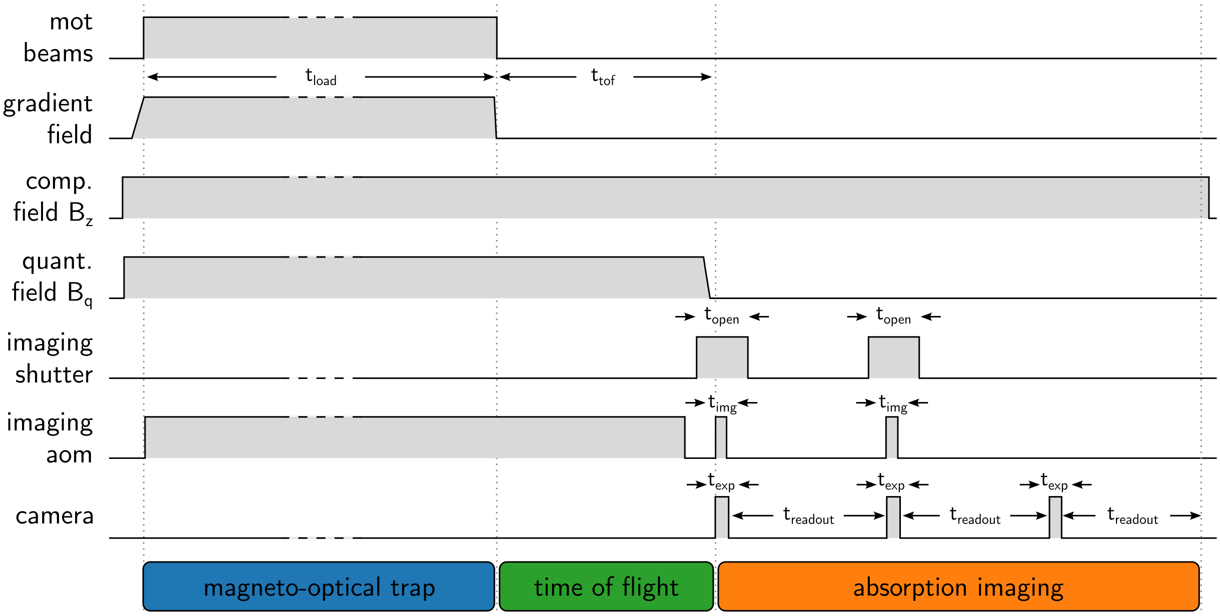

Figure 4.13: Experimental magneto optical trap and absorption imaging sequence. After MOT loading for t_{load} atoms fall for t_{tof} and are imaged using a $t_{\text{img}} \leq t_{\text{exp}}$ long absorption imaging pulse and camera exposure window. Reference and background image are taken after atoms are lost, limited by the camera readout time.

spectroscopy and for imaging, spatially homogeneous magnetic fields are needed. Additionally, stray magnetic fields and magnetic field gradients from surrounding components such as IGPs and vacuum gauges, as well as the Earth's magnetic field need to be compensated.

For all of these fields, pairs of electromagnets in Helmholtz configuration are an ideal choice, since they create a homogeneous magnetic field within its center when the two opposing coils carry an equal current in the same direction and create a linear gradient field when carrying an equal current but in the opposite direction. Furthermore, electromagnets allow tuning of the field strengths by changing its current, which support fine-tuning the magnetic field zero point to the location of the atoms and optimizing the systems' performance. This makes them advantageous over permanent magnet solutions, which have limited tunability but are often used for their zero power consumption and lack of cooling needs when optimized field strengths and gradients are known.

(Anti-)Helmholtz coil Assuming infinitesimally thin wires, the axial magnetic field B_z on the axis z of a circular current loop with radius r, current I and loop number N can be obtained from the Biot-Savart law and is given by

$$B_z(z) = \mu_0 \, I \, N \, \frac{r^2}{2\left(r^2 + z^2\right)^{3/2}} \, . \tag{4.26}$$

The magnetic field of two opposing circular coils with radius r and distance d, where the current direction in the two coils is the same (opposite) (±) can then be calculated from $B_z^{\pm}(z) = B_z(z - {}^{d}\!/_{2}) \pm B_z(z + {}^{d}\!/_{2})$. In good approximation for the application here, we can always assume $z \leqq r$. A Taylor expansion around $(z/r) = 0$ to third order gives

$$\begin{aligned} B_z^{\pm}(z) = \mu_0\, I\, N \Bigg[&\frac{1}{2}\frac{r^2\,(1 \pm 1)}{\left(r^2 + (d/2)^2\right)^{3/2}} + \frac{3}{4}\frac{d\, r^3\,(1 \mp 1)}{\left(r^2 + (d/2)^2\right)^{5/2}} \left(\frac{z}{r}\right) \\ &+ \left(-\frac{3}{2}\frac{r^4}{\left(r^2 + (d/2)^2\right)^{5/2}} + \frac{15}{8}\frac{d^2\, r^4}{\left(r^2 + (d/2)^2\right)^{7/2}} \right) (1 \pm 1) \left(\frac{z}{r}\right)^2 + \mathcal{O}\left(\frac{z}{r}\right)^3 \Bigg] . \end{aligned} \tag{4.27}$$

In the configuration of identical current orientation (+) the first order cancels for any distance of the coils, but the second order cancels as well for the **Helmholtz configuration** when $d = r$. The magnetic field along the symmetry axis is then given by

$$B_z^{+}(z) = \mu_0\, I\, N \frac{8}{5\sqrt{5}\, r} + \mathcal{O}\left(\frac{z}{r}\right)^3 . \tag{4.28}$$

If magnitude of the current in the two coils is equal but its orientation opposite to each other (−) the zeroth and second order of the expansion vanishes and the resulting field is linear in z, where the maximum gradient is given by again spacing the coils by $d = r$, the **Anti-Helmholtz configuration**. The field then reads

$$B_z^{-}(z) = \mu_0\, I\, N \frac{48}{25\sqrt{5}\, r^2}\, z + \mathcal{O}\left(\frac{z}{r}\right)^3 . \tag{4.29}$$

For this configuration, it can be shown that the orthogonal magnetic field B_ρ along $\rho = \sqrt{x^2 + y^2}$ is also approximately linear to third order [183]. Directly following then from the Gauss law for magnetism $\vec{\nabla} \cdot \vec{B} = 0$ (in cylindrical coordinates) this gradient has to be half as strong as the one along z and with opposite sign, creating a spherical quadrupole symmetry for the field,

$$\frac{\partial B_z}{\partial z} = -2\,\frac{\partial B_\rho}{\partial \rho} = \frac{48}{(25\sqrt{5})}\frac{\mu_0\, I\, N}{r^2} . \tag{4.30}$$

Rectangular coils For better optical access to the central vacuum chamber and more compact nesting of multiple coils within each other, pairs of rectangular coils feature a larger enclosed volume for the same field and are a good choice over classically round Helmholtz coils. The magnetic field of a rectangular coil can be estimated using the Biot-Savart law for a superposition of the individual fields of four finite length wire segments. For a single rectangular coil of side lengths $a \times b$ the on-axis magnetic field can therefore be approximated as [184, eq. (4.6)]

$$B_z(z) = \frac{\mu_0\, I}{4\pi}\frac{a\, b}{\sqrt{(a/2)^2 + (b/2)^2 + z^2}} \left(\frac{1}{(a/2)^2 + z^2} + \frac{1}{(b/2)^2 + z^2} \right) \tag{4.31}$$

The optimal spacing for the Helmholtz condition of two rectangular coils made up of multiple loops can then be obtained easiest numerically or experimentally. A good approximation found here is to consider the coil as a square coil of effective side length $\tilde{a} = (a + b)/2$. In this case, the optimal spacing – the distance, where the second order derivative of the field at the origin vanishes – is given by $d \approx 0.5445\,\tilde{a}$ [184, 185]. The magnetic field at the origin then reads [184]

$$B_z(z = 0) \approx 1.296\, \mu_0\, I\, N/\tilde{a} \qquad \text{at} \quad d \approx 0.5445\,\tilde{a} \tag{4.32}$$

and is therefore just about 9.4 % weaker than the field of a round Helmholtz coil pair with radius $r = \tilde{a}/2$.

Switching For fast switching of the magnetic gradient and guiding field coils, the main limitation is the inductance L of the coil. For a coil of radius r, number of turns N and overall thickness of all conductors t it can be approximated for $r \gg r$ as [183]

$$L \approx \mu_0 \, r \, N^2 \left(\log \left(\frac{16\, r}{t} \right) - 2 \right) . \tag{4.33}$$

The response of the current I when suddenly switched off at time $t = 0$ (by opening the circuit) then follows an exponential decay $I(t) = I_0 \, \exp\left(-t/\tau\right)$, where the characteristic switching time is given by

$$\tau = \frac{L}{R} , \tag{4.34}$$

where the coils' resistance $R = \rho \, l/A$ can be calculated from its length $l \approx 2\pi \, r \, N$ and its conductor cross-section A. In section 4.5.3 it will be shown, that the switching time can be further reduced by clamping the circuits' voltage during switch-off.

4.5.1 Gradient field coils

In MOT operation a spatial magnetic gradient field is required to make the scattering force of the circular polarized light field not only velocity-dependent as in an optical molasses, but also position-dependent. A zero of the magnetic field at the center of the trap ensures that the atoms see no Zeeman splitting and the light field is therefore far red-detuned to all atomic levels resulting in no significant light force. Atoms outside the center are Zeeman shifted by the gradient field and brought into resonance with the circular polarized light fields and therefore experience a restoring force towards the center of the trap. The strength of the magnetic gradient for magneto optical operation is typically on the order of 5 G/cm to 30 G/cm.

Two magnetic gradient field coil designs were built during this work. The first design is water cooled and allows gradient field strengths well beyond 20 G/cm and was used for studying the parameter landscape of MOT operation optimizing atom number and temperature, as described in chapter 4. The construction of the coil however limits the switching time needed for high imaging contrast in the sequence for isotope shift spectroscopy, as described in chapter 6. Therefore, reason a convection cooled magnetic gradient field coil with a non-metallic support and low inductance was manufactured as a replacement.

First generation gradient field coil The coil is constructed from 6 mm × 6 mm square, hollow copper tubing [1] with an inner diameter of 4 mm to allow as direct water cooling as possible. The tubing is made from oxygen free, high conductive copper (OFHC) to reduce its specific electrical resistance and allow bending the material more easily. It is isolated electrically from itself using 0.17 mm thick silicon impregnated braided glass fiber sleeves[2] and wound onto a support frame made

---

[1] Luvata Tool #6835; 6.0(1) mm × 6.0(1) mm profile, 4.0(1) mm inner diameter, 1 mm corner radius; oxygen free copper according to ASTM C10200 and EN CW008A; 0.20 kg/m; soft temper (H035). [2] Siltex GI 1011 Fiberglass Sleeve Silicone Impregnated; specified for −60 °C to 220 °C.

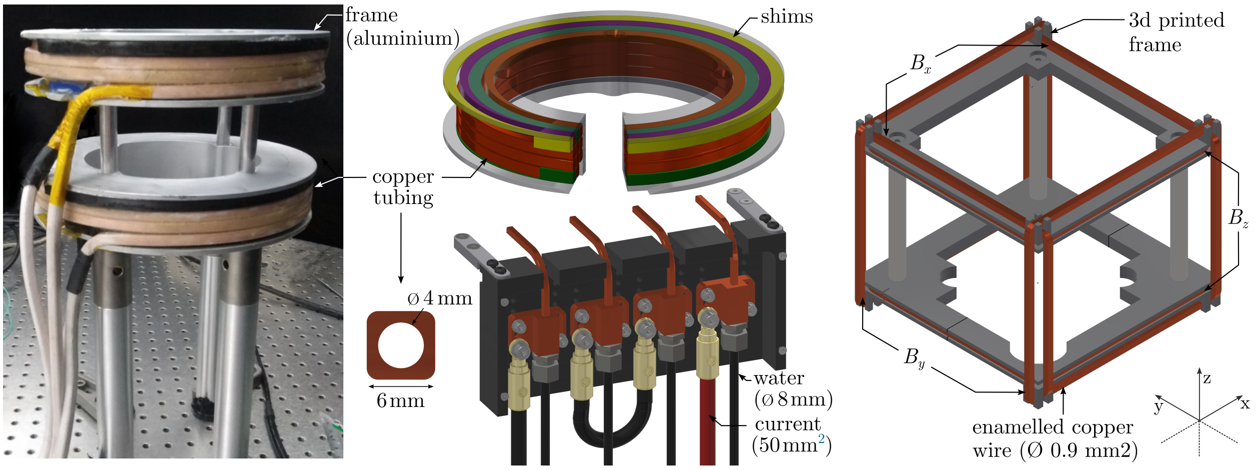

Figure 4.14: First generation magnetic field coils. Magnetic gradient coils in anti-Helmholtz configuration spaced by and supported to the table by aluminum posts (left). The hollow 6 mm × 6 mm square copper tubing is wound onto an aluminum frame with the help of 3D printed shims (top center). Electrical contact and water cooling connection to the hollow copper tubing is realized by an adapter station on the edge of the optical table (bottom center). Here the copper tubing of the top and bottom coil are connected in series and to the power supply using $50\,\mathrm{mm}^2$ diameter stranded isolated wire, the water cooling to the 17 °C house water via 8 mm outer diameter plastic tubing. Magnetic field compensation coils (right) fitting the gradient coils in (a) made from three pairs of rectangular coils of $0.9\,\mathrm{mm}^2$ cross-section enamelled copper wire wound onto a 3D printed support structure. The support is spaced by metal rods and clamped around the gradient coil frame for added rigidity.

from aluminum. The coil was wound starting with the first inner radial layer doing four axial windings up and then changing to the next radial layer, winding down and repeating this pattern for the other layers. The support frame features two slits with 22 mm radii for guiding the copper tubing in and out smoothly. About $N = 12$ windings are enclosed like this in a square $A_{\mathrm{tot}} = 27.4\,\mathrm{mm} \times 27.4\,\mathrm{mm}$ cross-section.

While winding the coil, heat conductive epoxy was applied to fix the copper tubing in place permanently and therefore compensating for the repulsive outward Lorentz force of the coil during operation. The Lorentz force also asks for a robust mounting of the two coils with respect to each other, since two current loops with opposing current direction repel themselves as well.[1] To address this, aluminum spacers and pedestal pillar posts, electrically isolated by nylon washers and nylon screws, act as a coil spacer and support structure as shown in figure 4.14.

Initially, a non-conductive fiber reinforced high strength machining plastic was considered as the support material to prevent eddy currents within the material when switching the magnetic fields. An estimation of the eddy currents was unfortunately neglected and the idea discarded. In hindsight this was a wrong decision as the metallic, circular continues support frame is the dominant limitation of the switching time, while the copper coil itself has a exceptionally low intrinsic inductance. Using equation 4.33 approximating the effective overall thickness of the coil $t \approx 4\sqrt{A_{\mathrm{tot}}/\pi} = 61.8\,\mathrm{mm}$ from

---

[1] For two coils of radius r separated by distance d this Lorentz force is in between the two scaling regimes; $d \ll r$ where the current experience the other coil as a straight line resulting in a $\propto d^{-1}$ scaling of the force and $d \gg r$ where the two coils see each others as dipoles resulting in a $\propto d^{-4}$ scaling of the repulsion force.

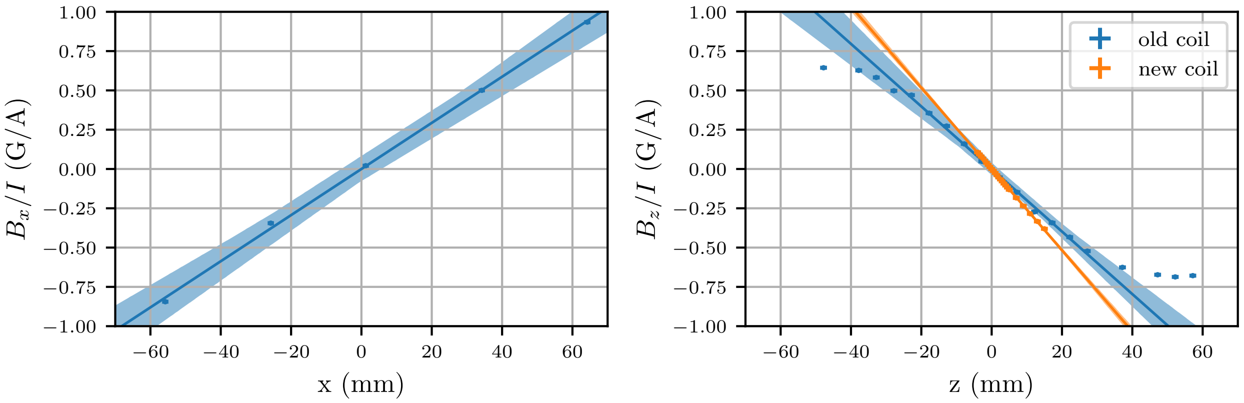

Figure 4.15: Magnetic field measurement of the gradient field coils. The magnetic field is measured axially using a Hall probe along three orthogonal axes with their origin located at the center of the coil. Displayed here is exemplary the field B_i in $i = x, z$ direction divided by the current I. The shaded area indicates the $3\,\sigma$ error band of the linear fit (line). For the vertical axis z only data points in the center are considered for the fit. First generation gradient field coil field measured at a current of 100.00(3) A (blue), second generation coils at a current of 49.90(3) A (orange).

the overall square coil cross-section A_{tot}, the number of loops $N \approx 12$ and mean radius $r = 78\,\mathrm{mm}$ the inductance is $L \approx 14\,\mu\mathrm{F}$. With a specific conductance of $1/\rho = 58.0\,\mathrm{S/m}$ for oxygen free copper, a conductor cross-section of $A = 22.6\,\mathrm{mm}^2$ and a coil length of about $l \approx 2\pi\, r\, N = 5.9\,\mathrm{m}$ the electrical resistance is about $R = 4.5\,\mathrm{m\Omega}$ per coil and following equation 4.34 the characteristic switching time is $\tau = 3.2\,\mathrm{ms}$. The electrical resistance was measured to 6.79(2) mΩ for the top and 6.39(5) mΩ for the bottom coil (at 100 A). This is in good agreement with the expectation considering the additional length of the coil connections of about 2.5 m per coil (adding up to about 1 mΩ per coil) and added contact resistance to the power supply.

Approximating the coil geometry following equation 4.30, the coil is designed for a field gradient of about $\partial B/\partial z \approx 0.213\,(\mathrm{G/cm/A}) \cdot I$. For a gradient of $\partial B/\partial z = 10\,\mathrm{G/cm}$ ($20\,\mathrm{G/cm}$) this requires a current of $I = 47\,\mathrm{A}$ ($94\,\mathrm{A}$). The magnetic field was measured along the vertical and two horizontal axes for varying currents using a Hall probe[1] and is shown exemplary in figure 4.15 for a current of 100 A. The magnetic gradient averaged over multiple measurements with varying field strengths is $\partial B/\partial z = -0.202(2)\,\mathrm{G/(cm\,A)}$ and $\partial B/\partial \rho = -0.146(3)\,\mathrm{G/(cm\,A)}$. Note that slight deviation of the gradient along z from the expectation can be accounted to the imprecise number of loops that originate from the complex coil geometry during layer changes. The deviation from $\partial B/\partial z = 2\,\partial B/\partial \rho$ is accounted to the finite volume of the coil and individual field contribution of loops that lie closer to the center of the coil, but the more homogeneous gradient at the position of the atoms is appreciated. A numerical field analysis accounting for the position of individual loops using the python package `Magpylib` [186] confirms this deviation.

In order to improve the stability of the magnetic field strength, avoid displacement of the magnetic field zero during operation, and shield the vacuum chamber and surrounding optics from heat, the electrical power in the coil must be dissipated as efficiently as possible. For a gradient of $\partial B/\partial z = 10\,\mathrm{G/cm}$ ($20\,\mathrm{G/cm}$) this requires dissipating about $P = 28\,\mathrm{W}$ ($113\,\mathrm{W}$) of resistive heat for both coils

---

[1] Two magnetic hall probes were used here: Magnet Physik HU-SA1-264605 and Group3 DTM-151.

(including connection leads) via the internal water cooling. To address this, a water distribution providing 17 °C cold cooling water in the flow and 20 °C water in the return line at a pressure difference of about 2 bar was installed in the lab. The cooling water and electrical contact of the coil copper tubing is realized by an adapter station on the edge of the optical table as shown in figure 4.14. Here the copper tubing is hard soldered on a small ~10 mm round copper piece, which is then soft soldered into a copper adapter featuring a M8 terminal for a ring terminal connecting to the 50 mm^2 cross-section electrical connection leads. The copper adapter then allows the installation of a water fitting, where 8 mm outer diameter, black, non-transparent[1] plastic tubing connects the hollow copper coil to the house cooling water. Restricting the temperature increase of the cooling water to $\Delta T = 0.5\,\mathrm{K}$ this would require a flow rate of $Q = 0.8\,\mathrm{L/min}$ $(3.2\,\mathrm{L/min})$. Following the Darcy-Weissbach equation for turbulent flow this corresponds to a pressure difference of $\Delta p = 0.4\,\mathrm{bar}$ $(1.44\,\mathrm{bar})$. These requirements are sufficiently provided by the house cooling water. Utilizing the full cooling power with $\Delta p = 2\,\mathrm{bar}$ and allowing up to $\Delta T = 3\,\mathrm{K}$ temperature difference should even allow dissipating up to $P = 950\,\mathrm{W}$ of power reaching gradient field strengths of up to $\partial B/\partial z = 58\,\mathrm{G/cm}$ at a current of $I = 270\,\mathrm{A}$. This allows enough flexibility for optimizing the magnetic field gradient for MOT operation.

Second generation gradient field coil For improving the switching time of the first generation coil design the only change required would have been to replace the aluminum support frame using a rigid, non-metallic material like fiber-reinforced machining plastics. Due to the high time effort for machining and manufacturing this design, an alternative approach was chosen. After studying the MOT properties and optimizing the atom number and temperature with respect to the gradient field using the previous set of gradient coils, it became clear that the optimum gradient strength lies around 10 G/cm and not exceed 20 G/cm, even during fast sequences of cloud compression that create minimal heating. Therefore, a passively cooled coil design was selected.

The coil is manufactured by directly water jet cutting a circular structure of $N = 12$ loops into a 25 mm thick oxygen free copper plate, as displayed in figure 4.16. The resulting coil cross-section therefore leaves only a minimal air gap of about 0.9 mm, which was later filled with epoxy to add stability to the otherwise really flexible coil.[2] The coil then being solid in itself just requires a support frame for the correct coil spacing, here solved by a two-piece 3D printed structure that directly clamps around the edges of the central cube of the vacuum chamber. Four through holes at the inner edge of the coil allow clamping the two coils firmly together using three headless stainless steel screws, that are isolated from the coil using Kapton tape and Nylon washers and hex nuts. The fourth hole is the start/end of the coil and a 4 mm diameter brass rod with brass washer and nut interconnects the two coils through the support frame. At the connection points to the coil pure indium was added into the through hole bore to increase the electrical conductivity between the brass rod and the copper coil. Two 50 mm^2 isolated stranded wire connect via M6 ring terminals to two threaded holes at the other end of the coil.[3]

Following equation 4.30 with an effective radius of $r = 70\,\mathrm{mm}$, the expected coils field gradient is

---

[1] Important to avoid any algae forming inside the tubing. [2] The size of this gap is limited by the three-axis water jet cutter, which, given the thickness of the plate, bulges for smaller gaps. Electric discharge machining would be a more expensive, but viable alternative allowing even smaller gaps increasing the current density of the coil further. [3] These four connection points appeared to be the hot spots of the coil, a redesign might consider increasing the clamping surface and a tighter clamping mechanism for the brass rod, potentially replacing it with copper as well.

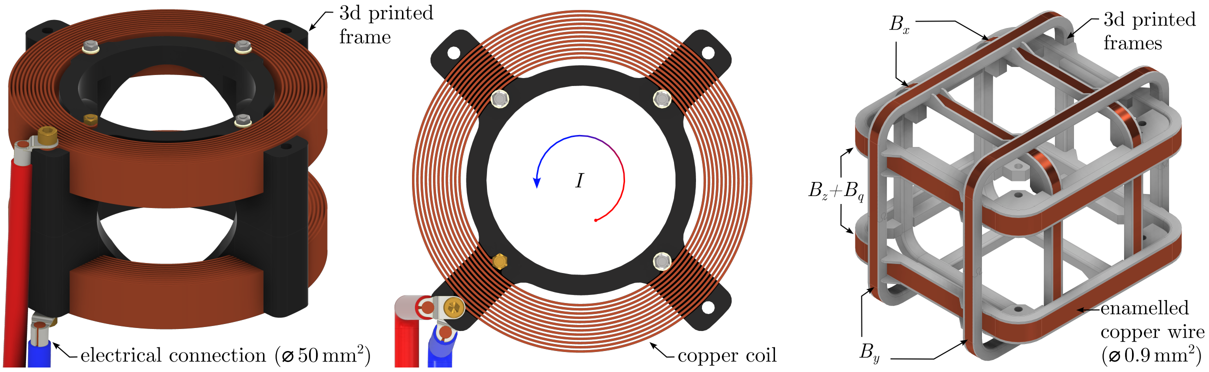

Figure 4.16: Second generation magnetic field coils. Magnetic gradient coils in a side (left) and top-down view (center). Compatible compensation and guiding field coils (right) that rest on the 3D printed gradient coil support frame.

about $\partial B/\partial z \approx 0.264\,(\mathrm{G/cm})/\mathrm{A} \times I$, about 24 % higher than the previous design due to the reduced size and increased current density. This reduces the required current for a magnetic field gradient of $\partial B/\partial z = 10\,\mathrm{G/cm}$ ($20\,\mathrm{G/cm}$) to $I = 37.8\,\mathrm{A}$ ($75.7\,\mathrm{A}$). While the number of loops $N = 12$ stayed the same, the new design further allowed to increase the conductor cross-section by 22 % now forming a rectangular $1.1 \times 25\,\mathrm{mm}^2$ profile. This gives an electrical resistance of $R = 3.3\,\mathrm{m\Omega}$ per coil and reduced the total power to $P = 10\,\mathrm{W}$ ($40\,\mathrm{W}$) of resistive heat, about a third less in comparison to the first generation design. This includes the 4 mm diameter brass rod with an electrical conductivity of about $1/\rho = 16.7\,\mathrm{S/m}$ that interconnects the upper and lower coil with a resistance of about $0.4\,\mathrm{m\Omega}$.

A measurement of the magnetic field is shown in figure 4.15 for a current of 49.90(3) A, which results in an axial magnetic field gradient of $\partial B/\partial z = -0.258(2)\,\mathrm{G/(cm\,A)}$, agreeing with the theoretical expectation for the thin coil model stated above.

4.5.2 Compensation and quantization field coils

The compensation field coils are required to zero the magnetic field at the location of the atoms. Non-zero field contributions originate from the Earth's magnetic field (north: ~0.20 G, east: ~0.01 G, vertical (z): ~0.45 G at the location in Bonn [187]), fields from surrounding permanent magnets (IGPs and vacuum gauges) and electronics and furthermore also imperfections in the construction and alignment of the gradient coil field zero with respect to the vacuum chamber. Three pairs of Helmholtz coils are an ideal choice to compensate the field along all directions.

To improve the precision of the isotope shift spectroscopy measurement presented in chapter 6, a homogeneous magnetic field aligned with the polarization of the spectroscopy light pulse is required. This quantization/guiding field coil then aligns the atomic spin with respect to the light polarization. With the ideally linear polarized spectroscopy laser light entering the vacuum chamber in the horizontal ($x \times y$) plane, a vertical (z) polarization and magnetic field axis is most convenient. Given typical Zeeman shift strengths of about ~2 MHz/G and transition linewidths of up to ~10 MHz (see section 2.2) this requires field strengths of up to ~30 G to split the relevant magnetic hyperfine levels of the atoms for the short duration of the spectroscopy pulse.

Construction The first-generation compensation coils were made by winding 0.9 mm^2 enamelled copper wire onto 3D printed supports mounted with stainless steel pillars[1], with approximately 20 rectangular windings per coil. Despite small deviations from Helmholtz configuration, the magnetic field remained sufficiently homogeneous over the MOT region, with center field strengths of 1.062 G/A, 1.074 G/A, and 1.567 G/A for x, y, and z, respectively.

The second-generation design introduced pre-wound coils on 3D printed supports (except for y) and corrected field inhomogeneities by adopting Helmholtz spacing and increasing the windings to $N = 40$, achieving stronger fields (4.272 G/A for x, 3.609 G/A for y, and 3.723 G/A for z) with lower power consumption. To enable a fast-switchable vertical quantization field B_q, an additional coil with equal windings is mounted in parallel to the z compensation coil. As quickly switching off an electromagnet can be realized easier than switching it on, this coil will be permanently turned on during static MOT operation and its additional field be compensated by a higher current (in opposite direction) in the z compensation coil. The total vertical field is thus $B_z + B_q$, and switching off B_q creates a quantization field during spectroscopy pulses.

4.5.3 Fast digital and analog field control

For time-of-flight imaging and spectroscopy sequences after MOT operation, fast switching of both the trapping laser light and the magnetic gradient field is required. Dynamics in the MOT take place on time scales of the scattering rate $\tau_{\text{scat}} = 1/R_{\text{scat}} \geq 2/\Gamma \approx 0.2\,\text{ms}$. With typical trap temperatures for mercury (see 4.7), atoms within the trap have mean velocities on the order of $v = \sqrt{k_B T/m} \approx 100\,\text{mm/s}$. Given initial cloud radii down to $\sim 50\,\mu\text{m}$ this lead to doubling of cloud size during free fall in about a $\sim 1\,\text{ms}$ or faster. To gain precise knowledge of the initial cloud radii, this requires switching the current within the gradient field coils much faster than these time scales. This will also keep the cloud density as high as possible during imaging of low abundant isotopes during isotope shift spectroscopy. Fast imaging light pulses on the order of 100 µs during time-of-flight require even faster switching of the guiding and compensation field currents.

Snubber circuit The characteristic switching time constant for a coil of inductance L and resistance R is $\tau = L/R$ as given by equation 4.34. A circuit with added capacity and switching characteristics of a non-ideal current source might further extend this time. The switching time constant can however be reduced drastically using a so-called Snubber circuit, where the switch-off voltage U_S is clamped by switching the current using a transistor and providing another sink for the power. Following Faraday's law, the change in the magnetic flux Φ_B induces the voltage

$$U_S = -\frac{\mathrm{d}\Phi_B}{\mathrm{d}t} = -L\,\frac{\mathrm{d}I}{\mathrm{d}t}\,, \tag{4.35}$$

and the current then decays linearly $I(t) = I_0\,(1 - t/\tau)$, where the switch-off time is given by

$$\tau = \frac{L\,I_0}{U_S}\,. \tag{4.36}$$

For a fixed magnetic field strength B (or magnetic gradient strength) determining the necessary total current $N\,I$, and given the proportionality of the inductance L with the square of the loop number N,

---

[1] Designed and built by Quentin Lavigne.

this time constant follows $\tau \propto BN/U_S$ [188]. This asks for low-inductance coils made out of as few loops as possible and for high switching voltages. To protect electronic transistor-based switches and to avoid damage to the insulation of all circuit components, including the cables and the coil conductor loops itself, the switching voltage U_S has to be chosen carefully. Snubber circuits usually involve an RC-circuit. For this application, special snubber capacitors with increased protection against impulse-like voltage spikes are also available. Additionally, the linear decay of the current in a realistic circuit will be altered by the capacitive and resistive impedances of the coils, their supply line, and the imperfect switch characteristics. These factors lead to non-constant voltage, additional exponential decay, and potential overshooting or undershooting of the current.

Gradient field control

The snubber circuit built for fast gradient field control is shown in figure 4.17. We employ a fast insulated-gate bipolar transistor (IGBT) module[1] with an integrated emitter-controlled diode to disconnect the power supply and short the coil via an appropriate resistive load. These IGBT modules are made for high frequency switching applications of high currents featuring low switching losses and an integrated protection diode rated for the switching current and voltage. The model chosen here can drive 150 A (DC) to 300 A (repetitive peak collector current at 1 ms pulse length) and features a collector-emitter voltage of 1200 V that allows fast switching times in the µs-range.

To drive the required gate-emitter voltage from our time control system, the workshop designed an IGBT driver board that converts the TTL level BNC connection from the digital interface to 15 V via a fast, but standard bipolar transistor and IGBT gate drive optocoupler with about 500 ns response time, which should not limit the overall coil switching time. When switching the IGBT to its closed state, clamping the voltage to the collector-emitter voltage, the coil current flows through the IGBT integrated diode and an external high-power snubber resistor R_S. An additional snubber capacitor C_S absorbs the initial transient current, and the resistor dissipates the pulse energy as heat. Together they also form a low-pass filter that smoothens out fast voltage and current spikes.

Various combination of resistors and capacitors were tested to improve the switching performance, where we aim for fastest switch-off time in compromise to a slight overshoot of the current and magnetic field. We settled on low-inductance snubber capacitors[2]. While they promise even shorter switching times, they did not show any improvement in speed. However, they promise high pulse reliability and overvoltage protection. A combination of a $R_S = 4.7\,\Omega$ resistor[3] and $C_S = 1\,\mu\mathrm{F}$ capacitor[4] showed the best performance.

Both the IGBT and the resistor come in a metal package with solid M5/M6 screw terminals for low-resistance connections and feature a large backplate, where we attach a big ($\sim 300\,\mathrm{cm}^2$) extruded aluminum heat sink, which dissipates the pulse energy via forced convection aided by a series of low-noise computer fans. All components are housed in a rack-mountable crate and are interconnected with $35\,\mathrm{mm}^2$ to $50\,\mathrm{mm}^2$ stranded single-core copper wire and M6 sized ring cable lugs for low resistance, as they are the dominating points of power dissipation. The overall system adds $\leq 15\,\mathrm{m}\Omega$ of resistance, when operating the coil at maximum set current (100 A).

---

[1] Infineon FD150R12RT4. [2] Wima Snubber MKP film capacitor line. [3] TE Connectivity HSC2004R7J, 200 W power dissipation, 3600 V isolation voltage. [4] Wima MKP4O141007E00KSSD, 1 kV (DC) insulation voltage, 75 V/µs to 150 V/µs pulse rise time.

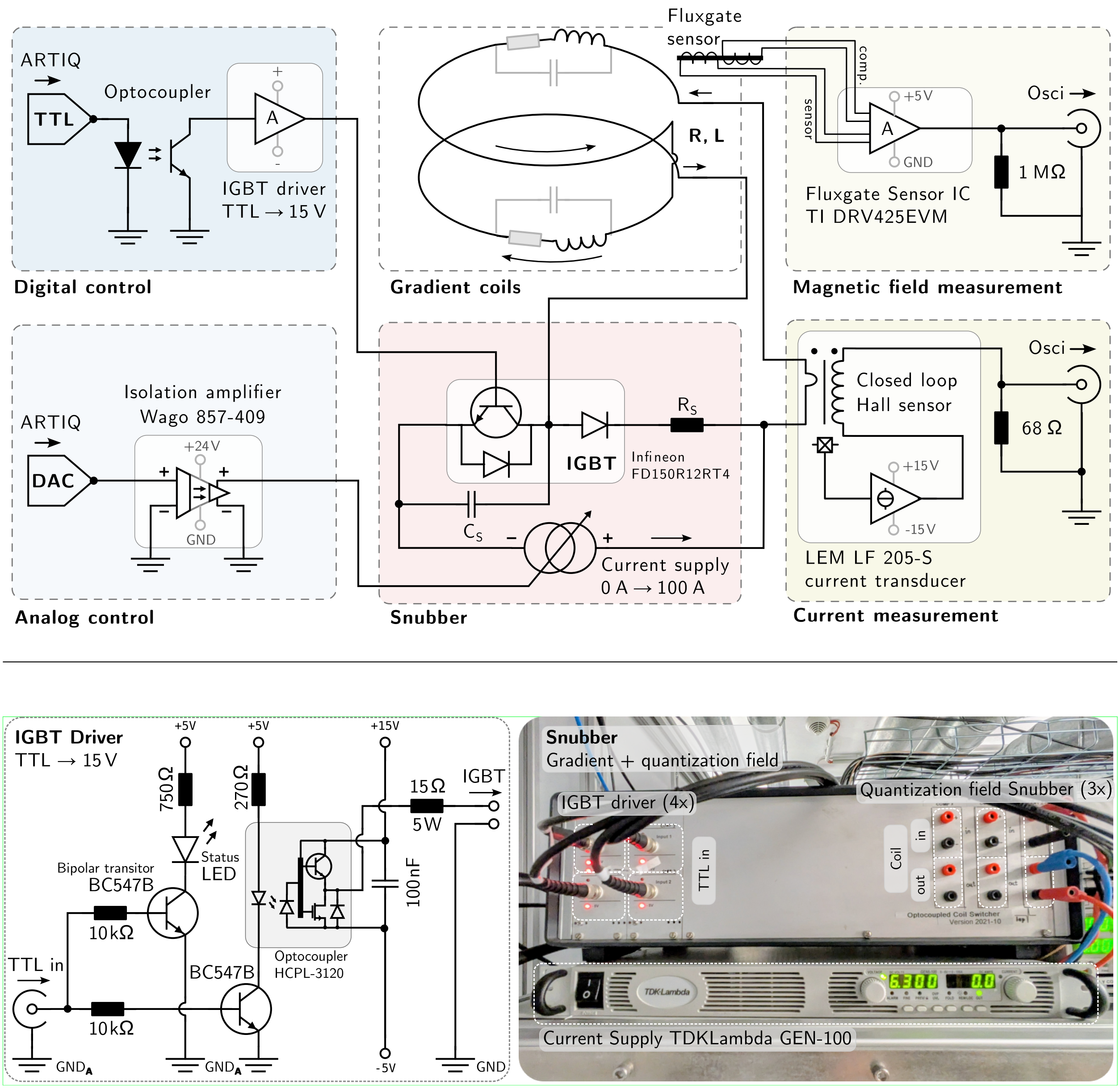

Figure 4.17: Fast analog and digital control and measurement setup for the magnetic gradient field coils (top). Analog and digital controls provided by the time control system are electrically isolated and act on the current supply analog set point and snubber circuit IGBT module respectively. The coil response is monitored on a fast oscilloscope with a closed loop Hall sensor measuring the DC and AC current, as well as a fast fluxgate sensor measuring the magnetic field. The IGBT driver (bottom, left) amplifies the TTL signal from the control system to drive the IGBTs for coil switching, its circuit layout is designed by our electronics workshop (credits: Achim Brähler, Eberhard Kalb). A rack-mountable crate (bottom, right) houses four IGBT driver boards, the gradient field snubber circuit and three snubber circuits for compensation and quantization field coils. The 100 A IGBT driver is located inside, attached to the back of the box, where a large extruded aluminum heat sink dissipates the power and 50 mm^2 cross-section high-current terminal blocks establish connections to the gradient field coil power supply and the gradient coils (not shown).

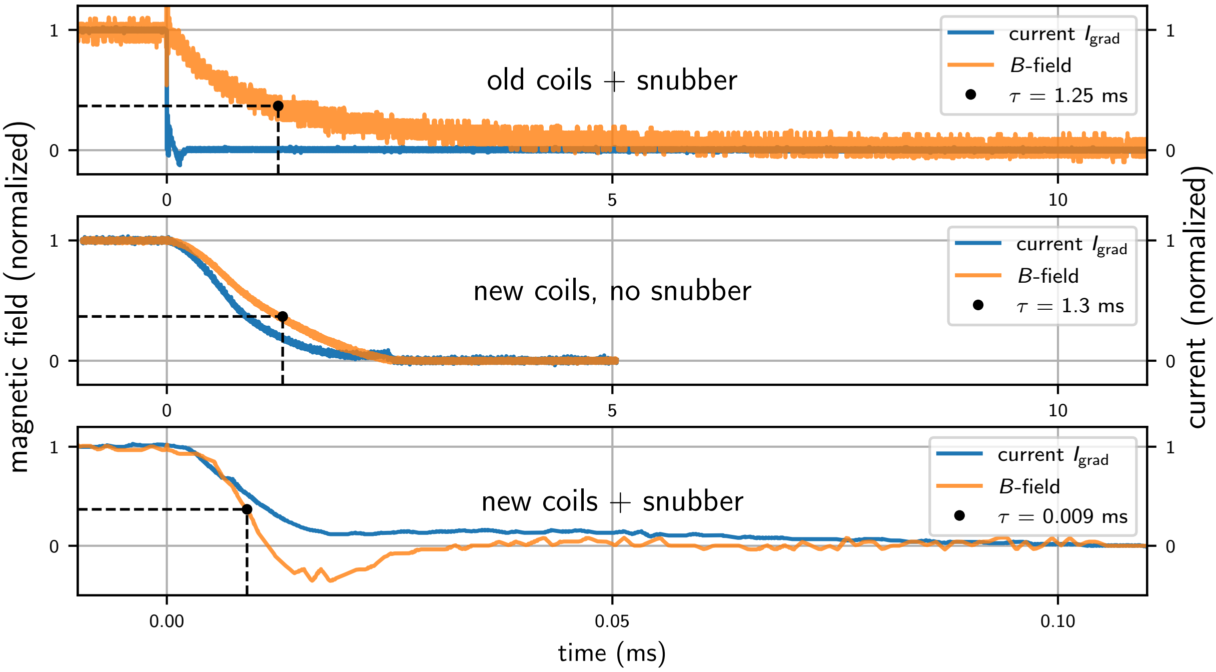

Figure 4.18: Current and magnetic field response of the gradient field coils switched with and without the Snubber circuit at a current of $I_{grad} = 100\,\mathrm{A}$. While the two coil impedances are comparable, the old coil setup switch-off time is limited by eddy currents in the aluminum coil support structure to 6 ms to 7 ms, as visible by the strong difference in current against field response. In the new gradient field coil the snubber circuit allows reducing the switch-off time by two orders of magnitude to about 30 µs. Note the different time axis scales.

We monitor the magnetic field response on a daily basis using an open-loop fluxgate sensor[1] measuring the magnetic field close to the coil and vacuum chamber and a closed loop Hall sensor[2] measuring the current at the connection leads. As the fluxgate sensor shows slight saturation effects, to resolve the magnetic field signal better, a fast, high-sensitivity magnetic field probe[3] with 100 kHz bandwidth is used. The typical current response of the gradient field is shown in figure 4.18, showing the first and second generation gradient coil switch-off behavior with and without snubber control. At the strongest gradient – limited by the power supply maximum current of 100 A – the snubber reduces the 1/e decay time of the field from $\tau = 1.3\,\mathrm{ms}$ to about 9 µs for the new gradient coil, while the old gradient coil does not see a strong improvement in its switching behavior. The total switching time – the time it takes the current to decay completely – is about 6 ms to 7 ms for the old gradient field coil, 2.5 ms to 3 ms for the new gradient field coil without and 40 µs to 50 µs with snubber. The difference between current and field response shows that the switching time of the first generation gradient field coil is mainly limited by the coil's mutual inductance to its frame, which results in eddy currents, rather than by its general construction. We confirmed this by switching a coil with a similar shape that was wound with a cross-section of $35\,\mathrm{mm}^2$ insulated stranded wire. Bringing an empty, otherwise identical aluminum frame in close contact with the coil increased the switching time by more than an order of magnitude.

---

[1] Texas Instrument DRV425EVM, DC to 47 kHz bandwidth. [2] LEM LF 205-S current transducer, DC to 100 kHz bandwidth. [3] Projekt Elektronik FM 210 Teslameter.

Analog control The gradient field strength is controlled via an analog input on the current supply, which is fed from a digital analog controller of the lab control system described below. Analog opto-isolators[1] in the BNC line ensure electronic isolation between control system and coils, as we could observe ground-loop induced disturbances in electronic signals over the entire lab, when switching the gradient field via the Snubber circuit. We characterized the field response to the analog control via measurements of the step-response for medium-sized current steps and modeled the setup as a linear control system. Using an analytical model for the impulse-response $h(t)$ of the control system then allows predicting the system's response $B(t)$ to a control voltage $U(t)$ as the convolution

$$B(t) = (U * h)(t) = \int_{-\infty}^{+\infty} \mathrm{d}\tau \;\; U(\tau)\, h(t-\tau)\,. \tag{4.37}$$

We can then use the knowledge of $h(t)$ to deconvolve a desired target magnetic field $B(t)$ or gradient field ramp $\partial_z B(t)$ obtaining the required voltage control signal $U(t)$. We program sinusoidal current ramps for an alternative to the fast switch-off from the snubber circuit, to allow for more adiabatic, but fast gradient field changes between defined strengths. The system's step response, impulse response, and an example for a smooth switch-on sinusoidal ramp are shown in figure 4.19. With the deconvolution routine, we establish ramp speeds down to 2 ms to 3 ms for ramps from $I_{\text{grad}} = 50\,\text{A}$ to 0 A. Their application for improved molasses cooling operation will be discussed in the outlook of this chapter.

Guiding field control

The compensation and quantization field control follows the gradient field control design closely, the analog control being completely identical. For digital control we also implement a snubber circuit for fast switching. Here 16 A metal-oxide-semiconductor field-effect transistorss (MOSFETs)[2] replace the much higher current capable IGBT from the gradient field control setup, as we need to switch currents of $\ll 10\,\text{A}$ only. We use an additional metal-oxide varistor[3] (= voltage-dependent resistor) in series to a $10\,\Omega$ resistor as a voltage-clamp to protect the MOSFET from high-voltage transients that appear during switching. All components are matched to the varistor's clamping voltage of 93 V. The TTL driver from the control system is again being isolated via an optocoupler and the IGBT driver board shown in figure 4.17. The complete digital snubber control is housed together with the gradient field control in a rack-mountable aluminum crate, also shown in figure 4.17.

4.6 Electronic time control

Precise and flexible time control at (sub)-microsecond resolution is critical for the experimental sequences in this thesis. Additionally, quantum optics experiments require phase-stable frequency generators to feed the AOMs, EOMs, and other lab hardware for precise control over the atoms. The sequence programming should be as intuitive and flexible as possible to enable quick debugging of experiments, modifications, iterations, and extensions to additional methods. The latter include extended cooling sequences, Zeeman slowing, ODT loading, and advanced measurement sequences,

---

[1] WAGO 857-409 bipolar signal conditioner and isolation amplifier. [2] ST 511-STP16NF06L. [3] TDK B72205S0300K101.

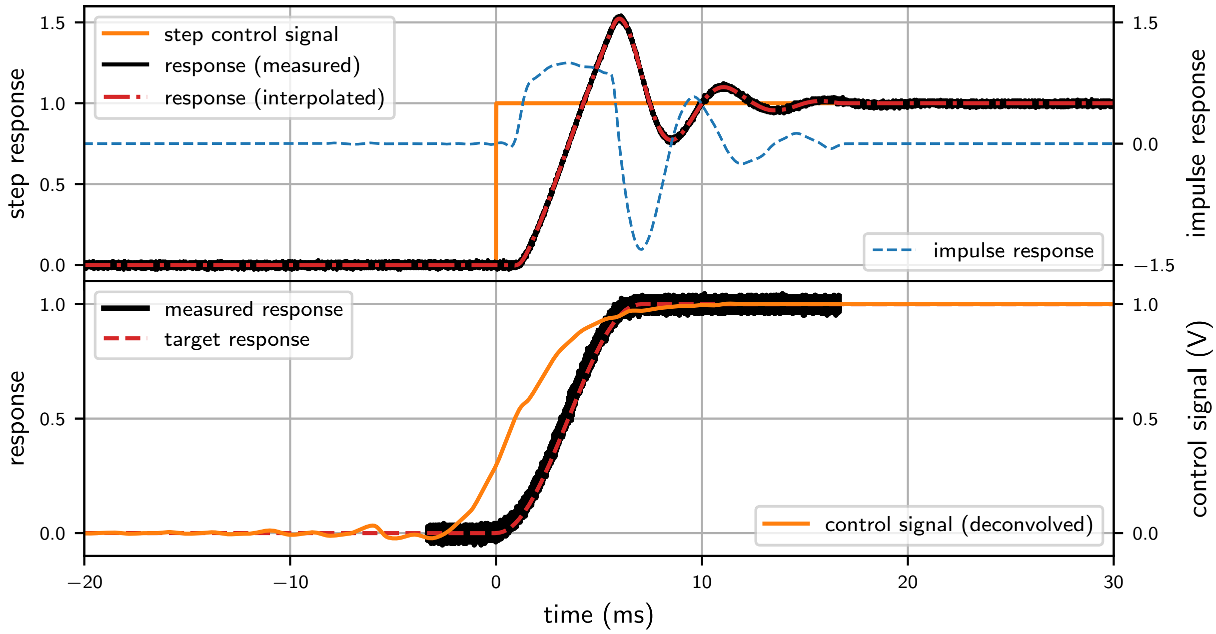

Figure 4.19: Gradient field coils magnetic field response to a step control signal (top) and an optimal control signal for a smooth sinusoidal ramp (bottom). The magnetic field response is measured with the fast DRV425 fluxgate sensor (black) and all measurements are performed with the second generation gradient coils at a current of $I_{\text{grad}} = 50\,\text{A}$. The step response (top, black) is interpolated via a spline (red), from which we extract the impulse response (blue). For execution of a sinusoidal switch-on curve (bottom), we deconvolve the target response (red) with the impulse response, the resulting control signal (orange) then leads to the desired system response.

while ensuring reproducibility and transparent data.

Modern hardware implementation utilizes the fast FPGA architecture, which typically executes a set of digital commands at clock rates in the 100 MHz regime. We compared various commercial hardware solutions and software implementations run by other labs around the world. Implementation of the time control system was approached by two ways during this thesis work, the first based on a Swabian Instruments PulseStreamer 8/2 and external RF frequency generators, which was later upgraded to the Sinara open hardware system [189] with integrated RF generation controlled by a customized software control based on the ARTIQ open software control system [190].

The design of a superordinate framework for flexible and reproducible sequence programming, including data acquisition, storage, and analysis, is presented below, along with the two systems.

4.6.1 Hardware control

Swabian Instruments PulseStreamer 8/2

We started with a system based on a small FPGA Swabian Instruments PulseStreamer 8/2 module, that features eight digital channels with TTL logic and two digital-to-analog channels at 1 GSa/s and 125 MSa/s sampling rate respectively. Its high-resolution digital pulse generator is capable of producing deterministic sequences with nanosecond timing. Here, pulse sequences of 5 s to 15 s length are generated for each experimental shot – atom loading + interrogation + detection – and are sent precompiled to the FPGA hardware in table form and then executed in real time. All external hardware that needs active communication – CCD cameras, RF frequency generators, signal generators, coil power supplies – are preprogrammed outside the real-time execution via custom written Python drivers that interface the hardware via the VISA protocol by means of GPIB, RS232, USB, or Ethernet depending on the device. The Andor CCD camera driver controls the CCD chip cooling, prepares the camera sensor for acquisition of multiple frames, sets the acquisition settings (gain, read-out clock speed, ...) and acquires the images. Analog control of e.g., the magnetic field coils, is either directly established via the two 14 bit, −1.0 V to 1.0 V analog channels of the PulseStreamer or by preprogramming an external Rohde & Schwarz HMF2550 arbitrary waveform generator.

For external frequency generators, we chose low-noise Rohde & Schwarz SML01 (9 kHz to 1.1 GHz) and SML02 (9 kHz to 2.2 GHz) VCO-PLL, that provide frequencies into the GHz range. The limited RF amplitude output of +12 dBm is typically amplified by a broad range of MiniCircuit RF amplifiers when necessary. A Rohde & Schwarz SMC100A VCO-PLL frequency generator with fast pulse modulation feeds the imaging AOM to enable the 150 μs long absorption imaging pulses. We preprogram all frequency and RF power sweeps via VISA and execute real time events via external TTL input from the PulseStreamer. All RF frequency generators used in this work are phase-locked to a stable 10 MHz rubidium frequency standard[1] for absolute and long-time frequency stability.

ARTIQ Sinara open hardware system

With the limitations in channel count and the need for external (RF) hardware, we upgraded the lab control to the Sinara hardware [189] and the Advanced Real-Time Infrastructure for Quantum physics (ARTIQ) control software system [190]. The ARTIQ control system offers a hybrid platform combining a Python-based high-level interface with a real-time, FPGA-based execution environment based on the modular Sinara open hardware ecosystem.

A variety of modules, including RF generators, are integrated via a back-plane architecture and controlled through ARTIQ's (distributed) real-time input/output (DRTIO) system, which schedules events deterministically down to nanosecond timescales. We utilize five types of hardware modules, that are all implemented as crate-mountable Eurocard Extension Module (EEM) boards.

Digital inputs and outputs at TTL level are provided by multiple DIO-BNC modules via multichannel BNC interfaces. The outputs drive all external hardware in the lab, while the input can be used for conditional programming. The latter will function as a 50 Hz line trigger, when high-resolution spectroscopy and electric dipole moment (EDM) measurements demand for an improved noise control and reproducibility in the lab. A 16 bit, 32-channel Zotino digital-to-analog converter board provides ±10 V output at 1 MSa/s update rate and drives all magnetic field coils.

On the frequency side, a low-noise Mirny four-channel PLL/VCO-based microwave frequency synthesizer provides a frequency range of 53 MHz to > 4 GHz and allows e.g., the driving of EOM carrier shifts for laser stabilization. Additionally, multiple four-channel Urukul frequency synthesizers based on a AD9910 1 GSa/s, 1 MHz to 400 MHz DDS board are used to drive all AOMs. In the latter setup, it also provides optical power stabilization functionality in combination with the Sampler analog-to-digital converter board via the FPGA-based SuServo PID lock loop.

---

[1] Stanford Research Systems FS725, 20 year aging of $< 5 \times 10^{-9}$.

Timing control is performed via two synchronized Kasli FPGA core devices, that run the ARTIQ kernel and control the individual EEM modules. Distributed over two 19 inch rack mountable crates, that are synchronized and phase-stabilized via a low-latency fiber connection, the lab is equipped with a future-proof electronics control setup.[1]

All non-real-time hardware communication is handled by the host CPU lab computer over Ethernet using kernel-to-host remote procedure calls (RPC) for tasks like configuring devices or retrieving measurement results outside the deterministic timeline. For this, we wrote Python-based drivers and Non-Deterministic Software Protocol (NDSP) server communication layers for all external hardware (cameras, power supplies including coil driver, shutter driver, oscilloscopes, . . .). This software stack runs on the main lab computer and handles asynchronous messaging, device setup, and data transfer in coordination with the host, while ensuring separation from the real-time (RTIO) execution on the FPGA. Automatic data analysis routines (atom number and temperature determination by optical density fitting, . . .) are also implemented to run asynchronous to the data experiment sequence to reduce sequence time as much as possible. All lab control is managed via a Python package, that includes data management tools, analysis routines, and the experiment sequence programming framework described below.

4.6.2 Sequence programming

While the PulseStreamer requires programming of the (pulse) sequence via a table of digital and analog signal against time, the ARTIQ control system supports the generation of sequences on a dynamic basis, as well as conditional branching based on live measurement. The latter is being programmed via ARTIQ Python – a domain-specific subset of Python to describe the experiment logic that then compiles to run deterministically on the Sinara FPGA hardware. For both systems a module-based sequence timing was developed.

The experiment is separated into modules that group hardware access and timing. An exemplary sequence is shown in figure 4.20. Here we load the atoms from the background gas via the MOT for a time t_{load} and compress the cloud via the gradient field and detuning control for t_{compress}. Atoms are then transferred into the ODT and we detect the ODT cooled atoms in time-of-flight via absorption imaging after a free fall time t_{tof}. All modules shown here – `mot` (MOT), `dt` (ODT) and `img` (absorption imaging) – are implemented as class objects and their individual functions as ARTIQ Python real-time kernel methods, that are executed on the Kasli FPGA and Sinara EEM modules.

Each module's methods define a specific, but variable point in time. For example, it may define the start of atom loading or the location of the absorption imaging beam pulse. These points depend on various experimental parameters that can be programmed via a customized graphical user interface, as shown in figure 4.21. With respect to this point, two times, t_{init} and t_{final}, are specified for each method. We define the initial time, t_{init}, required for the preparation of the method, including analog ramping of coil currents and shutter control. We characterize all hardware delays in the lab, including cable delays and hardware response times, to the sub-µs level ahead of this point in time. Also, we define a final time t_{final} that includes the physical length of the experimental execution and potential dead times originating from e.g., data acquisition transfer delay.

---

[1] Note that the open-source and open hardware nature of the system however requires extensive initial setup and expertise compared to a turn-key commercial system, which we only found out the hard way.

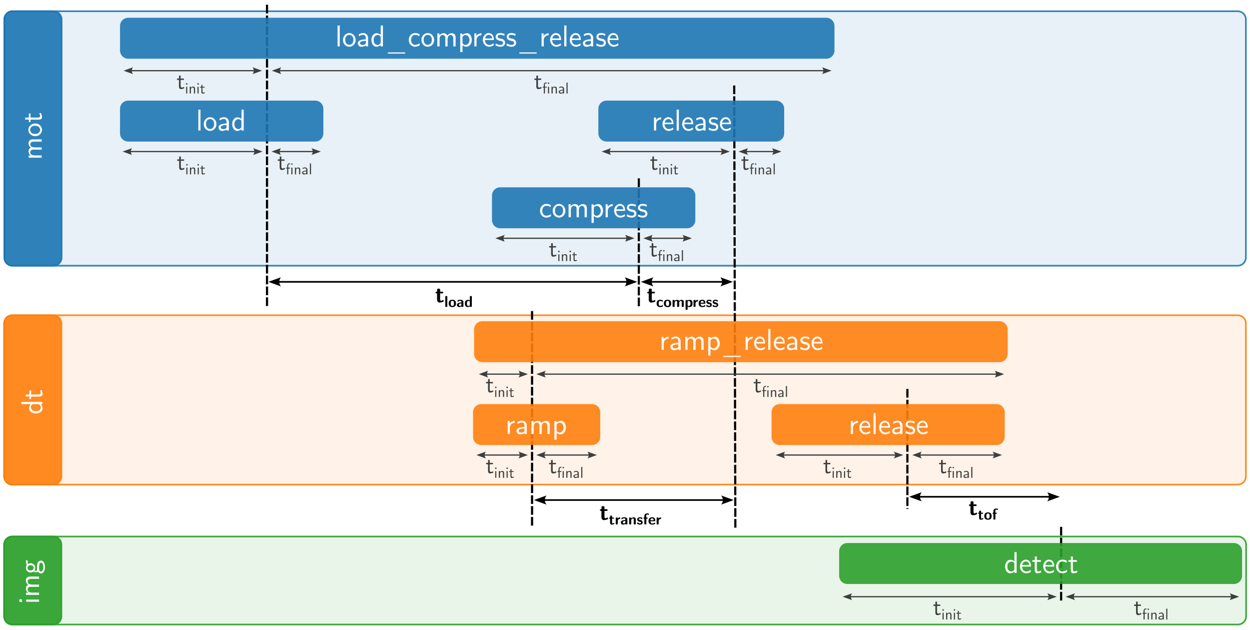

Figure 4.20: Graphical visualization of the experiments modular sequence programming. Displayed is a MOT loading and compression phase (`mot`), the transfer to an ODTs that is slowly ramped up (`dt`) and an absorption imaging sequence as defined in the detect method of the imaging module (`img`).

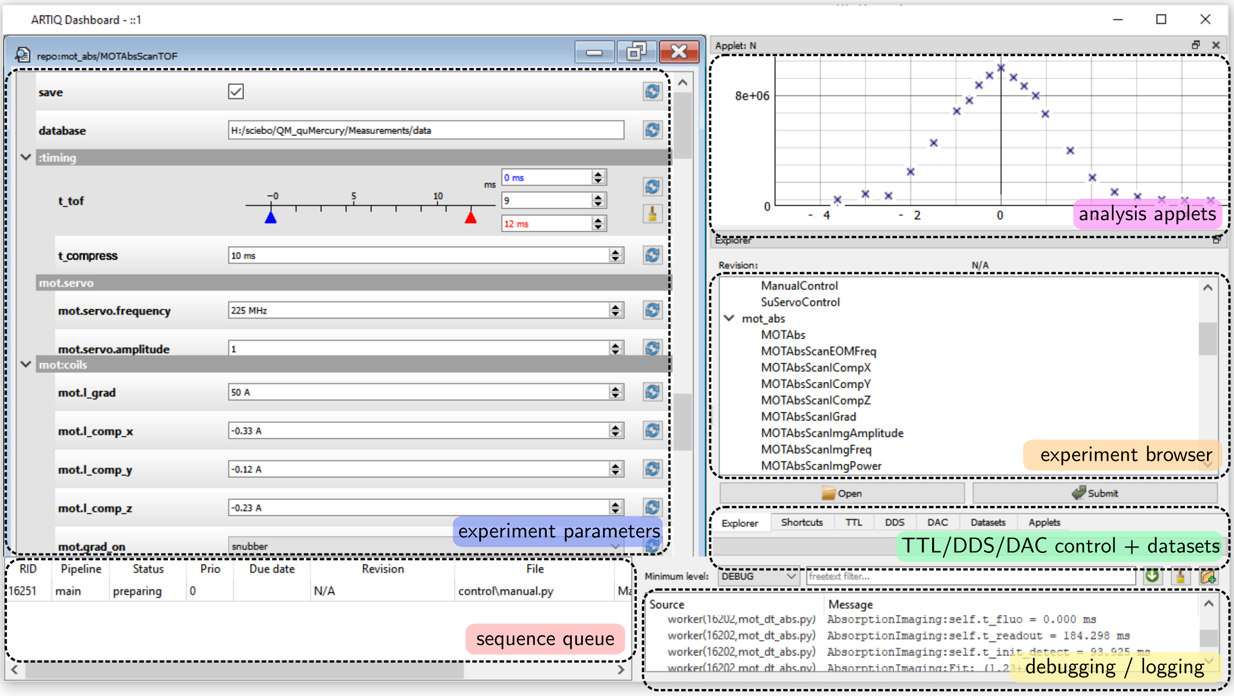

save ☑

database H:/sciebo/QM_quMercury/Measurements/data

t_tof 0 ms 9 12 ms

t_compress 10 ms

mot.servo.frequency 225 MHz

mot.servo.amplitude 1

mot.I_grad 50 A

mot.I_comp_x -0.33 A

mot.I_comp_y -0.12 A

mot.I_comp_z -0.23 A

mot.grad_on snubber

RID	Pipeline	Status	Prio	Due date	Revision	File
16251	main	preparing	0		N/A	control\manual.py

Minimum level: DEBUG

```
Source                           Message
worker(16202,mot_dt_abs.py)   AbsorptionImaging:self.t_fluo = 0.000 ms
worker(16202,mot_dt_abs.py)   AbsorptionImaging:self.t_readout = 184.298 ms
worker(16202,mot_dt_abs.py)   AbsorptionImaging:self.t_init_detect = 93.925 ms
worker(16202,mot_dt_abs.py)   AbsorptionImaging:Fit: (1.2
```

Figure 4.21: Reduced visualization of the customized ARTIQ experiment graphical user interface with experiment parameter control, live debugging, hardware control, analysis tools and sequence scheduling methods.

This design allows experiments to be easily extended by new modules and additional or modified methods, and allows for a rather quick debugging procedure. All experimental sequences include the option to convert any control parameter, like the time-of-flight duration t_{tof} or the AOM imaging beam detuning, into a scan variable, also allowing multidimensional scans and optimization runs over many experimental parameters. The dataset structure is then automatically extended to hold all experimental parameters for each shot of the measurement.

Data storage and measurement reproducibility Our measurements consist of atomic images obtained through absorption or fluorescence imaging. The reproducibility of these images is controlled by a wide range of experimental parameters, most of which are managed via the central control software. We chose to use the binary NetCDF/HDF5 format [191] as a standard format for storing experimental data for its support of large, structured datasets and wide compatibility with analysis tools. We implement self-explanatory NetCDF structures datasets that store both the raw data, and results of automatically performed analysis routines.

To ensure reproducibility of the experimental sequences, we integrate the Git version-control system with the data storage workflow by recording the Git commit identifier of the lab control software in the HDF5 file each time an experiment sequence is executed. This links the dataset to the exact software version used during runtime. If the repository is in a dirty state (with uncommitted changes), we store the latest commit identifier and flag the file as debugging data, helping distinguish exploratory runs from validated results.

4.7 Magneto-optical trap characterization

Building on the work presented above, the MOT characterization is presented in the publication [1]

> Quentin Lavigne, Thorsten Groh and Simon Stellmer, *Magneto-optical trapping of mercury at high phase-space density*, Physical Review A **105**, 033106 (2022). DOI: `https://doi.org/10.1103/PhysRevA.105.033106`.

Summary

In the publication, we summarize the experimental setup described thus far. In a short form we present the source and vacuum chamber design, as discussed in more depth in chapter 3 and the optical and magnetic field setup, which is discussed in this chapter.

We load MOTs of all seven stable isotopes of mercury from the background gas, as provided by the mercury source. We characterize the loading efficiency – loading rate and final atom number – of the MOT in dependence on both the source temperature and the natural abundance of the individual isotopes. As the source temperature increases, the MOT loading rate increases to up to 1.6×10^8 atoms per second. However, at this point the steady-state atom number is limited by the one-particle losses induced by collisions between the cloud atoms and the residual background gas atoms, which at high source temperatures is dominated by Hg. We conclude that installing a ZS or a 2D-MOT should enable the Hg loading rate to be increased selectively, thereby enhancing the number of atoms in the MOT. With regard to isotope dependence, we observe that the number of bosonic isotopes observed in the MOT is approximately proportional to their respective natural abundance. By contrast, the number of atoms trapped in the MOT for fermionic isotopes is three to five times lower, due to the more complex hyperfine structure.

We systematically investigate the effect of key experimental parameters – namely, laser detuning, optical intensity and magnetic field gradient – on the MOT's loading efficiency and steady-state atom number. The analysis is based on absorption imaging, as discussed in section 4.4.2 and shown in the experimental sequence in figure 4.13. We find that the achievable atom numbers are not limited by laser power at the selected cooling beam size. For the most abundant isotope, ^{202}Hg, we achieve record atom numbers on the order of 5×10^7, indicating efficient cooling and capture under optimized conditions. High atom numbers are achieved for a cooling beam detuning of about $\Delta = -10\,\Gamma$ and around a magnetic gradient strength of 10 G/cm, at which point the atom number increases linearly with the saturation parameter s_0.

In addition, we investigate the achievable atomic cloud temperatures and examine the differences in cooling efficiency specific to each isotope. To achieve this, we use TOF imaging, in which we probe the falling cloud at different fall times (in steps of 0.5 ms) up to approximately ≈ 12 ms, at which point the cloud density decreases to the point of disappearing contrast. For the bosonic isotopes, our temperature measurements are consistent with standard Doppler cooling theory and the absence of ground-state hyperfine structure. For ^{202}Hg, the lowest temperature ($T = 84(5)\,\mu$K) is obtained with a detuning of $\Delta = -1\,\Gamma$ and at low cooling beam intensities, while in this regime the magnetic gradient field strength has no drastic effect on the temperature. In contrast, the fermionic isotopes, which possess non-zero nuclear spin, exhibit evidence of sub-Doppler cooling mechanisms enabled by polarization gradients and multilevel structure, as discussed previously in section 4.1.2. We demonstrate that these effects enable the fermionic species MOTs to reach sub-Doppler temperatures. The minimum temperatures are achieved for ^{201}Hg, allowing slightly more efficient Sisyphus polarization gradient cooling. We reach temperatures down to $T = 30.9(2.3)\,\mu\mathrm{K}$, as averaged over multiple shots at the same cooling parameters.

We also analyze the size of the atomic cloud as described by one-dimensional Doppler theory, as given by equation (4.14). While we observe good agreement with the scaling for MOT-sized clouds with (vertical) radii in the range of 25 µm to 200 µm, the Doppler theory predicts a size around 20 % lower, which we attribute to imperfect beam profiles and radiative heating mechanisms.

For ODT loading and estimation of degenerate quantum gas production, we determine the phase-space density as a function of cooling beam detuning and intensity. We find that maximizing phase-space density critically depends on maintaining small detunings ($\Delta \approx -\Gamma$) and low saturation parameters ($s_0 < 1$). The latter effectively suppresses cloud heating caused by the reabsorption of scattered photons. We estimate a phase-space density of a few parts in 1×10^{-7} for the trapped atoms, which provides a favorable starting point for further cooling in ODTs.

By optimizing the experimental parameters, we achieved nearly a tenfold increase in the number of trapped atoms compared to previous reports. Given the technical limitations of imperfect beam shaping in the deep-UV, we expect to improve these numbers. Additionally, we provide concrete evidence that upgrading the mercury source to a proposed Zeeman-slowed atomic beam source will further increase the number of atoms in the future. This in-depth study of laser cooling in mercury demonstrates the potential of our system for future studies requiring ultracold, high-density mercury samples. These studies include precision spectroscopy, EDM searches, and evaporative cooling toward quantum degeneracy.

Contents

A reprint of the publications is included in Appendix A of this document. The table of contents of the publication is given below and links to the respective sections in the paper.

4.8 Outlook

4.8.1 Improving trapping and cooling

Increasing phase-space density

As we will see in the following chapter, transferring magneto-optically cooled atoms to an ODT is the most effective method of achieving evaporation cooling towards quantum degeneracy, given that magnetic trapping of the atomic ground state is prohibited. This method is also ideal for interrogating mercury atoms over a long period of time in future electric dipole moment measurements. To achieve good transfer efficiencies, it is necessary to increase the MOT atom number and phase-space density as much as possible. There are multiple methods for improving cooling performance and phase-space density in the in the Hg isotope MOT exist, some of which we have started to test and others for which this thesis lays the technological foundation. A selection of suggested experimental upgrades and their influence on MOT cooling are discussed below.

Increasing atom numbers Improvements in beam quality of the MOT cooling beams is predicted to improve atom loading. Here the new compact 254 nm laser system setup shown in figure 4.4, which is currently being constructed, is expected so solve this problem. We improve the beam quality by adding a beam shaping and spatial mode cleaning stage consisting of a two-lens telescope and a pinhole. With this, we can create a nicely rounded transversal beam profile and also correct the astigmatism mode cleaning with less than 10 % power loss. New UV-grade fused silica AOMs[1] were purchased. The AOMs are selected for their large aperture openings of $1.5 \times 2\,\mathrm{mm}^2$, which eliminates the need for strong focusing of the laser beam. The reduced incident intensity greatly reduces the risk of UV-induced solarization damage to the AOMs, which should significantly increase their lifetime, as discussed in more detail below. The AOM's optical medium features Brewster's angle incidence, which further reduces UV damage compared to alternative AR coatings. With about 85 % diffraction efficiency at 254 nm over the desired frequency bandwidth, they also outperform the previous AOMs and promise more power available for MOT and future ZS.

Not relying on large-focal-length telescopes around the AOMs also significantly reduces the length of the beam path. This also reduces the MOT position instability originating from the FHG beam pointing. All new optics have been tested successfully, and an engineer and our mechanical workshop have already certified the feasibility of enclosing the system in a protective environment with an oxygen-argon mix. We will soon employ the system for laser cooling and imaging.

Optical molasses cooling phase Cooling magneto-optical trapped atoms in an additional optical molasses phase is a well-known technique to lower the atomic temperature further. The authors of [192] e.g., recommend "to switch off the magnetic field of the MOT a few ms before the laser fields are extinguished, because the short resulting optical molasses cooling phase establishes the lowest possible temperatures and a quasi-thermal distribution in the trap". We first attempted to directly load an optical molasses from the background gas, but the small capture velocity of about $v_c^{(\mathrm{molasses})} \approx 0.2\,\mathrm{m/s}$, as estimated already in section 4.1.2, already predicts that trapping large number of atoms is going to

---

[1] Opto-Electronic MQ200-A1,5-244.266-Br, 244 nm to 266 nm spectral bandwidth, center frequency 200 MHz at 4 W RF power, 8.1 mrad to 8.9 mrad separation angle.

be challenging. Furthermore, optical molasses operation is very sensitive to residual magnetic fields and magnetic field gradients, as the resulting Zeeman shifts can lead to imbalanced forces. So far, no proper signal of direct molasses cooling from the background gas could be observed.

Transferring MOT cooled atoms into a molasses phase as a second cooling phase instead, seems to be limited by magnetic fields. Switching the magnetic gradient field using the Snubber control was observed to lead to strong acceleration of the atomic cloud away from the trap center. While short molasses phases could be observed already, so far no temperature reduction could be observed. To potentially circumvent the heating a fast, but moderate switch-off – avoiding overshoots and residual magnetic field ringing – was implemented on the basis of the current supplies analog control via ARTIQ. Additionally, fast analog control of compensation and quantization coils was also established on the same way. For this purpose, the optimal control scheme was already established in software.

Magneto-optical trap compression Fast analog magnetic field control also enables MOT compression schemes. To achieve this, we load the MOT at large laser light detuning and moderate gradient field strength, for which high atom numbers are achieved. The gradient is then dynamically ramped to higher values, which decreases the cloud size, as suggested by the $(\partial B/\partial z)^{-1/2}$ scaling of the MOT radius in equation 4.14. A similar scaling behavior is observed for the dependency of the cooling light detuning, which is typically ramped closer to resonance at the same time. While the compression of an ideal gas leads to heating, the strong density increase can lead to improvement in the phase space density. As in first experimental attempts we even observe cooling, we also suspect that the Doppler temperature limit scaling with the detuning, equation 4.10 and specific thermalization rates can even reduce the temperature.

Controlling the MOT light detuning dynamically during an experiment sequence is challenged by the optical setup. As discussed before, due to limited laser power in the UV, we set up the MOT cooling light in a single-pass AOM at a fixed, optimum modulation frequency. When detuned, this changes the Bragg condition and diffraction angle, leading to strong misalignment of the MOT beams within the chamber. To leave the MOT AOM at a fixed frequency, a fast dynamic frequency control via the ultrastable cavity lock feedback on the 1015 nm master laser was established. Here, the carrier shift that establishes the frequency offset of the laser to the selected cavity resonance is ramped linearly in time. To establish this, the RF frequency generator providing the carrier shift was already replaced with an ARTIQ DDS driver board, as the original phase-lock-loop voltage-controlled oscillator switches off and looses its phase when stepped in frequency. The DDS frequency was being extended to reach the $\leq 1.5\,\mathrm{GHz}$ range required for locking, as discussed before. While first implemented to allow for a simpler nearly static control of the MOT detuning, where the laser frequency is slowly ramped ($\sim$ MHz/s) at the beginning of the experimental sequence, the SHG cavity locks are stable and responsive enough, that this locking scheme allows dynamic frequency sweeps in the UV of tens of MHz within milliseconds. Future extensions of the experiment to a ZS, as discussed below, could also benefit from this by allowing UV laser frequency control without the need for an additional AOM.

An early analysis seems to suggest optimal transfer times of ~30 ms for a linear compression ramp from around 10 G/cm to $\geq 20\,\mathrm{G/cm}$ in gradient field strength and from $\Delta = -15\Gamma$ to -10Γ down to $\sim -1\Gamma$ in detuning. So far, tested for bosonic ^{202}Hg, this improved phase space density by an order of magnitude to $\sim 1 \times 10^{-6}$, while interestingly also reducing the temperature to $T \approx 140\,\mu\mathrm{K}$. Temperatures down to $T \approx 70\,\mu\mathrm{K}$ could be achieved, when simultaneously also ramping the cooling light intensity to less than 1 %. This additional compression and cooling phase already allowed improving stable dipole trapping, as presented in section 5.2.2.

At the time of writing, investigation of both MOT compression and additional molasses cooling is still being investigated. Future analysis will show whether these upgrades can further reduce phase space density and improve ODT loading.

Improving reliability

The experiment's main limitation is still its long-term operation and reliability. Here, UV degradation of the optics is one of the bigger challenges in this regard. Upgrading the optical setup and enclosing it in a pressurized oxygen and argon environment (see figure 4.4) is expected to solve this problem. An oxygen atmosphere protects the optics from solarization damage by passivating defect sites caused by UV exposure. However, pure oxygen poses safety risks due to its high reactivity, significantly increasing the risk of combustion and fire when in contact with flammable materials. Therefore, argon is added to improve safety.

Hydrogen-loaded photonic crystal fibers Since the beam pointing issues still might need to be addressed in the future also for other applications (spectroscopy, EDM measurements, ...), multiple active and passive beam stabilization solution were discussed. For passive beam stabilization and mode cleaning, hydrogen loaded large mode photonic crystal fibers were acquired for testing. While the fiber itself already allows transmission of UV light at around 250 nm [193], here only low powers (~0.3 mW) were incident and absorption dropped to about 1.44 dB/m. UV solarization is explained by the interaction of UV light with impurities or dopants in the silica glass material forming color-centers [194] that then absorb the light. Loading the fibers with high pressure (a few hundred bars) hydrogen can mitigate the absorption by modifying the UV-induced color-centers [195–197]. The commercially available NKT LMA-10-UV fibers were hydrogen loaded at the Physikalisch-Technische-Bundesanstalt (PTB). The absorption at ~235 nm is about 3 dB/m, but we expect better performance at 254 nm and improved power handling and long-term stability in comparison with the unloaded fiber.[1] Although low transmission and additional losses during fiber coupling, as well as the lack of polarization maintenance, limit the application, incorporating rigidly mounted centimeter-short fibers into the optical setup for mode cleaning to convert beam pointing into power fluctuations should result in low losses and acceptable polarization properties.[2]. At the time of writing testing of the fiber is still in progress.

4.8.2 UV laser development for addressing the singlet transition

While it is hard to reach high powers for laser cooling, the singlet transition at 184.9 nm however represents an excellent candidate for high-resolution imaging of cold atomic clouds. Here the broad

---

[1] Personal communication with Fabian Wolf (2024). Thanks to Fabian Wolf and the team of Piet Schmidt for supplying the optical fibers.

[2] Power fluctuations can then be compensated for by the AOM stabilization feedback. Polarization drifts are expected to be small, and light field polarization can be cleaned using polarization beam splitter after the fiber.

linewidth promises large photon scattering rates and the small wavelength down to around 100 nm resolution when diffraction limited.

For this we recently started setting up a continuous-wave laser system, based on a tunable intracavity-doubled vertical-cavity surface-emitting laser (VECSEL)[1] providing about 2 W at a wavelength of 431.3 nm. VECSELs combine the benefits of solid-state and quantum-well semiconductor lasers offering high power, but a significantly lower cost than e.g., titanium-sapphire laser systems. They are also more durable due to their large emitting area and provide stable output that is free from relaxation oscillations and amplified spontaneous emission.

The blue laser light is frequency doubled to 215.7 nm in a nonlinear, Brewster-cut beta barium borate (BBO) crystal. The conversion efficiency to the deep-UV is enhanced by a monolithic bowtie cavity[2] stabilized by a Hänsch-Couillaud locking scheme and equipped with a Brewster window for outcoupling of the UV laser light. We aim to reach about 50 mW to 100 mW of converted light at 215.7 nm.

Laser light at 184.9 nm is planned to be generated by sum-frequency conversion in combination with 1299.1 nm light provided by another tunable, single-frequency VECSEL laser that operates directly in the infrared[3]. For this conversion, we set up another bowtie cavity[2] for enhancement of the 1 W infrared light provided by the second laser. We use a nonlinear cesium lithium borate (CLBO) crystal in a type-I phase-matching condition for sum-frequency generation. The CLBO crystal has a UV transmission cutoff near 180 nm, thereby enabling efficient operation within the desired spectral range. We will heat the crystal to an elevated temperature of around 150 °C to improve its damage resistance, as CLBO is highly hygroscopic. The incoupling of the 215.7 nm light and outcoupling of the 184.9 nm light utilizes the dispersion in the crystal and is achieved using small mirrors, that reflect the UV laser beams in and out of the cavity beam path. A prism separates the UV wavelengths of seed laser and converted light after outcoupling. In the first stage, our goal is to generate at least 1 mW of continuous-wave laser light at 184.9 nm.

4.8.3 Zeeman slower design

Increasing atom numbers loaded into a MOT while simultaneously improving the atomic lifetime of trapped atoms by decreasing the background vacuum pressure, can be realized by employing a collimated atomic beam source in combination with a ZS [198], or by loading from an additional (2D-)MOT [199–202] located in a differentially pumped chamber. So far, attempts to increase the loading rate of mercury MOTs is solely focussed on operation of a 2D-MOT [58, 104, 203]. For more efficient use of the limited optical power in the UV, we propose a high-flux low-velocity source of mercury atoms based on a 1 m long ZS, as presented below.

Zeeman slower working principle Following the derivation in section 4.1, the acceleration for an atom at longitudinal position z and velocity v as mediated by the radiation pressure force is given by

$$a(z,v) = -a_{\max}\frac{s_0(z)}{1+s_0(z)+(2\,\Delta(z,v)/\Gamma)^2}\,, \qquad \text{where} \qquad a_{\max} = \frac{\hbar\,k\,\Gamma}{2\,m}\,. \tag{4.38}$$

---

[1] Vexlum VALO SHG. [2] Custom monolithic enhancement cavity provided by Agile Optic. [3] Vexlum VALO SF.

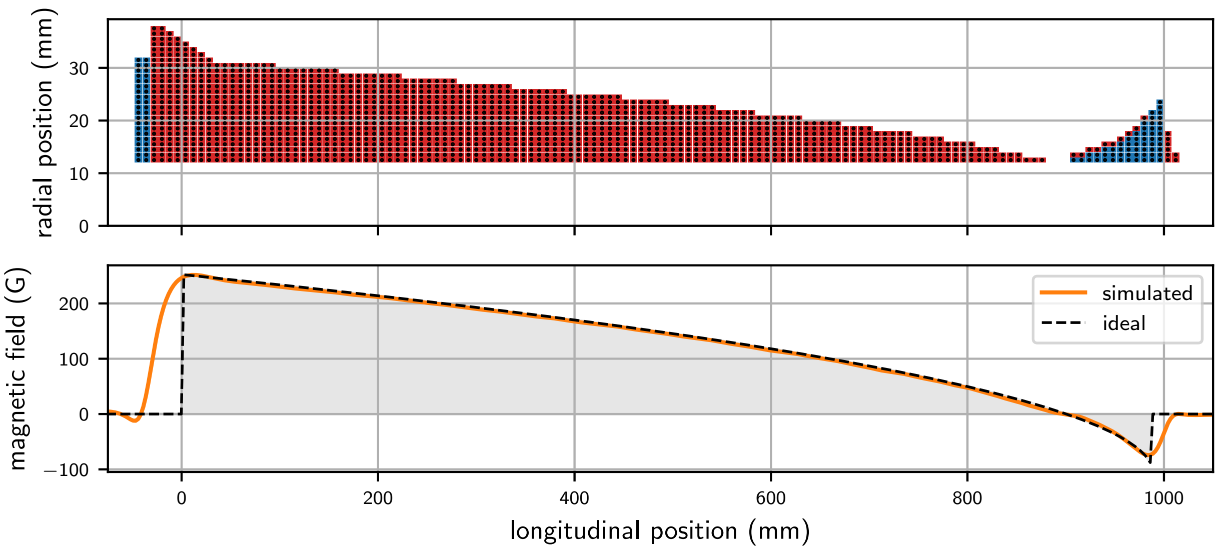

Figure 4.22: Coil layout (top) and simulated magnetic field (bottom) of the ZS. The color coded coil cross-sections indicate right- and left-handed currents of $|I_{ZS}| = 8\,\mathrm{A}$.

The detuning in presence of a magnetic field $B(z)$ is given by $\Delta(z,v) = \Delta_0 + k\,v - \Delta\mu\,B(z)/\hbar$, where Δ_0 is the laser detuning for an atom at rest in absence of any magnetic field. The ZS field $B(z)$ now compensates for the Doppler shift, such that the acceleration a is constant along the full atomic trajectory. While maximum and constant deceleration is reached at the resonance condition $0 = \Delta_0 + k\,v - \Delta\mu\,B(z)/\hbar$, with imperfections in $B(z)$ this is experimentally hard to ensure for narrow lines. Instead, slowing at slight red detuning is preferred, such that atoms can not leave the resonance condition towards large blue detuning. The effective detuning is defined via the safety factor ε, such that $a(z,v) = -\varepsilon\,a_{\max}\,s_0/(1+s_0)$ along the slower. The most efficient restoring force against velocity changes is achieved at $\varepsilon = 0.75$, where $-\mathrm{d}\,a/\mathrm{d}\,v$ is maximal, as illustrated in the inset of figure 4.23. From the new resonance condition we obtain the ideal ZS field for an atom with initial velocity v_i and final velocity v_f the velocity:

$$B(z) = B_0\sqrt{1 - \frac{z}{L}\left(1 - \left(\frac{v_f}{v_i}\right)^2\right)} + B_s\sqrt{(1+s_0)\,\frac{1-\varepsilon}{\varepsilon}} + B_c\,, \quad \text{for } 0 \le z \le L\,, \tag{4.39}$$

and $B(z) = 0$ else. The magnetic field amplitude is given by $B_0 = -\hbar\,k\,v_i/\Delta\mu$, $B_s = \hbar\,\Gamma/(2\,\Delta\mu)$ and the field offset $B_c = \hbar\,\Delta_0/\Delta\mu$ is freely adjustable via the initial laser detuning Δ_0.

Design All ZS parameters are optimized for the best numerically simulated slowing efficiency and loading rate of the MOT, where we conservatively constrain the required optical power to 30 mW, which is easily obtained by recycling the zeroth order of the MOT AOM[1]. We aim for a maximum initial velocity of $v_i = 190\,\mathrm{m/s}$, a final velocity of $v_f = 5\,\mathrm{m/s}$ to $8\,\mathrm{m/s}$, a saturation parameter of $s_0 = 5$ and a safety factor of $\varepsilon = 0.7$. This results in a deceleration of $a = 0.58\,a_{\max}$ and a slower length of $L \approx 1\,\mathrm{m}$. By choosing the laser detuning −225 MHz detuned to the MOT light, we aim for a spin flip

---

[1] Tuning of the ZS detuning with respect to the MOT detuning is planned to be fine-tunable via a homogenous offset field provided by two independently controllable additional windings in the ZS coil.

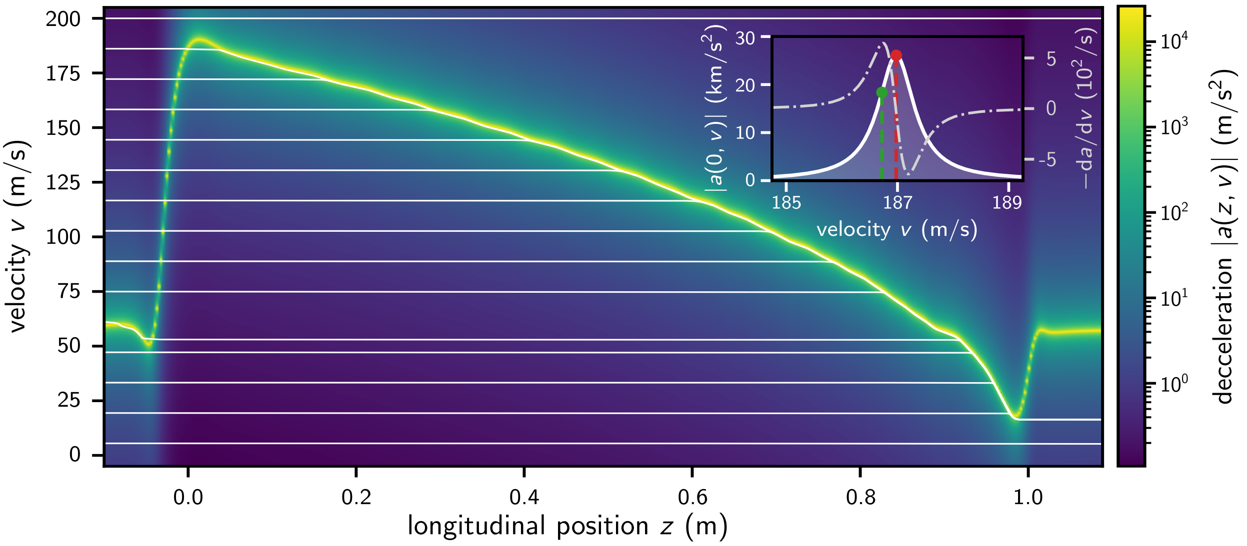

Figure 4.23: Predicted ZS deceleration (colored density plot) and one-dimensional simulation of atom trajectories through the ZS (white lines). Atoms with longitudinal velocities below the design capture velocity $v < v_{\text{init}} = 190\,\text{m/s}$ eventually come into resonance with the ZS beam, follow the deceleration trajectory, and slow down to the target velocity v_{final}. The inset shows the acceleration profile at $z = 0$ and its derivative. For stability, we operate at a safety factor of $\varepsilon = 0.7$ (green marker), slightly below the point of maximum slope and away from the peak deceleration (red marker).

ZS with a 901 mm long decreasing field section and maximum field strength of 252 G and an 88 mm long increasing field section.

Construction The magnetic field design is based on flat $8 \times 1\,\text{mm}^2$ enamelled copper wire wound onto a 22 mm inner diameter, double walled, water-cooled aluminum tube. The latter supports the coils without the CF16 vacuum tube, connecting source and main chamber, which allows vacuum baking the chamber without the ZS in place and measuring the internal magnetic field. The latter is important as the narrow linewidth makes the ZS very sensitive to small magnetic field imperfections, where atoms can leave the resonance condition. The increasing field ZS section is recessed into the main chamber to reduce the distance between ZS exit and MOT location to just 60 mm for efficient capture. This design also allows utilizing the MOT gradient field to bring the final ZS field of −98 G quickly back to zero. This should result in the atoms exiting the ZS abruptly, reducing atom loss by removing pushback light forces on the last section. The chosen coil configuration and winding pattern and the simulated magnetic field are shown in figure 4.22.

Simulation A one-dimensional simulation of atom trajectories subject to this field is shown in figure 4.23, which shows that residual deviations from the theoretically ideal field configuration are much smaller than the linewidth. Atoms therefore stay in resonance along the whole length of the slower. We estimate the atom flux that can be captured by the MOT by conducting an in-depth, two-dimensional simulation of atom trajectories under experimentally realistic parameters. This simulation takes into account the emission pattern and flux of the microchannel array nozzle, as described in section 3.1.3. An exemplary Monte-Carlo dataset of atom trajectories – taking into account the gravitational sag over the long travel distance, the atomic beam broadening due to imperfect nozzle collimation and

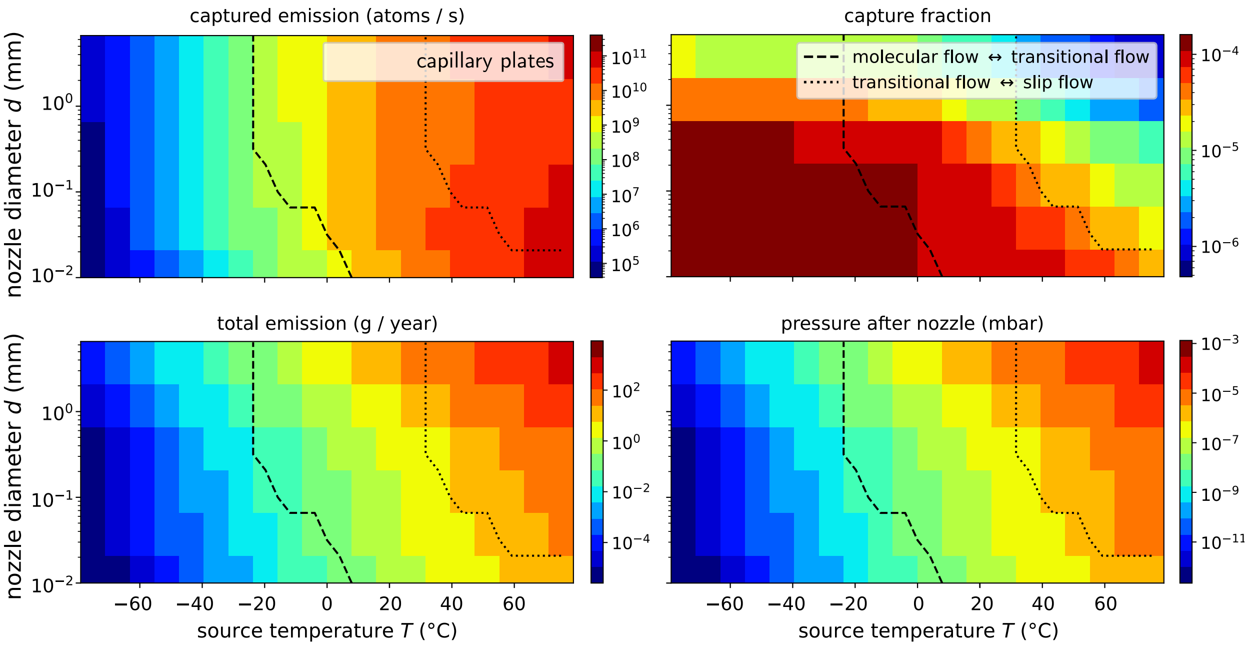

Figure 4.24: Simulation of the ZS performance in dependence of the collimator nozzle diameter d_{coll} and source temperature T, showing the captured emission in the MOT (= MOT loading rate, top left), the capture fraction (top right) of the total source emission (bottom left) and the vacuum pressure behind the nozzle (bottom right). We consider experimental constraints, restricting the total nozzle aperture to 5 mm and the microchannel collimator length to $L_{\text{coll}} \leq 100\,\text{mm}$ while keeping the collimation angle $\beta_{\text{coll}} = d_{\text{coll}}/L_{\text{coll}}$ at $\leq 0.14°$. We denote the transitions between flow regimes (dashed, dotted) and the optimal region for operation of the capillary plate nozzle with $d = 25\,\mu\text{m}$ and $50\,\mu\text{m}$ (hatched).

photon scattering of the ZS beam – is shown in figure 3.6. Atoms slowed by the ZS scatter about 6000 to 23 000 photons from the slowing beam and the resulting random walk in velocity space leads to a transversal velocity component of 0.36 m/s to 0.69 m/s, which is very comparable to the transversal velocity distribution of the source. Free fall under gravity reduces the capture range to about $v > 57\,\text{m/s}$, as slower atoms spend too much time (> 32 ms) in the ZS and do not reach the MOT. Depending on the initial velocity, gravity displaces atoms by −1.9 mm to −5.1 mm ($v = 57\,\text{m/s}$ to $190\,\text{m/s}$), which needs to be compensated for by a slight tilt of the source chamber axis to efficiently target the trapping region; we assume a MOT capture radius of $r_C \leq 3.1\,\text{mm}$ and capture velocity $v_C \leq 9.7\,\text{m/s}$.

A simulation of the ZS deceleration and resulting MOT capture performance for various nozzle geometries and varying source temperature T is shown in figure 4.24. Driven by the simulation results, we choose a $d_{\text{coll}} = 25\,\mu\text{m}$ and $50\,\mu\text{m}$ diameter capillary plate over a traditional microtube array or a single collimator tube. For an optimal operation region of $-5\,°\text{C} < T < 60\,°\text{C}$, we estimate a fraction of 3×10^{-5} to 5×10^{-5} emitted by the source and captured by the MOT, which results in a capturable atom flux of 1×10^{9} atoms/s to 4×10^{10} atoms/s at a total mass throughput of the machine of 1 g/yr to 5 g/yr, while keeping the achievable vacuum behind the collimator reasonable.

5 Dipole trapping of mercury

Optical dipole traps (ODTs) are ideally suited for electric dipole moment (EDM) measurements with mercury atoms, offering long storage and coherence times, high atomic densities, and compatibility with tightly spaced electrodes. Unlike magneto-optical traps (MOTs), ODTs operate without magnetic field gradients, avoiding perturbations in the magnetically sensitive measurement environment. They also offer tighter confinement and higher atomic densities than optical molasses, enabling operation near closely spaced ($\leq 1\,\mathrm{mm}$) electrodes that allow for stronger electric fields, thereby enhancing EDM sensitivity. By transferring laser-cooled atoms from a MOT into a deep ODT, we achieve the stable, high-quality samples required for precision EDM experiments. In order to hold the atoms in a science chamber dislocated from the MOT region in a magnetically shielded science vacuum chamber, transport of the atomic sample via an ODT is also required. The latter can be realized by using focus-tunable lenses [204, 205] or by moving the last focusing lens on an air-bearing stage [206, 207].

Moreover, ODTs for isotope shift spectroscopy in mercury could increase the interrogation times of the sample, allowing quantum enhancement of the spectroscopy methods. Here, three-dimensional optical lattice clock setups operating in the Lamb-Dicke regime reduce Doppler shifts and atomic interactions [208] and are the most ideal platforms to probe for isotope shifts on ultra-narrow clock lines, like demonstrated for instance in neutral ytterbium [209].

Evaporating mercury to degeneracy – not realized so far neither for bosonic nor fermionic species – does require ODTs for evaporative cooling, since the electronic structure of the ground state does not allow magnetic trapping of the electronic ground state.[1] Here, Fermi gases of ^{199}Hg used for probing the atomic EDM could improve the $\propto 1/\sqrt{N}$ scaling of the measurement sensitivity to $\propto 1/N$ by collective quantum effects as discussed before.

ODTs for generation and trapping of Fermi gases of mercury could also allow studies of impurity physics like Friedel oscillations [210, 211] mediated between a single bosonic impurity and the Fermi sea. Here, isotope-selective magic wavelength lattices would be required to trap a Fermi gas of ^{199}Hg or ^{201}Hg in an effectively two-dimensional trap, while an isotope-selective optical tweezer could be used to hold the bosonic impurity. Both ODTs would require vanishing light shifts for the opposite isotope to isolate the interaction to be scattering-based only. We discuss this application of ultracold gases of mercury in the outlook, section 5.3.2.

As we will see in the following, the ground state polarizability of mercury in the visible spectrum is about two orders of magnitude lower than that of other alkaline-earth-(like) elements and nearly all laser-cooled atomic species. This is because the atomic ground state can only be accessed through deep ultraviolet (UV) transitions. Overcoming the low polarizability is the main challenge.

So far we are not aware of any focussed beam ODT of mercury. For the operation of an optical

---

[1] Optically pumping to $^3\mathrm{P}_2$ could allow to magnetically trap atoms in the long-lived metastable state.

lattice clock in mercury, magic wavelength optical lattices are required to compensate for the light shift between the ground state and the relevant clock state. Such lattices have been successfully operated in the near UV region [39, 41–43]. Here, in-vacuum build up Fabry-Perot cavities are used to increase the effective available laser power at the location of the atoms by a large factor given by the finesse $\mathcal{F}$ of the cavity. In these application, however only single atoms per lattice side are loaded ($\gtrsim 10^3$ atoms in total), reducing the need for deep trap depths and large trapping volumes. For our applications much higher atom numbers are necessary, and trapping volumes need to hold large clouds of mercury. Other systems also requiring deep ODTs are experiments studying cold molecules. Here, high-power traps also based on high-finesse build up cavities were proposed [212] and are now reaching intensities of over 400 GW/cm^2, all operating at 1064 nm were high laser power is available [213–216]. Although build-up cavities provide high optical intensities, they reduce the flexibility of the trapping potential and strongly restrict atomic transport. The standing-wave lattice structure can restrict thermalization across lattice sites and therefore obstruct evaporative cooling for Bose-Einstein condensate (BEC) or Fermi gas formation. We therefore chose single focussed beam and crossed beam ODT for the application here.

Prediction of the atomic light shift for mercury was so far based on ab-initio electronic structure calculations [153, 217, 218], but focus only on magic optical lattice traps for clock operation. These type of electron structure calculations are unable to predict the location of the transition wavelengths to better than a few percent, which makes reducing uncertainties in the polarizability and light shift calculations challenging. For the $^1\mathrm{S}_0 \rightarrow {}^3\mathrm{P}_0$ transition, the magic wavelength lies at around 362.5 nm, predicted via configuration interaction many-body perturbation theory (CI-MBPT) [153, 217] and experimentally confirmed by [40, 219]. For the $^1\mathrm{S}_0 \rightarrow {}^3\mathrm{P}_2$ transition, the magic wavelength is predicted to be around 351.8 nm based on ab-initio electron structure calculations of the atomic transition energies and linewidths via a Complete Active Space Self-Consistent-Field (CASSCF) method and dynamical energy corrections [218].

For the polarizability calculation in section 5.1.1, in this thesis a data driven approach was attempted. This has the advantage of a smaller uncertainty in the known and spectroscopically measured transition. For so far unmeasured transitions, linewidths and wavelengths were taken from electron structure calculations in reference [218]. For other lines, a pragmatic scaling solution was chosen. The calculation presented here includes input from Raluca Aldea during her time as an intern in the group and Felix Affeld within his master thesis [91].

5.1 Dipole potential

The optical dipole potential originates from the coherent absorption and re-emission of scattered photons as derived in section 4.1. Expressing the dipole force from equation (4.8) as a conservative potential $\langle \vec{F}_{\mathrm{dip}} \rangle = -\nabla U_{\mathrm{dip}}$ and expanding the logarithm to first order in $s(\vec{r})$ for large detuning, gives the optical dipole potential

$$U_{\mathrm{dip}} = \frac{\hbar\,\Delta}{2} \log\left[s(\vec{r}) + 1\right] \approx \frac{\hbar\,\Delta}{2}\, s(\vec{r}) = \frac{\hbar\,|\Omega(\vec{r})|^2}{4\,\Delta}\,. \tag{5.1}$$

Since we neglected the co-rotating terms in equation (4.1) within the rotating wave approximation, this light shift derivation is not complete. Analogously to the counter-rotating terms leading to an energy correction $\propto (\omega - \omega_0)^{-1}$, by replacing $\omega \longrightarrow -\omega$ we can see that the fast oscillating terms contribute to lowest order an energy shift $\propto -(\omega + \omega_0)^{-1}$. This effect is known as the Bloch-Siegert shift [220] and must be considered when calculating the polarizability of very far-detuned ODTs, as we will see below.

A more precise derivation can be obtained by applying time-dependent perturbation theory to the Hamiltonian in equation 4.1. We define $|g'(t)\rangle = |g\rangle + |\delta g(t)\rangle$ to be the new perturbed ground state solving the time dependent Schrödinger equation $\partial_t|g'(t)\rangle = -i/\hbar\, H\,|g'(t)\rangle$ to first order, $\partial_t|\delta g(t)\rangle = -i/\hbar\, H_A\,|\delta g'(t)\rangle - i/\hbar\, H_{AF}\,|g\rangle$. Inserting the ansatz $|\delta g(t)\rangle = (a^{(+)}\,e^{-i\,\omega\,t} + a^{(-)}\,e^{-i\,\omega\,t})|e\rangle$ allows determination of the perturbation coefficients $a^{(\pm)}$ and the expectation value of the dipole moment to first order is then given by

$$\langle\vec{d}(t)\rangle = \langle g(t)|\vec{d}|\delta g(t)\rangle + \langle\delta g(t)|\vec{d}|g(t)\rangle = \frac{2\,\omega_0\,|\langle g|\hat{\epsilon}\cdot\vec{d}|e\rangle|^2\,E^{(+)}}{\hbar\,(\omega_0^2 - \omega^2)}e^{i\,\omega\,t} + \text{c.c.}\,, \qquad (5.2)$$

which confirms the argumentative derivation of the $\propto (\omega - \omega_0)^{-1} - (\omega + \omega_0)^{-1} \propto \omega_0/(\omega_0^2 - \omega^2)$ dependency. Expressing the dipole potential in terms of the atomic ground state AC polarizability $\alpha(\omega)$ then leads to

$$U_{\text{dip}} = -\frac{1}{2\,\epsilon_0\,c}\,\alpha(\omega)\,I(\vec{r})\,, \quad \text{where } \alpha(\omega) = 6\pi\,\epsilon_0\,c^3\,\frac{\Gamma}{\omega_0^2\,(\omega_0^2 - \omega^2)}\,. \qquad (5.3)$$

Here, the transition rate Γ is given by equation (4.4) and the electric field intensity is defined as $I(\vec{r}) = 2\,c\,\epsilon_0\,|E^{(+)}|^2$. These results also qualitatively agree with those of the classical Lorentz model derivation, which assumes that the field induces a dipole moment, $d = \alpha\,E$, that oscillates at the driving frequency. The polarizability, α, can be obtained by integrating the equation of motion for the driven electron and introducing an on-resonance damping rate of electron motion that resembles the transition rate, Γ, as described in reference [192].

5.1.1 Polarizability

For a multi-level atom the polarizability from equation (5.3) can to first order be summed over all possible excited states. Note that this gives the AC light shift for the ground state $|g\rangle$, while any higher lying state $|e\rangle$ coupled by the same light field shifts exactly in the opposite direction. The latter can be seen from a full quantum derivation in the dressed-state picture.

The complex atomic polarizability $\tilde{\alpha}$ is in general given by the quantum correlation function of the induced dipole moment operator $\vec{d}$. For a non-spherical atom it can be given in tensor form as

$$\tilde{\alpha}_{\mu\nu}(\omega) = \frac{i}{\hbar}\int_0^\infty \mathrm{d}t\,\left\langle\left[d_\mu(t),\,d_\nu(0)\right]\right\rangle\,e^{i\,\omega\,t} = \sum_{|e\rangle}\frac{(\omega_{ge}^2 - \omega^2) + i\,\Gamma_{ge}\,\omega}{\hbar\,\left[(\omega_{ge}^2 - \omega^2)^2 + \Gamma_{ge}^2\,\omega^2\right]}\,\langle g|d_\mu|e\rangle\,\langle e|d_\nu|g\rangle\,, \qquad (5.4)$$

where ω_{ge} and Γ_{ge} are the atomic resonance frequencies and linewidths and $[\cdot,\cdot]$ denotes the Hilbert space commutator [159].

Relevant for optical dipole trapping is only the real part of the polarizability tensor; the Kramers-

Heisenberg formula for the polarizability tensor is then given by

$$\alpha_{\mu\nu}(\omega) = \mathrm{Re}[\tilde{\alpha}_{\mu\nu}(\omega)] = \sum_{|e\rangle} \frac{2\,\omega_{ge}\,\langle g|d_\mu|e\rangle\,\langle e|d_\nu|g\rangle}{\hbar\,(\omega_{ge}^2 - \omega^2)}\,. \tag{5.5}$$

Fine structure

Consider the fine structure of an atom described by principal quantum number n, orbital momentum and spin quantum numbers L and J and the total momentum projection onto the quantization axis m. Using the Wigner-Eckart theorem [159, p. 7.241] we can rewrite the dipole matrix element for the transition $|i\rangle \longrightarrow |k\rangle$ between magnetic sublevels in the atomic fine structure via the projection to the coarser electronic structure. Introducing q as the projection of the electric field polarization vector $\hat{\epsilon}$ onto the quantization axis in the spherical basis with $q = 0$ for π-polarized and $q = \pm 1$ for $\sigma_\pm$-polarized light, we can write the magnitude of the dipole matrix elements as

$$\begin{aligned} |\langle i|\hat{\epsilon}\cdot\vec{d}|k\rangle| &= |\langle n_i, L_i, J_i m_i|\hat{\epsilon}\cdot\vec{d}|n_k, L_k, J_k m_k\rangle| \\ &= \left|\langle n_i, L_i, J_i||\vec{d}||n_k, L_k, J_k\rangle\sqrt{\frac{2\,J_i+1}{2\,J_k+1}}\langle J_k, m_k|J_i, m_i; 1, -q\rangle\right| \\ &= |\langle n_i, L_i, J_i||\vec{d}||n_k, L_k, J_k\rangle|\,\sqrt{2\,J_k+1}\begin{pmatrix} J_i & 1 & J_k \\ m_i & q & -m_k \end{pmatrix}, \end{aligned} \tag{5.6}$$

where in the last step we rewrite the Clebsch-Gordon coefficient in terms of the Wigner 3j-symbol $\langle j_1, m_1; j_2, m_2|j_3, -m_3\rangle = (-1)^{j_1-j_2-m_3+1}\sqrt{2\,j_3+1}\left(\begin{smallmatrix} j_1 & j_2 & j_3 \\ m_1 & m_2 & m_3 \end{smallmatrix}\right)$. The summed AC polarizability of any fine structure state $|i\rangle = |n_i, L_i, J_i, m_i\rangle$ given the electric field polarization q is then given by

$$\alpha_i(\omega) = 6\pi\,\epsilon_0\,c^3 \sum_k \sum_{m_k=-J_k}^{J_k} \frac{\Gamma_{J_i, J_k}\,(2\,J_k+1)}{\omega_{ik}^2\,(\omega_{ik}^2 - \omega^2)}\,\frac{\omega_{ik}}{|\omega_{ik}|}\begin{pmatrix} J_i & 1 & J_k \\ m_i & q & -m_k \end{pmatrix}^2. \tag{5.7}$$

Here, we now have rewritten the effective transition rates Γ between the two levels in terms of the atomic spontaneous decay rate $\Gamma_{J_i, J_k} = \omega_0^3/(3\pi\,\epsilon_0\,\hbar\,c^3)|\langle n_i, L_i, J_i||\vec{d}||n_k, L_k, J_k\rangle|^2$ from the fine-structure level J_k to the level J_i. Given in figure 2.3, these can be found tabulated as the linewidth for most transitions [87].[1] Note that here $\omega_{ik} = (E_i - E_k)/\hbar$ is the (signed) transition frequency between the relevant levels and the term $\omega_{ik}/|\omega_{ik}|$ ensures that lower lying levels are contributing to the polarizability with opposite sign. The resulting light shift is then given by equation (5.3) with $\alpha(\omega)$ given by the multi-level sum, equation (5.7).

This analysis holds for a description of the bosonic species with nuclear spin $I = 0$, for which the reduction of the dipole operator can be left at the fine structure level. For analysis of the trapping potential of fermionic species with $I \neq 0$, relevant for e.g., EDM measurements, the hyperfine structure becomes important and the reduction of the dipole operator in equation (5.6) is not sufficient.

---

[1] Note: In the remainder of this work the symbol Γ will be used as a shorthand for Γ_{J_i, J_k} to denote the linewidth any time a two-level description of the relevant levels is suitable.

Hyperfine structure

The derivation for the polarizability of the hyperfine levels is analogous to the fine structure, where we decompose the matrix elements via the Clebsch-Gordon coefficients of the relevant hyperfine levels. The polarizability tensor, equation (5.5), can be decomposed into three irreducible terms, a scalar part $\alpha^{(0)}$, where the resulting light shift is insensitive to the light field polarization, as well as a vector part $\alpha^{(1)}$ and a tensor part $\alpha^{(2)}$, that lead to a light field dependency sensitive to circular and linear polarization of the light field, respectively [159]. The total polarizability of level $|i\rangle$ with total spin quantum number F_i and associated magnetic sublevel m_i in dependence of light field frequency ω and polarization $\hat{\epsilon}$ can then be written as the sum of three terms

$$\alpha_i(\omega) = \alpha_i^{(0)}(\omega) + \alpha_i^{(1)}(\omega)\,(\hat{\epsilon}\cdot\hat{\sigma}_+ - \hat{\epsilon}\cdot\hat{\sigma}_-)\,\frac{m_i}{F_i} + \alpha_i^{(2)}(\omega)\,\frac{3\,|\hat{\epsilon}\cdot\hat{\pi}|^2-1}{2}\,\frac{3\,m_i^2 - F_i\,(F_i+1)}{F_i\,(2\,F_i-1)}\,, \tag{5.8}$$

where $\hat{\pi} = \hat{e}_z$ denotes the normal vector along the quantization axis of the atom indicating π-polarization and $\hat{\sigma}_\pm = \pm(\hat{e}_x \pm i\,\hat{e}_y)/\sqrt{2}$ are the normal vectors associated with $\sigma_\pm$-polarized light.

At large detuning of the light field to the atomic resonance the three polarizability components can be written [159] as

$$\begin{aligned}
\alpha_i^{(0)}(\omega) &= 2\pi\,\epsilon_0\,c^3 \sum_k \frac{1}{2\,J_i+1}\,\frac{(2\,J_k+1)\,\Gamma_{J_i,J_k}}{\omega_{ik}^2\,(\omega_{ik}^2-\omega^2)}\,\frac{\omega_{ik}}{|\omega_{ik}|}\,,\\
\alpha_i^{(1)}(\omega) &= 3\pi\,\epsilon_0\,c^3 \sum_k (-1)^{1-2\,J_i-J_k-F_i-I} \begin{Bmatrix} 1 & 1 & 1\\ J_i & J_i & J_k \end{Bmatrix} \begin{Bmatrix} J_i & J_i & 1\\ F_i & F_i & I \end{Bmatrix}\\
&\qquad\times \sqrt{\frac{6\,F_i\,(2\,F_i+1)}{F_i+1}}\,\frac{(2\,J_k+1)\,\Gamma_{J_i,J_k}}{\omega_{ik}^2\,(\omega_{ik}^2-\omega^2)}\,\frac{\omega_{ik}}{|\omega_{ik}|}\,,\\
\alpha_i^{(2)}(\omega) &= 3\pi\,\epsilon_0\,c^3 \sum_k (-1)^{-2\,J_i-J_k-F_i-I} \begin{Bmatrix} 1 & 1 & 2\\ J_i & J_i & J_k \end{Bmatrix} \begin{Bmatrix} J_i & J_i & 2\\ F_i & F_i & I \end{Bmatrix}\\
&\qquad\times \sqrt{\frac{40\,F_i\,(2\,F_i+1)\,(2\,F_i-1)}{3\,(F_i+1)\,(2\,F_i+3)}}\,\frac{(2\,J_k+1)\,\Gamma_{J_i,J_k}}{\omega_{ik}^2\,(\omega_{ik}^2-\omega^2)}\,\frac{\omega_{ik}}{|\omega_{ik}|}\,.
\end{aligned} \tag{5.9}$$

The vector and the tensor contributions are ill-defined for $F_i = 0$ for which the light shift contribution is zero. Note that the vector contribution also vanishes for $m_i = 0$ and results in light shifts of opposite sign for $\sigma_\pm$ polarized light. The resulting light shift is again given by equation (5.3).

Relevant levels

The relevant levels $|i\rangle$ to consider for loading an ODT from a MOT of mercury operated on the intercombination line, are the $6s^2\,{}^1S_0$ ground state with magnetic quantum number $m_g = 0$ in which the atoms should also be finally trapped, and the $6s\,6p\,{}^3P_1$ excited state with $m_e = \pm 1$. The latter is being pumped by the MOT light, when handing atoms over from one to the other trap. It is therefore important that the presence of the optical dipole potential for the ground state does not create a loss channel through the ${}^3P_1$ state. Either by forming a repulsive potential for excited atoms or by creating a relative light shift of the ${}^1S_0 \rightarrow {}^3P_1$ line, that detunes the MOT light too far into the red or blue and therefore either reduces or inverts its confining and cooling force.

Looking at the electronic level scheme, figure 2.3, it is clear that nearly all relevant transitions that couple to the ground and excited state of the intercombination line lie in the UV, except for the 436 nm $^3\mathrm{P}_1 \rightarrow {}^3\mathrm{S}_1$ line. This makes any ODT operating in the visible to infrared spectrum, where high power (single-mode) continuous-wave lasers are available, strongly detuned to any relevant transition. This emphasizes the shortcoming and insufficiency of the rotating wave approximation and indicates that in comparison to nearly all other laser cooled elements, obtaining sufficient trap depth for atoms cooled to around the Doppler limit is really challenging.

For calculation of the polarizability in the visible to infrared region the dominating contributions arise from the $^1\mathrm{S}_0 \rightarrow {}^1\mathrm{P}_1$ (185 nm) and $^1\mathrm{S}_0 \rightarrow {}^3\mathrm{P}_1$ (254 nm) line for the ground state, as well as for the $^3\mathrm{P}_1 \rightarrow {}^3\mathrm{S}_1$ (436 nm) and $^3\mathrm{P}_1 \rightarrow {}^3D_{1,2}$ (312.7 nm, 313.2 nm) transitions for the excited state. The linewidth of the $^3\mathrm{P}_1 \rightarrow {}^3\mathrm{D}_1$ transition and other contributing lines was experimentally unknown at the time of writing [87].[1]

Transition rates Γ_{J_i,J_k}

A more precise calculation of the light shift including the light field polarization dependency, and estimation contributions from unknown transitions is attempted here. This is also interesting for evaluating the feasibility of an ODT in the near UV. For this purpose, all relevant lines down to the ionization threshold of mercury were collected from two sources. Most transitions were taken from the NIST line or level database [87], when listed with their transition frequencies or relevant energy levels. We extract the vacuum wavelengths and linewidths from this dataset. Missing linewidths were estimated as described below. Theoretical predictions for otherwise unknown lines were taken from reference [218].

Noting the similarity of transition rates comparing lines in mercury and strontium, an electronically rather similar element, a mapping of some missing linewidths was performed. A subset of electronic transitions were compared, selecting all transitions from the NIST line database with non-missing transition rates that could be mapped using the orbital association. Mercury and strontium have similar s-orbital occupations, but mercury's overall electronic structure is much more complex due to the involvement of f- and d-electrons. Strontium's structure is simpler because it lacks these inner electron contributions in its ground state. Although this mapping of the electronic orbitals is crude, an approximately consistent scaling factor of $\Gamma_{\mathrm{Hg}}/\Gamma_{\mathrm{Sr}} = 2.0(9)$ between (Doppler-allowed) transition linewidths could be obtained. When we additionally assume a $\propto \omega^3$-scaling of the transition linewidth we obtain similar results within the large uncertainty. This allowed interpolation of missing mercury transition rates from strontium values given in reference [87] or if not listed here calculated from the total transition rates A_T for strontium, as given in reference [221]. The uncertainty of the strontium linewidth as well as the uncertainty in $\Gamma_{\mathrm{Hg}}/\Gamma_{\mathrm{Sr}}$ were propagated to the interpolated mercury linewidth. Using the data from reference [221] the code was also benchmarked to check for potential errors and the polarizability plots given in this work could be reproduced precisely.

Finally still unknown transition rates that could be neither obtained from the NIST database nor theory calculations nor interpolated from strontium data are assigned a fixed linewidth of $\Gamma_{J_i,J_l} = 2\pi \times 0(20)$ MHz generously accounting for realistic linewidths of the missing transitions. These transitions

---

[1] The linewidth of the $^3\mathrm{P}_1 \rightarrow {}^3\mathrm{D}_1$ transition was determined from experimental data later within this thesis, see chapter 6 or the master thesis work of Felix Affeld [91], respectively.

will therefore only contribute to the uncertainty of the polarizability, not the predicted magnitude.

Results

Summing equation (5.7) for the fine or equation (5.9) for the hyperfine structure, averaged over all relevant transitions and states, yields the polarizability for a given light field frequency and polarization. The polarizability of the $5s^2\,{}^1\mathrm{S}_0$ $m = 0$ and $6s\,6p\,{}^3\mathrm{P}_1$ $m = +1$ fine structure state for the bosonic isotopes of mercury for π-polarized light ($q = 0$) is shown in figure 5.1. The relevant atomic transitions contribute to the polarizability by introducing poles at the atomic resonances; their widths being proportional to the transition linewidth.

The obtained polarizability for the ${}^1\mathrm{S}_0$ ground state is dominated by the broad singlet ${}^1\mathrm{S}_0 \rightarrow {}^1\mathrm{P}_1$ transition at 185 nm and the intercombination line at 254 nm. With no other transition lying lower in energy / higher in wavelength this results in a very flat polarizability for the complete visible to infrared spectrum. The absolute polarizability is about two orders of magnitude lower in comparison to most laser cooled neutral atoms as discussed before. For the mercury ground state the resulting trap depth – directly proportional to the polarizability as given by equation (5.3) – is therefore nearly independent of the laser wavelength, where high power lasers are available. This supported the decision for this thesis to work at around 1064 nm, where high power semiconductor lasers and fiber lasers exist. Choosing a laser source with less detuning to the ground state transitions, like $\lambda = 532\,\mathrm{nm}$, where optically pumped semiconductor lasers can still provide power up to 20 W or more, is not beneficial. It only improves the ground state polarizability by about 10.6 % over the near infrared option at $\lambda = 1064\,\mathrm{nm}$, which is not compensating for the loss of available power at that wavelength. It also increases the trapping depth for the excited ${}^3\mathrm{P}_1$ state by more than a factor of two. This would lead to much larger relative light shifts that need to be compensated during loading from the MOT, as will be discussed below.

Magic wavelengths Magic wavelengths are wavelength for which the relative light shift between the ground and excited state vanishes. For mercury – useful for reduced systematic light shifts in EDM measurements of laser cooled samples – magic wavelengths only exist in the UV, with the most accessible lying around 357.9 nm. The large uncertainty in the excited state polarizability at this wavelength ($\alpha = 4.6(23.9) \times 10^{-40}\,\mathrm{Fm}^2$) is an added challenge, since high power UV laser systems feature mostly only a narrow wavelength tuning range. Note that the location of the magic wavelength in the UV-A spectrum was already predicted by electronic structure calculations [218]. Their value of 351 nm deviates from our value, likely explained by the large uncertainty in their determination of the energy levels and transition rates. Improved theoretical models and more experimental input to the calculations could render this wavelength range a viable option for a future magic wavelength ODT, when the atomic samples at pre-cooled at deeper trap depths. Trapping and cooling large atomic samples of mercury at even deeper UV laser wavelengths $< 260\,\mathrm{nm}$, where the ground state polarizability is enhanced, is at the current state of UV laser development not beneficial.

Hyperfine polarizability For the excited $6s\,6p\,{}^3\mathrm{P}_1$ state, as well as for the fermions that have nuclear moment contribution, the fine structure polarizability is not enough. We need to consider the scalar, vector and tensor contributions of the hyperfine structure given in equation (5.9). The polar-

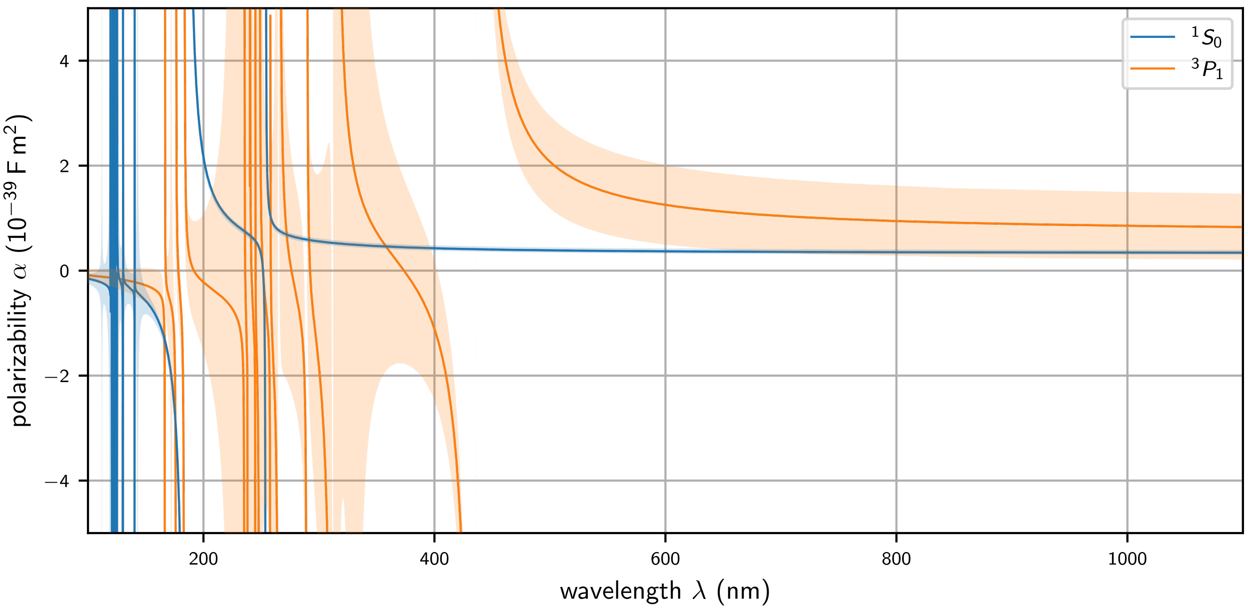

(a) Polarizability for the wavelength range from deep ultraviolet to near infrared.

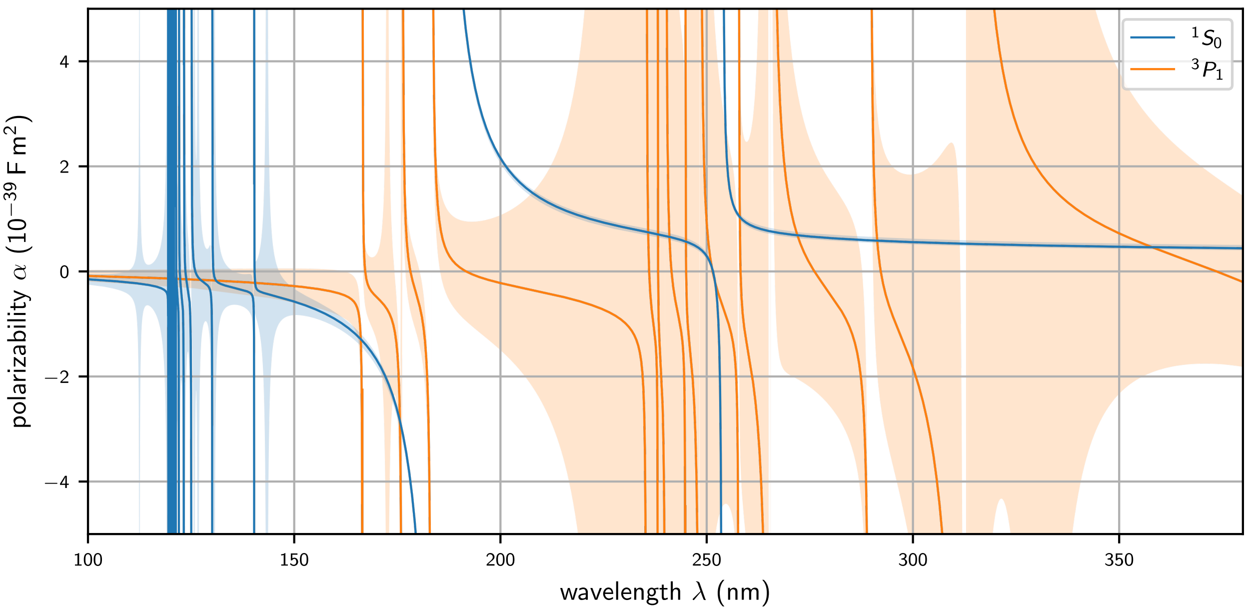

(b) Zoom into the ultraviolet wavelength region.

Figure 5.1: AC polarizability for the $^1\mathrm{S}_0$, $m = 0$ (blue) and $^3\mathrm{P}_1$ $m = +1$ (orange) state of neutral mercury given a light field polarization of $q = 0$ (π-polarized light). The shaded areas indicate the 1σ uncertainty of the calculation, originating in the uncertainty of the transition frequencies / energy levels and the linewidths. Here, unknown transition rates that could be neither obtained from theory calculations nor interpolated from strontium data are assigned a fixed linewidth of $\Gamma_{J_i,J_l} = 2\pi \times 0(20)$ MHz and therefore contribute only in the uncertainty of the polarizability. Poles in the polarizability plot indicate the location of the contributing transitions, that can be coupled from the relevant level, nearly all of them lying in the UV.

I	state	$\alpha^{(0)}$ ($10^{-40}\,\mathrm{Fm^2}$)	$\alpha^{(1)}$ ($10^{-40}\,\mathrm{Fm^2}$)	$\alpha^{(2)}$ ($10^{-40}\,\mathrm{Fm^2}$)
0	$\lvert{}^1\mathrm{S}_0, F = 0\rangle$	3.4(1.1)	0	0
	$\lvert{}^3\mathrm{P}_1, F = 1\rangle$	6.7(3.3)	1.6(2.3)	1.6(8)
1/2	$\lvert{}^1\mathrm{S}_0, F = 1/2\rangle$	3.4(1.1)	0	0
	$\lvert{}^3\mathrm{P}_1, F = 1/2\rangle$	6.7(3.3)	1.1(1.5)	0
	$\lvert{}^3\mathrm{P}_1, F = 3/2\rangle$	6.7(3.3)	1.6(2.3)	1.6(8)
3/2	$\lvert{}^1\mathrm{S}_0, F = 3/2\rangle$	3.4(1.1)	0	0
	$\lvert{}^3\mathrm{P}_1, F = 1/2\rangle$	6.7(3.3)	−0.5(8)	0
	$\lvert{}^3\mathrm{P}_1, F = 3/2\rangle$	6.7(3.3)	0.6(9)	−1.3(6)
	$\lvert{}^3\mathrm{P}_1, F = 5/2\rangle$	6.7(3.3)	1.6(2.3)	1.6(8)

Table 5.1: Hyperfine AC polarizability of the $6s^2\ {}^1\mathrm{S}_0$ and $6s\,6p\ {}^3\mathrm{P}_1$ level at $\lambda = 1064\,\mathrm{nm}$. Here, $\alpha^{(i)}$ denote the scalar ($i = 0$), vector ($i = 1$) and tensor ($i = 2$) polarizabilities.

izability at $\lambda = 1064\,\mathrm{nm}$ of the MOT ground and excited state is given for all hyperfine sublevels of bosonic and fermionic isotopes in table 5.1. Note that in this hyperfine description the polarizability components itself are independent of the magnetic sublevel and the polarization of the light field. The total ground state polarizability is independent of the isotope nuclear spin and hyperfine state, as the scalar polarizability just depends on J_i and the vector and tensor polarizability vanish. This is due to the first Wigner-6j symbol in equation (5.9) being $\left\{\begin{smallmatrix} 1 & 1 & n \\ J_i & J_i & J_k \end{smallmatrix}\right\} = 0$ for $n = 1, 2$, which forbids any coupling.

For the excited ${}^3\mathrm{P}_1$ state, however, the vector and tensor components differ and the resulting light shift is therefore sensitive to the light field polarization and the selected magnetic sublevel. This makes loading the ODT directly from the MOT slightly more complicated. Here, the circularly polarized light MOT beams in combination with the magnetic gradient field providing the quantization axis pump the atoms into the outermost fine structure levels during MOT operation. The atoms are therefore spatially sensitive to the light field polarization of the focussed ODT beam, that has to be set fixed in the lab reference frame.

5.1.2 Light shift and trap potential

The resulting light shift of all relevant MOT levels at an ODT wavelength of 1064 nm and for varying light field polarization with respect to the atomic quantization axis is given in table 5.2. As the vector and tensor components vanish for atoms in the atomic ground state, the resulting light shift is independent of polarization. For the ground state we obtain $U_{|g\rangle}/I = (-4.70(1.46))\,k_B \times \mathrm{mK}/(\mathrm{W}/\mu\mathrm{m}^2)$. This results in a trap depth of $U_{|g\rangle} = (-470(146))\,k_B \times \mu\mathrm{K}$ at a laser intensity of $I = 100\,\mathrm{mW}/\mu\mathrm{m}^2 = 10\,\mathrm{MW/cm^2}$. This is just enough to trap $T \approx 200\,\mu\mathrm{K}$ cold atoms from the MOT. The trap depth to temperature ratio is $\eta = |U_\mathrm{dip}/(k_B T)| = 2.35(73)$. Ideally $\eta \gg 1$ is preferred – typical experiments involving evaporative cooling operate at $\eta \approx 3$ to 10. We initially set our target low, as reaching these intensities while providing enough trapping volume is challenging.

As noted before, to load the atoms from the MOT into the ODT we however also need to consider that the excited state also experiences a light shift. The differential light shift of ground state $|g\rangle$ and excited state $|e\rangle$ then leads to a change of the MOT detuning $\Delta = \omega_\mathrm{mot} - \omega_0$ by shifting the atomic

I	state $\lvert i\rangle$		$U_{\mathrm{dip},\lvert e\rangle}$ / ($k_B \times$ mK)		Δ_{dip} / ($2\pi \times$ MHz)	
	$\lvert{}^1\mathrm{S}_0, F_g\rangle$	$\lvert{}^3\mathrm{P}_1, F_e\rangle$	π	$\sigma^\pm$	π	$\sigma^\pm$
0	0	1	−0.92(46)	−1.14(56)	−9.4(9.9)	−14(12)
1/2	1/2	1/2	−0.92(46)	−1.06(50)	−9.4(9.9)	−12(11)
	1/2	3/2	−1.14(47)	−1.35(57)	−14(10)	−18(12)
3/2	3/2	1/2	−0.92(46)	−0.85(47)	−9.4(9.9)	−8(10)
	3/2	3/2	−0.75(46)	−0.83(48)	−6(10)	−8(10)
	3/2	5/2	−1.14(47)	−1.35(57)	−14(10)	−18(12)

Table 5.2: Trap depth and relative light shift for all MOT cycling transitions of the possible hyperfine sublevels of the $5\mathrm{d}^{10}\,6\mathrm{s}^2\,{}^1\mathrm{S}_0$ ground and $5\mathrm{d}^{10}\,6\mathrm{s}\,6\mathrm{p}\,{}^3\mathrm{P}_1$ excited state at $\lambda = 1064\,\mathrm{nm}$. The trap depth is given in $k_B \times \mathrm{mK}$ at a peak intensity of $I = 100\,\mathrm{mW}/\mathrm{\mu m}^2$ for π- and $\sigma^\pm$-polarized light, respectively. The ground state shift is $U_{\mathrm{dip},\lvert g\rangle} = (-0.470(146))\,k_B \times \mathrm{mK}$ for all configurations due to the vanishing vector and tensor polarizabilities, see table 5.1.

resonance ω_0 as

$$\Delta \quad \longrightarrow \quad \Delta - \Delta_{\mathrm{dip}} = \Delta - \frac{U_{\mathrm{dip},\lvert e\rangle} - U_{\mathrm{dip},\lvert g\rangle}}{\hbar} \,. \tag{5.10}$$

This can result in a reduction of the MOT cooling efficiency and an increase of the MOT size if Δ_{dip} is positive, but more drastically to a blue-detuned MOT $\Delta - \Delta_{\mathrm{dip}} > 0$ and therefore heating of the cloud when $\Delta_{\mathrm{dip}} < \Delta < 0$. This could have a significant impact on the loading of the ODT and alternative loading strategies, such as rapid alternation between MOT cooling and dipole trapping light [192].

As shown in table 5.2 the excited MOT state also experiences an attractive potential, but the trap is about 2 to 2.5 times as deep compared to the ground state and depends slightly on the involved hyperfine state and light field polarization. The resulting relative light shift Δ_{dip} for the intercombination line is therefore predicted to be negative, while the uncertainty allows values close to zero or partially also a blue detuning of the trap. Since the large uncertainties are mainly accounted to the generous assumptions for the unknown transition linewidths, these error bars should be viewed with a grain of salt and are most likely too conservative. Furthermore, note that for the fermions the stable and high atom number MOTs are operated on the $F_{\lvert g\rangle} = 1/2 \rightarrow F_{\lvert e\rangle} = 3/2$ for ^{199}Hg and $F_{\lvert g\rangle} = 3/2 \rightarrow F_{\lvert e\rangle} = 5/2$ for ^{201}Hg, respectively, where the relative light shift is always negative also within their error bars.

We can also observe that the atoms who see the ODT light as a circular polarized light field experience a stronger trapping potential of the excited state and therefore also an increased relative light shift. For a linearly polarized ODT beam in the lab reference frame focussed to the center of the MOT these are mostly the atoms aligned with the ODT beam axis, since here the radially varying gradient field direction aligns the quantization axis with ODT wavevector. For an elongated cigar-shaped trapping volume resulting from a focussed Gaussian beam – as visualized in the master thesis of Sascha Heider [132] – these atoms are also the ones more likely to be trapped. While the ensemble of atoms will experience an averaged polarization and the resulting relative light shift will be spatially dependent and more complicated than this simple picture, we can still conclude, that a negative light shift is more likely and active light shift compensation during loading, as presented in section 5.2.2, to avoid blue detuning of the MOT light is probably advisable.

Trap potential

We consider the spatial intensity profile of a (focussed) Gaussian laser beam,

$$I(r,z) = I_0 \left(\frac{w_0}{w(z)}\right)^2 \exp\left(-\frac{2\,r^2}{w(z)^2}\right), \qquad w(z) = w_0 \sqrt{1 + \left(\frac{z}{z_R}\right)^2}, \tag{5.11}$$

with beam waist w_0 and Rayleigh length $z_R = \pi\, w_0^2/\lambda$. For a single beam trap near the focus, the ODT potential can be approximated as that of a harmonic oscillator,

$$U_{\text{dip}} = \frac{1}{2} m\,\omega_r^2\, r^2 + \frac{1}{2} m\,\omega_z^2\, z^2 - U_0 + \mathfrak{O}(\|\, z/z_R, r/w_0 \,\|^2)\,. \tag{5.12}$$

The radial and longitudinal trap frequencies are given by

$$\omega_r = \sqrt{\frac{4\,U_0}{m\,w_0^2}}, \qquad \omega_z = \sqrt{\frac{2\,U_0}{m\,z_R^2}}\,. \tag{5.13}$$

The peak trap depth U_0 is related to the peak intensity $I_0 = 2\,P_0/(\pi\, w_0^2)$ via equation (5.3), where P_0 is the laser power available at the location of the atoms.

5.2 Dipole trapping of mercury

In the time of writing this thesis, two laser systems for optical dipole trapping of mercury were constructed. The setup of the two systems was supported by the supervised master thesis work of Felix Affeld [91] and Sascha Heider [132], respectively. For more details on optical setups, alignment procedures and optimization, as well as characterization of optical components and laser noise, the reader is directed to their theses.

The first setup based on a 55 W Mephisto MOPA laser system at 1064 nm achieved first signatures of optical dipole trapping of mercury, but was strongly limited in trap depth and trap volume, as well as missing light shift compensation for loading from the MOT. For the second generation system, we upgraded the laser system to 300 W at 1070 nm using an ytterbium fiber laser, which allowed to increase both trap depth and volume. Additional upgrades to the electronic control system, see also section 4.6, including active control over the MOT detuning during ODT loading as well as stabilization and control of the ODT power are tackling the problems of the first generation attempt.

5.2.1 Mephisto MOPA laser setup

A continous-wave Coherent Mephisto MOPA laser at 1064 nm was selected as the base of this setup providing 55 W of peak power within a nicely round ($w_x/w_y < 1.1$) TEM$_{00}$ mode with good beam quality ($M^2 < 1.3$). It features a low relative intensity noise of < -130 dB/Hz at frequencies over 20 kHz with activated noise eater and < -100 dB/Hz without. The laser features a spectral linewidth of < 3 kHz, which while not necessary for dipole trapping, it reduces intensity noise and off-resonant scattering, leading to more stable, low-heating, and coherent atom trapping.

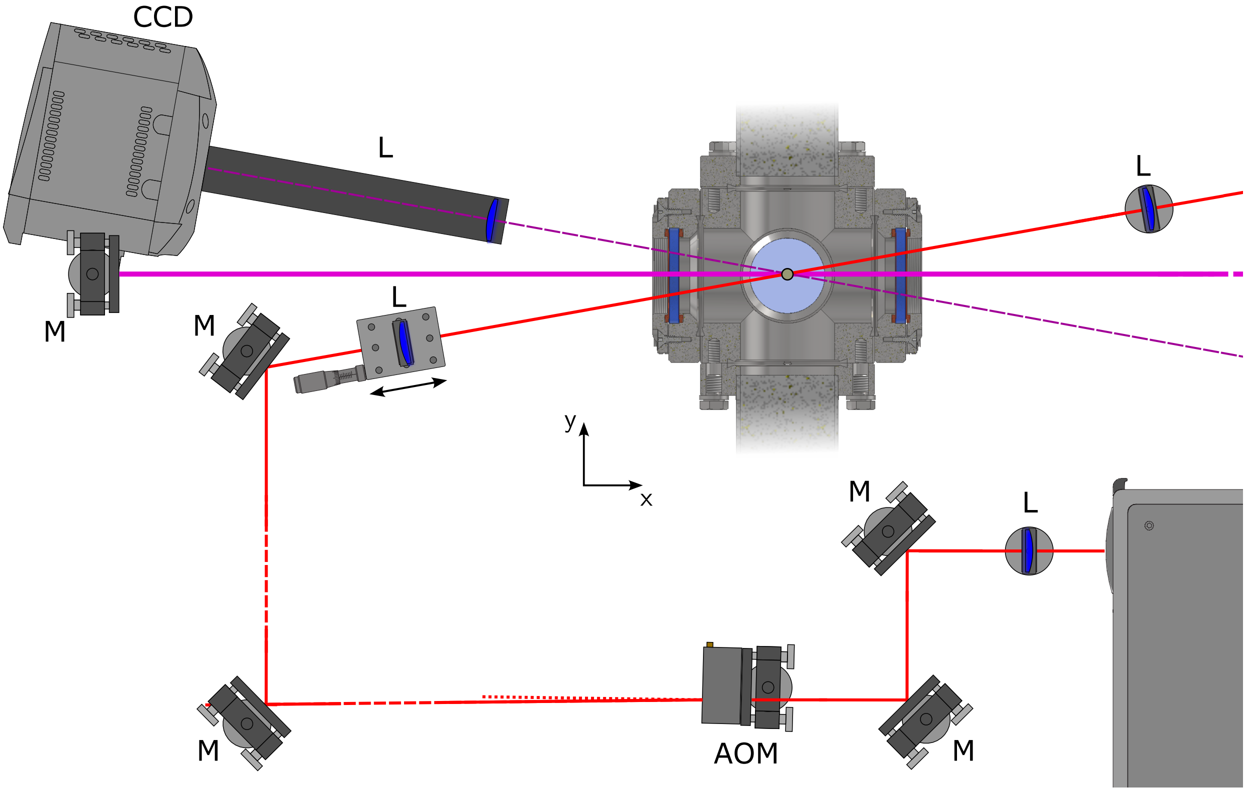

Figure 5.2: Top-down view of the optical dipole trap (ODT) setup based on a 55 W Mephisto MOPA laser system at 1064 nm. A $f = 125\,\mathrm{mm}$ lens (L) focusses the laser output over two adjustment mirrors (M) into the acousto-optic modulator (AOM). After a free expansion of the laser beam the 0th order AOM light is separated and beam dumped using a water cooled beam dump.

Optical setup

The laser output is focused to a beam waist of approximately 250 µm at the input of an acousto-optic modulator (AOM)[1]. The AOM achieves a diffraction efficiency of about 75 %. This results in roughly 37.5 W of power in the first-order diffracted beam. The beam is then expanded over a distance of approximately 2.5 m. After expansion, it is focused into the vacuum chamber using a single lens of variable focal length. The light is focused toward the atoms at an angle of incidence of 12° onto the vacuum chamber viewport. This allows any high-power reflection from the viewport to clear the MOT beam, especially the absorption and fluorescence imaging optics around the chamber. All ODT optics are selected based on their performance in high-power/high-intensity applications, which reduces the amount of absorbed and scattered light.[2] A sketch of the optical setup is shown in figure 5.2. More information on the optical setup, its characterization and optimization can be found in the thesis of Felix Affeld [91]. Multiple optomechanics (articulating AOM mount, periscope, beam alignment targets, …), as well as the (water cooled) beam dumps for trapping the high power ODT light for laser safety and to avoid any stray light reflections for imaging purposes were designed or adapted within this thesis.

One limiting optical component of the presented setup was the vacuum viewports of the chamber

---

[1] G&H 3080. [2] Mirrors: Thorlabs NB1-K14 with ≈ 99.94 % reflectivity and 20 kW/cm damage threshold; Lenses: Newport SPX___AR.1 high-purity fused silica series with reflectivity < 0.25 % at 1064 nm.

in this configuration, which were not originally planned for optical dipole trapping. Although they are anti-reflection coated for the deep UV, their transmission is measured to be just about 80 % [91] at the ODT wavelength. This limits the available power at the location of the atoms to about 30 W. See sections 3.2.2 and 5.2.2 for details and upgrades that address these issues.

Trap depth & geometry

As summarized in table 5.2, we need an intensity of about $100\,\mathrm{mW/\mu m^2}$ to generate a trap with $\eta = |U_{\mathrm{dip}}/(k_B T)| > 2$ for the approximately $T \approx 200\,\mathrm{\mu K}$ cold atoms from the MOT. We expand the ODT beam to 6.3(1) mm and focus it into the chamber using a 250 mm focal length lens. With $P_0 = 30\,\mathrm{W}$ this gives us a theoretical trap depth of $U_0 = -527(165)\,\mathrm{\mu K}$ at a waist of $w_{0x} = 12.9(4)\,\mathrm{\mu m}$ (horizontally) and $w_{0y} = 13.2(2)\,\mathrm{\mu m}$ (vertically). At $\eta = -2.6(8)$ this gives a properly deep trap for the target temperature of the MOT.

Camera-based beam profiling at this waist is not straightforward, and the beam profile data [91] is also compatible with an $M^2 = 1.3$ Gaussian beam, which would result in a trap depth of $U_0 = 311(97)\,\mathrm{\mu K}$ at a slightly larger waist of $w_{0x} = 16.8(5)\,\mathrm{\mu m}$ (horizontally) and $w_{0y} = 17.2(3)\,\mathrm{\mu m}$ (vertically). This just gives us $\eta = 1.6(5)$, which is slightly shallower, but should still allow trapping of at least part of the MOT.

The resulting trap size is still rather small, as also illustrated in figure 5.6. Following equation (5.13), the trap frequencies for this trap geometry are given by $(\omega_x, \omega_y, \omega_z) = 2\pi\times(13.5\,\mathrm{kHz},\ 13.2\,\mathrm{kHz},\ 247\,\mathrm{Hz})$ indicating the weak axial confinement of the ODT. The equipotential surfaces of the trap are represented by a long, narrow, cigar-shaped surface with an aspect ratio of about 1 : 50. This results in a small spatial overlap with the much larger MOT cloud. The main limitation here is the amount of available optical power, where we would prefer a similarly deep trap at larger beam foci and decreased Rayleigh length.

Noise analysis

The laser noise is analyzed via the relative intensity noise spectrum to determine the heating rate of the ODT at the trap frequencies [91]. Using the $w_0 \approx 13\,\mathrm{\mu m}$ beam parameters from above [91] these lie at $\omega_r \approx 2\pi \times 22.8\,\mathrm{kHz}$ radially and $\omega_z = 2\pi \times 420\,\mathrm{Hz}$ longitudinally and the corresponding heating time constants extracted from the power spectral density of relative intensity noise read $\tau_H^{(r)} = 1.1\,\mathrm{s}$ and $\tau_H^{(z)} = 51.2\,\mathrm{s}$, respectively, concluding that laser noise heating is not limiting the trap lifetime [91].

Beam-pointing stability of the ODT beams at higher frequencies can cause fluctuations in the spring constant and trap equilibrium position, which leads to subsequent heating [222]. Choosing stable optomechanics for the beam guiding and alignment mirrors[1], as well as for the periscope and focussing lens mounting (1.5 in diameter pedestal posts) compensate for the relatively long optical beam propagation. Laser beam-pointing noise was analyzed only on larger time scales ($\lesssim 10\,\mathrm{Hz}$) using a charge-coupled device (CCD) camera – limited by the intensity and shutter speed – where no disconcerting pointing instability was found.

---

[1] Newport Suprema SU100-F3K-254, 254 TPI actuators, stainless steel.

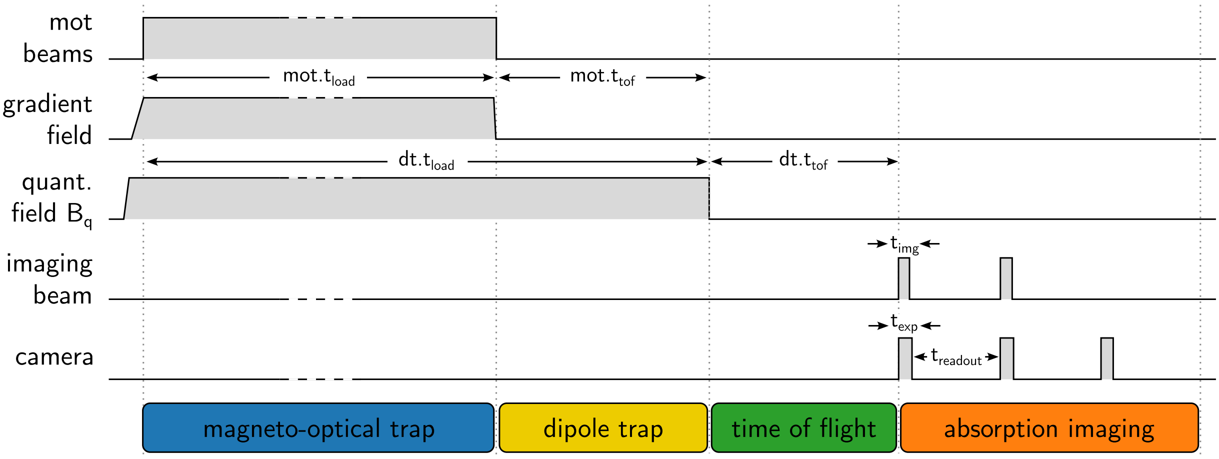

Figure 5.3: Simple experimental optical dipole trap (ODT) sequence. Here, the ODT light is switched on already during the MOT loading phase for a total time `dt.`t_{load}. After loading the MOT for `mot.`t_{load} the ODT light is left on for an additional amount of time `mot.`t_{tof} in which the uncaptured part of the MOT cloud falls freely under gravity. The temperature in the ODT can be characterized by an additional time-of-flight of the ODT atoms, `dt.`t_{tof}. A subsequent absorption imaging sequence, shown here in a simplified form (see section 4.4 for more details), consists of three images: one of the atoms, one of the reference beam, and one of the background. This sequence images the atoms in the ODT and the remaining MOT atoms.

Observation of unstable trapping

For the first loading attempts, a relatively simple control sequence was chosen, as shown in figure 5.3. Here, the ODT light is switched on with the beginning of the MOT loading phase. After loading the MOT the ODT light is left on for a time of flight duration t_{tof}, in which the uncaptured part of the MOT cloud falls freely under gravity. A subsequent absorption imaging sequence, see 4.4, images the atomic density inside the ODT, as well as remaining atoms in the MOT, that did not yet escape the field of view.

First signatures of weak trapping of mercury ^{202}Hg atoms are shown in figure 5.4. Stable trapping over longer time scales is however strongly limited by the weak confinement in the axial direction- The resulting optical density is too weak to be properly detected after a few milliseconds of MOT time of flight (TOF). However, this marks the first trapping of mercury atoms using a single beam ODT. More details on this attempt can be found in reference [91].

We also tested to switch off the gradient field a few ms shortly before the MOT light, as the resulting transition into an optical molasses should create a quasi-thermal distribution, which should make trap loading more insensitive to mechanical misalignments [192]. In this setup so far no significant improvement in the atom density or trap lifetime could be observed. Focussing the trapping light to even smaller foci (e.g., $w_0 \approx 8\,\mu\text{m}$) by replacement of the imaging lens did not provide any observable ODT signature even after extensive alignment. While not being excluded from technical shortcomings, the missing signature of an ODT signal at these trap waists is probably accounted to beam quality and the limited trapping volume compared to the achievable phase space density in the MOT. These observations led to the upgrade of the laser system, as presented in the following section.

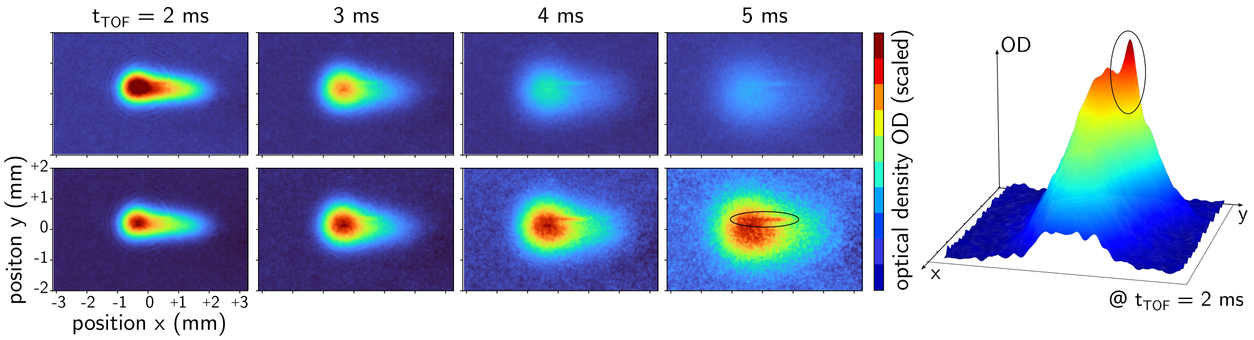

Figure 5.4: First signature of weak mercury optical dipole trapping. After ODT loading from a MOT, atoms are released in a free fall for a time t_{TOF}. The atomic densities are analyzed via absorption imaging following the sequence shown in figure 5.3. While most atoms from the MOT just fall freely and expand, a small cigar-shaped region of increased density (circled region) remains, indicating weak trapping inside the ODT. The top row shows the atomic / optical density using a common color scale, showing the density decrease and atom loss with time, while the lower row scales each image individually to enhance the contrast. Each column corresponds to a separate measurement. The 3d plot to the right shows the atomic density increase at the location of the ODT beam for a different shot with optimized optical alignment at $t_{\mathrm{TOF}} = 2\,\mathrm{ms}$. Data and visualization taken from reference [91].

5.2.2 Ytterbium fiber laser setup

To upgrade the laser power and trap depth, we selected a continuous-wave IPG YLR-300-LP-WC Ytterbium-doped fiber laser at a wavelength of 1070 nm. This system provides up to 300 W of optical power in the form of a collimated Gaussian beam with a diameter of 5.0 mm and a beam quality factor of $M^2 = 1.05(5)$. With upgrades of the vacuum viewports discussed below, this increases the power available at the atoms by a factor of about seven.

The use of a fiber laser with a spectral width of approximately 3 nm can adversely affect evaporative cooling, as demonstrated in experiments with rubidium [223]. In particular, the longitudinal multimode structure of such lasers can induce off-resonant excitation to weakly trapped hyperfine states. Although the dominant loss mechanism typically arises from the formation of ground-state molecules that are no longer confined by the trap, these additional losses due to spectral impurity can further reduce cooling efficiency and limit the final phase-space density. Achieving evaporation to degeneracy in all-fiber laser setups is still possible using e.g., fast evaporation ramps [223–225]. Successful evaporation to degeneracy could also be achieved in other species, such as sodium [226] and strontium [227], among others.

Optical setup

The optical setup presented here was supported in its construction by Sascha Heider during his supervised master's thesis work [132]. A sketch of the setup is shown in figure 5.5. The ytterbium fiber laser output is sent through a $\lambda/2$ zero-order waveplate and high power polarization beam splitter (PBS) cube[1]. This allows to coarsely adjust the laser power during alignment and improve the polarization extinction of the laser. The PBS is mounted such that it transmits a beam vertically polarized with

---

[1] Thorlabs PBS25-1064-HP.

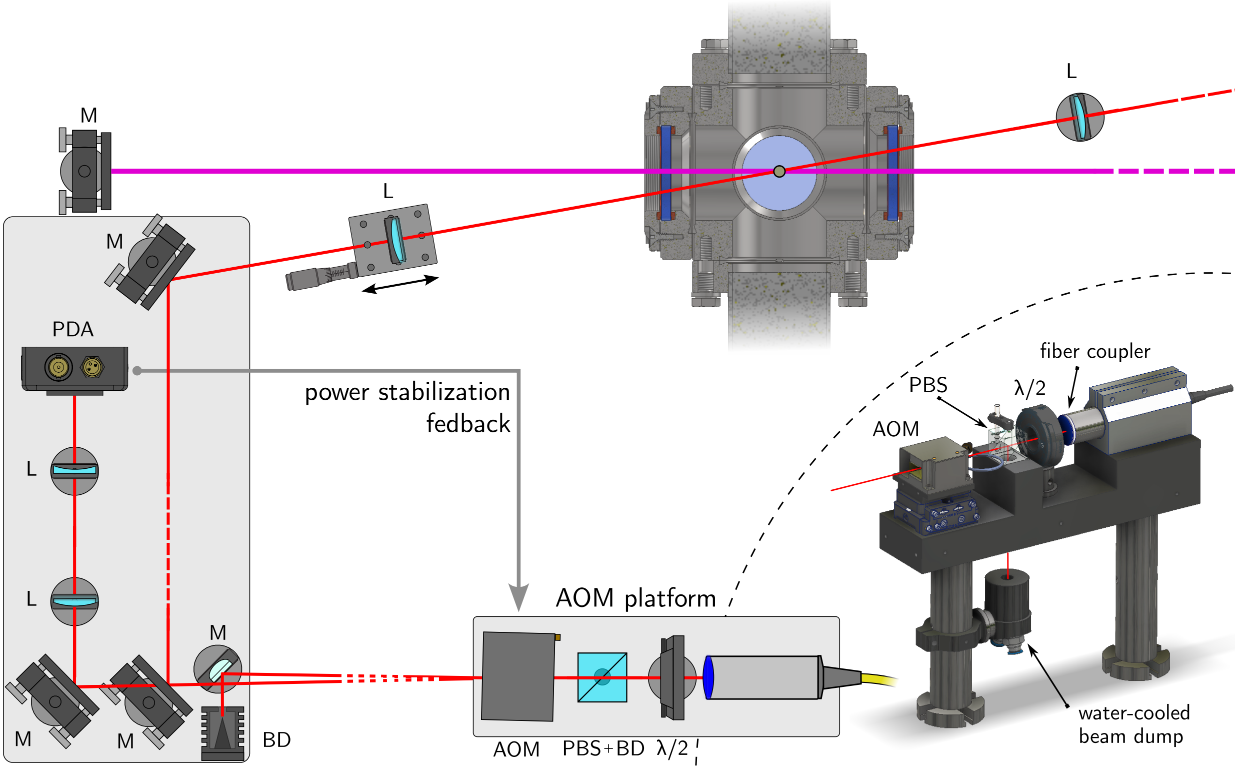

Figure 5.5: Optical dipole trap (ODT) setup based on a 300 W ytterbium fiber laser at 1070 nm. The fiber collimator is mounted rigidly on a platform (see bottom right inset) also housing a $\lambda/2$ waveplate, polarization beam splitter (PBS) and beam dump (BD) for manual power regulation during alignment, as well as an acousto-optic modulator (AOM) for digital power control including stabilization and switching. The zeroth order AOM light is dumped using a pickup mirror (M) into a water cooled beam dump. Power monitoring and stabilization is done by focussing the ODT light leaking through the first alignment mirror via a two-lens (L) telescope onto an amplified photodiode (PDA). The ODT light is focussed onto the atoms using a single lens setup mounted on a translation platform for focus adjustment. It is recollimated behind the chamber and beam dumped, as also any reflections from the vacuum viewports, that need to clear the magneto-optical beam path (violet) and the imaging optics (not shown, see figure 5.2).

respect to the optical table. The unused power is dumped into a custom high-power compatible beam dump mounted vertically below the platform. The number of optics is minimized to avoid reflections from additional optics.

To furthermore reduce the optical intensity and thermal lensing effects, also on the following optics, we select an AOM[1] featuring an about 10 mm diameter aperture quartz crystal. This allows transmission of the 5 mm diameter fiber coupler output without the need for additional lenses for focussing. To avoid incoupling optics, the AOM is mounted to a compact five-axis alignment stage[2]. The AOMs acoustic transducer setup is only designed for a beam diameter of 4 mm, which leads to a slightly elliptical first order beam ($w_{0,\updownarrow}/w_{0,\leftrightarrow} = 0.664(4)$) and limits the diffraction efficiency to about 74(3) %. This reduces the final trap depth along the direction of gravity, but future integration of a short telescope in front of the AOM is possible [132].

With the AOM requiring about 20 W of radio frequency (RF) power, a compact active water cooling

---

[1] Gooch & Housego I-M080-4C10G-4-GH60. [2] Thorlabs PY005/M.

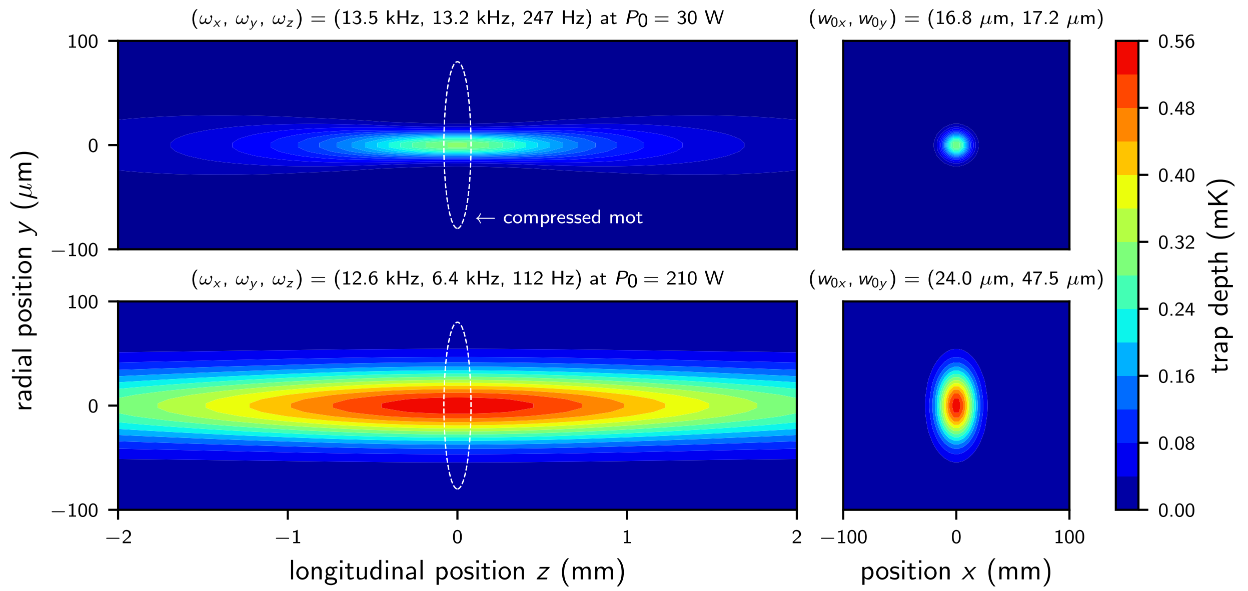

Figure 5.6: Comparison of the dipole trap potential between the old (top) and new (bottom) laser setup. The density plot shows the estimated dipole potential trap depth along all three beam axes. The cigar-shaped trapping volume depends on the beam waists w_{0x} along the horizontal and w_{0y} along the vertical axis, as well as the associated Rayleigh lengths $z_{Ri} = \pi\, w_{0i}^2\, M_i^2/\lambda$ $(i = x, y)$, with M_i^2 the beam quality factor (top: $M^2 \approx 1.3$, bottom: $(M_x^2, M_y^2) = (1.21, 1.36)$), as experimentally measured. The ellipse (dashed, white) indicates the MOT size of $\sigma \approx 80\,\mu\text{m}$, that can be reached after compression.

block was designed and retrofitted between AOM and stage. The AOM temperature is being actively monitored by the lab environmental surveillance system. After ~ 1.5 m of free propagation the zeroth order light (10.5 W to 300 W depending on the fiber laser amplifier current) is beam dumped, while the first order is steered towards the atoms using two high reflectivity mirrors[1] in fine-pitch high-stable adjustable mirror mounts.

A linear translation stage holding a $f = 150$ mm lens allows for focus adjustment of the ODT beam. First order light leaking through the first adjustment mirror is imaged onto an amplified photodiode, that allows to control and stabilize the trap depth via the FPGA-based ARTIQ SuServo proportional-integral-differential (PID) control loop.

All ODT optics are housed in aluminum enclosures around two rigid breadboard platforms at chamber height interconnected by protective lens tubes for laser safety reasons. See [132] for more details on noise analysis and the stabilization setup.

Trap depth & geometry

With upgrade of the vacuum viewports to broadband transmissive, nanostructured UV fused silica substrates featuring a reflectivity of just 0.38(13) % at 1070 nm, see section 3.2.2, the available power at the atoms increases to $P_0 \approx 210$ W. Using a 150 mm focal length lens for focussing, the potential depth with $\eta = 5.1$ can be doubled compared to the previous setup. At the same time, the trap volume is increased by a factor of 13 to a waist of $w_{0x} = 20.2(1)\,\mu\text{m}$, $w_{0y} = 31.5(1)\,\mu\text{m}$ along the horizontal and vertical axes, respectively. The resulting geometry of the dipole trap potential and the associated

---

[1] Thorlabs UM10-Y1HP picosecond Yb laser line mirror featuring a 99.9993 % reflectivity for the s-polarized light at 1070 nm.

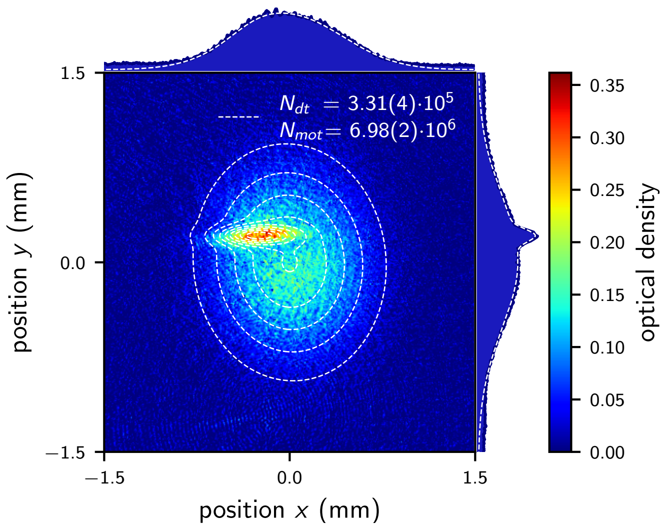

Figure 5.7: First stable optical dipole trapping of ^{202}Hg using the upgraded laser system. The MOT loads about 6.5×10^6 atoms, from which about 3.3×10^5 atoms can be transferred to the single beam ODT. The ODT is continuously operated at full power during MOT loading – about 210 W at the locations of the atoms – and the optical density is extracted from an absorption imaging pulse in free fall after a short time of flight of the MOT cloud, as shown in figure 5.3. A fit of two two-dimensional Gaussian profiles (white, dashed) to the optical density of the free-falling expanded MOT cloud and the dipole trapped allows estimation of the loading efficiency $N_{\mathrm{ODT}}/(N_{\mathrm{MOT}} + N_{\mathrm{ODT}}) \approx 4.57(5)\,\%$. The side plots show the integrated optical density.

trapping frequencies are shown in figure 5.6, indicating the massive increase in trap size and depth.

Preliminary results

Preliminary results[1] for successful optical dipole trapping are shown in figure 5.7. At the time of writing, about 3×10^5 mercury ^{202}Hg atoms can be transferred to the single beam ODT, as confirmed by absorption imaging. The loading process was characterized by a measured efficiency of approximately 5 %, defined as the ratio of atoms transferred from the MOT into the ODT. The successful transfer confirms that the trap depth and beam parameters of the ODT are sufficient to hold a sizable population of atoms, and that the overlap with the MOT region is adequately aligned to enable capture. The capture of a non-negligible fraction of the initial atomic ensemble in the ODT marks a significant step toward efficient optical trapping of more dense atomic clouds and demonstrates the viability of the current setup for further evaporative cooling.

5.3 Outlook

In the next step we will improve the loading efficiency. Here, better spatial and temporal overlap between the ODT and the MOT cloud can be achieved through more precise optical alignment. Plans to upgrade the two ODT incoupling mirrors and the linear translation stage by a piezo drive could provide computer-controlled optimization strategies. Furthermore, enhancements in the phase-space density of the atomic sample by means of improved cooling strategies, as outlined in chapter 4

---

[1] Thanks to Sascha Heider for taking over the operation of the lab and for providing these nice first results.

of this thesis, will provide better loading efficiency and higher atom numbers. Optimization of the freshly implemented MOT compression phase and resumed analysis of additional optical molasses phases for improved cooling are already on the way.

We will soon test ODT loading of fermionic mercury isotopes. They are of particular interest for future EDM measurements due to their sensitivity to symmetry-violating interactions, as discussed in chapter 7. Conveniently, these isotopes also feature sub-Doppler cooling mechanisms, which lead to a significant reduction in temperature and a corresponding increase in phase-space density. These properties make them ideal for more efficient trapping and following precision measurements within the ODT.

5.3.1 Crossed dipole trap setup

The next step is to extend the single beam ODT to a crossed beam configuration for increasing overall trap depth and atomic confinement in the longitudinal direction. The proposed setup is shown in figure 5.8. Behind the chamber, the horizontal ODT beam is re-collimated by a lens and corrected for its distance to the chamber by a three mirror periscope, that preserves its linear polarization. A vertical breadboard enables recycling of the beam for a crossed ODT configuration, with the second beam entering from above. An additional water-cooled, high-power AOM controls the intensity and trap depth of the vertical ODT beam and allows for motional excitations, as discussed below. A single lens with variable focus position sends the light towards the atoms under a slight angle with respect to the vertical (12°). At the time of writing, the setup is still under construction.

A crossed ODT setup also allows for an overall increase in trap size by especially improving the so far weak longitudinal confinement, which is currently limited by small beam waists and the resultingly large Rayleigh length. We estimate, that by switching to a $f = 200\,\mathrm{mm}$ focussing lens for both beams we relax the beam waist to about $w_{0x} = 63\,\mu\mathrm{m}$ and $w_{0y} = 32\,\mu\mathrm{m}$, while keeping the overall trap depth the same.[1]

The broad laser linewidth of the Yb fiber laser comes as an advantage, as – limited by the coherence length of $l_{\mathrm{coh}} = c/(\pi\,\delta\nu) = \lambda^2/(\pi\,\delta\lambda) \approx 121\,\mathrm{mm}$ – little to no interference is expected between the two crossed ODT beams, even without additional polarization or frequency control of the vertical beam. This potentially prohibits advanced polarization gradient based cooling strategies, but leads to a simpler trap potential.

5.3.2 Degenerate quantum gases of mercury

Quantum-degenerate gases of mercury could lead to the the creation of the heaviest BECs and Fermi gases studied to date. Mercury's rich atomic structure and the availability of multiple isotopes make it an incredibly versatile platform for fundamental research and precision measurements, with the potential to significantly enhance sensitivity.

Fermi gases of mercury are also interesting as quantum simulators of solid-state physics effects. They are a promising choice to study Friedel oscillations of the Fermi sea [210, 211], where the deep-UV imaging transition at 185 nm can be utilized to resolve spatial features in the order of the Fermi wavelength (see our proposal in reference [228]). The large selection of naturally abundant isotopes

---

[1] This takes into account the ~30 % reflection loss expected from the top viewports, that we were not able to upgrade to nanostructured windows, due to a faulty delivery of the manufacturer.

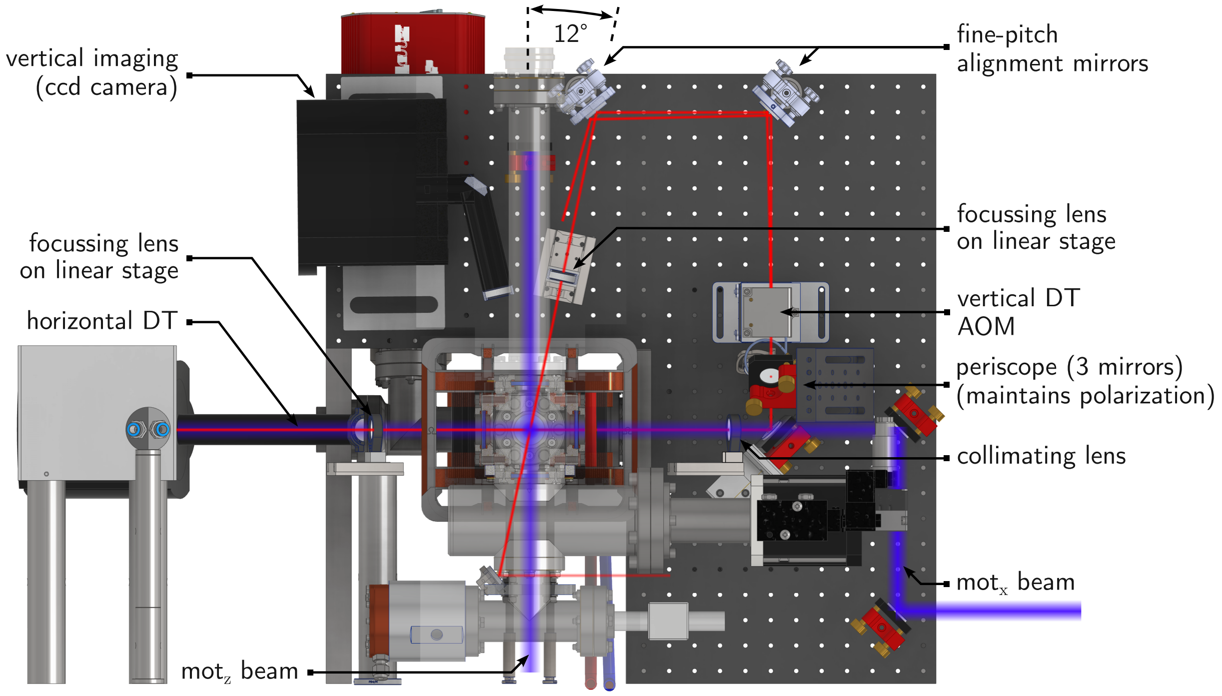

Figure 5.8: Crossed optical dipole trap setup being under construction. See the main text for a description.

should allow restricting the setup to intraspecies impurity-bath coupling without introducing other atomic elements, and to find an ideal combination of a fermionic bath and a bosonic impurity with good scattering properties.

Scattering lengths are essential in ultracold atomic gases because they determine the strength of interparticle interactions, which drive key phenomena such as thermalization, condensation, and superfluidity. Tuning the scattering length via optical or magnetic Feshbach resonances provides access to the strongly interacting regime and facilitates exploration of the BEC-BCS crossover. Magnetic Feshbach resonances usually require the application of magnetic fields to adjust the interaction strength. However, for mercury, the absence of magnetic trapping and the lack of a magnetic Feshbach resonance enhancement in the ground state make this approach unfeasible. Instead, optical Feshbach resonances, which use light to manipulate the interaction strength, offer an alternative way to tune the scattering length. Despite the absence of magnetic effects, these optical methods can still provide significant control over the interactions.

The outlook to degenerate quantum gases of mercury, their scattering and thermalization properties and their use for studying Friedel oscillations in mercury will be discussed below in more detail.

Mass scaling of scattering lengths

Cross-thermalization measurements provide access only to the absolute value of the scattering length, leaving its sign undetermined. Therefore, complementary theoretical models like the mass scaling relation [229] are a good way to gain a complete understanding of scattering properties across isotopes.

For alkaline-earth-like atoms with multiple stable isotopes, such as calcium, strontium, and ytterbium, the dependence of the scattering length a on the isotopic mass aligns along distinct branches

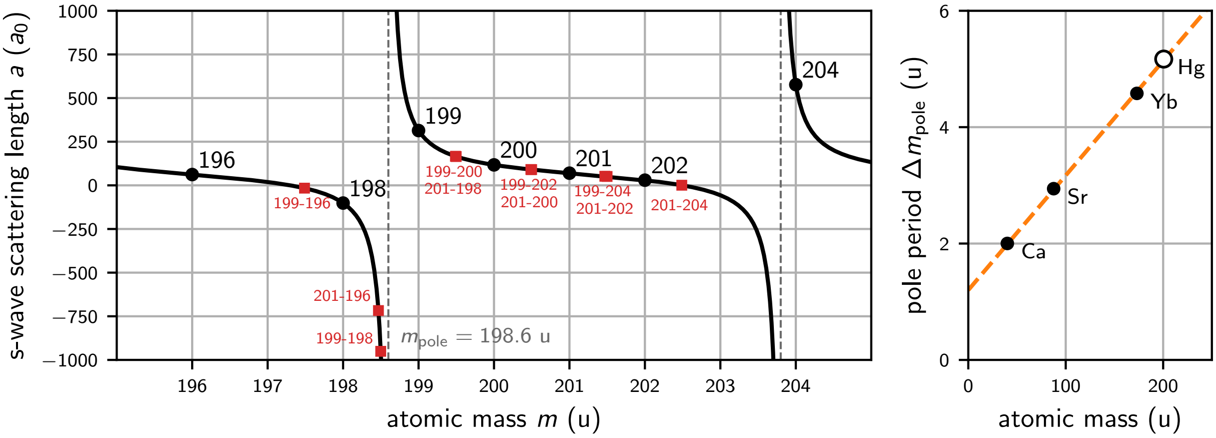

Figure 5.9: Mass scaling of s-wave scattering lengths for all naturally abundant mercury isotopes (black dots), assuming a pole at $m_{\mathrm{pole}} = 198.6\,\mathrm{u}$ with a $\Delta m_{\mathrm{pole}} = 5.2\,\mathrm{u}$ periodicity. Red squares show interisotope scattering lengths between fermionic (^{199}Hg, ^{201}Hg) and bosonic isotopes, highlighting possible impurity-bath physics interactions. Though the positions of the tangent branches cannot be predicted, the dashed orange line (right) suggests a periodicity of about $\Delta m_{\mathrm{pole}} \approx 5.2\,\mathrm{u}$ by following the scaling of the branch widths for Ca, Sr, and Yb.

of a tangent-like curve [229]. The scattering length can be written as

$$a(\mu) = \bar{a}(\mu)\left[1 - \tan\left(\phi(\mu) - \frac{\pi}{8}\right)\right] , \tag{5.14}$$

Here, $\bar{a}(\mu)$ represents the mean scattering length scale and $\phi(\mu)$ denotes the accumulated scattering phase dependent on the reduced mass $\mu = 1/(1/m_A + 1/m_{A'})$ of the two scattering partners [230]. For intraspecies and intraisotope scattering, where the two scattering partners have mass m, we can replace $2\,\mu \to m$. Figure 2.4 in reference [231] and figure 4 in Borkowski et al. [230] are illustrative examples of this scaling law. They demonstrate excellent agreement with experimental data and capture the full variation of scattering lengths across multiple isotopes for strontium and a composite system of ytterbium and rubidium, respectively.

If the scattering is dominated by the van der Waals $-C_6/r^6$ term, the associated scattering length scale is given by $\bar{a}(\mu) = 2^{-3/2}\,(\Gamma(3/4)/\Gamma(5/4))\,\left(2\,\mu\,C_6/\hbar^2\right)^{1/4}$ [230]. The Van der Waals coefficient for the mercury dimer, $C_6 = 392(4)\,E_h\,a_0^6$, was determined in reference [130], where E_h denotes the Hartree energy and a_0 the Bohr radius. From this, we obtain the scattering length offset in equation (5.14) to $\bar{a} = 62.2(4)\,\mathrm{a}_0$. Once the scattering length for a single isotope is experimentally measured, the scattering lengths of all remaining isotopes can be reliably predicted using this scaling.

In figure 5.9, we present a potential mass-scaling dependence of the scattering length for mercury isotopes. The position of the poles in equation (5.14) is determined by the depth and detailed shape of the molecular interaction potential in the $^1\mathrm{S}_0+^1\mathrm{S}_0$ scattering channel. However, accurately calculating the pole positions from first principles remains challenging due to the complex nature of the molecular potential and the sensitivity to short-range interactions. Since the exact pole positions are currently unknown, this plot serves as a hypothetical illustration based on the general scaling law.

The pole periodicity Δm_{pole} corresponds to the average mass increase required for the molecular ground-state $X\,^1\Sigma_g^+$ potential to support a new bound state. The value for mercury can be determined from the linear extrapolation of pole periodicity data from calcium, strontium, and ytterbium. We find $\Delta m_{\mathrm{pole}} \approx 5.2\,\mathrm{u}$. With the naturally abundant isotopes of mercury spanning 8 u, this ensures the presence of isotopes with large magnitudes and a wide range of scattering cross-sections. We will employ this scaling relation to estimate the feasibility of achieving strong impurity-bath interactions for a selected pair of fermionic and bosonic mercury isotopes discussed below.

Scattering length determination via cross thermalization

Measuring the scattering length via cross-thermalization – observing how two species equilibrate through collisions – provides a sensitive, indirect probe of the interaction strength. This is particularly crucial for mercury because the scattering lengths are unknown, and direct measurements are challenging. Nevertheless, as discussed below, due to the large number of isotopes, we expect a high likelihood of finding sufficiently large scattering lengths for thermalization in at least a few of the naturally abundant mercury isotopes.

In the crossed ODT setup, AOM control of the vertical beam power allows for motional excitation of the atomic cloud along the horizontal direction. By probing the temperature in the vertical direction in TOF, this cross-thermalization measurement scheme enables determination of the s-wave scattering length, as demonstrated in reference [232]. In the regime of small excitations, cross-dimensional thermalization results in exponential decay of temperature in the orthogonal direction with a characteristic time constant, $\tau = \alpha/(\bar{n}\,\sigma_S\,\langle \mathrm{v}\rangle_{\mathrm{th}})$, related to the total elastic scattering cross-section σ_S. Here, $\bar{n}$ is the mean number density of the cloud, $\langle \mathrm{v}\rangle_{\mathrm{th}}$ the average relative thermal velocity at the given temperature T. The number of collisions per rethermalization α can be obtained from Enskog kinetic theory in the limit of short times and small excitations [232]. Similar to our use in section 3.1.3 (page 30) for the estimate of the mean free path, the mean scattering cross-section σ_S can be directly related to the s-wave scattering length a, when taking into account other contributions, such as dipole-dipole interaction [232].

Evaporative cooling

For evaporative cooling we plan using exponential ramps in trap depth for evaporative cooling. We simulate atom temperatures and phase space density and optimize evaporation ramps via a kinetic numerical model based on the work in reference [233]. Even at the given vacuum background pressure, thermalization rates are expected to dominate the heating mechanism originating in atomic collisions with background gas particles and off-resonant ODT light scattering. We estimate that cooling to quantum degeneracy might be feasible in the crossed ODT setup, even in the background gas loaded vacuum chamber. The evaporation process will however strongly benefit from upgrading to a differentially pumped vacuum system, as presented in section 7.3.1. By installing a collimated atomic beam source (see section 3.1.3) combined with a Zeeman slower (ZS) (see section 4.8.3), we expect to not only increase atom numbers, but also reduce background collision induced atom loss. The latter will increase both atomic lifetimes and the expected evaporation efficiency. All of this should allow us to reach the critical phase space density necessary to form a condensate.

5.3.3 Studying impurity physics in Fermi gases of mercury

Ultracold atoms offer a clean and highly controllable platform for exploring impurity-bath physics, providing advantages over traditional solid-state systems. Although phenomena like bath-mediated bipolaron interactions and Friedel oscillations have been extensively discussed in condensed matter physics, they have yet to be realized in cold-atom experiments. The controlled observation of Friedel oscillations could help investigate the interaction between a single impurity and a bath on a fundamental level and provide insight into bath-mediated impurity-impurity interactions.

Friedel oscillations are periodic, spatial variations in the (electron) density of a Fermi gas resulting from quantum interference effects between the Fermi bath and impurities, like edges or point-like defects. These density modulations appear on length scales in the order of the Fermi wavelength λ_F, and they show a strong dimensionality dependence. Given an unperturbed Fermi sea density $n_0(r)$, the density perturbation $\delta n(r)$ induced by a single impurity located at $r = 0$ is given by

$$n(r) = n_0(r) + \delta n(r) = n_0(r) + C\,\frac{\sin\left(2\,k_F\,r + \varphi\right)}{r^D}\,. \tag{5.15}$$

Here, D denotes the dimensionality of the system, $k_F = 2\pi/\lambda_F$ is the Fermi wave vector and r is the radial distance from the impurity [234]. The amplitude C and the phase factor φ depend on the interaction strength between impurity and bath and are generally dimensionality dependent.

Friedel oscillations have been observed in two-dimensional electron gases of solid-state materials via scanning tunneling microscopy (STM). Experiments have focused especially on face-centered cubic (111) crystal surfaces of gold and silver, and the first measurements were made in copper [235]. This technique provides information about the Fermi surface, the band structure, and the coupling to impurities. However, it also limits investigations to time-independent observations. This restricts the study of temporal dynamics, including the emergence and propagation of impurity bath coupling. All dynamics take place on timescales much shorter than the typical duration of a STM scan. Additionally, impurities cannot be switched on or off dynamically.

Friedel oscillations in ultracold atomic Fermi gases

Compared to traditional solid-state systems, ultracold atomic gases provide a cleaner and more highly controllable platform for studying Friedel oscillations. Analysis of solid-state materials is often restricted to low-dimensional regimes, such as two-dimensional electron gases at surfaces or interfaces, constrained by the material's structure and geometry. In contrast, ultracold atoms can be precisely manipulated to create a variety of dimensional systems, ranging from one to three dimensions, through engineered trap potentials. This offers a much broader scope for exploring fundamental many-body phenomena. To date, Friedel oscillations have not been observed in ultracold atomic systems, and detecting them remains an open experimental challenge.

We envision probing Friedel oscillations in two-dimensional quantum degenerate Fermi gases of heavy mercury isotopes (^{199}Hg or ^{201}Hg). Individual bosonic mercury atoms can be used as tunable, localized scatterers whose potential strength and position are highly controllable. Here, mercury offers a wide range of both bosonic and fermionic isotopes, highly isotope-selective transitions for addressing and trapping, a clock transition suitable for detecting small energy shifts, and broad UV

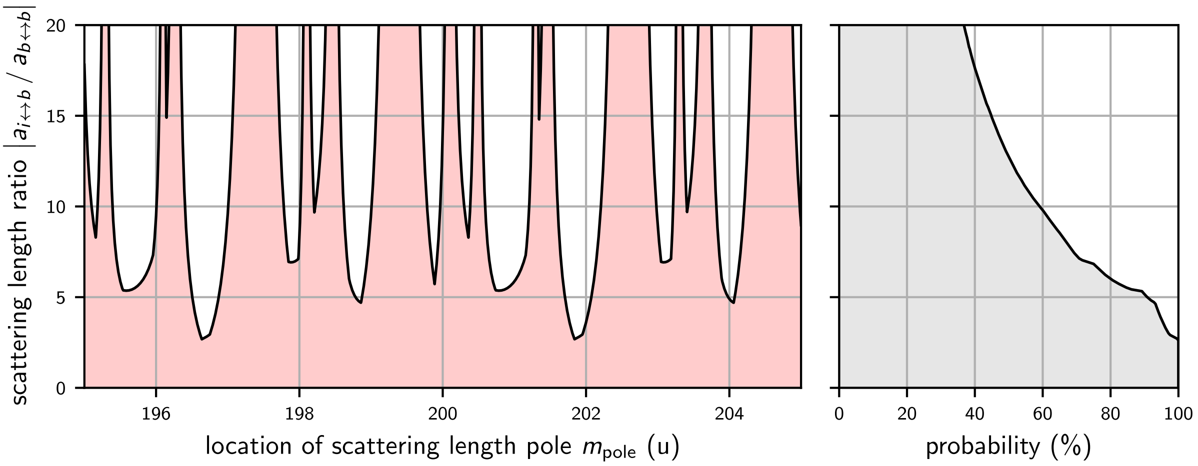

Figure 5.10: Impurity-bath to bath-bath s-wave scattering length ratio as a function of the location of the (yet unknown) scattering length pole m_{pole} (left) and the probability to find a specific ratio for all possible locations of the pole (right).

transitions that support high-resolution imaging.

A feasibility study performed in the group of H. Moritz (Hamburg) [211, 236] considered the detection of Friedel oscillations in one-dimensional tubes of lithium atoms. They found that an impurity with a size comparable to the Fermi wavelength and interaction strength near $2\,E_F$ can induce density modulations of around 10 %. While finite temperature reduces contrast – from 15 % at zero temperature to 10 % at $T/T_F = 0.1$ and 3 % at $T/T_F = 0.2$ – these values remain within detectable ranges under realistic conditions. The algebraic decay of the oscillations $\propto r^{-D}$ suggests an advantage in low-dimensional systems.

Impurity-bath interaction strength To estimate the feasibility of observing Friedel oscillations in ultracold quantum gases of mercury, we analyze the interisotope impurity-to-bath scattering length $a_{i\leftrightarrow b}$ and compare it to the intraspecies bath-to-bath scattering length $a_{b\leftrightarrow b}$. The ratio of the two scattering lengths gives us a measure for the relative interaction strength of the impurity-bath coupling and the potential magnitude of Friedel oscillations. As the location of the pole m_{pole} in the mass tuning dependency of scattering lengths is still unknown, we calculate the theoretical interaction strengths of impurity-bath and bath-bath coupling for varying pole positions. The ratio between the strongest impurity-bath and associated impurity-impurity scattering length $|a_{i\leftrightarrow b}/a_{b\leftrightarrow b}|$ is shown in figure 5.10.

From this calculation, we estimate the likelihood of finding a combination of a fermionic isotope (^{199}Hg or ^{201}Hg) forming the bath and a bosonic impurity that give a specific interaction strength ratio. The minimum achievable scattering wavelength ratio is always greater than 2.6, regardless of the pole's location. The probability of finding 10-times stronger impurity-bath than bath-bath interaction is about 60 %.

We ideally require $E_{\text{Friedel}}/E_F \gtrsim 1$, which requires large and ideally tunable impurity-bath scattering rates and strong two-dimensional trap confinement. Following the numerical modeling in reference [236], for realistic trap geometries, atom numbers and temperatures, we estimate that, for strong impurity-bath interaction and a good signal-to-noise ratio for observing Friedel oscillations, $a_{i\leftrightarrow b}$ is ideally as large as $1000\,a_0$.

To further control the impurity-bath interaction, two complementary approaches could be explored: optical Feshbach resonances with the impurity in the $^1\mathrm{S}_0$ ground state, or magnetic Feshbach resonances when it is excited to the long-lived $^3\mathrm{P}_2$ state. This may also permit dynamic tuning of interaction strength, which could allow time-resolved studies looking at emergence and propagation of impurities.

Experimental realization A potential future measurement of Friedel oscillations in ultracold mercury could involve loading the Fermi gas into a two-dimensional "pancake" trap. This trap geometry can be created by a vertical one-dimensional optical lattice at a magic wavelength of around 360 nm – as discussed above. A possible trap configuration could be realized by a 1 W of 360 nm light provided by e.g., a frequency-doubled Ti:Sapphire laser and focused to a waist of 50 µm. Under such conditions, the expected vertical trapping frequency would be $\omega_z \approx 33\,\mathrm{kHz}$ (harmonic oscillator length $a_z \approx 40\,\mathrm{nm}$), with radial trapping frequencies around $\omega_r \approx 57\,\mathrm{Hz}$, thereby realizing a regime close to a truly two-dimensional system.

A key experimental parameter and challenge is the density n of the Fermi gas, since the oscillation period $\lambda_F/2$ is comparable to the interparticle spacing. For typical atomic densities around $n_0 \approx 1 \times 10^{12}\,\mathrm{cm}^{-3}$, the spacing between oscillation peaks is smaller than about 0.5 µm, which necessitates high-resolution imaging. For realistic atom numbers and the trap geometry given above, the corresponding Fermi temperature would be $T_F \approx 1\,\mu\mathrm{K}$. In such a regime, the Fermi wavelength is estimated to be $\lambda_F = 2\pi/k_F \approx 200\,\mathrm{nm}$. This motivates working at low densities to keep λ_F large, but also introduces detection challenges such as increased atom shot noise.

This experiment must operate at extremely low atom densities and with excellent signal-to-noise ratios. Mercury's optical transitions in the deep-UV are highly promising for achieving the very high spatial resolution required for this experiment. When combined with a high numerical aperture objective (made of e.g., CaF_2 or MgF_2), the $^1\mathrm{S}_0 \rightarrow {}^1\mathrm{P}_1$ singlet transition at 185 nm offers a broad linewidth of and high photon scattering rates, making it well-suited for this application. The high scattering rates could even enable time-resolved studies of the system's dynamics. Development of a suitable laser source for this wavelength is underway as part of the "UVQuanT" ERC project, as already discussed in section 4.8.2. If a degeneracy parameter near $T/T_F = 0.1$ can be achieved – as demonstrated in similar experiments with Sr and Yb atoms – this would provide an excellent starting point for exploring many-body physics in 2D.

An indirect approach to observing Friedel oscillations could involve detecting bath-mediated spatial correlations between multiple impurity atoms. For this a few unconfined bosonic impurities can be co-trapped and cooled with the Fermi gas, as indicated in figure 5.11. If impurity-bath interactions dominate over direct impurity-impurity interactions, similar to the self-organization observed for mobile impurities on solid-state surfaces, spatial ordering could emerge. Analyzed by absorption imaging, correlation functions are then expected to peak at the length of the Fermi wavelength, offering indirect evidence of underlying density modulations.

Outlook Building on these observations, a single bosonic impurity could be confined in an isotope-selective optical tweezer engineered to induce minimal light shifts for the fermionic background. Using AC polarizability and trap depth calculations (presented above), in combination with precision isotope shift spectroscopy (presented in chapter 6), we identify magic wavelengths close to the 266 nm clock transition for selective trapping. A tweezer beam with 10 mW of power focused to a 1 µm waist

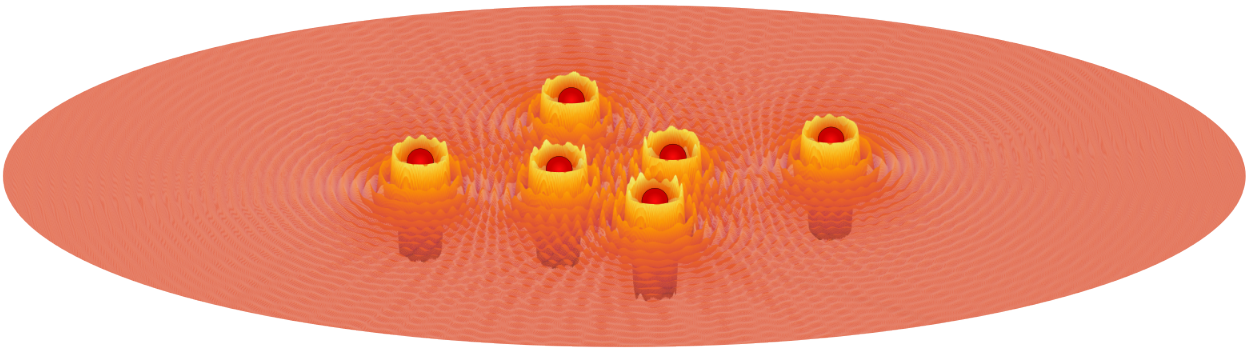

Figure 5.11: Artistic visualization of the simulation of Friedel oscillations in two-dimensional Fermi gases of mercury as induced by a few free bosonic impurities. The bath mediated interaction between the impurities can lead to a re-arrangement of the impurities to distances given by multiples of the Fermi wavelength λ_F.

is estimated to provide a trap depth of approximately $30\,E_{\mathrm{rec}}$ for the bosonic isotope, with negligible off-resonant photon scattering. This would allow precise isotope-selective control over the impurity's position and state, without directly disturbing the Fermi sea. A two-dimensional geometry offers the advantage of radial averaging to improve signal-to-noise despite the faster decay of the oscillations. Together with Feshbach resonance tuning of the scattering lengths, this setup could permit dynamic tuning of interactions and direct imaging of the fermionic response. Given the expected modulation amplitudes of only a few percent, direct in-situ detection via the 185 nm transition may still be challenging and potentially limited by shot noise.

The experimental control provided by optical Feshbach resonances in the cold-atom system allows for the study of nonequilibrium Friedel oscillation dynamics. Suddenly switching on the impurity-bath interaction enables the investigation of the buildup of the Friedel pattern over time. This sudden introduction of a scattering potential leads to a nontrivial dynamical response of the Fermi sea – a process connected to Anderson's infrared catastrophe. In the cold-atom system, optical Feshbach resonances allow one to alter the impurity-bath interaction on a nanosecond timescale. This is much faster than any other timescale of the system, effectively switching the impurity-bath interactions instantaneously. After establishing this protocol, one could also potentially explore the periodic modulation of the interaction strength in order to study driven Friedel oscillations and their behavior under time-dependent perturbations.

6 Isotope shift spectroscopy of laser cooled mercury

6.1 Isotope shifts

The isotope shift (IS) is the small energy shift of electronic levels induced by adding or removing neutrons between isotopes of the same element. Two main effects – the field shift (FS) and mass shift (MS) – contribute to this shift. We denote the IS on an electronic transition i with frequency ν_i between isotope with mass number A and A' as $\delta\nu_i^{A-A'}$. As motivated below, it can be approximated as

$$\delta\nu_i^{A-A'} \equiv \nu_i^{A} - \nu_i^{A'} = F_i\,\delta\big\langle r^2\big\rangle^{A-A'} + K_i\,\mu^{A-A'} + \sum_{\kappa} G_i^{(\kappa)}\,\Lambda_{(\kappa)}^{A-A'}\,, \tag{6.1}$$

where $\delta\big\langle r^2\big\rangle^{A-A'} = \big\langle r^2\big\rangle^{A} - \big\langle r^2\big\rangle^{A'}$ is the difference in nuclear charge radii between the two isotopes and $\mu^{A-A'} = \frac{1}{m_A} - \frac{1}{m_{A'}}$ the inverse nuclear mass difference. The $\Lambda_{(\kappa)}^{A-A'}$ denote higher order (nuclear) corrections and F_i, K_i and $G_i^{(\kappa)}$ are electronic factors that depend on the electronic transition i.

Field shift

The main contribution for the isotope-dependent level shift of electronic transitions in heavy elements like mercury is the FS – also called volume or Coulomb shift. It describes the change in the overlap of the electron wave function $\psi(\vec{r})$ with the nucleus and therefore is a nuclear size effect. As the number of neutrons changes, the size of the nucleus also changes, which in turn affects the spatial probability density of the protons. For spherical nuclei the resulting energy shift of a specific isotope can be approximated to first order as

$$\delta E_{\mathrm{FS}} = |\psi(r=0)|^2\,\frac{\pi\,a_0^3}{Z}\,f(Z)\,\big\langle r^2\big\rangle\,, \quad \text{where} \quad \langle r^2\rangle = \frac{\int \mathrm{d}^3\vec{r}\;\rho(\vec{r})\,r^2}{\int \mathrm{d}^3\vec{r}\;\rho(\vec{r})} \tag{6.2}$$

is the expectation value of the mean square charge radius of the nucleus with respect to its nuclear charge distribution $\rho(\vec{r})$ [69]. The FS between isotope A and A' therefore scales as the change in the difference of the two isotopes squared nuclear charge radii $\delta\,\big\langle r^2\big\rangle^{A-A'} = \big\langle r^2\big\rangle^{A} - \big\langle r^2\big\rangle^{A'}$.

The FS function $f(Z)$ depends on the nuclear charge number Z, the mass number A and a perturbation parameter n and incorporates the distortion of the electron wave function due to a finite-size nucleus ($n > -1$) which weakens the resulting FS compared to a point-like nucleus ($n = -1$). The real nuclear charge distribution is therefore treated as a perturbation of the point-like one $\rho(\vec{r}) \propto Z\,e/r_0^3\,(r/r_0)^{n-2}$ [69]. This simple model was first quantitatively introduced by Racah [237] and Rosenthal and Breit [238] in 1932. Using first isotope shift spectroscopy (ISS) data in mercury, Breit later also pointed out, that transitions involving no valence electrons in an s shell – and therefore no change in the probability density of the transition electron at the nucleus – also experience a FS due to screening effects involving other electrons that contribute to the total electron probability density $|\psi(\vec{r})|^2$. Transitions involving s-electrons are much more sensitive to FS effects.

For the $6s^2\ ^1S_0 \longrightarrow 6s6p\ ^3P_1$ intercombination line in Hg, ab initio (non-relativistic) Hartree-Fock calculations of the electron density at the nucleus [239] allowed first estimation of these screening effects by relating it to the ionic wavefunction, $\delta|\psi(\vec{r}=0)|^2 = |\psi_{6s^2}(0)|^2 - |\psi_{6s6p}(0)|^2 \approx \beta\,|\psi_{6s}(0)|^2$, where ψ_{6s} corresponds to the $^2S_{1/2}$ state of Hg$^+$ [69]. The screening ratio was determined to be $\beta = 0.74(5)$ [69]. With an estimation of $f(Z)$ ($\approx$ 66.1 GHz/fm^2 for Hg [240]) this enabled first explanation of observed ISs by theory and an order of magnitude estimation for other transitions of interest in many other elements. For the intercombination line, the FS is on the order of 5.3 GHz between neighboring pairs of even isotopes in Hg ($A' = A+2$), where the ground state contribution to the FS dominates strongly. Here, the FS in the Hg isotopes varies roughly linearly with mass number, while their MS remains nearly constant [241].

Mass shift

The next contribution to the IS is due to the finite nuclear mass m_A, called the MS, which consists of a normal mass shift (NMS) and specific mass shift (SMS). It originates from the diagonal and off-diagonal terms in the kinetic energy part $\mathcal{T}$ of the Hamiltonian for multielectron systems [242],

$$\mathcal{T} = \frac{\vec{P}^2}{2\,m_A} + \sum_{i=1}^{Z} \frac{\vec{p}_i^{\,2}}{2\,m_e} \xrightarrow[\text{CMS frame}]{} \frac{1}{2\,\mu}\sum_{i=1}^{Z} \vec{p}_i^{\,2} + \frac{1}{2\,m_A}\sum_{i>j} \vec{p}_i \cdot \vec{p}_j + \text{const.}, \tag{6.3}$$

where $\vec{P}$, $\vec{p}_i$ are the momentum operators associated with the nucleus and the individual electrons, respectively. In the stationary atom $\vec{P} + \sum_{i=1}^{Z} \vec{p}_i = 0$, which allows all diagonal terms in electron momentum operators $\vec{p}_i$ to be combined by converting to a description of motion within the center-of-mass (CMS) frame and by introducing the reduced mass $\mu = m_e\, m_A/(m_e + m_A)$ of the electron.

The resulting energy shift of the diagonal terms is the NMS, as also described by the Rydberg formula/Bohr model for hydrogen-like systems. It can be written as a small correction to the transition energy E_{ge}, given by $\delta E_{\text{NMS}} = -m_e/m_A\, E_{ge}$ as extracted by the virial theorem for the electromagnetic potential [242]. The additional off-diagonal electron-electron correlations $\vec{p}_i \cdot \vec{p}_j$ terms ($i \neq j$) add a second shift, called specific mass shift (SMS). This mass-polarization term can be estimated via electron structure calculations, when separating the radial and an angular part by rewriting the momentum operators [242]. Depending on the considered system and electronic levels, it can be as large as the NMS.

While the combined MS scales roughly as $1/m_A^2$ and therefore is strongest in hydrogen/deuterium (~670 GHz on the 1S-2S-transition, shifting the deuterium lines to shorter wavelength) and still dominates the IS for lighter elements like calcium, it is much weaker in heavy elements like mercury. On the $6s^2\ ^1S_0 \longrightarrow 6s6p\ ^3P_1$ intercombination line in Hg, the NMS is on the order of 3.2 GHz, while the SMS is about 14 MHz for ^{202}Hg - ^{200}Hg [69], only about 0.4 % of the NMS. The combined MS between two isotopes A and A' is generally separated into a MS parameter K, that incorporates the electronic level structure, and a nuclear term proportionality $\mu^{A-A'} \equiv \frac{1}{m_A} - \frac{1}{m_{A'}}$, the inverse mass difference, such that we can write $\delta E_{\text{MS}} = K\,\mu^{A-A'}$.

Higher order corrections

Additional higher order and potentially unknown corrections to the IS are incorporated in the electronic transition dependent factors $G_i^{(\kappa)}$ and isotope dependent (nuclear) parameters $\Lambda_{(\kappa)}^{A-A'}$. These corrections originating from atomic and nuclear structure effects are expected to be orders of magnitude smaller than the two leading first order terms and less than a handful of elements could be spectroscopically probed precisely enough to resolve additional terms, as will be discussed below. For heavy elements like mercury, higher order nuclear moment $\delta\left(\langle r^2\rangle^2\right)$ (quadratic FS (QFS)), $\delta\langle r^4\rangle$ (quartic FS), $\delta\langle r\rangle^6$, ... FS contributions are expected to be the next resolvable contributions.

Theory predictions

Resolving higher-order corrections to study nuclear or electronic structures and potential beyond standard model (BSM) interactions is challenging, as predicting nuclear charge radii and electronic factors – even in leading terms – is difficult for multi-nucleon and multi-electron systems, making precise comparison between theory and measurement nearly impossible. As an example, predictions for the FS in neutral Hg from relativistic mean-field theory is so far only precise to hundreds of megahertz [243]. Modern particle-hole configuration interaction algorithms like GRASP ("General-purpose Relativistic Atomic Structure Package") [244] are still mainly limited to few electron systems. Extensions via multiconfiguration Dirac-Fock (MCDF) calculations like FAC ("Flexible Atomic Code") [245] or more efficient configuration-interaction many-body perturbation theory approaches (CI+MBPT) like DIRAC ("program for atomic and molecular Direct Iterative Relativistic All-electron Calculations") [246] or AMBiT [247] can now handle more complex electron-electron correlations. Verifying experimentally measured parameters to better than the percent level is still really challenging and was only achieved in few special cases.

Currently, a more precise estimation of electronic parameters is only possible for highly simplified systems, such as one- or two-valence electron atoms and ions. The most interesting systems for ISS are highly charged ions, particularly heavy ones. Except for very spherical and light nuclei, their nuclear structure is just as complex and similarly hard to predict. Similarly, experimental determination of nuclear structure like more direct measurements of nuclear charge radii [71] still lack the precision when compared to optical measurements [248].

6.1.1 King plot analysis

Two-dimensional King plot

Resolving higher order corrections and studying their origins and isotope dependency can be performed by a King plot (KP) analysis. The "modified" (or "scaled") mass-normalized ISs $\overline{\delta\nu}_i^{A-A'} \equiv \delta\nu_i^{A-A'}/\mu^{A-A'}$ of two electronic transitions, i and j, are plotted against each other. To leading order, this gives a linear relationship,

$$\overline{\delta\nu}_i^{A-A'} = F_{ij}\,\overline{\delta\nu}_j^{A-A'} + K_{ij} + \sum_{\kappa} G_{ij}^{(\kappa)}\,\overline{\Lambda}_{(\kappa)}^{A-A'}. \tag{6.4}$$

Here, F_{ij}, K_{ij} and $G_{ij}^{(\kappa)}$ are again to very good approximation only electronic factors that depend on the two transitions; $F_{ij} = F_i/F_j$ is the FS slope ratio and $K_{ij} = (K_i - K_j\,F_{ij})$ a relative MS that together form the linear dependency between the modified ISs. Higher order correction terms expressed in the FS scaled electronic factor differences $G_{ij}^{(\kappa)} = (G_i^{(\kappa)} - G_j^{(\kappa)}\,F_{ij})$ can introduce a nonlinearity, as long as the (modified) nuclear parameters $\overline{\Lambda}_{(\kappa)}^{A-A'} \equiv \Lambda_{(\kappa)}^{A-A'}/\mu^{A-A'}$ do not align with $\delta\left\langle r^2\right\rangle^{A-A'}$ or the modified ISs itself.

The graphic visualization of $\overline{\delta\nu}_i^{A-A'}$ against $\overline{\delta\nu}_j^{A-A'}$ is called King plot (KP), named after William Henry King, who pioneered its use for extraction and study of electronic and nuclear parameters [69]. Analysis of ISS data via KP analysis is mostly limited to even isotopes only, as hyperfine interactions in non-zero nuclear spin isotopes can lead to very large (GHz-scale) shifts that are hard to predict precisely. In a linear KP, we can use an (orthogonal distance) linear regression analysis to extract the FS and MS ratios, nonlinearity indicates presence of higher order corrections that can be analyzed using the generalized KP analysis described below. The separation of nuclear and electronic factors allow for comparison of vastly different electronic transitions, including comparisons between atoms, ions and highly-charged ions. The latter allow for a wide range of ultra-narrow optical clock transitions to probe – a target of interest evolving in the last few years with the development of ion traps for precision spectroscopy. Less precise, but more common is ISS on highly ionized atoms on transitions in the x-ray regime and muonic atoms and ions [69].

Multi-dimensional King plot

As we eliminated $\delta\left\langle r^2\right\rangle^{A-A'}$ in the two-dimensional KP, in general any additional ISS measurement on an additional line can be used to remove higher order corrections, as long as the number of spectroscopically addressed isotopes n_A is large enough. “Given m transitions, $m-1$ nuclear parameters (including $\delta\langle r^2\rangle^{A-A'}$) can be traded for IS measurements” [249]. The largest dimension for which a KP linearity analysis is reasonable is given by $n_A - 2$, higher dimensional KP are already linear by definition. For $n_A = 5$ natural abundant bosonic Hg isotopes analyzed here, we can therefore absorb the next leading order correction $\Lambda_{(1)}^{A-A'}$ and construct a three-dimensional KP of transitions i, j and k:

$$\overline{\delta\nu}_i^{A-A'} = F_{ijk}\,\overline{\delta\nu}_j^{A-A'} + G_{ijk}^{(1)}\,\overline{\delta\nu}_k^{A-A'} + K_{ijk} + \sum_{\kappa>1} G_{ijk}^{(\kappa)}\,\overline{\Lambda}_{(\kappa)}^{A-A'}\,, \tag{6.5}$$

where the electronic coefficients are given by $G_{ijk} = G_{ik}/G_{jk}$ and $F_{ijk} = F_{ik} - G_{ijk}\,F_{jk}$ and analogously $K_{ijk} = F_{ik} - G_{ijk}\,F_{jk}$. While there is no control in selecting the nonlinearity to absorb, this technique gives information on the number of nonlinearity sources and can be used for further analysis allowing resolution of additional contributions and stricter bounds on new physics (NP) couplings.

Nonlinearity decomposition analysis

To determine the origin of higher order corrections and to distinguish them from potential NP contributions discussed below, we analyze the shape of the potential nonlinearity in a nonlinearity decomposition plot[1] [248, 250]. For n_A isotopes, the modified ISs between isotope pairs on electronic transition i form a $(n_A - 1)$-dimensional vector $\overline{\boldsymbol{\delta\nu}}_i$ with components $\overline{\delta\nu}_i^{A-A'}$. The two-dimensional KP relation for example can then be expressed as

$$\overline{\boldsymbol{\delta\nu}}_i = F_{ij}\,\overline{\boldsymbol{\delta\nu}}_j + K_{ij}\,\mathbb{1} + \sum_{\kappa} G_{ij}^{(\kappa)}\,\overline{\boldsymbol{\Lambda}}_{(\kappa)}\,, \tag{6.6}$$

---

[1] Sometimes also called “generalized King plot”.

where $\mathbb{1} = (1, \dots, 1)^\intercal$ is the $(n_A - 1)$-dimensional identity vector. For e.g., $n_A = 5$, we only need two additional terms with vectors $\overline{\mathbf{\Lambda}}_{(\kappa)}$ that are linearly independent of $\overline{\boldsymbol{\delta\nu}}_j$ and $\mathbb{1}$ to span the full space. Even without knowledge of the electronic pre-factors of higher order corrections, we can arbitrarily construct two (optionally orthogonal) vectors $\mathbf{\Lambda}_+$ and $\mathbf{\Lambda}_-$ in modified IS space to fully describe the set of experimental data via the projection

$$\left(F_{ij},\, K_{ij},\, \lambda_+,\, \lambda_-\right) = \left(\overline{\boldsymbol{\delta\nu}}_i \;\; \mathbb{1} \;\; \mathbf{\Lambda}_+ \;\; \mathbf{\Lambda}_-\right)^{-1} \cdot \overline{\boldsymbol{\delta\nu}}_j \equiv \mathbb{M}^{-1} \cdot \overline{\boldsymbol{\delta\nu}}_j\,. \tag{6.7}$$

We can then compare the observed nonlinearity in a generalized KP of λ_+ vs. λ_- – one data point per electronic transition pair i, j – to the expected nonlinearity shape originating from higher order corrections. We only require knowledge of the scaling of the nuclear coefficients $\mathbf{\Lambda}_{(\kappa)}$ and compare its projection $\mathbb{M}^{-1} \cdot \mathbf{\Lambda}_{(\kappa)}$. As long as the additional nonlinear terms do not align with the modified IS vectors, the identity vector or other contributions, they can be distinguished by a characteristic nonlinearity shape, which is defined by individual tuples (λ_+, λ_-). This technique can be easily scaled to higher-dimensional KP as long as there are enough isotope pairs.

Other King plots

There is a range of other KP that can be constructed, the here discussed mass-normalized $\overline{\boldsymbol{\delta\nu}}_i \rightleftharpoons \overline{\boldsymbol{\delta\nu}}_j$ being the most common one. Generalized **no-mass King plots** [251] can be constructed for example when the mass measurement uncertainty limits the modified IS uncertainty over the optical spectroscopy precision. For this the mass term $\mu^{A-A'}$ is expressed by a third IS measurement and the new projection matrix $\mathbb{M} = \left(\boldsymbol{\delta\nu}_i \;\; \boldsymbol{\delta\nu}_j \;\; \mathbf{\Lambda}_+ \;\; \mathbf{\Lambda}_-\right)$ is applied to measurements $\boldsymbol{\delta\nu}_k$ with $k \neq i, j$. The latest sub-Hz precision ISS in calcium uses mass-normalized KPs, even though mass measurement uncertainties were starting to limit the KP analysis. This was achieved by leveraging more precise isotope mass measurements from cryogenic Penning trap mass spectrometers, like PENTATRAP [249].

In the **dual King plot** [252] a multi-dimensional linearity among the different isotope pairs is established by exchanging the roles of the electronic and the nuclear factors, which promises to eliminate higher order standard model contributions and NP bounds without less knowledge of their electronic contributions. Here, the ratios of the nuclear factors $\delta\langle r^2\rangle^{A-A'}$ and $\mu^{A-A'}$ for varying pairs of isotopes are plotted against each other, providing a linear band of constraint from the IS data. This allows deducing more stringent constraints for nuclear factors that can also be used to benchmark nuclear theory [253].

Extraction of nuclear parameters

ISS offers a powerful tool for extracting nuclear parameters due to its high sensitivity to electron wave functions near the nucleus, where relativistic effects are pronounced [254]. As presented above, see section 2.1.2, probing the nuclear charge radius via ISS is a well-established method for studying the nuclear charge distribution and its anomalies. By comparing experimental and theoretical ISs and generalized KP – especially across multiple atomic transitions – studies of the effects and differences of changes in nuclear charge radii and nuclear deformation parameters, such as the quadrupole deformation parameter β_2, can be performed and used to benchmark nuclear theories [255]. Relativistic corrections, particularly those modifying the field IS via changes in $\langle r^{2\gamma}\rangle$, where $\gamma = \sqrt{1 - Z^2\alpha^2}$, and structural phenomena such as central charge density depletion in superheavy nuclei, also significantly affect FS contributions to the IS [256]. In the past, electronic x-ray, and muonic x-ray IS measurements have been a valuable addition to optical ISS. Transitions between energy levels of a muon bound to an atomic nucleus exhibit significant volume effects, allowing the extraction of $\delta\langle r^2\rangle$ and establishing muonic x-rays as a reliable alternative and cross-check to high-energy electron scattering for probing nuclear charge distributions [257]. A combined analysis using optical, electronic x-ray, and muonic x-ray IS data – while the latter so far limited in precision – enhances the sensitivity and provides a comprehensive approach to studying nuclear structure, including IS anomalies linked to variations in nuclear charge density [258].

Higher order FS corrections discussed above are historically written to enter the FS formula and modify the nuclear charge radii as [67, 259]

$$\delta\langle r^2\rangle^{A-A'} \longrightarrow \delta\langle r^2\rangle^{A-A'} + (C_2/C_1)\,\delta\langle r^4\rangle^{A-A'} + (C_3/C_1)\,\delta\langle r^6\rangle^{A-A'} + \dots \tag{6.8}$$

where the additional electronic factors C_i with $C_1 = F$ – called Seltzer moments [259] – are treated as higher order corrections. To our knowledge, no measurements have been made in Hg that could observe the KP nonlinearity associated with higher-order FSs or nuclear deformations (NDs). Seltzer moments are currently computed from electron structure calculations and are often approximated as nearly transition-independent (see, for example, [259]). To extract higher order contributions ISS data is compared to nuclear structure models or alternative measurements of the charge radii, as e.g., data from nuclear scattering using electrons or alpha particles, measurements of nuclear electric quadrupole transition probabilities or x-ray (muonic) ISS data (see e.g., [67]).

6.1.2 Search for new physics

ISS can also resolve a hypothetical NP coupling between electrons and neutrons [4, 35]. The electrons would experience a Yukawa-like potential, that in the point-charge approximation can be expressed as

$$V_{\mathrm{NP}}(r) = \frac{y_n\, y_e}{4\pi}\,\frac{e^{-r/\lambda\!\!\!^{-}_\phi}}{r} \equiv \alpha_{\mathrm{NP}}\,\frac{e^{-r/\lambda\!\!\!^{-}_\phi}}{r}\,, \quad \text{with } \lambda\!\!\!^{-}_\phi = \frac{\hbar}{m_\phi\, c}\,, \tag{6.9}$$

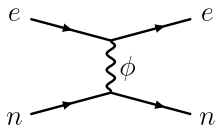

The force mediator is a NP boson ϕ with mass m_ϕ and with its Compton wavelength $\lambda\!\!\!^{-}_\phi$ determining the effective range of the interaction. The coupling strength is given by α_{NP} with y_e (y_n) representing the coupling constant between the new particle and an electron (neutron). This interaction would add an additional frequency shift

$$\delta\nu_i^{A-A'} \longrightarrow \delta\nu_i^{A-A'} + \alpha_{\mathrm{NP}}\, X_i\, h^{A-A'} \tag{6.10}$$

to the IS, equation (6.1), with the nuclear factor $\Lambda^{A-A'} = h^{A-A\prime} = A - A'$ being the difference in neutron number. The corresponding electronic factor $G_i = \alpha_{\mathrm{NP}}\, X_i$ is given by the coupling strength of the NP interaction α_{NP} and an electronic factor $X_i = (\hbar c/\alpha_{\mathrm{NP}})\,(\langle e|V_{\mathrm{NP}}(r)|e\rangle - \langle g|V_{\mathrm{NP}}(r)|g\rangle)$ that determines the sensitivity of the specific ground $|g\rangle$ and excited state $|e\rangle$ of the electronic transition i to this coupling.[1] While the NP coupling is slightly aligned with the MS $\mu^{A-A'}$ and its contribution

---

[1] Note, the coefficient X_i therefore in general depends on the mediator mass m_ϕ [253].

therefore slightly suppressed [251], it could be probed as a nonlinearity in the KP.

New physics bounds

New physics bounds can also be obtained from null measurements even in the presence of standard model (SM) nonlinearities when they are absorbed by additional IS measurements or their sources are understood well. For this purpose, the multidimensional KP formula with the addition of the BSM term[1],

$$\overline{\boldsymbol{\delta\nu}}_i = K_{\{i\}}\,\mathbb{1} + F_{\{i\}}\,\overline{\boldsymbol{\delta\nu}}_j + \sum_k G_{\{i\}}\,\overline{\boldsymbol{\delta\nu}}_k + \alpha_{\mathrm{NP}}\,X_{\{i\}}\,\overline{\boldsymbol{h}}\,, \tag{6.11}$$

is assumed to be linear/planar within experimental uncertainty up to the linearity-breaking BSM term and inverted to obtain a limit on α_{NP}. This limit can be interpreted as the ratio of the volume $V = \det(\overline{\boldsymbol{\delta\nu}}_1, \ldots, \overline{\boldsymbol{\delta\nu}}_n, \mathbb{1})$ spanned by just the $\overline{\boldsymbol{\delta\nu}}_i$ in the space of modified ISs and the volume $V_{\mathrm{th}}(\alpha_{\mathrm{NP}})$ of the above BSM coupling ansatz for $\alpha_{\mathrm{NP}} = 1$:

$$\alpha_{\mathrm{NP}} = \frac{V}{V(\alpha_{\mathrm{NP}} = 1)} = \frac{\det(\overline{\boldsymbol{\delta\nu}}_1, \ldots, \overline{\boldsymbol{\delta\nu}}_n, \mathbb{1})}{\frac{1}{(m-1)!}\,\varepsilon_{i_1 \ldots i_n}\,\varepsilon_{a_1 \ldots a_{n+1}}\,X_{i_1}\,\overline{h}^{a_1}\,\overline{\delta\nu}_{i_2}^{a_2} \ldots \overline{\delta\nu}_{i_n}^{a_n}}\,, \tag{6.12}$$

where $\varepsilon_{\ldots}$ denotes the Levi-Civita symbol and a sum over transition indices i and isotope pairs a is implied [249, 251]. Here, only the electronic factors X_i need to be computed using atomic many-body theory and all the rest of the analysis is data driven.

By varying the new boson mass m_ϕ in the calculation, an upper bound for a NP coupling strength α_{NP} can be estimated and also compared to bounds from other measurements, as discussed below. A recent exclusion plot of the BSM coupling resulting from these bounds is shown in figure 6.1. The largest boson masses that can be probed by ISS are limited by the nuclear charge radius r in comparison to the interactions effective range $\bar{\lambda}$, limiting sensitivity to $m_\phi \leq \hbar c / r \approx 1 \times 10^8$ eV [248]. The resonances in the sensitivity curve near $1 \times 10^4\ \mathrm{eV/c^2}$ result from a transition-dependent pole of the NP bounds, where $\overline{X}_i$ is zero [260]. SM nonlinearity sources need to be eliminated by including additional IS data in a multidimensional analysis or by subtracting theory predictions from electron and nuclear structure calculations from the IS data [249].

Review of King plot nonlinearities and new physics bounds

ISS has a long history in probing nuclear structure [69]. So far, additional contributions to the IS via KP nonlinearities have only been resolved in a few elements and first experimental constraints on BSM physics [4, 35] were just established recently using high-resolution ISS measurements in calcium and ytterbium. For a thorough overview of current measurements see e.g., the review in reference [248].

As shown in figure 2.2, the element calcium sits right at the $Z = 20$ nuclear shell closure and in-between the magic neutron numbers $N = 20, 28$, therefore possesses a very round nucleus with small nuclear deformation and five bosonic naturally abundant isotopes. While its spherical nucleus and low atomic mass decreases sensitivity to BSM couplings, higher-order nuclear effects and resulting nonlinearities are also being strongly suppressed, making Ca a good candidate for BSM searches.

---

[1] For simplicity, we abbreviated the m indices $i, j, k \in [1, m]$ of the electronic factors for the m transitions involved. A more detailed notation can be found in references [251] and [249].

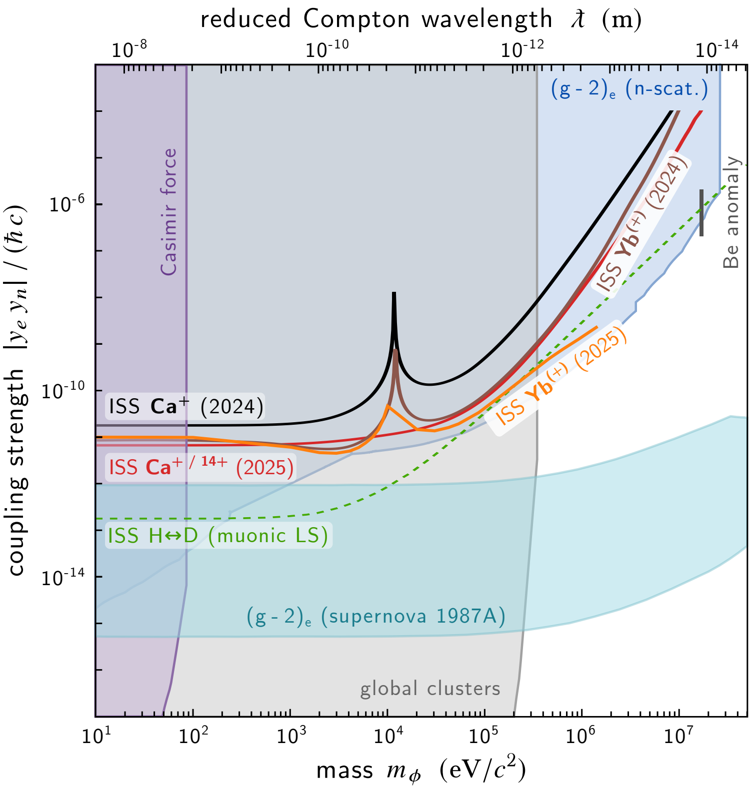

Figure 6.1: New physics exclusion plot for a new boson ϕ, with mass m_ϕ coupling neutrons and electrons with a coupling strength of $\alpha_{\mathrm{NP}} = y_n\, y_e/(4\pi)$. Solid lines show upper bounds for the coupling strength from recent high resolution ISS measurements: Ca$^+$ (2024, [260]), Ca$^+$/Ca^{14+} (2025, [249]); Yb$^{(+)}$ (2024, [261]) and Yb$^{(+)}$ (2025, [253]). Shaded areas indicate regions excluded by other measurements, as taken from reference [260]: Casimir fifth forces [262], cooling in horizontal branch stars of global clusters [263], measurements of the $(g-2)_e$ anomalous magnetic dipole moment of the electron [17] combined with data on star cooling in supernova SN1987A [264] and neutron scattering (e.g., [265]). The dashed line is an upper bound provided by ISs of hydrogen and deuterium extracted from Lamb shifts of muonic hydrogen and electron scattering experiments [266]. The range required for current BSM model explanations of the anomalous internal pair creation observed in ^{8}Be is indicated by the dark violet vertical bar [35–37].

Early KP analysis of Ca$^+$-ion spectroscopy at 100 kHz precision showed no significant deviation from linearity [267], and later measurements with sub-20 Hz accuracy confirmed this finding, providing first BSM bounds [260, 268]. More recent spectroscopy of ultra-narrow clock lines also in highly charged calcium ions, such as the $^3\mathrm{P}_0 \rightarrow {}^3\mathrm{P}_1$ transition in Ca^{14+}, has now achieved sub-Hz resolution. KP nonlinearities at the 900-sigma level were observed and accounted to second-order MSs and nuclear polarization contributions to the IS [249]. ISS of neutral Ca so far remains linear [165].

In contrast to calcium, early studies on neutral (Yb) and ionized (Yb$^+$) ytterbium have already shown clear KP nonlinearities, with a 300 Hz precision measurements already revealing a 3-sigma deviation [269]. Subsequent high-precision experiments, reaching Hz and even sub-Hz precision, not only confirmed these deviations but found even stronger nonlinearities [209, 250, 253, 261, 269, 270]. Multiple narrow transitions across five naturally abundant bosonic Yb isotopes have now been measured, enabling detailed decomposition of the nonlinearities. These studies show that the dominant contributions arise from nuclear structure, as the Yb nucleus is subject to strong nuclear deformations

(NDs) $\delta\langle r^4\rangle$ (see figure 2.2), rather than new-physics effects [248]. While BSM bounds obtained from recent Yb IS data [253] now compete with bounds set by Ca^+/Ca^{14+} KP comparison (see figure 6.1), this underscores the high sensitivity of heavy elements to nuclear SM effects. In the search for BSM physics, these SM contributions must be accounted for and limit the interpretation of IS data.

While so far limited to linear KP, additional platforms such as zinc ($Z = 30$, 4 even isotopes) [271], cadmium ($Z = 48$, 5 even isotopes) [272, 273], xenon ($Z = 54$, up to 7 even isotopes) [274] or tin ($Z = 50$, 7 even isotopes) [275, 276] sit close to nuclear shell closures and are therefore promising candidates for BSM bounds and to benchmark nuclear theory from ISS. Furthermore, highly charged ions [249, 277] are starting to be explored for their favorable nuclear and electronic properties and reduced sensitivity to perturbations from external electric and magnetic fields. With a wide range of ultra-narrow clock lines and options to sympathetically cool various elements in many different charge states, even when direct laser cooling is prohibited, these are discussed to offer outstanding potential for further improved BSM bounds on variations of fundamental constants [277] and fifth force carriers [248].

Note that the strict separation in nuclear and electronic coefficients – a consequence of lowest order perturbation theory [278] – is a very good approximation, but high precision spectroscopy on narrow clock lines could also probe for potential deviations [243, 248]. In special cases of electronic transitions i and j, where operators of second-order field or MS introduce off-diagonal matrix elements and mixing of closely spaced electronic levels, much stronger IS corrections can occur. Nuclear FS effects leading to "strong enhancement of second-order FS effect" [251] and up to 32 MHz-sized IS frequency corrections were observed in samarium – experimental details can be found in references [279, 280] and a theory model and explanation in reference [281].

6.1.3 Isotope shift spectroscopy in mercury

Possessing seven naturally abundant isotopes – five even and two odd – mercury ($Z = 80$) is an excellent candidate for ISS in the search for BSM physics. With ^{194}Hg having a half-life time of about 444 yr, even extensions to metastable radionuclides in a table-top experiment environment is possible. With its large mass, large nuclear charge, while sitting close to the nuclear shell closure of lead, mercury represents an excellent middle ground: it is not limited by recoil effects and reduced sensitivity to field-shift-mediated BSM couplings, as light nuclei like calcium. And SM induced nonlinearities arising from nuclear deformation are expected to be strongly suppressed in comparison to deformed nuclei like Yb. While for heavy systems, higher order nuclear contributions still can limit the KP analysis, the magnitude of the electronic factors X_i are strongly increased due to relativistic effects, which overall enhances these systems sensitivity to BSM couplings [248]. In addition, laser cooling of both neutral Hg and Hg^+ is well established.

Overview of isotope shift spectroscopy in mercury

IS measurements in mercury span a long history, from early arc spectra and vapor cell experiments to modern sub-MHz precision techniques [52, 168, 172, 282–285]. Beam-based and collinear laser spectroscopy techniques have expanded the accessible isotope range over many decades [64–68, 70, 77, 286, 287].

Ulm et al. investigated isotopes from ^{181}Hg to ^{206}Hg, extracting nuclear charge radii and magnetic dipole and electric quadrupole moments [67]. More recent studies at ISOLDE and other facilities extended these measurements to neutron-deficient isotopes as light as ^{177}Hg, revealing pronounced odd-even staggering in the charge radii consistent with shape coexistence, as discussed before [64, 65, 68, 70, 77].

Several optical transitions have been targeted in detail, with the 254 nm $^1S_0 \rightarrow {}^3\mathrm{P}_1$ intercombination line receiving the most attention in all systems. Other lines include measurements of Blaise and Chantrel at 405 nm, 408 nm, 436 nm, and 546 nm [284].

While early measurements were limited to hundreds of MHz to GHz uncertainty, Doppler-free saturation spectroscopy measurements by e.g., Gerstenkorn [168], Kroll [282], and Rayman [283] et al. reached the MHz to 100 kHz level of precision in the 80s and 90s. Measurements of Sansonetti et al. in 2010 achieved similar uncertainty of about 30 MHz on the 546 nm line [52]. Recent measurements of Witkowski et al. reported ISs on the 254 nm intercombination line with uncertainties between 56 kHz and 220 kHz [172] improving this sensitivity by more than one order of magnitude. These measurements were further refined in more recent work by Gravina et al. via comb-referenced Doppler-free saturation spectroscopy focussed on ^{200}Hg and ^{202}Hg for temperature metrology as a practical realization of the new kelvin definition [285].

Clock lines While potentially being addressable also in even isotopes – see the outlook for discussion – no direct IS measurements have yet been made on the neutral mercury $^1\mathrm{S}_0 \rightarrow {}^3\mathrm{P}_J$ $(J = 0, 2)$ clock lines. However, absolute frequency measurements have been made both for different isotopes in both neutral and singly ionized mercury.

Tyumenev et al. [93] and Petersen et al. [154] recently reported absolute frequency measurements of the $^1\mathrm{S}_0 \rightarrow {}^3\mathrm{P}_0$ line at 266 nm for the isotopes ^{199}Hg and ^{201}Hg. With absolute frequency determination of the ^{198}Hg resonance in reference [288] the ISs $\delta\nu^{199-198} = -0.662(11)$ GHz and $\delta\nu^{201-198} = -6.392(11)$ GHz can be determined [289]. Furthermore, multiconfiguration Dirac-Hartree-Fock (MCDHF) calculations in reference [289] provide estimates for the field ($F_{266} \approx -57.7\,\mathrm{GHz/fm^2}$) and MS coefficient ($K_{266} = -1.19(18)\,\mathrm{THz} \times \mathrm{amu}$). This gives an average $\delta\nu^{A-A'} = -4.72(46)$ GHz IS for pairs $A = A' + 2$ of even isotopes on the clock line, similar to the intercombination line, as the FS is dominated by the s-shell ground state wave function.

Bergquist et al. (for $^{198}\mathrm{Hg}^+$) [290] and Oskay et al. (for $^{199}\mathrm{Hg}^+$) [47] reported the frequencies of the $5\mathrm{d}^{10}6\mathrm{s}\ {}^2\mathrm{S}_{1/2} \rightarrow 5\mathrm{d}^9 6\mathrm{s}^2\ {}^2\mathrm{D}_{5/2}$ transition in single ionized mercury. From these, ISs can be extracted, and theoretical MCDHF estimates predict shifts on the order of as high as 1×10^4 GHz with hyperfine splittings between 1 GHz to 10 GHz [47] – very promising for high resolution ISS.

Isotope shift spectroscopy in laser cooled mercury

Being mostly interested in FS-like contributions that allow probing the atomic nucleus – NP couplings and nuclear moments –, for ISS we first chose the $^1\mathrm{S}_0 \rightarrow {}^3\mathrm{P}_1$ transition, that involves the s-shell electronic ground state. With ISs of the $^3\mathrm{P}_1 \rightarrow {}^3\mathrm{P}_1$, measured to the 100 kHz-level by the group of Jan Hall in the 90s [283], this promised FS-sensitive KP analysis and potential BSM-sensitivity. Note that the latter is suppressed for the wide dipole-allowed lines we initially address here. We later expanded our search to include optical transitions that do not involve S-state transitions, providing us a potential reference. Table 6.1 lists all the spectroscopy transitions we planned to target in our measurements.

For the spectroscopy of the $^1\mathrm{S}_0 \rightarrow {}^3\mathrm{P}_1$ intercombination line and the excited state transition $^3\mathrm{P}_1 \rightarrow {}^3\mathrm{D}_J$ with $J = 1, 2$, we utilize the suppressed Doppler broadening at low temperatures achievable in the magneto-optical trap (MOT). At typical cloud temperatures of $T \approx 100\,\mu\mathrm{K}$ to $200\,\mu\mathrm{K}$, the Doppler broadening is reduced from the GHz-range down to $\Gamma_D \approx 2\pi \times 600\,\mathrm{kHz}$ to $850\,\mathrm{kHz}$, which is smaller than the natural linewidth of the dipole-allowed transitions we spectroscopically address here. As we will see in the following, in this setting systematic shifts are dominated by light and recoil shifts. These can be reduced to just originating from the spectroscopy light itself by releasing the atoms from their trapping beams and addressing them in free fall.

More precise measurements would need to lever Doppler-free spectroscopy configuration by opposing lightfields and further cooling, by e.g., utilizing the optical dipole trap (ODT) setup presented above. Here, spectroscopy on the ultra-narrow optical clock transitions $^1\mathrm{S}_0 \rightarrow {}^3\mathrm{P}_J$ ($J = 0, 2$) in mercury are especially interesting for potential Hz to sub-Hz NP contributions. Here, atoms would ideally be confined in optical lattices, where any motional coupling between atom and photon (recoil + Doppler shifts) are suppressed in the Lamb-Dicke regime. In all spectroscopy environments we need to account for experimental imperfections like residual magnetic fields and other effects, that are sources of line shifts and increase the measurement uncertainty.

Transition $\vert g\rangle \rightarrow \vert e\rangle$	Wavelength λ (nm)	Natural linewidth $\Gamma/(2\pi)$ (MHz)	Saturation intensity I_{sat} (mW/cm^2)
$6s^2\ {}^1\mathrm{S}_0 \rightarrow 6s\,6p\ {}^3\mathrm{P}_1$	253.7	1.34	10.7
$6s\,6p\ {}^3\mathrm{P}_1 \rightarrow 6s\,6d\ {}^3\mathrm{D}_1$	313.2	15.4(2.6)	66(11)
$6s\,6p\ {}^3\mathrm{P}_1 \rightarrow 6s\,6d\ {}^3\mathrm{D}_2$	312.7	10.50	44.9
$6s\,6p\ {}^3\mathrm{P}_2 \rightarrow 6s\,7s\ {}^3\mathrm{S}_1$	546.2	7.80	6.3
$6s\,6p\ {}^3\mathrm{P}_1 \rightarrow 6s\,7s\ {}^3\mathrm{S}_1$	436.0	8.91	14.1
$6s^2\ {}^1\mathrm{S}_0 \rightarrow 6s\,6p\ {}^3\mathrm{P}_0$	265.7	$\ll$1 Hz	
$6s^2\ {}^1\mathrm{S}_0 \rightarrow 6s\,6p\ {}^3\mathrm{P}_2$	227.0	$\ll$0.1 Hz	

Table 6.1: Spectroscopy transitions interesting for ISS in mercury. The first three lines are experimentally studied within this work. The 546 nm line was measured elsewhere [283] and will be used for KP analysis later. The dipole allowed 436 nm line and the two strongly forbidden narrow clock lines are suggested for future measurements, as discussed in the outlook, section 6.5. Data is taken from reference [87], except for linewidth of the clock line transitions and $^3\mathrm{P}_1 \rightarrow {}^3\mathrm{D}_1$ transition, the latter being determined from excited state lifetime measurements [88–90] as explained in reference [91, appendix A.3].

Chapter overview

This chapter will present the experimental results and KP analysis of precision ISS on multiple dipole-allowed atomic transitions in mercury. Spectroscopy of laser cooled mercury by absorption imaging on the intercombination line $^1\mathrm{S}_0 \rightarrow {}^3\mathrm{P}_1$ at 253.7 nm including all naturally abundant bosonic isotopes is presented, and we achieve unprecedented precision. Further, we spectroscopically probe the $^3\mathrm{P}_1 \rightarrow {}^3\mathrm{D}_J$ ($J = 1, 2$) transitions that both are conveniently located at around 313 nm, for which we construct a frequency quintupled laser system and probe the atoms by depletion in the MOT. We observe slight nonlinearities in the subsequent two-dimensional KP analysis of the transitions, that we also perform in comparison to existing spectroscopy data on the $^3P_2 \rightarrow {}^3S_1$ line [283]. In a nonlinearity decomposition analysis we attempt to resolve potential nonlinearity origins, looking at nuclear and BSM effects. Finally, spectroscopy on the $^3P_1 \rightarrow {}^3S_1$ transition at 436 nm is proposed, for which a cavity stabilized laser system is constructed. An outlook on ISS on narrow clock lines will be given.

6.2 Spectroscopy on $^1S_0 \rightarrow {}^3P_1$

All spectroscopy schemes used in this thesis are illustrated in figure 4.13. For the spectroscopy on the $\Gamma = 2\pi \times 1.3\,\text{MHz}$ broad intercombination line at 253.7 nm, we probe the atoms in the absorption imaging sequence, shown in figure 4.13, for close to zero time of flight just after release.[1] We iterate between the isotopes, where we always jump back to ^{198}Hg and ^{202}Hg, the former for an improved literature comparison and the latter as it gives us the best signal to noise and therefore a good indicator for systematic shifts. We step the acousto-optic modulator (AOM) probe/imaging beam frequency in small steps starting from around the resonance outwards to avoid drifts in atom loading efficiency, that introduce asymmetries in the lineshape. For each AOM frequency we load the atoms for 5 s, probe the atom number via absorption imaging in free-fall and reload the MOT from the background gas after a short waiting time to avoid bias from the previous shot. We typically operate the imaging beam intensity at around $I = 0.3\,\text{mW/cm}^2$ and at a pulse length of $t_{\text{exp}} = 150\,\mu\text{s}$, which showed to be a good compromise between high contrast / low signal-to-noise and small systematic shifts, the latter discussed below. Given the saturation intensities listed in table 6.1, this makes the interaction stay in the low saturation limit ($s_0 \approx 0.03$), which avoids power broadening and excessive recoil shifts.

All systemic shifts described below are applied to each individual shot taking into account their correlations when fitting the lineshape and extracting the resonance frequencies. The full dataset, incorporating all systematics, is shown in figure 6.7, the extracted resonance frequencies showing the about one month long time span of the measurement campaign can be found in figure 6.10.

6.2.1 Frequency reference

The spectroscopy laser is stabilized to the ultrastable cavity described in section 4.3.3. The cavity resonances therefore act as a ruler in frequency space by providing cavity lines every free spectral range ($\delta_{\text{fsr}} \approx 3\,\text{GHz}$) and are used as a frequency reference for the hundreds of MHz to GHz scale ISs, measured in this work. The infrared (IR) master laser is offset from the cavity resonances by the fiber electro-optic modulator (EOM) frequency f_{eom}, as described before. The spectroscopy AOM then shifts the ultraviolet (UV) probe beam frequency with respect to the fundamental laser wavelength and the atomic resonances are probed by scanning the AOM frequency f_{aom} by a few to tens of MHz around a controlled center frequency. To ensure absolute frequency stability, all radio frequency (RF) signal generators – the phase lock loop (PLL) voltage controlled oscillator (VCO) controlling the master laser to cavity detuning and the direct digital synthesizer (DDS) boards that feed the AOMs in

---

[1] Experimentally there is a short $\leq 10\,\mu\text{s}$ delay between MOT light switch-off and imaging pulse/camera trigger to ensure negligible light shifts introduced by the MOT beams. The magnetic gradient field is switched off in-between MOT beam switch-off and camera trigger to remove any magnetic field change induced MOT dynamics.

State	Lifetime τ
6s 6p $^3P_0$	$\gg$ 1 s
6s 6p $^3P_1$	118.9(4) ns
6s 6p $^3P_2$	$\gg$ 1 s
6s 6d $^3D_1$	6.8(6) ns
6s 6d $^3D_2$	9.3(5) ns
6s 6p $^1P_1$	1.3 ns
6s 7s $^3S_1$	8.0(7) ns

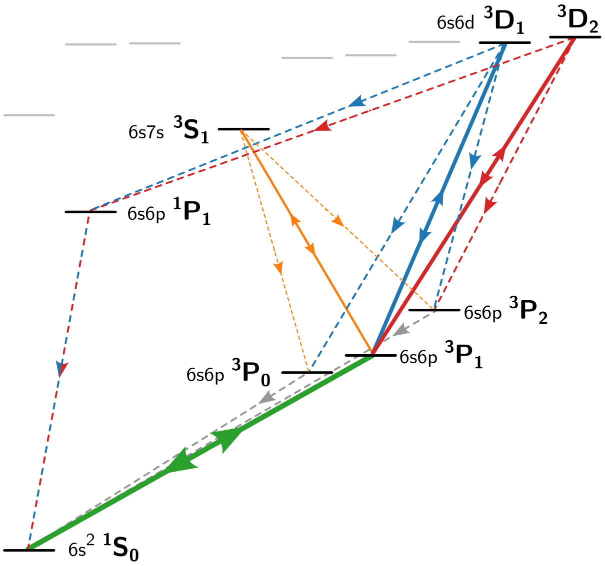

Figure 6.2: Spectroscopy scheme to address the $^1\mathrm{S}_0 \rightarrow {}^3\mathrm{P}_1$ intercombination line (green), as well as the excited MOT state $^3\mathrm{P}_1 \rightarrow {}^3\mathrm{D}_J$ with $J = 1, 2$ (blue, red) and $^3\mathrm{P}_1 \rightarrow {}^3\mathrm{S}_1$ (orange) transitions. While the MOT transition can be probed directly from the ground state via absorption imaging, spectroscopy of all other lines requires 254 nm light to pump the atoms to the $^3\mathrm{P}_1$ excited state. Here, a near-resonant spectroscopy probe pulse depletes the MOT atom number by absorption and subsequent decay (dashed lines) dominated by spontaneous emission to the indicated lower lying states, where effective atom loss is mainly a result of the long lifetimes (dashed gray) of the metastable $^3\mathrm{P}_{0,2}$ excited states. The table shows the excited state lifetimes as given in references [87, 88, 291].

the UV – are phase locked to a stable 10 MHz rubidium frequency standard[1], that is distributed over the lab. A single spectroscopy measurement stores the AOM frequencies f_aom of the scan, the EOM carrier shift frequency f_eom, the sign ± of the EOM sideband used for locking, and a cavity resonance index $i_\mathrm{cav} \in \mathbb{N}$. As introduced in equation (4.17), we reference all measurements to a fixed cavity line $i_\mathrm{cav} = 0$ that is located red detuned with respect to all mercury isotope resonances. All ISs therefore can be computed from the probe beam cavity detuning[2]

$$\delta_\mathrm{cav} \equiv \nu_\mathrm{probe} - 4\,\nu_{\mathrm{cav},\,0} = 4\;(i_\mathrm{cav}\,\delta_\mathrm{fsr} \pm f_\mathrm{eom}) + f_\mathrm{aom}\,. \tag{6.13}$$

From the atomic resonance frequencies, denoted as $\delta_\mathrm{cav}^{\star(A)} = \nu^{\star(A)} - 4\,\nu_{\mathrm{cav},\,0}$, of the individual isotopes with mass number A we then obtain the ISs as

$$\delta\nu^{A-A'} = \delta_\mathrm{cav}^{\star(A)} - \delta_\mathrm{cav}^{\star(A')}\,. \tag{6.14}$$

Note that for uncertainty determination we will need to take correlations between $\delta_\mathrm{cav}^{\star(A)}$ and $\delta_\mathrm{cav}^{\star(A')}$ into account, as they are derived from common references (e.g., δ_fsr, as determined below) and will be corrected by common systematic shifts.

Absolute atomic resonance frequencies would ideally be established by comparing to an optical frequency reference and SI time standard over a frequency comb, but at the time no optical clock

---

[1] Stanford Research Systems FS725, 20 year aging of $< 5 \times 10^{-9}$. [2] We denote $\nu_\mathrm{probe} = \nu_\mathrm{img}$ and $f_\mathrm{probe} = f_\mathrm{img}$ in this chapter for consistency with the notation for the spectroscopy probe beam in section 6.3.

in the group was yet in active operation. Therefore, we record the fundamental laser frequency on our HighFinesse wavemeter with about 10 MHz absolute accuracy in parallel to the measurement. As the wavemeter records the fundamental laser frequency in the IR, the absolute frequency of the atomic resonance of the individual isotope in the UV is then given by $\nu^\star = 4\,\nu_{\mathrm{IR}} + f^\star_{\mathrm{aom}}$, where $f^\star_{\mathrm{aom}}$ denotes the AOM frequency associated with the probe beam atomic resonance frequency $\nu^\star$. For the $^1\mathrm{S}_0 \rightarrow {}^3\mathrm{P}_1$ transition, we can also rely on the high-resolution Doppler-free saturation spectroscopy in reference [172] that is referenced to a representation of the SI second via a frequency comb and long-distance fiber link to about 100 kHz absolute accuracy.

Free-spectral range measurement

For determination of the relative cavity line positions, we position the 1015 nm laser frequency in-between two cavity resonances. With no frequency modulation on the EOM, the cavity transmission signal, as recorded by a reverse-biased photodetector, is at zero. We then apply sidebands at around $f_{\mathrm{eom}} \approx \delta_{\mathrm{fsr}}/2 \approx 1.5\,\mathrm{GHz}$, which allow probing the two cavity resonances that are located symmetrically around the laser frequency. We scan the laser about 500 kHz via the diode current and step the RF frequency in small steps and record the respective cavity transmission on a high-resolution oscilloscope. The laser now probes the two neighboring cavity resonances with its sidebands, as illustrated in figure 6.3.

For every step we determine the location of the maximum of the probed cavity transmission and average over five laser scans. Each EOM frequency step takes about 500 ms. An example for the recorded step-averaged transmission is shown in figure 6.4 as a function of the EOM frequency. A Lorentzian fit of the resonance gives us an estimate of the combined laser and cavity linewidth (see below), as well as the free spectral range: $\delta_{\mathrm{fsr}} = 2\,f^\star_{\mathrm{eom}}$. The fit uncertainty is only limited by the signal-to-noise of the transmission signal due to intensity noise and limited linewidth of the free-running laser. We determine the resonance location $2 \cdot f^\star_{\mathrm{eom}}$ to about 0.6 kHz in a single measurement. We do not

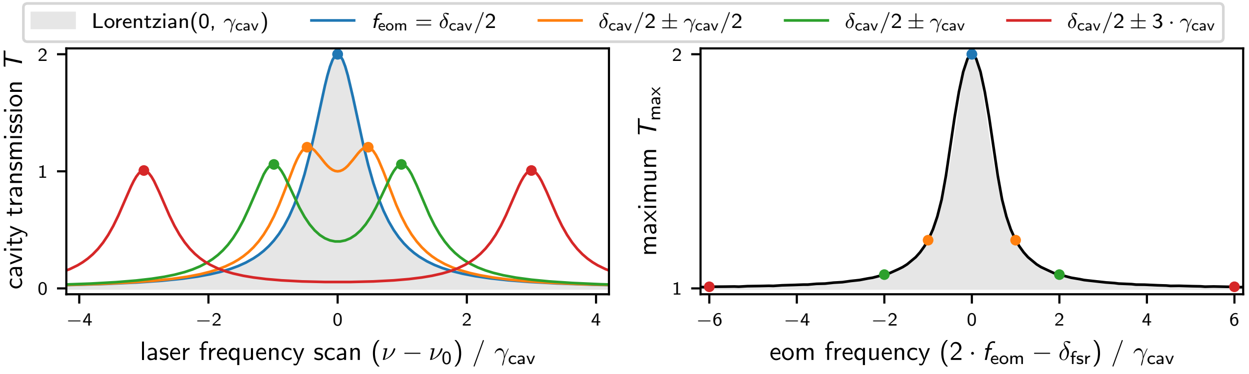

Figure 6.3: Free spectral range measurement principle showing the simulated cavity transmission T as recorded by a photodiode. With the laser frequency ν roughly centered between two cavity resonances, we step the EOM frequency f_{eom} around $\delta_{\mathrm{fsr}}/2$, scan the laser and record the respective cavity transmission T (left). The transmission maxima (colored dots) are graphed against the respective EOM frequency (right) to determine the free spectral range. Ignoring laser linewidth, the resulting lineshape closely reproduces the cavity profile (gray shaded area).

expect to resolve a linear drift of the cavity length outside this uncertainty and in this time window[1], but we repeat the measurement multiple times over the course of the ISS campaign, as shown in the right graph in figure 6.4. The FSR used for the determination of the ISs below is obtained from a weighted average to this data. We obtain:

$$\delta_\mathrm{fsr} = 2{,}992{,}455.6(3)\,\mathrm{kHz}\,, \tag{6.15}$$

which does not limit the ISS resolution.

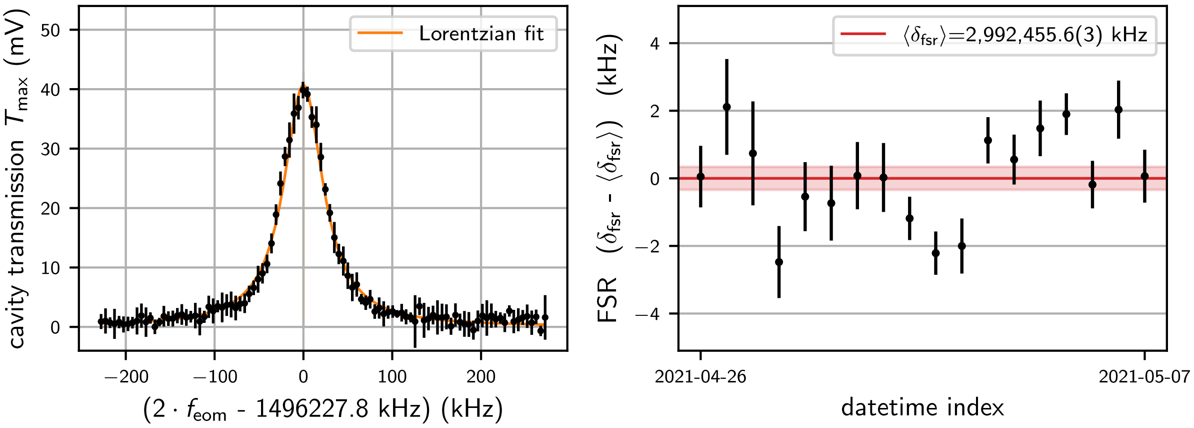

Figure 6.4: Measurement of the 1015 nm cavity free spectral range δ_fsr. A scan of the EOM frequency around $\delta_\mathrm{fsr}/2$ resolves the cavity lineshape in the cavity transmission maxima (left). A Lorentzian fit determines the FSR as the resonance position and combined laser cavity linewidth. Multiple measurements over the time period of the IS measurement campaign are averaged to determine the FSR (right). Note the nonlinear time axis.

6.2.2 Spectroscopy

An example dataset for the most abundant isotope ^{202}Hg is shown in figure 6.5 and all spectroscopy curves recorded during this measurement campaign for all isotopes is shown in figure 6.7. As illustrated, a Lorentzian or Voigt shaped fit to the data does result in a slight asymmetry in the residuals, which can easily lead to kHz shift in determination of the true atomic resonance. The origin of the asymmetry and a more appropriate fit model is discussed below.

Lineshape

Linear absorption spectroscopy with high energy UV photons leads to a probe beam recoil induced Doppler shift. Due to momentum conversation, every absorbed photon changes the atoms' velocity by $v_\mathrm{rec} = \hbar\, k/m$, which shifts the probe beam frequency by $\Delta_\mathrm{rec} = -k\, v_\mathrm{rec}$. We consider an atom initially at rest and analyze its light shift evolution during the probe beam exposure time t_exp. From equation (4.5), the coherent steady-state photon scattering rate of a two-level system at rest is given

---

[1] The cavity line in the infrared around 1015 nm drifts by about $\mathrm{d}\nu_\mathrm{IR}/\mathrm{d}t = -0.203(4)\,\mathrm{Hz/s}$ absolutely, as determined below in section 6.2.3. With ν_IR around the $\delta_\mathrm{fsr}/\nu_\mathrm{IR} = 98{,}779$-th cavity resonance, the free spectral range (FSR) itself is therefore expected to just drift by about $\mathrm{d}\delta_\mathrm{fsr}/\mathrm{d}t \approx (\delta_\mathrm{fsr}/\nu_\mathrm{IR})\,\mathrm{d}\nu_\mathrm{IR}/\mathrm{d}t = -65(1)\,\mathrm{Hz/yr}$.

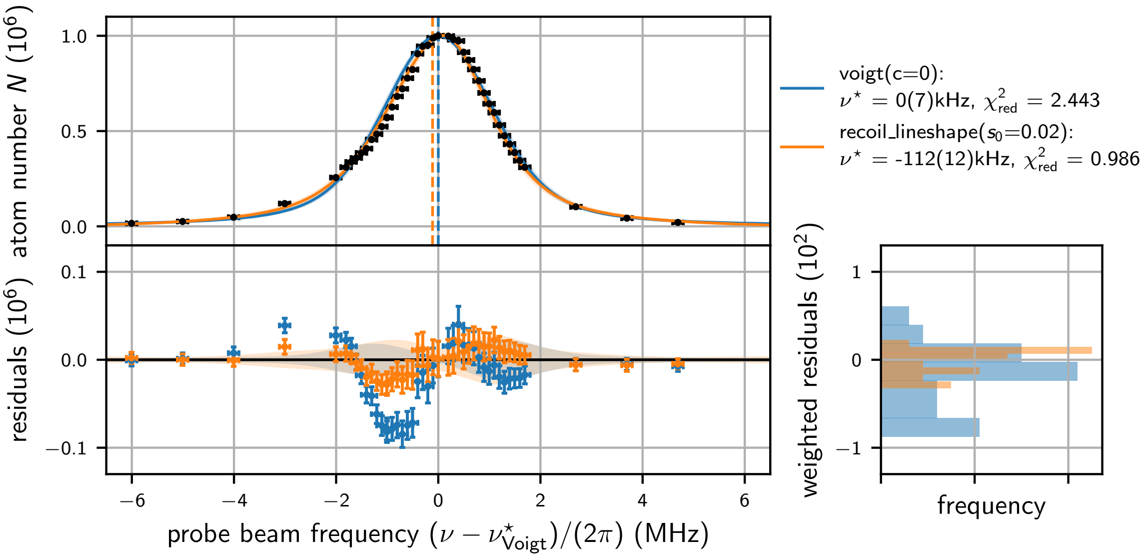

Figure 6.5: $^1S_0 \rightarrow {}^3P_1$ example spectroscopy data of ^{200}Hg comparing a symmetric Voigt fit function to the probe recoil induced Doppler shifted asymmetric lineshape. The frequency axis is given relative to the Voigt fit resonance, indicating the −112(12) kHz shift that the asymmetric fit function takes care of. The saturation parameter $s_0 = 0.0199(4)$ is extracted from the absorption imaging reference image and set fixed for the fit. The shaded area in the fit model indicates the $3\,\sigma$-uncertainty band. A histogram of the uncertainty weighted residuals (bottom right) is given as a measure for the fit quality. The data includes all systematic shifts and uncertainties discussed below.

by

$$R_{\text{sc}}(\Delta) = \frac{\Gamma}{2}\,\frac{s_0}{1 + s_0 + (2\,\Delta/\Gamma)^2}\,, \tag{6.16}$$

where $\Delta = \omega - \omega_0$ is the light field detuning of the probe beam and $s_0 = I/I_{\text{sat}}$ the saturation parameter. This corresponds to a Lorentzian lineshape centered at $\Delta = 0$ with a full width at half maximum (FWHM) of $\Gamma_s \equiv \Gamma\,\sqrt{1 + s_0}$. For low saturation ($s_0 \ll 1$), we can approximate $\Gamma_s \approx \Gamma$. If we also include a finite cloud temperature T, the line gets broadened by the Doppler shift due to the Maxwell-Boltzmann distributed atom velocities, the latter given in equation (4.15). The result is a Voigt profile detuning dependency – the convolution of a Lorentzian and a Gaussian lineshape – given by

$$\begin{aligned} R_{\text{sc}}(\Delta) &= \int_{-\infty}^{\infty}\!\mathrm{d}v\;\frac{\Gamma}{2}\,\frac{s_0}{1 + s_0 + (2\,(\Delta - k\,v)/\Gamma)^2} \times \frac{1}{v^\star\sqrt{\pi}}\,e^{-(v/v^\star)^2} \\ &= \pi\left(\frac{\Gamma}{2}\right)^2 \frac{s_0}{\sqrt{s_0+1}}\,V(\Delta,\,\Gamma_s,\,\Sigma_D)\,, \qquad \text{with} \quad \Sigma_D = \frac{\omega_0}{c}\sqrt{\frac{k_B\,T}{m}}\,, \end{aligned} \tag{6.17}$$

where Σ_D is the standard deviation of the Gaussian profile corresponding to the Doppler width.[1] Due to the finite atomic linewidth, the atom therefore scatters a photon after a time $t_{\text{scat}}(\Delta) \sim \mathit{Exp}(\lambda = R_{\text{scat}}(\Delta))$, where *Exp* denotes the exponential distribution with rate λ.

The total number of scattering events n_{scat} can then be estimated from the total scattering time t_{tot}

---

[1] The Doppler width (FWHM) is given by $\Gamma_D = \sqrt{8\ln(2)}\,\Sigma_D$.

that can fit into the probe beam exposure time t_{exp}:

$$t_{\text{exp}} \overset{!}{\geq} t_{\text{tot}} = \sum_{i=0}^{n_{\text{scat}}-1} t_{\text{scat}}(\Delta + i\,\Delta_{\text{rec}}) \quad \sim \quad \mathit{HypoExp}[\lambda_i = R_{\text{scat}}(\Delta + i\,\Delta_{\text{rec}})] \tag{6.18}$$

The total scattering time t_{tot} is following a hypoexponential distribution defined by n_{scat} rate parameters $[\lambda_i]_{i=0}^{n_{\text{scat}}-1}$, with a mean $\mu_H = \sum_i 1/R_{\text{scat}}(\Delta + i\,\Delta_{\text{rec}})$ and variance $\sigma_H^2 = \sum_i 1/R_{\text{scat}}^2(\Delta + i\,\Delta_{\text{rec}})$. We can approximate this distribution by a Gamma distribution $t_{\text{tot}} \sim \mathit{Gamma}\big[\alpha = \mu_H^2/\sigma_H^2,\ \lambda = \sigma_H^2/\mu_H\big]$ of denoted shape α and rate λ, as illustrated in figure 6.6. The mean number of scattering events for all atoms gives the absorption profile for the spectroscopy scheme and can be estimated from the statistical mean of this Gamma distribution:

$$n_{\text{scat}}(\Delta; s_0, t_{\text{exp}}) = \left(n \;\middle|\; t_{\text{exp}} \overset{!}{=} \langle t_{\text{tot}} \rangle_{\mathit{Gamma}[\alpha,\lambda]} \approx \int_0^{n-1} \mathrm{d}i \;\; \frac{1}{R_{\text{scat}}(\Delta + i\,\Delta_{\text{rec}})} \right), \tag{6.19}$$

which can be solved numerically.[1]

The resulting absorption profile is shown in figure 6.6 for realistic experimental parameters of a low intensity ($s_0 = 0.05$) probe beam and an exposure time of $t_{\text{exp}} = 150\,\mu\text{s}$. This indicates the slight asymmetric lineshape that forms, as the atom moves along the absorption profile in frequency space $\Delta \rightarrow \Delta + i\,\Delta_{\text{rec}}$ with every scattering event. While this not fully describes the data, where noise is dominated by atom number fluctuations and determination as described below, it strongly improves the residuals and fit quality. An improved model solving the time dependent optical Bloch equations in the duration of the probe beam pulse and also taking into account Doppler broadening of the line is could potentially describe the data even better.

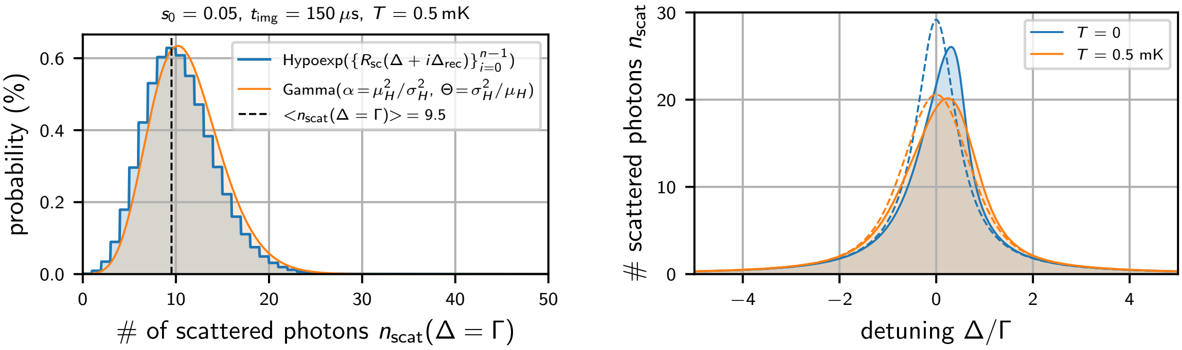

Figure 6.6: Lineshape model for the linear absorption spectroscopy of the $^1\mathrm{S}_0 \rightarrow {}^3\mathrm{P}_1$ transition. Probability distributions (left) showing the number of photons scattered by a single atom in the time interval of the probe beam pulse for realistic experimental parameters. Resulting lineshape (right) for the scattering with and without Doppler broadening following equation (6.19) with the scattering rate given by equation (6.16) for $T = 0$ (blue) and equation (6.17) for $T > 0$ (orange). The dashed line shows the lineshape without probe recoil induced Doppler shift.

---

[1] For computational performance the Voigt profile in the spectroscopy fits will be approximated by their sum instead of their convolution $V(\Delta, \Gamma_s, \Sigma_D) = L(\Delta, \Gamma_s) * G(\Delta, \Sigma_D) \approx \eta\, L(\Delta, \Gamma_s) + (1-\eta)\, G(\Delta, \Sigma_D)$, with η as defined in reference [292], which is accurate to $\leq 1\,\%$.

In the measurements presented for ISS we operate at $s_0 = 0.01$ to 0.03 for which every atom scatters about 4 to 15 photons at maximum (for $\Delta \approx 0$) in the given exposure time. In the fitting routine the saturation parameter is considered fixed and is instead extracted from the reference image of the absorption sequence weighted by the fitted atom position. The camera sensor is therefore being calibrated via an optical power meter.

6.2.3 Systematic shifts and uncertainties

A list of all systematic shift and uncertainty estimates is given in table 6.2. We approach the characterization and removal of these systematic corrections by calibration measurements and theory input including numerical models. They contribute to the uncertainty budget of the atom cavity detuning frequencies $\delta_{\mathrm{cav}}^{\star(A)}$ either via an uncertainty in the probe beam frequency ν_{probe}, via a shift or uncertainty in the atomic resonance frequency $\nu^{\star(A)}$ or via atom number uncertainties that propagate through the nonlinear fit. Extracting their individual contributions is not straightforward, as they have varying correlations in affecting the data and varying strength in shifting the fit-extracted resonance frequencies. We give an estimate for their approximate magnitude either directly from theory, or from analyzing their distribution over all measurements – which vary from shot to shot and isotope to isotope – or by considering them as nuisance parameters in a pull-method statistics analysis. The shifts, their origins and contributions to the overall IS will be discussed in more detail below.

Systematic	Correction	Estimated shift (kHz)	Source
Probe recoil	$a_I^A\, I_{\mathrm{probe}}$	33(15)	Photon recoil induced Doppler shift.
Zeeman shift	numerical model	−5(15)	Residual gradient field.
Reference drift	$a_{\mathrm{cav}}\, t$	1517(34)	Cavity aging/relaxation.
Probe frequency	$\pm\Delta f_{\mathrm{probe}}$	0(22)	Laser & cavity linewidth and lock offset.
Doppler shift	$\pm\Delta f_{\mathrm{Doppler}}$	0(20)	Residual cloud velocity $v_0 + g\, t_{\mathrm{tof}}$.
Light shift	$\pm\Delta f_{\mathrm{light}}$	0(0)	Probe beam induced, on- & off-resonant.
N fluctuations	$\pm\Delta N$	0(15)	MOT beam pointing and beam shape.
N determination	$\pm\Delta N_{od}$	0(5)	Atom number extraction from optical density.

Table 6.2: Uncertainty budget for the ${}^1\mathrm{S}_0 \rightarrow {}^3\mathrm{P}_1$ ISS. Uncertainties are given as shifts to the atom cavity detuning $\delta_{\mathrm{cav}}^{\star(A)}$, either direct in a frequency uncertainty or indirect via the atom number. All shifts and uncertainties are conservative approximations in magnitude only (rounded to 1 kHz) and an upper limit for all isotopes, as their individual contributions to the total uncertainty can not fully be isolated via the pull-method. The specified uncertainties in the result section can therefore be smaller than the sum of contributions given here. Explanations to the individual contributions can be found in the text.

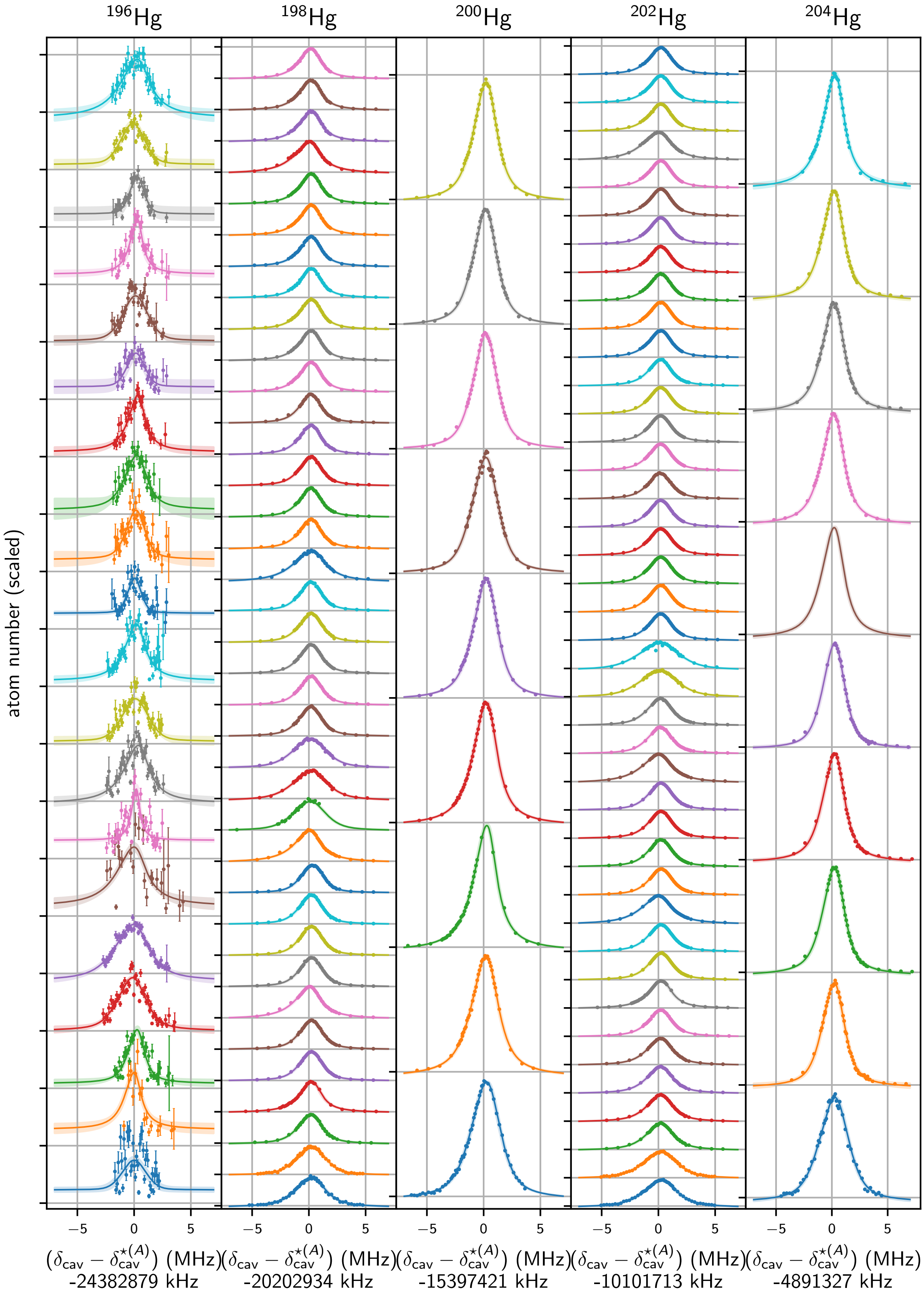

Figure 6.7: $^1S_0 \rightarrow {}^3P_1$ spectroscopy data incorporating all systematic shifts and uncertainties. Datasets are vertically offset for clarity.

Laser linewidth

The linewidth of the 1015 nm unlocked master laser is specified in the 10 kHz range typical for this kind of low-noise external cavity diode lasers [293]. We can use the cavity FSR measurement from above to give a limit to the spectral width of the free-running laser. The (averaged) fitted Lorentzian width of $\gamma_{\mathrm{tot}} = 59.2(3)$ kHz (FWHM) is the convolved linewidth of cavity and free running laser. The cavity linewidth can be estimated from both the FSR measurement and the cavity ring-down finesse measurement presented above. We obtain $\gamma_{\mathrm{cav}} = \gamma_{\mathrm{fsr}}/\mathcal{F} = 40.5(4)$ kHz at a finesse of $\mathcal{F} = 74\,120(660)$, see section 4.3.3. Assuming both laser and cavity to have Lorentzian lineshapes, the laser width can be approximated as $\gamma_{\mathrm{laser}} \lesssim \gamma_{\mathrm{tot}} - \gamma_{\mathrm{cav}} = 18.8(5)$ kHz.[1] For Gaussian dominated frequency noise the linewidth estimate is a factor of $\sim \sqrt{2}$ higher. Laser frequency drifts during the measurement render this an upper limit of the real linewidth of the free-running laser.

Linewidth narrowing The laser's spectral width is further reduced via the lock to the ultrastable cavity, where typically widths of a hundredth to a thousandth of the cavity linewidth below 1 kHz down to the Hz range [294] are achieved with similar stabilization setups. Missing a second laser we could not measure the linewidth of the master laser nor of the UV output directly. Using a very similar laser system (external cavity diode laser + tapered amplifier) at 872 nm, we reach a linewidth of < 1 Hz, as described in section 6.5. We give a conservative linewidth estimate of $\ll 1$ kHz for the master laser by analyzing the error signal of the cavity lock. We determine the error signal slope around resonance by a series of linear fits and interpolate from that the frequency range of the in-loop error signal when locked. With the discussed broadening due to amplifier stages and nonlinear conversion the UV laser linewidth discussed in section 4.3.3 is therefore conservatively estimated to be $\ll 16$ kHz. Laser linewidth is estimated to not limit the spectroscopy resolution, but a more rigorous analysis is recommended for future improvements of the latter.

Lock offset The ISS relies on relocking the laser to the individual cavity resonance, where we observe a slight offset change in the error signal, that potentially can change the lock point. We manually correct for this offset by hand before locking, slightly shifting the error signal to zero. As the true zero is therefore not known, we characterize the effect of these mV-sized offset drifts via an estimate of the error signal slope and assign an additional 15 kHz uncorrelated error to the frequency determination. We later characterized these drifts to originate from electronic ground loops in the lock electronics, as we could remove them with the installation of transformers for ground isolation, as shown in figure 4.8, and by isolating the locking electronics via optocouplers for all digital communication and by ensuring star-shaped routing of power and ground cable connections.

Light shifts

Probe beam induced off-resonant light shift The atoms are subject to light shifts originating from the AC polarizability of the ground and excited states of the spectroscopy transition at the probe beam wavelength itself due to non-resonant coupling to nearby transitions to other atomic levels. Estimating this shift from theory is challenging, since the AC polarizability as calculated in section 5.1.1 has many contributions from transitions with so far unknown transition probabilities.

---

[1] Lorentzian linewidths add linearly under convolution.

Probe transition $\lvert g\rangle \rightarrow \lvert e\rangle$	Ground state light shift $\delta\nu_{\lvert g\rangle}/I_{\mathrm{sat}}$ (Hz/I_{sat})	Excited state light shift $\delta\nu_{\lvert e\rangle}/I_{\mathrm{sat}}$ (Hz/I_{sat})
$6s^2\ {}^1S_0 \rightarrow 6s\,6p\ {}^3P_1$	-0.021(1)	0.005(88)
$6s\,6p\ {}^3P_1 \rightarrow 6s\,6d\ {}^3D_1$	-4(80)	0.9(2.8)
$6s\,6p\ {}^3P_1 \rightarrow 6s\,6d\ {}^3D_2$	-0.1(4.9)	0.7(1.3)
$6s\,6p\ {}^3P_1 \rightarrow 6s\,7s\ {}^3S_1$	-0.03(2)	0.54(71)

Table 6.3: Off-resonant AC Stark light shifts at the respective spectroscopy probe wavelength. The error bars are dominated by the uncertainty of the transitions with unknown linewidth that contribute to the AC polarizability. Here, all in the NIST line database [87] listed transitions are taken into account, where unknown transition probabilities are assigned a $\Gamma = 2\pi \times 0(100)$ MHz uncertainty, details can be found in section 5.1.1. The respective saturation intensities and probe beam wavelengths can be found in table 6.1.

For the $^1S_0 \rightarrow {}^3P_1$ transition, the ground state polarizability is dominated by the broad dipole allowed $^1S_0 \rightarrow {}^1P_1$ singlet transition at 185 nm. Other close resonant light shift contributions, as the one from the clock lines ($^1S_0 \rightarrow {}^3P_J$, $J = 0, 2$) are negligible. For the excited $^3P_1$ state, the NIST line database lists alone 63 transitions in the wavelength range of 200 nm to 300 nm with only a handful of lines with known linewidths. Using the approximate model for the AC polarizability, interpolating some transition probabilities as described in section 5.1.1 and calculating the light shift for the bosonic isotopes at the four given probe wavelengths results in light shifts in the mHz to Hz range as given in table 6.3.

The so far neglected counterrotating term in the Dipole shift is the Bloch-Siegert shift [220], given as $\delta\nu = \frac{\Omega^2}{8\pi\,\omega_0} = \frac{\Gamma^2}{16\pi\,\omega_0}\frac{I}{I_{\mathrm{sat}}}$ to first order [159]. While this can reach kHz magnitude at strong driving amplitudes, considering our sub-MHz Rabi frequencies this shift is only on the order of a few mHz and can therefore also be ignored completely.

An isotope dependence of the off-resonant light shift can only originate from the isotope-shifted position of the individual atomic resonances the probed level can couple to. Since these lines are many terahertz detuned, the isotopic variation in the light shift is orders of magnitude smaller than the shift itself, and we assume this effect negligible. Note that in this calculation we consider potential shifts originating from polarization-sensitive off-resonant coupling to Zeeman shifted $m_F = \pm 1$ excited ($^3P_1$) states to be small and ignore them.

Probe beam induced on-resonant light shift Driving a two-level system on-resonant, leads to a dressed state picture of atom + lightfield system, where the two levels are then shifted in their relative energy by $\hbar\sqrt{\Omega^2 + \Delta^2}$ (Rabi splitting). While this can lead to line broadening and splitting at large saturation, only asymmetric steady-state populations of the dressed states would introduce a shift. At the intensities involved here, we expect potential corrections to be negligible.

MOT beam induced near-resonant light shift In the setting of absorption imaging, light shifts induced by the MOT cooling beams are switched off by spectroscopically addressing the atoms in free fall. As we could still record remaining first order AOM diffraction of the MOT AOM when disabling the DDS integrated RF switch, we installed a second switch after the RF amplifier that feeds the AOM. No UV light could be detected on an amplified avalanche photodetector, restricting possible residual power to <10 nW per beam. We ensure to trigger the MOT light switch off slightly before (~ 3(2) µs) the snubber controlled magnetic gradient field switch off to reduce both atom loss and residual velocity components of the MOT cloud after release. Any residual light shifts from the MOT beams are considered common mode and too small to be considered here.

Doppler shifts

Doppler shifts $\vec{k} \cdot \vec{v}$ due to non-zero atomic velocity are identified to be the strongest systematics contribution. While most Doppler shifts originate from MOT dynamics and are common mode for all isotopes, the mass dependence of an atomic recoil induced velocity by photon scattering can render this shift to be slightly isotope dependent.

Recoil induced Doppler shifts We observe a linear dependence of the observed resonance frequencies on probe beam intensity of about $a_I^{202} = \delta\nu^{202}/I_{\text{probe}} = 167(64)\,\text{kHz}/(\text{mW}/\text{cm}^2)$ as characterized for ^{202}Hg and shown in figure 6.8. We assume this shift to dominantly originate from the probe beam recoil induced Doppler shift and characterize the shift by fitting the asymmetric lineshape model, equation (6.19), to all data, as discussed above. The linear calibration fit of the detected atomic resonance of isotope $A' = 202$ is extrapolated to all other isotopes A via their masses m_A. The data is then corrected according to

$$\delta^A_{\text{cav}} \rightarrow \delta^A_{\text{cav}} - aI_{\text{probe}} = \delta^A_{\text{cav}} - a_I^{A'} \frac{m_{A'}}{m_A} I_{\text{probe}} , \tag{6.20}$$

where the large nuclear masses render the isotope dependency small – about 0.16(6) kHz/amu at a mean intensity of $\langle I_{\text{probe}} \rangle = 0.195(3)\,\text{mW}/\text{cm}^2$. The intensity I_{probe} and its uncertainty are again extracted from the reference image of the absorption imaging sequence that shows the unperturbed probe beam, and we average the detected counts weighted by the fitted atom location for all shots individually. While not necessary for the correction, we benchmark the intensity determination, taking into account the sensor pixel size and imaging magnification to a diode-based powermeter, which shows good agreement in the measurement uncertainty.

Doppler broadening The finite temperature of the atomic cloud leads to Doppler broadening of the line as discussed in section 4.3.1. Following the formula for the Doppler width given in equation (6.17), it slightly increases the fit uncertainty on the spectroscopy lines, but does not contribute to any shift. We estimate a Gaussian width of $\Sigma_D = 2\pi \times 0.6(2)$ MHz for typical atom temperatures of $T = 0.5(3)$ mK at the given detuning and MOT beam intensity, which only slightly increases the Lorentzian natural linewidth with negligible uncertainty contribution.

Atomic motion Non-zero average velocities of the atomic cloud released from the MOT can originate from power imbalance in the opposing MOT beams and can be further amplified by imperfections in the beam shape and small misalignments of the retroreflection beam path. To suppress resulting Doppler shifts, we optimize the cooling light power balance to ensure MOT cloud trajectories are as straight as possible and follow a free fall behavior, but with only two imaging axes we can not fully

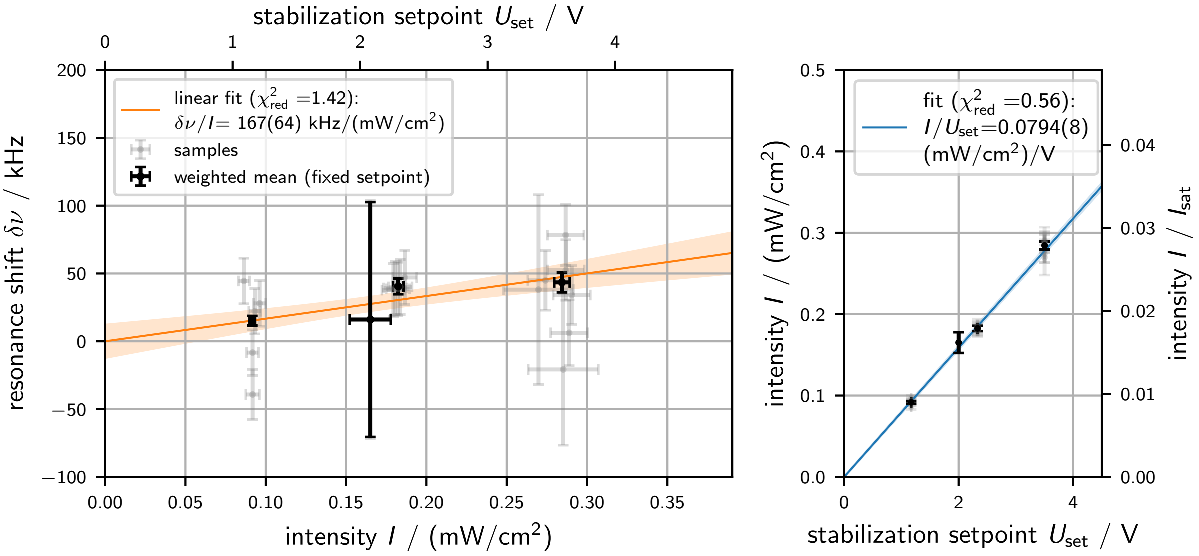

Figure 6.8: $^1\mathrm{S}_0 \rightarrow {}^3\mathrm{P}_1$ resonance shift in dependence of the optical beam power of the spectroscopy beam for four different intensity set points U_set of the probe beam power stabilization.

characterize the complete three-dimensional atom trajectory. From the atom trajectories we estimate velocities originating from the power imbalance to $\ll 1.5\,\mathrm{mm/s}$ and resulting shifts to $|\delta\nu_\mathrm{imb}| \ll 5\,\mathrm{kHz}$ and resulting isotope mass dependent contributions to $|\delta\nu^A_\mathrm{imb} - \delta\nu^{A'}_\mathrm{imb}| \ll 15(90)\,\mathrm{Hz/amu}$. Gravity induced velocity of the free-falling atoms is kept low, as the spectroscopy imaging pulse is located as close to the switch off point as experimentally feasible. Atom trajectories over the temporal duration of the spectroscopy pulse can lead to downward velocities of up to 100 mm/s, but already small angle misalignments between probe beam axis and gravity lead to Doppler shifts. With an estimate for the angle $\measuredangle(\mathrm{probe}, \mathrm{gravity}) = 90(3)^\circ$, this results in $|\delta\nu_\mathrm{grav}| \leq 20\,\mathrm{kHz}$ absolute shift and we assume this to be isotope independent within our stated uncertainty.

At the given atomic density, collisional broadening and shifts are negligible, contributing only a few hundred hertz to the linewidth – orders of magnitude smaller than the natural linewidth. Background gas collisions have an even smaller effect.

Zeeman shifts

Note that the measurement presented here could not yet benefit from the improved magnetic field control including updated gradient field coils and compensation fields, as introduced in section 4.5. Instead, the atoms fall in a non-zero residual magnetic gradient field that is induced by eddy currents in the coil support structure. This dominantly provides a vertical orientated guiding field for the falling atoms, but as the MOT is not point-like, individual atoms can experience different magnetic field directions, which defines their quantization axis for light field polarization. Due to the residual gradient field at the time of the spectroscopy pulse, Zeeman splitting of the excited $m_F = \pm 1$ can shift the atomic resonance, when the atomic quantization axis is aligned, such that the vertically polarized probe beam addresses $\sigma_\pm$ transitions. While a perfectly round cloud at the center of a quadrupole field just broadens the transition, inhomogeneities in the atomic cloud shape can probe different regions of magnetic field and amplify the shift. We measure only a minor influence of the applied gradient field strength on the atomic resonance as shown in figure 6.9.[1] As we can observe a slight quadratic behavior of the data, we analyze both the MOT shape and position of the MOT cloud for varying field strengths (the latter shown in the figure), but do not find any strong correlation to the observed shift. Therefore, we attempt a data-driven prediction for the observed shift. We model the influence of the two $m_F = 0 \to m_{F'} = \pm 1$ Zeeman shifted transitions on the resonance determination of the $m_F = 0 \to m_{F'} = 0$ magnetic insensitive transition. We numerically compute the sum of the three Lorentzian lineshapes

$$L_{\text{tot}}(\Delta) = L(\Delta - \Delta\mu\, B_{\text{eff}}/\hbar,\, \Gamma) + L(\Delta,\, \Gamma) + L(\Delta + \Delta\mu\, B_{\text{eff}}/\hbar,\, \Gamma) \tag{6.21}$$

for a varying effective magnetic field strengths $B_{\text{eff}} = m\, I_{\text{grad}}$ and determine the resulting signal's apparent resonance location (maximum determination). The parameter m models how the inhomogeneous cloud spatially samples the gradient field. As only asymmetric addressing of the $\sigma_\pm$-transitions lead to shifts of the resonance, we determine the ratio of the experimentally observed $m_F = 0 \to m_{F'} = -1$ transition strength $A_{-1}/A_0 = 1.208(16)$ and $m_F = 0 \to F' = +1$ transition strength $A_{+1}/A_0 = 1.009(17)$ from the gradient field calibration measurement. Assuming a Lorentzian linewidth of $\Gamma = 2\pi \times 2.157(69)$ MHz (measured), we obtain the "Zeeman shift model"-labeled resonance shift dependency (blue dashed) as shown in figure 6.9 with only the parameter m being free in the fit. While the dependency on the gradient field strength is expected – small fields induce less Zeeman shift of the $\Delta m_F = \pm 1$ transitions which therefore influence the center resonance stronger until the three lineshapes overlap, resulting in no shift at zero field – the data is not sufficient to compare the three fit models. In combination with analysis of the MOT position, the model confirms that, when operating at sufficiently large gradient field strengths, the three resonances are displaced far enough to be even insensitive to MOT movement within the gradient field.

In the ISS measurement, we load all isotopes at a MOT gradient field of $\partial B/\partial z = -10.1(1)$ G/cm ($I_{\text{grad}} = 50$ A), while for better contrast of the low atom numbers we probe some of the isotope ^{196}Hg MOTs at $-16.2(1)$ G/cm (80 A) instead. Only for ^{196}Hg this systematic therefore could contribute to an isotope dependent shift. We utilize the quadratic model for conservatively correcting all atom resonances to cavity detunings, according to

$$\delta^\star_{\text{cav}} \to \delta^\star_{\text{cav}} - \left[a_B\, (I_{\text{grad}} - I^{(0)}_{\text{grad}}) + b_B\right] . \tag{6.22}$$

For ^{196}Hg this results in a small shift and a larger added uncertainty of $-5(15)$ kHz in agreement with the observation and the three fit models.

Drift of the frequency reference

Systematic shift As the cavity spacer is aging, it undergoes structural relaxation which slightly changes the length of the cavity. As this drift is very well understood and no deviation from a linear length change is expected, we use the atoms themselves to calibrate the drift. A simultaneous linear

---

[1] As we were not able to measure this dependency on the original gradient coil setup, we simulate the slow gradient field switch off in the new (not eddy current limited) gradient field coils by analog ramping of the power supply current via the ARTIQ Zotino DAC controller, reproducing the original switch off behavior, as measured via fast magnetic field probes.

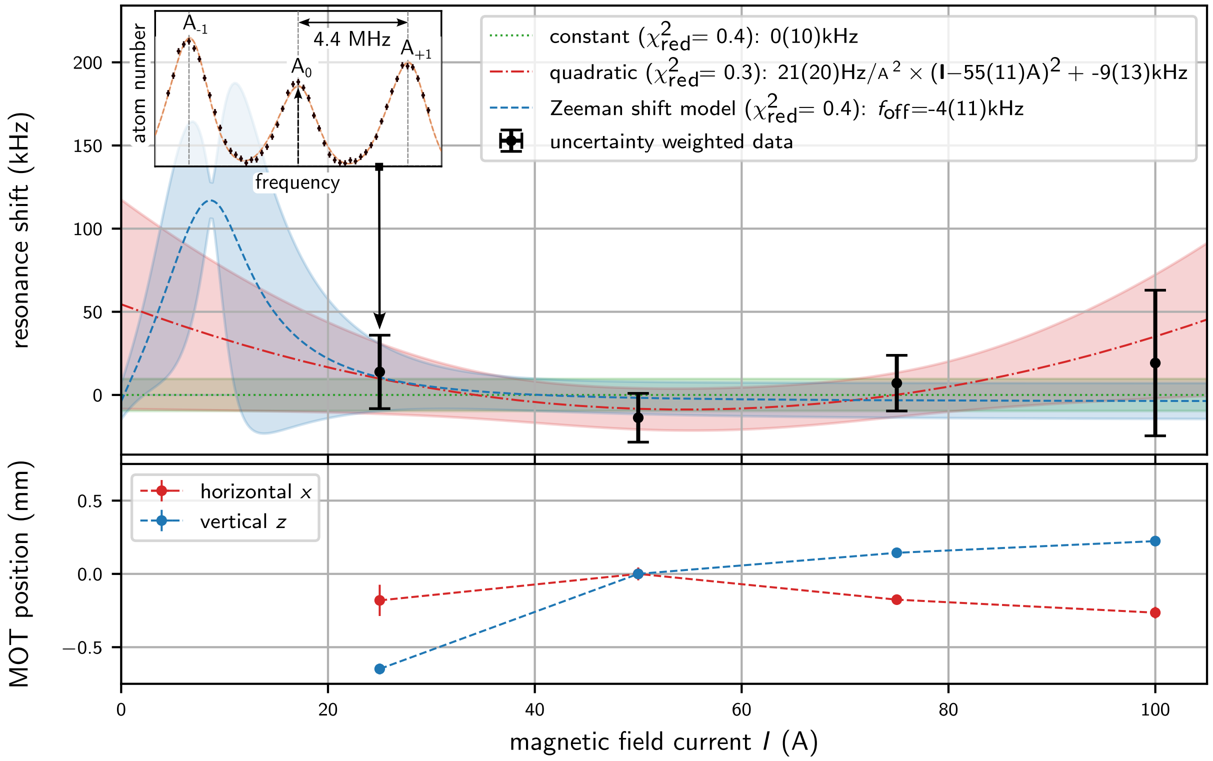

Figure 6.9: $^1\mathrm{S}_0 \rightarrow {}^3\mathrm{P}_1$ resonance shift of ^{202}Hg in dependence of the residual gradient field strength of the MOT. Each data point is averaged over two consecutive measurements, while the three different fits – constant (green), quadratic (red) and the Zeeman shift model explained in the text (blue) are applied to the raw data. The shaded areas indicate 1σ errorbands. The inset shows a spectroscopy measurement at a low magnetic field current of $I_{\mathrm{grad}} = 25\,\mathrm{A}$, where we could still load enough atoms for a qualitative analysis, indicating the three line amplitudes A_0, $A_{\pm 1}$, as used for the Zeeman shift model fit function (blue dashed). No significant sensitivity to the slight position-dependency of the MOT cloud (bottom) can be resolved.

fit to the atom resonance to cavity detuning against time

$$\delta^{\star(A)}_{\mathrm{cav}} = a_{\mathrm{cav}}\, t + \langle \delta^{\star(A)}_{\mathrm{cav}} \rangle \tag{6.23}$$

with a common slope a_{cav} for all isotopes A resolves and confirms the linearity of this drift. We show the results of the linear fit in combination with a weighted residual analysis in figure 6.10. Note that the data shown is adjusted for all other systematic shifts discussed before, the result being a very good fit quality, as the uncertainty estimates are rather conservative. We extract a slope of $a_{\mathrm{cav}} = -0.798(18)\,\mathrm{Hz/s}$ in the UV frequencies, which corresponds to a drift of $-0.200(4)\,\mathrm{Hz/s}$ in the IR, which agrees perfectly with the manufacturers' specification. This results in a maximum absolute drift of the frequency reference of 1517(34) kHz during the 22 days long IS measurement campaign.

While the fit quality is good, we can identify some outliers and a slight asymmetry in the residuals, especially considering the ^{196}Hg data. The outlier pairs at day 11 are shared between ^{196}Hg, ^{198}Hg and ^{202}Hg, indicating the presence of a local, not corrected systematic shift at that day. We estimate, that either a potential multimodality of the master laser diode or a spurious ground-loop induced

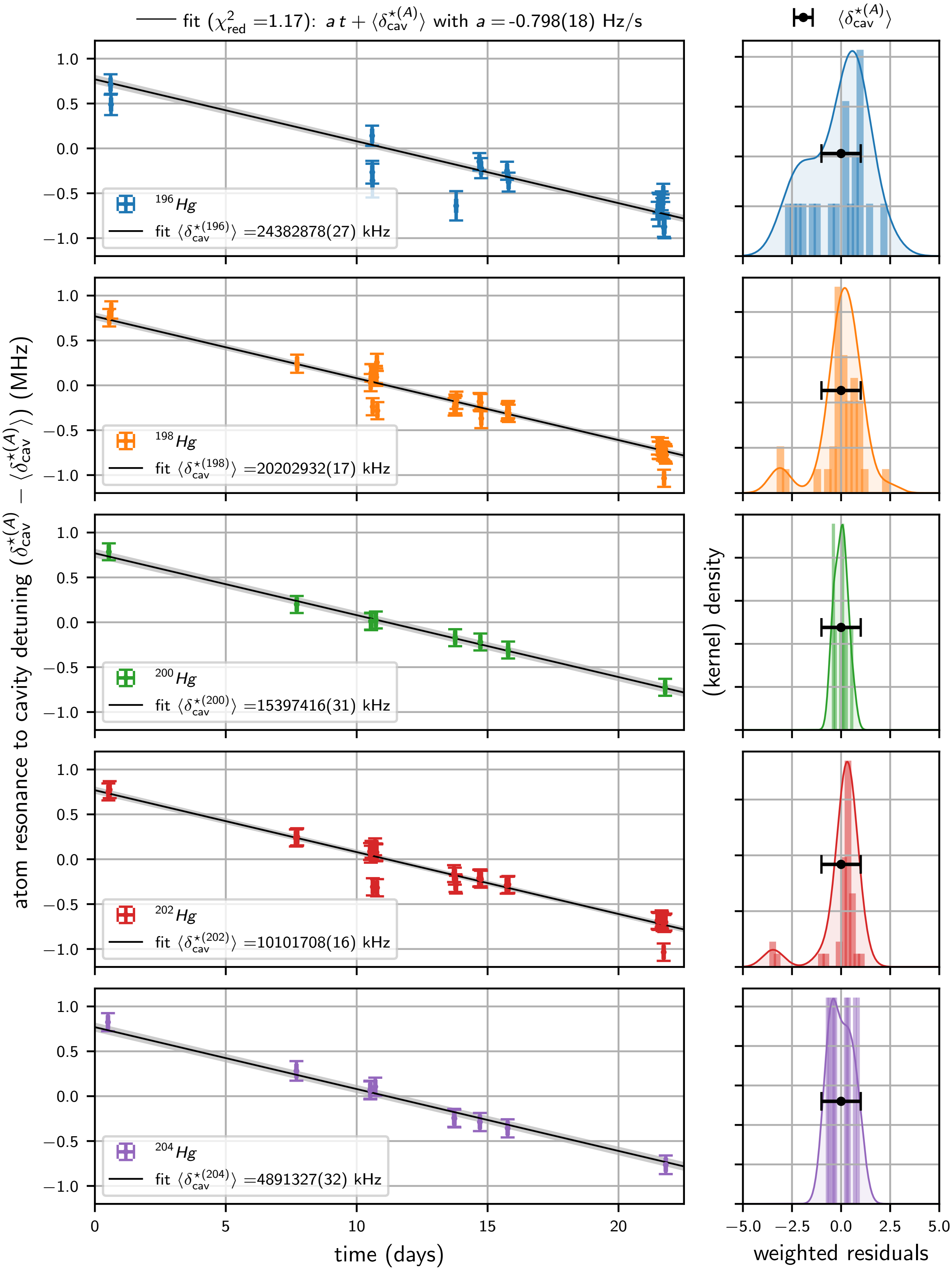

Figure 6.10: $^1\mathrm{S}_0 \rightarrow {}^3\mathrm{P}_1$ atom resonance to cavity detuning $\delta^{\star(A)}_{\mathrm{cav}}$ data samples for all five bosonic isotopes (A) taken over the measurement campaign (left column, upper plots). A corresponding simultaneous linear fit of all data with shared slope a accounts for the reference drift due to ultra-low expansion (ULE) cavity aging determines the resonance frequencies of the individual isotopes via the axis intercepts $\langle\delta^{\star(A)}_{\mathrm{cav}}\rangle$. The fit residuals are plotted against their timestamp (left column, lower plots) and their distribution is shown as a histogram and kernel density estimate (right column) to estimate fit bias.

electronic DC offset might have influenced the cavity lock error signal. Alternatively, an imperfect balance of cooling beam power originating from thermal drifts or a human error in positioning an iris or temporary beam dump in the optical beam path could potentially also introduce these shifts. As we don't have any other observable confirming these systematics, we do not exclude the data from the linear fit. Determining the atomic number and resonance for ^{196}Hg is particularly challenging due to low atomic densities – see figure 6.7. Consequently, this dataset exhibits the most pronounced asymmetry in the weighted residual distribution. Furthermore, the constant offset fitted to the spectroscopy data shows the largest variation across the entire dataset in this case, since the contrast of the far-detuned spectroscopy signal is too low to reliably extract atom numbers. The fit uncertainties stated below take into account all of these deviations in a symmetrized error bar.

6.2.4 Results

Atom resonance to cavity detuning We use the combined linear fit of the cavity drift, equation (6.23), to remove the remaining systematic from the data. The y-axis intercept provides us directly with the averaged atom resonance to cavity detuning $\langle \delta_{\mathrm{cav}}^{\star(A)} \rangle$. They are given including their total uncertainty estimates and their correlations in table 6.4. We determine the cavity to atom resonance detunings down to 16 kHz, about a hundredth of the observed linewidth.

The correlations indicate that parameter estimates are mostly independent, with expected negative interaction between the shared slope and the individual intercepts. The fit parameter confidence intervals were analyzed via the `kafe2` `python` toolbox's [295] contour profiler, which interfaces the `Minuit2` `C++` library maintained by the CERN ROOT team [296]. Here, nearly round confidence interval ellipsoids indicate good parameter estimates with small correlations and no signature of parameter bias.

Subtracting the time dependence of the frequency reference from the atom cavity detuning, the full systematic shift corrected frequencies then reads

$$\delta_{\mathrm{cav}}^{\star(A)} \to \delta_{\mathrm{cav}}^{\star(A)} \quad - \quad a I_{\mathrm{probe}} \quad - \quad a_B \left(I_{\mathrm{grad}} - I_{\mathrm{grad}}^{(0)} \right) - b_B \quad - \quad a_{\mathrm{cav}}\, t \,. \tag{6.24}$$

Averaging $\delta_{\mathrm{cav}}^{\star(A)}$ taking into account all systematic uncertainties and their correlations, we obtain the same results and uncertainties as given above. The shift-corrected $\delta_{\mathrm{cav}}^{\star(A)}$ are chosen as the horizontal axis in figure 6.7, so that the displayed spectroscopy data is adjusted from all systematic shifts and the resonances visually align with each other.

Isotope shifts Taking into account all correlations via the variance-covariance matrix we can compute the IS following equation (6.14). We obtain the values listed in table 6.5 for all combinations of isotopes. The gradient of the shift of isotopes – the relative shift between isotope pairs $(A,\, A+2)$ – is 4.872 888(17) GHz averaged over all isotope pairs considered here and increases from the light isotopes upwards. The exception being the heaviest isotope pair's shift $\delta\nu^{204-202}$, that sits the closest to the neutron shell closure and is most sensitive to onsets of nuclear deformations (NDs), as discussed in section 2.1.2. We resolve the IS to about 2 % to 3 % of the natural linewidth, dominated by systematic uncertainties and therefore provide a new potential benchmark for nuclear structure theory [77]. The combined systematic and statistical error are smallest for the best resolved isotopes ^{198}Hg and ^{202}Hg with 22 kHz of total uncertainty and increase to over 40 kHz for less resolved pairs. We analyze potential bias by computing the correlations, which we are also given in table 6.5, for simplicity reduced to ^{198}Hg as a fixed reference isotope. We identify weak positive correlations between the ISs, as they are subject to the same systematic corrections.

Comparison to literature We compare our spectroscopy results to experimental literature data [168, 172, 285, 297] (where available) and theoretical predictions [289] as shown in figure 6.11. While our values mostly agree with the older optical spectroscopy data from 1963 and 1977 within their error bars [168, 297], our uncertainties are more than two orders of magnitude smaller and only a comparison to the more recent Doppler-free absorption spectroscopy data in Witkowski et al. [172] and Gravina et al. [285] gives more insight. Therefore, we show the ISs with respect to ^{202}Hg, as Gravina et al. [285] probed $A = 200$ and 202 only. We observe a slight 2σ-deviation in the ^{198}Hg to ^{202}Hg IS with respect to Witkowski et al. and a stronger $> 3\sigma$-deviation with respect to

A	$\langle\delta_{\mathrm{cav}}^{\star(A)}\rangle$ (kHz)
196	24 382 878(27)
198	20 202 932(17)
200	15 397 416(31)
202	10 101 708(16)
204	4 891 327(32)

	a_{cav}	$\langle\delta_{\mathrm{cav}}^{\star(196)}\rangle$	$\langle\delta_{\mathrm{cav}}^{\star(198)}\rangle$	$\langle\delta_{\mathrm{cav}}^{\star(200)}\rangle$	$\langle\delta_{\mathrm{cav}}^{\star(202)}\rangle$	$\langle\delta_{\mathrm{cav}}^{\star(204)}\rangle$
a_{cav}	1.00	−0.32	−0.36	−0.03	−0.33	−0.04
$\langle\delta_{\mathrm{cav}}^{\star(196)}\rangle$	−0.32	1.00	0.12	0.01	0.11	0.01
$\langle\delta_{\mathrm{cav}}^{\star(198)}\rangle$	−0.36	0.12	1.00	0.01	0.12	0.02
$\langle\delta_{\mathrm{cav}}^{\star(200)}\rangle$	−0.03	0.01	0.01	1.00	0.01	0.00
$\langle\delta_{\mathrm{cav}}^{\star(202)}\rangle$	−0.33	0.11	0.12	0.01	1.00	0.01
$\langle\delta_{\mathrm{cav}}^{\star(204)}\rangle$	−0.04	0.01	0.02	0.00	0.01	1.00

Table 6.4: $^1\mathrm{S}_0 \rightarrow {}^3\mathrm{P}_1$ atom resonance to cavity detuning and associated correlations (including the shared slope parameter a_{cav}) as extracted from the simultaneous linear fit, as given in equation 6.23 and shown in figure 6.10. The given uncertainties are the combined systematic and statistical error bars originating from the analysis above.

$\delta\nu^{A-A'}$ (kHz)	A'			
A	196	198	200	202
196	0(0)			
198	−4 179 946(30)	0(0)		
200	−8 985 462(41)	−4 805 516(36)	0(0)	
202	−14 281 170(30)	−10 101 224(22)	−5 295 708(35)	0(0)
204	−19 491 551(42)	−15 311 605(36)	−10 506 089(45)	−5 210 382(36)

	$\delta\nu^{196-198}$	$\delta\nu^{200-198}$	$\delta\nu^{202-198}$	$\delta\nu^{204-198}$
$\delta\nu^{196-198}$	1.00			
$\delta\nu^{200-198}$	0.22	1.00		
$\delta\nu^{202-198}$	0.38	0.34	1.00	
$\delta\nu^{204-198}$	0.22	0.22	0.33	1.00

Table 6.5: ISs on the $^1\mathrm{S}_0 \rightarrow {}^3\mathrm{P}_1$ transition extracted from spectroscopy (top) and associated (symmetric) correlation matrix (bottom). Uncertainties represent the combined statistical and systematic uncertainty of the analysis. For simplicity the correlation matrix is shown for a fixed reference isotope $A' = 198$ only.

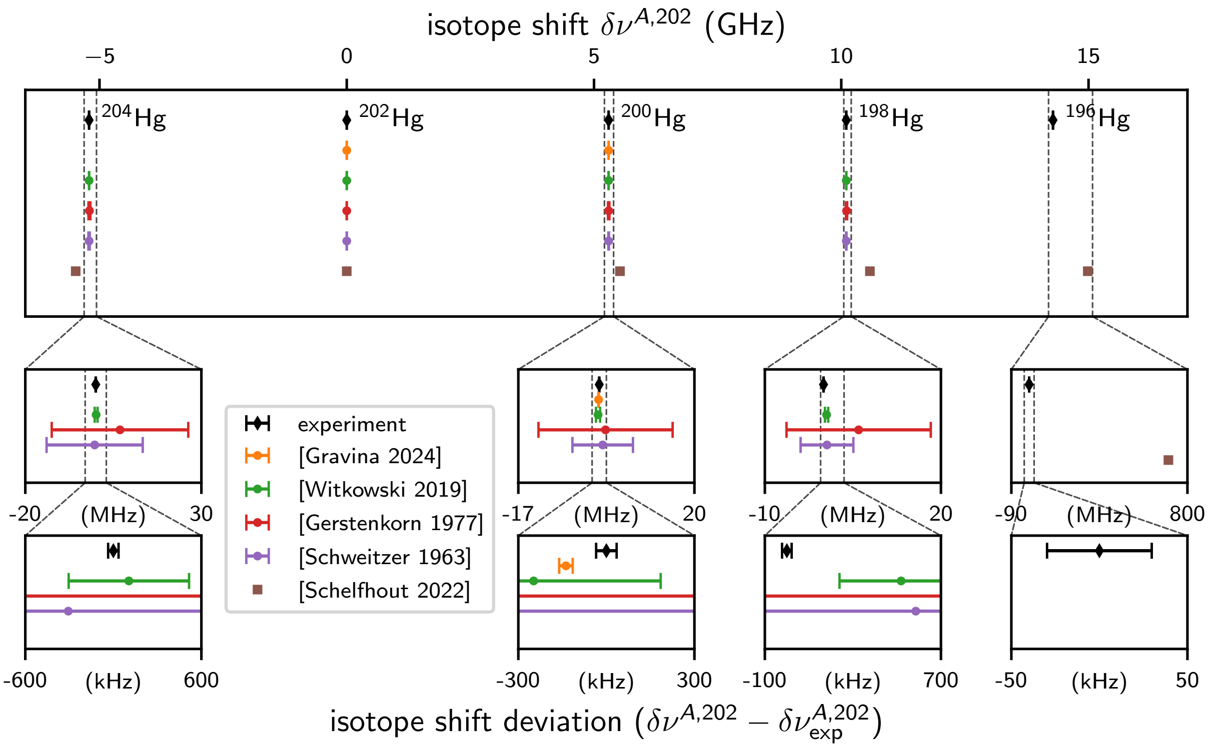

Figure 6.11: Comparison of our $^1\mathrm{S}_0 \rightarrow {}^3\mathrm{P}_1$ ISS data (diamond, black) compared to other experimental literature values [168, 172, 285, 297] (point) and theory prediction [289] (square, brown), where data is available. The subplots show the zoomed in IS deviation with respect to our experimental data.

Gravina et al.. As uncharacterized systematic shifts can be present in both the gas cell Doppler free absorption spectroscopy and our cold atom IS measurement, future measurements are required to find an explanation for these deviations. We suggest a spectroscopy interrogation of laser cooled Hg atoms loaded to the ODT as an option to cross-check these measurements. The theoretical predictions of ISs from multiconfiguration Dirac-Hartree-Fock calculations in Schelfhout et al. [289] has no specified uncertainty and our IS data agrees only approximately. We deviate 270 MHz for ^{204}Hg up to −704 MHz for ^{196}Hg, which is not surprising, as electronic structure calculations for heavy elements are not expected to predict atomic line frequencies to much better than 1 %. No comparison for the ^{196}Hg IS can be made, as to our knowledge the here obtained value represents the very fist measurement of the IS of this low abundant species.

6.3 Spectroscopy on $^3\mathrm{P}_1 \rightarrow {}^3\mathrm{D}_J$ $(J = 1, 2)$

As discussed in section 6.1.3, the previous experimental section focused on probing a transition involving the $^1\mathrm{S}_0$ ground state due to its sensitivity in probing nuclear structure via the FS. Building on this, we will now consider the Doppler-allowed 6s 6d $^3\mathrm{P}_1 \rightarrow$ 6s 6d $^3\mathrm{D}_J$ lines with $J = 1, 2$ that do not involve S-states. As we will discuss in more detail in section 6.4 on KP analysis, this approach provides complementary access to different FS-sensitivities and serves as a useful reference for isolating state-dependent KP-nonlinearities.

For the spectroscopy on the two $\Gamma/(2\pi) \approx 9$ MHz broad lines at around 313 nm, connecting the excited state $^3\mathrm{P}_1$ of the laser cooling transition to the $^3\mathrm{D}_J$ states, we probe the atoms by depleting the MOT atom numbers via probe light at the spectroscopy line resonance. The spectroscopy scheme is illustrated in figure 6.2. The individual mercury isotope is magneto-optically trapped on $^1\mathrm{S}_0 \rightarrow {}^3\mathrm{P}_1$, which pumps a small percentage of the atoms to the excited $^3\mathrm{P}_1$ state depending on MOT beam intensity and detuning.[1] Due to exposure to near-resonant probe light atoms can then be excited to the $^3\mathrm{D}_J$ state, that has a lifetime of about 8(2) ns – see table in figure 6.2 – and exhibits three ($J = 2$) or four ($J = 1$) distinct decay channels. The branching ratios let about 60 % of the atoms directly decay back to the $^3\mathrm{P}_1$ and the rest to the singlet and triplet states in the 6s 6p-shell [91]. At the level of the probe beam intensity (typically we use $s_0 \leq 0.01$), decay to $^3\mathrm{P}_1$ is dominated by spontaneous and not stimulated emission and atoms on this path are quickly broad back into the MOT cycle. Atoms that decay into the singlet $^1\mathrm{P}_1$ state also mostly remain trapped, as its lifetime is very short. The very long lifetime of the metastable triplet $^3\mathrm{P}_2$ and $^3\mathrm{P}_0$ states makes atoms transparent for the MOT cooling light and therefore leads to atom loss. The latter can be detected by a reduction of fluorescence counts on the $^3\mathrm{P}_1 \rightarrow {}^1\mathrm{S}_0$ transition, we typically reach a contrast of about 35 % as shown below.[2]

We initially planned the spectroscopy pulse to act in free fall after releasing the cooled cloud from the MOT, which both allows for reducing the light shift due to the MOT cooling beams[3] and strong suppression of Zeeman shifts, when also deactivating the magnetic gradient fields. For this purpose, we also chose the spectroscopy beam axis along the horizontal plane of the chamber and carefully align its polarization orthogonally to it. With the installed vertical magnetic guiding field coil pair, this allows addressing of π-polarized and magnetically insensitive $m_F = 0 \rightarrow m_{F'} = 0$ transitions. Atoms can then be spectroscopically addressed in a 1 ms to 5 ms time window after the switch off of the MOT cooling light.

We can either detect them by absorption imaging in free fall ($t_{\mathrm{img}} \approx 150\,\mu\mathrm{s}$ short exposure) or by recapturing the atoms within the MOT and imaging them by fluorescence as scattered from the cooling light beams. The option of fluorescence detection introduces a slight isotope abundance dependent atom number background by reloading atoms from the background gas. It however allows for much longer camera exposure times ($t_{\mathrm{exp}} = 1\,\mathrm{ms}$ to $100\,\mathrm{ms}$) and much higher photon collection counts, which increases the signal drastically and improves signal-to-noise. We therefore found this imaging scheme to be advantageous over absorption imaging for spectroscopy signal generation, which also pushed the installation of the second camera system, see section 4.4, forward.

While we could successfully test the overall spectroscopy scheme for the two most abundant bosonic isotopes ($^{202}\mathrm{Hg}$, $^{198}\mathrm{Hg}$), the lack of sufficient 313 nm laser power at the location of the atoms strongly limited the removal of atoms from the MOT and therefore also the signal contrast. This was mainly constraint by the bad diffraction efficiency of the spectroscopy AOM double-pass setup, described below, which we required to avoid a frequency-dependent movement of the spectroscopy probe beam. A

---

[1] Following equation (4.5) given a saturation parameter of ≈ 2.5 to 3.0 per MOT beam and a typical MOT detuning of $\Delta = -5\,\Gamma$ to $-15\,\Gamma$, optimized for high atom numbers, we obtain a steady-state excited state population of $\rho_{ee} = 2.0(1.1)\,\%$. [2] Collecting 313 nm fluorescence instead could be a valid alternative measurement scheme, as the scattering rate is also enhanced by the much broader line. At the time, however, we did not have a suitable spectral bandpass filter to remove the MOT pump light from the camera, so we ignored this option.

[3] Note that optical pumping to the excited $^3\mathrm{P}_1$ state always requires some form of light field at 254 nm, but choosing a slightly weaker pump beam with well-defined polarization and respective magnetic quantization field axis would allow addressing magnetically insensitive transitions and improved control over the light shifts.

single-pass setup leads to frequency-dependent beam pointing causing deformation of the spectroscopy lineshape, as the depletion scheme is much more sensitive to probe beam intensity compared to the ISS scheme via absorption imaging on the intercombination line. We estimated that this limitation in probe pulse intensity would not allow detection of the less abundant isotopes, where limited signal-to-noise requires much larger spectroscopy contrasts. Note that at the time of the ISS measurement campaign, the setup was still limited by the extended eddy current induced switch off time of the gradient coils, which slightly reduces the advantages of the scheme. We will revisit the originally planned measurement sequence, including further already implemented upgrades to the machine that removes the need for a double-pass AOM setup, in the outlook of this chapter, see section 6.5.

Due to the technical limitation at the time,[1] the data presented in the following originates in our first attempt of resolving the ISs of all bosonic isotopes based on a measurement scheme were we expose the laser cooled atomic cloud during MOT operation. The corresponding sequence is shown in figure 6.12. We load atoms in the MOT for a loading time[2] of $t_{\mathrm{load}} = 3\,\mathrm{s}$ and then expose the atoms to the spectroscopy light at 313 nm for $t_{\mathrm{spec}} = 150\,\mathrm{ms}$ and collect the 254 nm fluorescence on the charge-coupled device (CCD) camera.[3] The spectroscopy probe beam is vertically polarized and propagates along the y-axis of the vacuum chamber, as defined in figure 3.7. At the beginning of the sequence, a background image is recorded with cooling/pump beams but without MOT atoms. These fluorescence counts are subtracted from the spectroscopy image data to account for drifts in optical power that determine stray light contributions.

The here presented data is the result of two about 9 h long measurement campaigns, where we iterate between the isotopes, each probed about 20 times.[4] Different to the $^1\mathrm{S}_0 \rightarrow {}^3\mathrm{P}_1$ spectroscopy, we step the AOM probe beam frequency in small steps from red to blue detuning of the line, we will discuss the systematic shifts originating from this technique below.

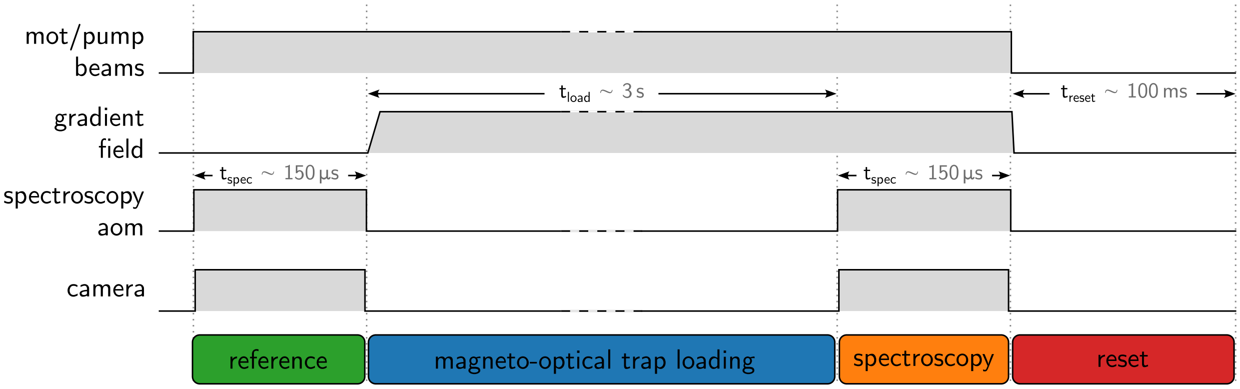

Figure 6.12: Sequence timing of the 313 nm spectroscopy measurement. The timing is not fully to scale, as indicated by the dashed lines.

---

[1] We lost both the source chamber and vacuum in the main chamber due to a power outage soon after and could not yet attempt a new measurement. [2] This was a compromise of sequence duration and most efficient MOT loading. The characteristic $1/e$ loading time was $\tau \approx 3.5(2)\,\mathrm{s}$ at the given background pressure and peak atom numbers are therefore only reached after about 15 s. [3] To not collect 313 nm fluorescence in the process, a narrowband spectral filter (Newport 10MLF10-254 Mercury Line Bandpass Filter, 253.7(3.0) nm center wavelength, 11(3) nm FWHM) can be installed on the CCD camera. We estimate the blocking band around 313 nm to be $OD > 8$. Note that the measured transmission of 19(1) % at 253.7 nm however reduces the collection efficiency of MOT fluorescence. [4] We filter out data when the laser fell out of lock due to acoustic disturbances.

6.3.1 Laser system at 313 nm

The UV light for $^3\mathrm{P}_1 \rightarrow {}^3\mathrm{D}_J$ spectroscopy is derived from the infrared by fifth harmonic generation via three consecutive nonlinear conversion stages. The fundamental frequency ν is converted towards the red via second-harmonic generation (SHG), the resulting photons via sum frequency generation (SFG) to the green and then again via SFG to the UV:

$$\nu \xrightarrow[2\times\nu]{\textbf{SHG}} (\nu, 2\nu) \xrightarrow[\nu+2\nu]{\textbf{SFG}} (\nu, 2\nu, 3\nu) \xrightarrow[2\nu+3\nu]{\textbf{SFG}} (\nu, 2\nu, 3\nu, 5\nu) = \mathbf{5\times\nu} \tag{6.25}$$

This system was first set up within the group in the master thesis of Maya Büki [298] for precision spectroscopy of the intercombination cooling transition ($^1\mathrm{S}_0 \rightarrow {}^3\mathrm{P}_1$) at 308 nm and the clock transition ($^1\mathrm{S}_0 \rightarrow {}^3\mathrm{P}_1$) at 310 nm of atomic zinc, reaching about 0.5 mW in the UV. This promised probe beam intensities of up to $s_0 = I/I_{\mathrm{sat}} = 0.40(18)$ for the here considered transitions, that are given in table 6.1. Here, we assume a beam waist of 1 mm and an AOM diffraction efficiency of 50 %. Providing more than enough for ISS, we decided to convert the system to work at around 313 nm. More details on the first implementation including results on laser spectroscopy of zinc can be found in reference [299]. More details on the individual frequency conversion stages for creation of 313 nm light discussed below can be found in the master thesis of Felix Affeld [91].

The full optical setup of the laser system and IR and UV frequency control for spectroscopy is shown in figure 6.13. We replaced the fiber seed laser with limited tuning range by a tunable, narrow linewidth external-cavity diode laser[1] operating in the telecom C band at around 1565 nm. The master laser providing ≤ 45 mW is fiber coupled (FC) and separated using a beam splitter (BS) into two paths. One for stabilization to the ultrastable cavity setup presented in section 4.3.3 and described below and one to seed an erbium-doped fiber amplifier[2] (FA) that amplifies the laser power up to 17.5 W.

Second harmonic generation to 782 nm We use a 5 % magnesium doped periodically poled lithium niobate $\mathrm{LiNbO_3}$ crystal (MgO:PPLN)[3] for SHG to 782.5 nm. The periodical structure and resulting nonlinear coefficient of the PPLN nonlinear crystal allows to circumvent limitations of normal birefringent phase matching (e.g., via angle and temperature tuning) for the two pump and the converted photon by quasi-phase matching. The change of ferroelectric domains within the crystal of poling period Λ simplifies the phase matching condition to $\Delta k = k_{2\nu} - 2\times k_\nu - 2\pi/\Lambda \approx 0$, which allows maintaining an optimal phase relation between input ν and generated photons $2\times\nu$ throughout the crystal and extends the range of wavelengths that can be efficiently converted over classical nonlinear crystals in bulk form. The crystal features nine periodically poled $0.5\times 0.5\,\mathrm{mm}^2$ wide gratings with poling periods between $\Lambda = 18.5\,\mu\mathrm{m}$ to $20.9\,\mu\mathrm{m}$ separated by regions of unpoled material and allows for a broad spectrum of fundamental wavelengths for SHG conversion.

A lens (L) focuses the beam to about $w_0 \approx 37\,\mu\mathrm{m}$, which we found to be optimal for conversion efficiency, agreeing with the prediction from the Boyd-Kleinman SHG theory, $L/(2\,z_R) \approx 2.84$ with $L = 40.0(5)$ mm the crystal length and $z_R = \pi w_0^2/\lambda$ the pump beam's Rayleigh length [300]. We find that adjusting the focus to the front end of the crystal gives us best efficiency illustrating the waveguide-like structure of the crystal structure. All focussing lenses (L) are mounted in adjustable lens tubes and the crystals are positioned with the help of a five axis pitch, yaw, and translation stage

---

[1] Toptica DLC DL Pro. [2] NKT Photonics Koheras BOOSTIK HP. [3] Covesion MSHG1550-0.5-40.

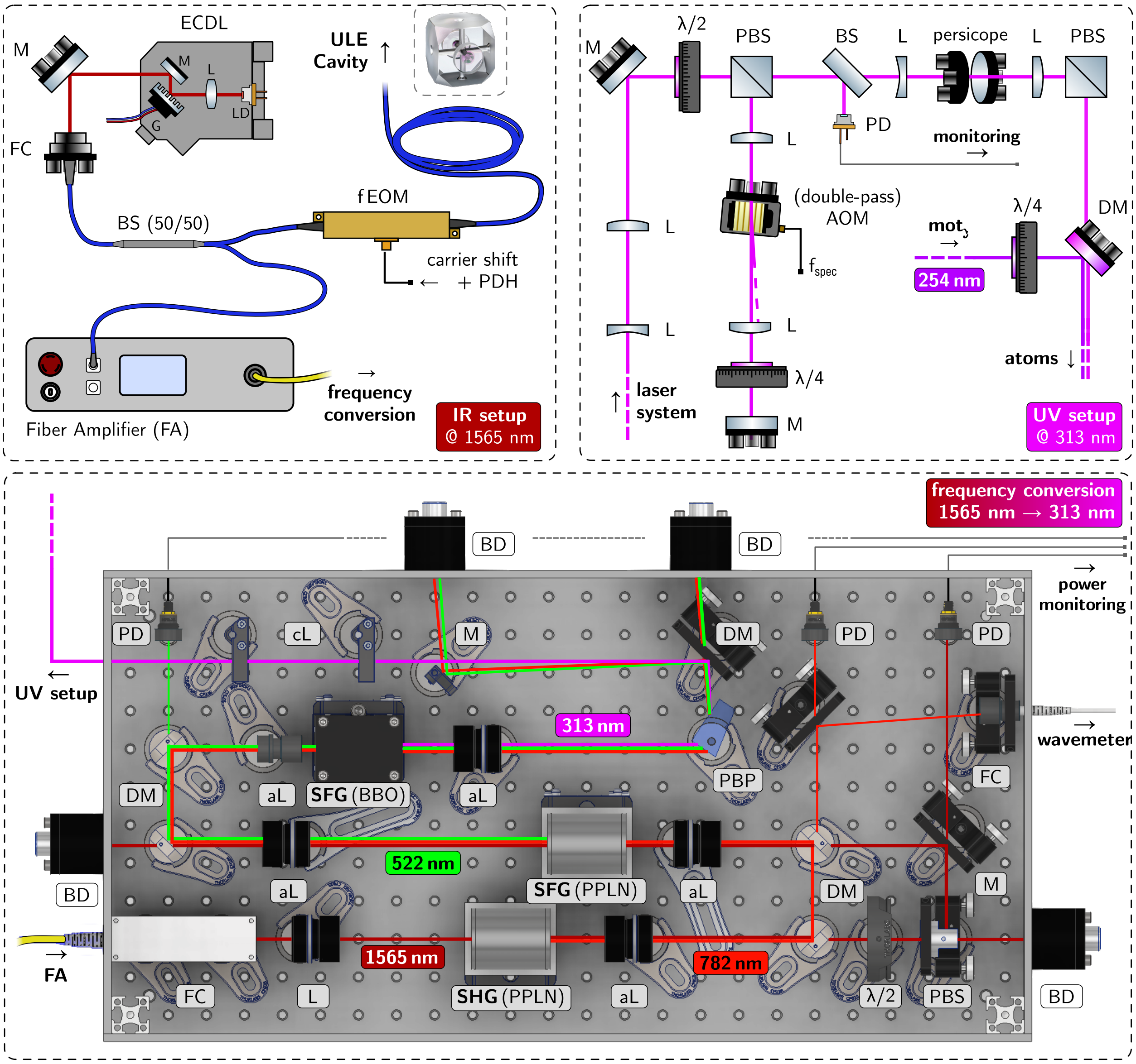

Figure 6.13: Optical setup of the laser system for spectroscopy of the $^3\mathrm{P}_1 \rightarrow {}^3\mathrm{D}_J$ ($J = 1, 2$) lines generated by fifth-harmonic generation (bottom), its frequency control in the infrared at 1565 nm (top left) and in the UV at 313 nm (top right). For a detailed description see the main text.

for optimizing coupling and phase matching.

We work in a type 0 phase-matching configuration where the input polarization of the pump beam (optimized by rotating the fiber coupler) is identical to that of the generated second harmonic. The crystal is enclosed in an oven[1] for temperature control and stabilization to <0.1 K. Using the $\Lambda = 19.7\,\mu\mathrm{m}$ poled crystal channel and adjusting the crystal temperature to 50.8(1) °C, we obtain a conversion efficiency of up to $\eta_{\mathrm{conv}} = P_{2\nu}/(P_\nu^2\, L) = 0.56(5)\,\%/(\mathrm{W\,cm})$, which drops to about $0.40(5)\,\%/(\mathrm{W\,cm})$ at full power. The converted light power follows the expected quadratic power scaling as shown in figure 6.14. This gives us approximately $P_{2\nu} = 4.9(5)$ W of power at 782 nm and has been shown to be very stable over long timescales.

---

[1] Covesion PV40.

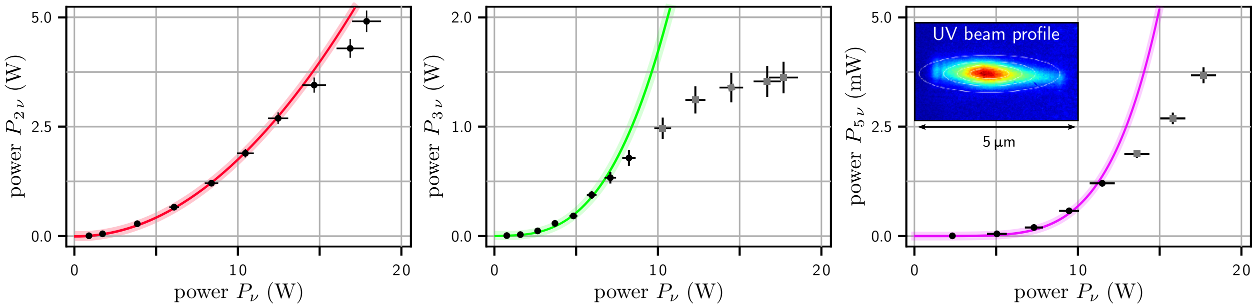

Figure 6.14: Conversion efficiency in the three nonlinear crystal frequency conversion stages of the 313 nm laser system. The power of the second-harmonic generation process $P_{2\,\nu}$ (left) and of the two sum frequency generation stages to third harmonic into the green $P_{3\,\nu}$ (middle) and fifth harmonic into the UV $P_{5\,\nu}$ (right) are shown with respect to the infrared pump power P_ν. The solid curves show the expected $P_{2\,\nu} \propto P_\nu^2$, $P_{3\,\nu} \propto P_\nu^3$, and $P_{5\,\nu} \propto P_\nu^5$ scaling laws, as fitted to the data (black data points). The significant deviation for higher infrared power (gray data points) is related to the green-induced infrared absorption (GRIIRA) effect, as explained in the text. All data and the photo of the UV beam profile are taken from reference [91].

Sum frequency generation to 522 nm For focussing and re-collimating converted and unconverted light, we use achromatic doublet lenses (aL) in all conversion stages. The second stage is also based on a MgO:PPLN waveguide crystal[1] of $L = 40$ mm length and same poling grating arrangement as in the first stage. From the nine gratings with $\Lambda = 6.00\,\mu$m to $8.36\,\mu$m sized domains, we find the best quasi phase matching conditions and best conversion efficiency at $\Lambda = 7.10\,\mu$m.

Sum frequency generation efficiency in PPLN at the desired wavelengths is strongly limited by effect of green-induced infrared absorption (GRIIRA) of crystal defect induced polarons and thermal effects [301]. To minimize these losses and avoid damage to the crystal, we reduce the power of the infrared light using a set of statically mounted dichroic mirrors (DM) in long-pass configuration and a combination of half waveplate ($\lambda/2$) and polarization beam splitter (PBS) cube. The latter are set up in kinematic mirror mounts to allow realignment of the 1565 nm beam to the 782 nm beam and efficient in-coupling to the SFG crystal.

Calibrated photodiodes (PDs) monitor the power of both infrared laser beams and the 782 nm light is fiber coupled to a single mode fiber for wavemeter readout[2] that allows for quick localization of the atomic resonances of the mercury isotopes. For SFG we focus into the five-axis stage-mounted and temperature controlled crystal to a waist of about 58(5) µm for the idler at 1565 nm and 49(5) µm for the signal wavelength at 782 nm and find optimal crystal temperature around 55 °C.

The discussed losses in the second conversion stage lead to a diversion from the expected scaling law $P_{3\,\nu} \propto P_\nu^3$ starting around $P_\nu = 10$ W of infrared input power and limit the overall conversion efficiency. The efficiency of $\eta_{\mathrm{conv}} = P_{3\nu}/(P_\nu\, P_{2\,\nu}\, L) = 2.7(2)\,\%/(\mathrm{W\,cm})$ for low input power reduces to about $0.45(6)\,\%/(\mathrm{W\,cm})$ at maximum input power, $P_\nu = 17.5$ W. The latter gives us up to $P_{3\,\nu} = 1.5(1)$ W of optical power in the green for conversion to the UV.

Sum frequency generation to 313 nm Conversion to 313 nm is performed by SFG of the near-infrared $2\,\nu$ and green $3\,\nu$ light in a beta barium borate (BBO) crystal. We use a bulk crystal instead

---

[1] Covesion MOPO515-0.5-40. [2] HighFinesse WS8-10.

of PPLN for its wide transparency range from ~ 190 nm to 3500 nm and strong birefringence. This allows us to use type I phase matching between idler, signal and generated photon $\vec{k}_{2\nu} + \vec{k}_{3\nu} = \vec{k}_{5\nu}$. For this we use a crystal with a cutting angle of 38°, which results in an extraordinary polarized output beam orthogonal to the vertical polarized pump fields. The crystal is housed in a self-built temperature controlled box that also acts as dust protection, as especially the UV light attracts dust by photoelectric charging of crystal surfaces.[1]

We focus the input beams to a waist of about 14(2) µm at 782 nm and 18(3) µm at 522 nm. This gives us about $P_{5\nu} = 0.8(1)$ mW of 313 nm light at a crystal temperature of about 60 °C, which is slightly more efficient than demonstrated in reference [299]. The UV laser light is separated by a Pellin-Brocca prism (PBP), after which a set of cylindrical lenses corrects for the elliptical beam profile – see the inset in figure 6.14 – that forms due to the spatial Poynting vector walk-off of the UV light in the nonlinear crystal ($\lesssim 3°$).

Laser lock The full frequency conversion laser system was transferred to a small footprint optical breadboard that can be enclosed for laser safety and dust protection, which makes the overall system easily transportable. The fiber coupled external-cavity diode laser (ECDL) master laser sits on a separate optical table close to the cavity lock setup, the latter explained in section 4.3.3 and shown in figure 4.8. The 1565 nm laser is split in a fiber BS that feeds fiber amplifier and cavity lock. Identical to the 1016 nm stabilization, we employ a fiber-coupled EOM[2] (fEOM) for Pound-Drever-Hall (PDH) sideband generation at $f_\mathrm{pdh} \approx 11$ MHz and for offsetting the laser system from the cavity resonances by $\pm f_\mathrm{eom}$ to address individual isotopes spectroscopically.

We ensure that the two cavity locks are not affecting each other by observing the error signal in presence and absence of the other laser light and compare the free spectral range in the locked state. Thermal affects are avoided by sending only 100 µW to 150 µW of total optical power (fundamental + shifted carriers + sidebands) to the cavity. To address this, we introduce a fiber attenuator between fiber BS and EOM (not shown), which also helps to suppress any unwanted back-reflections into the ECDL, as the latter is not equipped with an optical isolator. Only about 43 % of the modulated light is typically at the EOM sideband corresponding to the carrier shift f_eom that is locked to the cavity (at an optimized modulation depth of $\beta_\mathrm{eom} = 1.841$). The electronic setup is very similar to the RF circuit of the 1016 nm lock as shown in figure 4.8, and we reach comparable lock performance.

313 nm spectroscopy setup To prepare the 313 nm spectroscopy light for the atoms, we focus the beam using a telescope and adjust the polarization to the vertical for a double-pass AOM setup. Similar to the 254 nm setup, the double-pass AOM diffraction efficiency is again strongly limited by the large polarization sensitivity due to crystal birefringence. The single-pass efficiency achieved for a beam waist of 35 µm drops from about 50(1) % for *s*-polarized light to about 11(2) % for *p*-polarization [91, p. 66, Figure 7.17]. In contrast to the 254 nm setup, however, here we separate the outgoing and returning beams via the polarization. A calibrated photodetector monitors the spectroscopy beam (= second AOM order) intensity. A telescope adjusts the beam size to 911(10) µm in the horizontal and 1154(10) µm in the vertical direction. A periscope brings the beam up to vacuum chamber height.

The 313 nm light is superimposed with the circularly polarized MOT light along the y-axis of the

---

[1] At the very small UV powers involved here, we do not observe any degradation of the crystal surfaces due to solarization. [2] JenOptik PM1550.

vacuum chamber via a high-reflectivity 254 nm UV fused silica mirror acting as a dichroic mirror ($T \approx 80\,\%$ at 313 nm). Stepping the AOM frequency allows probing the lineshape of the transition. We typically scan the RF synthesizer by ±30 MHz around the AOM frequency that optimizes diffraction efficiency (around 217 MHz), which corresponds to a span of 120 MHz at the location of the atoms, enough to probe the about 10 MHz to 15 MHz wide lines. We keep the spectroscopy beam intensity approximately constant over the frequency range by a repeated calibration via the photodetector and a look-up table for the RF power required for each spectroscopy frequency. Dominated by the bad double pass efficiency this overall limits the probe beam power to just 30(5) µW at the location of the atoms. Note that moving the laser frequency via the laser lock offset to the cavity using the EOM, as was done for the MOT cooling beam (see the outlook in section 4.8), was not yet possible at that time. The PLL VCO frequency generator[1] used for EOM carrier shift generation did not allow for continuous frequency sweeps without losing the cavity lock.

6.3.2 Frequency reference

As described above, the spectroscopy laser is again stabilized to the ultrastable cavity, with the IR master laser offset from the cavity resonances by the carrier shift EOM frequency f_{eom}. With the UV laser being derived by the fifth-harmonic and given the double-pass AOM setup, that shifts the spectroscopy probe beam frequency by $2\,f_{\mathrm{aom}}$, the atom cavity detuning is given by

$$\delta_{\mathrm{cav}} \equiv \nu_{\mathrm{probe}} - 5\,\nu_{\mathrm{cav},\,0} = 5\,\left(i_{\mathrm{cav}}\,\delta_{\mathrm{fsr}} \pm f_{\mathrm{eom}}\right) + 2\,f_{\mathrm{aom}}\,.\,. \tag{6.26}$$

Here, ± again denotes the sign of the EOM sideband used for locking and $i_{\mathrm{cav}} \in \mathbb{N}$ the cavity resonance index. For the spectroscopy on $^3\mathrm{P}_1 \rightarrow {}^3\mathrm{D}_J$ ($J = 1, 2$) the ISs are on the order of 350 MHz, which allows to reference all measurements with respect to a single cavity resonance line $i_{\mathrm{cav}} = 0$ with sign -1. This removes the dependency on the cavity free spectral range. ISs can then again be obtained by equation (6.14) taking into account all correlations between observables.

For absolute frequency measurements of the atomic resonances of the different isotopes, the wavemeter recording of the second-harmonic $\nu_{782} = 2 \times \nu_{\mathrm{IR}}$ (located at around 782 nm) of the master laser can be utilized. Taking into account the fifth-harmonic generation process and the double-pass AOM, with the spectroscopy beam probing the atomic resonance $\nu^\star$ at an AOM frequency of $f^\star_{\mathrm{aom}}$, the following relation holds

$$\nu^\star = 5\,\nu_{\mathrm{IR}} + 2\,f^\star_{\mathrm{aom}} = (5/2)\,\nu_{782} + 2\,f^\star_{\mathrm{aom}}\,. \tag{6.27}$$

6.3.3 Spectroscopy

The experimental sequence described above computes and stores the background corrected fluorescence counts with their associated AOM and EOM frequencies and a combination of three reference images at the beginning, end and location of minimum atom number of the sequence. An exemplary dataset including all systematic uncertainties, that are discussed below, is shown in figure 6.15 as a function of the cavity detuning. The lineshape model used for extraction of the resonance frequency from a nonlinear fit will be discussed below. All spectroscopy curves for all isotopes recorded during this measurement campaign are shown in figure 6.16 and figure 6.17, respectively.

---

[1] Rhode & Schwarz SML-02.

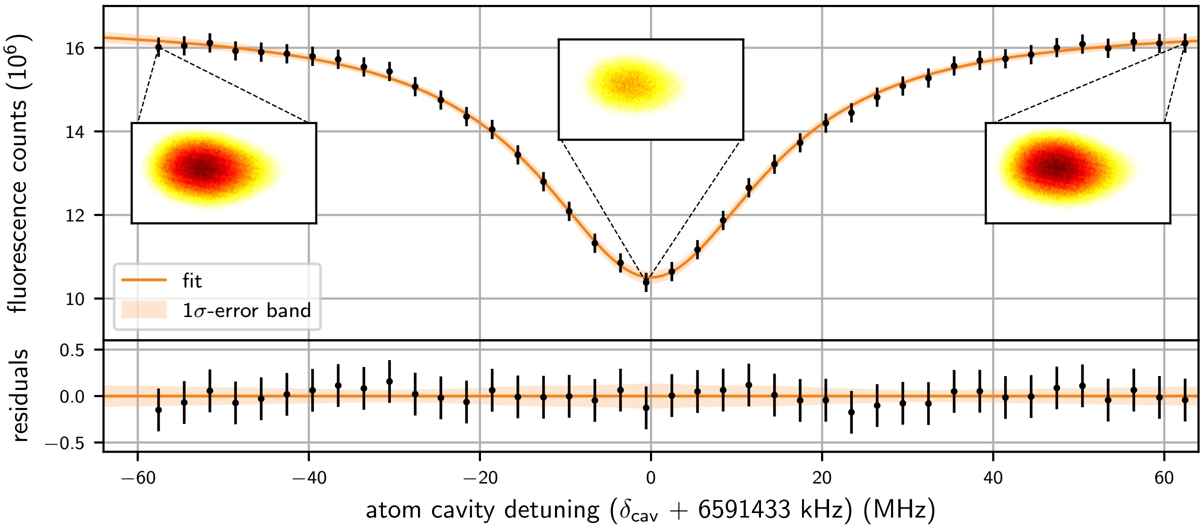

Figure 6.15: Exemplary data for the spectroscopy of ^{202}Hg via MOT depletion on the $^3\mathrm{P}_1 \rightarrow {}^3\mathrm{D}_1$ line. Each data point is the result of the spectroscopy measurement sequence shown in figure 6.12 for various spectroscopy AOM frequencies. The inset shows a false color display the atomic fluorescence as collected by the CCD camera at the respective atom cavity detuning, indicating the depleted MOT atom number on resonance. The fit model is defined in equation (6.31). Note that both the fluorescence counts and the fit residuals include horizontal error bars, that are smaller than the data points.

Lineshape

For determination of the lineshape we do not need to consider the full level spectrum that is involved in the excitation process, as shown in figure 6.2. Instead, we assume $N(t)$ atoms at given time t to be cycled on the $^1\mathrm{S}_0 \rightarrow {}^3\mathrm{P}_1$ transition, pumped by the MOT beam and detected via their fluorescence during the imaging pulse.

Assuming the atom loss during spectroscopy to be dominated by spectroscopy light the atom loss rate in dependence of the spectroscopy line detuning Δ is given by

$$R_{\mathrm{loss}}(\Delta) = \beta_{\mathrm{loss}} \, \frac{\Gamma}{2} \, \frac{1}{1 + (2\,\Delta/\Gamma)^2} \,, \tag{6.28}$$

where Γ, Δ are the linewidth of and detuning to the $^3\mathrm{P}_1 \rightarrow {}^3\mathrm{D}_J$ transition. β_{loss} is the fraction of atoms in the $^3\mathrm{D}_J$ state that get lost into the metastable states $^3\mathrm{P}_0$ and $^3\mathrm{P}_2$. For now, we assume the regime of low saturation ($s_0 \ll 1$) for the spectroscopy beam and ignore any Doppler broadening of the atoms. The number of atoms after time t can then be determined from

$$\frac{\mathrm{d}N}{\mathrm{d}t} = -R_{\mathrm{loss}}(\Delta)\, N \quad \Rightarrow \quad N(t) = N_0\, e^{-R_{\mathrm{loss}}(\Delta)\, t} \,. \tag{6.29}$$

The fluorescence flux recorded by the camera is directly proportional to the atom number. From equation (4.19), the total fluorescence counts in the probe beam and camera exposure time interval

$[0, t_{\mathrm{exp}}]$ is then given by

$$\begin{aligned} n_{\mathrm{fluo}}(\Delta) &= \epsilon_{\mathrm{qe}} \frac{\delta\Omega}{\Omega} \frac{\sigma I}{E_\nu} \int\limits_0^{t_{\mathrm{exp}}} \mathrm{d}t\, N(t) \\ &= \epsilon_{\mathrm{qe}} \frac{\delta\Omega}{\Omega} \frac{\sigma I}{E_\nu} \frac{N_0}{R_{\mathrm{loss}}(\Delta)} \left(1 - e^{-R_{\mathrm{loss}}(\Delta)\, t_{\mathrm{exp}}}\right) \\ &= n_0 \left[1 + (2\,\Delta/\Gamma)^2\right] \left[1 - \exp\left(-\frac{a}{1 + (2\,\Delta/\Gamma)^2}\right)\right] . \end{aligned} \tag{6.30}$$

Here, we introduced n_0 as the background fluorescence count in absence of spectroscopy light and a describing the amplitude of the resonance dip.

We observed a small linear temporal drift of the atom number during the long measurement sequence due to instability of the 254 nm laser power, that was not yet stabilized for the spectroscopy measurements presented here. As the AOM frequency is scanned linearly in time, we incorporate this drift into the resonance fit by introducing a linear background of slope s, $n_0 + s\,\Delta$. This modifies the fit function to

$$n_{\mathrm{fluo}}(\Delta) = (n_0 + s \cdot \Delta) \left[1 + (2\,\Delta/\Gamma)^2\right] \left[1 - \exp\left(-\frac{a}{1 + (2\,\Delta/\Gamma)^2}\right)\right] . \tag{6.31}$$

We characterize the MOT atom number in absence of spectroscopy beam exposure over time, the result of which confirms this observation. In a numerical study we fit the data with fixed positive and negative slopes of varying amplitude to study potential systematic shifts originating from this drift. Following this we conservatively add a systematic uncertainty of 70 kHz to the total uncertainty budget.

We tested various fit models including pure (inverted) Lorentzian, Gaussian and Doppler-broadened Voigt profiles, which did not shift the resonance significantly, but decrease the fit quality. Comparing the residuals especially in the wings confirmed our choice for an exponentially-modified Lorentzian, as derived above. We also extended the loss rate, equation 6.28, to a Voigt profile. However, this introduces strong correlations between the increased number of fit parameters, as observed in a contour plot analysis. Furthermore, it tends to overfit the data, which is already bounded by quite large systematic uncertainties. An exemplary dataset for the spectroscopy of ^{202}Hg-atoms on $^3\mathrm{P}_1 \rightarrow {}^3\mathrm{D}_1$ is shown in figure 6.15 as a function of the atom cavity detuning δ_{cav} defined above. The spectroscopy beam detuning Δ in the fit model, equation (6.31), is then written as $\Delta = 2\pi\,(\delta_{\mathrm{cav}} - \delta^\star_{\mathrm{cav}})$, where $\delta^\star_{\mathrm{cav}}$ denotes the resonance detuning with respect to the reference cavity line. The dataset already includes all systematic error corrections that will be further discussed below.

6.3.4 Systematic shifts and uncertainties

An overview of all systematic shifts and rough uncertainty estimates is given in table 6.6, the true systematics are computed for and applied to every individual data point including their correlation. They again contribute to the uncertainty budget of the atom cavity detuning frequencies $\delta^{\star(A)}_{\mathrm{cav}}$ either via an uncertainty in the probe beam frequency ν_{probe}, via a shift or uncertainty in the atomic resonance frequency $\nu^{\star(A)}$, or via atom number uncertainties that propagate through the nonlinear fit. We again characterize and remove these systematic corrections by calibration measurements and

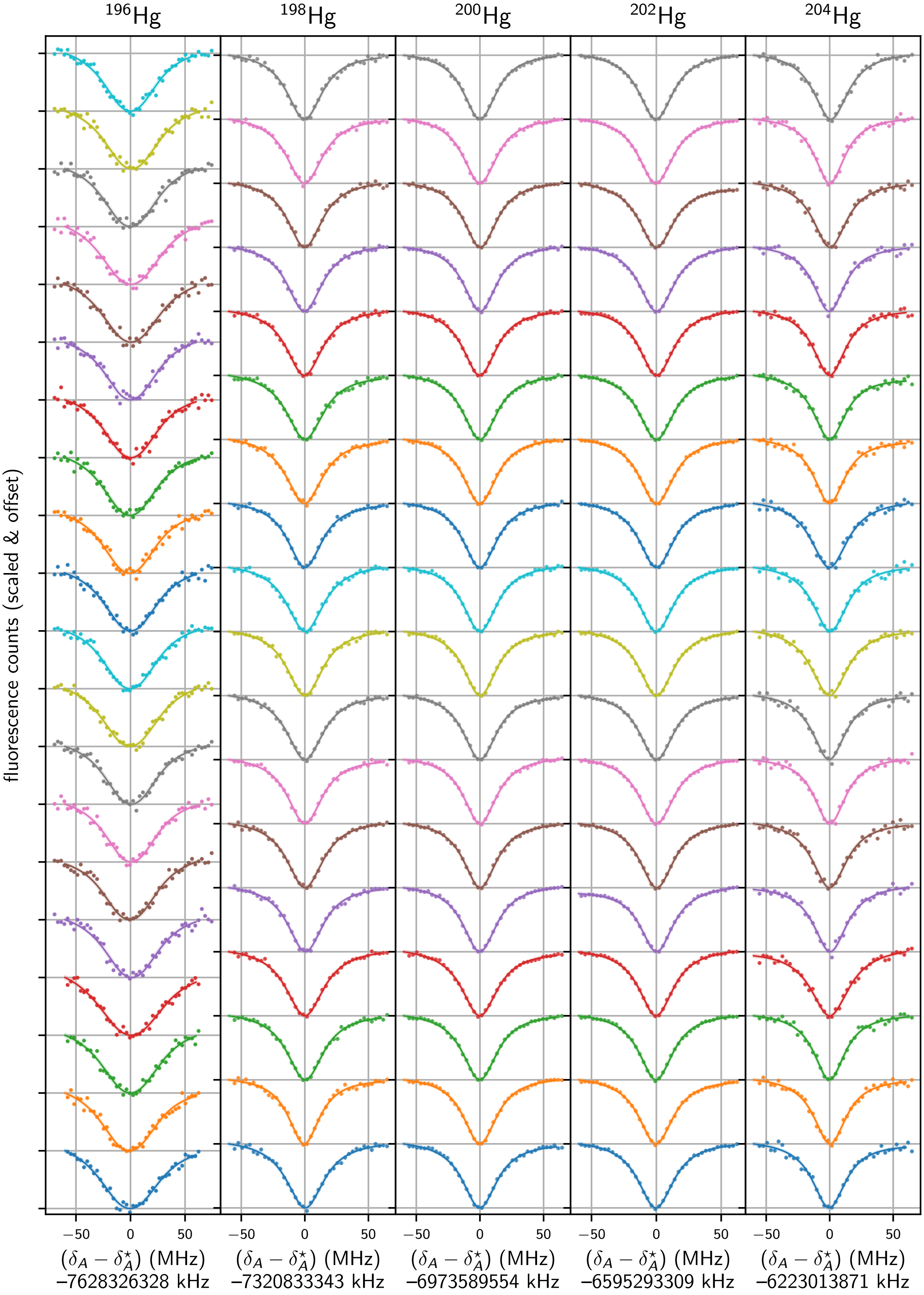

Figure 6.16: $^3P_1 \rightarrow {}^3D_1$ spectroscopy data incorporating all systematic shifts and uncertainties.

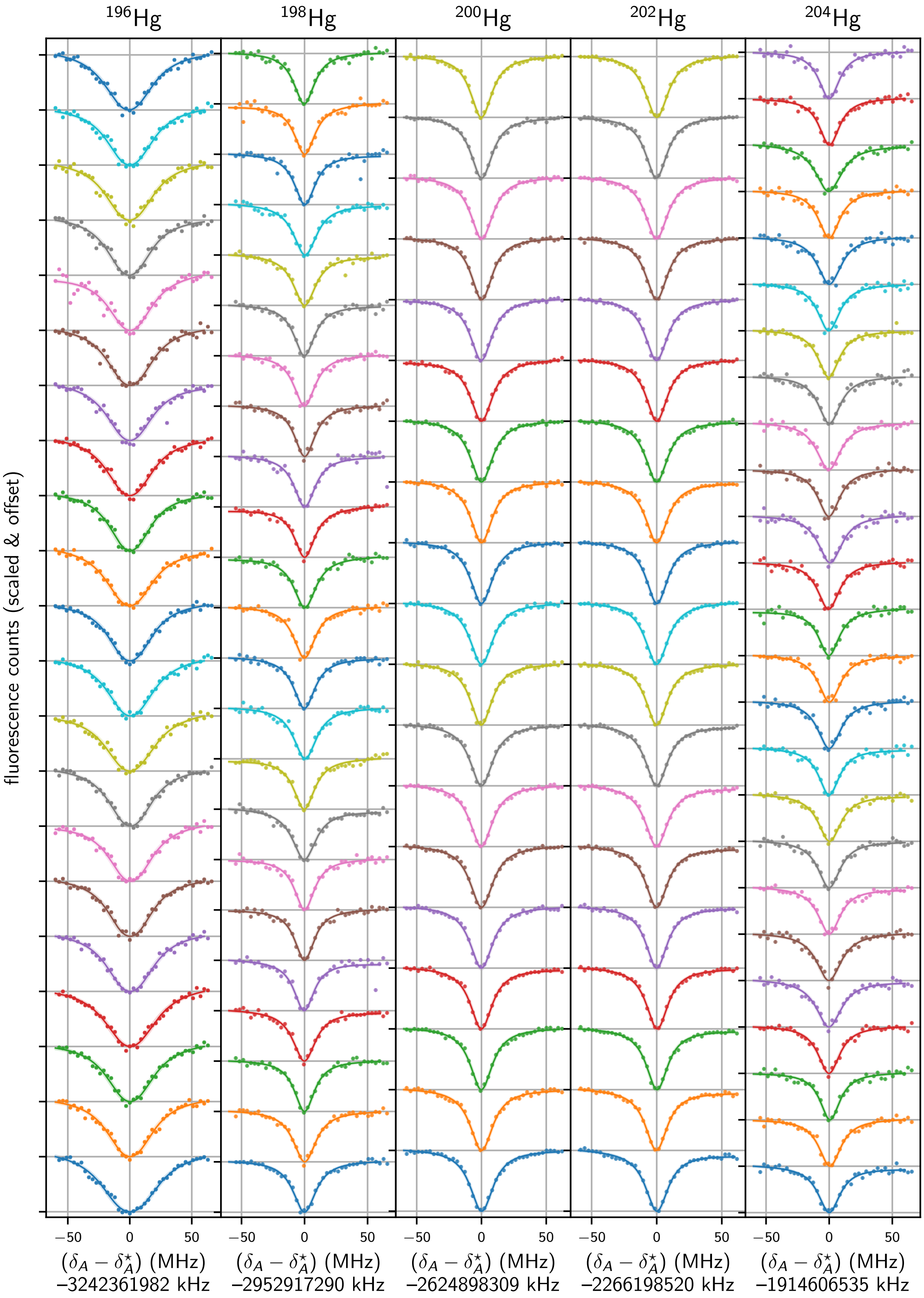

Figure 6.17: ^{3}P$_1$ → ^{3}D$_2$ spectroscopy data incorporating all systematic shifts and uncertainties.

theory input, as discussed in more detail below. For some of the uncertainties and shifts we follow the derivation of the $^1\mathrm{S}_0 \rightarrow {}^3\mathrm{P}_1$ spectroscopy systematics given in section 6.2.3.

Systematic	Correction	Estimated shift (MHz)	Source
Light shift	$\delta\nu_{\mathrm{light}}(\Delta_{\mathrm{mot}}, P_{\mathrm{mot}})$	3.90(17) −0.56(81) †	MOT beam power. and detuning induced.
Zeeman shift	$a_B\, \partial_z B + b_B$	0.00(22)	Residual gradient field.
Probe recoil	$\delta\nu_{\mathrm{probe}}$	0.00(15)	Photon recoil induced Doppler & Zeeman shift.
Reference drift	$a_{\mathrm{cav}}^{(313)}\, t$	0.026(1)	Cavity aging/relaxation.
Probe frequency	$\pm\Delta f_{\mathrm{probe}}$	0.000(15)	Laser & cavity linewidth and lock offset.
Atom number fluctuations	$\pm\Delta N$	0.000(70)	MOT beam pointing and power drift.

Table 6.6: Uncertainty budget for the $^3\mathrm{P}_1 \rightarrow {}^3\mathrm{D}_J$ ISS. Uncertainties are given as shifts to the atom cavity detuning $\delta_{\mathrm{cav}}^{\star(A)}$, either direct in a frequency uncertainty or indirect via the atom number. All shifts and uncertainties are conservatively approximations only, as their contributions to the total uncertainty cannot be fully isolated via the pull-method. The specified uncertainties in the result section can therefore be smaller than the sum of contributions given here. † = only for ^{196}Hg. Explanations to the individual contributions can be found in the text.

Laser linewidth & lock offset

We use the same tools to estimate the probe beam laser linewidth and lock offset as in the $^1\mathrm{S}_0 \rightarrow {}^3\mathrm{P}_1$ spectroscopy. While we here frequency convert to the fifth harmonic in three successive steps, the expected free-running laser linewidth is expected to be similar, as the laser noise sources are comparable – ECDL amplified by a fiber amplifier and successively frequency converted to the UV. The cavity lock shows to be much less affected by direct current (DC) offset drifts, and we do not have to correct for any changes during the measurement. We conservatively estimate a total uncertainty of 0(15) kHz.

Broadening mechanisms

Following equation (6.17), we estimate a Doppler broadened Gaussian width of $\Gamma_D = 2\pi \times 0.5(2)$ MHz for an atomic cloud temperature of $T = 0.6(4)$ mK, which only marginally increases the fit uncertainty on the spectroscopy lines, but does not contribute to any shift.

Pressure broadening and shifts are estimated to be negligible here [91]. In reference [302] the nitrogen pressure induced shifts of the $^1\mathrm{S}_0 \rightarrow {}^3\mathrm{P}_1$ line in a spectroscopy cell is estimate to −2.54(2) MHz/torr and the broadening to 9.01(4) MHz/torr. This effect is therefore strongly suppressed at the atomic density and background vacuum pressure present here [91]. We assume Hg-Hg collisional broadening and shifts to be negligible as well, also following the estimation in section 4.3.1. Transit time broadening is estimated to be $\Gamma_T \approx 2\pi \times 125$ Hz.

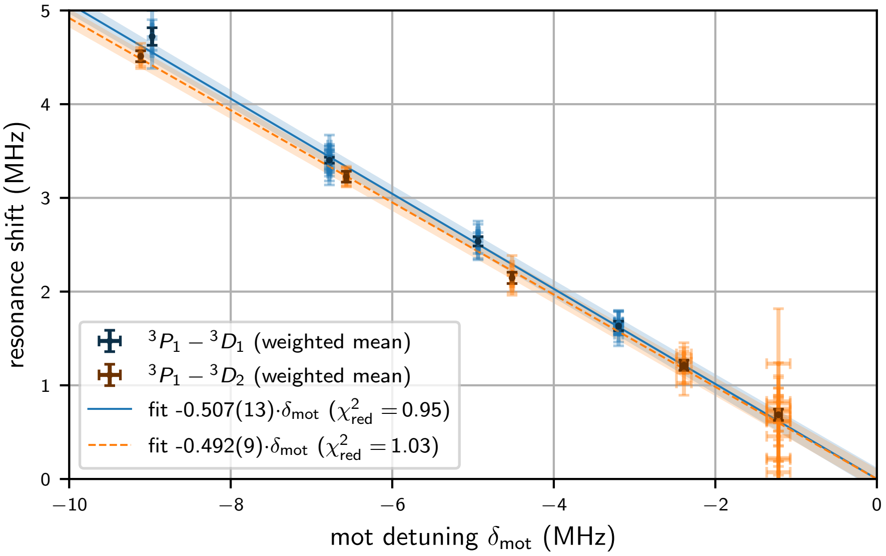

Figure 6.18: $^3\mathrm{P}_1 \rightarrow {}^3\mathrm{D}_J$ ($J = 1, 2$) resonance shift in dependence of the detuning of the MOT operated on the $^1\mathrm{S}_0 \rightarrow {}^3\mathrm{P}_1$ transition. The detuning is extracted from a separate absorption imaging spectroscopy following the methods in section 6.2 and the resonance shift is the fit intercept corrected atom resonance to cavity detuning as extracted from a exponential Lorentzian fit, as described above. The two datasets ($J = 1, 2$) show a very similar linear behavior, we therefore average the fitted slope for further analysis.

MOT beam induced near-resonant light shift

Light shift induced systematic shifts originating from the near resonant MOT cooling light is analyzed in dependence of MOT beam power P_{mot} and detuning Δ_{mot}. We measure the resonance shift on both lines for varying P_{mot}, Δ_{mot} repeatedly The former is monitored via a calibrated photodetector and the latter determined via absorption imaging spectroscopy on $^1\mathrm{S}_0 \rightarrow {}^3\mathrm{P}_1$ following section 6.2. Two measurements are performed, one for varying power at fixed MOT detuning and one with varying detuning at fixed MOT beam power. The results are shown in figure 6.18 and 6.19, from which we extract a linear dependency on both parameters.

For the MOT detuning dependency we find that two independent linear least square optimizations are both compatible with a fitted slope $a_\Delta = 0.502(7)\,\mathrm{MHz/MHz}$. This motivates that the observed light shift is strongly dominated by the shift of the $^3\mathrm{P}_1$ state by near-resonant coupling of the only a few linewidths detuned MOT cooling light. Off-resonant coupling to the $^3\mathrm{P}_1$ and $^3\mathrm{D}_J$ ($J = 1,\ 2$) states, as shown in table 6.3, are not expected to contribute significantly to the observed light shift or to shift independent of wavelength for the small range compared here. We therefore fit the dependency on the MOT cooling beam power with a shared slope linear model, as the $^3\mathrm{P}_1 \rightarrow {}^3\mathrm{D}_1$ data showed a rather noisy outlier at 5.3 mW of reference beam power. We obtain $a_P = 43(7)\,\mathrm{kHz/mW}$ of resonance shift with respect to the monitored MOT reference beam. Note that for all measurements here, the detected atom to cavity detuning was corrected by the drift of the cavity lines as described below.

As we observe linearity in P_{mot} and Δ_{mot}, we model the observed light shift, following equation (5.3), as a small linear change in the polarizability $\alpha(\Delta) \approx \alpha_0 + a_\alpha\,\Delta$, such that the observed $^3\mathrm{P}_1 \rightarrow {}^3\mathrm{D}_J$

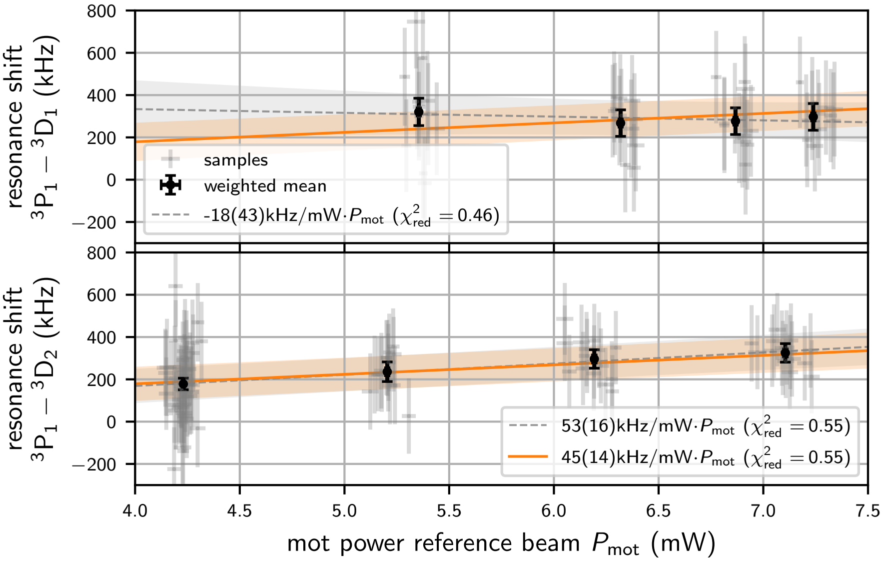

Figure 6.19: $^3\mathrm{P}_1 \to {}^3\mathrm{D}_J$ $((J = 1, 2))$ resonance shift in dependence of the optical beam power of the MOT operated on the $^1\mathrm{S}_0 \to {}^3\mathrm{P}_1$ transition. The power on the horizontal axis is a calibrated photodiode reference beam measurement at one of the MOT beams. The $^3\mathrm{P}_1 \to {}^3\mathrm{D}_1$ resonance fit is disturbed by an outlier at around 5.3 mW, which causes the slope of the individual linear regression (gray) to become negative. We therefore choose a combined fit with shared slope (orange) for further analysis. For the fits we use all data points (gray); the black error bar points indicate the weighted mean at every power set point.

$(J = 1,\ 2)$ atom resonance to cavity detuning shifts according to

$$\delta^\star_{\mathrm{cav}}(\Delta_{\mathrm{mot}},\ P_{\mathrm{mot}}) = \delta^\star_{\mathrm{cav}} - \frac{\alpha(\Delta_{\mathrm{mot}})}{2\,\epsilon_0\,h\,c}\,\frac{2\,P_{\mathrm{mot}}}{\pi\,w_0^2} = \delta^\star_{\mathrm{cav}} - \frac{1}{\epsilon_0\,h\,c\,\pi\,w_0^2}\,(\alpha_0 + a_\alpha\,\Delta_{\mathrm{mot}})\,P_{\mathrm{mot}}\,. \tag{6.32}$$

Here, w_0 is the effective MOT beam waist to convert power to intensity. Considering the two linear dependencies observed, we solve the system of equations,

$$\begin{aligned} \delta^\star_{\mathrm{cav}}(\Delta_{\mathrm{mot}},\ P^{(\Delta)}_{\mathrm{mot}}) &= a_\Delta\,\Delta_{\mathrm{mot}} + b_\Delta \\ \delta^\star_{\mathrm{cav}}(\Delta^{(P)}_{\mathrm{mot}},\ P_{\mathrm{mot}}) &= a_P\,P_{\mathrm{mot}} + b_P\,, \end{aligned} \tag{6.33}$$

for the unknowns α_0 and a_α. Here, a_Δ, b_Δ, are the slope and intercept, and $P^{(\Delta)}_{\mathrm{mot}}$ the mean MOT beam power during the measurement of the systematic shift detuning dependency. And a_P, b_P, are the slope and intercept, and $\Delta^{(P)}_{\mathrm{mot}}$ the MOT beam detuning during the measurement of the systematic shift power dependency. We therefore obtain the following correction model for the $^3\mathrm{P}_1 \to {}^3\mathrm{D}_J$ $(J = 1,\ 2)$ atom resonance to cavity detuning

$$\delta^\star_{\mathrm{cav}} \to \delta^\star_{\mathrm{cav}} - (a_\Delta\,\Delta_{\mathrm{mot}} + (b_\Delta - b_P))\,\frac{P_{\mathrm{mot}}}{P^{(\Delta)}_{\mathrm{mot}}}\,, \tag{6.34}$$

with the slope a_Δ given above, the mean power during the detuning measurement $P^{(\Delta)}_{\mathrm{mot}} = 6.5(2)$ mW, and the intercept difference given by $(b_\Delta - b_P) = -4.1(1)$ MHz.

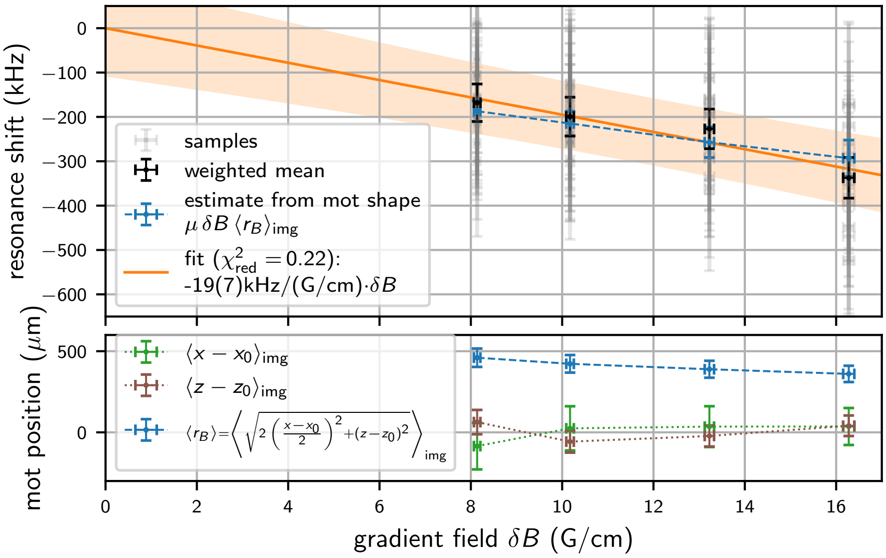

Figure 6.20: $^3P_1 \rightarrow {}^3D_2$ resonance shift of ^{202}Hg in dependence of the (vertical) gradient field strength of the MOT (top). The linear regression (orange) is applied to all collected data (gray error bars), the black error bars show the uncertainty weighted mean for each set point. The average MOT cloud position (bottom) in the horizontal (x, green) and vertical axis (z, brown) is extracted from the fluorescence image as described in the main text. Error bars originate from the 1σ standard deviation of the respective data set. The image weighted quadrupole field sensitive coordinate $\langle r_B \rangle_{\mathrm{img}}$ gives the model estimate for the resonance shift (blue).

Zeeman shifts

As we perform the spectroscopy sequence in the MOT, we need to consider Zeeman shifts originating from the coupling of the hyperfine structure components of the spectroscopy transition to the MOT gradient field, the latter defining the quantization axis for observing the vertically linearly polarized lightfield of the probe beam. Here, the position of the MOT within the gradient field, as well as spatial asymmetries in the MOT cloud, can lead to an on average non-zero magnetic field and therefore to a Zeeman shift. We characterize this shift by repeatedly probing the atomic resonance of the $^3P_1 \rightarrow {}^3D_2$ line in dependence of the gradient field strength as shown in figure 6.20. We observe a linear shift of slope $a_B = -20(5)\,\mathrm{kHz/(G/cm)}$, that leads to an atom resonance to cavity detuning correction of

$$\delta^{\star}_{\mathrm{cav}} \rightarrow \delta^{\star}_{\mathrm{cav}} - \left(a_B \frac{\partial B}{\partial z} + b_B \right) . \tag{6.35}$$

As we perform the full ISS measurement at a fixed gradient field, only changes of the MOT position and shape during the measurement can contribute to nonzero Zeeman shifts.

We confirm the atomic position dependency by a model based on the extraction of the two-dimensional MOT position in horizontal (x) and vertical (z) atom position from the fluorescence image. We determine the density weighted average atom positions $\langle x \rangle_{\mathrm{img}}$, $\langle z \rangle_{\mathrm{img}}$ in the camera image and determine the distance from their mean $\langle x - x_0 \rangle_{\mathrm{img}}$, $\langle z - z_0 \rangle_{\mathrm{img}}$. The position x_0, z_0 are then assumed to be the gradient field zero-crossing projections onto the $x\,z$-plane. The atoms approximately probe a quadrupole field with the field half the strength in the $x\,y$-plane with respect to the vertical axis with gradient $\partial B/\partial z$. We therefore compute the effective magnetic field induced Zeeman shift as

$$\delta\nu_{\mathrm{Zeeman}} = \frac{\Delta\mu}{\hbar}\frac{\partial B}{\partial z}\langle r_B\rangle_{\mathrm{img}} \tag{6.36}$$

with $\Delta\mu$ being a level and hyperfine averaged magnetic moment. Here, the quadrupole field sensitive position is defined and computed as

$$\langle r_B\rangle = \left\langle\sqrt{2\left(\frac{x - x_0}{2}\right)^2 + (z - z_0)^2}\right\rangle_{\mathrm{img}} \tag{6.37}$$

where due to limited information about the MOT shape along the y-axis, we assume an identical distribution as in x. We obtain a very close-fitting theoretical prediction of the experimentally measured Zeeman shift magnitude and its trend for an effective magnetic moment of $\Delta\mu/\hbar = 0.5\,\mathrm{MHz/G}$. This is in agreement with the expected Zeeman shift moments spanning $\Delta\mu/\hbar = 0.4\,\mathrm{MHz/G}$ to $5.3\,\mathrm{MHz/G}$ for the various $F = 1$ to $F = 2$ hyperfine components of the $^3\mathrm{P}_1 \rightarrow {}^3\mathrm{D}_2$ transition. We use this model to characterize the MOT movement and resulting shift during the ISS measurement campaign from the atomic density distribution in the fluorescence images. Therefore, we assign an additional (uncorrelated) systematic uncertainty of $\delta\nu_B = 0(220)\,\mathrm{kHz}$ to both the $^3\mathrm{P}_1 \rightarrow {}^3\mathrm{D}_1$ and $^3\mathrm{P}_1 \rightarrow {}^3\mathrm{D}_2$ atom to cavity detuning obtained.

Probe beam recoil induced shifts

Similarly to the $^1\mathrm{S}_0 \rightarrow {}^3\mathrm{P}_1$ spectroscopy, we observe a shift of the atomic resonance with probe beam power, as shown in figure 6.21, characterized for the $^3\mathrm{P}_1 \rightarrow {}^3\mathrm{D}_2$ transition. As we observe a slight linear behavior only for low optical power below 6 µW where we perform ISS, but a drastic deviation from the trend for higher powers, the origin of the shift is not fully understood.

Off-resonant light shifts originating from far detuned coupling of the $^3\mathrm{P}_1$ and $^3\mathrm{D}_J$ to other levels are negligible effects for the low probe beam intensities involved here, as shown in table 6.3. Recoil induced Doppler shifts would show in slight asymmetries of the lineshape that are not easily characterized due to the atom number drifts during the measurement, but are a possible systematic shift origin and can explain the observed shift magnitude. We observe a small radiation pressure induced shift of the MOT cloud position along the probe beam axis (= positive x-axis), as also shown in figure 6.21, which confirms our suspicion.

This displacement will also couple to gradient field induced Zeeman shifts, as described above, and not only the (fitted) MOT beam positions x_0, z_0, but potential deformation of the MOT cloud in 3D need to be considered. Different scaling in induced Doppler and Zeeman shift could then lead to the nonlinear dependency on the spectroscopy beam power that is observed. In the ISS measurement we operate at an average probe beam power of 3.49(2) µW with 0.8 µW of standard deviation for the full dataset. As the true origin of the shift can not be easily modeled with the available data, we conservatively assume an additional (uncorrelated) systematic uncertainty for all recorded frequencies, isotopes, and spectroscopy transitions. Following the trend observed in figure 6.21, we conservatively set this uncertainty to 0(150) kHz.

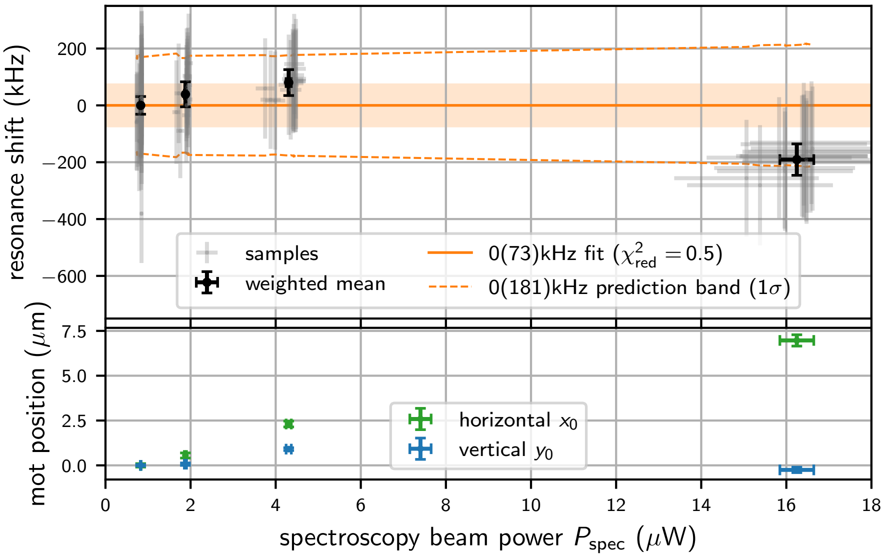

Figure 6.21: $^3\mathrm{P}_1 \rightarrow {}^3\mathrm{D}_2$ resonance shift in dependence of the probe beam power (top) and associated MOT beam positions (bottom) as extracted from a fit of the fluorescence images. We model the full dataset (gray error bars) with a constant fit (orange) and show the respective 1σ error and prediction band. The black error bars denote uncertainty weighted mean of the data for fixed power set points. We observe a radiation pressure / recoil induced MOT movement of about 7 µm along the probe beam axis.

Drift of the frequency reference

We use the slope of the linear cavity aging characterized in the $^1\mathrm{S}_0 \rightarrow {}^3\mathrm{P}_1$ ISS, see figure 6.10, to correct the small drift of the frequency reference that is present here. For the spectroscopy of the $^3\mathrm{P}_1 \rightarrow {}^3\mathrm{D}_1$ ($^3\mathrm{D}_2$) line we are locking the master laser to the 63,964th (64,085th) longitudinal cavity mode, while for the $^1\mathrm{S}_0 \rightarrow {}^3\mathrm{P}_1$ spectroscopy we operate the longitudinal mode index 98,711. This reduces the absolute frequency reference drift of the 1565 nm laser system. The drift in the IR is then translated by a factor of five and four to the UV at 313 nm and 254 nm, respectively. The frequency correction is then given by

$$\delta_{\mathrm{cav}} \rightarrow \delta_{\mathrm{cav}} - a_{\mathrm{cav}}^{(313)}\, t = \delta_{\mathrm{cav}} - a_{\mathrm{cav}}^{(254)} \frac{\lambda_{254}}{\lambda_{313}}\, t\,. \tag{6.38}$$

Here, $a_{\mathrm{cav}}^{(254)} \equiv a_{\mathrm{cav}} = -0.798(18)\,\mathrm{Hz/s}$ is the drift at $\lambda_{254} = 253.726\,875\,5(17)\,\mathrm{nm}$ as determined above. For the $^3\mathrm{P}_1 \rightarrow {}^3\mathrm{D}_1$ ($^3\mathrm{D}_2$) line the wavelength is given by $\lambda_{313} = 313.245\,882\,5(25)\,\mathrm{nm}$ ($312.657\,623\,4(24)\,\mathrm{nm}$). All wavelengths are taken from the National Institute of Standards and Technology (NIST) line database [87]. We obtain $a_{\mathrm{cav}}^{(313)} = -0.646(15)\,\mathrm{Hz/s}$ ($-0.647(15)\,\mathrm{Hz/s}$) and an absolute maximum shift of 20.4(5) kHz (25.4(6) kHz) for the 8.7 h (10.9 h) long ISS measurement campaign of the two transitions.

6.3.5 Results

Atom resonance to cavity detuning We subtract all systematic shifts discussed above and plot the systematic shift corrected frequencies

$$\delta_{\mathrm{cav}}^{\star(A)} \to \delta_{\mathrm{cav}}^{\star(A)} \;-\; (a_\Delta\,\Delta_{\mathrm{mot}} + (b_\Delta - b_P))\,\frac{P_{\mathrm{mot}}}{P_{\mathrm{mot}}^{(\Delta)}} \;-\; \left(a_B\,\frac{\partial B}{\partial z} + b_B\right) \;-\; a_{\mathrm{cav}}^{(313)}\,t \tag{6.39}$$

including all additional systematic uncertainties in figure 6.22 and 6.23. We obtain the final result for the atom resonance to cavity detuning $\langle\delta_{\mathrm{cav}}^{\star(A)}\rangle$ via a simultaneous uncertainty weighted fit of five individual constants that takes into account all correlations. The averaged atom resonance to cavity detunings are given in table 6.7. An uncertainty weighted mean reproduces the result very closely.

Limited by systematic uncertainties, we determine the cavity to atom resonance detunings down to about 400 kHz, about a 1/30 of the observed linewidth. The residuals show no significant asymmetries within the determined error bars. The correlations are not significantly strong for a potential bias, which is also confirmed by a confidence interval analysis of the fit parameter. The shift-corrected $\delta_{\mathrm{cav}}^{\star(A)}$ are again chosen as the horizontal axis in figure 6.16 and 6.17, so that the displayed spectroscopy data is adjusted from all systematic shifts and the resonances visually align with each other.

Isotope shifts Taking into account all correlations via the variance-covariance matrix, we can compute the ISs following equation (6.14). We obtain the values listed in table 6.8 for all combinations of isotopes and visualized with respect to reference isotope ^{198}Hg in figure 6.24.

The IS between isotope pairs (A, $A+2$) is about −361.7(2) MHz and −343.0(2) MHz for the two lines, respectively. The shift increases from the light isotopes upwards, with the exception being the heaviest isotope pair's shift $\delta\nu^{204-202}$. We resolve the ISs to 0.2 % to 0.4 % relatively, which corresponds to about 3.7 % to 11.2 % of the natural linewidth, limited by systematic uncertainties. The combined systematic and statistical errors give about 0.6 MHz to 1.2 MHz total uncertainty. We analyze potential bias by computing the correlations, which we are also given in table 6.8, for simplicity reduced to ^{198}Hg as a fixed reference isotope. We identify weak to medium-strong positive correlations between the ISs, as they are subject to the same systematic corrections.

Based on our knowledge, there does not appear to be any published ISS data or theoretical predictions for the two lines that we can use to compare our measurements to.

$^3\mathrm{P}_1 \to {}^3\mathrm{D}_1$	
A	$\langle\delta_{\mathrm{cav}}^{\star(A)}\rangle$ (MHz)
196	−7628.33(90)
198	−7320.83(41)
200	−6973.59(41)
202	−6595.29(42)
204	−6223.01(42)

$^3\mathrm{P}_1 \to {}^3\mathrm{D}_2$	
A	$\langle\delta_{\mathrm{cav}}^{\star(A)}\rangle$ (MHz)
196	−3242.4(1.1)
198	−2952.92(43)
200	−2624.90(45)
202	−2266.20(43)
204	−1914.61(45)

Table 6.7: $^3\mathrm{P}_1 \to {}^3\mathrm{D}_J$ ($J = 1, 2$) atom resonance to cavity detuning as extracted from the simultaneous constant fit, shown in figure 6.22 and 6.23. The given uncertainties are the combined systematic and statistical error bars originating from the analysis above. There are no significant correlations between the fit parameters.

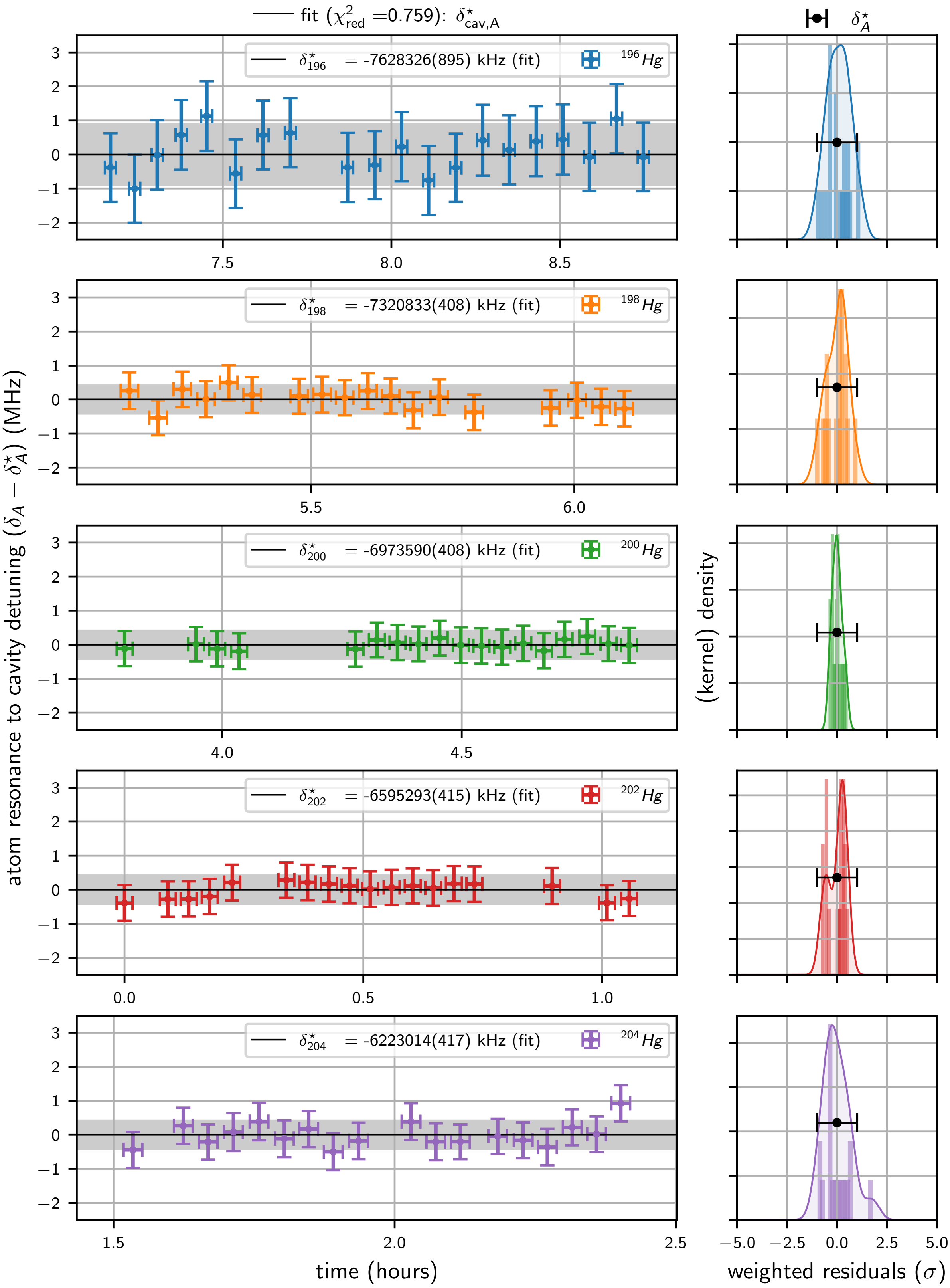

Figure 6.22: ^{3}P$_1$ → ^{3}D$_1$ atom resonance to cavity detuning δ_A data samples for all five bosonic isotopes (A) taken over the measurement campagne (left column). A corresponding simultaneous linear fit of all data with shared slope a accounts for the reference drift due to ULE cavity ageing determines the resonance frequencies of the individual isotopes via the axis intercepts $\delta^\star_A$. The distribution of weighted residuals is shown as a histogram and kernel density estimate (right column) to estimate fit bias.

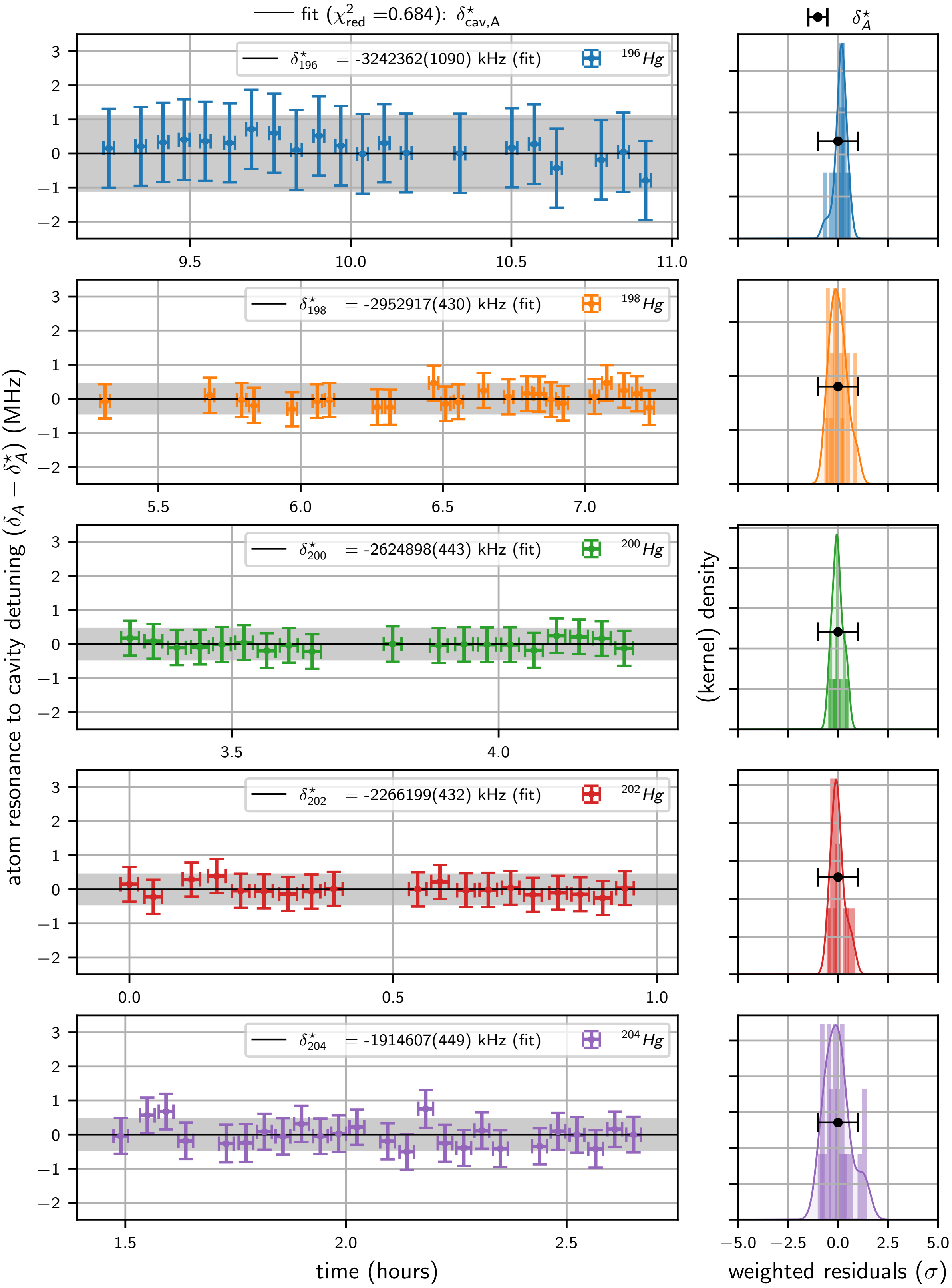

Figure 6.23: ^{3}P$_1$ → ^{3}D$_2$ atom resonance to cavity detuning δ_A data samples for all five bosonic isotopes (A) taken over the measurement campagne (left column). A corresponding simultaneous linear fit of all data with shared slope a accounts for the reference drift due to ULE cavity ageing determines the resonance frequencies of the individual isotopes via the axis intercepts $\delta^\star_A$. The distribution of weighted residuals is shown as a histogram and kernel density estimate (right column) to estimate fit bias.

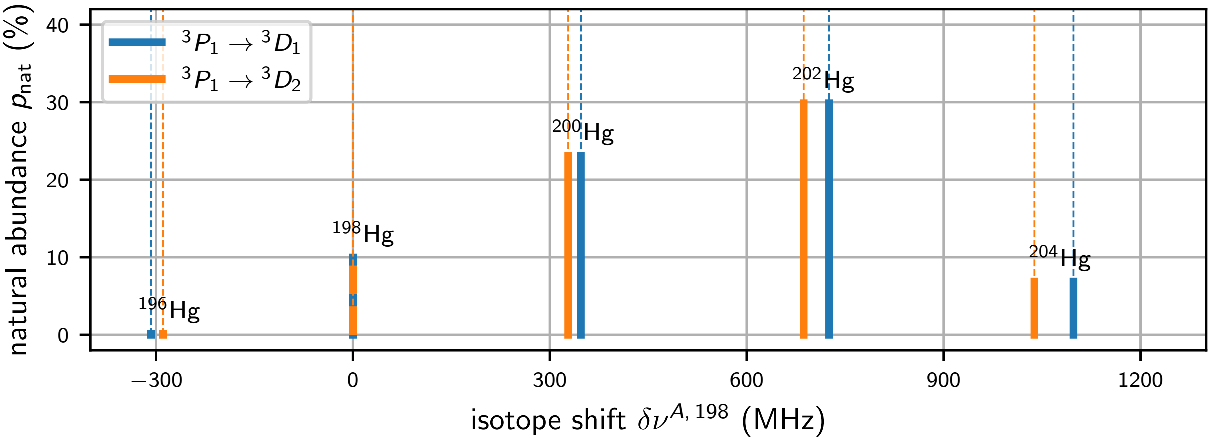

Figure 6.24: Graphical visualization of the ISs on the $^3P_1 \to {}^3D_J$ $(J = 1, 2)$ transitions as extracted from spectroscopy.

	$^3P_1 \to {}^3D_1$				
$\delta\nu^{A-A'}$ (MHz)	A'				
A	196	198	200	202	204
196	0(0)				
198	307.49(99)	0(0)			
200	654.74(99)	347.24(58)	0(0)		
202	1033.03(99)	725.54(59)	378.30(59)	0(0)	
204	1405.31(99)	1097.82(59)	750.58(59)	372.28(59)	0(0)
	$^3P_1 \to {}^3D_2$				
$\delta\nu^{A-A'}$ (MHz)	A'				
A	196	198	200	202	204
196	0(0)				
198	289.5(1.2)	0(0)			
200	617.5(1.2)	328.02(62)	0(0)		
202	976.2(1.2)	686.72(61)	358.70(62)	0(0)	
204	1327.8(1.2)	1038.31(63)	710.29(64)	351.59(63)	0(0)

	$^3P_1 \to {}^3D_1$			
	$\delta\nu^{196-198}$	$\delta\nu^{200-198}$	$\delta\nu^{202-198}$	$\delta\nu^{204-198}$
$\delta\nu^{196-198}$	1.00			
$\delta\nu^{200-198}$	0.29	1.00		
$\delta\nu^{202-198}$	0.29	0.50	1.00	
$\delta\nu^{204-198}$	0.29	0.49	0.49	1.00

	$^3P_1 \to {}^3D_2$			
	$\delta\nu^{196-198}$	$\delta\nu^{200-198}$	$\delta\nu^{202-198}$	$\delta\nu^{204-198}$
$\delta\nu^{196-198}$	1.00			
$\delta\nu^{200-198}$	0.26	1.00		
$\delta\nu^{202-198}$	0.26	0.49	1.00	
$\delta\nu^{204-198}$	0.25	0.48	0.49	1.00

Table 6.8: ISs (top) and associated correlation matrices (bottom) on the $^3P_1 \to {}^3D_J$ transitions as extracted from spectroscopy. Uncertainties represent the combined statistical and systematic uncertainty of the analysis. For simplicity the correlation matrix is shown for a fixed reference isotope $A' = 198$ only.

6.4 King plot analysis

In this chapter, we analyze the ISS datasets introduced earlier. These datasets consist of two previously unstudied transitions, $^3\mathrm{P}_1 \rightarrow {}^3\mathrm{D}_J$ ($J = 1, 2$), as well as high-precision data for the $^1\mathrm{S}_0 \rightarrow {}^3\mathrm{P}_1$ intercombination line, for which experimental uncertainties have been dramatically reduced. Notably, for the $^1\mathrm{S}_0 \rightarrow {}^3\mathrm{P}_1$ transition, we also present, for the first time, measurements for the isotope ^{196}Hg. We conduct a thorough King plot (KP) analysis to explore the linearity of electronic transition frequency shifts across all naturally abundant isotopes of mercury.

KP comparisons of previously published ISS data are strongly limited by measurement uncertainty and the range of spectroscopically addressed isotopes, underscoring the importance of our new, more precise data and its potential to advance our understanding of IS in mercury. We however present a detailed comparison of our data with existing spectroscopic data on the $^3\mathrm{P}_2 \rightarrow {}^3\mathrm{S}_1$ transition, which has comparable uncertainty levels to our measurements [283]. In this comparison, we observe significant nonlinearities in the two-dimensional KP analysis, and attempt to gain insight into the nature of the ISs.

6.4.1 Two-dimensional King plot analysis

We calculate the modified (= mass normalized) ISs $\overline{\delta\nu}_i^{A-A\prime} = \delta\nu_i^{A-A\prime}/\mu^{A-A\prime}$ with the inverse nuclear mass differences $\mu^{A-A'} = \frac{1}{m_A} - \frac{1}{m_{A'}}$ obtained from table 2.1 with the mass corrections for the total mass $Z\, m_e$ and binding energy $E_b(Z)$ of the electrons given by equation (2.1). The mass uncertainty does not limit the KP analysis compared to the spectroscopy resolution. For a fixed isotope pair selection of modified ISs, we only show results of neighboring pairs with $A' = A + 2$. The four ISS datasets then allow for six distinct two-dimensional KP. We check for a linear relationship by orthogonal distance regression taking into account the uncertainties of both lines. Three out of six KP are shown in figure 6.25 selected for their common horizontal axis given by the $^1\mathrm{S}_0 \rightarrow {}^3\mathrm{P}_1$ data, which provides the best measurement uncertainty. We also give the residuals as the (signed) orthogonal distance of the data points with respect to the linear regression line. Their error bars correspond to the projection of the data uncertainty ellipses along the perpendicular line, which is dominated by the $^3\mathrm{P}_1 \rightarrow {}^3\mathrm{D}_J$ ($J = 1, 2$) and $^3\mathrm{P}_2 \rightarrow {}^3\mathrm{S}_1$ datasets.

King plot linearity The orthogonal distance regression of the here measured $^1\mathrm{S}_0 \rightarrow {}^3\mathrm{P}_1 \rightleftharpoons {}^3\mathrm{P}_1 \rightarrow {}^3\mathrm{D}_1$ KP data strongly underfits the data with a reduced chi squared of $\chi^2_{\mathrm{red}} = 0.03$. The IS data is therefore very compatible with linearity. The $^1\mathrm{S}_0 \rightarrow {}^3\mathrm{P}_1 \rightleftharpoons {}^3\mathrm{P}_1 \rightarrow {}^3\mathrm{D}_2$ KP is also still linear with $\chi^2_{\mathrm{red}} = 1.00$ and a p-value of 0.37 confirming the two leading terms of the IS in equation (6.1) and equation (6.4) – first order FS and MS – dominate at the level of measurement precision. The linearity of KP also confirms the validity of separating nuclear and electronic factors in the IS. Any higher order (nuclear or BSM) corrections that could be resolved at this level of precision are only compatible with our data, when they align with the nuclear charge radii differences $\delta\langle r^2\rangle^{A-A'}$ or the inverse nuclear mass differences $\mu^{A-A'}$. For the $^1\mathrm{S}_0 \rightarrow {}^3\mathrm{P}_1 \rightleftharpoons {}^3\mathrm{P}_1 \rightarrow {}^3\mathrm{D}_2$ KP only the $\overline{\delta\nu}_i^{200-202}$ and $\overline{\delta\nu}_i^{202-204}$ modified IS residual indicates very slight deviations from linearity. The two-dimensional KP of $^3\mathrm{P}_1 \rightarrow {}^3\mathrm{D}_1 \rightleftharpoons {}^3\mathrm{P}_1 \rightarrow {}^3\mathrm{D}_2$ that does not involve any s-states is also strongly compatible with linearity resulting in a reduced chi squared of $\chi^2_{\mathrm{red}} = 0.74$ (not shown here). In the $^3\mathrm{P}_1 \rightarrow {}^3\mathrm{D}_J \rightleftharpoons {}^3\mathrm{P}_2 \rightarrow {}^3\mathrm{S}_1$ ($J = 1, 2$) KPs with $\chi^2_{\mathrm{red}} = 0.04$ and $\chi^2_{\mathrm{red}} = 1.12$, respectively, also no sources of nonlinearity can be

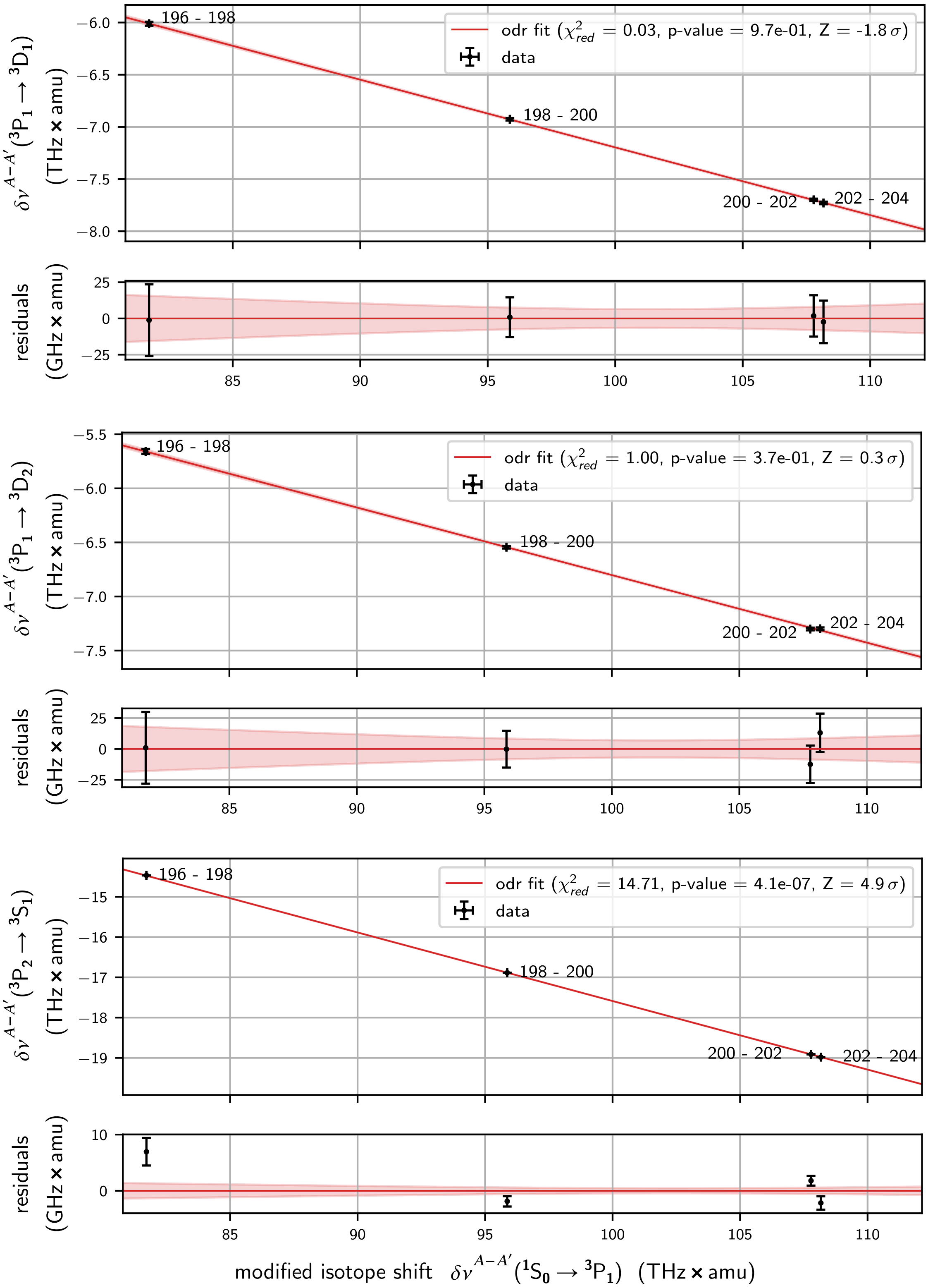

Figure 6.25: Two-dimensional KP analysis of the ISS data. Modified ISs $\overline{\delta\nu}_i^{A-A\prime} = \delta\nu_i^{A-A\prime}/\mu^{A-A\prime}$ are shown for neighboring isotope pairs $A' = A + 2$ and four electronic transitions i with respect to a common horizontal axis given by the $^1S_0 \to {}^3P_1$ data. For the orthogonal distance regression (red) we provide the 1σ uncertainty band (shaded), its residuals and the fit quality given by reduced chi-squared χ^2_{red}, p-value and significance Z as measures of nonlinearity.

observed. These three KP also show miniscule deviations from linearity only around ^{202}Hg and ^{204}Hg. This could hint at a not characterized systematic uncertainty or an onset of nuclear deformations (NDs) towards the neutron rich isotopes, but there is no significant evidence in any single dataset for this.

King plot nonlinearity We observe a clear nonlinearity in the KP analysis of our $^1\mathrm{S}_0 \rightarrow {}^3\mathrm{P}_1$ data when comparing it to the $^3\mathrm{P}_2 \rightarrow {}^3\mathrm{S}_1$ Doppler-free saturation spectroscopy data measured by the group of Jan Hall [283]. With a reduced chi square of $\chi^2_{\mathrm{red}} = 14.71$ and a p-value of 4.1×10^{-7} we need to reject the linearity hypothesis of the dataset with $Z = 4.9\,\sigma$ significance[1], which we confirm via Monte-Carlo methods. The combined orthogonal residuals read

$A - A'$	196 - 198	200 - 198	202 - 200	204 - 202
residuals (kHz)	360(130)	−94(47)	88(43)	−100(58)

(6.40)

and even fitting only a subset consisting of three isotope pairs does not restore linearity. A hidden systematic shift in our dataset would need to correct for up to 2.1 MHz shifts to restore linearity. This measurement demonstrates first signature of nonlinear contributions on the 100 kHz scale in mercury. It joins the so far short list of detected KP nonlinearities consisting of early IS measurements in samarium and recent precision measurements on ytterbium and calcium.

For KP referenced to a fixed reference isotope A', we analyze both KP with $A' = 202$ and $A' = 198$, as they provide the smallest measurement uncertainty in the IS. They agree with the findings above. The nonlinearity for the $^1\mathrm{S}_0 \rightarrow {}^3\mathrm{P}_1 \rightleftharpoons {}^3\mathrm{P}_2 \rightarrow {}^3\mathrm{S}_1$ data reduces slightly to 3.5σ significance. When we relax the rather conservative measurement uncertainties of our spectroscopy results in both the $^1\mathrm{S}_0 \rightarrow {}^3\mathrm{P}_1$ and $^3\mathrm{P}_1 \rightarrow {}^3\mathrm{D}_J$ transitions, we also obtain slight nonlinearities in both the $^1\mathrm{S}_0 \rightarrow {}^3\mathrm{P}_1 \rightleftharpoons {}^3\mathrm{P}_2 \rightarrow {}^3\mathrm{D}_J$ and $^3\mathrm{P}_2 \rightarrow {}^3\mathrm{S}_1 \rightleftharpoons {}^3\mathrm{P}_2 \rightarrow {}^3\mathrm{D}_J$ KP, while the $^3\mathrm{P}_1 \rightarrow {}^3\mathrm{D}_1 \rightleftharpoons {}^3\mathrm{P}_1 \rightarrow {}^3\mathrm{D}_2$ KP that does not involve any s-states remains linear. This could indicate higher order FS-like contributions. While the available data is still sparse, we will analyze potential nonlinearity origins in a decomposition analysis of the residuals below.

transition i	transition j	F_{ij}	K_{ij} (THz × amu)
$^1\mathrm{S}_0 \rightarrow {}^3\mathrm{P}_1$	$^3\mathrm{P}_1 \rightarrow {}^3\mathrm{D}_1$	−0.0649(7)	−0.71(8)
$^1\mathrm{S}_0 \rightarrow {}^3\mathrm{P}_1$	$^3\mathrm{P}_1 \rightarrow {}^3\mathrm{D}_2$	−0.0625(8)	−0.55(9)
$^1\mathrm{S}_0 \rightarrow {}^3\mathrm{P}_1$	$^3\mathrm{P}_2 \rightarrow {}^3\mathrm{S}_1$	−0.1703(1)	−0.556(6)
$^3\mathrm{P}_1 \rightarrow {}^3\mathrm{D}_1$	$^3\mathrm{P}_1 \rightarrow {}^3\mathrm{D}_2$	0.96(2)	0.1(2)
$^3\mathrm{P}_1 \rightarrow {}^3\mathrm{D}_1$	$^3\mathrm{P}_2 \rightarrow {}^3\mathrm{S}_1$	2.63(3)	1.3(3)
$^3\mathrm{P}_1 \rightarrow {}^3\mathrm{D}_2$	$^3\mathrm{P}_2 \rightarrow {}^3\mathrm{S}_1$	2.73(4)	1.0(3)

Table 6.9: Relative FS F_{ij} and MS K_{ij} parameters as extracted from two-dimensional KP analysis. The specified uncertainties are 1σ error bars from the orthogonal distance regression.

---

[1] The Z-score quantifies the significance of the deviation of the observed chi-square statistic from its expected value under the null hypothesis (i.e., the KP data follows a linear model). It is obtained by converting the chi-square p-value to the corresponding standard score on a standard normal distribution, representing the number of standard deviations the result deviates from the mean.

Extraction of electronic & nuclear parameters

Ignoring the nonlinearity of the $^1\mathrm{S}_0 \rightarrow {}^3\mathrm{P}_1 \rightleftharpoons {}^3\mathrm{P}_2 \rightarrow {}^3\mathrm{S}_1$ KP by assuming the weighted fit describes the original linear contribution, we can use the latter to extract the electronic parameter ratios of FS F_{ij} and MS K_{ij} of the all transitions i and j. The result is shown in table 6.9. For the comparison of the $^1\mathrm{S}_0 \rightarrow {}^3\mathrm{P}_1 \rightleftharpoons {}^3\mathrm{P}_2 \rightarrow {}^3\mathrm{S}_1$ transitions at 254 nm and 546 nm, we obtain a KP slope of $F_{546,254} = F_{546}/F_{254} = -0.1703(1)$. This value is in agreement with $-0.170\,47(11)$ as published by Witkowski et al. [172] and the less precise value of 0.1707(12) as provided by Ulm et al. [67]. The intercept of the linear regression is given by the FS normalized MS parameter difference $K_{ij} = (K_i - K_j\,F_{ij})$ of the two transitions i and j. We obtain $K_{546,254} = -0.556(6)$ THz × amu for the two lines in slight tension with the value 0.536(11) THz × amu given in reference [172].

To obtain the pure FS, F_i, and MS, K_i, parameters of the individual transitions i, we need to either obtain e.g., a single F_i from theory calculations, or compare the ISs to muonic or electronic x-ray measurement data. The latter probes dominantly only the FS and therefore is a good measure for the nuclear charge radii changes $\delta\langle r^2\rangle^{A-A'}$. Field shift factors F_i for the 254 nm intercombination line are the most precise values determined from theory and experiment for mercury. Together with theory predictions for the 185 nm singlet transition, they are given in reference [254], both experimentally – from electronic ($-53.9(5.3)$ GHz/fm^2) and muonic ($-57.4(2.9)$ GHz/fm^2) x-ray measurements – and from ab-initio MCDF calculations (-55.36 GHz/fm^2). In agreement, Witkowski et al. [172] give $E_{254} = -52.7(5.3)$ GHz/fm^2 from density functional theory electron structure calculations. From KP analysis, reference [172] obtains $E_{254} = -51.277(46)$ GHz/fm^2 when assuming $K_{546} = 682(203)$ GHz × amu as specified in reference [283] and in tension to $E_{254} = -51.63(17)$ GHz/fm^2 when assuming $\delta\langle r^2\rangle^{A-198}$ values given by [67]. For the latter, the authors of reference [172] assume the empirical relation between specific SMS to NMS $K_{254}^{(\mathrm{SMS})} = 0.0(5) \times K_{254}^{(\mathrm{NMS})}$, which holds for the 254 nm line in mercury, as the SMS is <1 % of the NMS as discussed before. Any of these values can be used to obtain FS and MS contributions from our data.

Due to the slight inconsistencies and partially large uncertainties of the FS parameters, we decide to use direct KP comparison of modified ISs $\overline{\delta\nu_i}^{A-A'}$ against modified nuclear charge radii differences $\overline{\delta\langle r^2\rangle}^{A-A'} \equiv \delta\langle r^2\rangle^{A-A'}/\mu^{A-A'}$ to determine the FS and MS factors of all transitions i. The mean squared charge radii differences are extracted from a combination of optical and x-ray IS measurements and absolute radii measurements from muonic spectra and electronic scattering experiments as given in reference [71]. The resulting KP are given in figure 6.26, the extracted FS and MS parameters in table 6.10. The so generated KP of the ~313 nm $^3\mathrm{P}_1 \rightarrow {}^3\mathrm{D}_J$ IS data is in agreement with a linear behavior. The 254 nm $^1\mathrm{S}_0 \rightarrow {}^3\mathrm{P}_1$ transition KP shows weak deviations from linearity, giving a reduced chi square of $\chi^2_{\mathrm{red}} = 2.54$ and a p-value of 7.9×10^{-2}. The same is true for the 546 nm (p → s) transition KP, which gives $\chi^2_{\mathrm{red}} = 3.14$ and a p-value of 4.3×10^{-2} (not shown here). This again indicates higher order corrections that are sensitive to the wave function overlap with the nucleus. To our knowledge, this is the first measurement of FS and MS parameters of the $^3\mathrm{P}_1 \rightarrow {}^3\mathrm{D}_J$ ($J = 1, 2$) lines in Hg. Their values are very similar as only inner shell electrons contribute significantly to the FS. The FS values of the $^1\mathrm{S}_0 \rightarrow {}^3\mathrm{P}_1$ and $^3\mathrm{P}_1 \rightarrow {}^3\mathrm{S}_1$ transitions agree with results from reference [172] and [283] within their (combined) error bars.

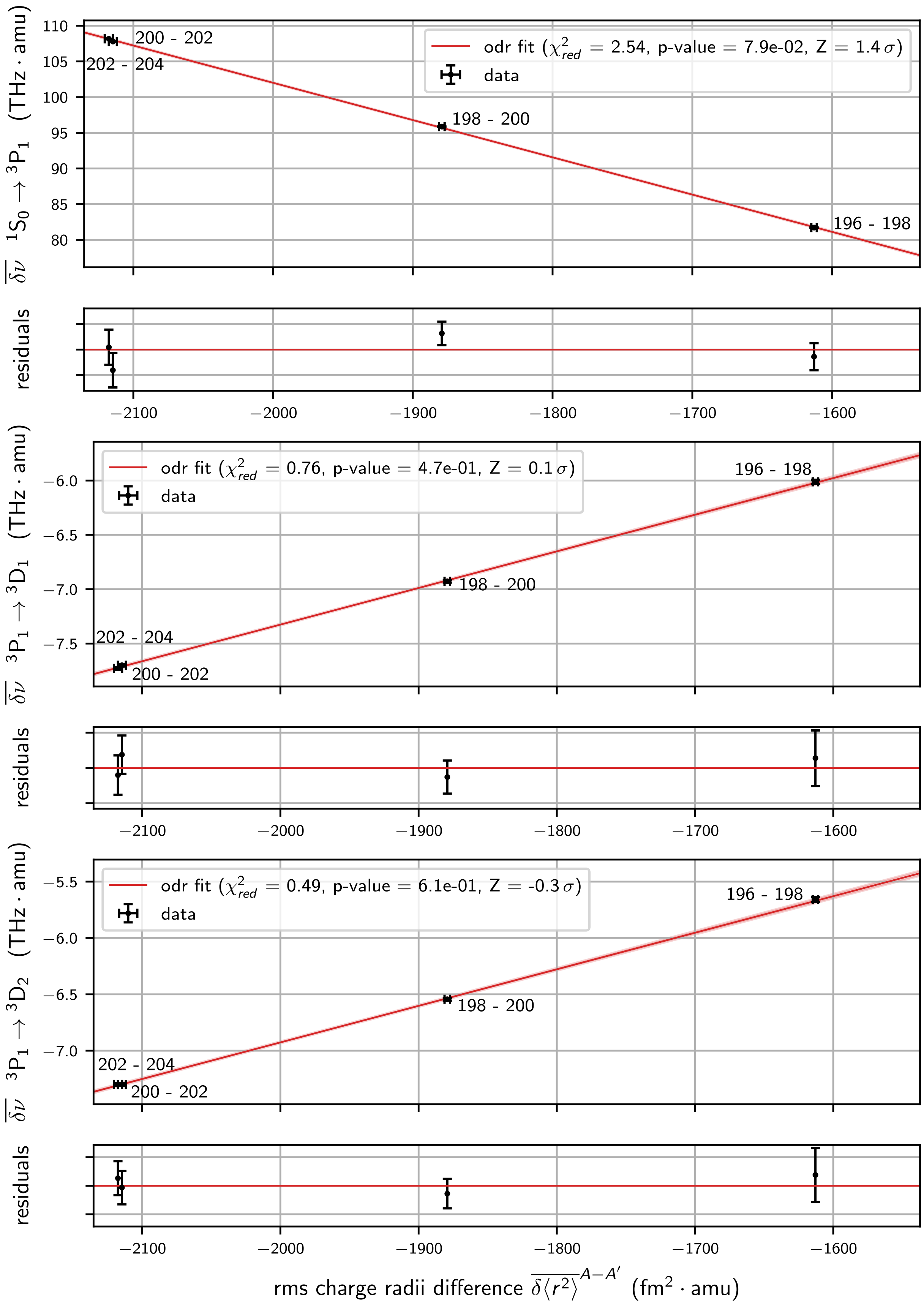

Figure 6.26: KP analysis via orthogonal distance regression (red) of the IS data for extraction of FS F_i and MS K_i parameters. Modified ISs $\overline{\delta\nu_i}^{A-A\prime}$ are shown for isotope pairs $A' = A + 2$ with respect to rms charge radii differences $\overline{\delta\langle r^2\rangle}^{A-A'}$ data from reference [71].

transition i	F_i (GHz/fm^2)	K_i (THz $\times$ amu)
$^1\mathrm{S}_0 \rightarrow {}^3\mathrm{P}_1$	−52.22(30)	−2.43(55)
$^3\mathrm{P}_1 \rightarrow {}^3\mathrm{D}_1$	3.370(43)	−0.585(86)
$^3\mathrm{P}_1 \rightarrow {}^3\mathrm{D}_2$	3.243(48)	−0.440(95)
$^3\mathrm{P}_2 \rightarrow {}^3\mathrm{S}_1$	8.909(50)	−0.112(94)

Table 6.10: Field shift F_i and MS K_i parameters as extracted from two-dimensional KP analysis of $\delta\nu_i^{A-A'}$ against nuclear charge radii $\delta\langle r^2\rangle^{A-A'}$ given in reference [71]. The specified uncertainties are 1σ error bars as extracted from a orthogonal distance regression.

Nonlinearity decomposition analysis

We analyze the two-dimensional KP nonlinearity origins using the generalized KP technique [251], as introduced in section 6.1.1. The basis vectors for the projection are given in equation (6.7), and we choose $\mathbf{\Lambda}_\pm$ in accordance with the definition found in recent literature (see e.g., reference [249]) as

$$\begin{aligned}\mathbf{\Lambda}_+ &= \left(\overline{\delta\nu}_i^{a_3} - \overline{\delta\nu}_i^{a_2},\, \overline{\delta\nu}_i^{a_1} - \overline{\delta\nu}_i^{a_4},\, \overline{\delta\nu}_i^{a_4} - \overline{\delta\nu}_i^{a_1},\, \overline{\delta\nu}_i^{a_2} - \overline{\delta\nu}_i^{a_3}\right)^\intercal ,\\ \mathbf{\Lambda}_- &= \left(\overline{\delta\nu}_i^{a_4} - \overline{\delta\nu}_i^{a_2},\, \overline{\delta\nu}_i^{a_1} - \overline{\delta\nu}_i^{a_3},\, \overline{\delta\nu}_i^{a_2} - \overline{\delta\nu}_i^{a_4},\, \overline{\delta\nu}_i^{a_3} - \overline{\delta\nu}_i^{a_1}\right)^\intercal .\end{aligned} \tag{6.41}$$

The isotope pairs are given by $a_1 = (196, 198)$, $a_2 = (198, 200)$, $a_3 = (200, 202)$, $a_4 = (202, 204)$.

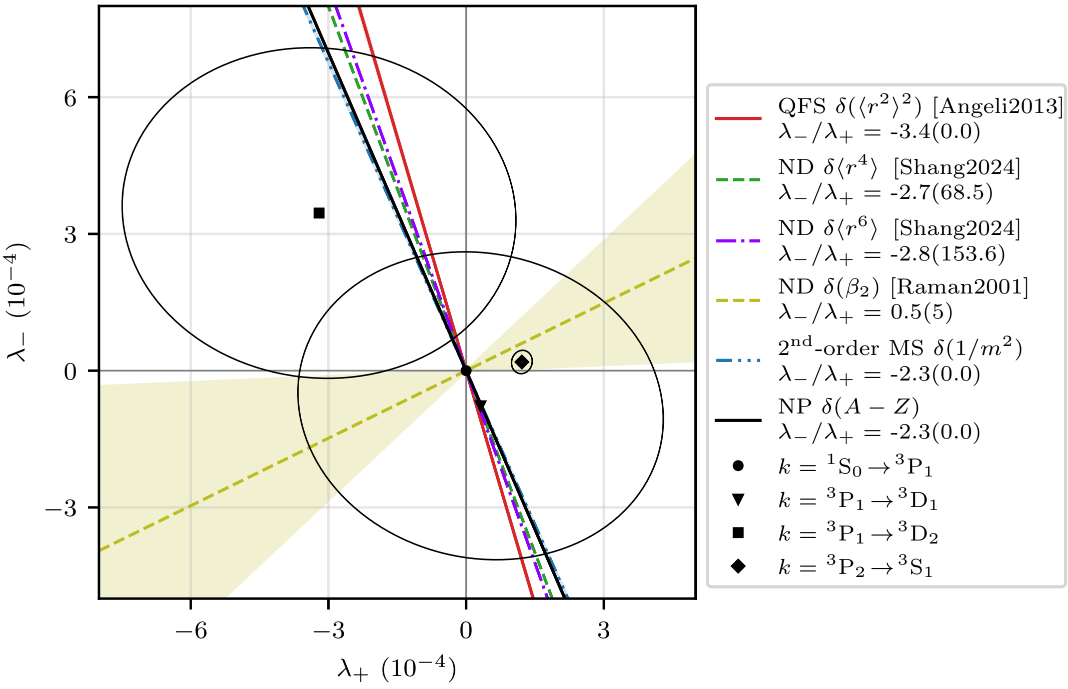

Figure 6.27: Nonlinear decomposition analysis of mass normalized ISs $\overline{\delta\nu}_k^{A-A'} = \delta\nu_k^{A-A'}/\mu^{A-A'}$ of all lines k projected via $\mathbb{M} = \left(\overline{\boldsymbol{\delta\nu}}_i \;\; \mathbb{1} \;\; \mathbf{\Lambda}_+ \;\; \mathbf{\Lambda}_-\right)$ with $i = {}^1\mathrm{S}_0 \rightarrow {}^3\mathrm{P}_1$ and projection vectors $\mathbf{\Lambda}_\pm$ given by equation (6.41). The various nonlinearity sources – with explanations in the main text – form lines through the origin with slopes λ_-/λ_+ as obtained from the projection. We show the corresponding 1σ uncertainty bands, but omit them for nuclear deformation (ND) $\delta\langle r^4\rangle$ and $\delta\langle r^6\rangle$ to improve visibility, as they span almost the entire plot.

We also compare our data to projections $\mathbb{M}^{-1} \cdot \overline{\mathbf{\Lambda}}_{(\kappa)}$ with $\overline{\Lambda}_{(\kappa)}^{A-A'} \equiv \Lambda_{(\kappa)}^{A-A'}/\mu^{A-A'}$ of potential higher order nuclear corrections and BSM couplings. While their absolute position in the nonlinear decomposition plot depend on the electronic prefactor $G_{ij}^{(\kappa)}$ that determines sensitivity of the IS to the nuclear property, even for variable $G_{ij}^{(\kappa)}$ they provide distinctive nonlinearity shapes, that are characterized by a fixed slope λ_-/λ_+. As $G_{ij}^{(\kappa)} = 0$ corresponds to linearity $\lambda_\pm = 0$, single sources of nonlinearity form lines through the origin.

We consider the next leading order correction to the mean squared nuclear charge radius, the quadratic field shift (QFS) $\delta\left(\langle r^2\rangle^2\right)$ from experimental values of the nuclear ground state charge radii given in reference [71]. Fourth order, $\delta\langle r^4\rangle^{A-A'}$, and sixth order, $\delta\langle r^6\rangle^{A-A'}$, moment nuclear charge radii differences – the former is also called quartic shift – are obtained from recent estimates that use a deep neural network for global prediction of nuclear charge distributions [303]. They result in quite large projection uncertainties, which render their location in the nonlinear decomposition plot rather vague.

The nuclear deformation parameter $\langle\beta_2\rangle$ is being extracted from reduced nuclear electric quadrupole transition probability, $B(E2)$, between the 0^+ nuclear ground state and the excited 2_i^+ states [67] via $\langle\beta_2\rangle^2 = \sum_i (4\pi/3\,Z\,R_0^2)^2\,B(E2,\,0^+ \rightarrow 2_i^+)$, with $R_0 = 1.2\,\mathrm{fm} \times A^{1/3}$. We use latest tabulated data for the transition to the first excited state $B(E2,\,0^+ \rightarrow 2_1^+)$ given in [304]. It is to note that truncating the sum is potentially unjustified near the $N = 126$ shell closure, as motivated by disagreements with nuclear deformation parameters extracted from ISS [67].

While strongly suppressed in Hg, we also estimate second order MS corrections $1/(m^A)^2 - 1/(m^{A'})^2$ from the binding energy and electron mass corrected masses m^A. As discussed before, BSM coupling between neutrons and electrons mediated by a potential boson is characterized by $\alpha_{\mathrm{NP}}\,X_i\,h^{A-A'}$. The characteristic slope of NP coupling can therefore just be extracted from the projections of the inverse nuclear mass normalized vector of neutron number $\overline{\boldsymbol{h}} = (2,2,2,2)^\intercal/\boldsymbol{\mu}$.

A nonlinear decomposition analysis of mass normalized, neighboring isotope pair KP data is shown in figure 6.27. While the uncertainty on the ISS data currently limits differentiation of nonlinearity origins and no single contribution can be extracted, the observed nonlinearity pattern of the $^1\mathrm{S}_0 \rightarrow {}^3\mathrm{P}_1 \rightleftharpoons {}^3\mathrm{P}_2 \rightarrow {}^3\mathrm{S}_1$ biases towards nuclear deformation $\langle\beta_2\rangle$ contributions and quadratic FSs $\delta\left(\langle r^2\rangle^2\right)$. We can also see that in this projection fifth force BSM couplings of a new boson are potentially aligned with nuclear deformation contributions and second order MSs. As shown in figure 6.28, nonlinear decomposition analysis of no-mass KP, where the raw IS vectors $\boldsymbol{\delta\nu}$ are projected onto $\mathbb{M} = \left(\boldsymbol{\delta\nu}_i \;\; \boldsymbol{\delta\nu}_j \;\; \mathbf{\Lambda}_+ \;\; \mathbf{\Lambda}_-\right)$ with $\mathbf{\Lambda}_\pm$ given by the non-modified $\boldsymbol{\delta\nu}$ analogously to equation (6.41), allow separation of these sources. This moves another IS line projection to the origin and quantitative nonlinearity analysis is only applicable for reduced measurement uncertainty and/or increased number of transitions.

6.4.2 Three-dimensional King plot analysis

As discussed in section 6.1.1, we can also analyze the IS data via multidimensional KP analysis, which can potentially absorb a nonlinearity via an additional modified IS vector. Figure 6.29 shows three out of four possible combinations of three-dimensional KP of modified IS that are representative of the full collection. While the data is in agreement with the linear relationship given by a two-dimensional plane in three-dimensional modified IS space, the measurement uncertainty is large and the orthogonal

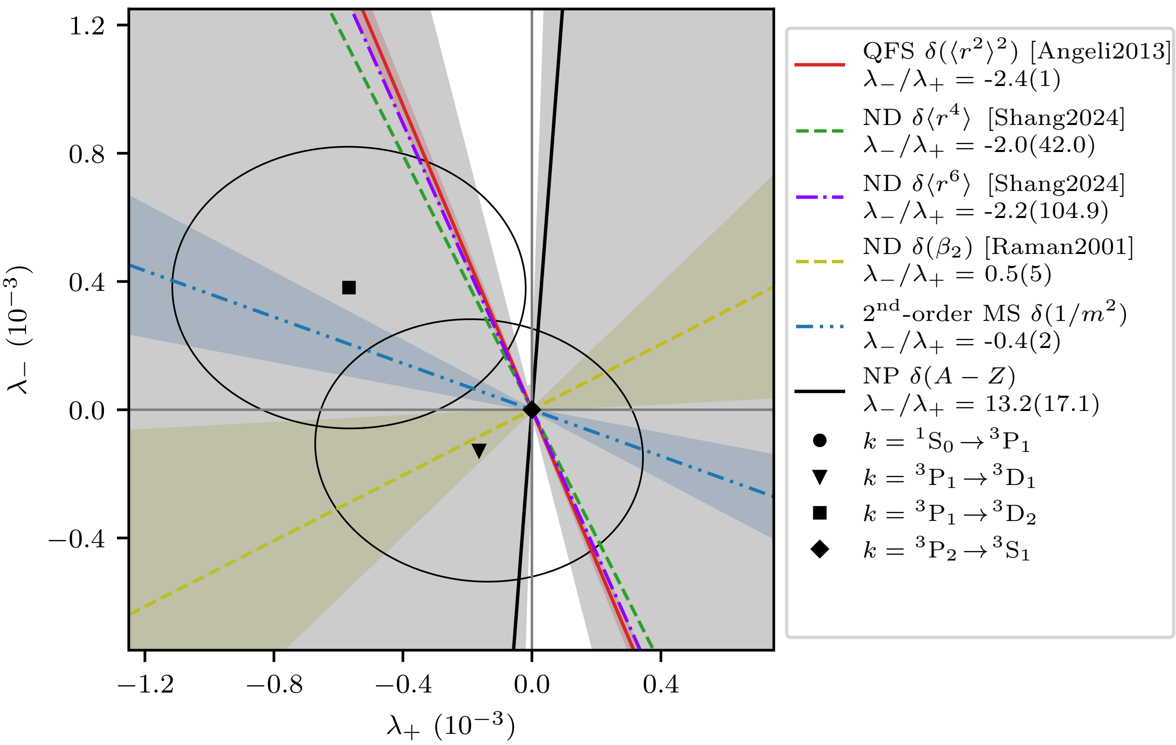

Figure 6.28: No-mass nonlinear decomposition analysis of IS $\delta\nu_k^{A-A'}$ of all lines k projected via $\mathbb{M} = \left(\boldsymbol{\delta\nu}_i\ \ \boldsymbol{\delta\nu}_j\ \ \boldsymbol{\Lambda}_+\ \ \boldsymbol{\Lambda}_-\right)$ with $i = {}^1\mathrm{S}_0 \to {}^3\mathrm{P}_1$ and $j = {}^3\mathrm{P}_2 \to {}^3\mathrm{S}_1$ and projection vectors $\boldsymbol{\Lambda}_\pm$ given by equation (6.41). The various nonlinearity sources – with explanations in the main text – form lines through the origin with slopes λ_-/λ_+ as obtained from the projection. We show the corresponding 1σ uncertainty bands, but omit them for nuclear deformation (ND) $\delta\langle r^4\rangle$ and $\delta\langle r^6\rangle$ for better visibility.

distance regression overfits the data. The removal of nonlinearity via three-dimensional KP analysis agrees with the guess that our data is subject to one single higher order (nuclear) correction term that is being absorbed here. The fitted field F_{ijk} and mass K_{ijk} shift parameters, as well as the third fit parameter $G^{(1)}_{ijk}$ that takes care of linearity in 2D, are given in table 6.11.

transition i	transition j	transition k	F_{ijk}	$G^{(1)}_{ijk}$	K_{ij} (THz × amu)	χ^2_{red}
${}^1\mathrm{S}_0 \to {}^3\mathrm{P}_1$	${}^3\mathrm{P}_1 \to {}^3\mathrm{D}_1$	${}^3\mathrm{P}_1 \to {}^3\mathrm{D}_2$	−0.5(1.6)	−6(25)	−5(18)	0.01
${}^1\mathrm{S}_0 \to {}^3\mathrm{P}_1$	${}^3\mathrm{P}_2 \to {}^3\mathrm{S}_1$	${}^3\mathrm{P}_1 \to {}^3\mathrm{D}_1$	−0.04(42)	0.1(2.5)	−0.6(1.3)	0.07
${}^1\mathrm{S}_0 \to {}^3\mathrm{P}_1$	${}^3\mathrm{P}_2 \to {}^3\mathrm{S}_1$	${}^3\mathrm{P}_1 \to {}^3\mathrm{D}_2$	−0.46(47)	−2.3(2.8)	−1.8(1.5)	1.31
${}^3\mathrm{P}_2 \to {}^3\mathrm{S}_1$	${}^3\mathrm{P}_1 \to {}^3\mathrm{D}_1$	${}^3\mathrm{P}_1 \to {}^3\mathrm{D}_2$	4(29)	−11(74)	−60(37)	0.06

Table 6.11: Relative FS F_{ijk}, MS K_{ijk} and first order correction $G^{(1)}_{ijk}$ parameters as extracted from three-dimensional KP analysis. The specified uncertainties are 1σ error bars from the orthogonal distance regression for which we also give the associated χ^2_{red}.

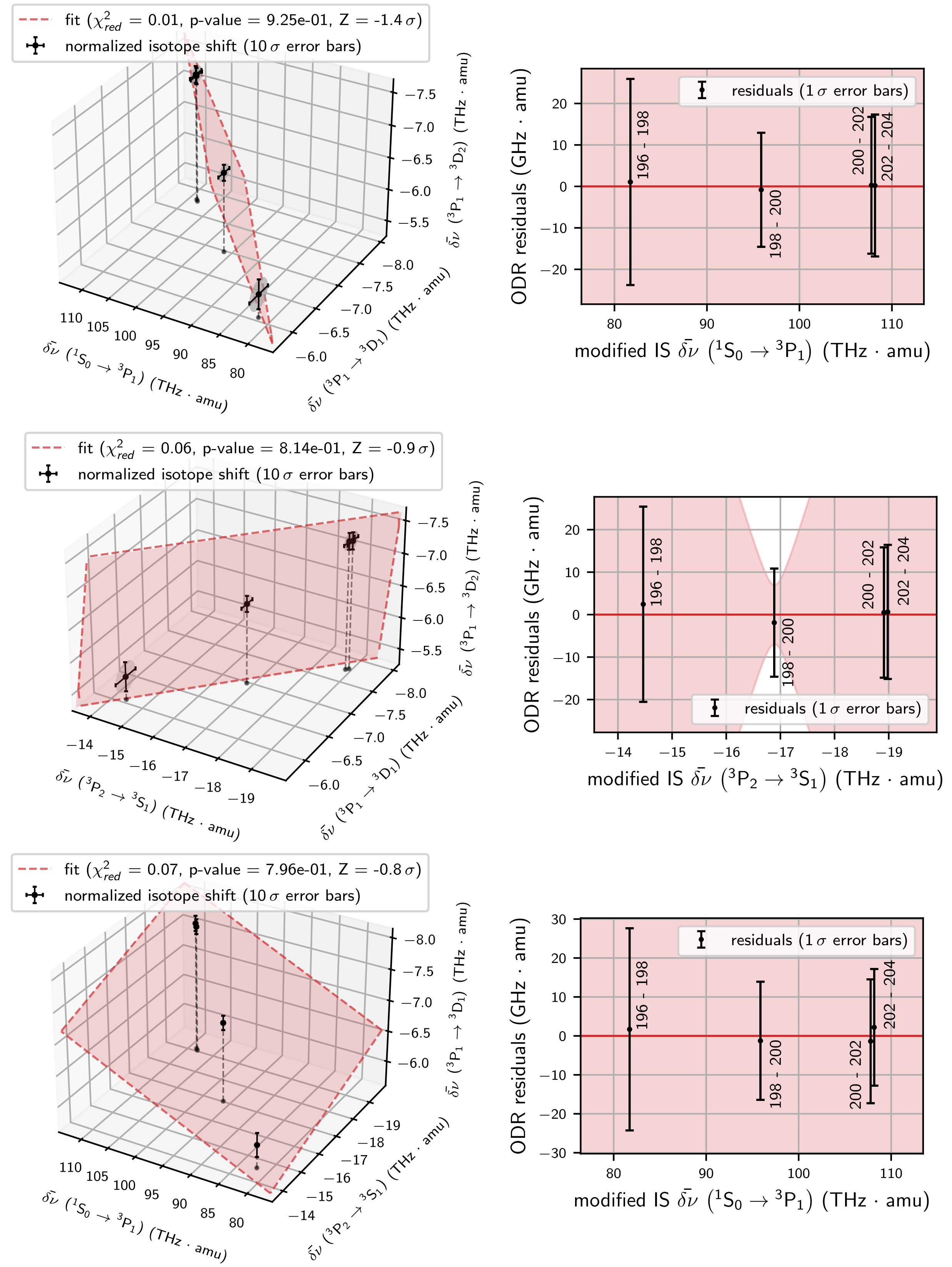

Figure 6.29: Three-dimensional KP analysis of the ISS data. Modified ISs $\overline{\delta\nu}_i^{A-A\prime} = \delta\nu_i^{A-A\prime}/\mu^{A-A\prime}$ (left) are shown for neighboring isotope pairs $A' = A + 2$ and triples (i, j, k) out of four electronic transitions together with the plane of linearity as given by orthogonal distance regression (red shaded). The fit residuals (right) and the fit quality given by reduced chi-squared χ^2_{red}, p-value and Z-score, are given as measures of (non)linearity.

6.5 Outlook

The work presented in this chapter reports the most precise ISS of mercury to date. In particular, we improve the measurement uncertainty of the $^1S_0 \rightarrow {}^3P_1$ intercombination line by approximately one order of magnitude compared to previous determinations, while for the first time providing comprehensive data for all naturally abundant isotopes, including the rare ^{196}Hg isotope. Furthermore, the inclusion of $^3P_1 \rightarrow {}^3D_J$ transitions, which directly connect to the $^3P_1$ state, highlights the sensitivity of s-electron transitions to (higher-order) FS contributions.

6.5.1 New physics bounds

In the broader context of BSM searches, it is clear that the ultimate constraints obtained from our study cannot compete with the exceptionally stringent bounds already set by ultra-narrow clock transitions in ytterbium [253] and, especially, by the latest highly charged-ion spectroscopy in Ca^{14+} [249]. Nevertheless, mercury offers an important complementary path. As discussed before, unlike ytterbium, where nuclear deformation imposes strong systematic limitations, mercury sits closer to a major nuclear shell closure. As such, further improvements in measurement resolution and uncertainty – potentially including future ISS on the Hg clock transitions discussed below – will not be comparably limited by nuclear structure effects. This makes mercury still a good candidate for BSM constraints that are competitive once uncertainties are further narrowed.

To derive BSM bounds, we can employ the generalized KP approach [251], see equation 6.12, as outlined in section. 6.1.2. For the subset of $^3P_1 \rightarrow {}^3D_J$ transitions incorporated into the KP analysis, the interpretation is straightforward since no nonlinearity must be accounted for. By contrast, in the case of s-state transitions, an outstanding challenge remains the identification of the dominant source of observed nonlinearity, either via theoretical modeling or further targeted measurements.

Atomic structure calculation

For translating our IS results into quantitative BSM constraints, it is crucial to compute the electronic structure coefficients X_i, which defines the coupling strength of a hypothetical new boson to electrons and neutrons. High-precision numerical methods such as configuration interaction combined with many-body perturbation theory (CI+MBPT), as implemented in state-of-the-art packages like AMBIT, have recently demonstrated excellent agreement with experiment even in complex atomic systems such as ytterbium and calcium [249, 253]. Nevertheless, the richness of the mercury electronic shell still poses a challenge for achieving the required precision in the X_i constants (see equations (6.10) and (6.12)).

Electron structure calculations can be applied not only to BSM sensitivity but also to the next-to-leading order SM contributions that induce apparent nonlinearities in the KP. A slightly weaker but more conservative constraint on BSM interactions can alternatively be obtained by empirically projecting the measured KP deviations onto known sources of SM nonlinearity or via regression-based estimates, without relying on full theoretical predictions. Any residual nonlinearity, together with the experimental uncertainty budget, is then translated into a bound on new physics couplings.

These calculations will be the next step in the current analysis.

6.5.2 Inclusion of odd isotopes

We so far limited the ISS and KP analysis to even isotopes only, as hyperfine interactions in non-zero nuclear spin isotopes can lead to very large (GHz-scale) shifts that are hard to predict precisely. The authors of [248] highlight the importance of accounting for these effects and explain the 100 kHz-nonlinearity observed in KP of neutral strontium including measurements on ^{87}Sr [305] by second order hyperfine splittings. This just recently motivated the inclusion of fermionic isotopes into ISS studies of wider lines also in the search for NP effects. Including fermionic isotopes will allow for increased statistics for KP analysis and more in-depth nonlinearity analysis tools, as the (modified) IS vector space increases in dimensions.

6.5.3 Improving the spectroscopy resolution

Improvements of the ISS precision or addition of further ISS data to the KP and nonlinearity decomposition analysis can really contribute to deeper insight into potential nuclear corrections and to distinguish them from potential BSM physics couplings. We plan to both improve measurement uncertainty on the $^1\mathrm{S}_0 \rightarrow {}^3\mathrm{P}_1$ and especially the $^3\mathrm{P}_1 \rightarrow {}^3\mathrm{D}_J$ transitions, as well as to add more lines and isotopes to the search. We expect to improve the error bars of the IS data presented here by a factor of at least five in the next measurement campaign by employing the originally anticipated measurement schemes in the absence of magnetic field gradients and free fall, which reduces light and recoil shifts from the pump fields.

6.5.4 Spectroscopy on $^3\mathrm{P}_1 \rightarrow {}^3\mathrm{S}_1$

As we observe KP nonlinearities when including the FS sensitive s-orbital involving transitions, we considered also probing the $^3\mathrm{P}_1 \rightarrow {}^3\mathrm{S}_1$ transition. This would add one more point to the 2D nonlinear decomposition plot, but also to check the (external) data used for analysis. Here, the spectroscopy scheme of MOT depletion in free fall, originally proposed for the $^3\mathrm{P}_1 \rightarrow {}^3\mathrm{D}_J$ transition, can be utilized, as the laser system provides more than enough power, as presented below. Absorption imaging of atoms within the $^3\mathrm{P}_1$ on 436 nm would be a viable alternative.

So far, we successfully tested the spectroscopy scheme on ^{202}Hg, but did not perform an ISS measurement campaign yet, as repairing the broken source chamber and a fixing a leak in the vacuum chamber required attention. The laser system and cavity lock were already employed for sub-100 kHz resolution ISS of the 423 nm singlet transition and KP analysis in neutral calcium [165]. This confirms the laser and lock meeting the requirements for future ISS on the $^3\mathrm{P}_1 \rightarrow {}^3\mathrm{S}_1$ spectroscopy in mercury.

436 nm laser system

For ISS of the $^3\mathrm{P}_1 \rightarrow {}^3\mathrm{S}_1$ line an ultrastable cavity referenced laser system is already constructed, as shown in figure 6.30. A diode laser provides fundamental light at 872 nm and is locked to another vibration-isolated and temperature-stabilized high-finesse ultrastable cavity[1], via a carrier-shifted Pound-Drever-Hall sideband triplet, a scheme already described before. The cavity acts as the frequency reference and reduces the laser linewidth to < 1 Hz, as measured by beat signal comparison to a second laser system at the same wavelength [165, 306].

---

[1] Menlo Systems ORC-Cubic. We measure a finesse of $\mathscr{F} > 80{,}000$ near the target wavelength.

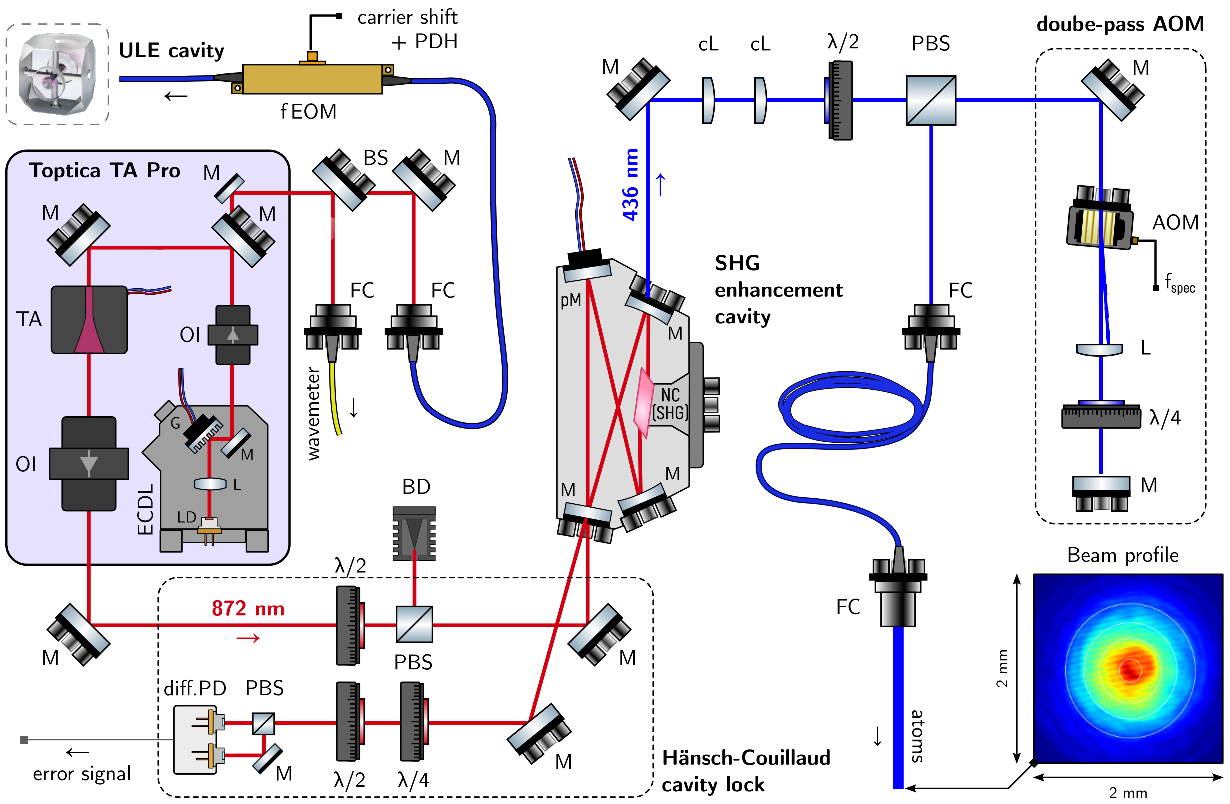

Figure 6.30: Optical setup of the 436 nm spectroscopy laser system. An external-cavity diode laser (ECDL) at 872 nm is send thorugh a tapered amplifier (TA) and optical isolator (OI). The amplified output is coupled to an enhancement cavity for second-harmonic generation (SHG) in a nonlinear crystal (NC). A fiber EOM (fEOM) carrier shifted sideband of the master laser is locked to a high-finesse ULE cavity via a Pound-Drever-Hall (PDH) scheme. The doubling cavity is locked to the laser frequency via a piezo mirror (pM) by a Hänsch-Couillaud scheme generated error signal. The 436 nm light is beam shaped by cylindrical lenses, frequency modulated by a double-pass AOM setup and fiber coupled. The inset shows the laser beam profile at the location of the atoms.

Frequency conversion to 436 nm is performed via second-harmonic generation (SHG) in BBO in a bow-tie enhancement cavity[1]. We lock the SHG cavity to the laser frequency via a Hänsch-Couillaud locking scheme [307], were a small portion of the incident is reflected by rotating the polarization utilizing the birefringence of the SHG crystal. When off-resonance, the reflected beam's polarization changes, and the difference between orthogonal polarization components is detected to produce an error signal on a differential/balanced photodetector. The nonlinear crystal is temperature-stabilized by a small heating element and the laser light is mode matched to the cavity via a spherical lens. We reach about 140 mW of power at 436 nm, but do not really optimize the incoupling to the SHG cavity and the conversion efficiency via the temperature, as we require less than a milliwatt for spectroscopy only. As the crystal introduces a walk off, the light exiting the cavity is beam-shaped and collimated via a pair of cylindrical lenses.

A double pass AOM[2] setup frequency shifts the laser frequency by $f_{\text{aom}} = 2 \times 80\,\text{MHz}$, the output is then fiber coupled into a polarization maintaining fiber and sent to the main optical table. We collimate the probe beam to 3.3(1) mm diameter, which gives us more than enough intensity at the

---

[1] Agile Optic IR to VIS standard SHG cavity. [2] Gooch and Housego 3080-120.

location of the atoms. The spectroscopy light is sent through the periscope mirrors of the MOT cooling beam x-axis which acts as a dichroic mirror with a transmission of 98.4(5) % at 436 nm and 45° incidence.

6.5.5 Clock line spectroscopy

Increasing sensitivity to NP coupling probably requires the spectroscopy of much narrower, dipole-forbidden transitions. Here, we can use the ultra-narrow $^1S_0 \rightarrow {}^3P_0$ clock intercombination line at 265.6 nm. While a single-photon transition of this line is highly forbidden, it is weakly allowed through hyperfine mixing for the odd mercury isotopes ^{199}Hg and ^{201}Hg with estimated linewidths in the Hz to mHz-range [93, 94]. For the bosonic mercury isotopes with $I = 0$, no hyperfine interaction is present and only highly suppressed E1-M1 two-photon decays could contribute to a natural linewidth [48] and the line is considered not directly addressable. Among various options also discussed for other alkaline-earth-metal-like systems [308], static magnetic fields can be utilized to enable direct optical excitation of forbidden electric-dipole transitions [309]. The clock line can also be probed indirectly via three-level quantum coherence linked via e.g., the $^1P_1$ level [310].

The ultra-narrow magnetic-quadrupole transition $^1S_0 \rightarrow {}^3P_2$ near 227 nm is another candidate for precision ISS of mercury. As spectroscopy requires little power, both wavelengths can easily be generated from the infrared by two successive SHG doubling stages – either cavity amplified or single pass. Here, phase-stable laser light at 267 nm with a fractional frequency uncertainty down to $5{\times}10^{-17}$ at 1 s was already realized in reference [311]. Laser development within our group successfully established over 100 mW of laser power at 214 nm and setup of a second laser system at 254 nm to 257 nm for magnetometry in mercury and ISS in xenon. Both Hg clock lines could also be probed by two-photon laser excitation, a wavelength region easily accessible by just SHG conversion. The two ultra-stable cavities used and characterized within this work already provide high-finesse mirror reflectivities for both the clock line fundamentals located at 1062.6 nm and 908 nm, respectively.

Finally, such a program would also allow a closed-loop IS scheme similarly to optical clock frequency ratio closure tests [46]. In Hg isotope shifts one could form a closed cycle using the transitions $^1S_0 \rightarrow {}^3P_1$, $^3P_1 \rightarrow {}^3S_1$, $^3S_1 \rightarrow {}^3P_2$, and $^3P_2 \rightarrow {}^1S_0$. Measuring such a closed set could provide a powerful internal consistency test for both SM and BSM analyzes of isotope shifts.

7 Towards electric dipole moment searches using laser-cooled mercury

7.1 Permanent electric dipole moments

The electric dipole moment $\vec{\mathcal{d}} = \int \mathrm{d}^3 r \; \rho(\vec{r})\, \vec{r}$ is the measure of the distribution of electric charge $\rho(\vec{r})$ in a system. While electric dipole moments in polar molecules can be simply described as $\vec{\mathcal{d}} = q\,\vec{r}$ with pointlike charges $\pm q$ separated along an intrinsic symmetry axis $\vec{r}$, a **permanent electric dipole moment (EDM)** $\vec{\mathcal{d}}$ of fundamental particles is fundamentally different.[1] As the spin $\vec{S}$ (or $\vec{F}$ for a composite system like an atom) is the only intrinsic vector of a particle, the permanent EDM must necessarily be aligned collinear to it, $\vec{\mathcal{d}} \parallel \vec{S}$, which can be seen as a consequence of the Wigner-Eckart theorem. For an eigenstate of such a system we would otherwise need an additional quantum number, a degeneracy not compatible with extensive observations in physics. A potential EDM of fundamental particles would therefore be aligned parallel or antiparallel to its spin, similarly to the magnetic moment $\vec{\mu}$.

Larmor precession Applying a controlled external magnetic field $\vec{B}$ to an atom induces a torque that leads to a Larmor precession of the atom's magnetic moment $\vec{\mu}$ around $\vec{B}$ with the time evolution $\mathrm{d}\vec{F}/\mathrm{d}t = \vec{\mu} \times \vec{B} = \gamma\, \vec{F} \times \vec{B}$. The angular frequency of this precession is the Larmor frequency given by

$$\omega_L = -\frac{g_F\, \mu_B}{\hbar}\, B \equiv \gamma\, B\,, \tag{7.1}$$

where γ is the gyromagnetic ratio associated to the total spin $\vec{F}$.

Analogously to the magnetic moment interacting with a magnetic field, the interaction of a permanent EDM $\vec{\mathcal{d}}$ with an electric field $\vec{E}$ is governed by the non-relativistic Hamiltonian $H_{\mathrm{EDM}} = -\vec{\mathcal{d}} \cdot \vec{E}$, identical to the interaction of an induced, non-permanent EDM discussed in section 4.1. The electric field induces a torque $\tau = \vec{\mathcal{d}} \times \vec{E}$, which aligns the dipole with the field and therefore minimizing its energy. This leads to a Larmor precession of $\vec{\mathcal{d}}$ around $\vec{E}$ and modifies the Larmor frequency from equation (7.1) by adding a term, such that

$$|\hbar\omega_L| = \left|\vec{\mu} \cdot \vec{B} + \vec{\mathcal{d}} \cdot \vec{E}\right|\,. \tag{7.2}$$

A potential permanent, nonzero EDM $\vec{\mathcal{d}}$ is therefore observable by detecting shifts in Larmor precession frequencies in presence of strong electric fields.

---

[1] We will distinguish between and denote induced and permanent EDM as $\vec{d}$ and $\vec{\mathcal{d}}$ respectively.

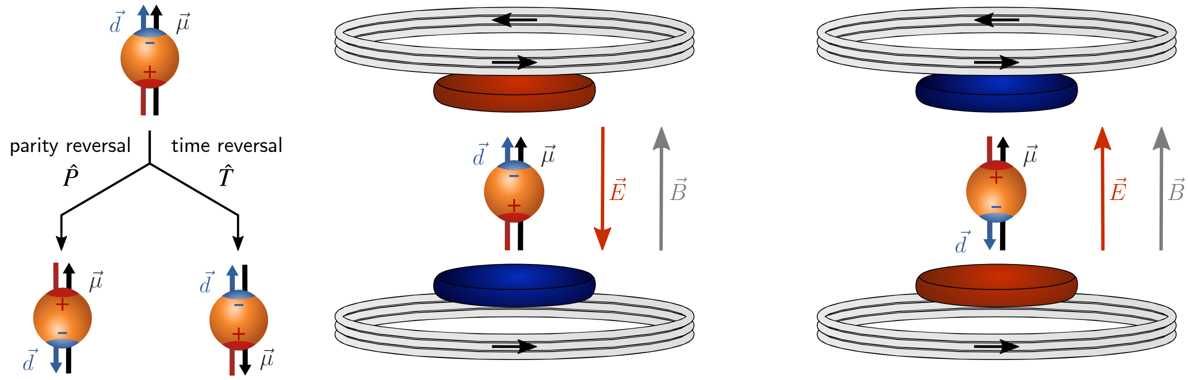

Figure 7.1: Permanent EDM $\vec{d}$ and magnetic moment $\vec{\mu}$ under parity T and time reversal transformation T (left). Experimental sketch of the EDM search (right). Magnetic moment $\vec{\mu}$ and EDM $\vec{d}$ are aligned to an external magnetic field $\vec{B}$ and electric field $\vec{E}$. Changing for instance the electric field polarity flips the EDM but not the magnetic moment.

7.1.1 Violation of charge and parity symmetry

As shown in figure 7.1, the EDM and magnetic moment transform differently under parity (T) and time reversal (T) operation, and the existence of a non-zero EDM of any fundamental particle would violate both T and T invariance. The EDM $\vec{d}$ changes its sign under the parity transformation P : $\vec{r} \to -\vec{r}$, the space-inversion/mirror operator, while the magnetic moment $\vec{\mu}$ is an axial vector/pseudovector and invariant under T, and the opposite being true for the time reversal operator T : $t \to -t$. Together with the operator of charge conjugation C : $q \to -q$, the combined transformation under charge, parity and time reversal symmetry (CPT) is the most fundamental symmetry in our universe. It applies to all physical phenomena in which Lorentz invariance is preserved – a concept that has been tested in numerous systems without evidence of its breakdown [312]. With the EDM interaction Hamiltonian H_{EDM} being both P and T odd, the existence of an EDM of any fundamental particle is therefore also a clear indication of combined charge and parity symmetry (CP) violation. As the amount of CP violation in the standard model (SM) is very small, a nonzero EDM measurement would therefore signal new sources of CP violation, directly probing beyond standard model (BSM) physics.

CP violation within the standard model In the SM of particle physics, CP violation refers to the breaking of the combined symmetries of charge conjugation, which exchanges particles with their antiparticles, and parity, the mirror transformation and a probe for chirality. Parity is conserved for all fundamental interactions of elementary particles, except for the weak force, as the SM Lagrangian only includes left-handed fermions in the weak interactions. Within the SM, CP violation is incorporated through a complex phase in the Cabibbo-Kobayashi-Maskawa (CKM) matrix, which governs the mixing of quark flavor eigenstates into mass eigenstates under the weak interaction. Since the experimental confirmation by observations in decays of kaons and B mesons in 1964 and around the 2000s, the discovery of spontaneous broken symmetry in subatomic physics gained a lot of attention.

Beyond standard model CP violation CP violation plays a crucial role in explaining the observed dominance of matter over antimatter in the universe, with constraints coming from cosmological observations of the cosmic microwave background. The majority of BSM theories that explain baryogenesis require significant CP violation. However, the amount of CP violation present in the SM is over ten orders of magnitude too small to explain the imbalance of matter and antimatter in our universe. The $\bar{\theta}_{\mathrm{QCD}}$ vacuum term in the Lagrangian of quantum chromodynamics is another source of CP violation in the SM. The unnatural small value of $\bar{\theta}_{\mathrm{QCD}}$ however represents a fine-tuning problem of theory parameters – the strong CP problem: the magnitude of the neutron electric dipole moment (nEDM) $d_n \approx \bar{\theta}_{\mathrm{QCD}} \cdot (6 \times 10^{-17}\,\mathrm{e} \cdot \mathrm{cm})$ predicted from this CP violating term, at current experimental upper bounds requires $|\bar{\theta}_{\mathrm{QCD}}| < 1 \times 10^{-9}$ [313].

At the fundamental level, EDMs therefore probe CP violation from multiple high-energy SM and BSM sources, that generate CP-violating operators at low energies, including quark EDMs (d_q), chromo-EDMs ($\tilde{d}_q$), the aforementioned strong CP-violating $\bar{\theta}_{\mathrm{QCD}}$ vacuum angle, and interactions between and in-between quarks and electrons [3]. Next to a direct generation of a potential permanent EDM of electrons d_e, this also can also lead to EDMs of neutrons d_n and protons d_p that together contribute to permanent EDM of larger system like atoms and molecules. As BSM theories like supersymmetry often predict electron and neutron EDMs near current experimental limits, EDM searches are therefore a key probe for CP violation and new physics (NP) [314].

7.1.2 Atomic EDM from Schiff moments and nuclear structure

Atomic electric dipole moments (aEDMs) originate from P and T symmetry violating interactions in the atomic nucleus, which manifest through the nuclear Schiff moment. CP-violating interactions between electrons and nucleons, and additional enhancements via nuclear magnetic quadrupole and higher order moments contributions are possible [3, 29, 84]. Actually, Schiff's theorem predicts the full screening of a point-like nuclear EDM by the electron cloud – an induced EDM is created, and cancelling any nuclear moment [315]. The finite size of the nucleus and the nuclear structure, however, lead to a non-vanishing Schiff moment, which allows residual P and T-violating interactions to survive and reduces the screening in atoms to about 10^{-3} [29]. As atomic or molecular systems are much easier to handle than fundamental particles, the former are still the preferred choice for EDM searches. EDM enhancing interactions are encapsulated in the Schiff moment operator $\vec{\mathcal{S}}$, which can be approximated as the sum

$$\vec{\mathcal{S}} = \vec{\mathcal{S}}^{(\mathrm{ch.})} + \vec{\mathcal{S}}^{(nucl.)} = \frac{|e|}{10} \sum_{i=1}^{Z} \left(r_i^2 - \frac{5}{3} \langle r^2 \rangle \right) \vec{r}_i \; + \; \frac{1}{6} \sum_{i=1}^{A} \left(r_i^2 - \langle r^2 \rangle \right) \vec{d}_i \,, \tag{7.3}$$

where the first term $\vec{\mathcal{S}}^{(\mathrm{ch.})}$ accounts for the nuclear charge distribution of the individual protons of charge $|e|$ determining the nuclear ground-state wave function and the second term $\vec{\mathcal{S}}^{(nucl.)}$ incorporates contributions originating in the non-zero EDMs $\vec{d}_i$ of the individual nucleons [29].

To leading order, the magnitude of the Schiff moment can be reduced to a sum of direct contributions from the neutron EDM, d_n, and proton EDM, d_p, and a combination of isoscalar (s), isovector (v), and isotensor (t) P, T-odd nucleon-nucleon and nucleon-pion interactions [29],

$$\mathcal{S} = a_n\, d_n + a_p\, d_p + \sum_{i \in \{s,\, v,\, (t)\}} \left(a_i\, g\, \bar{g}_i + A_i\, \bar{C}_i \right) \,. \tag{7.4}$$

The $\not{d}_n$ ($\not{d}_p$) are the neutron (proton) permanent EDM. The g is the standard strong pion-nucleon coupling constant, while the $\bar{g}_i$ are the P, T-odd (CP-violating) pion-nucleon coupling constants (with $i = s, v, t$ indicating isoscalar, isovector, and isotensor components, respectively). The C_i denote contact-interaction (short-range) CP-violating nucleon-nucleon coupling constants. The a and A are coefficients describing the nuclear structure response. The origin of nonzero EDM in atomic systems is therefore fully determined by nuclear effects, and knowledge about the nuclear shape to derive bounds on SM and BSM interactions from aEDM measurements is essential.

Nuclear deformation contributions

In paramagnetic atoms with unpaired electron spin like ^{133}Cs or ^{210}Fr, the valence electron wave functions near the nucleus are highly relativistic and the increasing penetration of s- and p-orbitals into the nuclear region enhances the Schiff moment. This makes these systems primarily sensitive to electron $\not{d}_e$ and spin-independent pseudoscalar-scalar electron-nucleon interactions [316]. The nuclear quadrupole moment induced aEDM contribution scales approximately as $\not{d} \propto \beta_2 \, Z^3 \, A^{2/3} / \Delta E$, where β_2 is the quadrupole deformation parameter, as introduced before, and ΔE is the energy splitting between opposite-parity nuclear ground states [84]. This Z^3 scaling with the nuclear charge – while not a contribution in Hg due to zero electron angular momentum – makes quadrupole deformed and heavy atoms particularly favorable for EDM searches.

Higher order moments, like nuclear octupole deformation $\langle \beta_3 \rangle$ in systems as ^{225}Ra or ^{223,225}Fr can further enhance the Schiff moment. Here, the pear shape of the nuclear charge density induces a Schiff moment scaling of $\mathcal{S} \sim \beta_2 \beta_3^2 \, Z \, A^{2/3} / \Delta E$ [3], which also favors heavy atoms.

Mercury EDM

The EDM of the diamagnetic atom like ^{199}Hg and ^{129}Xe is dominated by direct nuclear Schiff moments and CP violating interactions between the electrons and the nucleus [84, 317] that originate in the last term of the Schiff moment contributions in equation 7.4. For heavy atoms, the volume-effect of the Schiff moment induced EDM scales roughly at Z^2, as do direct contributions from nucleon EDMs. Relativistic effects scaling with Z enhance this coupling further [318]. While much weaker than in paramagnetic atoms, finite size effects and hyperfine interaction with the $I = 1/2$ nuclear spin can also introduce contributions from the electron EDM [318].

Nuclear structure theory is however still limited in predicting the dominating Schiff moment contributions. Reference [3] for instance compares latest results of a variety of nuclear (density functional theory) calculations giving a wide range of nucleon EDM coupling constants for ^{199}Hg,

$$\begin{array}{ccc}
\hline
a_0 \ (\mathrm{e \cdot fm^2}) & a_1 \ (\mathrm{e \cdot fm^2}) & a_2 \ (\mathrm{e \cdot fm^2}) \\
\hline
0.00004 \leftrightarrow 0.087 & -0.016 \leftrightarrow 0.087 & 0.009 \leftrightarrow 0.174 \\
\hline
\end{array}, \tag{7.5}$$

and similar results for elements like ^{129}Xe, that are being probed for an aEDM. While this motivates an improved nuclear structure theory supported by experimental studies of the mercury nucleus – such as high-resolution IS spectroscopy, discussed in the previous chapter – mercury still provides the tightest bound for aEDM searches, and also remains one of the best candidates for future searches [319].

Mercury is considered a crucial part of the set of EDM measurements that, together, provide the most important restrictions for CP-violating terms in the SM and BSM parameter space [3].

7.2 Probing CP violation via EDM measurements

The search for permanent EDMs of fundamental particles has been ongoing since the late 1950s, making it one of the longest-standing experimental efforts in precision physics. EDMs are typically being probed indirectly via spin precession induced Faraday effects, as discussed in the following section.

7.2.1 Detecting spin precession

As already illustrated in figure 7.1, probing a system with magnetic moment $\vec{\mu}$ and EDM $\vec{\not{d}}$ both aligned in external magnetic and electric fields $\vec{B}$ and $\vec{E}$, and alternating the field orientation between parallel $\vec{B} \upuparrows \vec{E}$ (+) and antiparallel $\vec{B} \updownarrows \vec{E}$ (−), the difference in Larmor frequency directly gives us the EDM. If we ensure that electric and magnetic field amplitudes E, B are constant/stable, following equation (7.1) we obtain

$$|\hbar\, \omega_{L,\pm}| = |2\, \mu\, B \pm 2 \not{d}\, E| \quad \Rightarrow \quad \not{d} = \frac{\hbar\, (\omega_{L,+} - \omega_{L,-})}{4\, E}\,, \tag{7.6}$$

Spin precession can be probed experimentally via the (linear) optical Faraday effect[1] [314]. The interaction between an external electric field $\vec{E}(t) \propto e^{i\, \omega\, t}$ propagating through a gas of mercury atoms with ground state $|g\rangle$ and excited state(s) $|e\rangle$ induces an electric dipole moment $\vec{d}$, which leads to a refractive index n. We can relate n to the complex polarizability $\tilde{\alpha}(\omega)$, which we discussed in the context of optical dipole traps (ODTs), see equation (5.4). This leads to a dispersive lineshape of the refractive index given by[2]

$$n(\omega) = \mathrm{Re}\left[\sqrt{1 + \frac{n\, \tilde{\alpha}(\omega)}{\epsilon_0}}\right] \approx 1 + \frac{n\, \mathrm{Re}[\tilde{\alpha}(\omega)]}{2\, \epsilon_0} = 1 + \frac{n}{\epsilon_0} \sum_{|e\rangle} \frac{\omega_{ge}\, |\langle g|d_z|e\rangle|^2}{\hbar\, (\omega_{ge}^2 - \omega^2)}\,, \tag{7.7}$$

featuring sharp transition(s) near the atomic resonance frequencies ω_{ge}; here n is the atomic number density of the sample. As the Zeeman shift of the m_F levels shifts these resonance locations, circularly polarized electric fields of different handedness experience different refractive indices and a relative phase retardation.

For EDM detection in mercury, we are primarily interested in the $\left|{}^1\mathrm{S}_0,\ F = 1/2,\ m_F = \pm 1/2\right\rangle$ ground state and the $\left|{}^3\mathrm{P}_1,\ F' = 1/2,\ m_{F'} = \pm 1/2\right\rangle$ excited state of ${}^{199}\mathrm{Hg}$ [320]. The ground state ${}^1\mathrm{S}_0$ has a single hyperfine level with $F = 1/2$ and two ground-state magnetic sublevels $m_F = \pm 1/2$ that form a clean two-level system that is ideal for coherent spin precession measurements. The excited $\left|{}^3\mathrm{P}_1\right\rangle$ state splits into $F' = 1/2$ and $F' = 3/2$, with corresponding magnetic sublevels and enables efficient optical pumping and detection. Although the $F' = 3/2$ level allows for cycling transitions, which can be useful for state preparation or detection, one uses the $F' = 1/2$ level in EDM experiments. This choice

---

[1] The explanation of the effect is also credited to Macaluso and Corbino, as well as Voigt for their independent studies on absorption spectra of alkali atoms in the presence of magnetic fields in the late 19th century [314].

[2] Simplified for a spherical atom, where the polarizability tensor is symmetric, $\tilde{\alpha}_{\mu\nu} = \tilde{\alpha}\, \delta_{\mu\nu}$.

simplifies the spectrum and avoids complications from optical pumping into dark states or off-resonant excitations. The $F = 1/2 \leftrightarrow F' = 1/2$ transition offers better control over the spin dynamics, which is essential for precision measurements of the aEDM. In contrast, ^{201}Hg, with $I = 3/2$, has a more complex hyperfine structure that introduces additional magnetic sublevels, increasing experimental complexity and sensitivity to systematic errors. Moreover, its nuclear structure leads to a smaller and less well-understood Schiff moment, reducing theoretical and experimental sensitivity to an EDM. These factors make ^{199}Hg the preferred choice for high-precision EDM searches.

We now consider a gas of ^{199}Hg atoms. For an incoming, e.g., linearly polarized light field oriented along the magnetic field axis, $\vec{k} \parallel \vec{B}$, (an equal superposition of σ_+ and σ_- polarization) propagating a distance L through the sample, the polarization rotates about an angle

$$\phi_{\text{Faraday}}(t) = \frac{\pi L}{\lambda}\,\left(n_+(\omega) - n_-(\omega)\right)\,\sin\left(\omega_L\, t\right). \tag{7.8}$$

This generates a signal that is modulated at the Larmor frequency ω_L and can be detected via polarization optics [320]. First optical detection of magnetic resonance via the Faraday effect in mercury dates back to investigations of Cohen-Tannoudji et al. in 1963 [321].

7.2.2 Overview of EDM searches

The first direct search for a nEDM was performed by Purcell and Ramsey in 1957, setting an upper limit of $|d_n| < 5 \times 10^{-20}\ e \cdot \text{cm}$ [322]. Since then, experimental techniques have improved by several orders of magnitude and a wide variety of atomic and molecular systems have been employed in the search for EDMs, offering complementary sensitivity to different sources of parity (P) and time-reversal (T) violation. Reference [3] provides a global analysis of CP violation in atoms and molecules, categorizing these systems into four classes based on their electronic configuration and nuclear spin, each with distinct sensitivities to underlying sources of EDM generation.

Class I includes open-shell molecular systems with spin-zero nuclei, such as ThO, HfF$^+$, and YbF, which are primarily sensitive to the electron electric dipole moment (eEDM) and scalar-pseudoscalar electron-nucleon interactions. Among these, ThO ($Z = 90$) [28] and HfF$^+$ ($Z = 72$) [27, 323] have outstanding sensitivity for eEDM searches due to their large internal electric fields and long coherence times. The most stringent bound on the eEDM to date comes from measurements of HfF$^+$ by a group led by Eric Cornell, yielding $|d_e| < 4.1 \times 10^{-30}$ e cm [27]. The other very promising Class I system is ThO [324, 325], where the previous eEDM bound of $|d_e| < 1.1 \times 10^{-29}$ e · cm at 90 % confidence level (CL) was set by the ACME II collaboration in 2018 [28], and further improvements are underway.

Class II comprises closed-shell systems with spin $I = 1/2$ nuclei, which are mainly sensitive to hadronic sources of CP violation including the neutron and proton EDMs and CP-odd nuclear forces, manifesting through nuclear Schiff moments. The most stringent aEDM limit is provided by measurements on room temperature vapors of ^{199}Hg, with a sensitivity of $\sigma_d = 3 \times 10^{-30}\ e$ cm [31]. Additional Class II systems include TlF [326], ^{129}Xe [327, 328], and Yb [329], as well as Ra [30, 330–332].

Class III includes open-shell systems with spin $I = 1/2$ nuclei such as Tl [333] and PbO [334], which offer mixed sensitivity to both electron and nuclear EDM contributions. **Class IV** is represented by systems such as ^{133}Cs [335], which are open-shell atoms with higher nuclear spin ($I > 1/2$), allowing sensitivity to CP violating tensor interactions and nuclear magnetic quadrupole moments.

Neutron EDM measurements Apart from atomic and molecular EDM searches, direct measurements of the nEDM are still being pursued today with increasing sensitivity. Two experiments are leading this effort: The **nEDM / n2EDM** experiment(s) at the Paul Scherrer Institute (PSI) and the **PanEDM** project at the Institut Laue-Langevin (ILL). We collaborate with the latter in developing ultraviolet (UV) lasers for magnetometry using mercury atoms as the sensor.

The nEDM/n2EDM project(s) utilizes a double-chamber spectrometer and an ultracold neutron source. An array of ^{199}Hg and ^{133}Cs co-magnetometers is used to extract the spatial magnetic field distribution including its gradients and correct for magnetic field drifts, that are minimized using both passive and active magnetic shielding and stabilization. It employs Ramsey's method of separated oscillatory fields, which creates a temporal interferometer sensitive to phase shifts induced by the interaction of the neutron spin with an applied electric field – a phase proportional to the EDM and spin polarization. The measurement provides the so far most stringent upper limit on the nEDM, with a value of $d_n = (0.0 \pm 1.1_{\text{stat}} \pm 0.2_{\text{sys}}) \times 10^{-26}\,\text{e} \cdot \text{cm}$ providing a bound of $|d_n| < 1.8 \times 10^{-26}\,\text{e} \cdot \text{cm}$ at 90 % CL.

The PanEDM project also uses a double-chamber Ramsey apparatus with ultracold neutrons and uses the SuperSUN cold neutron source. It is supported by a passive magnetic shield and a dual ^{199}Hg co-magnetometer system [34] with outstanding sensitivity [32, 33]. Both the upgraded n2EDM experiment at PSI and the PanEDM experiment at ILL now aim for an increased sensitivity of $\sigma_d = 1 \times 10^{-27}\,\text{e} \cdot \text{cm}$ and beyond. Future generation experiments also include the **nEDM@SNS** experiment at the Spallation Neutron Source at Oak Ridge National Laboratory, which is currently under construction. It utilizes ultracold neutrons in a superfluid ^{4}He environment with polarized ^{3}He as a co-magnetometer and aims to reach a sensitivity of $\sigma_d = 3 \times 10^{-28}\,\text{e} \cdot \text{cm}$ [336].

A global analysis incorporating measurements from all classes is necessary to disentangle and constrain the full parameter space of CP-violating interactions, including those arising from the electron, neutron, and proton EDMs, as well as from effective CP-odd four-fermion operators [3].

7.2.3 Searching atomic EDMs using mercury

Thermal vapor cell measurements The use of mercury for aEDM searches was already proposed in 1982 with initial experiments starting in Seattle in 1984 [318]. The most stringent constraints on an aEDM to date are imposed by the experimental findings of the University of Washington, which utilized room-temperature vapors of mercury through an over 20-year series of experiments, with EDM bounds given between 2001 [337] to 2016 [31].

The experimental setup of the latest measurement [31] consists of two cylindrical glass cells filled with gaseous ^{199}Hg(at a vapor pressure of 1.7×10^{-3} mbar at room temperature and about 0.6 bar of CO buffer gas. The cells are located inside a common homogenous magnetic field and feature shared electrodes that create opposing electric fields in the two regions. The atomic spin is transversely polarized via optical pumping for about 30 s. The Faraday effect induced by spin precession is probed using blue, linearly polarized laser light in two short measurement pulses over an overall spin precession time of about 200 seconds. With paraffin-coated cells, spin relaxation time of 250 s to 600 s could be reached – a strong feature of diamagnetic atoms, that is also exploited in measurements of ^{129}Xe, where even larger coherence times can be reached.

The dual-cell setup with a shared common electrode allows synchronous measurement of the two Larmor precession frequencies $\omega_{\pm}$, as given by equation (7.6). The system is sandwiched in-between two additional cells with no EDM sensitivity at zero electric field, used as magnetometers. The full setup is magnetically isolated via passive mu-metal shields for reducing systematic shifts. Spin precession during the probe beam phase and the in-between dark phase in absence of any interrogation results in characteristic Larmor frequencies of $\omega_L \approx \pm 10\,\mathrm{Hz}$ at a bias magnetic field of around $B = 10\,\mathrm{mG}$. The null measurement of resolved Larmor frequency differences in an electric field of about $E = 10\,\mathrm{kV/cm}$ feature a resolution of <0.1 nHz.

While early experiments relied on lamp-based light sources at 254 nm that provided excellent long-term reliability and stability also in similar experiments [318], later upgrades benefit from technology advancement in deep-UV continuous wave laser development. The probe laser light is detuned +10 GHz to the blue, halfway between the $F = 0 \to F' = 1/2$ and $F' = 3/2$ excited states of the ${}^1\mathrm{S}_0 \to {}^3\mathrm{P}_1$ transition. Especially for co-magnetometry this requires precise knowledge of the isotope shifts determining the vicinity of isotopic resonances and associated light shifts [33].

Measurement sensitivity The sensitivity of the EDM measurement is predominantly determined by the Larmor precession frequency measurement's uncertainty. Following the idea of the EDM being extracted from the frequency difference given in equation (7.6), under the assumption of perfectly stable electric and magnetic field, the ideally shot-noise limited EDM sensitivity is given by [320]:

$$\Delta d = \frac{\hbar}{2\,E\,\sqrt{N\,T\,\tau\,\epsilon}} \tag{7.9}$$

and therefore favors large atomic sample sizes N, large electric field strengths E, measurement interrogation times T and spin precession times τ. The parameter ϵ denotes imperfect detection efficiency from various sources and takes values $0 \leq \epsilon \leq 1$.

The external field strength E in EDM measurements is typically limited to a few 10 kV/cm due to arc discharges in the analyzed vapor and buffer gas. While polarizable molecules feature a strong enhancement of externally applied electric fields due to the induced inner EDM and are not limited by these constraints, aEDM searches in Hg would strongly benefit from higher electric field strengths limiting the measurement precision. Here, diamagnetic atoms like ${}^{199}\mathrm{Hg}$ have the advantage over paramagnetic atoms to be less sensitive to systematic effects from magnetic interaction such as leakage currents and motional induced magnetic fields $\vec{E} \times \vec{v}/c^2$ [338] that can mimic an EDM, and to spin depolarizing effects that limit spin coherence times [320].

Systematic uncertainties on the measured EDM are however strongly limited by the macroscopic size of the cell geometry and dominated by electric field correlated axial (and radial) motion of the atoms within the cell that, in combination with magnetic field gradients, is the dominating systematic uncertainty [31]. While the total uncertainty is currently dominated by statistics, required measurement time T for order-of-magnitude improvements render further progress impractical without a conceptual improvement, as the current measurement campaign took already about 10 months. Alternatively, increasing the probed sample sizes N strongly affects possible electric field strengths, where leakage currents pose already another systematic limit. Other systematic effects include imperfections in electric field reversal (notes as E^2 effects in reference [31]) and electric field inhomogeneities.

7.3 Probing electric dipole moments of laser-cooled mercury

The current ^{199}Hg measurement has reached fundamental limitations in its room-temperature vapor cell implementation, which motivates the development of a next-generation approach. The vision of this project is probing laser-cooled, tightly confined samples of ^{199}Hg atoms.

Similar to measurements on ^{225}Ra [30, 331, 332], this promises higher atomic densities, smaller physical size allowing strongly increased electric field strengths and reduced systematic errors. Going for ^{199}Hg instead of radioactive ^{225}Ra also has the advantage that radioactive elements often need to be produced artificially and therefore limit both the measurement time and the sample size. Experiments in radium for instance rely on spinless ^{226}Ra ($t_{1/2} = 1600\,\text{years}$) for testing and studying systematics, as the ^{225}Ra isotope of interest decays with a half-life time of just $t_{1/2} = 15\,\text{days}$ and sample sizes are limited to the $1\,\mu$Curie-range ($\approx 1\,\mu\text{g}$). While source operation in ultra-high vacuum (UHV) environment is not trivial either, here mercury has a clear advantage being the heaviest non-radioactive element in the periodic system that can be laser-cooled so far.

By confining atoms in an optical dipole trap and UHV, the maximum electric field strength is now in theory set by the vacuum breakdown voltage and leakage currents are strongly reduced. Field emission effects, surface roughness, and material properties of the electrodes in these experiments currently limit field strengths to about $500\,\text{kV/cm}$ [339]. However, as going from a glass cell container to an optical dipole trap confinement, much smaller sample volumes can be probed and electrodes can also be spaced much closer. This also strongly reduces systematic uncertainties by strongly reducing magnetic gradient fields and E-field inhomogeneities.

We also consider using techniques like spin squeezing out of the toolbox of quantum optics, that could increase the measurement sensitivity. Future iterations also aim at probing quantum degenerate gases of mercury, that have the potential for significant sensitivity gains via quantum Heisenberg scaling. This could change the sensitivity scaling from $1/\sqrt{N}$ to $1/N$.

7.3.1 A versatile quantum gas apparatus for EDM measurements

The measurements and method investigations presented in this thesis are all performed in the vacuum chamber presented in chapter 3. With the development of an UHV compatible mercury source chamber, that can be extended to an atomic beam source for Zeeman slower (ZS) operation, this establishes a solid foundation for future EDM measurements. High-resolution EDM measurements call for a magnetically shielded science chamber. For generating quantum degenerate gases we will further benefit from an improved background vacuum pressure. For both of these goals, a vacuum chamber design shown in figure 7.2 is proposed. The design is based on a ZS that provides both a source of slow atoms for better magneto-optical trap (MOT) loading, as discussed in section 4.8.3, and allows a strong vacuum pressure gradient between source and main chamber via a set of differential pumping stages. The latter should allow deeper UHV to extreme high vacuum (XHV) operation of the main MOT and quantum gas main chamber and the science cell. The planning of the experiment is well underway, but only a brief overview of the new machine's building blocks is provided here.

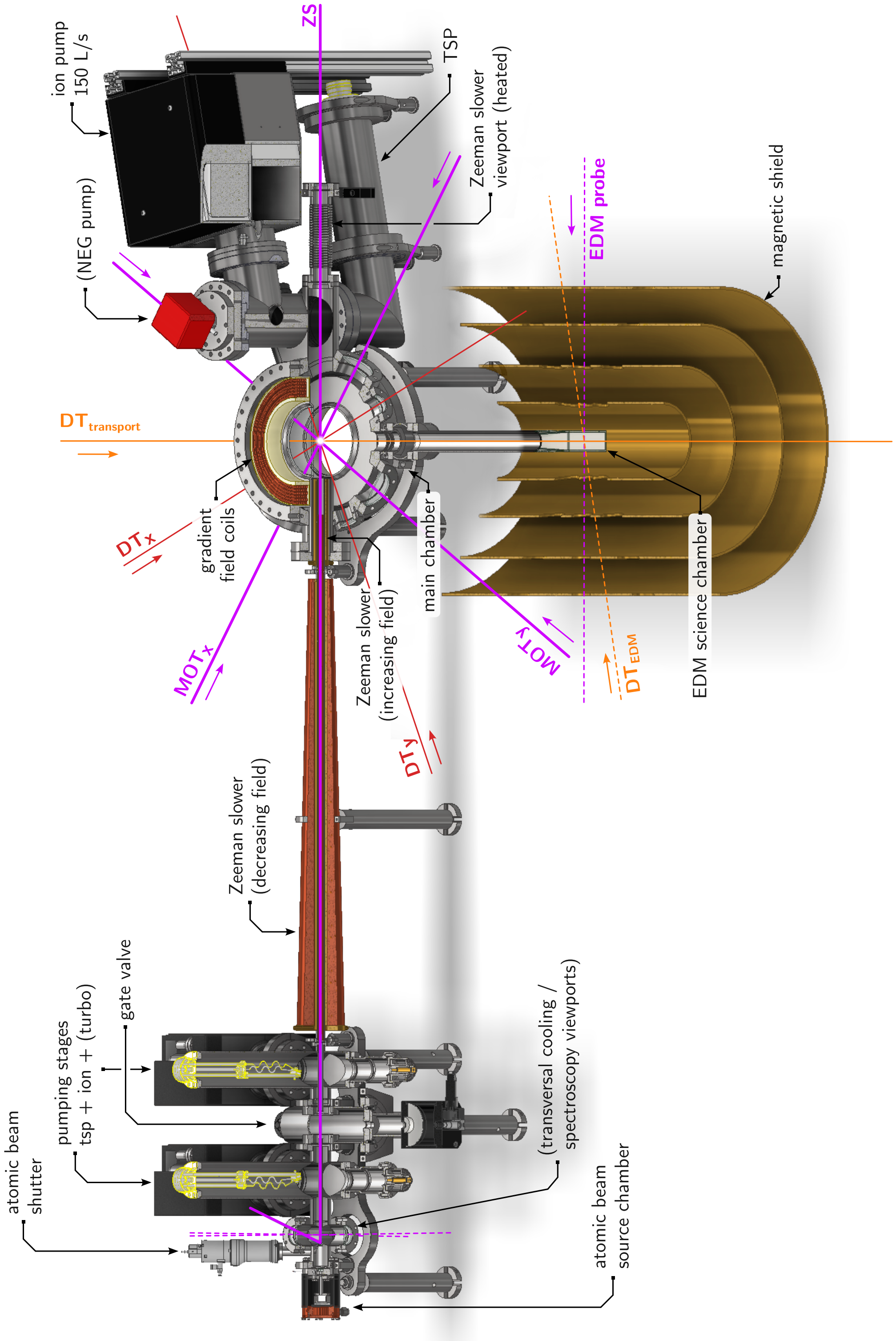

Figure 7.2: CAD drawing (cut view) of the planned vacuum chamber design for MOT loading from a differentially pumped ZS source and featuring a science chamber with electric field electrodes and magnetic shielding for future EDM measurements.

Source chamber

The source chamber contains the atomic beam source described in section 3.1.3. It also features a mechanical atomic beam shutter and four viewports for characterizing the atomic beam and optional transversal cooling. Each section has its own pumping station with a main ion getter pump (IGP) for long term operation, a titanium sublimation pump (TSP) to remove contaminants after baking and a full-metal angle valve for connection to a turbo molecular pump (TMP) during bake-out. The source is again being separated from the rest of the chamber via a pneumatic gate valve.

Main chamber

A set of three differential pumping stages – low conductance apertures and tube connections in combination with the pumping stations – within the ZS atomic beam path separate the main chamber from the source. It is simulated to hold a pressure difference of nine orders of magnitude and allow XHV vacuum pressures in the main chamber, when pumped by a combination of large ion pump and TSP. The optional installation of a NEG pump for better hydrogen pumping speed and pumping of mercury is motivated by the experience collected in the current setup. For optical access, we aim for a six beam MOT setup and viewports for horizontal and vertical ODTs and optical lattices. A recessed viewport on the top allows bringing a microscope objective close to the location of the atoms, which allows high-resolution imaging at high numerical aperture.

Science chamber

Being very sensitive to magnetic field variations, the science chamber for probing an electric dipole moment is separated and isolated from the main chamber. Transfer to an external EDM science glass chamber is planned to be established by transport in an optical dipole trap, where a crossed ODT setup can hold the laser-cooled atoms in-between the electric field electrodes.

For transport, the ODT focus can be moved by tunable or moving lenses. Here, the low polarizability of mercury will probably require reloading the atoms to a more tightly focussed single beam trap. Alternatively, keeping the trapping volume can be achieved by installation of a crossed ODT that is created by a single moving lens under a shallow angle.

The shielded part of the science cell extension is made of glass to avoid any metallic impurities and is pumped by the main chamber connection to reduce ion pump's magnetic field gradients at the location of the atoms. With the experimental experience presented here, based on the good UV compatibility and performance of the viewports in this work, we plan to bond nanostructured UV fused silica glass substrates using UHV compatible epoxy. Potentially, classical hard AR coatings could still be a viable UV resistant option here. Current investigations indicate that removing the substrates' Beilby layer before coating leads to strongly improved lifetimes under UV exposure.[1] This thin, amorphous surface film formed by plastic flow during polishing lacks crystalline structure can contain solarization-vulnerable contaminants and can be efficiently removed via ion beam etching.

---

[1] Personal communication with Stefan Truppe.

Magnetic shielding & fields

The science chamber is designed to feature a four layer magnetic shield made out of mu-metal[1], a metallic alloy with a very high magnetic permeability of $\mu_r = 50{,}000$ to $200{,}000$. In the simplest approximation, given the transversal and longitudinal field suppression of a cylindrical shield of diameter D and length L, is given by $S_\perp \approx \mu_r\, d/D + 1$ and $S_\| \approx 4\, N\, (S_\perp - 1)/(1 + D/(2\, L)) + 1$ with $N \approx 0.38(L/D)^{-1.3}$ for the geometry described here [340]. For our design of four stacked cylinders of increasing length and diameter – shown in figure 7.2 – with respective end caps, every shield contributes with a shielding factor of $S_\perp = 250$ to 1000 and $S_\| = 200$ to 300, respectively. Multi-layer shields ideally contribute multiplicative for large enough shield distances. Holes in the shield necessary for optical access reduce the shielding factor strongly, even though the introduced aperture field decreases exponentially with the distance from the hole. We estimate that the shield will suppress ambient static and low-frequency magnetic field changes by about −75 dB. Further suppression obtained by degaussing the shields through applying 50 Hz to 500 Hz AC magnetic fields to remove residual magnetization and internal fields should allow for suppression better than −80 dB [30].

We plan to utilize cylindrical cosine-theta coils both for degaussing and as the main quantization field driving the Larmor precession. In this type of coil, the current density varies with the cosine of the azimuthal angle θ around a cylinder $J(\theta) \propto \cos\theta$, which produces a very pure dipole field perpendicular to the cylinder axis and parallel to the EDM electrode stack.

Electrode design

The plan for the first EDM electrodes is based on a pair of plane-parallel copper electrodes mounted to a support frame made of Macor similar to the design used in the Radium experiment at Michigan State university [339], with the option to upgrade to a pair of niobium or titanium electrodes in the future. Here, electro-polishing and water pressure polishing of the electrodes as well as high voltage discharge-conditioning (that ablate microprotrusions on the electrode surfaces) [339] is planned to minimize surface inhomogeneities and increase the applicable voltage. In the first iteration we aim for an electrode distance of 0.5 mm that should allow voltages of up to 15 kV. The electrode was carefully designed to prevent electric breakdowns and leakage currents due to discharges at sharp corners, as the latter perfectly mimics an EDM signal. We simulate the electric field via a numerical finite-element method solving the electrostatic Laplace equation via successive over-relaxation algorithm, that validate the suitability of the design.

EDM readout

As an alternative to modified Faraday rotation readout schemes that utilize various forms of linear and nonlinear optical Faraday effects, as well as state preparation via optical pumping [314], we plan to read out the Larmor precession via dark state imaging [341]. Here, atoms are optically pumped with e.g., σ_+ polarized light into the $m_F = +1/2$ ground state that then forms a dark state for a σ_+ polarized absorption imaging pulse. Larmor precession of the spin polarized atoms then allows probing the $m_F = -1/2$ ground state population that also varies as $\propto \sin(\omega_L\, t)$. Alternative spin detection on the 120 MHz broad singlet transition at 185 nm could increase the number of scattered photons by about two orders of magnitude and reduce the associated photon shot noise by a factor of ten.

---

[1] ASTM A753 Alloy 4.

A Publication: Magneto-optical trapping of mercury at high phase-space density

This section presents a reprint of the journal article [1] as discussed section 4.7 of chapter 4. The complete citation reads:

> Quentin Lavigne, Thorsten Groh and Simon Stellmer, *Magneto-optical trapping of mercury at high phase-space density*, Physical Review A **105**, 033106 (2022). DOI: `https://doi.org/10.1103/PhysRevA.105.033106`

The article is included in this dissertation with the consent of all co-authors and the permission of the American Physical Society.

List of references

Since this publication uses a specific numbering system for its references, the bibliography is linked to the thesis bibliography via the table below.

reference in publication	equivalence in thesis	reference in publication	equivalence in thesis	reference in publication	equivalence in thesis
[1]	[24]	[13]	[342]	[25]	[343]
[2]	[344]	[14]	[107]	[26]	[145]
[3]	[19]	[15]	[58]	[27]	[146]
[4]	[345]	[16]	[346]	[28]	[347]
[5]	[153]	[17]	[31]	[29]	[348]
[6]	[154]	[18]	[330]	[30]	[349]
[7]	[350]	[19]	[35]	[31]	[351]
[8]	[40]	[20]	[172]	[32]	[352]
[9]	[41]	[21]	[251]	[33]	[353]
[10]	[46]	[22]	[354]	[34]	[355]
[11]	[56]	[23]	[356]	[35]	[357]
[12]	[155]	[24]	[358]	[36]	[359]

PHYSICAL REVIEW A **105**, 033106 (2022)

Magneto-optical trapping of mercury at high phase-space density

Quentin Lavigne, Thorsten Groh, and Simon Stellmer*
Physikalisches Institut, Rheinische Friedrich-Wilhelms-Universität, 53115 Bonn, Germany

(Received 21 December 2021; accepted 25 February 2022; published 15 March 2022)

We present a realization of a magneto-optical trap of mercury atoms on the $^1S_0 \rightarrow {}^3P_1$ intercombination line. We report on trapping of all stable mercury isotopes. We characterize the effect of laser detuning, laser intensity, and gradient field on the trapping performance of our system. The atom number for the most abundant isotope ^{202}Hg is 5×10^7 atoms. Moreover, we study the difference in cooling processes for bosonic and fermionic isotopes. We observe agreement with the Doppler cooling theory for the bosonic species and show sub-Doppler cooling for the fermionic species. We reach a phase-space density of a few parts in 10^{-7}, which constitutes a promising starting condition for dipole trap loading and evaporative cooling.

DOI: 10.1103/PhysRevA.105.033106

I. INTRODUCTION

All atoms in the class of alkaline-earth(-like) metal elements share a unique combination of properties: two valence electrons and a $J = 0$ ground state. The level structure decomposes into singlet and triplet states; the latter can be metastable and are connected to the single ground state via narrow intercombination lines. In recent years, this class of atoms has received widespread attention in the field of optical clocks [1], in quantum simulation based on laser-cooled atoms [2], and in low-energy searches for physics beyond the standard model [3,4]. Within this class of elements, mercury assumes a unique role: it is the heaviest element with stable isotopes that can be laser cooled, it has the highest ionization threshold, and as a consequence, all of its principal optical transitions are deep in the ultraviolet (UV) range. As the technology of UV lasers matured over the past few decades, cold-atom experiments with mercury atoms became feasible.

Magneto-optical trapping of mercury was first realized in seminal work by the group of Katori [5] and forms the basis of optical clocks based on mercury [6–10], benefiting in particular from its insensitivity to blackbody radiation shifts. Related research on laser cooling of mercury is also described in Refs. [11–15].

Here, we present a detailed study on laser cooling of mercury. The identification of optimal parameter ranges, in combination with increased laser power, has allowed us to substantially improve the atom number and phase-space density of laser-cooled samples compared to previous works. With these improvements, interesting experiments have come into reach [16], including a competitive measurement of the Hg electric dipole moment using laser-cooled atoms to search for physics beyond the standard model [17,18], isotope shift measurements [19–21], and evaporation towards degenerate quantum gases.

II. EXPERIMENTAL SETUP

In this work, laser cooling of neutral mercury is performed on the $^1S_0 \rightarrow {}^3P_1$ intercombination line at 254 nm, which has a linewidth of $\Gamma = 2\pi \times 1.3$ MHz and a corresponding Doppler temperature $T_D = 31\,\mu$K. The saturation intensity of this transition is $I_{\text{sat}} = 10\,\text{mW/cm}^2$. Note that precooling on the broad $^1S_0 \rightarrow {}^1P_1$ singlet transition is challenging due to its wavelength of 185 nm, for which high-power cw laser development is still in its infancy [22].

Our experimental apparatus, depicted in Fig. 1, is designed as a test setup to identify optimal parameters for laser cooling of mercury. The mercury atoms are loaded from the background gas. The atom source is composed of a stainless-steel reservoir filled with a few droplets of liquid mercury. This reservoir is cooled under vacuum by a four-stage Peltier element down to $-50\,^\circ$C. For loading of a magneto-optical trap (MOT), the oven is operated at a temperature of $-35\,^\circ$C, resulting in a partial pressure of about 5×10^{-6} mbar at the source. The source section is pumped with a 2 L/s ion pump to protect the in-vacuum electronics from mercury corrosion.

A CF40 tube with a length of 380 mm (conductivity $\sim$1.55 L/s) connects the source to the MOT chamber. The vacuum chamber, which is assembled from standard CF40 vacuum components, is pumped down to the range of 10^{-8} mbar by a 55 L/s ion pump and a standard titanium sublimation pump.

The magnetic quadrupole field required for atom trapping is generated by a pair of coils in anti-Helmholtz configuration. The coils are made of 6×6 mm^2 hollow-core square copper tubing and are water cooled. They consist of 12 windings each and have a diameter of 160 mm. These coils generate an axial gradient field $\partial B_z/\partial z$ of 0.20 G/(cm A). In typical operation, the axial gradient field is set to about 10 G/cm at a current of 50 A. The low inductance of the coils ($\sim$100 μH) enables us to quickly turn off ($<$1 ms) the magnetic field with an insulated-gate bipolar transistor. In practice, the switching time is limited by a metal frame to typically 6 ms. Three mutually orthogonal pairs of coils in Helmholtz configuration

---

[*] stellmer@uni-bonn.de

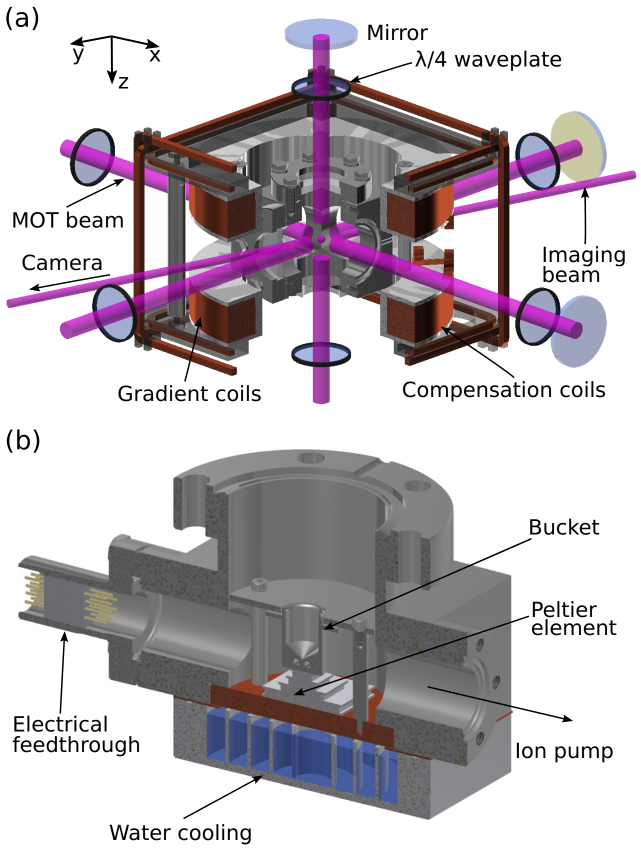

FIG. 1. Experimental setup. (a) Central region of the vacuum chamber, including coil systems and optics. (b) Cut-away view of the atomic source. A stainless-steel bucket filled with liquid mercury is temperature controlled via a four-stage Peltier element to set the vapor pressure in the vacuum chamber.

allow us to compensate for Earth's magnetic field and any other background field.

The light at 254 nm is generated by a commercial frequency quadrupled laser. The fundamental mode at 1016 nm is generated by a diode laser, which is stabilized to a commercial high-finesse cavity (Menlo, finesse 74 000 at 1016 nm) for linewidth reduction. A fiber-coupled phase modulator (Jenoptik PM1064) with 7-GHz bandwidth is used to imprint variable sidebands, which are used to steer the laser frequency with respect to the cavity mode.

The diode emission at 1016 nm is amplified by a tapered semiconductor amplifier, passed through a filter of $\sigma = 5.7\,\mathrm{GHz}$ transmission bandwidth to remove undesired incoherent background radiation (amplified spontaneous emission of the semiconductor laser), and amplified by a fiber amplifier to about 8 W. Two consecutive and resonant stages of second-harmonic generation generate more than 350 mW of UV power.

Polarization components are used to split the light at 254 nm into three pathways using a spectroscopy cell for monitoring purposes, the MOT beams, and the imaging beam. The light for the MOT is passed through an acousto-optical modulator (AOM) for intensity and frequency control before being split into three arms. The mean waist is increased up to $w_0 = 6.5\,\mathrm{mm}$. The three mutually orthogonal MOT beams are retroreflected and have a typical power P_{MOT} of 15 to 30 mW per beam, depending on the UV degradation of the optics. All beams are aligned with submillimeter accuracy to the center of the quadrupole field.

Absorption imaging is performed on the same optical transition. The imaging beam is passed through an AOM for frequency adjustment and switching; it is then focused through a 100-μm pinhole for mode cleaning, expanded to a waist of 7.5 mm, and delivered to the MOT region. It is linearly polarized and has a typical power of 1 mW. Our imaging system is composed of a single lens in the $2f$-$2f$ configuration to obtain a magnification of $M = 1$. A CCD camera (ANDOR model iXon3 885) with quantum efficiency in excess of 30% is used for imaging.

A typical measurement sequence consists of a 5-s-long MOT-loading phase in which the gradient field and the MOT beams are turned on. Then, the gradient field and MOT beam are switched off. The atom number and temperature of the atomic cloud are determined from standard time-of-flight (TOF) images.

III. RESULTS

A. Magneto-optical trapping of all seven stable isotopes

We begin our study by presenting magneto-optical trapping of all seven stable mercury isotopes (see Fig. 2). A list of the stable isotopes of mercury is provided in Table I: five bosonic isotopes with nuclear spin $I = 0$ and two fermionic isotopes, ^{199}Hg with $I = 1/2$ and ^{201}Hg with $I = 3/2$, exist. We adjust the waist of the MOT beams to $w_0 = 5.2\,\mathrm{mm}$ and set the power per beam to $P = 26\,\mathrm{mW}$, corresponding to a saturation parameter $s = I/I_{\mathrm{sat}}$ of $s = 6$. The magnetic field gradient is set to $\partial B_z/\partial z = 10\,\mathrm{G/cm}$. We scan the frequency of the MOT beams across the resonance frequency of each isotope. A maximum in atom number N is reached for a detuning Δ of about $-15\,\Gamma$ for the abundant bosonic isotopes. For the fermionic isotopes, the maximum atom number is obtained for ^{199}Hg at a detuning of about $-11\,\Gamma$ and for ^{201}Hg at about $-8\,\Gamma$.

We capitalize on the high laser power available, which allows us to increase the diameters of the MOT beams. We were able to observe a MOT of the least abundant isotope, ^{196}Hg, with a natural abundance of only 0.15%. This isotope was not detected in previous studies [5,6,11,13–15].

We observe that for the bosonic isotopes, the observed MOT atom numbers correspond, within the uncertainties, to the natural abundances. For that we normalize the peak MOT atom numbers N of each isotope to that of the most abundant isotope, ^{202}Hg. We then compare the normalized MOT atom numbers $N' = N/N_{202}$ of each isotope to its normalized natural abundance $A^{N'} = A^N/A^N_{202}$ (last column of Table I). The observed correspondence for the bosons is expected, as the electronic structures of these isotopes are exactly identical. This observation indicates that the MOT atom number is not yet saturated for the set of parameters used here.

For the fermions, however, we do observe a clear mismatch between the normalized atom number and isotope abundance: cooling and trapping efficiency is reduced by a factor of about

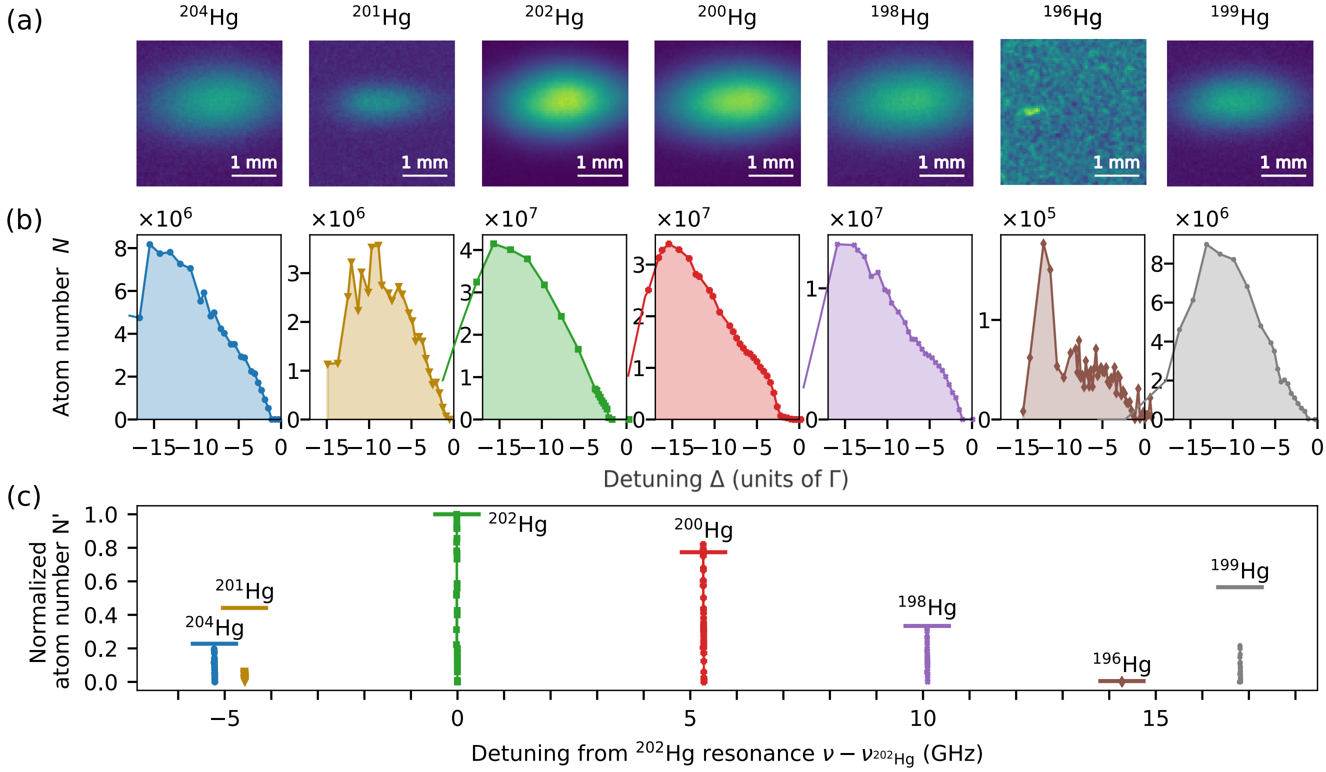

FIG. 2. Magneto-optical trapping of all stable Hg isotopes. (a) Absorption images of the MOTs after 0-ms time of flight. The image of ^{196}Hg is Gaussian filtered to increase visibility. (b) Number of trapped atoms N as a function of the detuning Δ for each isotope. (c) Normalized atom number as a function of the detuning from the ^{202}Hg resonance, with the same data as in (b). The horizontal lines represent the normalized isotope abundance.

3 for ^{199}Hg and by a factor of about 5 for ^{201}Hg. Compared to the bosonic isotopes, these two isotopes possess multiple m_F components in the $^1S_0$ ground state, as well as hyperfine and Zeeman structure in the $^3P_1$ excited state. The MOT is operated on the $F = 1/2 \rightarrow F' = 3/2$ transition for ^{199}Hg and on the $F = 3/2 \rightarrow F' = 5/2$ transition for ^{201}Hg. The reduced efficiency of fermionic MOTs was explained in Ref. [24] and is observed with many alkaline-earth-metal elements. In short, the vastly different g factors of the $^1S_0$ ground state ($g \approx 10^{-4}$) and the $^3P_1$ excited state ($g \approx 1.5$), as well as the multitude of Zeeman states, reduce cooling power and open up loss channels.

While the vast majority of magneto-optical traps are operated on $F \rightarrow F' = F + 1$ transitions, there is also an interest to study unconventional MOT operation for the cases $F' \leqslant F$. These cases are relevant for laser cooling of molecules and might use blue-detuned light [25]. Indeed, we observe stable magneto-optical trapping of the ^{199}Hg isotope on the $F = 1/2 \rightarrow F' = 1/2$ transition. With similar trap parameters we reach around $N = 1.1(2) \times 10^4$ atoms at a detuning of $\Delta \approx -3\,\Gamma$. This is a reduction of about two orders of magnitude with respect to the "ordinary" ^{199}Hg $F = 1/2 \rightarrow F' = 3/2$ MOT.

TABLE I. Naturally occurring mercury isotopes. For each isotope, we state the nuclear spin I; its natural abundance A^N [23]; the observed atom number normalized to the most abundant isotope, ^{202}Hg, N'; and the trapping efficiency $N'/A^{N'}$. The latter is expressed as the ratio of the normalized atom number and normalized natural abundance and shows a strong deviation from unity only for the fermionic isotopes.

Isotope	Spin statistics	Nuclear spin I	Natural abundance A^N	Normalized abundance $A^{N'}$	Normalized atom number N'	Trapping efficiency $N'/A^{N'}$
^{196}Hg	bosonic	0	0.15	0.0052	0.0043(13)	0.83
^{198}Hg	bosonic	0	9.97	0.3455	0.3220(12)	0.93
^{199}Hg	fermionic	1/2	16.87	0.5845	0.2166(10)	0.37
^{200}Hg	bosonic	0	23.10	0.8004	0.8200(12)	1.03
^{201}Hg	fermionic	3/2	13.18	0.4567	0.0862(7)	0.19
^{202}Hg	bosonic	0	29.86	1	1	1
^{204}Hg	bosonic	0	6.87	0.2380	0.1970(9)	0.83

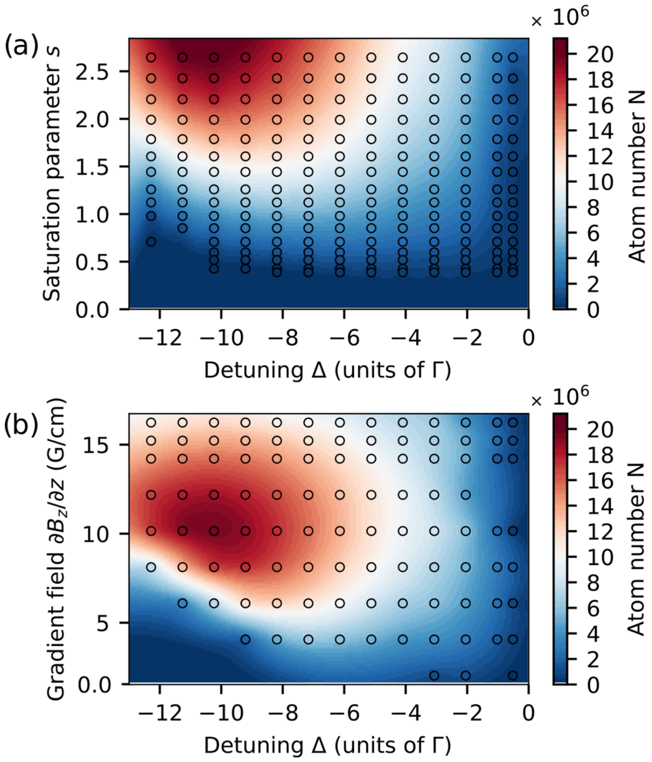

FIG. 3. Number of trapped atoms N as a function of (a) the detuning Δ and the saturation parameter s for a fixed magnetic gradient field of $\partial B_z/\partial z = 10\,\mathrm{G/cm}$ and (b) the detuning Δ and the magnetic gradient field $\partial B_z/\partial z$ for a fixed saturation parameter of $s = 2.6$.

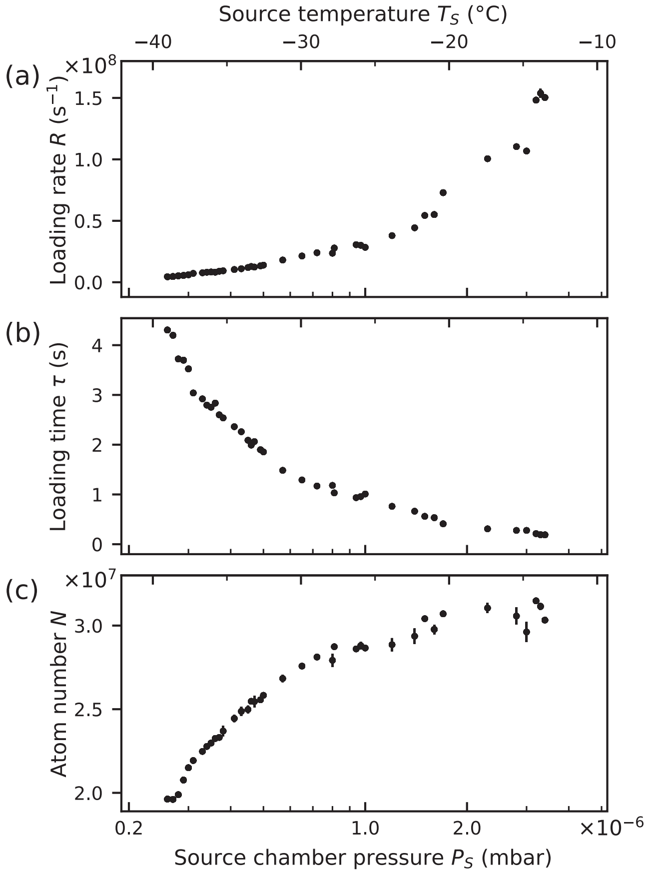

FIG. 4. Influence of the Hg partial pressure on (a) the initial loading rate, (b) the loading time, and (c) the equilibrium atom number. The partial pressure in the chamber cannot be measured directly; shown is the pressure reading of the small ion pump in the source chamber. The top axis shows the associated source temperature.

In the following, we will focus our studies on the most abundant isotope, ^{202}Hg. We will explore the key parameters such as laser detuning, intensity, and magnetic field gradient to optimize the performance of the experiment. These measurements significantly expand previous studies [8,12] to a broader parameter range.

B. Atom number

An important quantity of any cold-atom experiment is the atom number. For a fixed magnetic field gradient of $\partial B_z/\partial z = 10\,\mathrm{G/cm}$, we investigate the dependence of the atom number on the laser detuning Δ and on the saturation parameter $s = I/I_{\mathrm{sat}}$. The results are depicted in Fig. 3(a). In this contour plot, the circles indicate measurement points, and the color of the circle's filling denotes the measurement value. As a background, we provide a two-dimensional (2D) interpolation to improve the readability.

The atom number increases as the detuning increases and reaches a maximum of 2×10^7 atoms around $\Delta = -10\,\Gamma$. Beyond that maximum, the radiation pressure force becomes too weak to efficiently confine the atoms in the trap. At a detuning of $\Delta = -10\,\Gamma$, the atom number increases linearly with the saturation parameter s. Due to degradation of the laser and the optics, we could reach a saturation parameter of only $s \approx 3$ in this study. Up to this value, we do not observe saturation of the atom number.

Figure 3(b) shows the dependence of the atom number N on the magnetic field gradient $\partial B_z/\partial z$ and laser detuning Δ for a fixed saturation parameter, $s = 2.6$. An increase in the gradient field improves the atom number until it reaches a maximum around 10 G/cm, largely independent of detuning. Beyond this maximum, a reduction in the atom number is observed, explained by the reduction in capture volume at higher gradients fields. Typical atom numbers for the ^{202}Hg isotope are in the range of 10^7 atoms.

Our MOT is loaded from the background gas, and its equilibrium atom number depends on the loading rate (proportional to the Hg partial pressure) and the atom loss rate. Quite generally, the loss rate is a combination of one-body losses (induced by collisions with room-temperature Hg atoms and all other residual gas atoms), two-body losses (e.g., light-assisted collisions), and three-body losses (molecule formation). For the densities obtained in this study, we conclude that only one-particle losses are relevant.

We vary the Hg partial pressure by controlling the oven temperature T_s from $-37\,^{\circ}\mathrm{C}$ to $-13\,^{\circ}\mathrm{C}$. The loading rate increases linearly with partial pressure [see Fig. 4(a)]. The atom number saturates at a source temperature of around $-25\,^{\circ}\mathrm{C}$, which corresponds to about 1.6×10^{-6} mbar in the source section. At this point, the residual gas in the vacuum chamber is dominated by mercury, and the MOT atom number becomes independent of Hg partial pressure [see Fig. 4(c)]. Increasing the partial pressure further increases both the loading rate and the one-body loss rate, thus accelerating the loading dynamics, but does not increase the equilibrium atom number. A selective increase in the loading rate, and thus an increase in the MOT atom number, could be achieved through implementation of a Zeeman slower or a 2D MOT.

The maximum atom number, obtained with 35 mW of power per MOT beam ($s = 6.2$, before degradation of the optics), stands at 5×10^7 atoms. We believe that even higher atom numbers could be achieved with higher laser power and a cleaner mode profile.

C. Temperature

The series of mercury isotopes lends itself well to an investigation of laser-cooling mechanisms. On the one hand, the bosonic isotopes, which do not have a degenerate ground state, are particularly well suited to study simple Doppler cooling theory [26]. On the other hand, the fermionic isotope ^{199}Hg, which has a nuclear spin of $I = 1/2$, represents the simplest system which can support sub-Doppler cooling mechanisms, in particular Sisyphus cooling [27]. The dependence of cooling performance on the number of Zeeman substates can then be explored further through the ^{201}Hg isotope with a nuclear spin of $I = 3/2$.

1. Dependence of the temperature on trapping parameters

To measure the temperature T of the atomic cloud, we use the TOF technique: we release the atomic cloud from the MOT and record its ballistic expansion for a set of release times t_{TOF} via absorption imaging. The comparably narrow linewidth of 1.3 MHz leads to a comparably small absorption signal. For typical temperatures of the order of 100 μK and atom numbers of the order of 10^7, the absorption signal falls below the imaging photon shot noise at a TOF of about 10 ms. At this point of expansion, the cloud size $r \approx \sqrt{k_B T/m}\, t_{\mathrm{TOF}}$ does not yet dominate over the initial cloud size (see Sec. III D). Therefore, we cannot assume the initial cloud size is negligible, and each temperature measurement is obtained from a series of seven absorption images with the TOF varying between 0 and 7 ms. In this way, we can reconstruct the initial size and the expansion dynamics to infer the temperature. The radius of the cloud r accessible from our two-dimensional images for varying t_{TOF} corresponds to the rms of the fitted one-dimensional radii r_x and r_z along the x and z directions. Unless stated otherwise, temperatures given here are the rms temperature of all three dimensions.

The dependence of the temperature T on laser detuning Δ and the saturation parameter s is shown in Fig. 5(a). The temperature T increases with the saturation parameter s. Indeed, a high intensity of the MOT beams induces a heating mechanism which originates from reabsorption of scattered photons. The detuning Δ is the most critical parameter, and the lowest temperature, $T = 84(5)\,\mu$K, is obtained for a detuning of $\Delta = -\Gamma$. As shown in Fig. 5(a), a larger detuning leads to a temperature increase of the atomic cloud.

This is also expected from one-dimensional Doppler cooling theory [26], which relates the temperature T to the detuning Δ and the saturation parameter s,

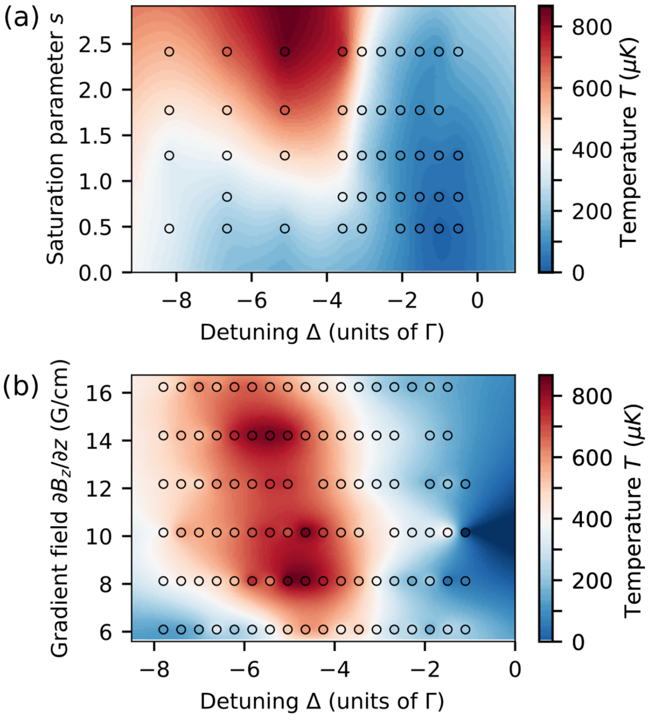

FIG. 5. Temperature T of the cloud of atoms as a function of (a) the detuning Δ and the saturation parameter s for a fixed magnetic gradient field $\partial B_z/\partial z = 10\,\mathrm{G/cm}$ and (b) the detuning Δ and the magnetic gradient field $\partial B_z/\partial z$ for a fixed saturation parameter $s = 2.6$.

$$T = \frac{\hbar\Gamma^2}{8k_B|\Delta|}\left[1 + 6s + \left(\frac{2\Delta}{\Gamma}\right)^2\right], \qquad (1)$$

where k_B is the Boltzmann constant and $\hbar$ is the reduced Planck constant.

The temperature of the cloud T has been measured as a function of the magnetic field gradient $\partial B_z/\partial z$ and the detuning Δ for a fixed saturation parameter $s = 2.6$ [see Fig. 5(b)]. The gradient does not have a significant influence on the temperature T, as predicted by the Doppler cooling theory. In general, the temperatures observed in the experiment are higher than those predicted by the Doppler cooling theory but follow the predicted dependence on detuning and the saturation parameter. This behavior was already observed in other experiments with alkaline-earth(-like) atoms [28–31].

2. Sub-Doppler cooling

We will now explore the lower limit of the temperature that can be achieved by laser cooling. As discussed above, the temperature depends only mildly on the gradient field and on the saturation parameter. Therefore, we fix these parameters to $\partial B_z/\partial z = 12.2\,\mathrm{G/cm}$ and $s = 2.7$ for the following study. The atom cloud has a pronounced oblate shape, and in the temperature regime studied here, the cloud barely expands beyond its initial size in the horizontal direction. Therefore, we will constrain our analysis to the temperature in the vertical (z) direction.

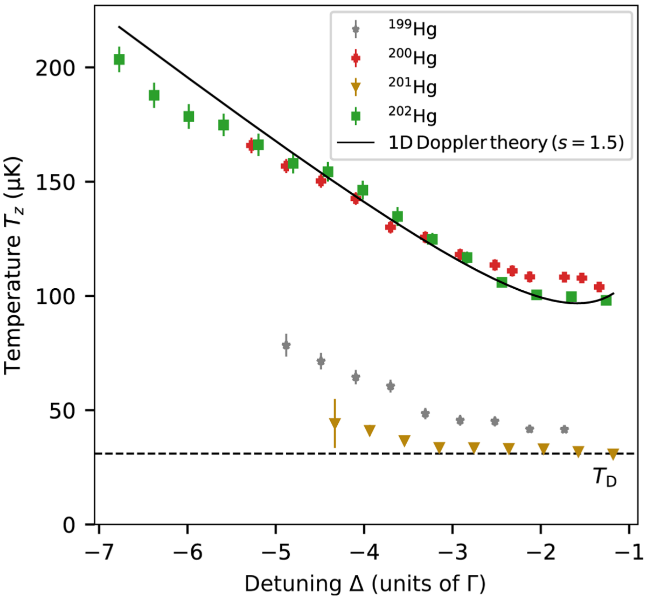

FIG. 6. Temperature T of the atomic cloud as a function of the detuning Δ, obtained for a saturation parameter of $s = 2.7$ and a fixed magnetic gradient field of $\partial B_z/\partial z = 12.2\,\mathrm{G/cm}$ for several mercury isotopes. The Doppler limit (dashed line) is the same for both bosonic and fermionic species.

The temperature of the atomic cloud T_z as a function of detuning Δ for two bosonic and two fermionic isotopes is presented in Fig. 6. Each data point is the weighted average of at least five time-of-flight sequences. Each sequence is composed of 0.5-ms steps and lasts until the disappearance of the signal. The temperature of the bosonic species ^{202}Hg (^{200}Hg) reaches a minimum at 98(2) μK [104(3) μK] at $\Delta = -1.6\,\Gamma$ ($\Delta = -1.5\,\Gamma$).

To compare our results with the Doppler theory, we now fit our data with the expression from Eq. (1), where we leave the saturation s as a free parameter. The model fits the measured temperatures well, but the derived saturation parameters are slightly lower [$s = 1.5(1)$ for ^{200}Hg and $s = 1.8(1)$ for ^{202}Hg] compared to the experimentally measured intensities. This difference is caused by the non-Gaussian profile of the MOT beams: when measuring the beam waist to determine the peak intensity of the beams, and thus the saturation parameter, we assume the beam shape is Gaussian. Degradation of the optics is proportional to the intensity and results in increased attenuation in the center of the beam. The beam profile acquires a flat top, which leads us to systematically overestimate the peak intensity.

In summary, we confirm that the cooling mechanism of bosonic mercury isotopes is properly described by Doppler theory [12]. The lack of degenerate ground states ($I = 0$) precludes sub-Doppler cooling mechanisms. This situation is different for the fermionic isotopes ^{199}Hg and ^{201}Hg, which do possess multiple Zeeman substates and indeed show temperatures substantially lower than their bosonic counterparts.

The cloud of ^{199}Hg atoms has a temperature $\sim$40 μK for a detuning between 2Γ and 3Γ. Above 3Γ, the temperature increases. The ^{201}Hg atoms reach the lowest temperature of 30.9(2.3) μK right at the Doppler temperature $T_D = 31\,\mu$K. These two fermionic species undergo Sisyphus cooling, but there is a subtle difference in the number of Zeeman substates. Indeed, ground-state-level degeneracy is the key parameter of sub-Doppler cooling because it affects the velocity capture range [29]. Thus, the richer atomic structure of ^{201}Hg is an asset to reach lower temperatures than ^{199}Hg. Mercury appears to be a promising system to study the interplay between Doppler and sub-Doppler cooling mechanisms [32,33].

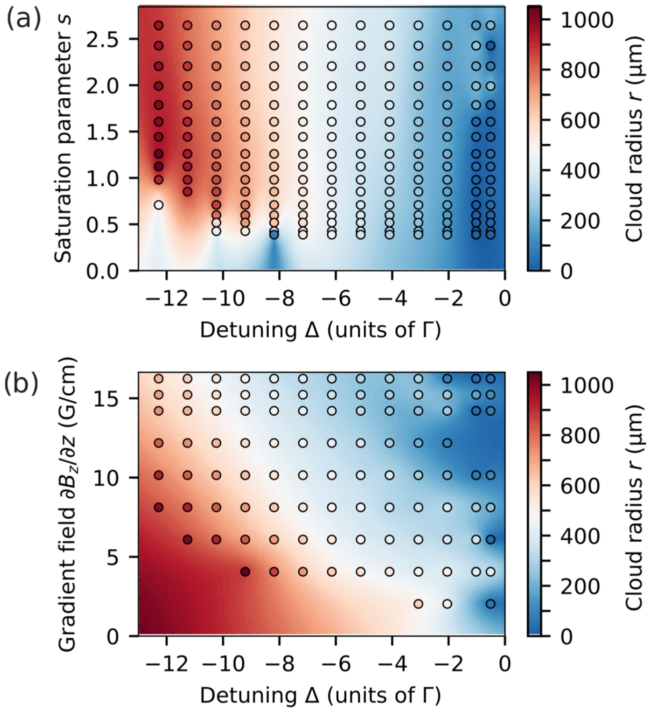

FIG. 7. Radius r of the atomic cloud as a function of (a) the detuning Δ and the saturation parameter s for a fixed magnetic gradient field $\partial B_z/\partial z = 10\,\mathrm{G/cm}$ and (b) the detuning Δ and the magnetic gradient field $\partial B_z/\partial z$ for a fixed saturation parameter $s = 2.6$.

D. Cloud size and atomic density

1. Cloud size and Doppler theory

The cloud radius is an important parameter when studying the performance of a MOT. From the same measurements used to generate Fig. 3(a), we extract the radius $r = \sqrt{r_x{}^2 + r_z{}^2}$ of the atomic cloud as a function of detuning Δ and saturation parameter s (see Fig. 7). We observe that the cloud size increases with detuning, it decreases with magnetic field gradient, and it is rather independent of the light intensity.

Considering the good agreement of the 1D Doppler theory for the bosonic species, we will compare the predicted radius of the cloud with our data in the z direction (see Fig. 8). Using the equipartition theorem, the radius r and temperature T of the cloud are related through

$$\frac{1}{2}\kappa r^2 = \frac{1}{2}k_B T. \tag{2}$$

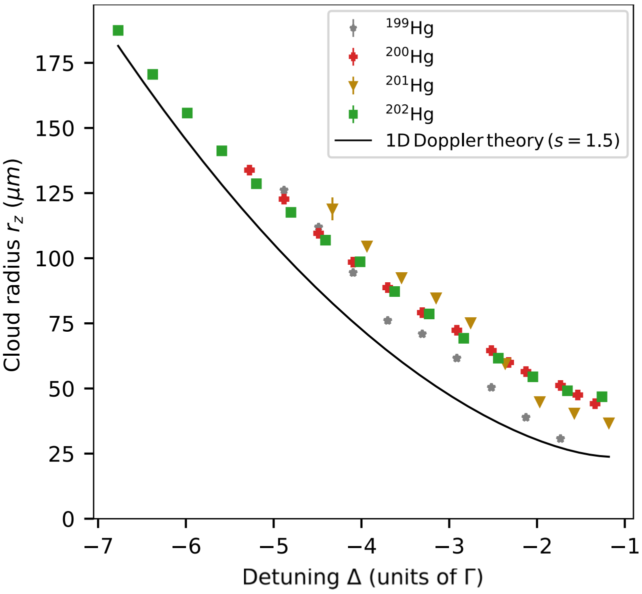

FIG. 8. Radius r_z of the cloud of atoms as a function of the detuning Δ with $s = 2.7$ and $\partial B_z/\partial z = 12.2$ G/cm for several mercury isotopes. The black line shows the Doppler theory prediction, assuming $s = 1.5$ as determined from the temperature measurement.

Here, k_B is the Boltzmann constant, and κ is the trap-spring constant, which can be expressed as

$$\kappa = \frac{8k|\Delta|}{\Gamma}\frac{s}{\left(1+6s+\left(\frac{2\Delta}{\Gamma}\right)^2\right)^2}g_j\mu_B\frac{\partial B_z}{\partial z}, \tag{3}$$

where μ_B is the Bohr magneton, g_j is the Landé factor of the excited state, and k is the photon wave vector [26].

Combining Eqs. (1), (2), and (3), we can obtain an expression for the radius of the cloud:

$$r_z = \sqrt{\frac{\hbar\Gamma^3}{64\Delta^2 k\, g_j\mu_B}\frac{\left[1+6s+\left(\frac{2\Delta}{\Gamma}\right)^2\right]^3}{s}\left(\frac{\partial B_z}{\partial z}\right)^{-1}}. \tag{4}$$

The dependence of cloud size on detuning is shown in Fig. 8: the cloud radius grows with the detuning. Moreover, the size of the cloud is largely independent of the atom number.

The radius in the vertical dimension is similar to the theory prediction for $s = 1.5$, as derived from the temperature measurement in Fig. 6. Using the experimentally determined saturation parameter of $s = 2.7$ provides around a 20% lower predicted radius than measured. Related studies have observed larger-than-expected cloud sizes as well [12]. The simple Doppler theory does not properly describe the experimental data. The discrepancy is likely explained by inhomogeneous and non-Gaussian beam profiles, as well as the effective repulsion between atoms from reabsorption of the cooling light.

2. *Atomic density*

We assume the atoms follow a three-dimensional Gaussian density distribution with a peak density $n = N/(2\pi)^{3/2}r_xr_yr_z$, where r_i is the cloud radius in direction i. This assumption is valid in the low-density regime and supported by absorption images with a very short time of flight. To maximize the density, we identify an optimum detuning near $\Delta = -\Gamma$ [see Fig. 9(a)]. The density favors large gradient fields and mild saturation parameters. The highest densities of the bosonic isotope ^{202}Hg are observed for a gradient field between 10 and 15 G/cm and reach a value of $n_{202} = 1.1(5)\times 10^{11}$ cm^{-3}. Increased loss mechanisms, such as light-assisted inelastic collisions [34], as well as photon reabsorption [35], lead to a saturation of the density for even higher gradient fields.

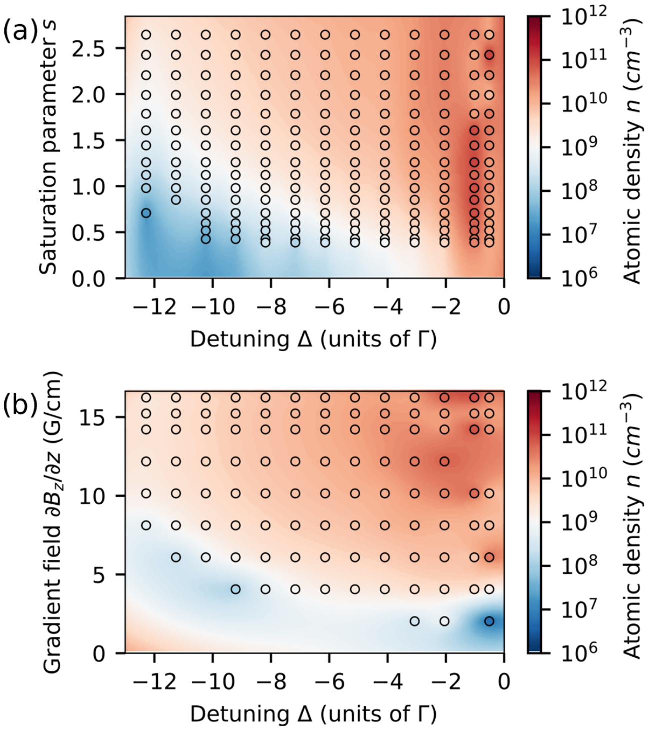

FIG. 9. Atomic density n of the atomic cloud as a function of (a) the detuning Δ and the saturation parameter s for a fixed magnetic gradient field $\partial B_z/\partial z = 10$ G/cm and (b) the detuning Δ and the magnetic gradient field $\partial B_z/\partial z$ for a fixed saturation parameter $s = 2.6$.

E. Phase-space density

The phase-space density ρ is the relevant quantity in the context of degenerate quantum gases [36]; it combines the atomic density n and the thermal de Broglie wavelength Λ. It is expressed as

$$\rho = n\Lambda^3 = n\left(\frac{\hbar\sqrt{2\pi}}{\sqrt{mk_BT}}\right)^3, \tag{5}$$

where k_B is the Boltzmann constant, $\hbar$ is the reduced Planck constant, and m is the mass of an atom.

The dependence of the phase-space density ρ on the detuning Δ and the saturation parameter s is shown in Fig. 10(a). The highest phase-space density is obtained for low saturation parameters $s \leqslant 1$, which avoids heating of the cloud through reabsorption of scattered photons. In terms of detuning, adjusting the frequency of the laser close to resonance is

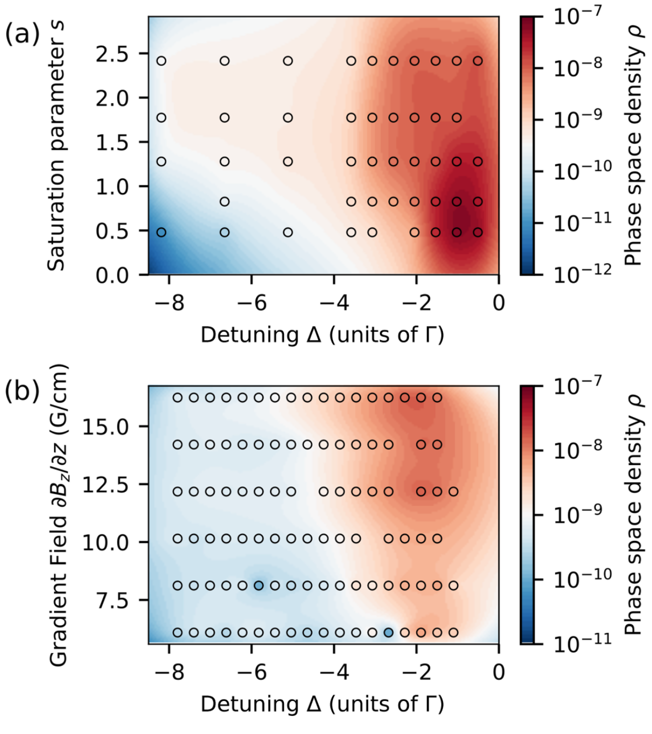

FIG. 10. Phase-space density ρ of ^{202}Hg as a function of (a) detuning Δ and the saturation parameter s for a fixed magnetic field gradient $\partial B_z/\partial z = 10\,\mathrm{G/cm}$ and (b) as a function of detuning Δ and magnetic gradient field $\partial B_z/\partial z$ at a fixed saturation parameter of $s = 2.6$.

beneficial to minimize the cloud temperature. Thus, favoring cooling over the atom number is the best strategy to maximize the phase-space density. In our experiment, a detuning of $\Delta \approx -\Gamma$ provides the highest phase-space density.

Moreover, the phase-space density grows with the gradient of the magnetic field [see Fig. 10(b)] as the trap volume is reduced. The highest phase-space density for the bosonic isotope ^{202}Hg is $\rho_{202} = 6.4(6) \times 10^{-8}$, reached at a gradient field of $\partial B_z/\partial z = 12.5\,\mathrm{G/cm}$ with about 5×10^5 atoms. For higher gradient fields, we expect that the scattering losses increase and reduce the phase-space density, as suggested by the parameters to obtain the highest atom number N in Fig. 3.

For the fermionic isotopes ^{199}Hg and ^{201}Hg, we also perform a measurement of the phase-space density as a function of detuning Δ and saturation s at a gradient of $\partial B_z/\partial z = 12.2\,\mathrm{G/cm}$. The picture resembles the bosonic case: the highest phase-space densities are obtained for small detuning and low intensity. Specifically, we obtain $\rho_{199} = 1.6(2) \times 10^{-7}$ and $\rho_{^{201}\mathrm{Hg}} = 4.7(4) \times 10^{-7}$.

These numbers provide a promising basis for dipole trap loading to further increase the phase-space density. Here, dynamic compression and cooling phases could be implemented. Evaporative cooling, *en route* to quantum degeneracy, will increase the phase-space density further.

IV. CONCLUSION

In conclusion, we have presented an in-depth study of laser cooling of mercury. With more laser power than available in previous experiments, we scanned the three-dimensional parameter space of the laser detuning, field gradient, and laser intensity. An optimum set of parameters allowed us to increase the number of trapped atoms by about an order of magnitude compared to previous studies. Inhomogeneities in the laser's mode profile reduce the cooling performance and lead to a discrepancy between the calculated and measured temperatures and MOT size in dependence of laser intensity. We showed that sub-Doppler cooling for the two fermionic isotopes closely follows theoretical expectations. We obtained phase-space densities of the order of 10^{-7} which appear to be a solid basis for dipole trap loading. It is interesting to note that the phase-space density obtained with the fermionic isotopes is about an order of magnitude larger than for the bosonic counterparts: clearly, the sub-Doppler cooling mechanisms overcompensate for the smaller capture efficiency. Work towards quantum degeneracy would benefit from the implementation of a Zeeman slower or 2D MOT to reduce the background pressure and improve the loading rate.

ACKNOWLEDGMENTS

We acknowledge fruitful discussions with Th. Walther, M. Witkowski, M. Zawada, A. Yamaguchi, A. Widera, M. Köhl, J. Kroha, and D. Meschede, and we thank F. Affeld for assistance in the operation of the experiment. Financial support from the DFG through SFB TR 185 "OSCAR," Project No. 277625399, as well as from the ERC, Project No. 757386, "quMercury," is gratefully acknowledged.

[1] A. D. Ludlow, M. M. Boyd, J. Ye, E. Peik, and P. O. Schmidt, Rev. Mod. Phys. **87**, 637 (2015).

[2] I. Bloch, J. Dalibard, and S. Nascimbène, Nat. Phys. **8**, 267 (2012).

[3] M. S. Safronova, D. Budker, D. DeMille, D. F. Jackson Kimball, A. Derevianko, and C. W. Clark, Rev. Mod. Phys. **90**, 025008 (2018).

[4] W. Cairncross and J. Ye, Nat. Rev. Phys. **1**, 510 (2019).

[5] H. Hachisu, K. Miyagishi, S. G. Porsev, A. Derevianko, V. D. Ovsiannikov, V. G. Pal'chikov, M. Takamoto, and H. Katori, Phys. Rev. Lett. **100**, 053001 (2008).

[6] M. Petersen, R. Chicireanu, S. T. Dawkins, D. V. Magalhães, C. Mandache, Y. Le Coq, A. Clairon, and S. Bize, Phys. Rev. Lett. **101**, 183004 (2008).

[7] J. J. McFerran, L. Yi, S. Mejri, S. Di Manno, W. Zhang, J. Guéna, Y. Le Coq, and S. Bize, Phys. Rev. Lett. **108**, 183004 (2012).

[8] S. Mejri, J. J. McFerran, L. Yi, Y. Le Coq, and S. Bize, Phys. Rev. A **84**, 032507 (2011).

[9] K. Yamanaka, N. Ohmae, I. Ushijima, M. Takamoto, and H. Katori, Phys. Rev. Lett. **114**, 230801 (2015).

[10] N. Ohmae, F. Bregolin, N. Nemitz, and H. Katori, Opt. Express **28**, 15112 (2020).

[11] P. Villwock, S. Siol, and T. Walther, Eur. Phys. J. D **65**, 251 (2011).
[12] J. J. McFerran, L. Yi, S. Mejri, and S. Bize, Opt. Lett. **35**, 3078 (2010).
[13] J. R. Paul, C. R. Lytle, Y. Kaneda, J. Moloney, T.-L. Wang, and R. J. Jones, in *SPIE LASE*, edited by J. E. Hastie (SPIE, San Francisco, 2013), p. 86060R.
[14] H.-L. Liu, S.-Q. Yin, K.-K. Liu, J. Qian, Z. Xu, T. Hong, and Y.-Z. Wang, Chin. Phys. B **22**, 043701 (2013).
[15] M. Witkowski, B. Nagoorny, R. Munoz-Rodriguez, R. Ciurylo, P. S. Zuchowski, S. Bilicki, M. Piotrowski, P. Morzynski, and M. Zawada, Opt. Express **25**, 3165 (2017).
[16] E. S. Fry and R. C. Thompson, Phys. Rev. Lett. **37**, 465 (1976).
[17] B. Graner, Y. Chen, E. G. Lindahl, and B. R. Heckel, Phys. Rev. Lett. **116**, 161601 (2016).
[18] R. H. Parker, M. R. Dietrich, M. R. Kalita, N. D. Lemke, K. G. Bailey, M. Bishof, J. P. Greene, R. J. Holt, W. Korsch, Z.-T. Lu, P. Mueller, T. P. OConnor, and J. T. Singh, Phys. Rev. Lett. **114**, 233002 (2015).
[19] J. C. Berengut, D. Budker, C. Delaunay, V. V. Flambaum, C. Frugiuele, E. Fuchs, C. Grojean, R. Harnik, R. Ozeri, G. Perez, and Y. Soreq, Phys. Rev. Lett. **120**, 091801 (2018).
[20] M. Witkowski, G. Kowzan, R. Munoz-Rodriguez, R. Ciuryło, P. S. Żuchowski, P. Masłowski, and M. Zawada, Opt. Express **27**, 11069 (2019).
[21] J. C. Berengut, C. Delaunay, A. Geddes, and Y. Soreq, Phys. Rev. Res. **2**, 043444 (2020).
[22] M. Scholz, D. Opalevs, P. Leisching, W. Kaenders, G. Wang, X. Wang, R. Li, and C. Chen, Appl. Phys. Lett. **103**, 051114 (2013).
[23] D. R. Lide, G. Baysinger, S. Chemistry, L. I. Berger, R. N. Goldberg, and H. V. Kehiaian, *CRC Handbook of Chemistry and Physics* (CRC Press, Boca Raton, FL, 2005).
[24] T. Mukaiyama, H. Katori, T. Ido, Y. Li, and M. Kuwata-Gonokami, Phys. Rev. Lett. **90**, 113002 (2003).
[25] K. N. Jarvis, J. A. Devlin, T. E. Wall, B. E. Sauer, and M. R. Tarbutt, Phys. Rev. Lett. **120**, 083201 (2018).
[26] P. D. Lett, W. D. Phillips, S. L. Rolston, C. E. Tanner, R. N. Watts, and C. I. Westbrook, J. Opt. Soc. Am. B **6**, 2084 (1989).
[27] J. Dalibard and C. Cohen-Tannoudji, J. Opt. Soc. Am. B **6**, 2023 (1989).
[28] C. Y. Park and T. H. Yoon, Phys. Rev. A **68**, 055401 (2003).
[29] X. Xu, T. H. Loftus, J. W. Dunn, C. H. Greene, J. L. Hall, A. Gallagher, and J. Ye, Phys. Rev. Lett. **90**, 193002 (2003).
[30] F. Y. Loo, A. Brusch, S. Sauge, M. Allegrini, E. Arimondo, N. Andersen, and J. W. Thomsen, J. Opt. B **6**, 81 (2004).
[31] S. L. Kemp, K. L. Butler, R. Freytag, S. A. Hopkins, E. A. Hinds, M. R. Tarbutt, and S. L. Cornish, Rev. Sci. Instrum. **87**, 023105 (2016).
[32] R. Chang, A. L. Hoendervanger, Q. Bouton, Y. Fang, T. Klafka, K. Audo, A. Aspect, C. I. Westbrook, and D. Clément, Phys. Rev. A **90**, 063407 (2014).
[33] Y. Yudkin and L. Khaykovich, Phys. Rev. A **97**, 053403 (2018).
[34] P. Julienne, A. Smith, and K. Burnett, Adv. At. Mol. Opt. Phys. **30**, 141 (1992).
[35] D. W. Sesko, T. G. Walker, and C. E. Wieman, J. Opt. Soc. Am. B **8**, 946 (1991).
[36] C. G. Townsend, N. H. Edwards, C. J. Cooper, K. P. Zetie, C. J. Foot, A. M. Steane, P. Szriftgiser, H. Perrin, and J. Dalibard, Phys. Rev. A **52**, 1423 (1995).

Bibliography

[1] Q. Lavigne, T. Groh, and S. Stellmer, “Magneto-optical trapping of mercury at high phase-space density”, Phys. Rev. A **105**, 033106 (2022).

[2] T. Groh, F. Affeld, and S. Stellmer, “Probing nuclear interactions through isotope shift spectroscopy of mercury”, arXiv, `10.48550/arXiv.2510.18514` (2025).

[3] K. Gaul and R. Berger, “Global analysis of $\mathcal{CP}$-violation in atoms, molecules and role of medium-heavy systems”, J. High Energy Phys. **2024**, 100 (2024).

[4] C. Delaunay, R. Ozeri, G. Perez, and Y. Soreq, “Probing atomic Higgs-like forces at the precision frontier”, Phys. Rev. D **96**, 093001 (2017).

[5] Planck Collaboration, “Planck 2018 results - VI. cosmological parameters”, Astron. Astrophys. **641**, A6 (2020).

[6] XENON Collaboration, “The XENONnT dark matter experiment”, Eur. Phys. J. C **84**, `10.1140/epjc/s10052-024-12982-5` (2024).

[7] PandaX Collaboration, “PandaX-xT: a deep underground multi-ten-tonne liquid xenon observatory”, Sci. China Phys. Mech. Astron. **68**, `10.1007/s11433-024-2539-y` (2024).

[8] LUX-ZEPLIN Collaboration, “First dark matter search results from the LUX-ZEPLIN (LZ) experiment”, Phys. Rev. Lett. **131**, 041002 (2023).

[9] KATRIN Collaboration, “Improved upper limit on the neutrino mass from a direct kinematic method by KATRIN”, Phys. Rev. Lett. **123**, 221802 (2019).

[10] S. Dell’Oro, S. Marcocci, M. Viel, and F. Vissani, “Neutrinoless double beta decay: 2015 review”, Adv. High Energy Phys. **2016**, 1–37 (2016).

[11] Super-Kamiokande Collaboration, “Search for proton decay via $\mathrm{p} \rightarrow e + \pi_0$ and $\mathrm{p} \rightarrow \mu + \pi_0$ with an enlarged fiducial volume in Super-Kamiokande I-IV”, Phys. Rev. D **102**, 112011 (2020).

[12] S. M. Brewer et al., “^{27}Al^{+} quantum-logic clock with a systematic uncertainty below 10^{-18}”, Phys. Rev. Lett. **123**, 033201 (2019).

[13] A. Aeppli, K. Kim, W. Warfield, M. S. Safronova, and J. Ye, “Clock with 8×10^{-19} systematic uncertainty”, Phys. Rev. Lett. **133**, 023401 (2024).

[14] W. F. McGrew et al., “Atomic clock performance enabling geodesy below the centimetre level”, Nature **564**, 87–90 (2018).

[15] C. G. Parthey et al., “Improved measurement of the hydrogen 1S-2S transition frequency”, Phys. Rev. Lett. **107**, 203001 (2011).

[16] A. Matveev et al., “Precision measurement of the hydrogen 1S-2S frequency via a 920-km fiber link”, Phys. Rev. Lett. **110**, 230801 (2013).

[17] X. Fan, T. G. Myers, B. A. D. Sukra, and G. Gabrielse, “Measurement of the electron magnetic moment”, Phys. Rev. Lett. **130**, 071801 (2023).

[18] D. Hanneke, S. Fogwell, and G. Gabrielse, “New measurement of the electron magnetic moment and the fine structure constant”, Phys. Rev. Lett. **100**, 120801 (2008).

[19] M. S. Safronova et al., “Search for new physics with atoms and molecules”, Rev. Mod. Phys. **90**, 025008 (2018).

[20] T. S. Roussy et al., “Experimental constraint on axionlike particles over seven orders of magnitude in mass”, Phys. Rev. Lett. **126**, 171301 (2021).

[21] A. Derevianko and M. Pospelov, “Hunting for topological dark matter with atomic clocks”, Nat. Phys. **10**, 933–936 (2014).

[22] M. Takamoto et al., “Test of general relativity by a pair of transportable optical lattice clocks”, Nat. Photon. **14**, 411–415 (2020).

[23] B. M. Roberts et al., "Search for transient variations of the fine structure constant and dark matter using fiber-linked optical atomic clocks", New J. Phys. **22**, 093010 (2020).

[24] A. D. Ludlow, M. M. Boyd, J. Ye, E. Peik, and P. O. Schmidt, "Optical atomic clocks", Rev. Mod. Phys. **87**, 637–701 (2015).

[25] T. E. Chupp, P. Fierlinger, M. J. Ramsey-Musolf, and J. T. Singh, "Electric dipole moments of atoms, molecules, nuclei, and particles", Rev. Mod. Phys. **91**, 015001 (2019).

[26] M. Athanasakis-Kaklamanakis et al., "Community input to the european strategy on particle physics: searches for permanent electric dipole moments", arXiv, `10.48550/ARXIV.2505.22281` (2025).

[27] T. S. Roussy et al., "An improved bound on the electron's electric dipole moment", Science **381**, 46–50 (2023).

[28] ACME Collaboration et al., "Improved limit on the electric dipole moment of the electron", Nature **562**, 355–360 (2018).

[29] J. Engel, "Nuclear Schiff moments and CP violation", Annu. Rev. Nucl. Part. S., `10.1146/annurev-nucl-121423-101030` (2025).

[30] R. H. Parker, "First EDM measurement of radium", PhD thesis (University of Chicago, 2015).

[31] B. Graner, Y. Chen, E. G. Lindahl, and B. R. Heckel, "Reduced limit on the permanent electric dipole moment of Hg 199", Phys. Rev. Lett. **116**, 161601 (2016).

[32] C. Abel et al., "Measurement of the permanent electric dipole moment of the neutron", Phys. Rev. Lett. **124**, 081803 (2020).

[33] B. Taubenheim, "Optical mercury magnetometry for fundamental physics experiments", PhD thesis (Technical University of Munich, 2018).

[34] D. Wurm et al., "The PanEDM neutron electric dipole moment experiment at the ILL", EPJ Web Conf. **219**, edited by T. Jenke et al., 02006 (2019).

[35] J. C. Berengut et al., "Probing new long-range interactions by isotope shift spectroscopy", Phys. Rev. Lett. **120**, 091801 (2018).

[36] A. J. Krasznahorkay et al., "Observation of anomalous internal pair creation in ^{8}Be: a possible indication of a light, neutral boson", Phys. Rev. Lett. **116**, 042501 (2016).

[37] J. L. Feng et al., "Protophobic fifth-force interpretation of the observed anomaly in ^{8}Be nuclear transitions", Phys. Rev. Lett. **117**, 071803 (2016).

[38] T. Walther and E. S. Fry, "Mercury – the Rosetta stone of physics?", J. Opt. B: Quantum Semiclassical Opt. **4**, S376–S383 (2002).

[39] M. Petersen et al., "Towards an optical lattice clock based on neutral mercury", in Ieee international frequency control symposium joint with the 21st european frequency and time forum (2007), pp. 649–654.

[40] S. Mejri, J. J. McFerran, L. Yi, Y. Le Coq, and S. Bize, "Ultraviolet laser spectroscopy of neutral mercury in a one-dimensional optical lattice", Phys. Rev. A **84**, 032507 (2011).

[41] K. Yamanaka, N. Ohmae, I. Ushijima, M. Takamoto, and H. Katori, "Frequency ratio of ^{199}Hg and ^{87}Sr optical lattice clocks beyond the SI limit", Phys. Rev. Lett. **114**, 230801 (2015).

[42] L. De Sarlo, M. Favier, R. Tyumenev, and S. Bize, "A mercury optical lattice clock at LNE-SYRTE", J. Phys. Conf. Ser. **723**, 012017 (2016).

[43] R. C. Zhao et al., "Recent progress of neutral mercury lattice clock in SIOM", J. Phys. Conf. Ser. **723**, 012022 (2016).

[44] E. J. Angstmann, V. A. Dzuba, and V. V. Flambaum, "Relativistic effects in two valence-electron atoms and ions and the search for variation of the fine-structure constant", Phys. Rev. A **70**, 014102 (2004).

[45] V. V. Flambaum and V. A. Dzuba, "Search for variation of the fundamental constants in atomic, molecular, and nuclear spectra", Can. J. Phys. **87**, 25–33 (2009).

[46] N. Ohmae, F. Bregolin, N. Nemitz, and H. Katori, "Direct measurement of the frequency ratio for Hg and Yb optical lattice clocks and closure of the Hg/Yb/Sr loop", Opt. Express **28**, 15112 (2020).

[47] W. H. Oskay et al., "Single-atom optical clock with high accuracy", Phys. Rev. Lett. **97**, 020801 (2006).

[48] E. A. Alden, K. R. Moore, and A. E. Leanhardt, "Two-photon E1-M1 optical clock", Phys. Rev. A **90**, 012523 (2014).

[49] E. Burt et al., "The Deep Space Atomic Clock: the first demonstration of a trapped ion atomic clock in space", Preprint, `10.21203/rs.3.rs-122117/v1` (2020).

[50] J. Reader, "Mercury-198 and the standard meter", Opt. Photonics News **28**, 38–43 (2017).

[51] T. J. Quinn, "Practical realization of the definition of the metre, including recommended radiations of other optical frequency standards (2001)", Metrologia **40**, 103–133 (2003).

[52] C. J. Sansonetti and D. Veza, "Doppler-free measurement of the 546 nm line of mercury", J. Phys. B: At. Mol. Opt. Phys. **43**, 205003 (2010).

[53] S. Gravina et al., "Comb-assisted mercury spectroscopy in the deep-ultraviolet: towards the development of a new primary thermometer", J. Phys. Conf. Ser. **2439**, 012015 (2023).

[54] B. J. Venema, P. K. Majumder, S. K. Lamoreaux, B. R. Heckel, and E. N. Fortson, "Search for a coupling of the Earth's gravitational field to nuclear spins in atomic mercury", Phys. Rev. Lett. **68**, 135–138 (1992).

[55] V. S. Prasannaa, A. C. Vutha, M. Abe, and B. P. Das, "Mercury monohalides: suitability for electron electric dipole moment searches", Phys. Rev. Lett. **114**, 183001 (2015).

[56] P. Villwock, S. Siol, and T. Walther, "Magneto-optical trapping of neutral mercury", Eur. Phys. J. D **65**, 251–255 (2011).

[57] T. Walther, "Prospects of trapping neutral mercury", J. Mod. Optic. **54**, 2523–2532 (2007).

[58] M. Witkowski et al., "Dual Hg-Rb magneto-optical trap", Opt. Express **25**, 3165–3179 (2017).

[59] J. S. Coursey, D. J. Schwab, J. J. Tsai, and R. A. Dragoset, "Atomic weights and isotopic compositions (version 4.1)", National Institute of Standards and Technology, Gaithersburg, MD. (2015).

[60] M. Wang, W. J. Huang, F. G. Kondev, G. Audi, and S. Naimi, "The AME 2020 atomic mass evaluation (II). tables, graphs and references", Chinese Phys. C **45**, 030003 (2021).

[61] E. Tiesinga, P. J. Mohr, D. B. Newell, and B. N. Taylor, "CODATA recommended values of the fundamental physical constants: 2018", Rev. Mod. Phys. **93**, 025010 (2021).

[62] J. Bonn, G. Huber, H.-J. Kluge, L. Kugler, and E. W. Otten, "Sudden change in the nuclear charge distribution of very light mercury isotopes", Phys. Lett. B **38**, 308–311 (1972).

[63] K. Heyde and J. L. Wood, "Nuclear shapes: from earliest ideas to multiple shape coexisting structures", Phys. Scripta **91**, 083008 (2016).

[64] S. M. C. Sels, "Laser spectroscopy of neutron-deficient mercury isotopes and commissioning of a gas-jet based RFQ ion guide", PhD thesis (Leuven University, 2018).

[65] T. Day Goodacre, "Developments of the ISOLDE RILIS for radioactive ion beam production and the results of their application in the study of exotic mercury isotopes", en, PhD thesis (The University of Manchester, 2017).

[66] T. Kühl et al., "Nuclear shape staggering in very neutron-deficient hg isotopes detected by laser spectroscopy", Phys. Rev. Lett. **39**, 180–183 (1977).

[67] G. Ulm et al., "Isotope shift of 182Hg and an update of nuclear moments and charge radii in the isotope range 181Hg-206Hg", Zeitschrift für Physik A Atomic Nuclei **325**, 247–259 (1986).

[68] S. Sels et al., "Shape staggering of midshell mercury isotopes from in-source laser spectroscopy compared with density-functional-theory and Monte Carlo shell-model calculations", Phys. Rev. C **99**, 044306 (2019).

[69] W. H. King, *Isotope shifts in atomic spectra*, Physics of Atoms and Molecules Ser. (Springer, New York, NY, 1984), 1215 pp.

[70] B. A. Marsh et al., "Characterization of the shape-staggering effect in mercury nuclei", Nat. Phys. **18**, 219–219 (2022).

[71] I. Angeli and K. P. Marinova, "Table of experimental nuclear ground state charge radii: an update", Atom. Data Nucl. Data **99**, 69–95 (2013).

[72] M. D. Seliverstov et al., "Electromagnetic moments of odd-A Po 193 – 203, 211 isotopes", Phys. Rev. C **89**, 034323 (2014).

[73] A. E. Barzakh et al., "Onset of deformation in neutron-deficient Bi isotopes studied by laser spectroscopy", Phys. Rev. C **95**, 044324 (2017).

[74] A. E. Barzakh et al., "Changes in mean-squared charge radii and magnetic moments of $^{179-184}$Tl measured by in-source laser spectroscopy", Phys. Rev. C **95**, 014324 (2017).

[75] A. E. Barzakh et al., “Laser spectroscopy studies of intruder states in ^{193,195,197}Bi”, Phys. Rev. C **94**, 024334 (2016).

[76] A. E. Barzakh et al., “Changes in the mean-square charge radii and magnetic moments of neutron-deficient Tl isotopes”, Phys. Rev. C **88**, 024315 (2013).

[77] T. Day Goodacre et al., “Laser spectroscopy of neutron-rich ^{207,208}Hg isotopes: illuminating the kink and odd-even staggering in charge radii across the $N = 126$ shell closure”, Phys. Rev. Lett. **126**, 032502 (2021).

[78] P. M. Goddard, P. D. Stevenson, and A. Rios, “Charge radius isotope shift across the N=126 shell gap”, Phys. Rev. Lett. **110**, 032503 (2013).

[79] H. De Witte et al., “Nuclear charge radii of neutron-deficient lead isotopes beyond $N = 104$ midshell investigated by in-source laser spectroscopy”, Phys. Rev. Lett. **98**, 112502 (2007).

[80] J. R. Stone and P.-G. Reinhard, “The Skyrme interaction in finite nuclei and nuclear matter”, Prog. Part. Nucl. Phys. **58**, 587–657 (2007).

[81] S. Marcos, R. Niembro, and M. López-Quelle, “Kink of the nuclear charge radius isotope shift and overlaps of the neutron and proton orbitals in lead”, Nucl. Phys. A **1047**, 122883 (2024).

[82] W. D. Myers and W. J. Swiatecki, “The nuclear droplet model for arbitrary shapes”, Ann. Phys-new. York. **84**, 186–210 (1974).

[83] S. G. Nilsson, “Binding states of individual nucleons in strongly deformed nuclei”, Kong. Dan. Vid. Sel. Mat. Fys. Med. **29N16**, 1–69 (1955).

[84] P. MohanMurthy, U. Silwal, and J. A. Winger, “A survey of nuclear quadrupole deformation in order to estimate the nuclear MQM and its relative contribution to the atomic EDM: searching for the best candidate to focus on an atomic EDM measurement: a nuclear physics perspective”, Interactions **245**, 1–18 (2024).

[85] S. Ebata and T. Nakatsukasa, “Octupole deformation in the nuclear chart based on the 3D Skyrme Hartree-Fock plus BCS model”, Phys. Scripta **92**, 064005 (2017).

[86] M. M. Sharma, G. A. Lalazissis, and P. Ring, “Anomaly in the charge radii of Pb isotopes”, Phys. Lett. B **317**, 9–13 (1993).

[87] A. Kramida, Y. Ralchenko, J. Reader, and NIST ASD Team, “NIST atomic spectra database (ver. 5.11)”, en, National Institute of Standards and Technology, Gaithersburg, MD, `10.18434/T4W30F` (2023).

[88] K. Blagoev et al., “Radiative lifetimes of 6s ns $^3S_1$ and 6s nd $^3D_1$ excited states of Hg I”, Phys. Rev. A **66**, 032509 (2002).

[89] M. Lukaszewski and D. Lecler, “Laser excitation of 6s 6d^6 $^3D_1$ level of mercury: transition probabilities and collisional excitation transfer”, Opt. Commun. **25**, 189–192 (1978).

[90] E. R. Mosburg and M. D. Wilke, “Some new transition probabilities for mercury I”, J. Quant. Spectrosc. Radiat. Transfer **19**, 69–81 (1978).

[91] F. Affeld, “Dipole trapping and isotope shift spectroscopy of mercury”, MA thesis (University of Bonn, 2022).

[92] M. S. Safronova, M. G. Kozlov, and C. W. Clark, “Blackbody radiation shifts in optical atomic clocks”, IEEE Trans. Ultrason. Ferroelectr. Freq. Control **59**, 439–447 (2012).

[93] R. Tyumenev et al., “Comparing a mercury optical lattice clock with microwave and optical frequency standards”, New J. Phys. **18**, 113002 (2016).

[94] S. G. Porsev, U. I. Safronova, and M. S. Safronova, “Theoretical study of the g factor and lifetime of the 6s6p 3P0 state of mercury”, Phys. Rev. A **96**, 012509 (2017).

[95] R. Santra, K. V. Christ, and C. H. Greene, “Properties of metastable alkaline-earth-metal atoms calculated using an accurate effective core potential”, Phys. Rev. A **69**, 042510 (2004).

[96] C. H. Greene, “Doubly excited states of the akaline-earth atoms”, Phys. Rev. A **23**, 661–678 (1981).

[97] C. H. Greene and M. Aymar, “Spin-orbit effects in the heavy alkaline-earth atoms”, Phys. Rev. A **44**, 1773–1790 (1991).

[98] S. Gravina et al., “Measurement of the mercury (6s6p) 3P1-state lifetime in the frequency domain from integrated absorbance data”, Phys. Rev. Res. **4**, 033240 (2022).

[99] H. Schüler and T. Schmidt, “Über Abweichungen des Atomkerns von der Kugelsymmetrie”, Zeitschrift für Physik **94**, 457–468 (1935).

[100] N. J. Stone, "Table of recommended nuclear magnetic dipole moments", International Atomic Energy Agency, International Nuclear Data Committee (2024).

[101] M. L. Huber, A. Laesecke, and D. G. Friend, *The vapor pressure of mercury* (National Institute of Standards and Technology, 2006).

[102] P. Villwock, "Kühlen und Fangen von neutralen Hg-Atomen", PhD thesis (Technical University of Darmstadt, 2010).

[103] H. John, "Entwicklung eines Systems zum Fangen und Kühlen von atomarem Quecksilber", PhD thesis (Technical University of Darmstadt, 2019).

[104] M. Petersen, "Laser-cooling of neutral mercury and laser-spectroscopy of the 1S0 - 3P0 optical clock transition", PhD thesis (Pierre and Marie Curie University - Paris VI, 2009).

[105] J. R. Paul, "Construction and characterization of a neutral Hg magneto-optical trap and precision spectroscopy of the $6\,^1S_0 \rightarrow 6\,^3P_0$ ^{199}Hg clock transition", PhD thesis (The University of Arizona, 2015).

[106] M. Witkowski, Personal communication, 2019.

[107] L. Hong-Li et al., "Magneto-optical trap for neutral mercury atoms", Chinese Phys. B **22**, 043701 (2013).

[108] G. Jangg and E. Lugscheider, "Die Löslichkeit von Quecksilber in verschiedenen Metallen", Monatshefte für Chemie **104**, 1269–1275 (1973).

[109] D. Burgess, "IUPAC/NIST solubility data series, NIST standard reference database 106", en, `10.18434/T4QC79` (2007).

[110] M. M. Karnowsky and F. G. Yost, *Mercury switch with non-wettable electrodes – US department of energy patent*, (1987) `https://patents.google.com/patent/US4652710A/en`.

[111] N. M. Irvin and A. S. Russell, "117. the solubilities of copper, manganese, and some sparingly soluble metals in mercury", J. Chem. Soc. (Resumed), 891 (1932).

[112] J. R. DiStefano, S. J. Pawel, and E. T. Manneschmidt, *Materials compatibility studies for the Spallation Neutron Source* (Office of Scientific and Technical Information (OSTI), 1998).

[113] B. J. Ward and J. C. Bill, "Investigation of getter-ion pump operation in systems containing oil and mercury vapour", Vacuum **16**, 659–662 (1966).

[114] M. Henini, "Molecular beam epitaxy: applications to key materials", Microelectron. J. **31**, 218–219 (2000).

[115] P. P. Chow, D. K. Greenlaw, and D. Johnson, "MBE growth of (Hg, Cd, and Te) compounds", Journal of Vacuum Science & Technology A: Vacuum, Surfaces, and Films **1**, 562–563 (1983).

[116] J.-P. Faurie, "Molecular beam epitaxy of Hg1-xCdxTe: growth and characterization", Prog. Cryst. Growth Ch. **29**, 85–159 (1994).

[117] Y. A. Čengel and A. J. Ghajar, *Heat and mass transfer, Fundamentals & applications*, en, Fifth (McGraw-Hill Education, Montigny-le-Bretonneux, France, 2010), 968 pp.

[118] J. R. Howell, *A catalog of radiation heat transfer configuration factors*, (2024) `https://www.thermalradiation.net/tablecon.html`.

[119] N. Ramsey, *Molecular beams*, Vol. 261, Oxford Classic Texts in the Physical Sciences 5 (Oxford University Press, London, England, 1956), p. 583.

[120] J. G. King and J. R. Zacharias, "Some new applications and techniques of molecular beams", in *Advances in electronics and electron physics volume 8*, Vol. 8 (Elsevier, 1956), pp. 1–88.

[121] D. R. Olander, "Molecular-beam sources fabricated from multichannel arrays. II. effect of source size and alignment", J. Appl. Phys. **40**, 4650–4657 (1969).

[122] S. P. Bennetts, "1000 times closer to a continuous atom laser. steady-state strontium with unity phase-space density", PhD thesis (University of Amsterdam, 2019).

[123] E. Wille, "Preparation of an optically trapped Fermi-Fermi mixture of ^{6}Li and ^{40}K atoms and characterization of the interspecies interactions by Feshbach spectroscopy", PhD thesis (University of Innsbruck, 2009).

[124] E. Staub, "Developing a high-flux atomic beam source for experiments with ultracold strontium quantum gases", MA thesis (Ludwig Maximilian University of Munich, 2019).

[125] C. Li et al., "Cascaded collimator for atomic beams traveling in planar silicon devices", Nat. Commun. **10**, `10.1038/s41467-019-09647-3` (2019).

[126] C. Li et al., "Robust characterization of microfabricated atomic beams on a six-month time scale", Phys. Rev. Res. **2**, 023239 (2020).

[127] K. Jousten, *Wutz Handbuch Vakuumtechnik, Theorie und praxis*, edited by W. Jitschin et al., 8th ed. (Springer Vieweg. in Springer Fachmedien Wiesbaden GmbH, Wiesbaden, 2004), pp. 16–23, 1853 pp.

[128] J. F. O'Hanlon, *A user's guide to vacuum technology*, Third (Wiley, Hoboken, NJ, 2003), 1516 pp.

[129] A. Bondi, "Van der Waals volumes and radii", The Journal of Physical Chemistry **68**, 441–451 (1964).

[130] K. T. Tang and J. P. Toennies, "The dynamical polarisability and van der Waals dimer potential of mercury", Mol. Phys. **106**, 1645–1653 (2008).

[131] H. S. W. Massey and C. B. O. Mohr, "Free paths and transport phenomena in gases and the quantum theory of collisions. II. the determination of the laws of force between atoms and molecules.", Proc. R. Soc. London A. **144**, 188–205 (1934).

[132] S. Heider, "Towards dipole trapping of mercury", MA thesis (University of Bonn, 2024).

[133] S. Crane and C. R. Ekstrom, "Nonmagnetic UHV optical viewports", in Proceedings of the 2005 ieee international frequency control symposium and exposition. (2005), pp. 297–300.

[134] P. Arora and A. S. Gupta, "Note: reliable and reusable ultrahigh vacuum optical viewports", Rev. Sci. Instrum. **83**, 046104 (2012).

[135] J. Kepler, *De cometis libelli tres I. astronomicus, theoremata continens de motu cometarum ... II. physicus, continens physiologiam cometarum novam ... III. astrologicus, de significationibus cometarum annorum 1607 et 1618*, la (typis Andrae Apergeri; sumptibus Sebastiani Mylii, 1619).

[136] P. Lebedew, "Untersuchungen über die Druckkräfte des Lichtes", Ann. Phys. **311**, 433–458 (1901).

[137] E. F. Nichols and G. F. Hull, "The pressure due to radiation.", Phys. Rev. **17**, 26–50 (1903).

[138] R. Frisch, "Experimenteller Nachweis des Einsteinschen Strahlungsrückstoßes", Zeitschrift für Physik **86**, 42–48 (1933).

[139] A. Ashkin, "Trapping of atoms by resonance radiation pressure", Phys. Rev. Lett. **40**, 729–732 (1978).

[140] T. W. Hänsch and A. L. Schawlow, "Cooling of gases by laser radiation", Opt. Commun. **13**, 68–69 (1975).

[141] S. Chu, L. Hollberg, J. E. Bjorkholm, A. Cable, and A. Ashkin, "Three-dimensional viscous confinement and cooling of atoms by resonance radiation pressure", Phys. Rev. Lett. **55**, 48–51 (1985).

[142] D. E. Pritchard, E. L. Raab, V. Bagnato, C. E. Wieman, and R. N. Watts, "Light traps using spontaneous forces", Phys. Rev. Lett. **57**, 310–313 (1986).

[143] W. Phillips, "Historical foreword: Jean Dalibard, the magneto-optical trap, and the ascent of physics with cold atomic gases", C. R. Phys. **24**, 5–13 (2024).

[144] E. L. Raab, M. Prentiss, A. Cable, S. Chu, and D. E. Pritchard, "Trapping of neutral sodium atoms with radiation pressure", Phys. Rev. Lett. **59**, 2631–2634 (1987).

[145] P. D. Lett et al., "Optical molasses", J. Opt. Soc. Am. B **6**, 2084–2107 (1989).

[146] J. Dalibard and C. Cohen-Tannoudji, "Laser cooling below the Doppler limit by polarization gradients: simple theoretical models", J. Opt. Soc. Am. B **6**, 2023 (1989).

[147] S. Chu, C. Cohen-Tannoudji, and W. D. Phillips, *The Nobel Prize in physics 1997*, (2025) `https://www.nobelprize.org/prizes/physics/1997/summary/`.

[148] M. H. Anderson, J. R. Ensher, M. R. Matthews, C. E. Wieman, and E. A. Cornell, "Observation of Bose-Einstein condensation in a dilute atomic vapor", Science **269**, 198–201 (1995).

[149] K. B. Davis et al., "Bose-Einstein condensation in a gas of sodium atoms", Phys. Rev. Lett. **75**, 3969–3973 (1995).

[150] B. DeMarco and D. S. Jin, "Onset of Fermi degeneracy in a trapped atomic gas", Science **285**, 1703–1706 (1999).

[151] J. E. Padilla-Castillo et al., "Magneto-optical trapping of aluminum monofluoride", arXiv, `10.48550/arXiv.2506.02266` (2025).

[152] C. J. Baker et al., "Laser cooling of antihydrogen atoms", Nature **592**, 35–42 (2021).

[153] H. Hachisu et al., "Trapping of neutral mercury atoms and prospects for optical lattice clocks", Phys. Rev. Lett. **100**, 053001 (2008).

[154] M. Petersen et al., “Doppler-free spectroscopy of the 1S0-3P0 optical clock transition in laser-cooled fermionic isotopes of neutral mercury”, Phys. Rev. Lett. **101**, 183004 (2008).

[155] J. J. McFerran, L. Yi, S. Mejri, and S. Bize, “Sub-Doppler cooling of fermionic Hg isotopes in a magneto-optical trap”, Opt. Lett. **35**, 3078 (2010).

[156] B. Rein, “Drei-Photonen Kohärenzeffekte in Quecksilberdampf”, PhD thesis (Technical University of Darmstadt, 2016).

[157] M. Witkowski, A. Linek, M. Zawada, and R. Ciuryło, “Development of a molecular Hg_2 clock to investigate fundamental physics”, J. Phys. Conf. Ser. **2889**, 012004 (2024).

[158] C. Lytle, “Spectroscopy of neutral mercury in a magneto-optical trap based on a novel ytterbium fiber-amplified cooling laser source”, PhD thesis (University of Arizona, 2016).

[159] D. A. Steck, *Quantum and atom optics* (2021).

[160] S. A. Hopkins and A. V. Durrant, “Parameters for polarization gradients in three-dimensional electromagnetic standing waves”, Phys. Rev. A **56**, 4012–4022 (1997).

[161] D. Haubrich, A. Höpe, and D. Meschede, “A simple model for optical capture of atoms in strong magnetic quadrupole fields”, Opt. Commun. **102**, 225–230 (1993).

[162] S. Eckel, D. S. Barker, E. B. Norrgard, and J. Scherschligt, “PyLCP: a Python package for computing laser cooling physics”, Comput. Phys. Commun. **270**, 108166 (2022).

[163] J. M. Supplee, E. A. Whittaker, and W. Lenth, “Theoretical description of frequency modulation and wavelength modulation spectroscopy”, Appl. Optics **33**, 6294 (1994).

[164] M. Gehrtz, E. A. Whittaker, and G. C. Bjorklund, “Quantum-limited laser frequency-modulation spectroscopy”, J. Opt. Soc. Am. B **2**, 1510 (1985).

[165] D. Röser, L. Möller, H. Keßler, and S. Stellmer, “Isotope-shift measurement of the 423-nm transition in neutral Ca”, Phys. Rev. A **110**, 032809 (2024).

[166] L.-S. Ma and J. L. Hall, “Optical heterodyne spectroscopy enhanced by an external optical cavity: toward improved working standards”, IEEE J. Quantum Electron. **26**, 2006–2012 (1990).

[167] J. F. Eble and F. Schmidt-Kaler, “Optimization of frequency modulation transfer spectroscopy on the calcium 4^1S_0 to 4^1P_1 transition”, Appl. Phys. B **88**, 563–568 (2007).

[168] S. Gerstenkorn, J. J. Labarthe, and J. Vergès, “Fine and hyperfine structures and isotope shifts in the arc spectrum of mercury. Part I. Experimental study of the infrared spectrum by fourier transform spectroscopy”, Phys. Scripta **15**, 167–172 (1977).

[169] C. Wieman and T. W. Hänsch, “Doppler-free laser polarization spectroscopy”, Phys. Rev. Lett. **36**, 1170–1173 (1976).

[170] D.-Q. Su et al., “Application of sub-Doppler DAVLL to laser frequency stabilization in atomic cesium”, Appl. Optics **53**, 7011 (2014).

[171] S. Yin et al., “Observation and optimization of DAVLL spectra on the $^1S_0 \rightarrow {}^3P_1$ transition of neutral mercury atom”, Opt. Commun. **285**, 5169–5174 (2012).

[172] M. Witkowski et al., “Absolute frequency and isotope shift measurements of mercury 1S0-3P1 transition”, Opt. Express **27**, 11069 (2019).

[173] K. P. Birch and M. J. Downs, “An updated edlén equation for the refractive index of air”, Metrologia **30**, 155–162 (1993).

[174] S. Häfner, “Ultra-stabile Lasersysteme für Weltraum- und Bodenanwendungen”, PhD thesis (University of Hannover, 2015).

[175] M. D. Álvarez, *Optical cavities for optical atomic clocks, atom interferometry and gravitational-wave detection* (Springer International Publishing, 2019), 1258 pp.

[176] H. Stoehr, “Diodenlaser mit Hertz-Linienbreite für ein optisches Calcium-Frequenznormal”, PhD thesis (University of Hannover, 2005).

[177] T. Nazarova, F. Riehle, and U. Sterr, “Vibration-insensitive reference cavity for an ultra-narrow-linewidth laser”, Appl. Phys. B **83**, 531–536 (2006).

[178] L. Jin et al., “Laser frequency instability of 2e-16 by stabilizing to 30-cm-long Fabry-Pérot cavities at 578 nm”, Opt. Express **26**, 18699 (2018).

[179] Corning Advanced Optics Incorporate, *ULE Corning Code 7972. Ultra low expansion glass*, (2016) `https://www.corning.com/media/worldwide/csm/documents/7972%20ULE%20Product%20Information%20Jan%202016.pdf`.

[180] Q.-F. Chen et al., "A compact, robust, and transportable ultra-stable laser with a fractional frequency instability of 1×10^{-15}", Rev. Sci. Instrum. **85**, 113107 (2014).

[181] J. Millo et al., "Ultrastable lasers based on vibration insensitive cavities", Phys. Rev. A **79**, 053829 (2009).

[182] Menlo Systems, *ORC-cylindric, ORC-cubic optical reference cavity*, (2024) `https://www.menlosystems.com/products/ultrastable-lasers/orc-cylindric-orc-cubic/`.

[183] T. Meyrath, *Electromagnet design basics for cold atom experiments*, tech. rep., Technical report (Atom Optics Laboratory Center for Nonlinear Dynamics, University of Texas at Austin, 2004).

[184] F. Fiorillo, *Characterization and measurement of magnetic materials*, en, Electromagnetism (Elsevier, San Diego, CA, 2005), 1647 pp.

[185] M. E. Rudd and J. R. Craig, "Optimum spacing of square and circular coil pairs", Rev. Sci. Instrum. **39**, 1372–1374 (1968).

[186] M. Ortner and L. G. Coliado Bandeira, "Magpylib: a free Python package for magnetic field computation", SoftwareX **11**, 100466 (2020).

[187] NCEI Geomagnetic Modeling Team and British Geological Survey, "World magnetic model 2020", `10.25921/11V3-DA71` (2019).

[188] T. J. Harrison, "Measuring the gap and investigating non-equilibrium in the BEC-BCS crossover", PhD thesis (University of Bonn, 2017).

[189] Sinara Contributors, *Sinara hardware for quantum physics experiments*, Sinara Project, (2024) `https://github.com/sinara-hw`.

[190] ARTIQ Developers, *ARTIQ: Advanced Real-Time Infrastructure for Quantum Physics*, ARTIQ Project (2024).

[191] R. Rew et al., *Unidata NetCDF*, en, (1989)

[192] R. Grimm, M. Weidemüller, and Y. B. Ovchinnikov, "Optical dipole traps for neutral atoms", in *Advances in atomic, molecular, and optical physics*, Vol. 42 (Elsevier, 2000), pp. 95–170.

[193] N. Yamamoto, L. Tao, and A. P. Yalin, "Single-mode delivery of 250 nm light using a large mode area photonic crystal fiber", Opt. Express **17**, 16933–16940 (2009).

[194] L. Skuja, H. Hosono, and M. Hirano, "Laser-induced color centers in silica", in Laser-induced damage in optical materials: 2000, Vol. 4347, edited by G. J. Exarhos, A. H. Guenther, M. R. Kozlowski, K. L. Lewis, and M. J. Soileau (2001).

[195] P. Karlitschek, G. Hillrichs, and K.-F. Klein, "Influence of hydrogen on the colour center formation in optical fibers induced by pulsed UV-laser radiation. part 1: all silica fibers with high-OH undoped core", Opt. Commun. **155**, 376–385 (1998).

[196] M. Oto, S. Kikugawa, N. Sarukura, M. Hirano, and H. Hosono, "Optical fiber for deep ultraviolet light", IEEE Photonics Technol. Lett. **13**, 978–980 (2001).

[197] Y. Colombe, D. H. Slichter, A. C. Wilson, D. Leibfried, and D. J. Wineland, "Single-mode optical fiber for high-power, low-loss UV transmission", Opt. Express **22**, 19783–19793 (2014).

[198] W. D. Phillips and H. Metcalf, "Laser deceleration of an atomic beam", Phys. Rev. Lett. **48**, 596–599 (1982).

[199] K. Gibble, S. Chang, and R. Legere, "Direct observation of s-wave atomic collisions", Phys. Rev. Lett. **75**, 2666–2669 (1995).

[200] C. J. Myatt, N. R. Newbury, R. W. Ghrist, S. Loutzenhiser, and C. E. Wieman, "Multiply loaded magneto-optical trap", Opt. Lett. **21**, 290 (1996).

[201] Z. T. Lu et al., "Low-velocity intense source of atoms from a magneto-optical trap", Phys. Rev. Lett. **77**, 3331–3334 (1996).

[202] K. Dieckmann, R. J. C. Spreeuw, M. Weidemüller, and J. T. M. Walraven, "Two-dimensional magneto-optical trap as a source of slow atoms", Phys. Rev. A **58**, 3891–3895 (1998).

[203] C. Guo et al., "Exploiting the two-dimensional magneto-optical trapping of Hg-199 for a mercury optical lattice clock", Phys. Rev. A **107**, 033116 (2023).

[204] J. Léonard et al., "Optical transport and manipulation of an ultracold atomic cloud using focus-tunable lenses", New J. Phys. **16**, 093028 (2014).

[205] F. Finger, "A transport laser with shape and amplitude control for ultracold strontium atoms", MA thesis (Technical University of Munich, 2018).

[206] E. W. Streed et al., "Large atom number Bose-Einstein condensate machines", Rev. Sci. Instrum. **77**, `10.1063/1.2163977` (2006).

[207] C. Gross, H. C. J. Gan, and K. Dieckmann, "All-optical production and transport of a large Li-6 quantum gas in a crossed optical dipole trap", Phys. Rev. A **93**, 053424 (2016).

[208] M. Takamoto, F.-L. Hong, R. Higashi, and H. Katori, "An optical lattice clock", Nature **435**, 321–324 (2005).

[209] K. Ono et al., "Observation of nonlinearity of generalized King plot in the search for new boson", Phys. Rev. X **12**, 021033 (2022).

[210] J. Friedel, "Metallic alloys", Il Nuovo Cimento **7**, 287–311 (1958).

[211] K. Riechers, K. Hueck, N. Luick, T. Lompe, and H. Moritz, "Detecting Friedel oscillations in ultracold Fermi gases", Eur. Phys. J. D **71**, `10.1140/epjd/e2017-80275-6` (2017).

[212] B. Friedrich and D. Herschbach, "Alignment and trapping of molecules in intense laser fields", Phys. Rev. Lett. **74**, 4623–4626 (1995).

[213] A. Singh et al., "Dynamics of a buffer-gas-loaded, deep optical trap for molecules", Phys. Rev. Res. **5**, 033008 (2023).

[214] C. Turnbaugh et al., "High-power near-concentric Fabry-Perot cavity for phase contrast electron microscopy", Rev. Sci. Instrum. **92**, `10.1063/5.0045496` (2021).

[215] O. Schwartz et al., "Laser phase plate for transmission electron microscopy", Nat. Methods **16**, 1016–1020 (2019).

[216] O. Schwartz et al., "Near-concentric Fabry-Pérot cavity for continuous-wave laser control of electron waves", Opt. Express **25**, 14453 (2017).

[217] A. Ye and G. Wang, "Dipole polarizabilities of ns^2 ^{1}S$_0$ and ns np ^{3}P$_0$ states and relevant magic wavelengths of group-IIB atoms", Phys. Rev. A **78**, 014502 (2008).

[218] A. Gogyan, P. Tecmer, and M. Zawada, "Multi-reference ab initio calculations of Hg spectral data and analysis of magic and zero-magic wavelengths", Opt. Express **29**, 8654 (2021).

[219] L. Yi, S. Mejri, J. J. McFerran, Y. Le Coq, and S. Bize, "Optical lattice trapping of Hg-199 and determination of the magic wavelength for the ultraviolet ^{1}S$_0$ - ^{3}P$_0$ clock transition", Phys. Rev. Lett. **106**, 073005 (2011).

[220] F. Bloch and A. Siegert, "Magnetic resonance for nonrotating fields", Phys. Rev. **57**, 522–527 (1940).

[221] M. M. Boyd, "High precision spectroscopy of strontium in an optical lattice: towards a new standard for frequency and time", PhD thesis (University of Colorado, Boulder, 2007).

[222] M. E. Gehm, K. M. O'Hara, T. A. Savard, and J. E. Thomas, "Dynamics of noise-induced heating in atom traps", Phys. Rev. A **58**, 3914–3921 (1998).

[223] T. Lauber, J. Küber, O. Wille, and G. Birkl, "Optimized Bose-Einstein-condensate production in a dipole trap based on a 1070-nm multifrequency laser: influence of enhanced two-body loss on the evaporation process", Phys. Rev. A **84**, 043641 (2011).

[224] K. J. Arnold and M. D. Barrett, "All-optical Bose-Einstein condensation in a 1.06 μm dipole trap", Opt. Commun. **284**, 3288–3291 (2011).

[225] L. Li et al., "All-fiber laser system for all-optical ^{87}Rb Bose Einstein condensate to space application", Appl. Optics **62**, 7844 (2023).

[226] R. Dumke et al., "All-optical generation and photoassociative probing of sodium Bose-Einstein condensates", New J. Phys. **8**, 64–64 (2006).

[227] S. Stellmer, R. Grimm, and F. Schreck, "Production of quantum-degenerate strontium gases", Phys. Rev. A **87**, 013611 (2013).

[228] S. Stellmer et al., *Precision control of single or few impurities in a fermionic bath*, Proposal for the Second Funding Period of Collaborative Research Center TR 185 *OSCAR* (*Open System Control of Atomic and Photonic Matter*), 2022.

[229] G. F. Gribakin and V. V. Flambaum, “Calculation of the scattering length in atomic collisions using the semiclassical approximation”, Phys. Rev. A **48**, 546–553 (1993).

[230] M. Borkowski et al., “Scattering lengths in isotopologues of the RbYb system”, Phys. Rev. A **88**, 052708 (2013).

[231] S. Stellmer, “Degenerate quantum gases of strontium”, PhD thesis (University of Innsbruck, 2013).

[232] A. Patscheider et al., “Determination of the scattering length of erbium atoms”, Phys. Rev. A **105**, 063307 (2022).

[233] A. J. Olson, R. J. Niffenegger, and Y. P. Chen, “Optimizing the efficiency of evaporative cooling in optical dipole traps”, Phys. Rev. A **87**, 053613 (2013).

[234] G. E. Simion and G. F. Giuliani, “Friedel oscillations in a Fermi liquid”, Phys. Rev. B **72**, 045127 (2005).

[235] M. F. Crommie, C. P. Lutz, and D. M. Eigler, “Imaging standing waves in a two-dimensional electron gas”, Nature **363**, 524–527 (1993).

[236] K. M. Hueck, “A homogeneous, two-dimensional Fermi gas”, PhD thesis (University of Hamburg, 2017).

[237] G. Racah, “Isotopic displacement and hyperfine structure”, Nature **129**, 723–724 (1932).

[238] J. E. Rosenthal and G. Breit, “The isotope shift in hyperfine structure”, Phys. Rev. **41**, 459–470 (1932).

[239] M. Wilson, “Ab initio calculation of screening effects on $|\psi(0)|^2$ for heavy atoms”, Phys. Rev. **176**, 58–63 (1968).

[240] F. A. Babushkin, “Isotope shift of spectral lines”, J. Exp. Theor. Phys. **42**, 1604 (1962), (Sov. Phys. JETP 15 (1962) p. 1113).

[241] X. Zhang, B.-Q. Lu, J.-G. Li, and H.-X. Zou, “Theoretical investigation on hyperfine structure and isotope shift for $5d^{10}$ 6s $^2S_{1/2}$ - $5d^9$ $6s^2$ $^2D_{5/2}$ clock transition in Hg^+”, Acta Phys. Sin-ch. Ed. **68**, 043101 (2019).

[242] A. Surzhykov and R. Müller, *Relativistic atomic theory – lecture notes*, (2018) `https://www.ptb.de/cms/fileadmin/internet/institute/fpm/QMatter_2019/VL06.pdf`.

[243] V. V. Flambaum, A. J. Geddes, and A. V. Viatkina, “Isotope shift, nonlinearity of King plots, and the search for new particles”, Phys. Rev. A **97**, 032510 (2018).

[244] C. Froese Fischer, G. Gaigalas, P. Jönsson, and J. Bieroń, “GRASP2018 – A Fortran 95 version of the General Relativistic Atomic Structure package”, Comput. Phys. Commun. **237**, 184–187 (2019).

[245] M. F. Gu, “The flexible atomic code”, Can. J. Phys. **86**, 675–689 (2008).

[246] T. Saue et al., “The DIRAC code for relativistic molecular calculations”, J. Chem. Phys. **152**, 204104 (2020).

[247] E. V. Kahl and J. C. Berengut, “Ambit: a programme for high-precision relativistic atomic structure calculations”, Comput. Phys. Commun. **238**, 232–243 (2019).

[248] J. C. Berengut and N. S. Oreshkina, “Second-order hyperfine structure and its impact on searches for new physics using isotope-shift spectroscopy”, Phys. Rev. A **112**, 022804 (2025).

[249] A. Wilzewski et al., “Nonlinear calcium King plot constrains new bosons and nuclear properties”, arXiv **134**, `10.48550/arxiv.2412.10277` (2024).

[250] J. Hur et al., “Evidence of two-source King plot nonlinearity in spectroscopic search for new boson”, Phys. Rev. Lett. **128**, 163201 (2022).

[251] J. C. Berengut, C. Delaunay, A. Geddes, and Y. Soreq, “Generalized King linearity and new physics searches with isotope shifts”, Phys. Rev. Res. **2**, 043444 (2020).

[252] Y. Yamamoto, “The dual King relation”, Phys. Lett. B **838**, 137682 (2023).

[253] T. Ishiyama et al., “Orders-of-magnitude improved precision spectroscopy of an inner-shell orbital clock transition in neutral ytterbium”, arXiv, `10.48550/arXiv.2505.04154` (2025).

[254] G. Torbohm, B. Fricke, and A. Rosén, “State-dependent volume isotope shifts of low-lying states of group-IIa and -IIb elements”, Phys. Rev. A **31**, 2038–2053 (1985).

[255] S. O. Allehabi, V. A. Dzuba, V. V. Flambaum, A. V. Afanasjev, and S. E. Agbemava, “Using isotope shift for testing nuclear theory: the case of nobelium isotopes”, Phys. Rev. C **102**, 024326 (2020).

[256] V. V. Flambaum and V. A. Dzuba, “Sensitivity of the isotope shift to the distribution of nuclear charge density”, Phys. Rev. A **100**, 032511 (2019).

[257] C. J. Foot, *Atomic physics*, Oxford master series in physics 7 (Oxford Univ. Press, Oxford & New York, 2005), 331 pp.

[258] L. Wilets, D. L. Hill, and K. W. Ford, "Isotope shift anomalies and nuclear structure", Phys. Rev. **91**, 1488–1500 (1953).

[259] E. C. Seltzer, "K x-ray isotope shifts", Phys. Rev. **188**, 1916–1919 (1969).

[260] T. T. Chang, B. B. Awazi, J. C. Berengut, E. Fuchs, and S. C. Doret, "Systematic-free limit on new light scalar bosons via isotope-shift spectroscopy in Ca^{+}", Phys. Rev. A **110**, l030801 (2024).

[261] M. Door et al., "Probing new bosons and nuclear structure with ytterbium isotope shifts", Phys. Rev. Lett. **134**, 063002 (2025).

[262] M. Bordag, G. L. Klimchitskaya, U. Mohideen, and V. M. Mostepanenko, *Advances in the Casimir effect*, edited by G. L. Klimchitskaya and [more], Vol. 145, International Series of Monographs on Physics Ser. v.145 (Oxford University Press, Oxford, 2009), pp. 1–768.

[263] J. A. Grifols, E. Massó, and S. Peris, "Energy loss from the sun and red giants: bounds on short-range baryonic and leptonic forces", Mod. Phys. Lett. A **04**, 311–323 (1989).

[264] G. Raffelt, "Limits on a CP-violating scalar axion-nucleon interaction", Phys. Rev. D **86**, 015001 (2012).

[265] V. V. Nesvizhevsky, G. Pignol, and K. V. Protasov, "Neutron scattering and extra-short-range interactions", Phys. Rev. D **77**, 034020 (2008).

[266] C. Delaunay, C. Frugiuele, E. Fuchs, and Y. Soreq, "Probing new spin-independent interactions through precision spectroscopy in atoms with few electrons", Phys. Rev. D **96**, 115002 (2017).

[267] F. Gebert et al., "Precision isotope shift measurements in calcium ions using quantum logic detection schemes", Phys. Rev. Lett. **115**, 053003 (2015).

[268] C. Solaro et al., "Improved isotope-shift-based bounds on bosons beyond the standard model through measurements of the $^2\mathrm{D}_{3/2} - {}^2\mathrm{D}_{5/2}$ interval in Ca^{+}", Phys. Rev. Lett. **125**, 123003 (2020).

[269] I. Counts et al., "Evidence for nonlinear isotope shift in Yb^{+} search for new boson", Phys. Rev. Lett. **125**, 123002 (2020).

[270] N. L. Figueroa et al., "Precision determination of isotope shifts in ytterbium and implications for new physics", Phys. Rev. Lett. **128**, 073001 (2022).

[271] D. Röser et al., "Hyperfine structure and isotope shifts of the (4s2) 1S0 - (4s4p) 1P1 transition in atomic zinc", Phys. Rev. A **109**, 012806 (2024).

[272] S. Hofsäss et al., "High-resolution isotope-shift spectroscopy of Cd I", Phys. Rev. Res. **5**, 013043 (2023).

[273] B. Ohayon et al., "Isotope shifts in cadmium as a sensitive probe for physics beyond the standard model", New J. Phys. **24**, 123040 (2022).

[274] N.-H. Rehbehn et al., "Narrow and ultranarrow transitions in highly charged Xe ions as probes of fifth forces", Phys. Rev. Lett. **131**, 161803 (2023).

[275] K. Matsubara, U. Tanaka, H. Imajo, S. Urabe, and M. Watanabe, "Laser cooling and isotope-shift measurement of Zn^{+} with 202-nm ultraviolet coherent light", Appl. Phys. B: Lasers Opt. **76**, 209–213 (2003).

[276] F. P. Gustafsson et al., "Tin resonance-ionization schemes for atomic- and nuclear-structure studies", Phys. Rev. A **102**, 052812 (2020).

[277] S. A. King et al., "An optical atomic clock based on a highly charged ion", Nature **611**, 43–47 (2022).

[278] S. A. Blundell, P. E. G. Baird, C. W. P. Palmer, D. N. Stacey, and G. K. Woodgate, "A reformulation of the theory of field isotope shift in atoms", J. Phys. B: At. Mol. Phys. **20**, 3663–3681 (1987).

[279] J. A. R. Griffith, G. R. Isaak, R. New, M. P. Ralls, and C. P. van Zyl, "Anomalies in the optical isotope shifts of samarium", J. Phys. B: At. Mol. Phys. **12**, L1–L7 (1979).

[280] J. A. R. Griffith, G. R. Isaak, R. New, and M. P. Ralls, "Anomalies in the optical isotope shifts of samarium", J. Phys. B: At. Mol. Phys. **14**, 2769–2780 (1981).

[281] C. W. P. Palmer and D. N. Stacey, "Theory of anomalous isotope shifts in samarium", J. Phys. B: At. Mol. Phys. **15**, 997–1005 (1982).

[282] M. Kroll, "Saturation spectroscopy and resonant degenerate four-wave mixing in Hg at 546.1 nm", Opt. Lett. **7**, 151 (1982).

[283] M. D. Rayman, C. G. Aminoff, and J. L. Hall, "Precise laser frequency scanning using frequency-synthesized optical frequency sidebands: application to isotope shifts and hyperfine structure of mercury", J. Opt. Soc. Am. B **6**, 539 (1989).

[284] J. Blaise and H. Chantrel, “Structures hyperfines de raies du spectre d’arc du mercure et moment quadrupolaire de ^{201}Hg”, J. Phys. Radium **18**, 193–200 (1957).

[285] S. Gravina et al., “Comb-referenced doppler-free spectrometry of the Hg200 and Hg202 intercombination line at 254 nm”, Phys. Rev. Lett. **132**, 213001 (2024).

[286] S. P. Davis, T. Aung, and H. Kleiman, “Isotope shifts of neutron-deficient mercury isotopes”, Phys. Rev. **147**, 861–866 (1966).

[287] J. Bonn, G. Huber, H.-J. Kluge, and E. W. Otten, “Spins, moments and charge radii in the isotopic series ^{181}Hg - ^{191}Hg”, Zeitschrift für Physik A Atoms and Nuclei **276**, 203–217 (1976).

[288] A. Kramida, “Re-optimized energy levels and Ritz wavelengths of 198Hg I”, J. Res. Nat. Inst. Stand. Technol. **116**, 599 (2011).

[289] J. S. Schelfhout and J. J. McFerran, “Multiconfiguration Dirac-Hartree-Fock calculations for Hg and Cd with estimates for unknown clock-transition frequencies”, Phys. Rev. A **105**, 022805 (2022).

[290] J. C. Bergquist et al., “Energy and radiative lifetime of the 5d^9 6s^2 ^{2}D$_{5/2}$ state in Hg II by Doppler-free two-photon laser spectroscopy”, Phys. Rev. Lett. **55**, 1567–1570 (1985).

[291] E. C. Benck, J. E. Lawler, and J. T. Dakin, “Lifetimes, branching ratios, and absolute transition probabilities in Hg I”, J. Opt. Soc. Am. B **6**, 11–22 (1989).

[292] T. Ida, M. Ando, and H. Toraya, “Extended pseudo-Voigt function for approximating the Voigt profile”, J. Appl. Crystallogr. **33**, 1311–1316 (2000).

[293] S. Bennetts et al., “External cavity diode lasers with 5 kHz linewidth and 200 nm tuning range at 1.55 μm and methods for linewidth measurement”, Opt. Express **22**, 10642 (2014).

[294] T. Nazarova, C. Lisdat, F. Riehle, and U. Sterr, “Low-frequency-noise diode laser for atom interferometry”, J. Opt. Soc. Am. B **25**, 1632 (2008).

[295] J. Gäßler, G. Quast, D. Savoiu, and C. Verstege, “Kafe2 – a modern tool for model fitting in physics lab courses”, arXiv, `10.48550/ARXIV.2210.12768` (2022).

[296] R. Brun et al., “Root-project/root: v6.18/02”, `10.5281/ZENODO.848818` (2019).

[297] W. G. Schweitzer, “Hyperfine structure and isotope shifts in the 2537-Å line of mercury by a new interferometric method”, J. Opt. Soc. Am. **53**, 1055 (1963).

[298] M. Büki, “A frequency quintupled laser for spectroscopy of the clock transition of zinc”, MA thesis (University of Bonn, 2020).

[299] M. Büki, D. Röser, and S. Stellmer, “Frequency-quintupled laser at 308 nm for atomic physics applications”, Appl. Optics **60**, 9915 (2021).

[300] G. D. Boyd and D. A. Kleinman, “Parametric interaction of focused gaussian light beams”, J. Appl. Phys. **39**, 3597–3639 (1968).

[301] R. G. Batchko, G. D. Miller, A. Alexandrovski, M. M. Fejer, and R. L. Byer, “Limitations of high-power visible wavelength periodically poled lithium niobate devices due to green-induced infrared absorption and thermal lensing”, in Technical digest. summaries of papers presented at the conference on lasers and electro-optics. (1998), pp. 75–76.

[302] J. P. Jacobs and R. B. Warrington, “Pressure shift and broadening of the 254-nm intercombination line of mercury by N2”, Phys. Rev. A **68**, 032722 (2003).

[303] T. S. Shang, H. H. Xie, J. Li, and H. Liang, “Global prediction of nuclear charge density distributions using a deep neural network”, Phys. Rev. C **110**, 014308 (2024).

[304] S. Raman, C. W. Nestor, and P. Tikkanen, “Transition probability from the ground to the first-excited 2^+ state of even-even nuclides”, Atom. Data Nucl. Data **78**, 1–128 (2001).

[305] H. Miyake, N. C. Pisenti, P. K. Elgee, A. Sitaram, and G. K. Campbell, “Isotope-shift spectroscopy of the 1S0-3P1 and 1S0-3P0 transitions in strontium”, Phys. Rev. Res. **1**, 033113 (2019).

[306] L. H. P. Möller, “Spectroscopy of the 1S0 - 1P1 transition of calcium on a thermal beam and a vapor cell”, MA thesis (University of Bonn, 2023).

[307] T. W. Hänsch and B. Couillaud, “Laser frequency stabilization by polarization spectroscopy of a reflecting reference cavity”, Opt. Commun. **35**, 441–444 (1980).

[308] G. Wang and A. Ye, “Possibility of using Zn as the quantum absorber for a laser-cooled neutral atomic optical frequency standard”, Phys. Rev. A **76**, 043409 (2007).

[309] A. Taichenachev et al., “Magnetic field-induced spectroscopy of forbidden optical transitions with application to lattice-based optical atomic clocks”, Phys. Rev. Lett. **96**, 083001 (2006).

[310] R. Santra, E. Arimondo, T. Ido, C. H. Greene, and J. Ye, “High-accuracy optical clock via three-level coherence in neutral bosonic 88 Sr”, Phys. Rev. Lett. **94**, 173002 (2005).

[311] B. Kraus et al., “Phase-stabilized UV light at 267 nm through twofold second harmonic generation”, Opt. Express **30**, 44992–45007 (2022).

[312] V. A. Kostelecký and N. Russell, “Data tables for Lorentz and CPT violation”, Rev. Mod. Phys. **83**, 11–31 (2011).

[313] M. Pospelov and A. Ritz, “Electric dipole moments as probes of new physics”, Ann. Phys-new. York. **318**, 119–169 (2005).

[314] D. Budker et al., “Resonant nonlinear magneto-optical effects in atoms”, Rev. Mod. Phys. **74**, 1153–1201 (2002).

[315] L. I. Schiff, “Measurability of nuclear electric dipole moments”, Phys. Rev. **132**, 2194–2200 (1963).

[316] T. Chupp and M. Ramsey-Musolf, “Electric dipole moments: a global analysis”, Phys. Rev. C **91**, 035502 (2015).

[317] V. A. Dzuba, V. V. Flambaum, J. S. M. Ginges, and M. G. Kozlov, “Electric dipole moments of Hg, Xe, Rn, Ra, Pu, and TlF induced by the nuclear Schiff moment and limits on time-reversal violating interactions”, Phys. Rev. A **66**, 012111 (2002).

[318] I. B. Khriplovich and S. K. Lamoreaux, *CP violation without strangeness, Electric dipole moments of particles, atoms, and molecules*, Texts and Monographs in Physics (Springer, Berlin, 1997), 1231 pp.

[319] R. Berger, “Laser-cooling of molecules in various charge states”, Talk at 88. Annual Conference of the DPG and DPG Spring Meeting, 2025.

[320] W. C. Griffith, “Limiting CP violation through search for a permanent electric dipole moment of mercury 199 atoms”, PhD thesis (University of Washington, 2005).

[321] J. Manuel and C. Cohen-Tannoudji, “Détection optique de la résonance magnétique par modulation de l’effet Faraday paramagnétique transversal à la fréquence de Larmor”, C. R. Acad. Sci. **257** (1963).

[322] J. H. Smith, E. M. Purcell, and N. F. Ramsey, “Experimental limit to the electric dipole moment of the neutron”, Phys. Rev. **108**, 120–122 (1957).

[323] W. B. Cairncross et al., “Precision measurement of the electron’s electric dipole moment using trapped molecular ions”, Phys. Rev. Lett. **119**, 153001 (2017).

[324] J. J. Hudson et al., “Improved measurement of the shape of the electron”, Nature **473**, 493–496 (2011).

[325] D. M. Kara et al., “Measurement of the electron’s electric dipole moment using YbF molecules: methods and data analysis”, New J. Phys. **14**, 103051 (2012).

[326] D. Cho, K. Sangster, and E. A. Hinds, “Search for time-reversal-symmetry violation in thallium fluoride using a jet source”, Phys. Rev. A **44**, 2783–2799 (1991).

[327] M. A. Rosenberry and T. E. Chupp, “Atomic electric dipole moment measurement using spin exchange pumped masers of 129 Xe and 3 He”, Phys. Rev. Lett. **86**, 22–25 (2001).

[328] N. Sachdeva et al., “New limit on the permanent electric dipole moment of Xe 129 using He 3 comagnetometry and SQUID detection”, Phys. Rev. Lett. **123**, 143003 (2019).

[329] T. A. Zheng et al., “Measurement of the electric dipole moment of Yb 171 atoms in an optical dipole trap”, Phys. Rev. Lett. **129**, 083001 (2022).

[330] R. H. Parker et al., “First measurement of the atomic electric dipole moment of Ra 225”, Phys. Rev. Lett. **114**, 233002 (2015).

[331] M. Bishof et al., “Improved limit on the ^{225}Ra electric dipole moment”, Phys. Rev. C **94**, 025501 (2016).

[332] G. Arrowsmith-Kron et al., “Progress towards an improved measurement of the radium-225 electric dipole moment”, in Fall meeting of the aps division of nuclear physics, Session E10.00001 (2024).

[333] B. C. Regan, E. D. Commins, C. J. Schmidt, and D. DeMille, “New limit on the electron electric dipole moment”, Phys. Rev. Lett. **88**, 071805 (2002).

[334] D. DeMille et al., “Investigation of PbO as a system for measuring the electric dipole moment of the electron”, Phys. Rev. A **61**, 052507 (2000).

[335] S. A. Murthy, D. Krause, Z. L. Li, and L. R. Hunter, "New limits on the electron electric dipole moment from cesium", Phys. Rev. Lett. **63**, 965–968 (1989).

[336] nEdm Collaboration, "Plans for a neutron EDM experiment at SNS", J. Phys. Conf. Ser. **69**, 012037 (2007).

[337] M. V. Romalis, W. C. Griffith, J. P. Jacobs, and E. N. Fortson, "New limit on the permanent electric dipole moment of 199 Hg", Phys. Rev. Lett. **86**, 2505–2508 (2001).

[338] S. Afach et al., "Measurement of a false electric dipole moment signal from ^{199}Hg atoms exposed to an inhomogeneous magnetic field", Eur. Phys. J. D **69**, 225 (2015).

[339] R. A. Ready et al., "Surface processing and discharge-conditioning of high voltage electrodes for the Ra EDM experiment", Nucl. Instrum. Methods Phys. Res., Sect. A **1014**, 165738 (2021).

[340] Sekels GmbH, *Magnetische Abschirmungen – Grundlagen, Lieferprogramm, Messtechnik* (2019).

[341] T. Rabga, "Upgrades for an improved measurement of the permanent electric dipole moment of radium", PhD thesis (Michigan State University, 2020).

[342] J. R. Paul et al., "Optically pumped external-cavity semiconductor lasers for precision spectroscopy and laser cooling of atomic Hg", in Vertical external cavity surface emitting lasers (vecsels) iii, Vol. 8606, edited by J. E. Hastie (2013), p. 86060.

[343] K. N. Jarvis, J. A. Devlin, T. E. Wall, B. E. Sauer, and M. R. Tarbutt, "Blue-detuned magneto-optical trap", Phys. Rev. Lett. **120**, 083201 (2018).

[344] I. Bloch, J. Dalibard, and S. Nascimbène, "Quantum simulations with ultracold quantum gases", Nat. Phys. **8**, 267–276 (2012).

[345] W. B. Cairncross and J. Ye, "Atoms and molecules in the search for time-reversal symmetry violation", Nat. Rev. Phys. **1**, 510–521 (2019).

[346] E. S. Fry and R. C. Thompson, "Experimental test of local hidden-variable theories", Phys. Rev. Lett. **37**, 465–468 (1976).

[347] C. Y. Park and T. H. Yoon, "Efficient magneto-optical trapping of Yb atoms with a violet laser diode", Phys. Rev. A **68**, 055401 (2003).

[348] X. Xu et al., "Single-stage sub-doppler cooling of alkaline earth atoms", Phys. Rev. Lett. **90**, 193002 (2003).

[349] F. Y. Loo et al., "Investigations of a two-level atom in a magneto-optical trap using magnesium", J. Opt. B: Quantum Semiclassical Opt. **6**, 81–85 (2003).

[350] J. J. McFerran et al., "Neutral atom frequency reference in the deep ultraviolet with fractional uncertainty $= 5.7 \times 10^{-15}$", Phys. Rev. Lett. **108**, 183004 (2012).

[351] S. L. Kemp et al., "Production and characterization of a dual species magneto-optical trap of cesium and ytterbium", Rev. Sci. Instrum. **87**, `10.1063/1.4941719` (2016).

[352] R. Chang et al., "Three-dimensional laser cooling at the Doppler limit", Phys. Rev. A **90**, 063407 (2014).

[353] Y. Yudkin and L. Khaykovich, "Laser cooling at resonance", Phys. Rev. A **97**, 053403 (2018).

[354] M. Scholz et al., "A bright continuous-wave laser source at 193 nm", Appl. Phys. Lett. **103**, 051114 (2013).

[355] P. S. Julienne, A. M. Smith, and K. Burnett, *Theory of collisions between laser cooled atoms*, Vol. 30, Advances in atomic, molecular, and optical physics v.30 (Elsevier, Boston, 1992), pp. 141–198, 351 pp.

[356] W. M. Haynes, *CRC handbook of chemistry and physics*, edited by J. R. Rumble, 102nd edition 2021-2022 (CRC Press, Boca Raton, 2014), 1 p.

[357] D. W. Sesko, T. G. Walker, and C. E. Wieman, "Behavior of neutral atoms in a spontaneous force trap", J. Opt. Soc. Am. B **8**, 946 (1991).

[358] T. Mukaiyama, H. Katori, T. Ido, Y. Li, and M. Kuwata-Gonokami, "Recoil-limited laser cooling of Sr-87 atoms near the Fermi temperature", Phys. Rev. Lett. **90**, 113002 (2003).

[359] C. G. Townsend et al., "Phase-space density in the magneto-optical trap", Phys. Rev. A **52**, 1423–1440 (1995).

Acronyms

AC alternating current.
aEDM atomic electric dipole moment.
AOM acousto-optic modulator.
AR anti-reflection.
ARTIQ Advanced Real-Time Infrastructure for Quantum physics.
BBO beta barium borate.
BEC Bose-Einstein condensate.
BS beam splitter.
BSM beyond standard model.
CAD computer-aided design.
CCD charge-coupled device.
CF ConFlat.
CKM Cabibbo-Kobayashi-Maskawa.
CL confidence level.
CLBO cesium lithium borate.
CP charge and parity symmetry.
CPT charge, parity and time reversal symmetry.
CTE coefficient of thermal expansion.
DAVLL dichroic atomic vapor laser locking.
DC direct current.
DDS direct digital synthesizer.
ECDL external-cavity diode laser.
EDM electric dipole moment.
eEDM electron electric dipole moment.
EEM Eurocard Extension Module.
EOM electro-optic modulator.
FEM finite element method.
FHG fourth-harmonic generation.
FMS frequency modulation spectroscopy.
FMTS frequency modulation transfer spectroscopy.
FPGA field programmable gate array.
FS field shift.
FSR free spectral range.
FWHM full width at half maximum.
GRIIRA green-induced infrared absorption.
HV high vacuum.
IGBT insulated-gate bipolar transistor.
IGP ion getter pump.
IR infrared.
IS isotope shift.
ISS isotope shift spectroscopy.
KP King plot.
LHC Large Hadron Collider.
MCDF multiconfiguration Dirac-Fock.
MCDHF multiconfiguration Dirac-Hartree-Fock.
MOSFET metal-oxide-semiconductor field-effect transistors.
MOT magneto-optical trap.
MS mass shift.
ND nuclear deformation.
nEDM neutron electric dipole moment.
NIST National Institute of Standards and Technology.
NMS normal mass shift.
NP new physics.
ODT optical dipole trap.
PBS polarization beam splitter.
PD photodiode.
PDH Pound-Drever-Hall.
PID proportional-integral-differential.
PLL phase lock loop.
PPLN periodically poled lithium niobate.
PS polarization spectroscopy.
PTB Physikalisch-Technische-Bundesanstalt.
QCD quantum chromodynamics.
QED quantum electrodynamics.
QFS quadratic field shift.
RAR random anti-reflection.
RF radio frequency.
RGA residual gas analyzer.
RIN relative laser intensity noise.
SFG sum frequency generation.
SHG second-harmonic generation.
SM standard model.
SMS specific mass shift.
STM scanning tunneling microscopy.
TEC thermoelectric cooler.
TFP thin film polarizers.
TMP turbo molecular pump.
TOF time of flight.
TSP titanium sublimation pump.
TTL transistor-transistor logic.
UHV ultra-high vacuum.
ULE ultra-low expansion.
UV ultraviolet.
VCO voltage controlled oscillator.
VECSEL vertical-cavity surface-emitting laser.
XHV extreme high vacuum.
ZS Zeeman slower.

Acknowledgements

First and foremost, I would like to thank Simon for the opportunity to work on this project, for your ongoing support and the trust you gave me throughout – even when things got a bit chaotic, broke, or took much longer than anticipated! I also thank my second supervisor, Prof. Daqing Wang, for taking the time to dive into this topic.

A special thanks goes to Quentin – for being an awesome lab buddy! While our plan to refresh each other's German and French vocabulary didn't quite take off, it was always fun to have you around. Thank you also to Markus for sharing the (only) lab space with me in those early days! Thanks to Felix and Sascha for their outstanding contributions during their Master's theses – your input left a lasting mark on this project.

To everyone else in the group who joined during my time – past and present, – David, Ali, Cedric, Andreas, Lukas, Alica, Benny, Christopher, Darius, Fabian, Felix, Frederik, Georg, Hans, Johanna, John, Jonas, Julian, Katrin, Lara, Maanas, Mahdi, Marc, Marcel, Marlon, Maya, Philipp, Raluca, Sahil, Stefan, Tessa, Thomas, and Vedang – and likely at least one name I've forgotten (sorry!). Thank you for the discussions, coffee breaks, barbecues, and everything in between. It was a real pleasure to work with you all! Special mentions to Anica and Jannik – thank you for being fantastic colleagues and for all the fun along the way!

A big thank you to the institute's organizational team! Special thanks to Beate, Anja: you made navigating the bureaucracy much easier, even when I came with last-minute requests and needed something urgently ordered. Thanks also to Norbert Jöpen and Richard for technical support – especially when the air conditioning or cooling water failed yet again! And thanks to Oliver and the rest of the team for support with all things IT: data storage, backups, server infrastructure, and everything else I had to wrestle with.

My sincere thanks go to the mechanical workshops: Alexander Christen, Sebastian Ismar, Martin Schaub, and the rest of the Zentralwerkstatt team, as well as Waldemar Graf. And the electronic workshop teams from PI and IAP, especially Achim Brähler, Eberhard Kalb, and Walter Honerbach. Your input and ideas made a real difference! Thanks also to Philipp Hänisch for reliable technical assistance.

I was lucky to work with a great group of researchers throughout this project – thank you to Julian Berengut and Ben Ohayon for productive discussions on isotope shift spectroscopy and King plot analysis, and to the teams around Stefan Truppe, Piet Schmidt, and Skyler Degenkolb and more for their thoughtful input.

Thanks as well to colleagues from other institutes: Frank and Dietmar – not least for helping move optical tables during the early days! From the IAP, special thanks to Wolfgang, Eduardo, Akos, Santosh (not only for exchanging ARTIQ complaints!), Cedric, Thilo, Lukas, and Nina! And from the Stefan Linden group: Hajo, Paul, and others – thank you for being excellent corridor neighbors in the early years.

I'm also very grateful to the team in Kaiserslautern – Jennifer, Sian, Felix, and the rest of the group around Artur Widera – for hosting me during my visit and answering my many (also stupid) questions about cold atom labs. Thanks to Suthep for support with ARTIQ questions. The broader SFB collaboration also deserves thanks for the good times, memorable retreats, and lively wine cellar and pub nights.

To the "crank turners" at Les Houches – thank you for making that week in the alps both scientifically enriching and unforgettably fun, and for being a source of valuable information over the years!

Finally, I owe a huge thank you to my family and friends! To my parents – thank you for sparking my curiosity for physics early on and for your unwavering support over the years. And to all my friends – thank you for your support and especially for reminding me there's a world outside the lab too. ♡